



**TÉCNICO**  
LISBOA

**UNIVERSIDADE DE LISBOA**  
**INSTITUTO SUPERIOR TÉCNICO**

**GFRP–concrete hybrid structural systems.  
Application to the development of a footbridge prototype**

**José Manuel Cabecinhas de Almeida Gonilha**

**Orientador: Doutor João Pedro Ramôa Ribeiro Correia**

**Co–orientador: Doutor Fernando António Baptista Branco**

**Tese aprovada em provas públicas para a obtenção do Grau de Doutor em  
Engenharia Civil**

**Qualificação atribuída pelo Júri: Aprovado com Muito Bom com Distinção**

**Júri:**

**Presidente: Presidente do Conselho Científico do IST**

**Vogais:**

**Doutor João Paulo Janeiro Gomes Ferreira  
Doutor Luís Filipe Pereira Juvandes  
Doutor José Manuel de Sena Cruz  
Doutor Luís Manuel Coelho Guerreiro  
Doutor João Pedro Ramôa Ribeiro Correia**

**2014**







**TÉCNICO**  
LISBOA

**UNIVERSIDADE DE LISBOA**  
**INSTITUTO SUPERIOR TÉCNICO**

**GFRP–concrete hybrid structural systems.  
Application to the development of a footbridge prototype**

**José Manuel Cabecinhas de Almeida Gonilha**

**Orientador: Doutor João Pedro Ramôa Ribeiro Correia**

**Co–orientador: Doutor Fernando António Baptista Branco**

**Tese aprovada em provas públicas para a obtenção do Grau de Doutor em  
Engenharia Civil**

**Qualificação atribuída pelo Júri: Aprovado com Muito Bom com Distinção**

**Júri:**

**Presidente: Presidente do Conselho Científico do IST**

**Vogais:**

**Doutor João Paulo Janeiro Gomes Ferreira**, Professor Associado (com  
Agregação) do Instituto Superior Técnico, da Universidade de Lisboa

**Doutor Luís Filipe Pereira Juvandes**, Professor Associado  
da Faculdade de Engenharia, da Universidade do Porto

**Doutor José Manuel de Sena Cruz**, Professor Associado  
da Escola de Engenharia, da Universidade do Minho

**Doutor Luís Manuel Coelho Guerreiro**, Professor Associado  
do Instituto Superior Técnico, da Universidade de Lisboa

**Doutor João Pedro Ramôa Ribeiro Correia**, Professor Associado  
do Instituto Superior Técnico, da Universidade de Lisboa

**Instituições Financiadoras:**

**Fundação para a Ciência e a Tecnologia (SFRH/BD/70041/2010)**

**Agência de Inovação (2009/003456)**



# Abstract

Fibre reinforced polymers (FRP), particularly glass fibre reinforced polymer (GFRP) pultruded profiles, have been increasingly used as structural materials over the last few decades owing to their high strength, low self-weight, ease of installation, corrosion resistance and electromagnetic transparency. However, the structural application of these materials presents some difficulties, namely regarding their high deformability, brittle failure, behaviour at elevated temperatures and lack of specific design codes, which have been hindering their widespread acceptance.

In order to overcome the aforementioned difficulties, in particular the high deformability, which often leads to structural designs governed by deformability or instability phenomena, seldom allowing the full exploitation of the material strength, hybrid structures (in which GFRP members are combined with concrete elements) have been pointed out as an alternative solution to all-GFRP structures.

On the other hand, recent developments on cementitious materials have shown the potential of steel fibre reinforced self-compacting concrete (SFRSCC) for substituting conventional rebar reinforced concrete on some structural applications, allowing the construction of thinner elements with good corrosion resistance.

The main objective of this thesis was to study the structural behaviour of GFRP–concrete hybrid structural systems and, in particular, their feasibility as footbridge structures. The pursuit of this objective led to the development of three research axes: (i) GFRP–concrete connection systems; (ii) static, creep and dynamic behaviour of GFRP–concrete structures; and (iii) development of a full-scale GFRP–SFRSCC footbridge prototype.

The research on GFRP–concrete connection systems comprised an extensive experimental campaign, which included three shear connection systems: (i) bonded; (ii) bolted (with different connector configurations); and (iii) hybrid, combining of both bonded and bolted connections. The rheological degradation of the mechanical response of the bonded and hybrid connection systems was also object of experimental investigations, using two accelerated aging processes: (i) thermal; and (ii) wet–dry cycles. Numerical models were developed to simulate the response of these connections, and were well able to predict the behaviour of bonded test specimens, including the correspondent degradation due to the aging processes. Although it was shown that the bonded connection presents better mechanical response than the bolted connection in the short-term, the degradation of the response of the bonded interface with the aging processes pointed out the advantage of adopting hybrid shear connection systems for GFRP–concrete structures.

A hybrid structural system comprising GFRP pultruded profiles and a thin slab of SFRSCC was proposed. Its behaviour was investigated with experimental studies on a hybrid GFRP–SFRSCC small(half)–scale prototype, which included: (i) static serviceability tests; (ii) a static failure test; (iii) creep tests; (iv) modal identification tests; and (v) dynamic tests under pedestrian loading. The experimental tests demonstrated the appropriate mechanical

behaviour of the prototype, proving the feasibility of the proposed structural system for footbridge applications. Additionally, the static serviceability tests have shown that it is possible to mitigate the deflections of these structures with a low-cost prestress system. Analytical and numerical investigations have shown that readily available design tools are able to predict the static and dynamic responses of hybrid GFRP–concrete structures with good accuracy. Furthermore, an analytical methodology for the determination of the creep behaviour was proposed, based on material creep laws and including the effects of the environmental conditions, showing good accuracy with experimental results.

A full-scale hybrid GFRP–SFRSCC footbridge prototype was designed and built, based on the knowledge obtained from the investigations on the small-scale prototype and the GFRP–concrete connection systems. The experimental testing of the full-scale prototype proved its adequate structural response, showing that it fulfils Eurocode requirements. Moreover, the analytical and numerical investigations showed that the models proposed were, again, able to predict the experimental results. Overall, it was shown that the developed prototype, to be installed in the city of Ovar, is a valid alternative to footbridge structures made of traditional materials.

**Keywords:** fibre reinforced polymers (FRP), glass fibre reinforced polymer (GFRP) pultruded profiles, steel fibre reinforced self-compacting concrete (SFRSCC), GFRP–concrete hybrid structures, GFRP–concrete connection, footbridge, experimental tests, static behaviour, dynamic behaviour, creep behaviour.

## Sumário

O recurso a materiais polímeros reforçados com fibras (FRP) e, em particular, a perfis pultrudidos em polímeros reforçados com fibras de vidro (GFRP), tem vindo a crescer nas últimas décadas graças à sua resistência, reduzido peso, facilidade de instalação, resistência à corrosão e transparência electromagnética. No entanto, a aplicação estrutural destes materiais apresenta algumas dificuldades, nomeadamente devido à sua elevada deformabilidade, rotura frágil, comportamento a temperaturas elevadas e falta de normas de dimensionamento específicas, que têm posto em causa a sua aceitação generalizada.

De modo a ultrapassar as dificuldades referidas anteriormente, nomeadamente a elevada deformabilidade, que conduz ao dimensionamento condicionado por limitações de flecha ou fenómenos de instabilidade, raramente permitindo explorar toda a resistência do material, as estruturas mistas (nas quais se combinam elementos em GFRP e em betão) têm sido apontadas como uma solução alternativa às estruturas somente em GFRP.

Por outro lado, desenvolvimentos recentes na investigação sobre materiais cimentícios têm demonstrado o potencial do betão auto-compactável reforçado com fibras de aço (BACFRA) na substituição do tradicional betão reforçado com varões, para algumas aplicações estruturais, permitindo a construção de elementos mais finos e com elevada resistência à corrosão.

O principal objectivo desta tese consistiu no estudo de sistemas estruturais mistos GFRP-betão e, em particular, na sua aplicabilidade a estruturas de pontes pedonais. Para alcançar este objectivo, foram desenvolvidos três eixos de investigação: (i) sistemas de ligação GFRP-betão; (ii) comportamento estático, dinâmico e em fluência de estruturas GFRP-betão; e (iii) desenvolvimento de um protótipo de ponte pedonal mista GFRP-BACFRA.

A investigação dos sistemas de ligação GFRP-betão incluiu uma extensa campanha experimental, com o estudo de três sistemas de conexão de corte: (i) colado; (ii) aparafusado (com diferentes configurações); e (iii) misto, combinando os sistemas colado e aparafusado. A degradação reológica do comportamento mecânico das ligações colada e mista foi também objecto de estudos experimentais, através da utilização de dois tipos de envelhecimento acelerado: (i) ciclos térmicos; e (ii) ciclos de molhagem-secagem. Foram desenvolvidos modelos numéricos para a simulação do procedimento experimental, que se mostraram capazes de prever a resposta dos provetes colados, incluindo a correspondente degradação provocada pelos processos de envelhecimento. Apesar de se ter demonstrado que a ligação colada apresenta um melhor comportamento mecânico do que a ligação aparafusada, a degradação do primeiro tipo de ligação com os processos de envelhecimento levou à recomendação do sistema de ligação misto para estruturas GFRP-betão.

Foi proposto um sistema estrutural misto com perfis pultrudidos de GFRP e uma laje fina em BACFRA. O seu comportamento foi estudado através de ensaios experimentais num protótipo de ponte pedonal mista GFRP-BACFRA à escala reduzida (metade do comprimento), incluindo: (i) ensaios estáticos em serviço; (ii) ensaio estático à rotura;

(iii) ensaios de fluência; (iv) ensaios de identificação modal; e (v) ensaios dinâmicos sob acções pedonais. Nestes ensaios demonstrou-se uma adequada resposta mecânica da estrutura, provando-se a aplicabilidade a pontes pedonais do sistema estrutura proposto. Adicionalmente, os ensaios estáticos em serviço mostraram que é possível diminuir as flechas destas estruturas recorrendo a um sistema de pré-esforço de baixo custo. Os estudos analíticos e numéricos mostraram que é possível prever os comportamentos estático e dinâmico deste tipo de estrutura recorrendo às ferramentas de dimensionamento já disponíveis. Foi ainda proposta uma metodologia para a previsão do comportamento em fluência de estruturas GFRP–betão, baseada nas leis de fluência dos materiais e que tem em conta as condições ambientais, que mostrou uma boa concordância com os resultados experimentais.

Com base no conhecimento adquirido através da investigação relativa ao protótipo pequeno e aos sistemas de ligação, foi dimensionado e construído um protótipo de ponte pedonal GFRP–BACFRA à escala real. Os ensaios experimentais a este protótipo mostraram a sua adequada resposta estrutural, tendo sido cumpridos os requisitos dos Eurocódigos. Para além disto, os estudos analíticos e numéricos mostraram que os modelos propostos foram, mais uma vez, capazes de prever os resultados experimentais. Globalmente, demonstrou-se que o protótipo desenvolvido, que será instalado na cidade de Ovar, é uma alternativa válida às pontes pedonais com estruturas em materiais tradicionais.

**Keywords:** polímeros reforçados com fibras (FRP), perfis pultrudidos em polímeros reforçados com fibras de vidro (GFRP), betão auto-compactável reforçado com fibras de vidro (BACFRA), estruturas mistas GFRP–betão, ligações GFRP–betão, pontes pedonais, ensaios experimentais, comportamento estático, comportamento dinâmico, fluência.

## Acknowledgements

I would like to begin by expressing my gratitude to Professor João Ramôa Correia, scientific supervisor of this thesis, whose contribution was crucial for the development of this work. It has been a pleasure to work with Professor João Ramôa Correia, to whom I am grateful for his support and guidance, which were available to me at all times. His deep knowledge and incredible work ethic have inspired me, contributing to my formation as a researcher and civil engineer.

I would also like to express my gratitude to Professor Fernando Branco, scientific co-supervisor of this thesis, whose insight and vast experience were particularly helpful whenever I thought I had found an insuperable problem.

I would also like to thank my colleagues and fellow researchers at *Instituto Superior Técnico* (IST), particularly to Cristina López, Francisco Nunes, João Firmo, João Sousa, José Sampaio, Luís Valarinho, Manuel Correia, Mário Arruda, Mário Garrido, Mário Sá and Tiago Morgado, who were always available to discuss any subject and ready to help me with whatever I might need.

I am grateful for the contribution of all the partners of the Pontalumis project, namely Professor Joaquim Barros and Professor José Sena-Cruz from *Minho University* (UM), Eng. Tomé Santos and Eng. Mário Alvim from *ALTO Perfis Pultrudidos, Lda.*, and Professor João Ramôa Correia, Professor Fernando Branco, Eng. Ana Aquino and Eng. Joana Sousa from IST.

I would also like to thank Professor José Sena-Cruz for kindly helping me with the thermal cycle aging of the shear connection test specimens, which was performed at UM.

I am also grateful to Professor Elsa Caetano and Professor Álvaro Cunha from *Faculdade de Engenharia of Porto University* (FEUP) for their participation in the modal identification analysis of the small-scale prototype, which would have not been possible to perform without their expertise.

I want to thank Mrs. Maria Helena Salvado for all her help, which made my day-to-day work much easier. I also want to thank the technicians who made the experimental campaign of this thesis possible, namely Mr. Fernando Alves, Mr. Fernando Costa, Mr. Leonel Silva and Mr. João Lopes.

The present research was funded by the *Portuguese Foundation for Science and Technology* (FCT, grant SFRH/BD/70041/2010) and by the *Portuguese Innovation Agency* (ADI, project 2009/003456), whose support is greatly acknowledged. I would also like to thank to my research centre *Instituto de Engenharia de Estruturas, Território e Construção* (ICIST) and to the *Department of Civil Engineering, Architecture and Georesources* (DECivil) at IST for providing me the work conditions needed to develop my work.

I would like to acknowledge the industry partners who made the experimental campaign of this thesis possible by generously providing the materials, namely: *ALTO Perfis Pultrudidos*,

*Lda.; S&P Clever Reinforcement Ibérica, Lda.; Sika Portugal, Produtos de Construção e Indústria, S.A.; Tecnipor and INTEC — Sociedade Técnica de Equipamentos Industriais, S.A.*

I am very grateful for my family's support, for the love of my parents and sister, with whom I can count on for making my life easier when it could get more difficult. I want to express the deepest of gratitude to my beloved wife Rita who is always selflessly ready to put others (particularly me) before herself and who provided me with all the love and support I needed, asking little in return. This work would not have been possible without her. I want to thank my beautiful daughter Carmo who has been the biggest blessing, always cheering me up and putting a smile on my face. I can not express how grateful I am for having you both in my life.



# Contents

<b>Abstract</b>	<b>i</b>
<b>Sumário</b>	<b>iii</b>
<b>Acknowledgements</b>	<b>v</b>
<b>Table of contents</b>	<b>vii</b>
<b>List of Figures</b>	<b>xiii</b>
<b>List of Tables</b>	<b>xxxi</b>
<b>Notation</b>	<b>xxxv</b>
<b>1. Introduction</b>	<b>1</b>
1.1. Context and motivation . . . . .	1
1.2. Objectives and methodology . . . . .	2
1.3. Main scientific contributions . . . . .	4
1.4. Document organization . . . . .	5
<b>2. State-of-the-art</b>	<b>7</b>
2.1. Preliminary remarks . . . . .	7
2.2. FRP construction . . . . .	8
2.3. FRP materials . . . . .	11
2.3.1. Fibre reinforcement . . . . .	11
2.3.2. Polymeric matrix . . . . .	13
2.3.2.1. Other components . . . . .	14
2.4. GFRP pultruded profiles . . . . .	15
2.4.1. GFRP pultruded structural shapes . . . . .	17
2.4.2. Properties of GFRP pultruded profiles . . . . .	18
2.4.3. Structural applications of GFRP pultruded profiles . . . . .	20
2.4.4. Summary . . . . .	23
2.5. SFRSCC . . . . .	23
2.6. Hybrid GFRP–concrete structural systems . . . . .	24
2.7. Actions and requirements for footbridges . . . . .	29
2.7.1. Static behaviour . . . . .	29
2.7.1.1. Loads . . . . .	29
2.7.1.2. Requirements . . . . .	30
2.7.2. Dynamic behaviour . . . . .	31
2.7.2.1. Loads . . . . .	31
2.7.2.2. Requirements . . . . .	35
2.8. Concluding remarks . . . . .	37

<b>3. Structural concept and description of the Pontalumis Project</b>	<b>39</b>
3.1. Preliminary remarks . . . . .	39
3.2. Pontalumis project — Development of a prototype of a pedestrian bridge in GFRP–ECC . . . . .	39
3.3. Structural concept . . . . .	40
3.4. Preliminary design . . . . .	42
3.5. Concluding remarks . . . . .	50
<b>4. Materials</b>	<b>51</b>
4.1. Preliminary remarks . . . . .	51
4.2. GFRP profiles . . . . .	51
4.2.1. Experimental programme . . . . .	51
4.2.2. Material characterization tests . . . . .	52
4.2.2.1. Tensile tests . . . . .	52
4.2.2.2. Compressive tests . . . . .	57
4.2.2.3. Off-axis tensile tests . . . . .	63
4.2.2.4. Flexural tests . . . . .	66
4.2.2.5. Interlaminar shear tests . . . . .	69
4.2.2.6. Summary of results . . . . .	71
4.2.3. Full-scale flexural tests . . . . .	72
4.2.3.1. Serviceability tests . . . . .	72
4.2.3.2. Failure tests . . . . .	75
4.2.3.3. Analytical simulation . . . . .	89
4.2.3.4. Numerical simulation . . . . .	100
4.3. SFRSCC . . . . .	107
4.3.1. Experimental programme . . . . .	107
4.3.2. Material characterization tests . . . . .	107
4.3.2.1. Tests on cubes . . . . .	107
4.3.2.2. Tests on cylinders . . . . .	109
4.3.2.3. Tests on small-scale beams . . . . .	110
4.3.2.4. Summary . . . . .	111
4.3.3. Full-scale flexural tests . . . . .	112
4.4. Other materials . . . . .	114
4.4.1. GFRP angle profiles . . . . .	114
4.4.2. Stainless steel . . . . .	115
4.4.3. Epoxy adhesive . . . . .	115
4.4.4. Epoxy mortar . . . . .	116
4.4.5. Conventional concrete . . . . .	116
4.4.6. Regular steel . . . . .	117
4.5. Concluding remarks . . . . .	117
<b>5. GFRP–concrete shear connection</b>	<b>119</b>
5.1. Preliminary remarks . . . . .	119
5.2. Experimental tests . . . . .	120
5.2.1. Experimental programme and test series . . . . .	120
5.2.1.1. Preliminary tests . . . . .	120
5.2.1.2. Un-aged specimens . . . . .	121
5.2.1.3. Aged specimens . . . . .	122
5.2.2. Specimen preparation . . . . .	124
5.2.3. Test setup, instrumentation and procedure . . . . .	126

5.2.4.	Results and discussion — preliminary tests . . . . .	129
5.2.4.1.	Series P–A . . . . .	129
5.2.4.2.	Series P–M1 . . . . .	129
5.2.4.3.	Series P–M2 . . . . .	131
5.2.4.4.	Series P–M3 . . . . .	132
5.2.4.5.	Series P–M4 . . . . .	133
5.2.4.6.	Series P–AM . . . . .	134
5.2.4.7.	Comparative analysis . . . . .	135
5.2.5.	Results and discussion — un-aged specimens . . . . .	136
5.2.5.1.	Series A . . . . .	136
5.2.5.2.	Series M . . . . .	138
5.2.5.3.	Series AM . . . . .	139
5.2.5.4.	Comparative analysis . . . . .	141
5.2.6.	Results and discussion — aged specimens . . . . .	143
5.2.6.1.	Thermal cycles . . . . .	143
5.2.6.2.	Wet–dry cycles . . . . .	148
5.2.6.3.	Summary . . . . .	156
5.3.	Numerical simulations . . . . .	157
5.3.1.	Objectives . . . . .	157
5.3.2.	Description of the FE models . . . . .	157
5.3.2.1.	Geometry, elements and boundary conditions . . . . .	157
5.3.2.2.	Material properties . . . . .	158
5.3.2.3.	GFRP–concrete interface constitutive laws . . . . .	159
5.3.2.4.	Type of analyses . . . . .	160
5.3.3.	Results and discussion . . . . .	160
5.3.3.1.	Un-aged specimens . . . . .	160
5.3.3.2.	Specimens aged with thermal cycles . . . . .	161
5.3.3.3.	Specimens aged with wet–dry cycles . . . . .	163
5.4.	Final remarks . . . . .	166
<b>6.</b>	<b>Small-scale prototype</b>	<b>169</b>
6.1.	Preliminary remarks . . . . .	169
6.2.	Characteristics of the prototype . . . . .	169
6.3.	Construction of the prototype . . . . .	171
6.4.	Static behaviour of the prototype . . . . .	179
6.4.1.	Context . . . . .	179
6.4.2.	Monitoring of precamber effects . . . . .	179
6.4.3.	Serviceability tests (without prestress) . . . . .	179
6.4.4.	Serviceability tests with prestress . . . . .	181
6.4.5.	Failure test . . . . .	183
6.4.6.	Analytical simulation . . . . .	186
6.4.6.1.	Serviceability behaviour without prestress . . . . .	186
6.4.6.2.	Serviceability behaviour with prestress . . . . .	187
6.4.6.3.	Failure behaviour . . . . .	190
6.4.7.	Numerical simulation . . . . .	193
6.4.7.1.	Serviceability behaviour without prestress . . . . .	194
6.4.7.2.	Serviceability behaviour with prestress . . . . .	195
6.4.7.3.	Failure behaviour . . . . .	195
6.4.8.	Conclusions . . . . .	197

---

6.5.	Dynamic behaviour of the prototype . . . . .	199
6.5.1.	Modal identification . . . . .	199
6.5.1.1.	Context . . . . .	199
6.5.1.2.	Experimental tests . . . . .	200
6.5.1.3.	Analytical simulation . . . . .	205
6.5.1.4.	Numerical simulation . . . . .	209
6.5.1.5.	Conclusions . . . . .	211
6.5.2.	Behaviour under pedestrian loads . . . . .	212
6.5.2.1.	Context . . . . .	212
6.5.2.2.	Experimental tests . . . . .	212
6.5.2.3.	One pedestrian tests . . . . .	213
6.5.2.4.	Crowd tests . . . . .	216
6.5.2.5.	Numerical simulation . . . . .	218
6.5.2.6.	Conclusions . . . . .	221
6.6.	Creep behaviour of the prototype . . . . .	222
6.6.1.	Context . . . . .	222
6.6.1.1.	Creep response of the GFRP material . . . . .	223
6.6.1.2.	Creep response of the SFRSCC material . . . . .	226
6.6.2.	Experimental tests . . . . .	227
6.6.2.1.	Experimental series . . . . .	227
6.6.2.2.	Experimental results . . . . .	229
6.6.3.	Analytical simulation . . . . .	234
6.6.3.1.	Model proposal . . . . .	234
6.6.3.2.	Assessment of GFRP material creep models . . . . .	235
6.6.3.3.	Prediction of long-term response . . . . .	237
6.6.4.	Conclusions . . . . .	239
6.7.	Final remarks . . . . .	240
<b>7.</b>	<b>Full-scale prototype</b>	<b>241</b>
7.1.	Preliminary remarks . . . . .	241
7.2.	Characteristics and design of the prototype . . . . .	241
7.2.1.	Ultimate limit states . . . . .	243
7.2.1.1.	Longitudinal direction . . . . .	244
7.2.1.2.	Transverse direction . . . . .	248
7.2.2.	Serviceability limit states . . . . .	251
7.3.	Construction of the prototype . . . . .	252
7.4.	Static behaviour of the prototype . . . . .	257
7.4.1.	Overview . . . . .	257
7.4.2.	Serviceability tests . . . . .	257
7.4.3.	Analytical simulation . . . . .	259
7.4.4.	Numerical simulation . . . . .	260
7.4.5.	Conclusions . . . . .	263
7.5.	Dynamic behaviour of the prototype . . . . .	263
7.5.1.	Modal identification . . . . .	263
7.5.1.1.	Experimental tests . . . . .	263
7.5.1.2.	Analytical simulation . . . . .	266
7.5.1.3.	Numerical simulation . . . . .	266
7.5.2.	Behaviour under pedestrian loads . . . . .	267
7.5.2.1.	Overview . . . . .	267
7.5.2.2.	Experimental tests . . . . .	268

7.5.2.3. Numerical simulation . . . . .	271
7.5.3. Conclusions . . . . .	273
7.6. Creep behaviour of the prototype . . . . .	275
7.6.1. Overview . . . . .	275
7.6.2. Experimental test . . . . .	276
7.6.3. Analytical simulation . . . . .	276
7.6.4. Conclusions . . . . .	280
7.7. Final remarks . . . . .	281
<b>8. Conclusions and future developments</b>	<b>283</b>
8.1. Conclusions . . . . .	283
8.1.1. GFRP–concrete connection systems . . . . .	284
8.1.2. Static, creep and dynamic behaviour of GFRP–concrete structures .	285
8.1.3. Development of a full-scale GFRP–SFRSCC footbridge prototype .	287
8.2. Future developments . . . . .	287
<b>Bibliography</b>	<b>291</b>
<b>Appendix</b>	<b>301</b>
<b>A. Appendix A — Material characterization tests</b>	<b>303</b>
A.1. Introduction . . . . .	303
A.2. GFRP tensile coupon tests . . . . .	303
A.3. GFRP compressive coupon tests . . . . .	304
A.4. GFRP off-axis tensile coupon tests . . . . .	306
A.5. GFRP flexural coupon tests . . . . .	307
A.6. GFRP interlaminar shear coupon tests . . . . .	308
A.7. SFRSCC compressive cube tests . . . . .	308
A.8. SFRSCC compressive cylinder tests . . . . .	309
<b>B. Appendix B — GFRP–SFRSCC shear connection tests</b>	<b>311</b>
B.1. Introduction . . . . .	311
B.2. Preliminary tests . . . . .	311
B.2.1. Series P–A . . . . .	311
B.2.2. Series P–M1 . . . . .	312
B.2.3. Series P–M2 . . . . .	312
B.2.4. Series P–M3 . . . . .	313
B.2.5. Series P–M4 . . . . .	313
B.2.6. Series P–AM . . . . .	314
B.3. Un-aged specimens . . . . .	314
B.3.1. Series A . . . . .	314
B.3.2. Series M . . . . .	315
B.3.3. Series AM . . . . .	315
B.4. Aged specimens . . . . .	316
B.4.1. Thermal cycles . . . . .	316
B.4.1.1. Series A–Th–T1 . . . . .	316
B.4.1.2. Series A–Th–T2 . . . . .	316
B.4.1.3. Series A–Th–T3 . . . . .	317
B.4.2. Wet–dry cycles . . . . .	317
B.4.2.1. Series A–H–T1 . . . . .	317

B.4.2.2. Series A–H–T2 . . . . .	318
B.4.2.3. Series A–H–T3 . . . . .	318
B.4.2.4. Series AM–H–T3 . . . . .	319
<b>C. Appendix C — One pedestrian dynamic test on the small-scale prototype</b>	<b>321</b>
C.1. Introduction . . . . .	321
C.2. Walk slow . . . . .	321
C.2.1. Centred path . . . . .	321
C.2.2. Eccentric path . . . . .	323
C.3. Walk . . . . .	325
C.3.1. Centred path . . . . .	325
C.3.2. Eccentric path . . . . .	327
C.4. Walk fast . . . . .	329
C.4.1. Centred path . . . . .	329
C.4.2. Eccentric path . . . . .	331
<b>D. Appendix D — One pedestrian dynamic test on the full-scale prototype</b>	<b>335</b>
D.1. Introduction . . . . .	335
D.2. Walk slow . . . . .	335
D.2.1. Centred path . . . . .	335
D.2.2. Eccentric path . . . . .	336
D.3. Walk . . . . .	337
D.3.1. Centred path . . . . .	337
D.3.2. Eccentric path . . . . .	338
D.4. Walk fast . . . . .	339
D.4.1. Centred path . . . . .	339
D.4.2. Eccentric path . . . . .	340
D.5. Walk fast . . . . .	341
D.5.1. Centred path . . . . .	341
D.5.2. Eccentric path . . . . .	342

## List of Figures

2.1.	Monsanto House of the Future. . . . .	8
2.2.	Futuro House. . . . .	8
2.3.	CFRP flexural strengthening. . . . .	9
2.4.	CFRP shear strengthening. . . . .	9
2.5.	CFRP axial strengthening. . . . .	9
2.6.	CFRP strengthening of masonry structure. . . . .	9
2.7.	CFRP strengthening of timber structure. . . . .	9
2.8.	CFRP prestress cables. . . . .	9
2.9.	GRC telecommunication tower prototype. . . . .	10
2.10.	FRP reinforcement bars with different coating finish. . . . .	10
2.11.	Application of CFRP reinforcement bars. . . . .	10
2.12.	Steel-GFRP hybrid road bridge. . . . .	11
2.13.	Steel-GFRP hybrid road bridge. . . . .	11
2.14.	Eyecatcher building. . . . .	11
2.15.	<i>Novartis</i> Campus Entrance Building. . . . .	11
2.16.	Fibre reinforcement rovings: a) unidirectional; b) spun; and c) mock. . . . .	12
2.17.	Fibre reinforcement mats: (a) continuous mat with random fibre orientation; (ii) weaves $0/90^\circ$ ; (iii) complex mat, $0/90^\circ$ membrane and random fibre orientation; and (iv) bidirectional complex mat, $0/\pm 45/90^\circ$ membrane and random fibre orientation. . . . .	13
2.18.	Pultrusion process assembly line. . . . .	16
2.19.	Pultrusion of an I-shape profile: a) pulling of the dry fibres; b) first stretch of cured FRP; and c) general view of the pultrusion line. . . . .	16
2.20.	Typical fibre architecture of pultruded laminates. . . . .	17
2.21.	Typical first generation pultruded profiles. . . . .	17
2.22.	Typical second generation pultruded profiles. . . . .	18
2.23.	Tensile stress <i>vs.</i> strain relationship of GFRP pultruded profiles and other materials. . . . .	19
2.24.	Comparison between the physical and mechanical properties of GFRP pultruded profiles and other materials: density (left); thermal expansion coefficient (middle); and thermal conductivity (right). . . . .	20
2.25.	Aberfeldy footbridge. . . . .	21
2.26.	Bonds Mill lifting bridge. . . . .	21
2.27.	Pontresina footbridge. . . . .	21
2.28.	Pontresina footbridge helicopter transportation. . . . .	21
2.29.	Kolding footbridge. . . . .	22
2.30.	Lleida footbridge. . . . .	22
2.31.	West Mill road bridge. . . . .	22
2.32.	Klipphausen road bridge. . . . .	22
2.33.	Steel-GFRP hybrid footbridge (courtesy of Mário Sá). . . . .	22

2.34.	Typical stress–strain relationship of SFRC. . . . .	24
2.35.	Cross–section of the hybrid beam proposed by Deskovic <i>et al.</i> . . . . .	26
2.36.	Cross–section of the hybrid beam proposed by Garcia. . . . .	26
2.37.	Cross–section of the hybrid beams used in the Asturias bridge. . . . .	27
2.38.	G/CFRP–concrete hybrid bridge built in Spain. . . . .	27
2.39.	Carbon Shell System with GFRP panel deck (top) and concrete deck (bottom). . . . .	27
2.40.	Hybrid Tube System. . . . .	27
2.41.	Cross–section of a hybrid GFRP–concrete sandwich panel. . . . .	28
2.42.	Cross–section of hybrid GFRP–concrete deck systems. . . . .	29
2.43.	Service vehicle load model: $Q_{SV1} = 80$ kN, $Q_{SV2} = 40$ kN and $x$ is the bridge direction. . . . .	30
2.44.	Correlation between the pacing rate ( $f_s$ ), the speed ( $v_s$ ) and the stride length ( $l_s$ ). . . . .	32
2.45.	Vertical load–time function for different types of motion. . . . .	32
2.46.	Load–time function overlap. . . . .	33
2.47.	Correlation between the pacing rate ( $f_s$ ), the peak load/static weight ratio and the contact duration ( $t_p$ ). . . . .	33
2.48.	Horizontal load–time functions for a) transverse and b) longitudinal directions. . . . .	33
2.49.	Impact factor ( $k_p$ ) <i>vs.</i> relative contact duration ( $t_p/T_p$ ). . . . .	34
2.50.	Comparison between the vertical acceleration limits proposed in several documents. . . . .	36
2.51.	Comparison between the horizontal acceleration limits proposed in several documents. . . . .	36
2.52.	ISO 10137 RMS vertical acceleration limits for footbridge structures. . . . .	37
2.53.	ISO 10137 RMS horizontal acceleration limits for footbridge structures. . . . .	37
3.1.	Idealized cross–section. . . . .	41
3.2.	Live load configurations over the transverse direction, (i) uniform distribution, (ii) live load on the cantilevers, and (iii) live load on the interior span. . . . .	43
3.3.	Optimized spacing as a function of the slab thickness ( $h_c$ ) for different live load configurations and envelope. . . . .	44
3.4.	Design values of resistant and acting bending moments ( $M_{rd,cT}$ and $M_{sd,cT}$ , respectively) as a function of the slab thickness ( $h_c$ ). . . . .	45
3.5.	General geometry of the GFRP profiles for the main girders. . . . .	45
3.6.	Geometry of the I400 GFRP profiles used as main girders of the full–scale prototype (dimensions in mm). . . . .	48
3.7.	Evolution of the long–term midspan deflections ( $\delta_{ms}(50 \text{ yrs})$ ) as a function of the slab thickness ( $h_c$ ). . . . .	49
3.8.	Evolution of the fundamental vibration frequency ( $f$ ) as a function of the slab thickness ( $h_c$ ). . . . .	49
3.9.	Resistant and acting design forces as a function of the slab thickness ( $h_c$ ). . . . .	49
4.1.	Coupon extraction: separation of the flanges from the web. . . . .	52
4.2.	Coupon extraction: cutting off–axis coupons. . . . .	52
4.3.	Coupon tensile tests: I200 specimen. . . . .	53
4.4.	Coupon tensile tests: I400 specimen. . . . .	53
4.5.	Coupon tensile tests: axial stress ( $\sigma_{t,L}$ ) <i>vs.</i> strain ( $\varepsilon_{t,L}$ ) of I200 web specimens. . . . .	54
4.6.	Coupon tensile tests: axial stress ( $\sigma_{t,L}$ ) <i>vs.</i> strain ( $\varepsilon_{t,L}$ ) of I200 flange specimens. . . . .	54
4.7.	Coupon tensile tests: axial <i>vs.</i> transverse strain of I200 web specimen. . . . .	54



4.8.	Coupon tensile tests: axial <i>vs.</i> transverse strain of I200 flange specimen. . .	54
4.9.	Coupon tensile tests: failure mode of I200 specimens. . . . .	55
4.10.	Coupon tensile tests: axial stress ( $\sigma_{t,L}$ ) <i>vs.</i> strain ( $\varepsilon_{t,L}$ ) of I400 web specimens. . .	55
4.11.	Coupon tensile tests: axial stress ( $\sigma_{t,T}$ ) <i>vs.</i> strain ( $\varepsilon_{t,T}$ ) of I400 flange specimens. . . . .	55
4.12.	Coupon tensile tests: axial stress ( $\sigma_{t,L}$ ) <i>vs.</i> strain ( $\varepsilon_{t,L}$ ) of I400 flange specimens. . . . .	56
4.13.	Coupon tensile tests: failure mode of I400 specimens tested in the longitudinal direction. . . . .	57
4.14.	Coupon tensile tests: failure mode of I400 specimens tested in the transverse direction. . . . .	57
4.15.	Coupon compressive tests: I200 specimen. . . . .	58
4.16.	Coupon compressive tests: I400 specimen. . . . .	58
4.17.	Coupon compressive tests: axial stress ( $\sigma_{c,L}$ ) <i>vs.</i> strain ( $\varepsilon_{c,L}$ ) in the longitudinal direction of I200 web specimens. . . . .	59
4.18.	Coupon compressive tests: axial stress ( $\sigma_{c,L}$ ) <i>vs.</i> strain ( $\varepsilon_{c,L}$ ) in the longitudinal direction of I200 flange specimens. . . . .	59
4.19.	Coupon compressive tests: axial stress ( $\sigma_{c,T}$ ) <i>vs.</i> strain ( $\varepsilon_{c,T}$ ) in the transverse direction of I200 web specimens. . . . .	59
4.20.	Coupon compressive tests: axial stress ( $\sigma_{c,T}$ ) <i>vs.</i> strain ( $\varepsilon_{c,T}$ ) in the transverse direction of I200 flange specimens. . . . .	59
4.21.	Coupon compressive tests: axial stress ( $\sigma_{c,L}$ ) <i>vs.</i> strain ( $\varepsilon_{c,L}$ ) in the longitudinal direction of I400 web specimens. . . . .	61
4.22.	Coupon compressive tests: axial stress ( $\sigma_{c,L}$ ) <i>vs.</i> strain ( $\varepsilon_{c,L}$ ) in the longitudinal direction of I400 flange specimens. . . . .	61
4.23.	Coupon compressive tests: axial stress ( $\sigma_{c,T}$ ) <i>vs.</i> strain ( $\varepsilon_{c,T}$ ) in the transverse direction of I400 web specimens. . . . .	61
4.24.	Coupon compressive tests: axial stress ( $\sigma_{c,T}$ ) <i>vs.</i> strain ( $\varepsilon_{c,T}$ ) in the transverse direction of I400 flange specimens. . . . .	61
4.25.	Coupon off-axis tensile tests: I200 specimen. . . . .	64
4.26.	Coupon off-axis tensile tests: I400 specimen. . . . .	64
4.27.	Coupon off-axis tensile test: specimen types A and B, respectively, tested at a $+10^\circ$ (top) or $-10^\circ$ (bottom) off-axis direction. . . . .	64
4.28.	Coupon off-axis tensile tests: $\tau_{LT}$ <i>vs.</i> $\gamma_{LT}$ — I200 specimens. . . . .	65
4.29.	Coupon off-axis tensile tests: $\tau_{LT}$ <i>vs.</i> $\gamma_{LT}$ — I400 specimens. . . . .	65
4.30.	Coupon off-axis tensile tests: failure mode of I200 specimen. . . . .	66
4.31.	Coupon off-axis tensile tests: failure mode of I400 specimen. . . . .	66
4.32.	Coupon flexure test before specimen failure. . . . .	67
4.33.	Coupon flexure test after specimen failure. . . . .	67
4.34.	Coupon flexure tests: $\sigma_{f,L}$ <i>vs.</i> $\varepsilon_{f,L}$ — web specimens. . . . .	68
4.35.	Coupon flexure tests: $\sigma_{f,L}$ <i>vs.</i> $\varepsilon_{f,L}$ — flange specimens. . . . .	68
4.36.	Coupon interlaminar shear test before specimen failure. . . . .	70
4.37.	Coupon interlaminar shear test after specimen failure. . . . .	70
4.38.	Coupon interlaminar shear tests: $\tau_{is,L}$ <i>vs.</i> $d_{is,L}$ — web specimens. . . . .	70
4.39.	Coupon interlaminar shear tests: $\tau_{is,L}$ <i>vs.</i> $d_{is,L}$ — flange specimens. . . . .	70
4.40.	Full-scale flexural serviceability tests: test setup for the I200 profile. . . .	73
4.41.	Full-scale flexural serviceability tests: test setup for the I400 profile. . . .	73
4.42.	Full-scale flexural serviceability tests: determination of the full-section moduli ( $E_{full}$ and $G_{full}$ ) for the I200 profile. . . . .	74

4.43.	Full-scale flexural serviceability tests: determination of the full-section moduli ( $E_{full}$ and $G_{full}$ ) for the I400 profile. . . . .	74
4.44.	Full-scale flexural failure tests: 4-point bending load configuration. . . . .	76
4.45.	Full-scale flexural failure tests: I200 profile — positioning of string pot displacement transducers. . . . .	77
4.46.	Full-scale flexural failure tests: I200 profile — positioning of the strain gauges at midpan section (dimensions in mm). . . . .	77
4.47.	Full-scale flexural failure tests: test setup of the I200 specimen. . . . .	77
4.48.	Full-scale flexural failure tests: I200 profile — load <i>vs.</i> deflections. . . . .	78
4.49.	Full-scale flexural failure tests: I200 profile — load <i>vs.</i> midspan axial strains. . . . .	78
4.50.	Full-scale flexural failure tests: configuration of the local buckling wave in the I200 profile (near one of the loading sections). . . . .	79
4.51.	Full-scale flexural failure tests: damage detail on the top flange and web of the I200 profile (near one of the loading sections). . . . .	79
4.52.	Full-scale flexural failure tests: I200 profile — Load <i>vs.</i> upper flange deflections. . . . .	80
4.53.	Full-scale flexural failure tests: I200 profile — Upper flange differential vertical deflection and application of the modified Southwell method. . . . .	80
4.54.	Full-scale flexural failure tests: I400 profiles — scheme of the vertical displacement measurement apparatus. . . . .	81
4.55.	Full-scale flexural failure tests: I400 profiles — vertical displacement measurement apparatus. . . . .	81
4.56.	Full-scale flexural failure tests: I400 profiles — positioning of the strain gauges in the cross-section (dimensions in mm). . . . .	82
4.57.	Full-scale flexural failure tests: I400 profile — strain gauge rosette used in specimen P400-2. . . . .	82
4.58.	Full-scale flexural failure tests: I400 profiles — test setup for the longer specimens. . . . .	83
4.59.	Full-scale flexural failure tests: I400 profiles — test setup for the shorter specimen. . . . .	83
4.60.	Full-scale flexural failure tests: P400-1 specimen — load <i>vs.</i> midspan deflection. . . . .	83
4.61.	Full-scale flexural failure tests: P400-2 specimen — load <i>vs.</i> midspan deflection. . . . .	83
4.62.	Full-scale flexural failure tests: P400-3 specimen — load <i>vs.</i> midspan deflection. . . . .	84
4.63.	Full-scale flexural failure tests: P400-1 specimen — load <i>vs.</i> axial strains. . . . .	85
4.64.	Full-scale flexural failure tests: P400-2 specimen — load <i>vs.</i> axial strains. . . . .	85
4.65.	Full-scale flexural failure tests: P400-2 specimen — load <i>vs.</i> rosette strains. . . . .	86
4.66.	Full-scale flexural failure tests: P400-2 specimen — shear stress <i>vs.</i> distortion. . . . .	86
4.67.	Full-scale flexural tests: failure mode of specimen P400-1, front side view. . . . .	87
4.68.	Full-scale flexural tests: failure mode of specimen P400-1, back side view. . . . .	87
4.69.	Full-scale flexural tests: failure mode of specimen P400-2, global view. . . . .	88
4.70.	Full-scale flexural tests: failure mode of specimen P400-2, damage on the web-flange junction. . . . .	88
4.71.	Full-scale flexural tests: failure mode of specimen P400-3, global view. . . . .	89
4.72.	Full-scale flexural tests: failure mode of specimen P400-3, damage on the web-flange junction. . . . .	89
4.73.	Midspan deflection stiffness <i>vs.</i> span: analytical and numerical results for the I200 profile. . . . .	91

4.74.	Midspan deflection stiffness <i>vs.</i> span: analytical and numerical results for the I400 profile. . . . .	91
4.75.	Bending moment and shear force diagrams along the length of the beam. .	99
4.76.	Axial and shear stress distributions along the depth of the web of the I400 profile. . . . .	99
4.77.	Overall perspective of the I200 specimen FE model. . . . .	101
4.78.	Overall perspective of the I400 specimens FE models (P400-1 specimen). .	101
4.79.	FE analysis: first buckling mode configuration for the I200 specimen. . .	102
4.80.	FE analysis: Tsai-Hill failure index distribution of the I200 specimen for $F = 34.9$ kN (half-model). . . . .	103
4.81.	FE analysis: first buckling mode configuration for the P400-1 specimen. . .	103
4.82.	FE analysis: Tsai-Hill failure index distribution of the P400-1 specimen for $F = 91.1$ kN (half-model). . . . .	104
4.83.	FE analysis: first buckling mode configuration for the P400-2 specimen. . .	105
4.84.	FE analysis: Tsai-Hill failure index distribution of the P400-2 specimen for $F = 91.1$ kN (half-model). . . . .	105
4.85.	FE analysis: first buckling mode configuration for the P400-3 specimen. . .	106
4.86.	FE analysis: Tsai-Hill failure index distribution of the P400-3 specimen for $F = 141.7$ kN (half-model). . . . .	106
4.87.	Compressive tests on SFRSCC cube specimens. . . . .	108
4.88.	Elasticity modulus tests on SFRSCC cylinder specimens. . . . .	110
4.89.	Splitting tensile strength tests on SFRSCC cylinder specimens. . . . .	110
4.90.	Positioning of the strain gauges and displacement transducers in the midspan section. . . . .	112
4.91.	Flexural tests on SFRSCC slabs: test setup. . . . .	112
4.92.	Flexural tests on SFRSCC slabs: load <i>vs.</i> average deflection curves. . . .	113
4.93.	Flexural tests on SFRSCC slabs: load <i>vs.</i> average strain curves. . . . .	113
4.94.	Flexural tests on SFRSCC slabs: initial crack opening. . . . .	113
4.95.	Flexural tests on SFRSCC slabs: crack opening in the brink of failure (overall and detail views). . . . .	113
5.1.	Scheme of the push-out tests: frontal view (left) and section view A-A (right).	120
5.2.	Preliminary test specimens: adhesive provided for specimens P-A and P-AM only; and bolts and negatives provided for specimens P-M1 and P-AM only. . . . .	121
5.3.	Preliminary test specimens: (a) P-M2; (b) P-M3; (b) P-M4. . . . .	121
5.4.	Un-aged test specimens: adhesive provided for specimens A and AM while the cellophane film was provided for specimens M only; bolts and negatives provided for specimens AM and M; and strain gauges used in 2 specimens of series A. . . . .	122
5.5.	Thermal cycle aging: objective and real (measured) temperature curves. . .	123
5.6.	Thermal cycle aging: objective and real (measured) $RH$ curves. . . . .	123
5.7.	Thermal cycle aging: specimens inside the climate chamber. . . . .	124
5.8.	Wet-dry cycle aging: specimens inside the wet-dry chamber. . . . .	124
5.9.	Surface preparation of a SFRSCC slab for the adhesive bonding. . . . .	125
5.10.	Surface preparation of a SFRSCC slab (with negative) for the adhesive bonding. . . . .	125
5.11.	Preparation of the adhesively bonded specimens: application of the resin. .	125
5.12.	Preparation of the adhesively bonded specimens: application of the weight.	125
5.13.	Preparation of the adhesively bonded specimens: installation of strain gauges.	126

5.14.	Preparation of the adhesively bonded specimens: specimens instrumented with strain gauges. . . . .	126
5.15.	Preparation of the bolted specimens: drilling of the profiles. . . . .	126
5.16.	Preparation of the bolted specimens: embedded length of the connectors. .	126
5.17.	Preparation of the bolted specimens: aspect after installation of the bolts. .	127
5.18.	Preparation of the bolted specimens: series M specimens provided with cellophane film. . . . .	127
5.19.	Preparation of the bolted specimens: sealing of the GFRP–SFRSCC joints (M series only). . . . .	127
5.20.	Preparation of the bolted specimens: filling of the negatives with epoxy mortar.	127
5.21.	Test setup: specimens P–A, P–M1 and P–AM. . . . .	128
5.22.	Test setup: specimens P–M2, P–M3 and P–M4. . . . .	128
5.23.	Test setup: specimens A, M and AM. . . . .	128
5.24.	Test setup: specimens A–Th, A–H and AM–H. . . . .	128
5.25.	Shear connection tests: load <i>vs.</i> relative displacement curves for P–A specimens. . . . .	129
5.26.	Specimen P–A–6: a) beginning of the test; b) failure of the specimen; c) detail of the web–flange junction failure — complete separation; and d) detail of the failure at the interface — complete separation. . . . .	130
5.27.	Shear connection tests: load <i>vs.</i> relative displacement curves for P–M1 specimens. . . . .	130
5.28.	Specimen P–M1–2: a) beginning of the test; b) beginning of the crushing, and of bolts’ deformation; c) failure due to crushing of the flange; and d) detail of the interaction between the bolts and the profile. . . . .	131
5.29.	Shear connection tests: load <i>vs.</i> relative displacement curves for P–M2 specimens. . . . .	131
5.30.	Specimen P–M2–1: a) beginning of the test; b) deformation on the bolts/beginning of GFRP flange crushing on the GFRP flange; c) collapsed specimen; d) detail of the GFRP flange crushing. . . . .	132
5.31.	Shear connection tests: load <i>vs.</i> relative displacement curves for P–M3 specimens. . . . .	132
5.32.	Specimen P–M3–4: a) linear stage; b) non–linear stage (deformation of the bolts on the left side only); c) crushing of the GFRP flange; d) crushing of the GFRP flange — detail. . . . .	133
5.33.	Shear connection tests: load <i>vs.</i> relative displacement curves for P–M4 specimens. . . . .	133
5.34.	Specimens P–M4–4: a) linear stage; b) non–linear stage — deformation of the bolts; c) collapsed specimen; and d) detail of the GFRP flange crushing.	134
5.35.	Shear connection tests: load <i>vs.</i> relative displacement curves for P–AM specimens. . . . .	134
5.36.	Specimen P–AM–2: a) beginning of the test; b) failure of the web–flange junction; c) failure of the SFRSCC–adhesive interface; d) failure of both bolts of the same flange. . . . .	135
5.37.	Shear connection tests: load <i>vs.</i> relative displacement curves for all preliminary series. . . . .	135
5.38.	Shear connection tests: $F_{u,lin.}/A_{neg}$ <i>vs.</i> $A_{neg}$ for all P–M specimens. . . .	137
5.39.	Shear connection tests: $F_{u,non-lin.}/Nr$ <i>vs.</i> $Nr$ for all P–M specimens. . . .	137
5.40.	Shear connection tests: load <i>vs.</i> relative displacement curves for series A. .	137

5.41. Specimen A-1: a) beginning of the test; b) detail of the web-junction damage; c) detail of the GFRP-SFRSCC debonding; d) debonding in the SFRSCC. . . . .	138
5.42. Shear connection tests: strain measurements at the interface for specimen A-4. . . . .	138
5.43. Shear connection tests: load <i>vs.</i> relative displacement curves for series M. . . . .	139
5.44. Specimen M-2: a) beginning of the test; b) deformation of the bolts; c) crushing of the GFRP flanges; d) damage on the SFRSCC (after failure). . . . .	139
5.45. Shear connection tests: load <i>vs.</i> relative displacement curves for series AM. . . . .	140
5.46. Specimen AM-2: a) beginning of the test; b) collapsed specimen; c) debonding and crushing of the flange; d) web-flange junction failure. . . . .	140
5.47. Shear connection tests: load <i>vs.</i> relative displacement curves for all un-aged series. . . . .	141
5.48. Shear connection tests: load <i>vs.</i> relative displacement curves of series P-M4 and M. . . . .	142
5.49. Shear connection tests: load <i>vs.</i> relative displacement curves for series A-Th-T1. . . . .	143
5.50. Specimen A-Th-T1-2: a) beginning of the test; b) collapsed specimen; c) debonding failure in the SFRSCC; d) debonded surfaces. . . . .	144
5.51. Shear connection tests: load <i>vs.</i> relative displacement curves for series A-Th-T2. . . . .	144
5.52. Specimen A-Th-T2-3: a) beginning of the test; b) collapsed specimen; c) SFRSCC failure surface; d) GFRP failure surface. . . . .	145
5.53. External signs of fibre corrosion in A-Th-T3 series, specimens: a) A-Th-T3-1; b) A-Th-T3-2; c) A-Th-T3-4; d) A-Th-T3-7. . . . .	145
5.54. Shear connection tests: load <i>vs.</i> relative displacement curves for series A-Th-T3. . . . .	146
5.55. Specimen A-Th-T3-2: a) beginning of the test; b) collapsed specimen; c) incomplete debonding; d) failure surfaces. . . . .	146
5.56. Shear connection tests: comparison of load <i>vs.</i> relative displacement curves for different durations of thermal cycles aging (A series). . . . .	147
5.57. Ultimate load <i>vs.</i> number of thermal cycles. . . . .	148
5.58. Stiffness <i>vs.</i> number of thermal cycles. . . . .	148
5.59. External signs of fibre corrosion in A-H-T1 series, specimens: a) A-H-T1-2; b) A-H-T1-3; c) A-H-T1-4; d) A-H-T1-4. . . . .	149
5.60. Shear connection tests: load <i>vs.</i> relative displacement curves for series A-H-T1. . . . .	149
5.61. Specimen A-H-T1-3: a) beginning of the test; b) collapsed specimen; c) uncomplete debonding; d) failure surfaces. . . . .	150
5.62. External signs of fibre corrosion in A-H-T2 series, specimens: a) A-H-T2-1; b) A-H-T2-2; c) A-H-T2-3; d) A-H-T2-4. . . . .	150
5.63. Shear connection tests: load <i>vs.</i> relative displacement curves for series A-H-T2. . . . .	151
5.64. Specimen A-H-T2-3: a) beginning of the test; b) collapsed specimen; c) failure surfaces; d) debonding in the epoxy resin. . . . .	151
5.65. External signs of fibre corrosion in A-H-T3 series, specimens: a) A-H-T3-3; b) A-H-T3-3; c) A-H-T3-4; d) A-H-T3-4. . . . .	151
5.66. Shear connection tests: load <i>vs.</i> relative displacement curves for series A-H-T3. . . . .	152
5.67. Specimen A-H-T3-1: a) beginning of the test; b) collapsed specimen; c) web-flange junction failure; d) failure surfaces. . . . .	153
5.68. External signs of fibre corrosion in AM-H-T3 series, specimens: a) AM-H-T3-1; b) AM-H-T3-2; c) AM-H-T3-3; d) AM-H-T3-3. . . . .	153

5.69.	Shear connection tests: load <i>vs.</i> relative displacement curves for series AM–H–T3. . . . .	153
5.70.	Specimen AM–H–T3–3: a) beginning of the test; b) collapsed specimen; c) crushing of the flange; d) web–flange junction failure. . . . .	154
5.71.	Shear connection tests: comparison of load <i>vs.</i> relative displacement curves for different durations of wet–dry cycles aging (A series). . . . .	155
5.72.	Shear connection tests: comparison of load <i>vs.</i> relative displacement curves for different durations of wet–dry cycles aging (AM series). . . . .	155
5.73.	Ultimate load <i>vs.</i> number of wet–dry cycles. . . . .	155
5.74.	Stiffness <i>vs.</i> number of wet–dry cycles. . . . .	155
5.75.	Ultimate load <i>vs.</i> duration of aging. . . . .	157
5.76.	Stiffness <i>vs.</i> duration of aging. . . . .	157
5.77.	Overview of the FE model. . . . .	158
5.78.	Bi–linear shear bond–slip law adopted. . . . .	159
5.79.	Shear connection tests: load <i>vs.</i> relative displacement curves for series A — experiments and FE model. . . . .	161
5.80.	Shear connection tests: strain measurements at the interface for specimen A–4 — experimental and numerical results. . . . .	161
5.81.	Shear connection tests: load and Tsai–Hill index <i>vs.</i> relative displacement curves obtained with the FE model. . . . .	161
5.82.	Shear connection tests: load <i>vs.</i> relative displacement curves for series A specimens aged with thermal cycles — experiments and FE model. . . . .	162
5.83.	Ultimate load <i>vs.</i> duration of thermal cycles aging: experimental and numerical results. . . . .	163
5.84.	Stiffness <i>vs.</i> duration of thermal cycles aging: experimental and numerical results. . . . .	163
5.85.	Shear connection tests: load and Tsai–Hill index <i>vs.</i> relative displacement curves obtained with the FE model considering thermal cycles aging. . . . .	164
5.86.	Shear connection tests: load <i>vs.</i> relative displacement curves for A specimens aged with wet–dry cycles — experiments and FE model. . . . .	165
5.87.	Ultimate load <i>vs.</i> duration of wet–dry cycles aging: experimental and numerical results. . . . .	165
5.88.	Stiffness <i>vs.</i> duration of wet–dry cycles aging: experimental and numerical results. . . . .	165
5.89.	Shear connection tests: load and Tsai–Hill index <i>vs.</i> relative displacement curves obtained with the FE model considering wet–dry cycles aging. . . . .	166
6.1.	Small–scale prototype cross–section. . . . .	170
6.2.	Side– and top–view of the small–scale prototype. . . . .	170
6.3.	Details of the concrete jackets and connections between main and secondary girders. . . . .	170
6.4.	Dimensions of the precast SFRSCC slabs. . . . .	171
6.5.	Roughening of the slab. . . . .	172
6.6.	Roughening of the slab (detail). . . . .	172
6.7.	Mark–up for drilling of the bolts position. . . . .	172
6.8.	Mark–up for drilling for the main/secondary girders connection. . . . .	172
6.9.	Drilling of the flanges. . . . .	173
6.10.	Drilling of the flanges (detail). . . . .	173
6.11.	Drilling of the webs. . . . .	173
6.12.	Embedded length of the bolts. . . . .	173

6.13.	Embedded length of the threaded rods. . . . .	173
6.14.	Group of bolts installed. . . . .	173
6.15.	Group of threaded rods installed. . . . .	173
6.16.	Tailoring of the formwork. . . . .	174
6.17.	Installation of the formwork. . . . .	174
6.18.	Final aspect of the formwork. . . . .	174
6.19.	Final aspect of the formwork (side view). . . . .	174
6.20.	Casting of the concrete. . . . .	174
6.21.	Vibration of the concrete. . . . .	174
6.22.	Cutting of the square-section profiles. . . . .	175
6.23.	Drilling of the angle-section profiles. . . . .	175
6.24.	Dimensions of the midspan secondary girder (mm). . . . .	175
6.25.	Final aspect of the midspan secondary girder. . . . .	175
6.26.	Assembly of the main and secondary girders. . . . .	176
6.27.	Final aspect of the assembled girders. . . . .	176
6.28.	Construction details: a) installation of plastic spacers; b) trimming of slabs' outer edges; c) trimming of a slab's inner edge; and d) geometrical incompatibility. . . . .	176
6.29.	Bonding of the elements: a) precamber props; b) dusting of the surface; application of the adhesive on the c) main girders; and d) on the SFRSCC slabs. . . . .	177
6.30.	Assembly of the prototype: a) fastening of the central pair of slabs; b) moving a slab with the aid of a moving crane; and c) final placing of the slabs by manual labor. . . . .	177
6.31.	Aspect of the small-scale prototype after the bonding of the slabs. . . . .	177
6.32.	Preparation for sealing the negatives: a) and b) sealing of the SFRSCC– GFRP junctions; c) components of the epoxy mortar; and d) mixing of the epoxy mortar. . . . .	178
6.33.	Sealing the negatives: a) pouring the epoxy mortar; b) sealed negative; and c) final aspect of the prototype. . . . .	178
6.34.	Permanent instrumentation of the small-scale prototype: position of electric strain gauges at the midspan section. . . . .	178
6.35.	Axial strains measured upon the removal of the precamber props (position 0 mm corresponds to $\varepsilon_c1$ to $\varepsilon_c3$ , <i>i.e.</i> the top of the deck). . . . .	180
6.36.	Small-scale prototype serviceability tests: midspan deflections for load con- figuration 1: a) load stage 1; b) load stage 2; and c) load stage 3. . . . .	181
6.37.	Small-scale prototype serviceability tests: load configuration 2. . . . .	181
6.38.	Small-scale prototype serviceability tests: structure loaded in load configu- ration 2. . . . .	182
6.39.	Small-scale prototype serviceability tests with prestress: a) positioning of the prestress rebars; b) applying prestress; prestress rebar c) without and d) with applied force. . . . .	182
6.40.	Small-scale prototype serviceability tests with prestress: midspan average deflection <i>vs.</i> prestress force per rebar. . . . .	183
6.41.	Small-scale prototype failure test: test configuration. . . . .	184
6.42.	Small-scale prototype failure test: load <i>vs.</i> midspan average deflections up to failure. . . . .	185
6.43.	Small-scale prototype failure test: load <i>vs.</i> midspan average strains up to failure. . . . .	185

6.44.	Small-scale prototype failure test: (a) prototype after failure; (b) GFRP main girder web-flange junction failure; (c) complete separation of web and flange followed by web buckling; and (d) detail of web-flange separation. . . . .	185
6.45.	Small-scale prototype failure test: deformed configuration immediately prior to failure. . . . .	186
6.46.	Prestress: rotation around the theoretical support. . . . .	188
6.47.	Small-scale prototype serviceability behaviour with prestress: experimental test <i>vs.</i> analytical simulation. . . . .	189
6.48.	Small-scale prototype failure behaviour: midspan deflections. Experimental tests and analytical predictions. . . . .	191
6.49.	Analytical prediction of the axial ( $\sigma$ ) and shear ( $\tau$ ) stress distributions along the depth of the web for $x = 1.025$ m. . . . .	193
6.50.	Tri-dimensional illustration of the FE model. . . . .	193
6.51.	Small-scale prototype serviceability behaviour without prestress for load configuration 1: a) load stage 1; b) load stage 2; and c) load stage 3. Experimental test <i>vs.</i> FE model prediction. . . . .	194
6.52.	Small-scale prototype serviceability behaviour with prestress: experimental results <i>vs.</i> analytical and numerical predictions. . . . .	195
6.53.	Small-scale prototype flexural behaviour up to failure: midspan deflections. Experimental tests, analytical and numerical predictions. . . . .	196
6.54.	Small-scale prototype flexural behaviour up to failure: midspan average strains results for a) experimental tests, b) analytical and c) numerical predictions. . . . .	197
6.55.	Small-scale prototype failure behaviour: analytical and numerical axial ( $\sigma$ ) and shear ( $\tau$ ) stress distributions along the depth of the web for $x = 1.025$ m. . . . .	198
6.56.	Small-scale prototype modal identification tests: top plan view and instrumentation (S# load points and A# acceleration measurement points). . . . .	200
6.57.	Small-scale prototype modal identification tests: example of impact load being applied. . . . .	201
6.58.	Small-scale prototype modal identification tests: impact at point S1 and corresponding deck acceleration recorded at points A1 and A5. . . . .	201
6.59.	Small-scale prototype modal identification tests, output-only method: example of the FFT of the half-sum and half-difference of accelerations at A6 and A10 for an impact load at S2. . . . .	202
6.60.	Small-scale prototype modal identification tests: example of FRF amplitude relating excitation at point S2 with acceleration measured at point A6. Measured and synthesized in range 0–40 Hz, and coherence. . . . .	203
6.61.	Small-scale prototype modal identification tests: mode shapes attained (normalized to maximum deformation). . . . .	204
6.62.	Small-scale prototype modal identification: mode shapes (normalized to maximum deformation). Experimental results <i>vs.</i> analytical predictions. . . . .	209
6.63.	Small-scale prototype modal identification: mode shapes (normalized to maximum deformation). Experimental results <i>vs.</i> analytical and numerical predictions. . . . .	210
6.64.	Pedestrian induced actions: experimental evaluation of load-time functions. . . . .	213
6.65.	Load-time functions for pedestrian action (slow, normal and fast walk): tests <i>vs.</i> Bachmann and Ammann. . . . .	213
6.66.	Small-scale prototype behaviour under pedestrian loads tests: instrumentation and motion positioning (dimensions in meters). . . . .	214
6.67.	Small-scale prototype one pedestrian test. . . . .	215



6.68.	Small-scale prototype one pedestrian tests: accelerations attained at A3 for slow walk at the cantilever. . . . .	215
6.69.	Small-scale prototype crowd test. . . . .	217
6.70.	Small-scale prototype crowd tests: vertical accelerations. . . . .	217
6.71.	Small-scale prototype crowd tests: horizontal accelerations. . . . .	217
6.72.	Small-scale prototype crowd tests: expected vertical accelerations (RMS). Experimental tests <i>vs.</i> ISO 10137. . . . .	218
6.73.	Small-scale prototype crowd tests: expected horizontal accelerations (RMS). Experimental tests <i>vs.</i> ISO 10137. . . . .	218
6.74.	Small-scale prototype one pedestrian tests: accelerations attained at A3 for slow walk at the cantilever. Experimental and numerical results. . . . .	219
6.75.	Small-scale prototype one pedestrian tests: accelerations attained at A1 for fast walk at the centre. Experimental and numerical results. . . . .	219
6.76.	Small-scale prototype one pedestrian tests: accelerations attained at A3 for fast walk at the centre. Experimental and numerical results. . . . .	219
6.77.	Small-scale prototype one pedestrian tests: maximum accelerations attained for slow walk at the centred path. . . . .	220
6.78.	Small-scale prototype one pedestrian tests: maximum accelerations attained for normal walk at the centred path. . . . .	220
6.79.	Small-scale prototype one pedestrian tests: maximum accelerations attained for fast walk at the centred path. . . . .	221
6.80.	Small-scale prototype one pedestrian tests: maximum accelerations attained for slow walk at the eccentric path. . . . .	221
6.81.	Small-scale prototype one pedestrian tests: maximum accelerations attained for normal walk at the eccentric path. . . . .	221
6.82.	Small-scale prototype one pedestrian tests: maximum accelerations attained for fast walk at the eccentric path. . . . .	221
6.83.	Evolution of the elasticity and shear moduli of the GFRP material with time according to different creep models. . . . .	225
6.84.	Small-scale prototype creep tests: instrumentation at midspan. . . . .	228
6.85.	Small-scale prototype creep tests: load configuration. . . . .	228
6.86.	Small-scale prototype loaded for creep test: a) test 1; b) test 2; and c) test 3. . . . .	229
6.87.	Small-scale prototype creep test 1: environmental conditions — temperature and relative humidity. . . . .	230
6.88.	Small-scale prototype creep test 1: evolution of the midspan deflections and Findley's power law regressions. . . . .	230
6.89.	Small-scale prototype creep test 1: evolution of strains at midspan and Findley's power law regressions. . . . .	231
6.90.	Small-scale prototype creep test 1: axial strain distributions across the depth of the cross-section and neutral axis depth, measured from the top of the SFRSCC slab at the beginning and end of the test. . . . .	231
6.91.	Small-scale prototype creep test 2: evolution of the temperature. . . . .	232
6.92.	Small-scale prototype creep test 2: evolution of midspan deflections and Findley's power law regressions. . . . .	232
6.93.	Small-scale prototype creep test 3: environmental conditions — temperature and relative humidity. . . . .	233
6.94.	Small-scale prototype creep test 3: evolution of midspan deflections and Findley's power law regressions. . . . .	233
6.95.	Small-scale prototype creep tests: comparison between the creep deflections of all tests. . . . .	233

6.96.	Small-scale prototype creep test 1: analytical predictions <i>vs.</i> experimental results. . . . .	236
6.97.	Small-scale prototype creep test 2: analytical predictions <i>vs.</i> experimental results. . . . .	236
6.98.	Small-scale prototype creep test 3: analytical predictions <i>vs.</i> experimental results. . . . .	236
6.99.	Small-scale prototype creep test 1 long-term predictions: analytical <i>vs.</i> regressions. . . . .	237
6.100.	Small-scale prototype creep test 2 long-term predictions: analytical <i>vs.</i> regressions. . . . .	237
6.101.	Small-scale prototype creep test 3 long-term predictions: analytical <i>vs.</i> regressions. . . . .	237
6.102.	Small-scale prototype creep test 1: experimental and predicted axial strain distributions ( $\varepsilon_{EXP}$ and $\varepsilon_{MOD}$ , respectively) across the depth of the cross-section and neutral axis depth, measured from the top of the SFRSCC slab ( $NA_{EXP}$ and $NA_{MOD}$ , respectively). . . . .	238
7.1.	Full-scale prototype cross-section. . . . .	242
7.2.	Side- and A-A section-view of the full-scale prototype. . . . .	242
7.3.	Details of the connections between main and secondary girders of the full-scale prototype. . . . .	243
7.4.	Design web shear stress ( $\tau_{sd}$ ) distribution at the support section. . . . .	246
7.5.	Idealized stress-strain relationship of the SFRSCC. . . . .	249
7.6.	Axial stress distribution over the SFRSCC slab at transverse failure. . . . .	250
7.7.	Beginning of the pultrusion of the I400 profiles. . . . .	252
7.8.	Pultrusion of the I400 profiles in progress. . . . .	252
7.9.	Assembled girders. . . . .	253
7.10.	Girders on the transport truck. . . . .	253
7.11.	Construction of the formwork. . . . .	253
7.12.	Formwork ready for the cast. . . . .	253
7.13.	Casting of the SFRSCC slab. . . . .	254
7.14.	Regularization of the slab surface. . . . .	254
7.15.	Final aspect of the slab after being cast. . . . .	254
7.16.	Concrete jackets and stainless steel connectors. . . . .	254
7.17.	Drilling of the SFRSCC slab. . . . .	255
7.18.	Installation of the stainless steel connectors. . . . .	255
7.19.	Application of the epoxy adhesive layer. . . . .	255
7.20.	Installation of the girders on the deck. . . . .	255
7.21.	Installation of the washers and nuts. . . . .	256
7.22.	Aspect of the assembled structure. . . . .	256
7.23.	Rotation of the full-scale prototype. . . . .	256
7.24.	Final aspect of the full-scale prototype. . . . .	256
7.25.	Serviceability tests on the full-scale prototype: load configurations. . . . .	258
7.26.	Axial strain gauges positioning at the midspan section of the full-scale prototype. . . . .	258
7.27.	Full-scale prototype serviceability tests: scheme of load configurations. . . . .	259
7.28.	Tri-dimensional view of the FE model of the full-scale prototype. . . . .	261
7.29.	Full-scale prototype modal identification tests: instrumentation (dimensions in mm). . . . .	263
7.30.	Full-scale prototype modal identification test ongoing. . . . .	264

7.31.	Full-scale prototype modal identification tests: accelerations at positions A1 and A2. . . . .	264
7.32.	Full-scale prototype modal identification tests: accelerations at positions A3 and A4. . . . .	264
7.33.	Full-scale prototype modal identification tests: FFT of the half-sum and half-difference of accelerations at A1 and A2. . . . .	265
7.34.	Full-scale prototype modal identification tests: FFT of the half-sum and half-difference of accelerations at A3 and A4. . . . .	265
7.35.	Full-scale prototype FE model: modal shapes. . . . .	267
7.36.	Full-scale prototype response under pedestrian behaviour tests: instrumentation (dimensions in mm). . . . .	268
7.37.	Full-scale prototype one pedestrian tests: pedestrian running in the eccentric path. . . . .	268
7.38.	Full-scale prototype one pedestrian tests: accelerations at position A1 when the pedestrian walked normally in the centred and eccentric paths. . . . .	269
7.39.	Full-scale prototype crowd tests in progress. . . . .	270
7.40.	Full-scale prototype crowd tests: accelerations at A1 and A2. . . . .	271
7.41.	Full-scale prototype crowd tests: accelerations at A1 and A2. . . . .	271
7.42.	Full-scale prototype crowd tests: comparison between the experimental expected vertical accelerations (RMS) and the ISO 10137 limits. . . . .	271
7.43.	Full-scale prototype one pedestrian tests: accelerations at A1 for normal walk in the centred path, experimental and numerical results. . . . .	272
7.44.	Full-scale prototype one pedestrian tests: accelerations at A1 for normal walk in the eccentric path, experimental and numerical results. . . . .	272
7.45.	Full-scale prototype one pedestrian tests: maximum accelerations for slow walk in the centred path, experimental and numerical results. . . . .	274
7.46.	Full-scale prototype one pedestrian tests: maximum accelerations for normal walk in the centred path, experimental and numerical results. . . . .	274
7.47.	Full-scale prototype one pedestrian tests: maximum accelerations for fast walk in the centred path, experimental and numerical results. . . . .	274
7.48.	Full-scale prototype one pedestrian tests: maximum accelerations for run in the centred path, experimental and numerical results. . . . .	274
7.49.	Full-scale prototype one pedestrian tests: maximum accelerations for slow walk in the eccentric path, experimental and numerical results. . . . .	275
7.50.	Full-scale prototype one pedestrian tests: maximum accelerations for normal walk in the eccentric path, experimental and numerical results. . . . .	275
7.51.	Full-scale prototype one pedestrian tests: maximum accelerations for fast walk in the eccentric path, experimental and numerical results. . . . .	275
7.52.	Full-scale prototype one pedestrian tests: maximum accelerations for run in the eccentric path, experimental and numerical results. . . . .	275
7.53.	Full-scale prototype loaded in the creep test. . . . .	276
7.54.	Full-scale prototype creep test: air temperature ( $T$ ) and relative humidity ( $RH$ ) during the test period. . . . .	277
7.55.	Full-scale prototype creep test: experimental results and Findley's power law fitting. . . . .	277
7.56.	Full-scale prototype creep test: experimental results <i>vs.</i> analytical predictions. . . . .	279
7.57.	Full-scale prototype creep test: long-term midspan deflection predictions. . . . .	279
7.58.	Full-scale prototype midspan deflection creep predictions with 20°C and 25°C average temperature. . . . .	280



C.26.	Small-scale prototype one pedestrian tests: accelerations attained at A16 for normal walk at the centred path. Experimental and numerical results. .	326
C.27.	Small-scale prototype one pedestrian tests: accelerations attained at A17 for normal walk at the centred path. Experimental and numerical results. .	326
C.28.	Small-scale prototype one pedestrian tests: accelerations attained at A18 for normal walk at the centred path. Experimental and numerical results. .	326
C.29.	Small-scale prototype one pedestrian tests: accelerations attained at A19 for normal walk at the centred path. Experimental and numerical results. .	327
C.30.	Small-scale prototype one pedestrian tests: accelerations attained at A20 for normal walk at the centred path. Experimental and numerical results. .	327
C.31.	Small-scale prototype one pedestrian tests: accelerations attained at A1 for normal walk at the eccentric path. Experimental and numerical results. . .	327
C.32.	Small-scale prototype one pedestrian tests: accelerations attained at A2 for normal walk at the eccentric path. Experimental and numerical results. . .	327
C.33.	Small-scale prototype one pedestrian tests: accelerations attained at A3 for normal walk at the eccentric path. Experimental and numerical results. . .	328
C.34.	Small-scale prototype one pedestrian tests: accelerations attained at A4 for normal walk at the eccentric path. Experimental and numerical results. . .	328
C.35.	Small-scale prototype one pedestrian tests: accelerations attained at A5 for normal walk at the eccentric path. Experimental and numerical results. . .	328
C.36.	Small-scale prototype one pedestrian tests: accelerations attained at A16 for normal walk at the eccentric path. Experimental and numerical results.	328
C.37.	Small-scale prototype one pedestrian tests: accelerations attained at A17 for normal walk at the eccentric path. Experimental and numerical results.	328
C.38.	Small-scale prototype one pedestrian tests: accelerations attained at A18 for normal walk at the eccentric path. Experimental and numerical results.	328
C.39.	Small-scale prototype one pedestrian tests: accelerations attained at A19 for normal walk at the eccentric path. Experimental and numerical results.	329
C.40.	Small-scale prototype one pedestrian tests: accelerations attained at A20 for normal walk at the eccentric path. Experimental and numerical results.	329
C.41.	Small-scale prototype one pedestrian tests: accelerations attained at A1 for fast walk at the centred path. Experimental and numerical results. . . . .	329
C.42.	Small-scale prototype one pedestrian tests: accelerations attained at A2 for fast walk at the centred path. Experimental and numerical results. . . . .	329
C.43.	Small-scale prototype one pedestrian tests: accelerations attained at A3 for fast walk at the centred path. Experimental and numerical results. . . . .	330
C.44.	Small-scale prototype one pedestrian tests: accelerations attained at A4 for fast walk at the centred path. Experimental and numerical results. . . . .	330
C.45.	Small-scale prototype one pedestrian tests: accelerations attained at A5 for fast walk at the centred path. Experimental and numerical results. . . . .	330
C.46.	Small-scale prototype one pedestrian tests: accelerations attained at A16 for fast walk at the centred path. Experimental and numerical results. . . .	330
C.47.	Small-scale prototype one pedestrian tests: accelerations attained at A17 for fast walk at the centred path. Experimental and numerical results. . . .	330
C.48.	Small-scale prototype one pedestrian tests: accelerations attained at A18 for fast walk at the centred path. Experimental and numerical results. . . .	330
C.49.	Small-scale prototype one pedestrian tests: accelerations attained at A19 for fast walk at the centred path. Experimental and numerical results. . . .	331
C.50.	Small-scale prototype one pedestrian tests: accelerations attained at A20 for fast walk at the centred path. Experimental and numerical results. . . .	331

C.51.	Small-scale prototype one pedestrian tests: accelerations attained at A1 for fast walk at the eccentric path. Experimental and numerical results. . . . .	331
C.52.	Small-scale prototype one pedestrian tests: accelerations attained at A2 for fast walk at the eccentric path. Experimental and numerical results. . . . .	331
C.53.	Small-scale prototype one pedestrian tests: accelerations attained at A3 for fast walk at the eccentric path. Experimental and numerical results. . . . .	332
C.54.	Small-scale prototype one pedestrian tests: accelerations attained at A4 for fast walk at the eccentric path. Experimental and numerical results. . . . .	332
C.55.	Small-scale prototype one pedestrian tests: accelerations attained at A5 for fast walk at the eccentric path. Experimental and numerical results. . . . .	332
C.56.	Small-scale prototype one pedestrian tests: accelerations attained at A16 for fast walk at the eccentric path. Experimental and numerical results. . .	332
C.57.	Small-scale prototype one pedestrian tests: accelerations attained at A17 for fast walk at the eccentric path. Experimental and numerical results. . .	333
C.58.	Small-scale prototype one pedestrian tests: accelerations attained at A18 for fast walk at the eccentric path. Experimental and numerical results. . .	333
C.59.	Small-scale prototype one pedestrian tests: accelerations attained at A19 for fast walk at the eccentric path. Experimental and numerical results. . .	333
C.60.	Small-scale prototype one pedestrian tests: accelerations attained at A20 for fast walk at the eccentric path. Experimental and numerical results. . .	333
D.1.	Full-scale prototype one pedestrian tests: accelerations attained at A1 for slow walk at the centred path. Experimental and numerical results. . . . .	335
D.2.	Full-scale prototype one pedestrian tests: accelerations attained at A2 for slow walk at the centred path. Experimental and numerical results. . . . .	335
D.3.	Full-scale prototype one pedestrian tests: accelerations attained at A3 for slow walk at the centred path. Experimental and numerical results. . . . .	336
D.4.	Full-scale prototype one pedestrian tests: accelerations attained at A4 for slow walk at the centred path. Experimental and numerical results. . . . .	336
D.5.	Full-scale prototype one pedestrian tests: accelerations attained at A1 for slow walk at the eccentric path. Experimental and numerical results. . . . .	336
D.6.	Full-scale prototype one pedestrian tests: accelerations attained at A2 for slow walk at the eccentric path. Experimental and numerical results. . . . .	336
D.7.	Full-scale prototype one pedestrian tests: accelerations attained at A3 for slow walk at the eccentric path. Experimental and numerical results. . . . .	337
D.8.	Full-scale prototype one pedestrian tests: accelerations attained at A4 for slow walk at the eccentric path. Experimental and numerical results. . . . .	337
D.9.	Full-scale prototype one pedestrian tests: accelerations attained at A1 for normal walk at the centred path. Experimental and numerical results. . . . .	337
D.10.	Full-scale prototype one pedestrian tests: accelerations attained at A2 for normal walk at the centred path. Experimental and numerical results. . . . .	337
D.11.	Full-scale prototype one pedestrian tests: accelerations attained at A3 for normal walk at the centred path. Experimental and numerical results. . . . .	338
D.12.	Full-scale prototype one pedestrian tests: accelerations attained at A4 for normal walk at the centred path. Experimental and numerical results. . . . .	338
D.13.	Full-scale prototype one pedestrian tests: accelerations attained at A1 for normal walk at the eccentric path. Experimental and numerical results. . . . .	338
D.14.	Full-scale prototype one pedestrian tests: accelerations attained at A2 for normal walk at the eccentric path. Experimental and numerical results. . . . .	338

D.15. Full-scale prototype one pedestrian tests: accelerations attained at A3 for normal walk at the eccentric path. Experimental and numerical results. . .	339
D.16. Full-scale prototype one pedestrian tests: accelerations attained at A4 for normal walk at the eccentric path. Experimental and numerical results. . .	339
D.17. Full-scale prototype one pedestrian tests: accelerations attained at A1 for fast walk at the centred path. Experimental and numerical results. . . . .	339
D.18. Full-scale prototype one pedestrian tests: accelerations attained at A2 for fast walk at the centred path. Experimental and numerical results. . . . .	339
D.19. Full-scale prototype one pedestrian tests: accelerations attained at A3 for fast walk at the centred path. Experimental and numerical results. . . . .	340
D.20. Full-scale prototype one pedestrian tests: accelerations attained at A4 for fast walk at the centred path. Experimental and numerical results. . . . .	340
D.21. Full-scale prototype one pedestrian tests: accelerations attained at A1 for fast walk at the eccentric path. Experimental and numerical results. . . . .	340
D.22. Full-scale prototype one pedestrian tests: accelerations attained at A2 for fast walk at the eccentric path. Experimental and numerical results. . . . .	340
D.23. Full-scale prototype one pedestrian tests: accelerations attained at A3 for fast walk at the eccentric path. Experimental and numerical results. . . . .	341
D.24. Full-scale prototype one pedestrian tests: accelerations attained at A4 for fast walk at the eccentric path. Experimental and numerical results. . . . .	341
D.25. Full-scale prototype one pedestrian tests: accelerations attained at A1 for run at the centred path. Experimental and numerical results. . . . .	341
D.26. Full-scale prototype one pedestrian tests: accelerations attained at A2 for run at the centred path. Experimental and numerical results. . . . .	341
D.27. Full-scale prototype one pedestrian tests: accelerations attained at A3 for run at the centred path. Experimental and numerical results. . . . .	342
D.28. Full-scale prototype one pedestrian tests: accelerations attained at A4 for run at the centred path. Experimental and numerical results. . . . .	342
D.29. Full-scale prototype one pedestrian tests: accelerations attained at A1 for run at the eccentric path. Experimental and numerical results. . . . .	342
D.30. Full-scale prototype one pedestrian tests: accelerations attained at A2 for run at the eccentric path. Experimental and numerical results. . . . .	342
D.31. Full-scale prototype one pedestrian tests: accelerations attained at A3 for run at the eccentric path. Experimental and numerical results. . . . .	342
D.32. Full-scale prototype one pedestrian tests: accelerations attained at A4 for run at the eccentric path. Experimental and numerical results. . . . .	342





# List of Tables

2.1.	Typical properties of the most common fibre reinforcements. . . . .	12
2.2.	Typical properties of the most common thermosetting resins. . . . .	14
2.3.	Typical mechanical properties of GFRP pultruded profiles. . . . .	19
2.4.	Typical physical and thermal properties of GFRP pultruded profiles. . . .	20
2.5.	Recommend values of $\psi$ for footbridges. . . . .	30
2.6.	Parameters of pedestrian motion proposed by Bachmann and Ammann. . .	31
2.7.	Acceleration ranges for different comfort levels. . . . .	36
3.1.	Summary of activities and tasks of the Pontalumis project. . . . .	40
3.2.	Geometrical properties of the iterations of the parametric study regarding the GFRP profiles. . . . .	46
3.3.	Summary of the parametric study results regarding the geometry of the GFRP profiles. . . . .	48
4.1.	Coupon tensile tests: summary of results for I200. . . . .	53
4.2.	Coupon tensile tests: summary of results for I400. . . . .	56
4.3.	Coupon tensile tests: I200 <i>vs.</i> I400. . . . .	57
4.4.	Coupon compressive tests: summary of results for I200 web specimens. . .	60
4.5.	Coupon compressive tests: summary of results for I200 flange specimens. .	60
4.6.	Coupon compressive tests: summary of results for I400 web specimens. . .	62
4.7.	Coupon compressive tests: summary of results for I400 flange specimens. .	62
4.8.	Coupon compressive tests: I200 <i>vs.</i> I400. . . . .	63
4.9.	Coupon off–axis tensile tests: summary of results. . . . .	66
4.10.	Coupon flexural tests: summary of results of the web specimens (I200). . .	68
4.11.	Coupon flexure tests: summary of results of the flange specimens (I200). .	69
4.12.	Coupon interlaminar shear tests: summary of results (I200). . . . .	71
4.13.	Summary of the main mechanical properties of the GFRP material for both I200 and I400 profiles: experimental data and values declared by the manufacturer. . . . .	71
4.14.	Full–scale flexural serviceability tests: spans tested, maximum loads ( $F_{max}$ ) and midspan deflection ( $\delta_{max}$ ) attained. . . . .	73
4.15.	Geometrical properties of the profile sections. . . . .	74
4.16.	Full–scale flexural serviceability tests: results and comparison with coupon testing. . . . .	75
4.17.	Full–scale flexural failure tests: determination of the elasticity modulus ( $E_{full}$ ) with axial strain measurements (I200). . . . .	79
4.18.	Full–scale flexural failure tests: determination of the elasticity modulus ( $E_{full}$ ) with axial strain measurements for I400 specimens. . . . .	85
4.19.	Full–scale flexural failure tests: summary of main results for the I400 specimens. . . . .	89

4.20.	Cross-section properties of the profiles with the mechanical properties derived from coupon and full-scale testing. . . . .	90
4.21.	GFRP profiles serviceability behaviour: stiffness ( $K$ ) derived from experimental and analytical results. . . . .	92
4.22.	Critical stresses of the several walls of the I200 cross-section. . . . .	94
4.23.	Critical stress of the I200 cross-section: experimental results <i>vs.</i> analytical predictions. . . . .	94
4.24.	Material strength and critical stress for each local failure mode. . . . .	96
4.25.	Failure load and forces for each specimen considering each failure mode. . .	98
4.26.	Component mix proportions for the SFRSCC used in the small- and full-scale prototypes. . . . .	107
4.27.	Summary of the compressive tests on small-scale prototype SFRSCC cube specimens. . . . .	108
4.28.	Summary of the test results on small-scale prototype SFRSCC material cylinder specimens. . . . .	110
4.29.	Summary of the flexural test results on full-scale prototype SFRSCC material coupons. . . . .	111
4.30.	Summary of the SFRSCC main mechanical properties derived from coupon testing. . . . .	111
4.31.	Flexural tests on SFRSCC slabs: summary of results. . . . .	114
4.32.	Summary of the mechanical properties of the square tubular GFRP profiles. .	115
4.33.	Mechanical properties of the L60×8 GFRP section provided by the manufacturer. . . . .	115
4.34.	Conventional concrete, used in the concrete jackets of the small-scale prototype, component mix proportion. . . . .	116
5.1.	Accelerated aging: series, number of specimens and number of cycles. . . .	124
5.2.	Shear connection tests: summary of all preliminary series results. . . . .	136
5.3.	Shear connection tests: comparison of the results for all P–M series. . . .	136
5.4.	Shear connection tests: summary of all un-aged series results. . . . .	141
5.5.	Shear connection test: summary of the results of series aged with thermal cycles. . . . .	147
5.6.	Shear connection tests: summary of the results of series aged with wet–dry cycles. . . . .	154
5.7.	Shear connection FE model, thermal cycles: calibration parameters, numerical results and comparison with experimental results. . . . .	162
5.8.	Shear connection FE model, wet–dry cycles: calibration parameters, numerical results and comparison with experimental data. . . . .	164
6.1.	Small-scale prototype serviceability tests with prestress: midspan average deflection ( $\delta_{ms}$ ) and stiffness ( $K$ ) for applied loads and prestress. . . . .	183
6.2.	Small-scale prototype failure test: failure load ( $F_u$ ), average midspan deflection at failure ( $\delta_{ms-u}$ ), stiffness ( $K$ ) and neutral axis position ( $NA$ ) with reference to the top of the cross-section. . . . .	184
6.3.	Small-scale prototype serviceability behaviour — load configuration 2: experimental and analytical estimates of average midspan deflection ( $\delta_{ms}$ ), stiffness ( $K$ ), curvature ( $\chi$ ) and neutral axis position ( $NA$ ) with reference to the top of the cross-section. . . . .	187

6.4.	Small-scale prototype serviceability behaviour with prestress: midspan average deflection ( $\delta_{ms}$ ) and stiffness ( $K$ ) for loads and prestress. Experimental test <i>vs.</i> analytical simulation. . . . .	190
6.5.	Small-scale prototype failure behaviour: failure load ( $F_u$ ), midspan average deflection at failure ( $\delta_{ms-u}$ ), stiffness ( $K$ ) and neutral axis position ( $NA$ ). Experimental test and analytical simulations. . . . .	191
6.6.	Small-scale prototype serviceability behaviour without prestress for load configuration 2: average midspan deflection ( $\delta_{ms}$ ), stiffness ( $K$ ), curvature ( $\chi$ ) and neutral axis position ( $NA$ ) with reference to the top of the cross-section. Experimental results, analytical and numerical predictions. . . . .	195
6.7.	Small-scale prototype serviceability behaviour with prestress: midspan average deflection ( $\delta_{ms}$ ) and stiffness ( $K$ ) for loads and prestress. Experimental test <i>vs.</i> analytical simulation. . . . .	196
6.8.	Small-scale prototype failure behaviour: failure load ( $F_u$ ), midspan average deflection at failure ( $\delta_{ms-u}$ ), stiffness ( $K$ ) and neutral axis position ( $NA$ ). Experimental test, analytical and numerical simulations. . . . .	198
6.9.	Numerical failure analysis for the small-scale prototype — maximum Tsai-Hill index for GFRP laminates and maximum stresses in the SFRSCC. . . . .	199
6.10.	Small-scale prototype modal identification tests: vibration frequencies and nature of identified modes (output-only method). . . . .	202
6.11.	Small-scale prototype modal identification tests: vibration frequencies, damping ratios and nature of identified modes (input-output method). . . . .	204
6.12.	Small-scale prototype mode frequencies: experimental results <i>vs.</i> analytical and numerical (FE) predictions. . . . .	210
6.13.	Main characteristics of pedestrian motion: experimental tests <i>vs.</i> Bachmann and Ammann. . . . .	214
6.14.	Small-scale prototype one pedestrian tests: maximum accelerations (mean $\pm$ standard deviation). . . . .	216
6.15.	Small-scale prototype one pedestrian tests: experimental maximum accelerations (average $\pm$ standard deviation) <i>vs.</i> numerical predictions. . . . .	220
6.16.	Parameters of the GFRP creep model proposed by Bank. . . . .	224
6.17.	Parameters of the GFRP creep models derived from EuroComp. . . . .	224
6.18.	Time-dependent moduli proposed by the Italian guidelines. . . . .	225
6.19.	Small-scale prototype creep tests: relevant data. . . . .	229
6.20.	Small-scale prototype creep tests: Findley power law regression parameters. . . . .	234
6.21.	Small-scale prototype predictions of long-term creep deflections: analytical model and regressions. . . . .	238
7.1.	Design loads and partial safety factors considered in the design of the full-scale footbridge prototype. . . . .	243
7.2.	Material characteristic strengths relevant for the design (MPa). . . . .	244
7.3.	Summary of ULS design in the longitudinal direction. . . . .	248
7.4.	Summary of ULS design in the transverse direction. . . . .	251
7.5.	Summary of SLS design. . . . .	252
7.6.	Summary of the results of the serviceability tests on the full-scale prototype. . . . .	259
7.7.	Full-scale prototype serviceability tests: load parameters. . . . .	260
7.8.	Full-scale prototype serviceability tests: analytical <i>vs.</i> experimental results. . . . .	260
7.9.	Full-scale prototype serviceability tests: numerical, analytical and experimental results. . . . .	262
7.10.	Full-scale prototype modal identification tests: summary of results. . . . .	265

7.11.	Full-scale prototype modal identification tests: experimental results <i>vs.</i> analytical predictions. . . . .	266
7.12.	Full-scale prototype modal identification tests: experimental results, analytical and numerical predictions. . . . .	266
7.13.	Full-scale prototype one pedestrian tests: summary of the experimental results.	269
7.14.	Full-scale prototype one pedestrian tests: experimental results <i>vs.</i> numerical predictions. . . . .	273
A.1.	Coupon tensile tests: results for I200. . . . .	303
A.2.	Coupon tensile tests: results for I400. . . . .	304
A.3.	Coupon compressive tests: results for I200 web specimens. . . . .	304
A.4.	Coupon compressive tests: results for I200 flange specimens. . . . .	305
A.5.	Coupon compressive tests: results for I400 web specimens. . . . .	305
A.6.	Coupon compressive tests: results for I400 flange specimens. . . . .	305
A.7.	Coupon off-axis tensile tests results. . . . .	306
A.8.	Coupon flexural tests: results of the web specimens (I200). . . . .	307
A.9.	Coupon flexure tests: results of the flange specimens (I200). . . . .	307
A.10.	Coupon interlaminar shear tests results (I200). . . . .	308
A.11.	Results of the compressive tests on small-scale prototype SFRSCC cube specimens. . . . .	308
A.12.	Results of the compressive tests on small-scale prototype conventional concrete (jackets) cube specimens. . . . .	309
A.13.	Test results on small-scale prototype SFRSCC material cylinder specimens.	309
B.1.	GFRP-SFRSCC shear connection tests: results for series P-A. . . . .	311
B.2.	GFRP-SFRSCC shear connection tests: results for series P-M1. . . . .	312
B.3.	GFRP-SFRSCC shear connection tests: results for series P-M2. . . . .	312
B.4.	GFRP-SFRSCC shear connection tests: results for series P-M3. . . . .	313
B.5.	GFRP-SFRSCC shear connection tests: results for series P-M4. . . . .	313
B.6.	GFRP-SFRSCC shear connection tests: results for series P-AM. . . . .	314
B.7.	GFRP-SFRSCC shear connection tests: results for series A. . . . .	314
B.8.	GFRP-SFRSCC shear connection tests: results for series M. . . . .	315
B.9.	GFRP-SFRSCC shear connection tests: results for series AM. . . . .	315
B.10.	GFRP-SFRSCC shear connection tests: results for series A-Th-T1. . . . .	316
B.11.	GFRP-SFRSCC shear connection tests: results for series A-Th-T2. . . . .	316
B.12.	GFRP-SFRSCC shear connection tests: results for series A-Th-T3. . . . .	317
B.13.	GFRP-SFRSCC shear connection tests: results for series A-H-T1. . . . .	317
B.14.	GFRP-SFRSCC shear connection tests: results for series A-H-T2. . . . .	318
B.15.	GFRP-SFRSCC shear connection tests: results for series A-H-T3. . . . .	318
B.16.	GFRP-SFRSCC shear connection tests: results for series AM-H-T3. . . . .	319

# Notation

## Roman Lower Case

$1,2$	laminate direction
$a$	geometrical parameter; half-buckle wave length
$a_{free}^{ss}$	length of half-wave bucke of free-simply supported plate
$a_{full}$	linear regression parameter
$a_{RMS}$	root mean squared acceleration
$a_{v,max}$	maximum vertical acceleration
$b$	geometrical parameter, cross-section width
$b_{bot}$	GFRP profile bottom flange's width
$b_{cj}$	concrete jacket width
$b_f$	plate width
$b_{full}$	linear regression parameter
$b_{is}$	interlaminar shear specimen width
$b_s$	specimen width
$b_{top}$	GFRP profile top flange's width
$ct$	SFRSCC deck transverse cantilever
$di$	deflection at position $i$
$d$	pedestrian traffic density; distance between support and pre-stress rebar rotation point; thickness of the deck.
$d_{cr}$	cracking midspan deflection; critical displacement
$d_{cy}$	concrete cylinder diameter
$d_f$	coupon flexural test displacement
$d_{is}$	coupon interlaminar shear test displacement
$d_{ms}$	midspan deflection
$d_{post-cr}$	post-cracking midspan deflection
$d_{soft}$	softening displacement
$d_u$	ultimate displacement
$d_w$	GFRP web depth
$ds$	connection specimens free length
$dx$	infinitesimal length
$e$	prestress eccentricity
$f$	vibration frequency
$f_0$	fundamental vibration frequency
$f_{au}$	tensile strength of the epoxy adhesive
$f_{bending}$	fundamental bending vibration frequency
$f_c$	concrete compressive strength

$f_{ck}$	concrete characteristic compressive strength
$f_{cm}$	concrete average compressive strength
$f_{cr,k}$	characteristic cracking stress
$f_{cr}$	cracking stress
$f_{eq,i}$	SFRSCC $i^{th}$ equivalent flexural tensile strength
$f_{m,c}$	compressive strength of the epoxy mortar
$f_{m,f}$	flexural strength of the epoxy mortar
$f_n$	vibration frequency of mode $n$
$f_{post-cr}$	post-cracking stress
$f_{R,i}$	SFRSCC $i^{th}$ residual flexural tensile strength
$f_{R,ik}$	characteristic SFRSCC $i^{th}$ residual flexural tensile strength
$f_s$	pedestrian action frequency
$f_{torsion}$	fundamental torsional vibration frequency
$f_{yk}$	characteristic yielding stress of steel
$g_k$	self-weight
$h$	GFRP profile's height
$h_0$	equivalent thickness
$h_c$	SFRSCC deck thickness
$h_t$	height of the cross-section
$k$	shear area factor; boundary conditions coefficient; interface stiffness; thickness factor
$k_\theta$	rotational spring stiffness
$k_{LT}$	shear buckling coefficient
$k_p$	pedestrian action dynamic impact factor
$k_w$	warping boundary conditions coefficient
$l$	prestress rebars' free length
$l_s$	pedestrian stride length
$l_t$	SFRSCC deck width
$l_s$	connection specimens slab length
$m$	cross-section mass; Findely's law stress dependent coefficient
$m_\sigma$	empirical stress dependent coefficient
$m'_\sigma$	empirical stress dependent coefficient
$m_\tau$	empirical stress dependent coefficient
$m'_\tau$	empirical stress dependent coefficient
$n$	vibration mode number; Findely's law stress independent coefficient
$n_E$	elasticity modulus stress independent coefficient
$n_G$	shear modulus stress independent coefficient
$p_n$	vibration frequency of mode $n$
$q_{cp}$	quasi-permanent load
$q_{fk}$	pedestrian traffic uniformly distributed load
$q_{LL}$	live load
$q_p$	uniformly distributed pedestrian load
$q_{rd}$	design resistant load
$q_{sd}$	design uniformly distributed load
$q_{SW}$	self-weight
$sp$	SFRSCC deck central span
$t$	time; plate thickness
$t_0$	age of concrete at loading

$t_{bot}$	GFRP profile bottom flange's thickness
$t_f$	plate thickness
$t_{is}$	interlaminar shear specimen width
$t_p$	pedestrian action contact duration
$t_s$	specimen thickness
$t_T$	corrected concrete age
$t_{top}$	GFRP profile top flange's thickness
$t_w$	GFRP profile web thickness
$u$	perimeter
$v_{min}$	minimum design shear strength
$v_s$	pedestrian speed
$x$	longitudinal development
$y$	perpendicular direction to the loading plane; linear function
$z$	transverse (loading) direction; vertical displacement
$z_g$	distance between load application point and shear centre
$\bar{z}_n$	flexure modal shape of mode $n$
$z_{NA}$	vertical distance to the neutral axis

## Roman Capital

$A$	cross-section area
$A_c$	concrete area
$A_{eff}$	effective area
$A_n$	arch amplitude for mode $n$
$A_{specimen}$	cross-section area of the specimen
$A_w$	GFRP profile's web area
$B_n$	arch amplitude for mode $n$
$C_1$	bending moment diagram parameter
$C_2$	bending moment diagram parameter
$C_n$	arch amplitude for mode $n$
$D_L$	longitudinal flexural plate stiffness
$D_{LT}$	longitudinal to transverse flexural plate stiffness
$D_n$	arch amplitude for mode $n$
$D_S$	torsional plate stiffness
$D_T$	transverse flexural plate stiffness
$E$	elasticity modulus
$E_0$	instantaneous elasticity modulus
$E_a$	elasticity modulus of the epoxy adhesive
$E_c$	elasticity modulus of concrete
$E_{c,28}$	elasticity modulus of concrete at 28 days of age
$E_{c,X}$	compressive elasticity modulus in X-direction
$E_{full}$	full-section elasticity modulus
$E_{f,X}$	flexural elasticity modulus in X-direction
$E_{m,c}$	compressive elasticity modulus of the epoxy mortar
$E_{m,f}$	flexural elasticity modulus of the epoxy mortar

$E_s$	elasticity modulus of steel
$E_{t,X}$	tensile elasticity modulus in X-direction
$E_t$	creep elasticity modulus
$E_X$	elasticity modulus in X-direction
$F$	load
$F_{cm}$	shear force
$F_{cr}$	critical load; cracking load
$F_{cu,X}$	ultimate compressive load in the X-direction
$F_{cu}$	ultimate compressive load
$F_f$	flexural load
$F_{fu,X}$	ultimate flexural load in the X-direction
$F_{fu-i,X}$	initial failure flexural load in the X-direction
$F_{is,X}$	interlaminar shear load in the X-direction
$F_{isu,X}$	ultimate interlaminar shear load in the X-direction
$F_{max}$	maximum load
$F_p$	pedestrian action force
$F_{tu,X}$	ultimate tensile load in the X-direction
$F_u$	ultimate load
$F_{uk}$	characteristic load
$F_{uk}$	design load
$F_{Wk}$	wind loads
$G$	shear modulus, pedestrian static weight
$G_0$	instantaneous shear modulus
$G_{full}$	full-section shear modulus
$G_t$	creep shear modulus
$G_{XY}$	shear modulus between X and Y directions
$I$	second moment of area about X
$I_p$	polar moment of inertia
$I_t$	torsional constant
$I_w$	warping constant
$I_X$	second moment of area about X
$J$	torsional constant
$K$	stiffness; stiffness coefficient
$K_{sec}$	secant stiffness
$L$	longitudinal span; longitudinal direction
$L_{cant}$	transverse cantilever length
$L_{cy}$	concrete cylinder length
$L_{eff}$	effective length
$L_{f,0}$	span of coupon flexural tests
$L_{int}$	transverse interior span
$L_T$	plate transverse width
$M$	bending moment
$M_{cr,local}$	local buckling critical bending moment
$M_{cr}$	cracking bending moment
$M_{cr}^{global}$	global buckling critical bending moment
$M_F$	bending moment caused by vertical loads



$M_{max}$	maximum bending moment
$M_{post-cr}$	ultimate post-cracking bending moment
$M_{rd,cT}$	transverse design resistant bending moment of the deck
$M_{rd}$	design resistant bending moment
$M_{rk}$	characteristic resistant bending moment
$M_{sd}$	design applied bending moment
$M_{SW}$	bending moment caused by self-weight
$M_{trans,sd}^-$	design transverse negative bending moment
$M_{trans,sd}^+$	design transverse positive bending moment
$M_u$	ultimate bending moment
$M_X$	bending moment about X direction
$N$	number of pedestrians
$NA$	neutral axis position
$Nr$	number of bolts
$Q_c$	construction loads
$Q_{flk}$	pedestrian traffic horizontal load
$Q_{fwk}$	pedestrian traffic concentrated load
$Q_{serv}$	service vehicle loads
$Q_{Sn,k}$	snow loads
$Q_{SV1}$	emergency vehicle first axis load
$Q_{SV2}$	emergency vehicle second axis load
$Q_{Wk}$	wind forces
$R^2$	coefficient of determination
$R_b$	strength per bolt
$R_{bd}$	design strength per bolt
$R_{bk}$	characteristic strength per bolt
$R_{cj,k}$	characteristic strength of the concrete jackets
$R_d$	design strength
$R_k$	characteristic strength
$R_{sd}$	design support reaction
$RH$	relative humidity
$S$	shear strength between X and Y directions
$S_d$	design loads
$T$	transverse direction; torsion moment; temperature
$T_0$	reference temperature
$T_1$	period of exposure to vibrations
$T_g$	glass transition temperature
$T_k$	thermal actions
$T_p$	pedestrian action pace period
$V$	shear force
$V_{rd}$	design resistant shear load
$V_{sd}$	design shear load
$V_u$	ultimate shear force
$V_X$	shear load in X direction
$W$	first moment of area
$W/C$	water to cement ratio
$X$	strength in X direction
$Y$	strength in Y direction

**Greek symbols**

$\alpha$	live load distribution factor
$\alpha_i$	amplitude factor of the $i^{th}$ harmonic
$\beta$	distortion angle
$\beta_c$	creep coefficient
$\gamma$	specific weight
$\gamma_G$	design partial safety factor for permanent loads
$\gamma_{M,mat}$	design partial safety factor of material $mat$
$\gamma_Q$	design partial safety factor for live loads
$\gamma_{XY}$	distortion between X and Y directions
$\delta$	deflection
$\delta_{c,X}$	compressive relative displacement in X-direction
$\delta_{ms}$	midspan deflection
$\delta_{ms-u}$	ultimate midspan deflection
$\delta_p$	vertical deflection due to prestress
$\delta_{si}$	vertical deflection at position $i$
$\varepsilon_i$	axial strain at position $i$
$\varepsilon_{au}$	ultimate tensile strain of the epoxy adhesive
$\varepsilon_{c,X}$	compressive strain in X-direction
$\varepsilon_{cr}$	cracking strain
$\varepsilon_{cu,X}$	ultimate compressive strain in X-direction
$\varepsilon_{f,X}$	strain in flexure for X-direction
$\varepsilon_{fu,X}$	ultimate strain in flexure for X-direction
$\varepsilon_{fu-i,X}$	Initial failure strain in flexure for X-direction
$\varepsilon_{t,X}$	tensile strain in X-direction
$\varepsilon_{tu,X}$	ultimate tensile strain in X-direction
$\varepsilon_{tu,Xk}$	characteristic ultimate tensile strain in X-direction
$\varepsilon_X$	strain in X-direction
$\zeta_{rest.}$	coefficient of restrain
$\theta$	angle between $L$ and 1 directions; infinitesimal rotation angle
$\theta_L$	rotation of the supports caused by loads
$\theta_P$	rotation of the supports caused by prestress
$\theta_T$	total rotation of the supports
$\lambda$	pedestrian equivalent density coefficient; creep model parameter
$\varpi$	RMS limit curves multiplication factor
$\rho$	specific mass
$\varrho$	creep model parameter
$\sigma$	axial stress
$\sigma_{c,X}$	compressive stress in X-direction
$\sigma_{cr,local}$	local buckling stress
$\sigma_{cu,X}$	compressive strength in X-direction
$\sigma_{cu,Xk}$	characteristic compressive strength in X-direction
$\sigma_{f,X}$	flexural stress in X-direction
$\sigma_F$	axial stress caused by the vertical loads
$\sigma_{free}^{ss}$	critical stress of free–simply supported plate

$\sigma_{fu,X}$	flexural strength in X-direction
$\sigma_m$	empirical stress dependent coefficient
$\sigma_{max}$	maximum stress
$\sigma_{ss}^{ss,var.lin.}$	critical stress of a simply supported plate subjected to linear variation stress
$\sigma_{SW}$	axial stress caused by the self-weight
$\sigma_{t,X}$	tensile stress in X-direction
$\sigma_T^{crush}$	transverse crushing stress
$\sigma_{tu,X}$	tensile strength in X-direction
$\sigma_{tu,Xd}$	design tensile strength in X-direction
$\sigma_{tu,Xk}$	characteristic tensile strength in X-direction
$\sigma_{u,X}$	strength in X-direction
$\sigma_X$	stress in X-direction
$\tau$	shear stress
$\tau_{ak}$	characteristic shear strength of the bonded interface
$\tau_{cr}$	critical shear stress
$\tau_F$	shear stress caused by the vertical loads
$\tau_{isu,L}$	interlaminar shear strength in X-direction
$\tau_{isu,L}$	interlaminar shear stress in X-direction
$\tau_m$	shear strength of the epoxy mortar; empirical stress dependent coefficient
$\tau_{max}$	maximum shear strength
$\tau_{SW}$	shear stress caused by the self-weight
$\tau_{u,XY}$	shear strength between X and Y directions
$\tau_{XY}$	shear stress between X and Y directions
$\tau_{XYk}$	characteristic shear strength between X and Y directions
$\nu_c$	Poisson ratio of concrete
$\nu_X$	X direction Poisson ratio
$\nu_{XY}$	X to Y direction Poisson ratio
$\phi$	slope of the deflection; torsion rotation angle
$\bar{\phi}_n$	torsion modal shape for mode $n$
$\varphi$	creep coefficient
$\varphi_0$	constant creep coefficient
$\varphi_i$	phase angle of the $i^{th}$ harmonic
$\chi$	cross-section curvature; Trevino's aging coefficient
$\chi_{rk}$	characteristic ultimate cross-section curvature
$\psi$	load reduction factor; pedestrian synchronization coefficient
$\Delta G_i$	load amplitude of the $i^{th}$ harmonic
$\Delta t_i$	period at temperature $T(\Delta t_i)$
$\Delta$	time-dependent deformations
$\Delta \delta_s$	deflection differential
$\Delta_0$	instantaneous deformations
$\Delta_P$	force on prestress rebars due to vertical loads
$\Delta_s$	elongation of prestress rebars
$\Omega$	cross-section area

**Acronyms**

AASHTO	American Association of State Highway and Transportation Officials
ADI	Portuguese Innovation Agency
ALTO	ALTO Perfis Pultrudidos, Lda.
ASTM	American Society of Testing and Materials
BS	British Standard
CFRP	carbon fibre reinforced polymer
CoV	coefficient of variation
ECC	engineered cementitious composites
EFDD	Enhanced Frequency Domain Decomposition
EN	European norm
eVDV	estimated vibration dose value
FE	finite element
FFT	fast Fourier transform
FRC	fibre reinforced concrete
FRF	frequency response functions
FRP	fibre reinforced polymer
GFRP	glass fibre reinforced polymer
GRC	glass fibre reinforced concrete
HBM	Hottinger Baldwin Messtechnik GmbH
ISO	International Organization for Standardization
IST	Instituto Superior Técnico
LERM	Laboratório de Estruturas e Resistência dos Materiais
LFRD	Load Factor and Resistance Design
OHBDC	Ontario Highway Bridge Design Code
PC	personal computer
PVC	Polyvinyl Chloride
QREN	Quadro de Referência Estratégica Nacional
RC	reinforced concrete
REFER	Portuguese National Railway Network Company
RILEM	International Union of Laboratories and Experts in Construction Materials
RMS	root mean squared
SÉTRA	Service d'Études Techniques des Routes et Autoroutes
SF	safety factor
SFRC	steel fibre reinforced concrete
SFRSCC	steel fibre reinforced self-compacting concrete
SLS	serviceability limit states
SYNPEX	advanced load models for synchronous pedestrian excitation and optimised design guidelines for steel foot bridges
TML	Tokyo Sokki Kenkyujo Co., Ltd.
ULS	ultimate limit states
UM	University of Minho
VDV	vibration dose value

# 1. Introduction

## 1.1. Context and motivation

The construction industry and structural engineering have known significant evolutions with the introduction of new building materials. In particular, the use of iron, following the industrial revolution, allowed erecting taller and longer span buildings and bridges. The introduction of reinforced concrete, on the other hand, was a key factor for the rapid reconstruction of Europe after the World War Two [1].

At the turn of the millennium, the construction industry faces important challenges with regard to maintenance, repair and substitution costs of existing structures owing to their durability problems [2], in particular regarding the corrosion phenomenon in steel and reinforced concrete structures. In this regard, ASCE's 2013 Report Card for America's Infrastructure identifies the growth of structurally deficient bridges in the USA, estimating that the elimination of this backlog by 2028 would require an annual investment of 20.5 billion dollars per year, representing a 60% increase when compared to the current investment [3].

On the other hand, the boost of urban density and growth of road and railway networks, particularly in developed countries, has increased the need for structural systems of easy erection, which avoid the use of large cranes. Moreover, the inherent economic competitiveness of the construction industry has been stimulating the search for structures with higher speeds of construction and with improved functionality. Such demands have been met with the development of innovative structural systems, including new materials, lighter and with improved durability, while providing high mechanical performance.

In this context, fibre reinforced polymers (FRP) are being increasingly used as an alternative to traditional structural materials (steel, concrete and timber). FRP materials, often referred to as advanced composites, are constituted by a polymeric matrix (*e.g.* polyester, vinylester, epoxy) reinforced by continuous fibres (most often glass, carbon or aramid). These composite materials have been used in many commercial applications since the 1940s, in the aerospace, naval, automotive and petrochemical industries, combining their lightweight and improved durability with a good mechanical performance. Owing to these characteristics, together with a progressive cost reduction, FRP materials have been increasingly regarded by the construction industry as promising structural materials, with growing applications since the mid-1990's [4].

Within the FRP materials, glass fibre reinforced polymer (GFRP) pultruded profiles are one of the types with more potential for structural applications due to (i) the possibility of producing any cross-section and (ii) their relative low cost. In fact, owing to their high strength, lightness, ease of installation, electromagnetic transparency, thermal insulation

and corrosion resistance, GFRP pultruded profiles have been increasingly used as structural members both in bridge and building structures (*cf.* Chapter 2).

However, GFRP pultruded profiles also present some technical limitations, namely (i) the brittle failure, (ii) the low elasticity and shear moduli, which make the design often governed by deformation limits or instability phenomena, and (iii) their fire behaviour, preventing their use in building structures without specific protection systems [5]. The two last disadvantages, together with the lack of widely accepted design guidelines and codes, have been hindering the widespread use and acceptance by structural engineers of GFRP pultruded profiles.

In order to overcome the aforementioned limitations, several hybrid structural systems combining GFRP and cementitious materials have been proposed, which have proven to be effective in reducing the overall deformability and proneness to instability phenomena of the GFRP material (*cf.* Chapter 2).

The recent developments of cementitious materials, by their turn, and of fibre reinforced concrete (FRC) in particular, have demonstrated the potential of these materials for structural applications, including the possibility of completely substituting regular reinforced concrete in some applications. Moreover, the development of steel fibre reinforced self-compacting concrete (SFRSCC) has proven the ability to build very thin structural members while maintaining good corrosion resistance [6].

The present thesis was developed in the framework of the Pontalumis project, funded by the Portuguese Innovation Agency (ADI) and promoted in partnership between *Instituto Superior Técnico* (IST) of the *University of Lisbon*, *University of Minho* (UM) and *ALTO Perfis Pultrudidos, Lda.* (ALTO). The project aimed at the development of a footbridge prototype, which could be easily installed over any transportation axes. In this context, the structural system to be developed should (i) present lightweight and be easy to install, (ii) be available for pre-fabrication while offering ease of transportation, (iii) present low electromagnetic interference and, more generally, (iv) comply with structural performance requirements defined in the regulation, and (v) offer improved durability. Taking these objectives into account, a hybrid GFRP–SFRSCC structural solution was proposed and thoroughly investigated.

## 1.2. Objectives and methodology

The study of hybrid GFRP–concrete structural systems was the main objective of this PhD thesis, particularly regarding their feasibility as footbridge structures. The research developed may be divided in three main axes of development:

- GFRP–concrete connection systems;
- Static, creep and dynamic behaviour of GFRP–concrete structures;
- Development of a full-scale GFRP–SFRSCC footbridge prototype.

The first research axis, **GFRP–concrete connection systems**, aimed at:

1. Studying several GFRP–concrete connection systems: bonded, bolted and hybrid (combining bonding and bolting);

2. Studying the long–term mechanical degradation (durability) of the bonded connection systems;
3. Proposing a connection system for the footbridge prototype to be developed.

In order to achieve the aforementioned goals, an experimental campaign was conducted comprising push–out tests on hybrid GFRP–SFRSCC specimens with different connection systems: (i) bonded; (ii) bolted (with different connector configurations); and (iii) hybrid. Additionally, the degradation of the structural performance of the bonded connection systems (more susceptible to the deleterious effects of environmental agents) was object of further study by testing specimens previously subjected to accelerated aging processes, namely (i) thermal, and (ii) wet–dry cycles. Numerical models were developed, simulating the test procedure, in order to allow for a better understanding of the mechanical behaviour of the bonded connections, including the degradation of such properties by the accelerated aging processes. Finally, the research conducted allowed the proposal of a connection system to be used in GFRP–concrete structures and, in particular, in the prototypes to be developed within the scope of this PhD thesis and of the Pontalumis project.

The main objectives of the second research axis, **static, creep and dynamic behaviour of GFRP–concrete structures**, were the following:

1. To study the short– and long–term responses of GFRP–concrete structures;
2. To study the accuracy of readily available analytical and numerical tools in predicting the structural behaviour of GFRP–concrete structures;
3. To assess the feasibility of the proposed structural system (including its constructability) for footbridge applications.

This research axis was developed by performing a comprehensive experimental study of a GFRP–SFRSCC small(half)–scale prototype, including: (i) static serviceability tests; (ii) a static failure test; (iii) creep tests; (iv) modal identification tests; and (v) dynamic tests under pedestrian loading. The results of the experimental tests were compared with analytical and numerical simulations, using readily available design tools. Regarding the creep behaviour of GFRP–concrete structures, a new prediction method was proposed, which accounts for the environmental conditions on the evolution of the creep deformations of the constituent materials. The results of these investigations showed the feasibility of the structural concept for footbridge applications and allowed the design of the full–scale prototype.

Finally, the main objectives of the third research axis, **development of a full–scale GFRP–SFRSCC footbridge prototype**, were the following:

1. To design and build a full–scale GFRP–SFRSCC footbridge prototype;
2. To characterize the behaviour of the structure by means of non–destructive test methods, regarding its static, creep and dynamic responses;
3. To validate the design and general conclusions obtained with reference to the small–scale prototype.

The full–scale prototype was built by ALTO, in accordance with the design developed in this PhD thesis, and included a new type of GFRP pultruded profiles, especially developed for this purpose (whose height is the double of that of the largest profile produced by ALTO until now). After the construction was completed, the structure was subjected to non–destructive static, creep and dynamic tests, allowing its thorough characterization. The results of these tests were compared with the design predictions, in order to further validate the models

used, and with design requirements in order to guarantee that the novel structure complied with serviceability and ultimate limit states' safety requirements. Presently, the GFRP–SFRSCC footbridge structure is being prepared to be installed in real service conditions for general public use in a prime central area of the city of Ovar.

### 1.3. Main scientific contributions

The research presented in this thesis provided scientific contributions regarding GFRP–concrete structures, relevant for both the scientific community and the construction industry. The main scientific contributions are highlighted in this section.

The research on GFRP–concrete connection systems improved the understanding regarding the behaviour of adhesively bonded, bolted and hybrid (redundant) connections and provided a significant amount of experimental data. These data included different mechanical connectors geometries and the influence of thermal and humidity cycles on the mechanical response of adhesively bonded connection systems. The numerical investigations on the latter connections system have shown that the influence of aging can be included in finite element (FE) models, which may be relevant for the design of particular cases.

The research on the static behaviour of GFRP–concrete structures has proven the ability of available analytical and numerical tools in predicting the service and failure behaviour of such structures. Furthermore, the possibility of introducing a low-cost prestress system for GFRP–concrete structures was also demonstrated. Additionally, the experimental studies on the static behaviour of isolated GFRP pultruded beams has allowed the assessment of existing analytical formulae and numerical tools regarding the analysis of the flexural behaviour of these members. Furthermore, the response of GFRP beams under concentrated loads, namely their web-crippling behaviour, specially relevant for support sections, was studied in collaboration with a MSc thesis [7]. This investigation included experiments on different profiles, allowing the assessment of the ability of analytical and numerical tools in predicting the web-crippling behaviour.

Other main contributions concern the research on the dynamic behaviour of GFRP–concrete structures. The assessment of the structural response under pedestrian loads, and the ability of FE models in predicting it, constitutes data of the utmost importance for their application in footbridge structures. Additionally, the assessment of the accuracy of FE models and simple analytical formulae in the determination of the modal parameters of GFRP–concrete structures is a significant step for the acceptance of this structural system by structural engineers.

The research on the creep behaviour of GFRP–concrete structures has resulted from the proposal of (adapted) material creep models of the constituent materials in order to predict the creep deformations of these structures under different environmental conditions. This contribution is particularly relevant since the design of GFRP–based structures is often governed by deformability requirements, and the existent GFRP creep laws may not be suitable to describe the creep behaviour of GFRP–concrete structures. The research conducted on this thesis has also shown that creep in GFRP–concrete hybrid structures has much less magnitude compared to equivalent all–GFRP structures.

The construction (and testing) of the full-scale hybrid GFRP–SFRSCC footbridge prototype constituted the final proof of concept of this structural system for footbridge applications.



Furthermore, the investigations performed with respect to the full-scale prototype have contributed to further validate the conclusions formulated based on the small-scale prototype investigations and allowed the further development of the proposed creep model.

The following publications resulted from the scientific contributions described above:

- J.R. Correia, F.A. Branco, J.A. Gonilha, N. Silva, and D. Camotim. GFRP pultruded flexure members: assessing of existing design methods. *Structural Engineering International*, 20(4):362–369, 2010 [8];
- J.A. Gonilha, J.R. Correia, and F.A. Branco. Dynamic response under pedestrian load of a GFRP–SFRSCC hybrid footbridge prototype: Experimental tests and numerical simulation. *Composite Structures*, 95:453–463, 2013 [9];
- J.A. Gonilha, J.R. Correia, and F.A. Branco. Creep response of GFRP–concrete hybrid structures: application to a footbridge prototype. *Composites Part B*, 53:193–206, 2013 [10];
- J.A. Gonilha, J.R. Correia, F.A. Branco, E. Caetano, and A. Cunha. Modal identification of a GFRP–concrete hybrid footbridge prototype: experimental tests and analytical and numerical simulations. *Composite Structures*, 106:724–733, 2013 [11];
- J.A. Gonilha, J.R. Correia, and F.A. Branco. Structural behaviour of a GFRP–concrete hybrid footbridge prototype: experimental tests and numerical and analytical simulations. *Engineering Structures*, 60:11–22, 2014 [12];
- J.A. Gonilha, J. Barros, J.R. Correia, J. Sena-Cruz, F.A. Branco, L.F. Ramos, D. Gonçalves, M.R. Alvim, and T. Santos. Static, dynamic and creep behaviour of a full-scale GFRP–SFRSCC hybrid footbridge. *Composite Structures*, 118:496–509, 2014 [13];
- L.A. Fernandes, J.A. Gonilha, J.R. Correia, N. Silvestre, and F. Nunes. Web-crippling of GFRP pultruded profiles. Part 1: experimental study. *Composite Structures*, in press, 2014 (DOI: 10.1016/j.compstruct.2014.09.027) [14];
- L.A. Fernandes, F. Nunes, J.R. Correia, N. Silvestre, and J.A. Gonilha. Web-crippling of GFRP pultruded profiles. Part 2: numerical analysis and design. *Composite Structures*, in press, 2014 (DOI: 10.1016/j.compstruct.2014.09.026) [15].

## 1.4. Document organization

The present thesis is organized in eight chapters.

The first and current chapter introduces the thesis theme and frames it in the context of civil engineering, describing the objectives and methodology of the research and its main scientific contributions.

Chapter 2 presents a brief overview of the use of FRP structural solutions in the construction industry, describing also the general characteristics of these materials, including the typical properties of their constituents and their main fields of application in civil engineering structures. Additionally, this chapter presents the general mechanical and physical properties of GFRP pultruded profiles, their shapes, examples of application and a summary of their main advantages and disadvantages. Similarly, the general properties of SFRSCC materials are presented in this chapter. A review of previously proposed hybrid GFRP–concrete

structural systems is also described in this chapter, as well as an overview of the actions and requirements for footbridge structures.

Chapter 3 describes the details of the Pontalumis project, which framed the development of this thesis, and presents the hybrid GFRP–SFRSCC structural concept. Subsequently, the preliminary design of the full-scale prototype, which led to the definition of its general geometry, is described.

The experimental characterization of the main materials used in the construction of the prototypes is presented in Chapter 4, including the thorough coupon testing of the GFRP profiles and SFRSCC. In addition to coupon testing, this chapter also presents experimental investigations on the isolated structural members, *i.e.* flexural tests on GFRP beams and SFRSCC slabs. The results of the GFRP beam tests are compared with the predictions of analytical and/or numerical models. The final part of the chapter describes the remaining materials used in the construction of the prototypes, including their main mechanical properties obtained through experimental testing or provided by the manufacturers.

Chapter 5 concerns the research on GFRP–concrete connections. The first part of the chapter presents the experimental campaign, describing the experimental programme, the tests series and procedures and, finally, the experimental results and discussion. The second part of the chapter refers to the numerical investigations developed in order to simulate the behaviour of the tested adhesively bonded specimens, including the evolution of their mechanical behaviour when subjected to different aging processes.

Chapter 6 refers to the investigations conducted concerning the small-scale prototype. The chapter presents the characteristics of the prototype and a step-by-step description of its construction. Subsequently, the experimental, analytical and/or numerical investigations regarding the static, dynamic and creep behaviour of the prototype are presented and their results are discussed.

Chapter 7 introduces the full-scale prototype, presenting its characteristics and formal design, as well as the description of its construction process. As for the previous chapter, the experimental, analytical and/or numerical investigations regarding the static, dynamic and creep behaviour of the full-scale prototype are presented and discussed.

Chapter 8 summarizes the main conclusions of the present research and formulates recommendations for future developments.

Additional experimental data are presented in the appendixes at the end of the document.

## 2. State-of-the-art

### 2.1. Preliminary remarks

A composite material results from the combination of two or more materials, combined in order to create a new material with enhanced characteristics and properties, when compared to those of its individual components. Concrete, which combines cement, water, coarse and fine aggregates, is an example of a composite material that is widely used in the construction industry.

Fibre reinforced polymer (FRP) materials are modern and advanced composite materials that combine polymeric resins with fibre reinforcement. These materials have been used in defense industry applications (namely in naval and aeronautic applications) since the 1930's and have been introduced in the oil, energy, chemical, paper, water, waste treatment and automobile industries since the 1950's [5].

More recently, in spite of earlier pioneer applications in the late 1950's and early 1960's [5], since the mid-1990's there has been an increasing growth of FRP structural applications in the construction industry [4]. Section 2.2 presents an overview of FRP structural applications in the construction industry.

The general characteristics of FRP materials are presented in Section 2.3. Section 2.4 addresses the main properties of glass fibre reinforced polymer (GFRP) pultruded profiles, the type of FRP materials used in the present thesis. This section also presents some examples of the application of GFRP pultruded profiles in bridge structures.

Engineered cementitious composites (ECC) are cement based materials that can be designed to present tensile strain-hardening behaviour when reinforced with randomly distributed discrete fibres. In the past few years, the research on these materials, and particularly on fibre reinforced concrete (FRC), has shown significant progress [6, 16]. Section 2.5 presents the general characteristics of FRC materials, in particular, steel fibre reinforced self-compacting concrete (SFRSCC), which constitutes the deck of the hybrid footbridge structural system proposed herein.

A similar concept to that which led to the development of composite materials may be applied to the design of hybrid structural systems, *i.e.*, one or more structural materials may be combined in structures, enhancing the exploitation of each materials' best properties, while avoiding their potential disadvantages. A small review of hybrid FRP-concrete structural solutions is presented in Section 2.6.

Section 2.7 presents an overview of the specific actions and requirements for footbridge structures, namely regarding the (i) static and (ii) dynamic behaviours. Finally, Section 2.8 presents the concluding remarks of the chapter.

## 2.2. FRP construction

As mentioned earlier, pioneer applications of FRP composites in the construction industry date back from the late 1950's and 1960's [5], namely with the construction of iconic house prototypes such as the Monsanto House of the Future (Figure 2.1) and the Futuro House (Figure 2.2). These projects were, ultimately abandoned due to their lack of economic competitiveness and the rejection of the architectural community [5]; nevertheless, several FRP constructions were built between 1956 and 1972 [17].



Figure 2.1.: Monsanto House of the Future [18].



Figure 2.2.: Futuro House [19].

In the last two decades of the past century, the use of FRP as structural materials in the construction industry has known significant growth [4]. In fact, the growing need of structural renovation, both due to the durability problems and increasing load demands on existing infrastructure, together with the cost reduction of FRP materials, owing to the evolution of the manufacturing processes [5], have increased the attractiveness of these materials.

The structural applications of FRP materials in the construction industry can be divided in four fields [20]: (i) repair and strengthening; (ii) FRP-reinforced concrete; (iii) hybrid new structures; and (iv) all composite new structures.

The most common structural application of FRP materials in the construction industry is the repair and strengthening of existing structures, in particular the external strengthening of concrete structures with carbon fibre reinforced polymer (CFRP) materials [21]. Figures 2.3 to 2.5 show, respectively, the strengthening of concrete elements with CFRP materials with regard to: (i) the flexural strength (*Burj al Arab* tower in Dubai); (ii) the shear strength (*ADIA* tower in Abu Dhabi); and (iii) the axial strength (Corkerhill road bridge in the UK).

Similar techniques have been used to retrofit masonry structures (Figure 2.6, historic building in Mantua, Italy) and timber structures (Figure 2.7, private house in Switzerland). Additionally, another technique for the strengthening of existing structures with FRP materials is the introduction of external prestress with FRP cable systems, as shown in Figure 2.8 for the Verdasio road bridge in Switzerland.

Another application of FRP materials is FRP-reinforced concrete, in which the traditional steel reinforcing bars are substituted by: (i) short-length fibres or textile FRP reinforcement; and/or (ii) FRP bars or internal prestress cables. The first type of FRP-reinforced concrete,



*Figure 2.3.: CFRP flexural strengthening [22].*



*Figure 2.4.: CFRP shear strengthening [22].*



*Figure 2.5.: CFRP axial strengthening [22].*



*Figure 2.6.: CFRP strengthening of masonry structure [23].*



*Figure 2.7.: CFRP strengthening of timber structure [22].*



*Figure 2.8.: CFRP prestress cables [24].*

in particular glass-fibre reinforced concrete (GRC), has been used mostly in non-structural applications and, more recently, in some structural applications such as telecommunication towers [25], as shown in Figure 2.9. FRP bars (Figure 2.10) and internal FRP prestress cables, on the other hand, have been used in direct substitution of traditional steel rebars in order to enhance the corrosion resistance of such concrete structures [26]. Figure 2.11 presents the application of CFRP reinforcement bars on the concrete deck of a hybrid steel-concrete road bridge in Vermont, USA.



Figure 2.9.: GRC telecommunication tower prototype [25].



Figure 2.10.: CFRP reinforcement bars with different coating finish [27].



Figure 2.11.: Application of CFRP reinforcement bars [28].

More recently, FRP structural elements have also been used in hybrid structural solutions, where, typically, FRP materials are used in the replacement of some components made of traditional materials, such as girders, cables or slabs. However, the full exploitation of the FRP materials is often prevented, since the design concepts are mostly oriented towards the use of traditional materials [20]. One of the most common applications of FRP elements in hybrid structures is the use of FRP decks with steel or concrete girders. Figures 2.12 and 2.13 present examples of two road bridge structures in Germany and the U.K., respectively, comprising steel girders and GFRP decks.

The use of all-FRP structures in building applications has been hindered by the poor performance of these materials to fire exposure [5], although some all-FRP buildings have been erected, such as the Eyecatcher building (Figure 2.14), a 5-storey, 15 m tall GFRP





Figure 2.12.: Steel-GFRP hybrid road bridge [29].



Figure 2.13.: Steel-GFRP hybrid road bridge [29].

structure in Basel, Switzerland, and the *Novartis* Campus Entrance Building (Figure 2.15) in Lausanne, Switzerland, which comprises an all-FRP roof, made of GFRP sandwich panels, supported by a glass load-carrying façade.



Figure 2.14.: Eye-catcher building [24].



Figure 2.15.: *Novartis* Campus Entrance Building [24].

## 2.3. FRP materials

Fibre reinforced polymers are composite materials comprising two phases: (i) the fibre reinforcement; and (ii) the polymeric resin. The first phase provides most of the strength and stiffness, governing the mechanical behaviour. The second phase is responsible for transferring the internal stresses between the fibre reinforcement, protecting the fibres from the environmental agents and providing the geometrical stability of the material.

### 2.3.1. Fibre reinforcement

As mentioned earlier, the fibre reinforcement is responsible for supporting the mechanical solicitations to which the composite material is subjected to. The most common reinforcing fibres are aramid, carbon (standard modulus) and glass (E-glass) [4]. Their main mechanical, physical and thermal properties are summarized in Table 2.1.

**Aramid fibres**, also known by the trade name *Kevlar*, were used in the first generation of FRP prestressing tendons in the 1980s [4]. Their main advantages are the good tenacity

Table 2.1.: Typical properties of the most common fibre reinforcements (adapted from [2]).

Property	Aramid	Carbon	E-Glass
Tensile strength (MPa)	2800–3600	2600–3600	3500
Elasticity modulus (GPa)	80–190	200–400	73
Strain at failure (%)	2.0–4.0	0.6–1.5	4.5
Density (g/cm <sup>3</sup> )	1.4	1.7–1.9	2.6
Fibre diameter ( $\mu\text{m}$ )	12	6–7	3–13
Coefficient of thermal expansion ( $10^{-6}/\text{K}$ )	-3.5	axial: -1.3 to -0.1 radial: 18.0	5.0–6.0

and toughness properties, however, their relatively low compressive strength, reduced long-term strength and high sensitivity to UV radiation, makes them less attractive for civil engineering structural applications [5].

**Carbon fibres** are used in the construction industry mostly in repair and strengthening applications, such as strengthening sheets and fabrics, strengthening strips and prestressing tendons [4]. The main advantages of this type of fibre are the high tensile strength and elasticity modulus, high fatigue and creep resistance and low self-weight, while its main disadvantage is the relatively high cost [5]. Carbon fibres are produced with different grades, namely standard modulus (SM), intermediate modulus (IM), high strength (HS) and ultrahigh modulus (UM) [4].

**Glass fibres** are the most commonly used fibre reinforcement in the construction industry, owing to their high strength and relatively low cost [5], being used in several FRP products such as reinforcing bars, strengthening fabrics and structural profiles [4]. There are several grades of glass fibres available, namely: (i) E-glass, known for its high electric resistivity, which is used in most GFRP structural applications; (ii) S-glass, known for its high strength, which is used primarily in aerospace applications; (iii) A-glass, window glass; and (iv) C-glass, corrosion resistant, also known as AR-glass, alkali-resistant, which is used for specialized products, such as GRC [4]. The main disadvantages of this type of fibre are their relatively low elasticity modulus, the reduced long-term strength (generally lower than 60% of the instantaneous strength) and the reduced resistance to moisture and alkaline environments [4, 5].

Fibre reinforcements can be produced with different geometries, normally combined to create an FRP material. In particular, fibres can be produced in continuous filaments known as rovings, which may be (i) unidirectional (Figure 2.16a); (ii) spun (Figure 2.16b); or (iii) mock (Figure 2.16c), the last two types being also known as yarns.

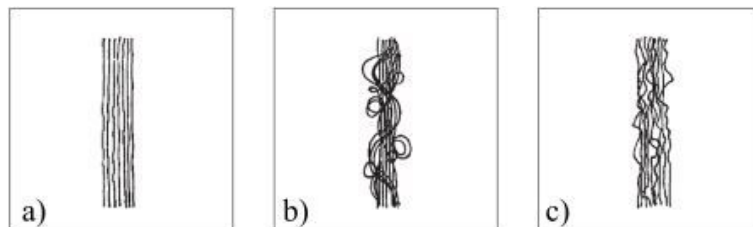


Figure 2.16.: Fibre reinforcement rovings: a) unidirectional; b) spun; and c) mock (adapted from [30]).

In order to obtain fibre reinforcement in more than one direction, the fibres may be combined in textile products, such as: (i) continuous mats with random fibre orientation (Figure 2.17a);



(ii) weaves ( $0/90^\circ$  orientation, Figure 2.17b); (iii) complex mats, with  $0/90^\circ$  membrane and random fibre orientation (Figure 2.17c); and (iv) bidirectional complex mats, with  $0/\pm 45/90^\circ$  membrane and random fibre orientation (Figure 2.17d).

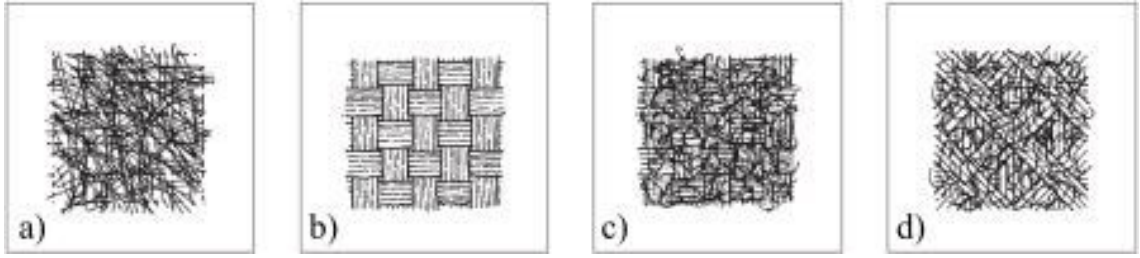


Figure 2.17.: Fibre reinforcement mats: (a) continuous mat with random fibre orientation; (ii) weaves  $0/90^\circ$ ; (iii) complex mat,  $0/90^\circ$  membrane and random fibre orientation; and (iv) bidirectional complex mat,  $0/\pm 45/90^\circ$  membrane and random fibre orientation (adapted from [30]).

Usually, fibres are provided with a chemical superficial treatment with a substance named *sizing* (made of starch, oil or wax), which acts as lubricant and antistatic agent, protecting the fibres during the processing, enhancing the ability of the bundles of fibres to remain together as units, promoting the bonding with the polymeric matrix and, for glass fibres, providing protection against moisture degradation during the service live [5]. Additionally, for further protection to corrosion and mechanical deterioration, the surface of FRP materials can be provided with a thin outer layer mat called overlay veil or surface veil [30].

### 2.3.2. Polymeric matrix

The main functions of the polymeric matrices are: (i) to guarantee the load transfer/distribution between the fibres; (ii) to hold the fibres in the intended position, thereby preventing them to buckle under compressive stresses; and (iii) to protect the fibres from environmental degradation agents, such as moisture. Nevertheless, it should be mentioned that the matrices also have an important role in the mechanical response to some types of solicitations, namely shear stresses and compressive stresses (owing to the fact that they must prevent fibre buckling, as mentioned earlier) [5].

The polymeric resins may be divided into two main groups: (i) thermoplastic; and (ii) thermosetting resins [5].

**Thermoplastic resins**, owing to their weak molecular connections, allow welding, recycling and reprocessing. On the other hand, when compared to thermosetting resins, they present poor fibre impregnation and adhesive properties. Furthermore, their high viscosity does not allow high processing speed, raising the manufacturing cost of the FRP materials. Polypropylene, polyamide, polyethylene and polybutylene are examples of this type of resin [5].

**Thermosetting resins** show good fibre impregnation and provide very good adhesive properties. Additionally, owing to their low viscosity, they allow high processing speeds. These characteristics have made them more attractive for FRP applications, being used in most commercial FRP products [5]. On the other hand, once cured, these resins are no longer fusible, owing to the strong molecular structures developed during the polymerization process, meaning they cannot be welded or reprocessed. Table 2.2 presents the main

mechanical, physical and thermal properties of polyester, vinylester, epoxy and phenolic thermosetting resins.

*Table 2.2.: Typical properties of the most common thermosetting resins (adapted from [5]).*

Property	Epoxy	Phenolic	Polyester	Vinylester
Tensile strength (MPa)	60–80	30–50	20–70	68–82
Elasticity modulus (GPa)	2.0–4.0	3.6	2.0–3.0	3.5
Strain at failure (%)	1.0–8.0	1.8–2.5	1.0–5.0	3.0–4.0
Density (g/cm <sup>3</sup> )	1.20–1.30	1.00–1.25	1.20–1.30	1.12–1.16
Glass transition temperature (°C)	100–270	260	70–120	102–150

Epoxy resins present excellent adhesive properties and very good environmental durability [4]. These resins present high viscosity and relatively long curing periods, making them harder to process, but, on the other hand, they present considerably lower shrinkage than their polyester counterparts [5]. These resins are generally used in high-performance applications, in terms of strength, stiffness, service temperature and durability and, more commonly, are used together with carbon fibres [30]. Additionally, epoxy resins are often used on their own as structural adhesives [31].

Phenolic resins maintain their adhesive properties and dimensional stability at relatively high temperatures, being much less flammable and producing less smoke when submitted to intense heat or fire conditions, when compared to their thermosetting counterparts [5]. They are economically competitive but difficult to reinforce and cure. Furthermore, these resins present a brownish color that is difficult to pigment in order to produce a final FRP product in a different color than that of the resin [4].

Polyester resins are the most commonly used in FRP applications owing to the good balance between their mechanical, chemical, electrical and physical properties and their relatively low cost. They present a good dimensional stability and reduced viscosity, which makes them easy to process. Furthermore, it is possible to change the matrix composition during the polymerisation process [5].

Finally, vinylester resins were developed in order to achieve improved mechanical and chemical properties, such as those of epoxy resins, with the fluidity and the ease of processing of polyester resins. As a result, these resins present an intermediate cost between those of the polyester and epoxy resins [5]. Vinylester resins are used for applications requiring improved durability, such as reinforcing FRP bars for concrete (owing to the need of protecting the fibres from the alkaline environment), with most of the commercial FRP bars using these resins [4].

### 2.3.2.1. Other components

The polymeric matrices of FRP materials can comprise additional constituents other than the base resins described earlier. These constituents may be divided into three categories: (i) polymerisation agents; (ii) fillers; and (iii) additives. They can be added to the matrices in order to improve the material processing, to reduce its cost, to induce the polymerisation reactions and/or to tailor specific properties of the final FRP product [5].

**Polymerisation agents** induce the initiation of the polymerisation reaction on the base resin. Polyester and vinylester resins require low quantities of polymerisation agents (0.25%

to 1.50%, by weight of resin), using, typically, heat activated organic peroxides. Epoxy resins, on the other hand, require larger quantities of polymerisation agents (25% to 50%, by weight of resin), normally curing agents (or hardeners) of the amine type [4].

The introduction of **fillers** in the matrix is performed in order to achieve two separate results: (i) reducing the cost of the final product; and (ii) improving some of the FRP properties. Fillers may be used in order to reduce the matrix shrinkage (preventing/reducing cracking), to improve the dimensional stability, the hardness, the fatigue resistance, the creep behaviour or the chemical resistance. Additionally, fillers may enhance the fire performance of the FRP material by reducing (i) the organic content of the matrix, and (ii) the flammability and smoke production of the final composite material (*e.g.* alumina trihydrate or calcium sulfate fillers). Other commonly used fillers are calcium carbonate and aluminum silicate [5]. It should be mentioned that the introduction of fillers may lead to improvements on some physical and chemical properties of the matrices, but it usually leads to a decrease of the main mechanical properties and durability of the final FRP materials [4]. In this context, typical pultruded FRP profiles and bars have 10% to 30%, by weight, of filler in the matrix; small pultruded parts with primarily unidirectional reinforcement generally present less than 5% of filler content by weight; while the matrix of FRP strips generally does not include fillers [4].

**Additives** are added to the matrix of FRP materials in order to ease the processing or to improve a wide range of characteristics of the final FRP product. Typically, these products are used in reduced quantities (<1% by weight of resin) but may, nevertheless, change the physical and mechanical properties of the FRP materials significantly [5]. Additives are usually added in order to obtain: a given colour (pigments or colourants); protection to UV agents, namely discolouration, gloss loss, cracking and disintegration (UV stabilizers); reduction of void contents; reduction of shrinkage (low profile or shrink additives); inhibition of polymer oxidation (antioxidants); reduction of flammability and smoke production (flame retardants); increase toughness (elastomeric materials); increase of electrical conductivity (metal and/or carbon particles); reduction of electrical charge attraction (antistatic agents); promotion of cellular structure, in order to reduce the density, the costs, the shrinkage and improving electrical and thermal insulation (foaming agents); and facilitate the removal from the molds (release agents) [5].

## 2.4. GFRP pultruded profiles

As mentioned earlier, GFRP materials are the most common FRP materials in structural engineering applications [5]. Additionally, GFRP pultruded profiles are the most common FRP structural parts for new construction. They are manufactured by a cost-effective method named pultrusion, which was first developed in the USA in the 1950s [4], allowing the production of high-quality FRP profiles with constant section.

The pultrusion process allows the production of virtually any type of cross-section, including open cross-sections, such as I- and U-shaped, wide-flange or angle sections; closed cross-sections (tubular); multi-cellular closed-form panels with internal webs. Additionally, this manufacturing process has no limitations in terms of length of the profiles [5].

Figure 2.18 schematizes the pultrusion process assembly line. On the left-hand side, at the beginning of the assembly line, the fibre reinforcements (rovings and mats) are preformed, with the aid of a guiding plate, into a resin bath (depicted in Figure 2.18) or a resin injection

system, in which the resin is only added to the fibres inside the curing die, depending on the producer/assembly line. After the fibres are duly impregnated in the polymeric matrix, the composite is pulled through the preformer into the forming and curing die, where it gains its final shape owing to the polymerization of the matrix, which occurs at temperatures ranging from  $90^{\circ}\text{C}$  to  $180^{\circ}\text{C}$  [4]. It should be mentioned that the surface veil, when provided, is added before the reinforcement enters the preformer, as shown in Figure 2.18. Finally, the pulling system pulls the cured profiles, towards a cut-off saw, where they are cut to the desired dimension.

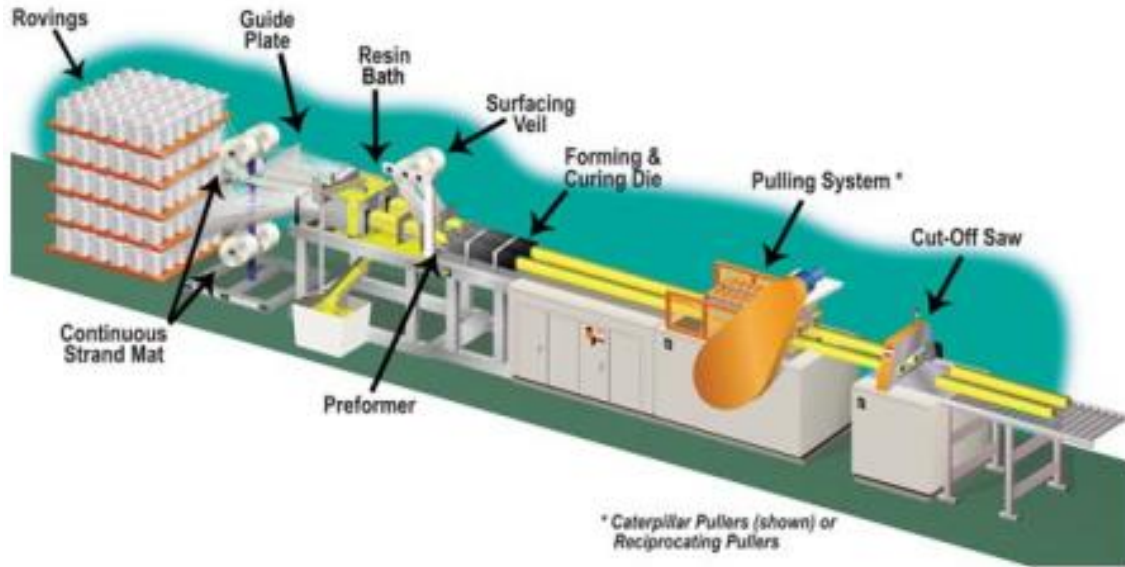


Figure 2.18.: Pultrusion process assembly line [32].

Regarding the productivity of the pultrusion process, it may vary with the type of machine used, as well as with the shape of the cross-section. Generally, for current profile cross-sections, production occurs at an average rate of 2 m/min. The pultrusion process presents the best productivity/cost ratio, when compared to other manufacturing processes [5].

As an illustrative example of the pultrusion process, Figure 2.19 shows several steps of the pultrusion of I400 GFRP profiles (*cf.* Section 4.2), produced by *ALTO, Perfis Pultrudidos, Lda.*



Figure 2.19.: Pultrusion of an I-shape profile: a) pulling of the dry fibres; b) first stretch of cured FRP; and c) general view of the pultrusion line.

The final GFRP pultruded profiles are constituted by laminates/walls combining several layers with different types of reinforcement, as schematized in Figure 2.20. The fibre rovings provide the axial reinforcement, while the mats, containing fibres in several directions, provide reinforcement in the transverse directions, contributing for the mechanical response

to in-plane shear loading [5]. The surface veil, a protection and optional reinforcement layer, generally consists of a thin short and randomly orientated fibre mat. The outer layer is provided with an increased resin content, providing protection against environmental chemical and mechanical (impact) degradation agents, also providing a smooth surface finishing [5].

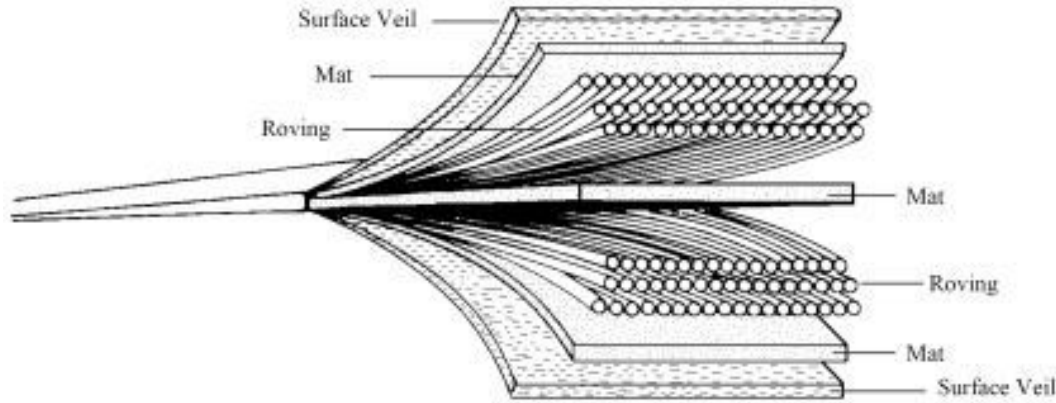


Figure 2.20.: Typical fibre architecture of pultruded laminates (adapted from [33]).

#### 2.4.1. GFRP pultruded structural shapes

According to Keller [34], pultruded structural shapes can be divided in two categories: (i) first generation profiles; and (ii) second generation profiles.

The first generation profiles basically mimic the structural shapes used in the metallic construction, namely thin-walled open and closed cross-sections, as depicted in Figure 2.21.

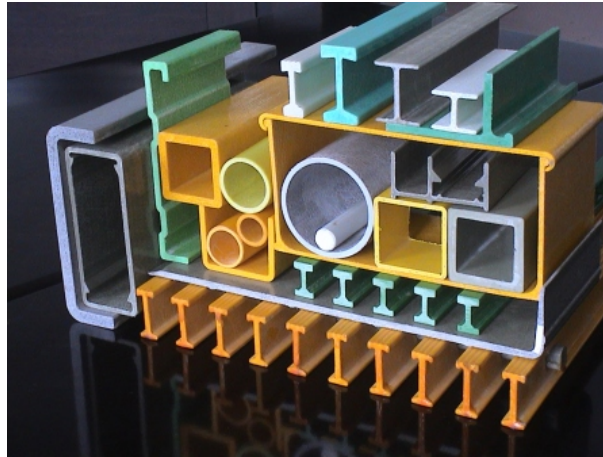
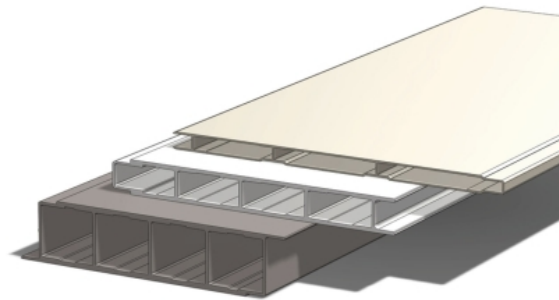


Figure 2.21.: Typical first generation pultruded profiles [35].

First generation profiles have been used in most GFRP structural applications at this point [5]. However, there are some disadvantages inherent to this type of geometry in association with the GFRP material properties, such as the sensitivity to impact loads, the proneness to instability phenomena, especially under compression, and the high deformability, which prevent the full exploitation of the material's potential in most applications. In order to overcome these problems, two different solutions have been proposed: (i) the use

of hybrid structural solutions, in which GFRP profiles are combined with other traditional materials (further discussed in Section 2.6); and (ii) the development of material-adapted shapes, which led to the introduction of second generation GFRP pultruded profiles.

Second generation pultruded profiles, developed in the last few years, encompass multi-cellular cross-sections, as depicted in Figure 2.22. These profiles were designed as slab elements, spanning between main girders and have been mostly used in bridge applications, both in new structures and in the replacement of traditional decks [5]. The connection between the profiles is generally performed by adhesive bonding, which is sometimes complemented with a mechanical connection system.



*Figure 2.22.: Typical second generation pultruded profiles [36].*

Although the second generation pultruded profiles have been designed in order to make a better use of the GFRP material properties, their application field is limited to horizontal elements and to secondary structural parts (typically the transverse spans of bridges). In this regard, it should be noted that the development of material-adapted structural forms and shapes can last generations [34], and according to Correia [5], this process has just started in what concerns GFRP pultruded profiles for structural engineering applications.

#### **2.4.2. Properties of GFRP pultruded profiles**

The engineering properties of GFRP pultruded profiles, which depend on the type of fibres and polymeric matrix used, the fibre content and architecture, and on the fibre-matrix interaction, are generally given by each manufacturer. Unlike what occurs for traditional construction materials, such as steel and concrete, the properties of GFRP pultruded profiles are not standardized, presenting relatively high variations among manufacturers. Nevertheless, EN 13706 [37] established two material grades for GFRP profiles, with minimum requirements, which, on the other hand, appear to be insufficient to characterize such a broad spectrum of material properties. Furthermore, according to Bank [4], the material properties based on coupon testing, often provided by the manufacturers, can be taken as lower bounds for the material characteristics. However, additional data is required to perform probability-based design methods [5], such as those included in the Eurocodes. This lack of information leads to the adoption of overly conservative material safety partial design factors, such as those proposed by the EuroComp guidelines [38], hindering the competitiveness and widespread use of these materials.

Table 2.3 summarizes the typical mechanical properties of GFRP profiles, while Figure 2.23 compares the mechanical behaviour of these pultruded parts with those of traditional materials, among which structural steel is pointed out as the main competitor of GFRP profiles [5].

Table 2.3.: Typical mechanical properties of GFRP pultruded profiles (adapted from [5]).

Property	Direction	
	Longitudinal	Transverse
Tensile strength (MPa)	200–400	50–80
Compressive strength (MPa)	200–400	70–140
Shear strength (MPa)	25–30	
Elasticity modulus (GPa)	20–40	5–9
Shear modulus (GPa)	3–4	
Poisson ratio (–)	0.23–0.35	0.09–0.15

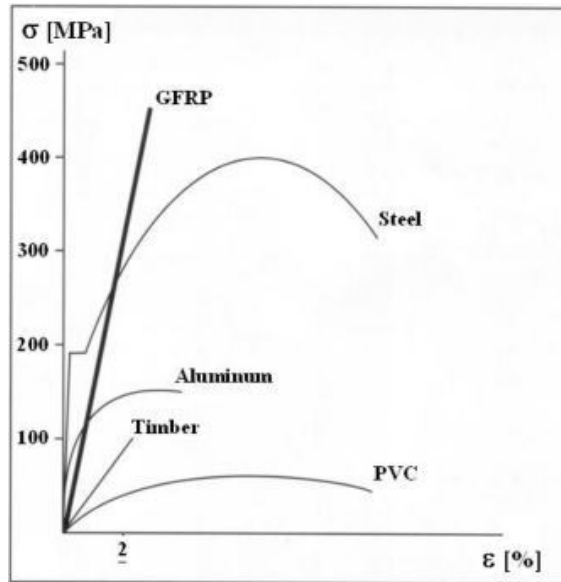


Figure 2.23.: Stress vs. strain relationship of GFRP pultruded profiles and other materials (adapted from [5]).

Figure 2.23 shows that the GFRP material presents linear-elastic behaviour up to failure, unlike the ductile behaviour presented by structural steel. Additionally, the comparison between these materials shows that they present similar tensile strength, while the elasticity modulus of GFRP is significantly lower than that of steel (10% to 20%). As mentioned earlier, the relatively low elasticity modulus of the GFRP material associated with the thin-walled shapes of first generation profiles (*cf.* Section 2.4.1) contributes to the fact that the design of GFRP pultruded profiles is often governed by deformability criteria or instability phenomena [4].

Regarding the physical and thermal properties of GFRP profiles, Table 2.4 summarizes the typical (i) fibre contents, (ii) density ( $\rho$ ), (iii) thermal expansion coefficient ( $\alpha$ ), and (iv) thermal conductivity ( $\lambda$ ). Figure 2.24 compares the three last properties of the GFRP material to those of PVC, aluminum (AL), steel (ST) and timber (T).

Table 2.4.: Typical physical and thermal properties of GFRP pultruded profiles (adapted from [5]).

Property	Direction	
	Longitudinal	Transverse
Fibre content, by weight (%)	50–70	
Density ( $\text{kN/m}^3$ )	15–20	
Thermal expansion coefficient ( $10^{-6}/\text{K}$ )	8–14	16–22
Thermal conductivity ( $\text{W}/(\text{m}\cdot\text{K})$ )	0.20–0.58	

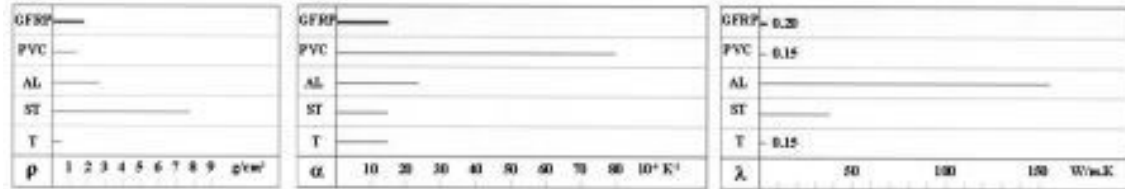


Figure 2.24.: Comparison between the physical and mechanical properties of GFRP pultruded profiles and other materials (adapted from [5]): density (left); thermal expansion coefficient (middle); and thermal conductivity (right).

Again, in comparison to steel, GFRP profiles present lower self-weight (20% to 25% of that of steel), similar thermal expansion coefficient and much lower thermal conductivity coefficient.

### 2.4.3. Structural applications of GFRP pultruded profiles

GFRP pultruded profiles have been mostly used in a wide range of non-structural applications in the construction industry [5]. On the other hand, these materials have been increasingly used in structural applications, predominantly in bridge structures, while the application in building structures has been less frequent (*e.g.* the Eyecatcher building, *cf.* Figure 2.14).

The Aberfeldy bridge (Figure 2.25), built in 1992, was the first all-composite footbridge in the UK. This structure, with a length of 131 m, comprises a second generation GFRP pultruded deck, suspended from GFRP towers by aramid-FRP cables.

In 1994, the Bonds Mill lifting bridge (Figure 2.26) was the first all-composite vehicular bridge built in the UK and, additionally, the first all-composite bascule bridge. This structure was built with second generation GFRP pultruded profiles, fully exploiting the materials' lightness with significant savings on the mechanical elevation system.

The Pontresina footbridge, built in 1997 in Switzerland (Figure 2.27), is a two-span all-GFRP structure, which is used during the winter for ski touring. The structure comprises first generation GFRP pultruded profiles installed in a truss system for both 12.5 m spans, one presenting bolted connections, while the other has bonded connections. Owing to its lightness, the bridge is removed every year in the spring before the water rises, being reinstalled in the autumn. These operations are performed with a helicopter (Figure 2.28).

The Kolding footbridge (Figure 2.29) in Denmark, also built in 1997, was the first worldwide composite bridge crossing a railway line. The structure presents two spans, with 13 m and 27 m, supported by cables anchored in a central tower. First generation GFRP pultruded profiles were used for all elements of the structure, including the cables, guaranteeing the





Figure 2.25.: Aberfeldy footbridge [39].



Figure 2.26.: Bonds Mill lifting bridge [40].



Figure 2.27.: Pontresina footbridge [24].



Figure 2.28.: Pontresina footbridge helicopter transportation [24].

electromagnetic transparency of the bridge, not interfering with the railway electrification. Another advantage of using GFRP pultruded profiles was the ease of erection of the structure, with the bridge being installed in three 8 hours night sessions, also not interfering with the normal traffic of the railway.

In 2001, the construction of the Lleida footbridge (Figure 2.30) in Spain, crossed a roadway, a regular railway and the (projected) high-speed railway, thereby presenting similar installation and performance requirements than those of the Kolding footbridge. The 38 m span arch structure was built exclusively with first generation GFRP pultruded profiles and was installed in only 3 hours.

The West Mill road bridge (Figure 2.31), built in 2002, was one of the first all-composite road bridges in the UK, presenting a 10 m single span, made of second generation GFRP pultruded profiles. In 2005, a similar road bridge was built in Germany, the Klipphausen bridge (Figure 2.32), becoming the first all-GFRP road bridge in the European continent.



Figure 2.29.: Kolding footbridge [29].



Figure 2.30.: Lleida footbridge [41].



Figure 2.31.: West Mill road bridge [29].



Figure 2.32.: Klipphausen road bridge [29].

In addition to all-composite structures, GFRP profiles, mainly second generation profiles, have been used as the deck of hybrid bridge structures, in combination with steel or concrete main girders, in both rehabilitation and new construction. As an example of such applications, Figures 2.12 and 2.13 (page 11) show steel-GFRP hybrid bridge structures in Germany and in the UK, respectively.

Complementing the previous examples, it should be mentioned that a hybrid steel-GFRP footbridge bridge has been constructed very recently (2013) in Viseu, Portugal, as shown in Figure 2.33. This 13.5 m long footbridge comprises two steel main girders and a 2.5 m wide deck made of GFRP pultruded second generation profiles.

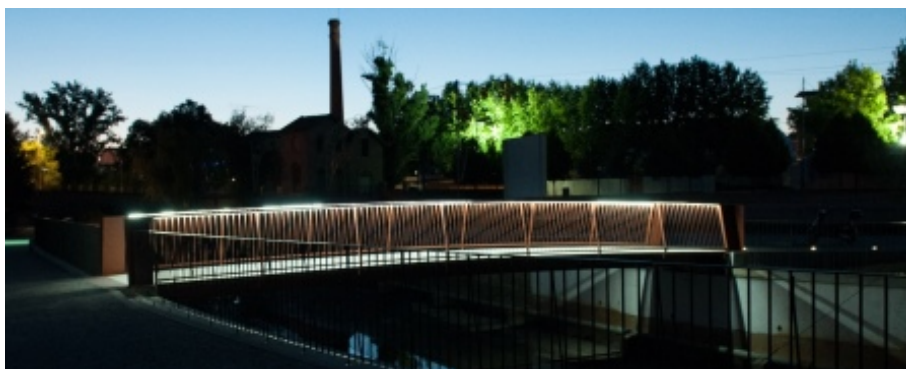


Figure 2.33.: Steel-GFRP hybrid footbridge (courtesy of Mário Sá).

#### 2.4.4. Summary

In summary, GFRP pultruded profiles are materials with great potential for structural applications in the construction industry. When compared to traditional materials, namely reinforced concrete and structural steel, these materials present the following advantages:

- High strength-to-weight ratio;
- Low self-weight;
- High fatigue strength;
- Thermal insulation;
- Ease of erection and transportation;
- High corrosion resistance;
- Improved durability;
- Low maintenance costs.

On the other hand, GFRP pultruded profiles present the following disadvantages or limitations, when compared to traditional materials:

- High deformability and susceptibility to instability phenomena, owing to the relatively low elasticity and shear moduli, which may hinder the full exploitation of the material properties;
- Brittle failure behaviour, in contrast with current design practice, which often aims at exploiting the ductile failure behaviour of traditional materials;
- Fire behaviour, often requiring protective (onerous) measures, owing to the flammability and smoke production of the material, especially in building applications;
- Lack of specific design codes, preventing a wide acceptance by structural engineers;
- Necessity of further investigations and material adapted structural concepts, namely concerning some specific design aspects, such as connection systems;
- Initial cost competitiveness, which, nevertheless, has been improving in recent years. In this regard, it should be mentioned that, owing to the low maintenance costs, GFRP pultruded profiles may allow significant savings when considering life-cycle costs.

### 2.5. SFRSCC

As mentioned earlier, the recent developments in fibre reinforced concrete (FRC) research have shown the potential of these materials for structural applications in the construction industry [6]. Moreover, the enhanced tensile post-cracking strength exhibited by FRC materials, when compared to that of traditional concrete, allows replacing traditional rebar reinforced concrete (RC) in some structural applications, with technical and economical advantages [6].

FRC materials may be divided into two main categories regarding their tensile behaviour: (i) tensile hardening; and (ii) tensile softening [6]. According to the Model Code 2010 [42],

the tensile hardening classification should be attributed to materials that present a tensile strain higher than 1% at their ultimate tensile stress.

Research on steel fibre reinforced concrete (SFRC), in particular, has shown that the corrosion resistance of these materials may be significantly increased if the steel fibres are provided with a minimum cement paste coating, with thicknesses of 0.1 mm to 0.2 mm for water-to-cement ratios of 0.5 [43]. The use of self-compacting concrete can guarantee such fibre coating, owing to its high flowable mixtures and high fine particles and paste contents [44]. Figure 2.34 presents the typical stress-strain relationship of SFRC materials recommended by RILEM [45].

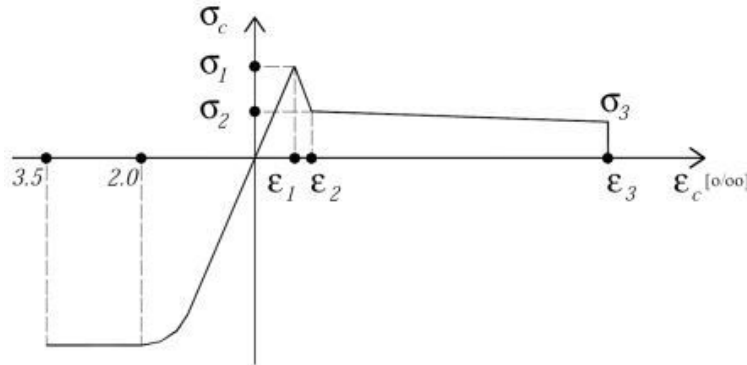


Figure 2.34.: Typical stress-strain relationship of SFRC (adapted from [45]).

In this context, the use of steel fibre reinforced self-compacting concrete (SFRSCC), owing to its high post-cracking tensile strength and small cover thickness requirements, allows the execution of very thin structural elements, especially when compared to an equivalent RC element, guaranteeing the proper fibre coating. In this regard, it should be mentioned that, for some structural solutions, such as the hybrid GFRP-concrete footbridge concept proposed herein (*cf.* Chapter 3), the total thickness of traditional RC elements may be governed by rebar cover requirements, leading to heavier structures and, consequently, further loading of the remaining structural elements, resulting in more onerous structures. Furthermore, the recent developments on self-compacting concrete have allowed the production of cost-competitive SFRSCC materials with a fibre content higher than 1%, by volume, which present tensile hardening behaviour [44].

The main difficulties of SFRC materials, and particularly of SFRSCC materials, concern the control of the fibre distribution and orientation, which depend on the fresh-state properties of the mix, the casting method, the dynamic effects and the formwork geometry [44]. In fact, these parameters can greatly influence the post-cracking behaviour [46], namely with regard to the flexure and shear strengths, and to the crack width and spacing [44].

Thereafter, the use of isolated SFRSCC elements in structural applications has been limited to research projects [44].

## 2.6. Hybrid GFRP-concrete structural systems

In general, the development of hybrid structural solutions aims at the exploitation of each materials' best properties and characteristics, while overcoming their main disadvantages.

As mentioned earlier, GFRP materials are susceptible to instability phenomena when subjected to compressive stresses, owing to their relatively low elasticity modulus (*cf.* Section 2.4), therefore performing better when subjected to tensile stresses. Cementitious materials, on the other hand, due to their low tensile strength, perform better when subjected to compressive stresses. In this context, hybrid GFRP–concrete structural solutions have been developed so that GFRP materials are mainly subjected to tensile stresses, while the concrete material is mainly under compressive stresses.

Thereafter, several authors have presented GFRP–concrete structural systems aiming at avoiding the aforementioned disadvantages, while maintaining the attractiveness of GFRP structural solutions, namely their strength, lightness, ease of erection, and durability.

Deskovic *et al.* [47] presented one of the first FRP–concrete structural systems, which consisted of a beam element comprising a compressive layer of concrete shuttered by a GFRP box section with elongated webs, supporting shear stresses, and a CFRP strip on the bottom plate of the box section, which supported most of the tensile stresses (Figure 2.35). The authors studied two types of connections between the GFRP and the concrete: (i) epoxy adhesive bond; and (ii) epoxy adhesive bond and steel connectors. The first connection system proved to be inadequate, since failure occurred prematurely at the bonded interface, while the latter connection system allowed a progressive failure mode (first by tensile rupture of the CFRP strip and secondly by crushing of the concrete), which was aimed at by the authors in order to create a pseudo–ductile failure.

Another hybrid beam was proposed by Hall and Mottram [48], which comprised a GFRP pultruded walkway panel with T–upstands and a concrete layer, cast onto the GFRP material. In addition to the T–upstands, which acted as shear connectors, some beams were provided with an epoxy layer between the GFRP and concrete materials. These structural elements showed a linear behaviour for service conditions and presented shear failure in the concrete material, with few specimens presenting failure due to the premature debonding of the concrete–adhesive interface.

Garcia [49] also presented a hybrid beam element, comprising a concrete compressive layer on top, two GFRP webs, which enclosed part of the concrete layer, and a hybrid G/CFRP laminate bottom plate (Figure 2.36). Additionally, wooden stiffeners were provided to the GFRP webs in order to increase the buckling resistance of these laminates. Moreover, the connection between the GFRP and the concrete elements was guaranteed by an epoxy adhesive. The tested prototype presented linear behaviour and failed due to web buckling.

Canning *et al.* [50] and Hullat *et al.* [51] studied hybrid beam elements with similar cross–sections to that proposed by Deskovic *et al.* [47] (Figure 2.35). In the first study, the authors tried to avoid web shear failure by using GFRP sandwich panels with foam cores as webs, while in the second study the authors reinforced the webs with additional GFRP laminates, testing reinforced and un–reinforced beams. In both studies, the influence of different GFRP–concrete connection systems was investigated, namely: (i) mechanical connection with indents on the vertical faces of the shuttering; (ii) epoxy adhesive bond applied between the GFRP and the hardened concrete; (iii) mechanical connection materialized by bolts, displaced horizontally, connecting the concrete and the GFRP shuttering; (iv) epoxy adhesive bond, with the epoxy being applied with two different injection techniques; and (v) epoxy adhesive bond materialized with an epoxy adhesive suitable for fresh concrete. The experiments showed that the best connection system to ensure the shear transfer between the GFRP and the concrete was the epoxy resin bond, particularly the techniques applied

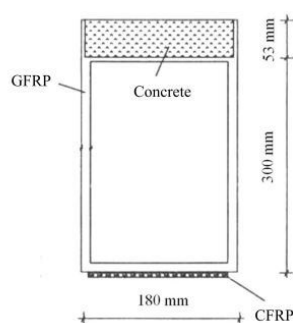


Figure 2.35.: Cross-section of the hybrid beam proposed by Deskovic *et al.* (adapted from [47]).

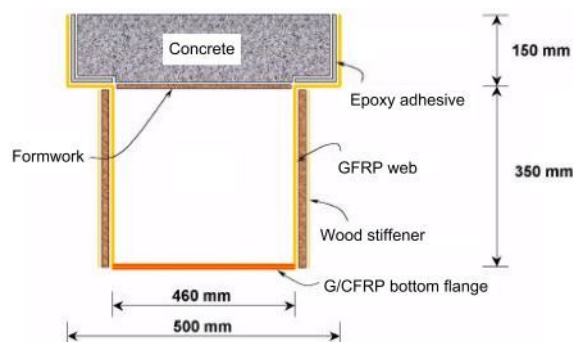


Figure 2.36.: Cross-section of the hybrid beam proposed by Garcia (adapted from [49]).

to the the hardened concrete. Furthermore, the beams tested in these studies presented three distinct failure modes: (i) GFRP–concrete connection failure; (ii) concrete crushing; and (iii) local buckling of the webs; all failure modes presented limited ductility.

Ribeiro *et al.* [52] also reported investigations on GFRP–concrete beams with a cross-section variation to that proposed by Deskovic *et al.* [47]. In this study, the beams comprised different U-shaped GFRP profiles (combined to form different cross-sections) with a polymeric concrete compressive layer. Premature failure in the GFRP–concrete interface was prevented by sandpapering the interface surfaces of the GFRP material and by applying a layer of silane adhesion promoter before the concrete casting. The cross-sections tested were idealized to promote crushing failure of the concrete, which was deemed to be a visible warning sign of failure.

The Asturias road bridge was the first vehicular bridge constructed with FRP (CFRP) materials in Spain [53]. This 46 m long structure, with four spans, presents a hybrid CFRP–concrete cross-section, with CFRP box girders and a 200 mm thick RC compressive layer. The CFRP–concrete connection was materialized by GFRP pultruded profiles displaced transversely (Figure 2.37). The CFRP box girders were produced by moulding fibre prepreps around a stay-in-place polyurethane mould [54]. The construction of the bridge required the total highway closure for three days.

More recently, two similar road brides were built in Spain, on the M111 highway [54]. In order to enhance the economic competitiveness of the hybrid structural solution, the box girders were substituted by beams with an open cross-section (Figure 2.38) in order to allow the reuse of the molds. More importantly, some of the carbon fibres used in the FRP laminates, particularly in the webs, were substituted by glass fibres, comprising G/CFRP–concrete hybrid structures.

Two different hybrid structural systems were developed by Seible *et al.* [56] for bridge applications: (i) the Carbon Shell system, used in the Kings Stormwater Channel Bridge, which can be adapted to both column and beam applications; and (ii) the Hybrid Tube System, used in the I-5/Gilman bridge.

The Carbon Shell System comprises CFRP tubes, filled with lightweight concrete cast *in situ*. In order to enhance the adherence between both materials, the CFRP tubes have an internal nervurated surface. When used as girders, the hybrid tubes can be associated with FRP panels decking system or with traditional concrete slabs (Figure 2.39). The hybrid



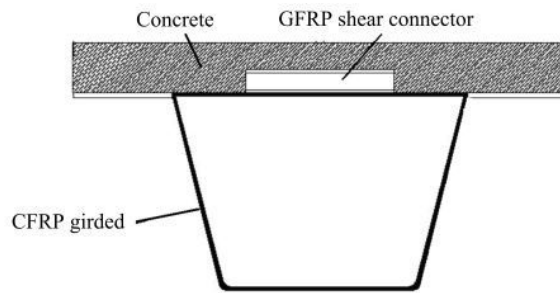


Figure 2.37.: Cross-section of the hybrid beams used in the Asturias bridge (adapted from [55]).



Figure 2.38.: G/CFRP-concrete hybrid bridge built in Spain (adapted from [54]).

tubes and the deck present a mechanical connection system, provided by shear connectors embedded in the tubes during the casting of the concrete.

The Hybrid Tube System comprises FRP hollow girders connected with an FRP permanent formwork, which is snap-locked to the girders' top flanges. The deck is made of a polypropylene fibre reinforced concrete, which, owing to the shape of the FRP formwork, behaves as an arch structure. The shear connection between the girders and the concrete deck is materialized by CFRP connectors, which are snap-locked to the girders' top flanges (Figure 2.40). The bottom flange of the hollow girders is a G/CFRP laminate, while the remaining plates are all-GFRP.

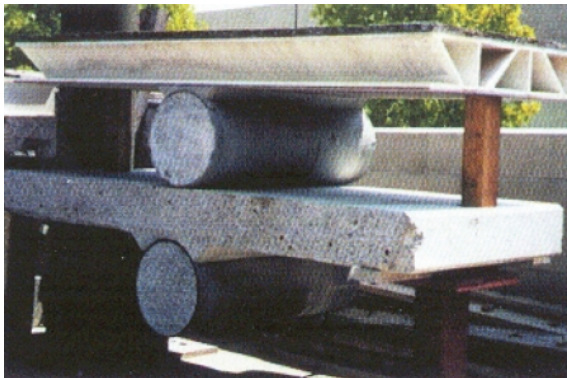


Figure 2.39.: Carbon Shell System with GFRP panel deck (top) and concrete deck (bottom) [56].

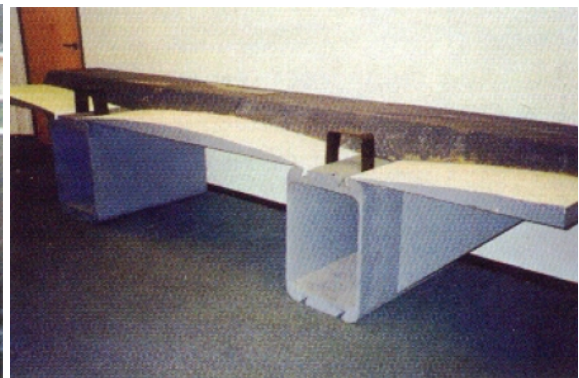


Figure 2.40.: Hybrid Tube System [56].

Black [57] reported the construction of three bridges in the USA with hybrid GFRP-concrete deck structures. The hybrid decks were installed on steel or prestressed RC main girders and comprised GFRP panels with corrugated profiles, which acted both as permanent formwork and bottom reinforcement of the concrete. In order to enhance the bond between the GFRP panels and the concrete cast *in situ*, a coating of epoxy adhesive filled with coarse limestone aggregates was provided to the panels. Additionally, the concrete of the deck was reinforced by FRP individual bars and by bidirectional FRP bar grids.

More recently, Gai *et al.* [58] presented an experimental study on a similar hybrid system, which also used a GFRP–concrete mechanical connection materialized by GFRP dowels. The authors have reinforced the feasibility of such structural systems, proving their ability to present ductile failure behaviour.

A hybrid GFRP–concrete sandwich panel (Figure 2.41) has been proposed by Keller *et al.* [59] for bridge deck applications. The hybrid sandwich comprises: (i) GFRP panels with T-upstands, acting both as permanent formwork and tensile skin; (ii) a lightweight concrete core; and (iii) a ultra high performance reinforced concrete compressive skin. The experimental investigations included the study of the influence of the GFRP–lightweight concrete connection, in particular the effect of adding an epoxy adhesive bond, and the influence of two different lightweight concretes. The results showed that the panels with bonded interfaces presented higher strength (+104%) than their un-bonded counterparts; however, the former panels presented brittle failure, while the latter presented a ductile failure. This study showed encouraging results regarding the feasibility of the proposed structural solution for bridge deck applications.

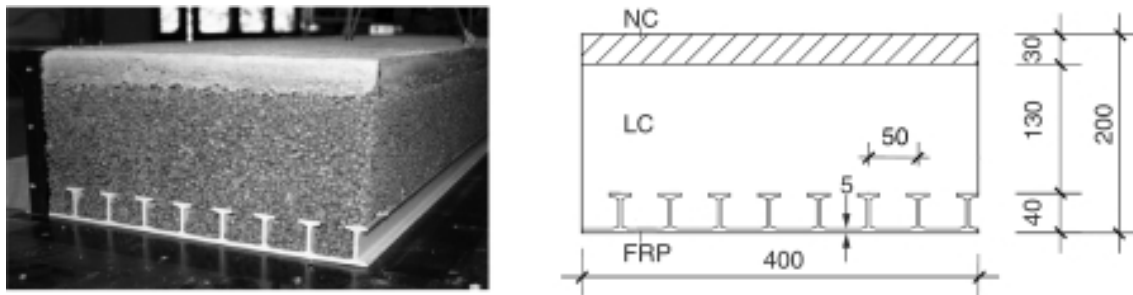


Figure 2.41.: Cross-section of a hybrid GFRP–concrete sandwich panel [59].

Correia *et al.* [60–62] have proposed a straightforward GFRP–concrete hybrid structural system, comprising I-shaped GFRP profiles and RC slabs, forming hybrid beams. The experimental investigations included the study on the influence of the connection system between both materials, namely: (i) mechanical connection materialized by steel bolts; and (ii) bonded connection materialized by an epoxy adhesive. The results have shown that the bonded connection leads to an overall better performance of the hybrid beams. Furthermore, these studies have shown the feasibility of the proposed GFRP–concrete hybrid system for structural applications, highlighting the importance of providing an adequate detailing of the solution for improved structural responses.

Recently, Zheng *et al.* [63] have proposed a hybrid GFRP–concrete bridge deck structural solution, comprising an arch concrete slab supported by hybrid (i) GFRP tubes filled with FRP reinforced concrete, or (ii) GFRP–concrete–steel beams (Figure 2.42). The connection between the hybrid beams and the concrete slab is guaranteed by stainless steel studs. Additionally, an FRP tying rod is provided to connect the beams transversely, enhancing the lateral restraints. The authors reported experimental results on 1/3 scale specimens, showing the feasibility of the proposed solution.



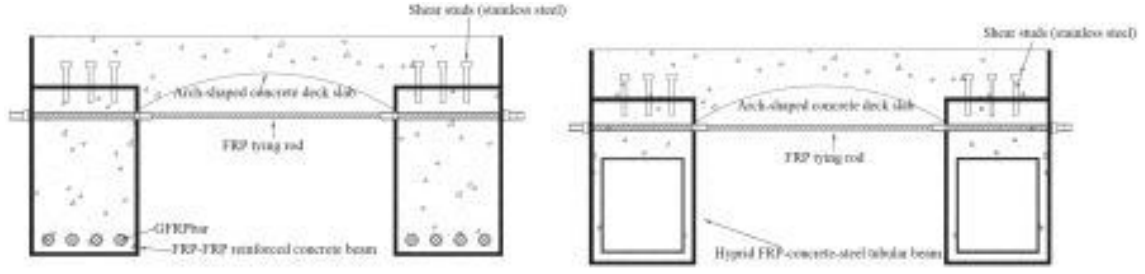


Figure 2.42.: Cross-section of hybrid GFRP-concrete deck systems [63].

## 2.7. Actions and requirements for footbridges

This section presents the specific design actions and requirements for footbridge structures, with particular emphasis on the Eurocode regulations [64,65]. The section is divided in two subsections: (i) static behaviour; and (ii) dynamic behaviour.

### 2.7.1. Static behaviour

#### 2.7.1.1. Loads

Eurocode 1 [65] presents three straightforward static vertical load models for footbridge structures, which are mutually exclusive: (i) uniformly distributed load ( $q_{fk}$ ); (ii) concentrated load ( $Q_{fwk}$ ); and (iii) service vehicles load ( $Q_{Serv}$ ).

The uniformly distributed load model should be applied in the deck of the footbridge structures in order to achieve the most unfavorable combination. The characteristic value of the uniformly distributed load is,

$$q_{fk} = 2.0 + \frac{120}{L + 30}, \quad 2.5 \leq q_{fk} \leq 5.0 \quad (\text{kN/m}^2) \quad (2.1)$$

where  $L$  represents the loaded length (typically the span), in meters.

The concentrated load ( $Q_{fwk}$ ) should be used in the safety verification of local effects. The characteristic value should be taken as 10 kN acting on a square surface with 0.10 m sides.

The service vehicles load, on the other hand, should only be considered where no permanent obstacles prevent vehicles to be driven onto the bridge deck. The service vehicle load can be taken as the load model presented in Figure 2.43, where  $Q_{SV1} = 80$  kN,  $Q_{SV2} = 40$  kN and  $x$  is the bridge direction.

Eurocode 1 [65] also provides a horizontal static load model to be used in combination with the vertical uniformly distributed load or with the service vehicle load. This horizontal load ( $Q_{flk}$ ), relevant for the design of piers, abutments and support systems, should be taken as 10% or 60% of the total vertical load when used, respectively, in combination with the uniformly distributed load or the service vehicle load.

Additionally, the same document [65] provides accidental load models for footbridges, namely due to the collision of vehicles with piers or decks and due to the accidental presence of vehicles on the bridge.

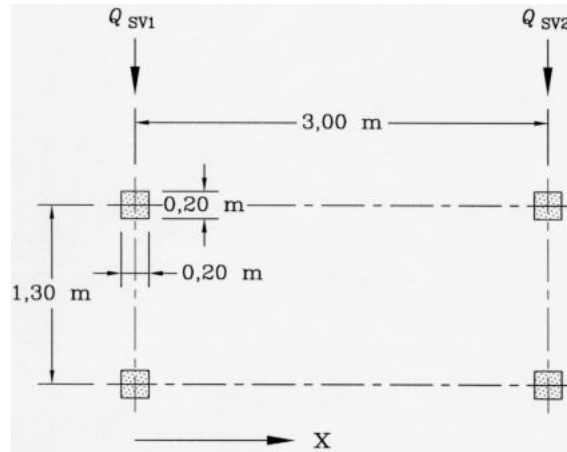


Figure 2.43.: Service vehicle load model:  $Q_{SV1} = 80$  kN,  $Q_{SV2} = 40$  kN and  $x$  is the bridge direction [65].

Owing to the fact that footbridge piers and decks are generally more sensitive to collision forces than those of road bridges, Eurocode 1 [65] recommends the protection of these elements to collision impacts, where relevant, namely by providing road restraint systems at appropriate distances before the piers. Nevertheless, for stiff piers, the document recommends a minimum point load of 1000 kN applied in the direction of the vehicle travel, or 500 kN applied perpendicularly to that direction. Both loads should be applied, separately, at a distance of 1.25 m from the ground surface.

Regarding the loads due to the accidental presence of vehicles on the footbridge, the vehicle load model presented in Figure 2.43 is recommended.

Table 2.5 presents the recommended variable reduced values ( $\psi$ ) for footbridges, including those for the traffic actions reported earlier, as well as others to be used with general actions (not specific of footbridges), namely wind forces ( $F_{Wk}$ ), thermal actions ( $T_k$ ), snow loads ( $Q_{Sn,k}$ ) and construction loads ( $Q_c$ ). It should be noted that the Eurocode 0 [64] dismisses the quasi-permanent load of the traffic actions, since the corresponding  $\psi_2$  are null.

Table 2.5.: Recommend values of  $\psi$  for footbridges (adapted from [64]).

Action	Symbol	$\psi_0$	$\psi_1$	$\psi_2$
Traffic loads	$q_{fk} + Q_{flk}$	0.4	0.4	0
	$Q_{fwk}$	0	0	0
	$Q_{Serv} + Q_{flk}$	0	0	0
Wind forces	$F_{Wk}$	0.3	0.2	0
Thermal actions	$T_k$	0.6	0.6	0.5
Snow loads	$Q_{Sn,k}$	0.8	0	0
Construction loads	$Q_c$ (during execution)	1.0	0	1.0

### 2.7.1.2. Requirements

The Eurocode regulations [64, 65] do not provide specific requirements for footbridges regarding their static behaviour (in addition to the general requirements all structures must comply with). In fact, these documents do not specify deflection limits for footbridge structures.

The AASHTO LFRD Guide specifications for the design of pedestrian bridges [66], on the other hand, specifies a maximum deflection of  $1/360$  of the span length, when subjected to the unfactored pedestrian live load, which corresponds to a uniformly distributed load of  $4.24 \text{ kN/m}^2$ .

Regarding FRP footbridges, Demitz *et al.* [67] suggest that the maximum deflection on such structures should be limited to  $1/400$  of the span length, although these authors do not provide a load combination for which this limit should be verified.

The Italian guidelines for FRP structures [68] recommend that the maximum deflection of FRP footbridges should be limited to  $1/100$  of the span length, when subjected to the characteristic (rare) load combination.

## 2.7.2. Dynamic behaviour

### 2.7.2.1. Loads

One of the main concerns in footbridge design is the dynamic response to pedestrian actions [69]. In this context, the characterization of pedestrian loads is of the utmost importance. Bachmann and Ammann [70] presented a thorough study on the characterization of pedestrian actions for several types of motion, setting the most relevant parameters of such characterization, namely: (i) the frequency or pacing rate ( $f_s$ ); (ii) the speed ( $v_s$ ); (iii) the stride length ( $l_s$ ); and (iv) the load–time function. Although these parameters are highly variable from individual to individual, and even dependent on the footwear and type of pavement, the authors have proposed some "standard" values, namely those provided in Table 2.6 for the first three parameters.

Table 2.6.: Parameters of pedestrian motion proposed by Bachmann and Ammann [70].

Motion	$f_s$ (Hz)	$v_s$ (m/s)	$l_s$ (m)
Slow walk	1.7	1.1	0.60
Normal walk	2.0	1.5	0.75
Fast walk	2.3	2.2	1.00
Jog	2.5	3.3	1.30
Sprint	$>3.2$	5.5	1.75

According to the authors [70], these parameters are mutually dependent, as shown in Figure 2.44.

Regarding the vertical load–time functions, Bachmann and Ammann [70] proposed a set of functions for different types of motion, as shown in Figure 2.45.

Regarding the walking motion functions, it should be noted that there is an overlap of time for which both feet are in contact with the pavement, whereas for the running motions (jog and sprint) there is a period of time where none of the feet is in contact with the pavement. The overlap of feet leads to an overlap of loads, exemplified in Figure 2.46. Another important aspect of the load–time curves is that, as the duration of contact between the foot and the pavement decreases the peak load increases, as shown in Figure 2.47. Furthermore, the two peak loads observed for the slower motion types, corresponding to

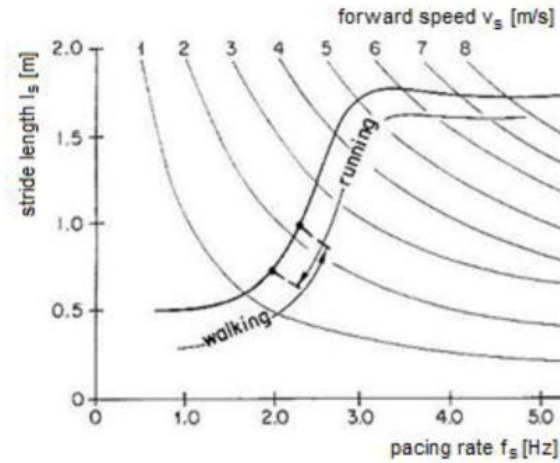


Figure 2.44.: Correlation between the pacing rate ( $f_s$ ), the speed ( $v_s$ ) and the stride length ( $l_s$ ) [70].

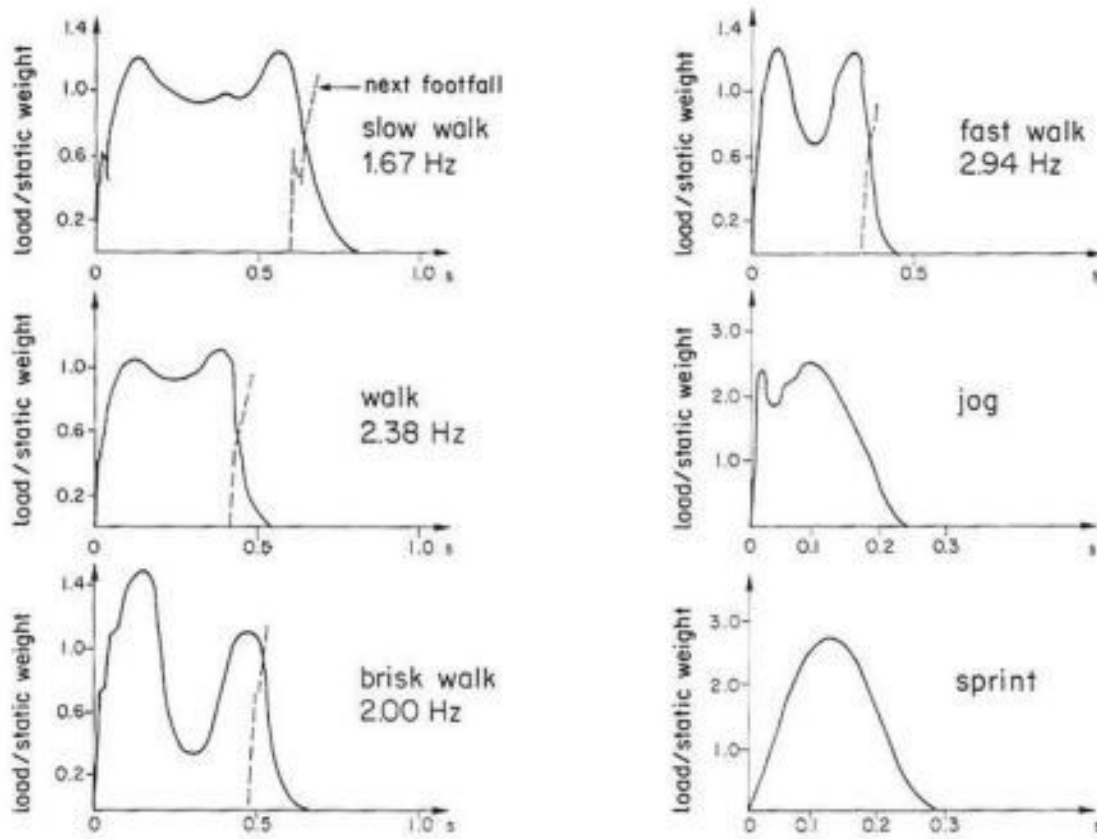


Figure 2.45.: Vertical load-time function for different types of motion [70].

the contact of the heel and ball of the foot, degenerate in a single peak load for the sprint motion.

Zivanovic *et al.* [71], in their literature review, presented horizontal load-time functions for both the transverse and longitudinal directions, shown in Figure 2.48, which were first reported by Andriacchi *et al.* [72] as an illustrative example taken from tests performed with seventeen different subjects with an average weight of 75.7 kgf.

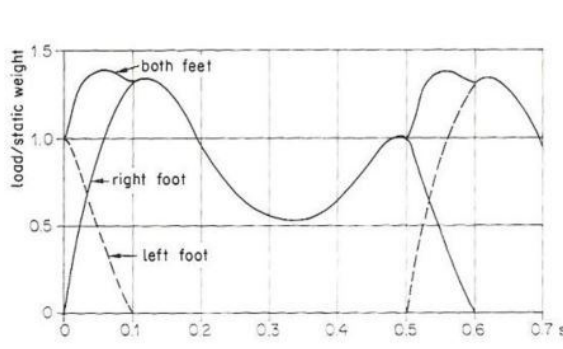


Figure 2.46.: Load-time function overlap [70].

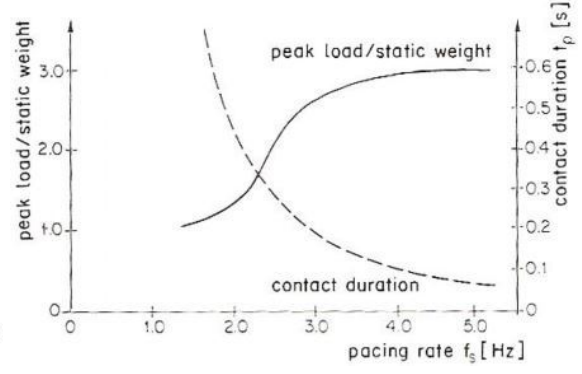
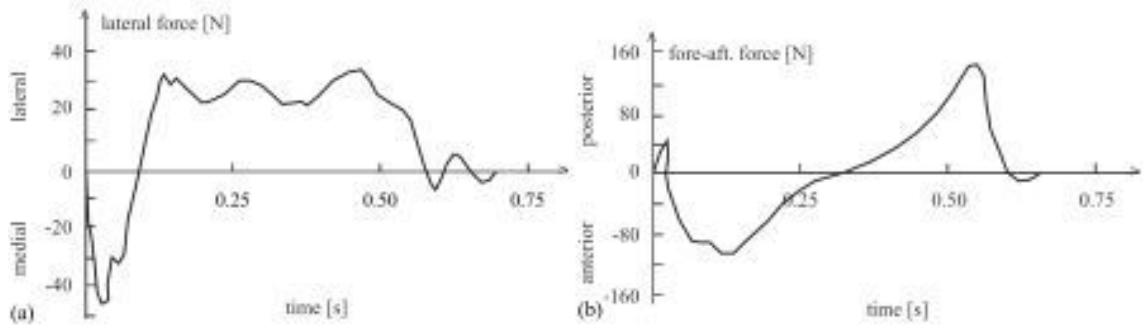

 Figure 2.47.: Correlation between the pacing rate ( $f_s$ ), the peak load/static weight ratio and the contact duration ( $t_p$ ) [70].


Figure 2.48.: Horizontal load-time functions for a) transverse and b) longitudinal directions (adapted from [71]).

According to Bachmann and Ammann [70], the walking motions, *i.e.* motions presenting foot contact overlap, can be estimated by,

$$F_p(t) = G + \Delta G_1 \cdot \sin(2\pi f_s t) + \Delta G_2 \cdot \sin(4\pi f_s t - \varphi_2) + \Delta G_3 \cdot \sin(6\pi f_s t - \varphi_3) \quad (2.2)$$

where,  $G$  is the static weight of the pedestrian,  $\Delta G_i$  is the load amplitude of the  $i^{th}$  harmonic and  $\varphi_i$  is the phase angle of the  $i^{th}$  harmonic. For the vertical loads, the authors suggest a linear variation of  $\Delta G_1$  from  $0.4G$  at  $f_s = 2.0$  Hz to  $0.5G$  at  $f_s = 2.4$  Hz, while  $\Delta G_2$  and  $\Delta G_3$  may be taken as  $0.1G$ . In order to estimate the horizontal loads,  $\Delta G_1$  and  $\Delta G_3$  can be taken as  $0.1G$  and  $\Delta G_2$  can be taken as zero. It should also be noted that, when estimating horizontal loads, the frequency ( $f_s$ ) should be taken as half of the pacing rate due to the the period inherent to the load-time functions themselves (*cf.* Figure 2.48). The phase angles can be estimated as  $\pi/2$ .

In order to estimate the load-time functions of the running motions, the same authors [70] propose using Eq. (2.3),

$$F_p(t) = \begin{cases} k_p \cdot G \cdot \sin(\pi \times \frac{t}{t_p}), & \text{if } t \leq t_p \\ 0, & \text{if } t_p < t \leq T_p \end{cases} \quad (2.3)$$

where  $T_p$  is the pace period ( $f_s^{-1}$ ) and  $k_p$  is a dynamic impact factor, varying with the ratio  $t_p/T_p$ , which can be determined from Figure 2.49.

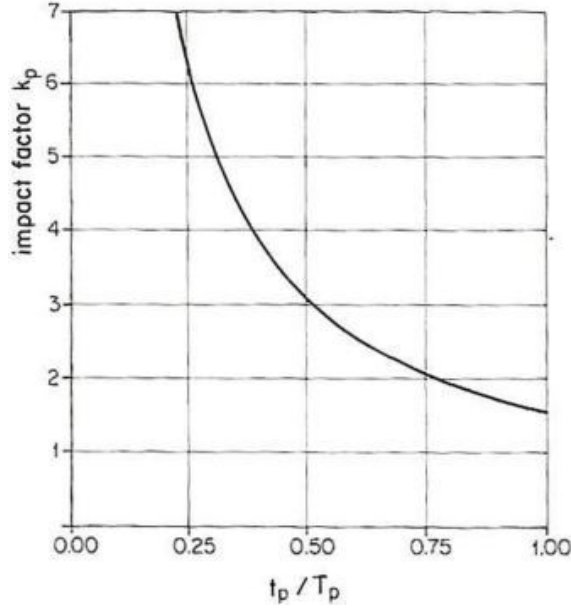


Figure 2.49.: Impact factor ( $k_p$ ) vs. relative contact duration ( $t_p/T_p$ ) [70].

Matsumoto *et al.* [73] presented one of the first load models considering the effects of several pedestrians, which was achieved by multiplying the load applied by one pedestrian by the square root of the number of pedestrians present in the footbridge ( $\sqrt{N}$ ),

$$F_p(t) = \sqrt{N} \cdot \sum G\alpha_i \sin(2\pi f_p t - \varphi_i) \quad (2.4)$$

where  $\alpha_i$  is the amplitude factor of the  $i^{th}$  harmonic. It should be noted, however, that this model does not account for pedestrian synchronization, a problem which was perceived later, namely with the excessive vibration of the Solferino and Millennium bridges [69, 74].

The latter load model is included in ISO 10137 [75], while an improved version accounting for pedestrian synchronization is proposed in the British national annex to the Eurocode 2 [76]. These models were initially designed to be used with one degree of freedom equivalent oscillator, simulating the footbridge. Thereafter, the major difficulty in their use is the complexity of the analysis required in order to apply them to an actual structural model, *i.e.* simulating different concentrated loads at the position of each feet and combining them in a time-history analysis, which is aggravated when simulating the structural response to the actions of several pedestrians.

In this context, several pedestrian load models have been proposed with uniformly distributed loads instead of concentrated loads, namely the models proposed by the British national annex to the Eurocode 2 [76], the French guide for footbridge design (SÉTRA) [74] and the SYNPEX guidelines [77], all based on the original Matsumoto model (*cf.* Eq. (2.4)),

$$q_p(t) = d \cdot \lambda \cdot \psi \cdot [\alpha_i \cdot G \cdot \sin(2\pi \cdot f_p t)] \quad (2.5)$$

where  $d$  is the traffic density, *i.e.* the number of pedestrians over the bridge surface,  $\lambda$  is a coefficient accounting for the equivalent number of pedestrians travelling the footbridge and  $\psi$  is a coefficient accounting for the effects of the synchronization of the pedestrians movement. These coefficients vary between the different documents, with SÉTRA [74] and SYNPEX [77] guidelines suggesting different  $\lambda$  coefficients for (i) sparse to dense crowds ( $d < 1.0$  pedestrians/m<sup>2</sup>), and for (ii) very dense crowds ( $d \geq 1.0$  pedestrians/m<sup>2</sup>). Additionally, it should be mentioned that the two last documents recommend a null  $\psi$  coefficient for vibration frequencies ( $f_p$ ) over 5.0 Hz, while the British national annex to the Eurocode 2 [76] sets that same coefficient at zero for vibration frequencies ( $f_p$ ) over 8.0 Hz.

### 2.7.2.2. Requirements

The Eurocode 0 [64] sets two different criteria for verification of pedestrian comfort in footbridges, (i) an indirect criterion, and (ii) a direct criterion. The indirect criterion is based on the risk of resonance phenomena due to pedestrian loading, setting the minimum fundamental frequencies at 5.0 Hz for vertical vibrations and 2.5 Hz for horizontal (transverse) vibrations.

When the indirect criterion for pedestrian comfort is not met, Eurocode 0 [64] recommends flat-out structural accelerations limits, when the footbridge is subjected to pedestrian loading of 0.7 m/s<sup>2</sup> for vertical accelerations and 0.2 m/s<sup>2</sup> or 0.4 m/s<sup>2</sup> for horizontal accelerations for regular or exceptional traffic, respectively.

Other regulations suggest a similar approach to that of Eurocode 0 [64], namely by limiting the maximum structural accelerations. The British Standard BS 5400 [78] and the Ontario Highway Bridge Design Code (OHBDC) [79] recommend the maximum vertical acceleration limit to be related with the first vertical vibration mode frequency ( $f_0$ , in Hz), as stated in Eqs. (2.6) and (2.7), respectively:

$$a_{v,max} = 0.5 \times f_0^{0.5} \text{ (m/s}^2\text{)} \quad (2.6)$$

$$a_{v,max} = 0.25 \times f_0^{0.78} \text{ (m/s}^2\text{)} \quad (2.7)$$

The SÉTRA [74] and SYNPEX [77] guidelines, on the other hand, suggest that the maximum acceleration limits should be related with three comfort levels (to be defined by the owners): (i) maximum; (ii) medium; and (iii) minimum. Table 2.7 summarizes the maximum vertical and horizontal acceleration ranges for each comfort level proposed in these documents.

In addition, the SÉTRA [74] guideline recommends that the horizontal accelerations should be limited to 0.10 m/s<sup>2</sup> in order to avoid the so-called "lock-in" effect. This phenomenon is described as the unconscious synchronization of the movement of the pedestrians in a crowd with the vibration frequencies of the footbridge. This phenomenon has only been reported with regard to horizontal vibrations, with the best known cases being the Solferino and the Millennium bridges, both presenting relatively low horizontal vibration frequencies (0.80 Hz and 0.80 Hz to 0.95 Hz, respectively [80]).

The different acceleration limits proposed by the aforementioned documents are compared in Figures 2.50 and 2.51 regarding vertical and horizontal vibrations, respectively.

Table 2.7.: Acceleration ranges for different comfort levels (adapted from [74, 77]).

Comfort level	Vertical acceleration (m/s <sup>2</sup> )	Horizontal acceleration (m/s <sup>2</sup> )
Maximum	< 0.50	< 0.15 (SÉTRA) < 0.10 (SYNPEX)
Medium	0.50 — 1.00	0.15 — 0.30 (SÉTRA) 0.10 — 0.30 (SYNPEX)
Minimum	1.00 — 2.50	0.30 — 0.80
Unacceptable	> 2.50	> 0.80

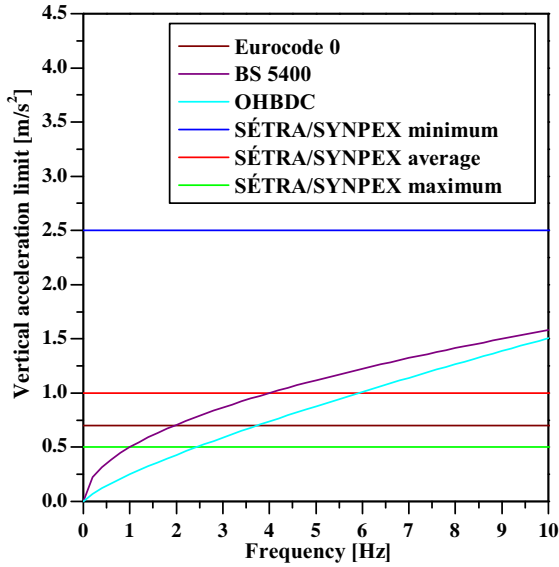


Figure 2.50.: Comparison between the vertical acceleration limits proposed in several documents.

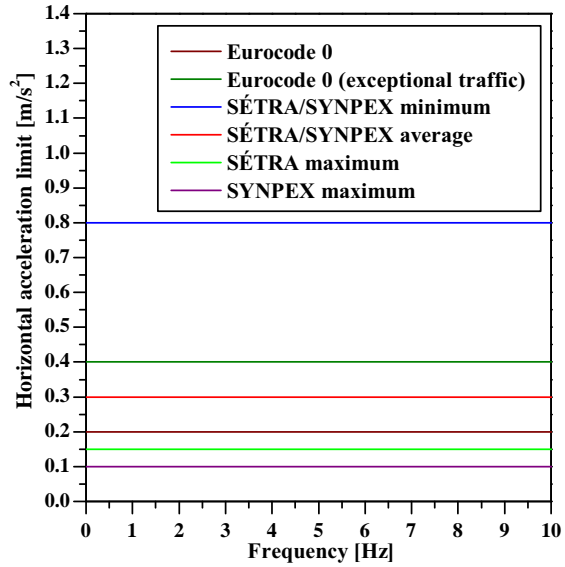


Figure 2.51.: Comparison between the horizontal acceleration limits proposed in several documents.

The above mentioned pedestrian comfort criteria refer to maximum acceleration limits, which may be quasi instantaneously surpassed without loss of comfort to the users. Thereby, different comfort criteria have been proposed, namely by British Standards BS 6841 [81] and BS 6471-1 [82] and by ISO 10137 [75]. BS 6841 [81] provides root mean squared (RMS) acceleration limits for pedestrian comfort. These RMS accelerations are provided as base-curves, in the frequency domain (between 1 Hz and 80 Hz), which can be adapted for several service situations for building structures by multiplying factors. It should be mentioned that this document does not provide multiplying factors for footbridge structures. BS 6471-1 [82] introduces the Vibration Dose Value (VDV) concept, which can be explained as the cumulative measurement of the vibrations received by a human during a certain period of time.

ISO 10137 [75], on the other hand, presents both RMS base-curves and multiplying factors, including multiplying factors for footbridges, and the VDV concept. With regard to footbridge structures, this document considers two distinct situations concerning vertical vibrations: (i) a pedestrian walking on the footbridge, for which a multiplying factor of 60 is recommended; and (ii) a pedestrian standing on the footbridge while other pedestrians travel the deck, where a multiplying factor of 30 is suggested. Concerning horizontal accelerations,



ISO 10137 [75] suggests adopting a multiplying factor of 60. Figures 2.52 and 2.53 present the RMS acceleration base limit curves as well as the resulting multiplied limits for both vertical and horizontal directions, respectively. It should be mentioned that, according to Zivanovic *et al.* [71], these multiplying factors are not based on known published research on vibrations on footbridges.

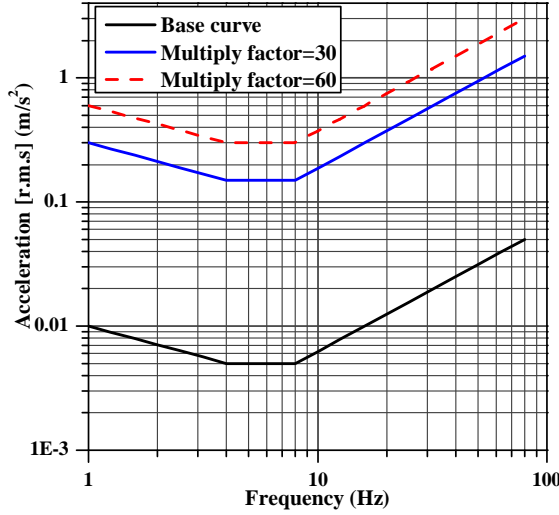


Figure 2.52.: ISO 10137 [75] RMS vertical acceleration limits for footbridge structures.

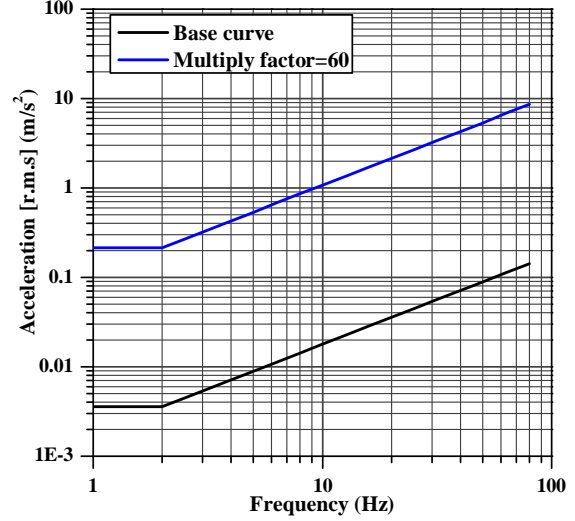


Figure 2.53.: ISO 10137 [75] RMS horizontal acceleration limits for footbridge structures.

## 2.8. Concluding remarks

In this chapter, several examples of FRP structural applications in the construction industry were presented, with a particular emphasis on applications of GFRP pultruded profiles. The general properties of these materials were described, highlighting their advantages and disadvantages, and showing their high potential for civil engineering structural applications.

The general properties of SFRSCC materials were also presented, demonstrating the potential of these cementitious materials in replacing regular reinforced concrete in some structural applications, namely those requiring small thickness elements.

Several hybrid GFRP-concrete structural solutions were presented, both in field studies and research applications, highlighting the advantages of designing hybrid structures comprising these materials. This brief review of existing solutions suggests the potential of the hybrid GFRP-SFRSCC footbridge structural solution proposed herein (*cf.* Chapter 3). Nevertheless, it is clear that there are some research fields, regarding the behaviour of GFRP-concrete structures, which need to be further developed. In fact, research on the dynamic behaviour of these structures, which is of the utmost importance for bridge applications, has not yet been reported, nor on their creep behaviour. Additionally, there are no reports on experimental tests regarding the static flexural behaviour (up to failure) of complete full-scale GFRP-concrete structures. All these aspects are addressed in this thesis, aiming at improving the overall knowledge on GFRP-concrete structures.

Finally, a summary of the specific actions and design requirements for footbridge structures was presented with regard to the static and dynamic behaviour, the latter being dominated with concerns due to the dynamic effects of pedestrian loading.

### 3. Structural concept and description of the Pontalumis Project

#### 3.1. Preliminary remarks

The present chapter describes the Pontalumis project, which framed the work developed in the present thesis, providing information regarding its objectives, partners, activities and tasks. The structural concept of the hybrid GFRP–concrete footbridge proposed herein is also described and the preliminary design, which led to the definition of the geometry of the full-scale prototype, is presented.

This chapter is divided in five sections: (i) preliminary remarks; (ii) Pontalumis project — development of a prototype of a pedestrian bridge in GFRP–ECC, which presents the research project; (iii) structural concept, which describes the structural concept and the objectives of the hybrid solution; (iv) preliminary design, where the geometry of the full-scale prototype is defined; and (v) concluding remarks.

#### 3.2. Pontalumis project — Development of a prototype of a pedestrian bridge in GFRP–ECC

The present work was developed in the scope of the Pontalumis project, which aimed at the development of a footbridge prototype that can be easily installed over any transportation axis. In this regard, three fundamental requirements were set for the structural system: (i) lightness and ease of installation; (ii) possibility of pre-fabrication with easy transportation; and (iii) low electromagnetic interference (in order to avoid interference with the electrification of some transport systems, such as trains or trams). In this context, the structural solution to be developed within this project is a hybrid GFRP–concrete structure. The GFRP material was chosen owing to its lightness, strength-to-weight ratio and electromagnetic transparency (*cf.* Section 2.4), while the concrete was chosen in order to increase the stiffness of the structural system and to prevent instability phenomena (*cf.* Section 2.6). However, in order to maintain the lightness of the structure, a steel fibre reinforced self-compacting concrete (SFRSCC) was chosen allowing the use of very thin concrete elements without bar reinforcement (*cf.* Section 2.5), instead of an engineering cementitious composite which had first been envisaged for this concept (hence the acronym "ECC" used in the title of the project).

This project was developed in partnership between *Instituto Superior Técnico* (IST) of the *University of Lisbon*, *University of Minho* (UM) and *ALTO Perfis Pultrudidos, Lda.*

(ALTO), the industrial partner, a Portuguese manufacturer of FRP products. The project was divided in seven main activities: (i) preliminary studies; (ii) acquisition and development of theoretical and technical know-how for the development of the project; (iii) development; (iv) construction of prototypes; (v) experimental tests; (vi) technical specifications; and (vii) dissemination of results. Table 3.1 summarizes the tasks attributed to each partner within each main activity.

Table 3.1.: Summary of activities and tasks of the Pontalumis project.

Activity	Task description	Partner
I — Preliminary studies	1 — Economical advantages	ALTO
	2 — Technical advantages	IST / UM
II — Formation activities	1 — Technics of pre- and post-tension in GFRP profiles	ALTO
	2 — State-of-the-art on GFRP-concrete structures	IST
	3 — Numerical modelling of hybrid structures	UM
III — Development	1 — Numerical modelling up to failure	UM
	2 — Analytical modelling	IST
	3 — Manufacturing of optimized GFRP profiles	ALTO
	4 — Manufacturing and characterization of the SFRSCC	UM
	5 — Evaluation of the numerical model	UM
	6 — Evaluation of the analytical models	IST
	7 — Parametric studies	IST
IV — Prototypes	1 — GFRP profiles	ALTO
	2 — GFRP-SFRSCC hybrid specimens for connection tests	ALTO / UM
	3 — Construction of the footbridge prototypes	ALTO / UM
V — Tests	1 — GFRP coupons under different environmental conditions	UM
	2 — GFRP profiles under different environmental conditions	UM
	3 — GFRP-SFRSCC connection tests under cyclic loading	UM
	4 — GFRP-SFRSCC connection tests under static loading	IST
	5 — Dynamic tests on the footbridge prototypes	IST
VI — Specifications	1 — Design recommendations and technical specifications	IST / UM
VII — Dissemination of results	1 — Development of a web site	ALTO
	2 — Reports and papers in scientific journals and conferences	All
	3 — Final seminar	All

The Pontalumis project was funded by the *Portuguese Innovation Agency* (ADI), project 2009/003456, through the *Quadro de Referência Estratégica Nacional* (QREN). The financial support allowed performing all the tasks summarized in Table 3.1, as well as pursuing additional tasks, such as the development of a small-scale prototype in IST, described in this work.

### 3.3. Structural concept

As mentioned earlier (*cf.* Section 2.6), the main objective of adding different materials to a structural system, thereby developing a hybrid structure, is to make use and enhance the best characteristics of the constituent materials, while overcoming their limitations. The structure to be developed in this work is a simply supported footbridge. Thereafter, the main solicitations comprise gravity loads, causing transverse forces and positive bending moments, *i.e.* compressing the top fibres and tensioning the bottom fibres of the cross-section. In this regard, the cross-section of the structural system proposed presents a thin

SFRSCC compression lamina, which acts as the deck of the footbridge, connected to GFRP profiles positioned underneath it.

Regarding the overall dimension of the prototypes (width and span length), a survey of the existent footbridges over the Portuguese railways, based in the *National Railway Network Company (REFER)* database, performed within the scope of the Pontalumis project, showed that the vast majority (76%) of these structures presented a single span [83]. The most common width was found to lay in the range between 2.0 m and 3.0 m, more specifically 30% between 2.0 m and 2.5 m, and 31% between 2.5 m and 3.0 m [83]. In what concerns the span length, the survey showed that 15% of the existing footbridges have spans between 10.0 m and 15.0 m, while ranges between 15.0 m and 20.0 m, and 20.0 m and 25.0 m were the most common, corresponding to 28% and 29%, respectively [83]. In this context, the width of the full-scale prototype was defined as 2.0 m with a maximum length of 12.0 m (11.5 m span). It should be mentioned that the maximum span length chosen is not among the most common ranges (15.0 m and 25.0 m), since all partners agreed that due to (i) the economical constraints regarding the development of the GFRP profiles, (ii) the possibility of transporting the assembled structure without special transportation requirements, and (iii) the novelty of the structural solution it would be advisable for the development of the Pontalumis project to set the maximum length between 10 m and 12 m.

Therefore, the cross-section idealized for this footbridge structure comprised a SFRSCC deck connected to two GFRP pultruded profiles acting as main girders, as shown in Figure 3.1.

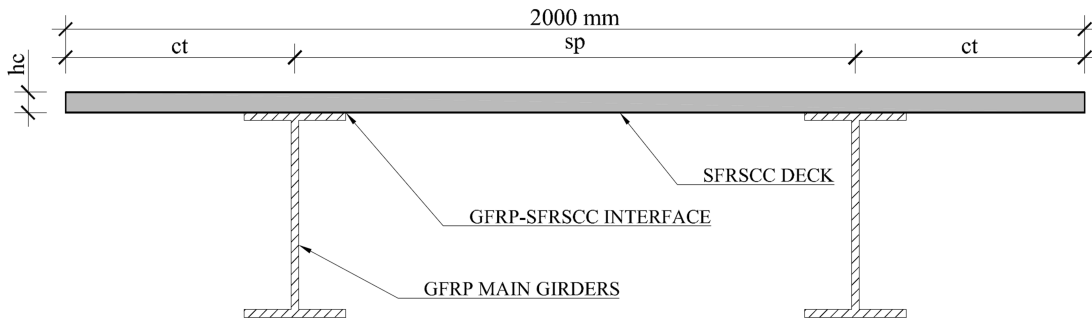


Figure 3.1.: Idealized cross-section.

As can be easily perceived from Figure 3.1, for positive bending moments along the longitudinal direction, compressive stresses will develop in the top fibres of the cross-section, where the SFRSCC layer is located, while tensile stresses will develop in the bottom fibres, where the GFRP profiles are positioned. The positioning of the elements in the cross-section, associated with this stress distribution, allows each material to contribute to the overall behaviour of the structure with their best mechanical properties: (i) compressive properties for the SFRSCC, which, despite of the fibre reinforcement, is a cementitious material and, (ii) tensile properties for the GFRP material. Furthermore, the thickness of the SFRSCC slab ( $h_c$ ) and the geometry of the GFRP profiles should be conjugated in order to position the neutral axis of the cross-section in the vicinity of the GFRP-concrete interface, enhancing the full exploitation of each materials' best properties.

Another advantage of the present structural system is avoiding the triggering of local instability phenomena in the GFRP profiles' top flanges (which may be compressed if the neutral axis lays on the webs of the profiles) owing to the support of the SFRSCC slab, enhancing the full-exploitation of the FRP material strength. In this context, and in order to provide a continuous interface, the connection between the GFRP elements and the SFRSCC

slab should be provided by (i) adhesive bonding, and (ii) a bolted connection system using stainless steel studs/bolts. The adhesive connection is expected to govern the behaviour of the interface in terms of stiffness, while the bolts are expected to provide a redundant connection system in case of premature deterioration of the adhesive due to vandalism, environmental and/or rheological phenomena. Notwithstanding, the bolted connection may also be used, depending on the number of connectors provided, to create a progressive collapse mechanism for the interface failure (*cf.* Chapter 5).

Regarding the structural behaviour in the transverse direction, and owing to the high tensile strength and ductility in tension of the SFRSCC material, when compared to regular concrete [84], the SFRSCC slab ensures the transmission of the applied loads to the GFRP profiles without any bar reinforcement.

Additional elements, namely concrete jackets and secondary girders, are also included in the proposed hybrid GFRP–concrete structural system. The secondary girders, materialized by GFRP pultruded profiles, connecting the main girders, should be used in order to ensure that the section behaves as a whole when subjected to eccentric loading without excessive torsion deformations. In fact, due to the relatively low warping constants of the proposed cross-section, eccentric loading could result in large warping deformations, overloading one of the main girders and the thin SFRSCC slab in the transverse direction.

In what concerns the concrete jackets, these are defined for the support sections in order to avoid premature failure of the webs, in these sections, due to web crushing or buckling in the transverse direction (known as web-crippling), which are very relevant phenomena in FRP thin-walled structures [4, 5, 7, 14, 15].

### 3.4. Preliminary design

This section presents a summary of the preliminary design stage of the Pontalumis full-scale prototype, which allowed the definition of its geometry, namely (i) the definition of the GFRP profiles geometry, and (ii) the slab thickness. This early design stage was based on parametric studies, which were conducted using very simple analytical equations and approximate material properties.

Regarding the material properties, these were defined based on literature references for the GFRP material [5], considering the elasticity modulus in the longitudinal direction ( $E_L$ ) as 37.0 GPa, the shear modulus ( $G_{LT}$ ) as 3.5 GPa, the axial strength in the longitudinal direction ( $\sigma_{u,L}$ ) as 425.5 MPa and the shear strength ( $\tau_{u,LT}$ ) as 30.0 MPa. The properties of the SFRSCC material were also defined based on the literature [84] and preliminary compression tests on cylinder coupons (*cf.* Section 4.3.2.2), setting the elasticity modulus ( $E_c$ ) as 37.0 GPa and the cracking strength ( $f_{cr}$ ) as 6.0 MPa. Regarding the partial safety coefficients of the materials, the following values were adopted for this early stage of the design process: (i) 3.2 for the GFRP material ( $\gamma_{M,GFRP}$ ); and (ii) 1.5 for the SFRSCC material ( $\gamma_{M,c}$ ). The partial safety coefficient adopted for the GFRP material at this early stage of the design process was based on the recommendations of the EuroComp guidelines [38]. Nevertheless, it should be mentioned that the recommendations provided in that document may lead to overly conservative partial safety coefficients, namely when compared to those proposed by the (more recent) Italian Guidelines [68], which recommend coefficients of 1.5 (or even slightly lower). For the SFRSCC material the partial safety factor adopted was that recommended by the Eurocode 2 [85] for regular concrete materials.

Considering the idealized cross-section of the proposed structural system shown in Figure 3.1, the transverse spacing between the main girders ( $sp$ ) was one of the first parameters to be set. Owing to the fact that there is no bar reinforcement in the slab and, therefore, the SFRSCC material must resist the applied loads by itself, the main criterion used to define this spacing was to have similar positive and negative transverse bending moments, so as to optimize the use of the SFRSCC material strength. Thereafter, the optimal spacing between main girders ( $sp$ ) may be found as a function of the total width of the deck ( $l_t$ ) and a non-dimensional parameter ( $\alpha$ ) accounting for different live load configurations, as expressed in Eq. (3.1),

$$sp = \frac{\alpha}{2 + \alpha} \cdot 2\sqrt{2}l_t \quad (3.1)$$

where the parameter  $\alpha$  may be given as a function of the live load configuration and of the relation between the live load ( $q_{LL}$ ) and the self-weight of the slab ( $g_{SW}$ ), including the correspondent load safety factors ( $\gamma_Q$  and  $\gamma_G$ , respectively). For the present study, three live load configurations were considered, namely: (i) uniform distribution, (ii) live load on the cantilevers, and (iii) live load on the inner span, as illustrated in Figure 3.2.

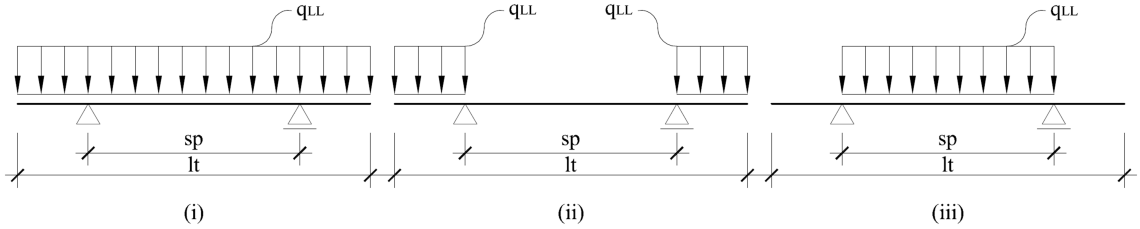


Figure 3.2.: Live load configurations over the transverse direction, (i) uniform distribution, (ii) live load on the cantilevers, and (iii) live load on the inner span.

The  $\alpha$  parameter may then be calculated, for each of these configurations and, additionally, for the governing bending moment envelope with the expressions provided in Eq. (3.2):

$$\begin{aligned} \alpha &= 1, & \text{for (i) uniform live load} \\ \alpha &= \sqrt{\frac{g_{SW} \cdot \gamma_G + q_{LL} \cdot \gamma_Q}{g_{SW} \cdot \gamma_G}}, & \text{for (ii) live load on cantilevers} \\ \alpha &= \sqrt{\frac{g_{SW} \cdot \gamma_G}{g_{SW} \cdot \gamma_G + q_{LL} \cdot \gamma_Q}}, & \text{for (iii) live load on interior span} \\ \alpha &= \sqrt{\frac{2g_{SW} \cdot \gamma_G + q_{LL} \cdot \gamma_Q}{2(g_{SW} \cdot \gamma_G + q_{LL} \cdot \gamma_Q)}}, & \text{for (iv) bending moment envelope} \end{aligned} \quad (3.2)$$

Figure 3.3 presents the evolution of the spacing between main girders ( $sp$ ) with the self-weight or thickness of the SFRSCC deck ( $g_{SW}$  and  $h_c$ , respectively). These results were calculated considering the following parameters: (i)  $q_{LL} = 5.0 \text{ kN/m}^2$ ; (ii)  $\gamma_Q = 1.50$ ; (iii)  $\gamma_G = 1.35$  (*cf.* Section 2.7); and (iv) a specific weight of the SFRSCC of  $24.0 \text{ kN/m}^3$  (*cf.* Section 4.3).

The results shown in Figure 3.3 indicate that as the slab thickness and self weight increase (*i.e.*, the influence of the live load diminishes), all curves converge for the uniform distribution load configuration ( $sp \approx 1172 \text{ mm}$ ).

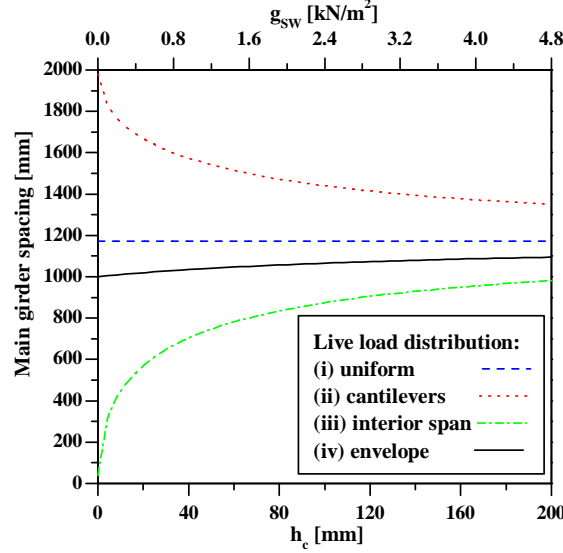


Figure 3.3.: Optimized spacing as a function of the slab thickness ( $h_c$ ) for different live load configurations and envelope.

From Figure 3.3, it is clear that the optimal spacing between the main girders is directly linked with the slab thickness ( $h_c$ ) due to the influence of the self-weight ( $g_{SW}$ ) in Eq. (3.2). Therefore, in order to set the spacing between the main girders ( $sp$ ), it is also necessary to ensure the ability of the slab to safely resist the applied loads in the transverse direction by defining its thickness ( $h_c$ ). The design resistant bending moment of the slab in the transverse direction ( $M_{rd,cT}$ ) may be found by multiplying its first moment of area by its cracking strength ( $f_{cr}$ ) as indicated in Eq. (3.3):

$$M_{rd,cT} = \frac{h_c^2}{6} \frac{f_{cr}}{\gamma_{M,c}} \quad (3.3)$$

On the other hand, considering the optimal main girder spacing ( $sp$ ), *i.e.* the positive and negative bending moments present the same value, the design value of the bending moment ( $M_{sd,cT}$ ) may be determined with Eq. (3.4):

$$M_{sd,cT} = (g_{SW} \cdot \gamma_G + q_{LL} \cdot \gamma_Q) \times \frac{ct^2}{2} \quad (3.4)$$

Figure 3.4 shows the evolution of the design values of the resistant and acting bending moments ( $M_{rd,cT}$  and  $M_{sd,cT}$ , respectively) as a function of the slab thickness ( $h_c$ ).

As expected, the design resistant bending moment increases ( $M_{rd,cT}$ ) with higher slab thicknesses ( $h_c$ ). The design acting bending moment ( $M_{sd,cT}$ ), on the contrary, is almost constant, showing a decreasing trend with the slab thickness ( $h_c$ ). In fact, in spite of the self-weight increase, the variation of the optimal spacing between main girders ( $sp$ ) causes the design load bending moment ( $M_{sd,cT}$ ) to diminish. Finally, comparing the results obtained from Eqs. (3.3) and (3.4), it can be shown that the safety of the structure regarding bending in the transverse direction is only ensured (considering the material properties listed above) with slab thicknesses ( $h_c$ ) higher than 39.29 mm.

In this context, a parametric study regarding the geometry of the profile was conducted considering the minimum thickness of the slab which ensures safety in the transverse



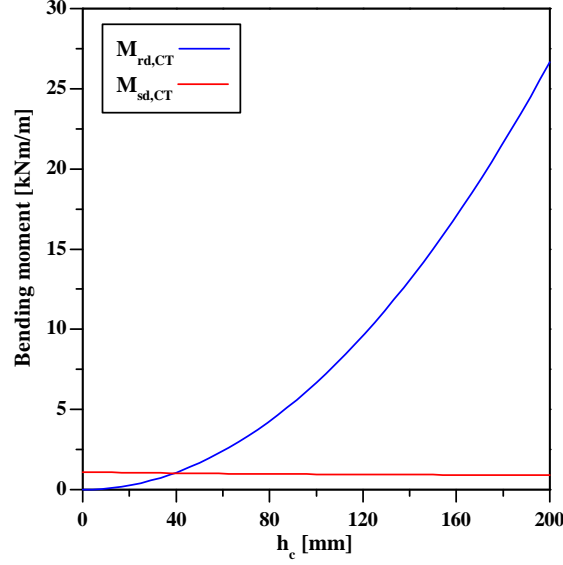


Figure 3.4.: Design values of resistant and acting bending moments ( $M_{rd,CT}$  and  $M_{sd,CT}$ , respectively) as a function of the slab thickness ( $h_c$ ).

direction ( $h_c = 40$  mm) and a longitudinal span ( $L$ ) of 11.5 m, corresponding to the maximum length defined in the Pontalumis project (12.0 m). Together with ALTO, an I-shaped cross-section was chosen due to the ease of production and versatility (in terms of other applications) of such sections, with the generic dimensions shown in Figure 3.5.

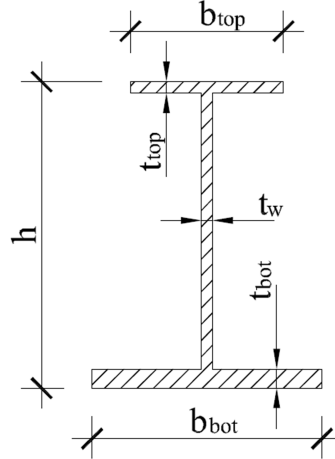


Figure 3.5.: General geometry of the GFRP profiles for the main girders.

Considering the general geometry presented in Figure 3.5, the first iteration of the parametric study consisted of testing a bi-symmetric I-shaped profile with a height ( $h$ ) of 400 mm, a flange width ( $b_{top} = b_{bot}$ ) of 200 mm and a constant thickness ( $t_{top} = t_{bot} = t_w$ ) of 15 mm. Several iterations were performed with the aim of reducing the area of the profiles, thereby reducing the cost of the structure. The cross-sections' dimensions of all iterations are provided in Table 3.2, which also presents their relative reduction of area when compared with the first iteration.

Regarding the serviceability limit states (SLS) criteria, the parametric study considered the verification of (i) the long-term maximum deflections, and (ii) the pedestrian comfort criteria.

Table 3.2.: Geometrical properties of the iterations of the parametric study regarding the GFRP profiles.

Iteration	$h$ mm	$b_{top}$ mm	$b_{bot}$ mm	$t_w$ mm	$t_{top}$ mm	$t_{bot}$ mm	Symmetry	Area %
1	400	200	200	15	15	15	Bi-symmetric	100
2	435	100	75	17.5	10	10	Mono-symmetric	78
3	400	100	100	20	10	10	Bi-symmetric	83
4	350	100	125	20	10	10	Mono-symmetric	77
5	325	100	150	20	10	10	Mono-symmetric	74
6	400	100	200	15	10	15	Mono-symmetric	83
7	400	100	200	17.5	10	15	Mono-symmetric	92
8	400	100	200	17.5	10	12.5	Mono-symmetric	88
9	400	100	150	17.5	10	15	Mono-symmetric	85
10	350	100	200	15	10	15	Mono-symmetric	77
11	350	100	200	17.5	10	15	Mono-symmetric	84
12	350	100	200	17.5	10	12.5	Mono-symmetric	80
13	350	100	150	17.5	10	15	Mono-symmetric	77

The long-term deflections were calculated for each iteration based on the following assumptions: (i) the creep behaviour of the GFRP material follows the laws proposed by Bank [4] for creep in flexure (*cf.* Section 6.6.3); (ii) the creep behaviour of the SFRSCC follows the creep law proposed by Eurocode 2 [85]; and (iii) the creep deflections are caused by the quasi-permanent load combination ( $q_{cp}$ ) which, for footbridges, can be considered as the self-weight of the structure (*cf.* Section 2.7). Thereafter, the long-term mid-span deflections ( $\delta_{ms}(t)$ ) of the footbridge structure may be calculated with Eq. (3.5) [4],

$$\delta_{ms}(t) = \frac{5 \cdot q_{cp} L^4}{384 EI(t)} + \frac{q_{cp} L^2}{GkA(t)} \quad (3.5)$$

where  $t$  represents time,  $EI(t)$  is the flexural stiffness of the hybrid cross-sections over time and  $GkA(t)$  is their shear stiffness over time. Regarding the last parameter, a common simplification was assumed [4,5] that the shear stresses are supported only by the web of the profiles, thus considering a constant shear area equal to the area of the webs of the profiles ( $A_w$ ), *i.e.*  $GkA(t) = A_w G_{LT}(t)$ .

In the absence of specific limits regarding the maximum deflections for composite/hybrid footbridge structures (*cf.* Section 2.7), a maximum long-term deflection of  $L/400$  was deemed as acceptable at this stage of the design, corresponding to 28.75 mm.

In what concerns the pedestrian comfort, the Eurocode 0 [64] indirect criterion was used, therefore only iterations with a fundamental vibration frequency higher than 5.0 Hz (*cf.* Section 2.7) were considered acceptable. In this earlier stage of the design process, the fundamental flexural vibration frequency ( $f$ , in Hz) was calculated disregarding the shear deformability of the structure, using the well known expression stated by Eq. (3.6), based on the Bernoulli beam theory [86],

$$f = \frac{\pi}{2L^2} \sqrt{\frac{EI}{\rho A}} \quad (3.6)$$

where  $EI$  is the instantaneous flexural stiffness of the hybrid cross-sections, while  $\rho A$  represents their mass by unit of length in the longitudinal direction.

In what concerns the ultimate limit states (ULS) analysis, two failure modes were considered: (i) web shear failure, and (ii) flexural failure of the cross-section. It should be noted that the following equations were devised per unit of width. Assuming the same simplifications considered above regarding the shear stresses, the design resistant shear force ( $V_{rd}$ ) was computed with Eq. (3.7),

$$V_{rd} = \frac{\tau_{u,LT} A_w}{\gamma_{M,GFRP}} \quad (3.7)$$

where  $\tau_{u,LT}$  is the in-plane shear strength of the GFRP profiles' webs. The design value of the acting shear force ( $V_{sd}$ ) was calculated with Eq. (3.8):

$$V_{sd} = (g_{SW} \cdot \gamma_G + q_{LL} \cdot \gamma_Q) \frac{L}{2} \quad (3.8)$$

The design resistant bending moment ( $M_{rd}$ ), on the other hand, which was governed by the tensile failure of the bottom fibres of the GFRP profiles in all iterations, was computed using Eq. (3.9),

$$M_{rd} = EI \cdot \frac{\sigma_{u,L}}{E_L(h_t - NA)\gamma_{M,GFRP}} \quad (3.9)$$

where,  $h_t$  is the total height of the cross-section, and  $NA$  is the neutral axis position with respect to the top of the cross-section. Finally, the design value of the acting bending moment ( $M_{sd}$ ) was calculated with Eq. (3.10):

$$M_{sd} = (g_{SW} \cdot \gamma_G + q_{LL} \cdot \gamma_Q) \frac{L^2}{8} \quad (3.10)$$

Table 3.3 presents the summary of SLS and ULS verifications for each of the 13 iterations performed. SLS verifications include the long-term midspan deflections for a loading period of 50 years ( $\delta_{ms}(50 \text{ yrs})$ ) and the assessment of the fundamental vibration frequency ( $f$ ). The verification of the ULS is presented in terms of the ratio between the the design load ( $q_{sd} = g_{SW} \cdot \gamma_G + q_{LL} \cdot \gamma_Q$ ) over the design ultimate load ( $q_{rd}$ ) and includes the failure mode (both failure modes considered are brittle).

The results presented in Table 3.3 show that only the geometry used in iteration 10 is not able to verify the ULS requirements, while five geometries are not able to fulfill the SLS requirements considered (iterations 4, 5, 10, 12 and 13 do not comply with the long-term deflection requirements, *i.e.*  $\delta_{ms}(50 \text{ yrs}) \leq L/400$ , while iterations 4, 5 and 13 do not fulfill the indirect pedestrian comfort criterion either, *i.e.*  $f \geq 5 \text{ Hz}$ ). These results confirm that FRP based structures are often governed by SLS requirements instead of ULS requirements, which commonly govern the design of traditional structures, avoiding the full exploitation of the FRP materials' strength. Another important result is the possibility of saving up to 22% of GFRP material using iteration 2 without compromising the structural requirements.

Considering the parametric study presented above, the section chosen for the construction of the full-scale prototype was that corresponding to the first iteration, a bi-symmetric

Table 3.3.: Summary of the parametric study results regarding the geometry of the GFRP profiles.

Iteration	Failure		$\delta_{ms}(50 \text{ yrs})$		$f$
	$q_{rd}/q_{sd}$	mode	mm	$L/$	Hz
1	1.02	Web shear	22.7	507	5.85
2	1.28	Flexure	26.2	439	5.36
3	1.31	Flexure	28.1	409	5.14
4	1.14	Flexure	36.0	319	4.52
5	1.09	Flexure	40.1	287	4.01
6	1.03	Web shear	22.0	523	5.93
7	1.19	Web shear	21.1	545	6.02
8	1.19	Web shear	22.5	511	5.81
9	1.20	Web shear	23.7	485	5.66
10	0.90	Flexure	28.9	398	5.13
11	1.05	Flexure	27.8	414	5.20
12	1.05	Flexure	29.8	386	5.01
13	1.05	Flexure	31.5	365	4.87

I-shaped section (I400 —  $400 \times 200 \times (15) \text{ mm}^2$ ) shown in Figure 3.6. It should be mentioned that although considerable savings could be achieved using a different section for the main girders, as demonstrated by the results of the parametric study (*cf.* Table 3.3), the industrial partner ALTO preferred the I400 bi-symmetric cross-section due to (i) the ease of the technical manufacturing process, and (ii) to its commercial advantages, being easier to adapt to different structures.

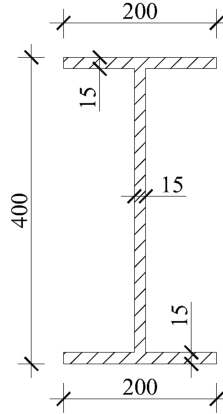


Figure 3.6.: Geometry of the I400 GFRP profiles used as main girders of the full-scale prototype (dimensions in mm).

Having set the geometry of the GFRP main girders, the influence of the slab thickness ( $h_c$ ) in the fulfillment of the SLS and ULS was also studied (using Eqs. (3.5) to (3.10)). Figure 3.7 presents the evolution of the long-term midspan deflections for a loading period of 50 years ( $\delta_{ms}(50 \text{ yrs})$ ) as a function of the slab thickness ( $h_c$ ), while Figure 3.8 presents the evolution of the fundamental vibration frequency ( $f$ ).

Figure 3.7 shows that the deflection limit state requirements ( $\delta_{ms}(50 \text{ yrs}) \leq L/400$ ) are only met for thicknesses under 60 mm within the thickness range considered ( $0 \text{ mm} \leq h_c \leq 250 \text{ mm}$ ). Concerning the pedestrian limit state comfort, Figure 3.8 shows

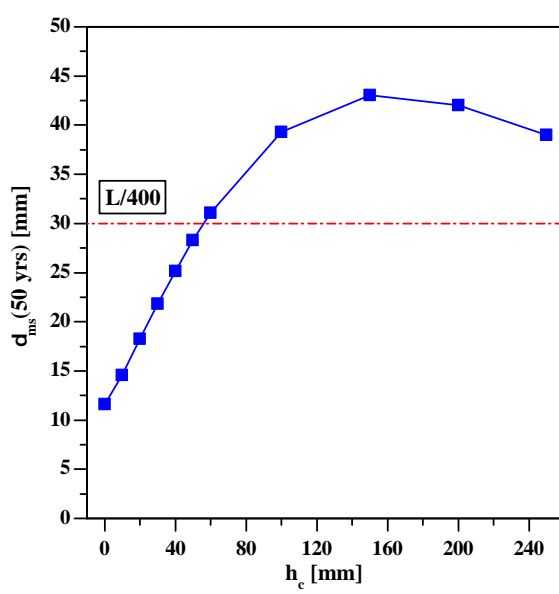


Figure 3.7.: Evolution of the long-term midspan deflections ( $\delta_{ms}(50 \text{ yrs})$ ) as a function of the slab thickness ( $h_c$ ).

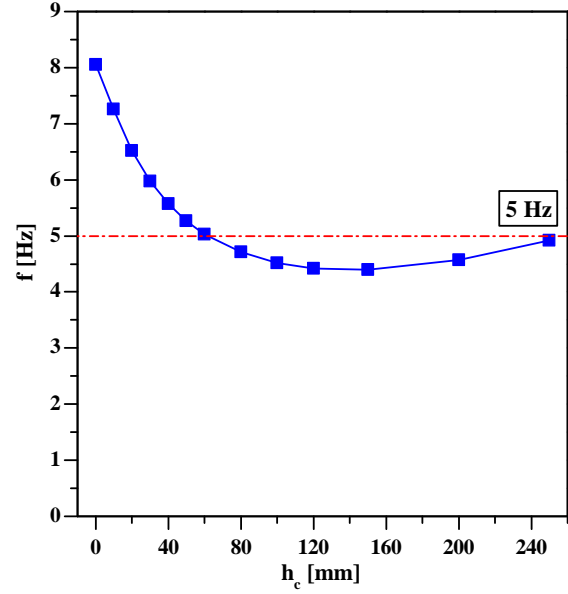


Figure 3.8.: Evolution of the fundamental vibration frequency ( $f$ ) as a function of the slab thickness ( $h_c$ ).

that the indirect criterion ( $f \geq 5 \text{ Hz}$  [64]) is only fulfilled (within the studied range) by thicknesses not higher than 60 mm.

Regarding the fulfilment of the ULS, Figure 3.9 presents the variation of the applied and resistant shear forces and bending moments ( $V_{sd}$  and  $V_{rd}$  and,  $M_{sd}$  and  $M_{rd}$ , respectively) with the evolution of the slab thickness ( $h_c$ ).

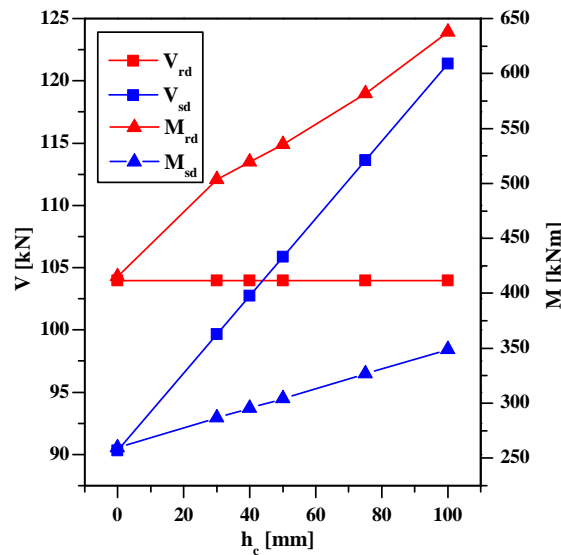


Figure 3.9.: Resistant and acting design forces as a function of the slab thickness ( $h_c$ ).

Figure 3.9 indicates that the ULS requirements are met for slab thicknesses ( $h_c$ ) up to 40 mm with failure being governed by the shear strength of the GFRP profiles (webs).

The results of the latter parametric study led to the definition of the thickness of the slab ( $h_c$ ) for the full-scale prototype around 40 mm, which corresponds to an optimal spacing ( $sp$ ) of 1034 mm, considering the bending moment envelope (*cf.* Figure 3.3). Taking into account ease of construction requirements, the spacing between main girders ( $sp$ ) was set as 1100 mm, with the length of the cantilevers ( $ct$ ) being set as 450 mm. This geometry comprised a negative design bending moment in the transverse direction with an absolute magnitude -25.7% lower than its positive counterpart.

### 3.5. Concluding remarks

This chapter presented the hybrid GFRP–concrete structural concept developed within this work and in the Pontalumis project.

The parametric study conducted has shown the feasibility of the structural system proposed for footbridges. In addition, it was shown that the preliminary design can be easily performed using very simple analytical formulae. This early design stage allowed the definition of the basic geometry of the full-scale prototype, namely the geometry of the cross-section, including the GFRP profiles to be used as the main girders of that prototype and the thickness of the deck.

## 4. Materials

### 4.1. Preliminary remarks

This Chapter presents the mechanical characterization of the main constituent materials of the small- and full-scale footbridge prototypes, which are fully described in Chapters 6 and 7, respectively.

The experimental investigations regarding the GFRP main and secondary girders used in the construction of the above mentioned prototypes included (i) coupon tests in order to determine the mechanical properties of the materials, and (ii) full-scale flexural tests on the isolated beams in order to investigate their bending behaviour. Similarly, the experimental investigations regarding the concrete (SFRSCC) used in the prototypes' decks included (i) coupon and (ii) full-scale flexural tests. The experimental results derived from the full-scale flexural tests on GFRP beams were also compared with analytical and numerical predictions.

The present Chapter is divided in five main sections that address the following issues: (i) preliminary remarks; (ii) GFRP profiles, where the experimental, analytical and numerical investigations regarding the GFRP girders are presented; (iii) SFRSCC, which presents the experimental investigations concerning the SFRSCC slabs; (iv) other materials, presenting the characteristics of the remaining materials used in the construction of both prototypes, derived from testing or reported in the literature; and, finally, the (v) concluding remarks.

### 4.2. GFRP profiles

#### 4.2.1. Experimental programme

The GFRP profiles constituting the main and secondary girders are made of E-glass fibre rovings and mats embedded in an isophthalic polyester resin matrix and were produced by *ALTO, Perfis Pultrudidos, Lda*. Their main mechanical properties were derived from small-scale material characterisation tests, performed in coupons extracted from the flanges and webs, using a diamond saw blade, as illustrated in Figures 4.1 and 4.2.

The small-scale coupon material characterization tests included: (i) tensile tests; (ii) compressive tests; (iii) off-axis tensile tests; (iv) flexure tests; and (v) interlaminar shear tests.



Figure 4.1.: Extracting coupons: separating the flanges from the web.



Figure 4.2.: Extracting coupons: cutting off-axis coupons.

The full-scale flexural tests were performed on pultruded profiles with cross-sections I200 ( $200 \times 100(\times 10)$  mm<sup>2</sup>) and I400 ( $400 \times 200(\times 15)$  mm<sup>2</sup>) used in the construction of the small- and full-scale prototypes, respectively. The main objective of these tests was to experimentally determine (i) the global elasticity and shear moduli ( $E_{full}$  and  $G_{full}$ , respectively), and (ii) the failure modes and respective failure loads and stresses.

## 4.2.2. Material characterization tests

### 4.2.2.1. Tensile tests

The coupon tensile tests were performed in order to determine the tensile strength ( $\sigma_{tu,X}$ ), the elasticity modulus ( $E_{t,X}$ ) and the Poisson ratio ( $\nu_{XY}$ ), where the subscript  $t$  denotes tension,  $u$  denotes ultimate,  $X$  the tensile direction and  $Y$  the in-plane orthogonal direction with respect to  $X$ .

These tests were performed using a multipurpose universal test machine (from *Instron*, model 1343) with a load capacity of 250 kN. The tests were performed according to the specifications of EN ISO 527 [87], namely testing, at a speed of 2 mm/min, specimens with the following dimensions (with an 1% error margin): (i) 250 mm of length; (ii) 150 mm of free length; and (iii) 25 mm of width. The thickness of the specimens depended on the profiles they were extracted from: (i) 10 mm for the I200 profile, and (ii) 15 mm for the I400 profile. During the tests, data was gathered with a datalogger (from *HBM*, model *Spider8*) at a rate of 5 Hz and stored in a PC.

Regarding the I200 profile, 15 specimens were tested in tension in the longitudinal direction ( $X = L$ ), 8 extracted from the web and 7 extracted from the flanges. A longitudinal strain gauge was installed in 4 specimens of each series (web and flanges) and, additionally, a transverse strain gauge was added to one of the latter specimens. The strain gauges used were manufactured by *HBM*, model *HBM-1-LY11-10/120*.

Regarding the I400 profile, 18 specimens were tested in tension. Of these, 6 web specimens and 6 flange specimens were tested in the longitudinal direction, while 6 web specimens were tested in the transverse direction ( $X = T$ ). Three specimens of all series were instrumented with a longitudinal strain gauge, from *TML*, model *FLK-1-11-3L*.



Figures 4.3 and 4.4 show specimens from I200 and I400 profiles, respectively, being tested.

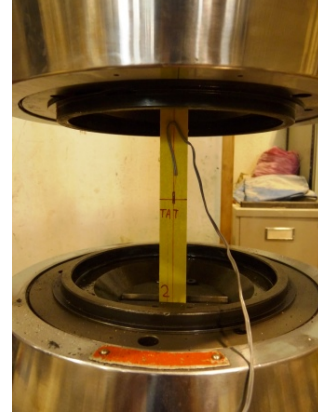


Figure 4.3.: Coupon tensile tests: I200 specimen.

Figure 4.4.: Coupon tensile tests: I400 specimen.

All specimens were tested up to failure allowing the determination of the ultimate tensile strength in each direction. The tensile strength ( $\sigma_{tu,X}$ ) may be obtained by dividing the ultimate load ( $F_{tu,X}$ ) by the specimens' area ( $A_{specimen}$ ), as described in Eq. 4.1:

$$\sigma_{tu,X} = \frac{F_{tu,X}}{A_{specimen}} \quad (4.1)$$

The tensile elasticity modulus ( $E_{t,X}$ ), on the other hand, was obtained from the linear regression of the stress *vs.* strain curves, for strains varying from 500  $\mu\text{m}$  to 2500  $\mu\text{m}$  [87]. Finally, the Poisson ratio ( $\nu_{LT}$ ) was derived from the linear regression of strains in the  $Y$  direction *vs.* strains in the  $X$  direction. This regression was performed for the aforementioned longitudinal strain range. Figures 4.5 and 4.6 present the axial stress ( $\sigma_{t,L}$ ) *vs.* strain ( $\varepsilon_{t,L}$ ) curves for the I200 specimens, extracted from the flanges and webs, respectively.

Figures 4.5 and 4.6 show that the behaviour of all specimens was linear, as expected in FRP materials. It should be noted that, since the strain gauges debonded before the specimens' failure, it was not possible to determine the ultimate strain ( $\varepsilon_{tu,L}$ ) nor to plot the latter results up to the failure of the specimens. Table 4.1 summarizes the results obtained for the specimens extracted from the I200 profile, both for the web and the flanges. The complete results for each specimen are detailed in Table A.1 (page 303).

Table 4.1.: Coupon tensile tests: summary of results for I200.

Plate	Web				Flanges			
Property	$F_{tu,L}$ kN	$\sigma_{tu,L}$ MPa	$E_{t,L}$ GPa	$\nu_{LT}$ -	$F_{tu,L}$ kN	$\sigma_{tu,L}$ MPa	$E_{t,L}$ GPa	$\nu_{LT}$ -
Average	94.17	376.69	32.85	0.29	102.67	410.67	35.94	0.30
Std. Dev.	1.86	7.44	1.09	-	4.65	18.60	2.35	-
CoV	2.0%	2.0%	3.3%	-	4.5%	4.5%	6.5%	-

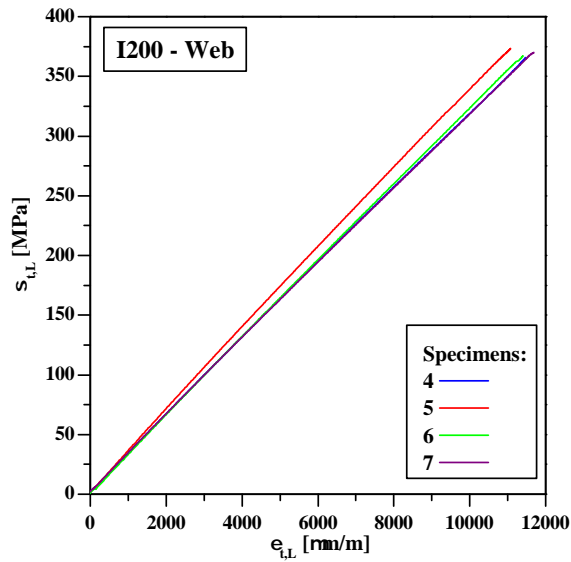


Figure 4.5.: Coupon tensile tests: axial stress ( $\sigma_{t,L}$ ) vs. strain ( $\varepsilon_{t,L}$ ) of I200 web specimens.

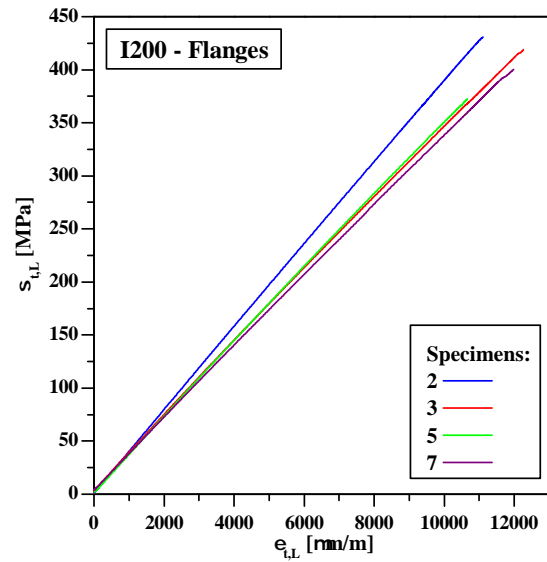


Figure 4.6.: Coupon tensile tests: axial stress ( $\sigma_{t,L}$ ) vs. strain ( $\varepsilon_{t,L}$ ) of I200 flange specimens.

Figures 4.7 and 4.8 present the regressions performed in order to determine the Poisson ratio for the web and the flanges, respectively, and the corresponding coefficient of determination ( $R^2$ ).

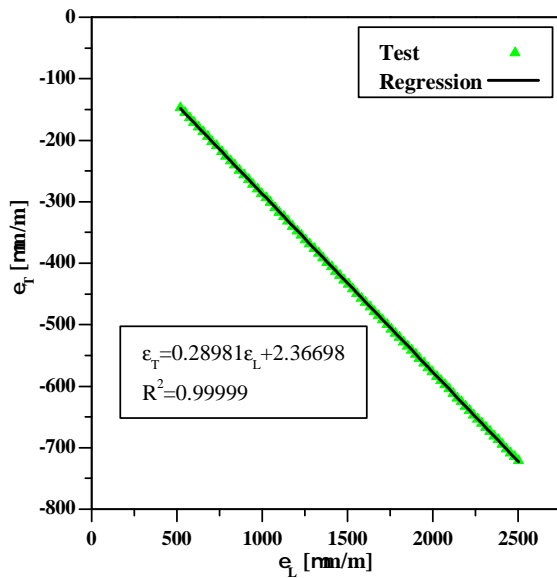


Figure 4.7.: Coupon tensile tests: axial vs. transverse strain of I200 web specimen.

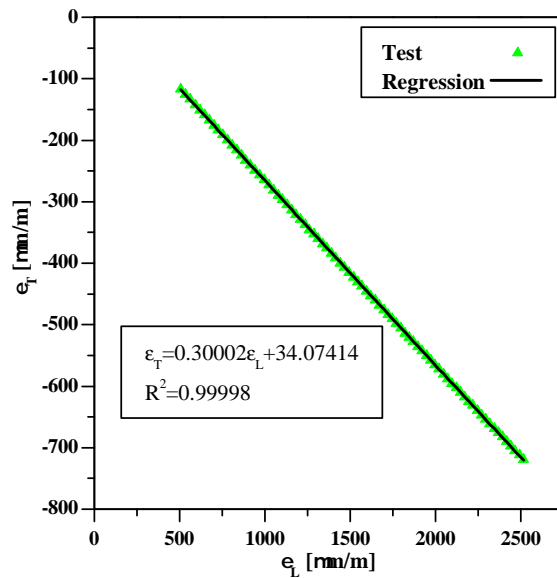


Figure 4.8.: Coupon tensile tests: axial vs. transverse strain of I200 flange specimen.

The results of the coupon tensile tests show a good consistency between different specimens with the coefficient of variation (CoV) ranging from 2.0 to 6.5% regarding the ultimate load/stress and the elasticity modulus. It can be observed that the ultimate strength ( $\sigma_{tu,L}$ ) of the web is 8.3% lower than that of the flanges, while the elasticity modulus ( $E_{t,L}$ ) of the

web is 8.6% lower. In what concerns the Poisson coefficient, whilst the transverse strains were only measured in one specimen of the web and in one of the flanges, the regressions performed presented very high coefficients of determination ( $R^2$ , cf. Figures 4.7 and 4.8).

Figure 4.9 illustrates the failure mode of the specimens, which presented fibre failure and ply separation in the thickness direction, a typical failure mode in FRP tensile tests.



Figure 4.9.: Coupon tensile tests: failure mode of I200 specimens.

In what concerns the specimens extracted from the I400 profile, Figures 4.10 to 4.12 present the axial stress ( $\sigma_{t,X}$ ) vs. strain ( $\varepsilon_{t,X}$ ) curves. The first two figures refer to web specimens tested in the longitudinal and transverse directions, respectively, while the last corresponds to the flange specimens tested in the longitudinal direction.

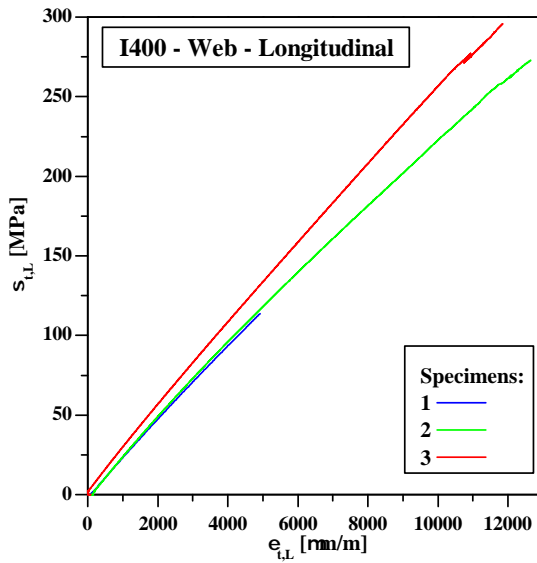


Figure 4.10.: Coupon tensile tests: axial stress ( $\sigma_{t,L}$ ) vs. strain ( $\varepsilon_{t,L}$ ) of I400 web specimens.

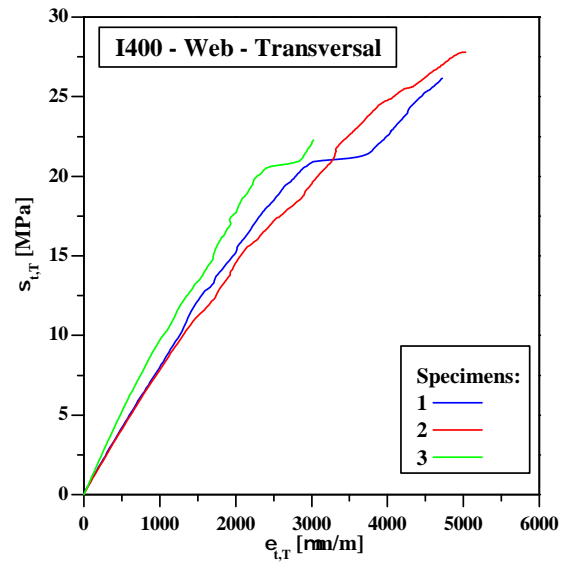


Figure 4.11.: Coupon tensile tests: axial stress ( $\sigma_{t,T}$ ) vs. strain ( $\varepsilon_{t,T}$ ) of I400 flange specimens.

Figures 4.10 and 4.12 show that, similarly to what was observed in the tests with I200 specimens, the behaviour of all specimens extracted from the I400 profile and tested in the longitudinal direction was linear. Regarding the tests in the transverse direction, it may be depicted from Figure 4.11 that the behaviour of the specimens was linear until the vicinity of failure, in which a non-linear behaviour was exhibited. The non-linearity of the specimens

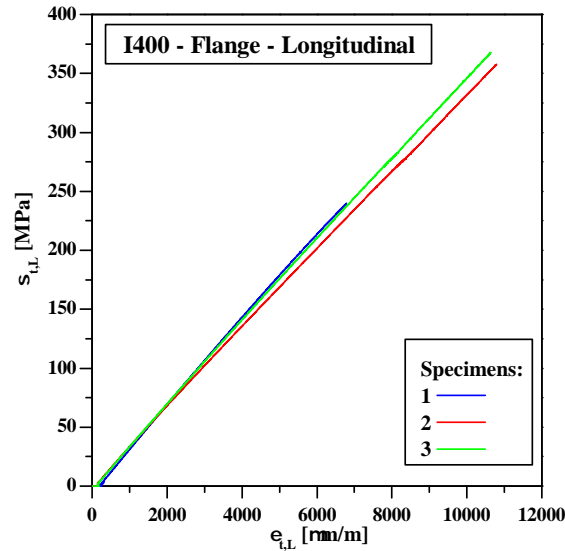


Figure 4.12.: Coupon tensile tests: axial stress ( $\sigma_{t,L}$ ) vs. strain ( $\varepsilon_{t,L}$ ) of I400 flange specimens.

tested in the transverse direction in the brink of collapse is most likely due to the lower fibre content in that direction, which increases the role of the polymeric matrix in the material behaviour. As already stated for the tests with I200 specimens, it should be noted that some of the strain gauges debonded before the specimens' failure and, therefore, it was not possible to determine the ultimate strain ( $\varepsilon_{tu,X}$ ) nor to plot the strain results up to failure. Table 4.2 summarizes the results obtained in these tests (for the complete results refer to Table A.2, page 304).

Table 4.2.: Coupon tensile tests: summary of results for I400.

Plate	Web						Flanges		
Direction	Longitudinal			Transverse			Longitudinal		
Property	$F_{tu,L}$ kN	$\sigma_{tu,L}$ MPa	$E_{t,L}$ GPa	$F_{tu,T}$ kN	$\sigma_{tu,T}$ MPa	$E_{t,T}$ GPa	$F_{tu,L}$ kN	$\sigma_{tu,L}$ MPa	$E_{t,L}$ GPa
Average	104.59	278.90	23.98	10.54	28.09	7.73	126.35	336.94	35.71
Std. Dev.	8.92	23.78	1.60	1.06	2.84	0.90	14.07	37.51	1.83
CoV	8.5%	8.5%	6.7%	10.1%	10.1%	11.6%	11.1%	11.1%	5.1%

The analysis of Table 4.2 shows that the results are consistent, with CoV ranging from 5.1% to 11.6%. The web presents a lower longitudinal elasticity modulus ( $E_{t,L}$ ) when compared to the flanges (-32.8%) and a lower longitudinal strength (-17.2%). These differences are likely due to the multidirectional architecture of fibres in the webs, where, unlike the flanges, the great majority of fibres is oriented in the longitudinal direction. Even so, the longitudinal elasticity modulus ( $E_{t,L}$ ) of the web is significantly higher than its transverse elasticity modulus ( $E_{t,T}$ , +210.2%), showing that the majority of the fibres are also oriented in the longitudinal direction.

The I400 specimens presented two distinct failure modes, illustrated in Figures 4.14 and 4.13: (i) the specimens tested in the longitudinal direction presented evidence of separation of the fibre plies (delamination) along the thickness, similarly to the failure mode of the I200 specimens; while (ii) the specimens tested in the transverse direction presented a fracture in one of its sections.



Figure 4.13.: Coupon tensile tests: failure mode of I400 specimens tested in the longitudinal direction.

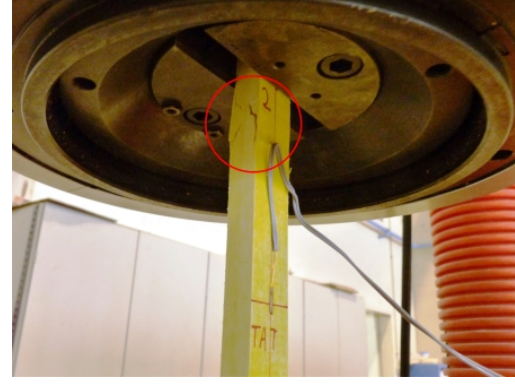


Figure 4.14.: Coupon tensile tests: failure mode of I400 specimens tested in the transverse direction.

Table 4.3 compares the average longitudinal strength and elasticity modulus in tension of the GFRP material comprising the I200 and the I400-sections. This comparison shows that the GFRP material of the I400 profile presents a significantly lower strength, both for the flanges and the webs, when compared to the I200 profile (-18.0% and -26.0%). The profiles present a similar longitudinal elasticity modulus for the flanges, while the I400 profile presents a significant reduction of this parameter for the webs when comparing with the I200 profile (-27.0%, a similar reduction to that observed in strength). These results show that the increase of thickness (from 10 mm for the I200 profile to 15 mm for the I400 profile) occurred together with a decrease of material strength due to the differences in the fibre contents and architecture, a feature of GFRP profiles structural designers should be aware of.

Table 4.3.: Coupon tensile tests: I200 vs. I400.

Average		I200	I400	diff.
$\sigma_{tu,L}^{flanges}$	MPa	410.67	336.94	-18.0%
$E_{t,L}^{flanges}$	GPa	35.94	35.71	-0.7%
$\sigma_{tu,L}^{web}$	MPa	376.69	278.90	-26.0%
$E_{t,L}^{web}$	GPa	32.85	23.98	-27.0%

#### 4.2.2.2. Compressive tests

The coupon compression tests were performed in order to determine the compressive strength ( $\sigma_{cu,X}$ ), the ultimate strain in compression ( $\varepsilon_{cu,X}$ ) and the elasticity modulus in compression ( $E_{c,X}$ ) for the longitudinal and transverse directions.

These tests were performed using a press tester from *Form+Test Seidner* with a load capacity of 200 kN. The tests were performed according to the specifications of ASTM D 695 [88], by testing, at a speed of 1.3 mm/min, specimens with the following dimensions (with an 1% error margin): (i) 40 mm of length; and (ii) 12.7 mm of width, in order to have a slenderness between 11 and 16. The continuous measurement of the displacements between the upper and bottom plates of the press was performed with an electric displacement transducer (from *APEK* with a 50 mm stroke and 0.01 mm precision), which measured the displace-

ment between plates. Data was gathered with a datalogger (from *HBM*, model *Spider8*) at a rate of 5 Hz and stored in a PC. It should be referred that the test speed was set manually in each test and a 1.5 mm/min average velocity was in fact obtained. This small difference (+15.4%) compared to the test standard requirements [88] was deemed as acceptable.

In what concerns the I200 profile, 15 specimens extracted from the flanges were tested, 8 longitudinally and 7 transversely, while 16 specimens extracted from the web were tested, 8 in each direction. Regarding the I400 profile, 12 specimens extracted from the web were tested, 6 in each direction, while 13 specimens extracted from the flanges were tested, 7 in the longitudinal direction and 6 in the transverse one. Figures 4.15 and 4.16 show specimens from the I200 and I400 profiles, respectively, being tested.

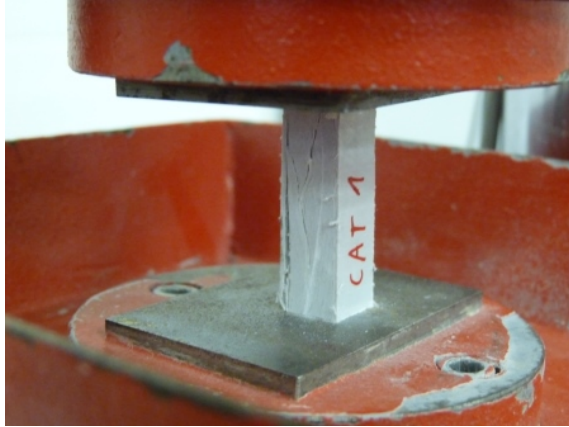


Figure 4.15.: Coupon compressive tests: I200 specimen.



Figure 4.16.: Coupon compressive tests: I400 specimen.

The compressive stress ( $\sigma_{c,X}$ ) was determined by dividing the compressive load ( $F_{c,X}$ ) by the specimens' minimum area ( $A_{specimen}$ ), similarly to what was done for the tension tests (*cf.* Eq. (4.1)), while the compressive strains ( $\varepsilon_{c,X}$ ) were estimated by dividing the relative displacement between plates ( $\delta_{c,X}$ ) by the initial length of the specimens ( $l_{c,X}$ ), as defined in Eq (4.2). Regarding the determination of the elasticity modulus in compression ( $E_{c,X}$ ), it was estimated by performing a linear regression between the compressive stress ( $\sigma_{c,X}$ ) and the (estimated) compressive strains ( $\varepsilon_{c,X}$ ) within the linear-elastic range of the plot.

$$\varepsilon_{c,X} = \frac{\delta_{c,X}}{l_{c,X}} \quad (4.2)$$

It should be mentioned that this test procedure is known to underestimate the elasticity modulus in compression [14], owing to the effects of the material local crushing on the extremities of the specimens, which are not accounted for in the previous formulae (Eq. (4.2)).

Figures 4.17 and 4.18 plot the axial compressive stress ( $\sigma_{c,L}$ ) *vs.* the estimated axial strain ( $\varepsilon_{c,L}$ ) curves obtained for the specimens extracted from the web and flanges, respectively, of the I200 profile, when tested in the longitudinal direction. Figures 4.19 and 4.20 plot the equivalent curves for specimens tested in the transverse direction ( $\sigma_{c,T}$  *vs.*  $\varepsilon_{c,T}$ ).

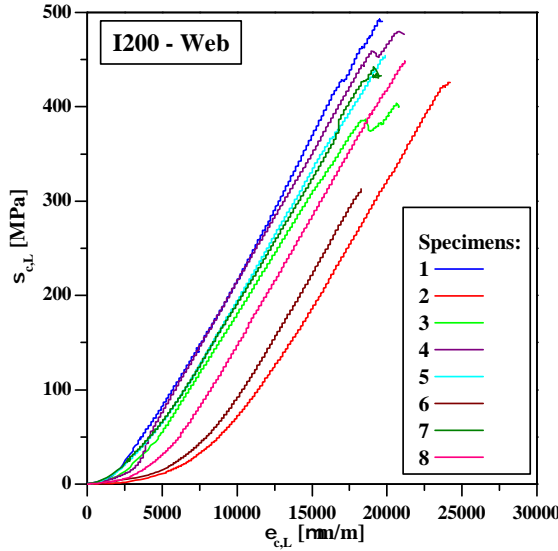


Figure 4.17.: Coupon compressive tests: axial stress ( $\sigma_{c,L}$ ) vs. strain ( $\varepsilon_{c,L}$ ) in the longitudinal direction of I200 web specimens.

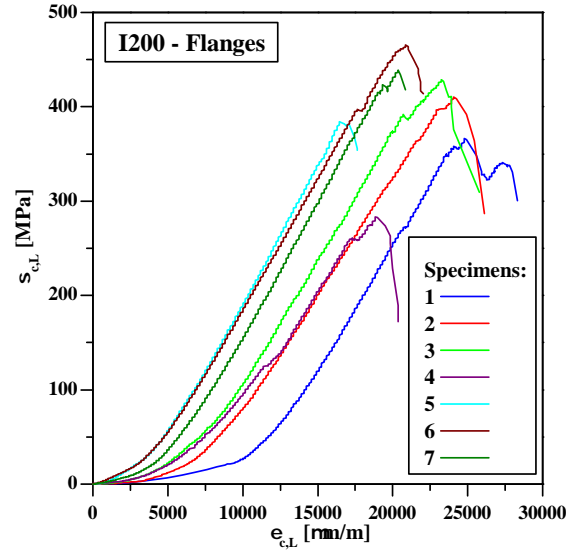


Figure 4.18.: Coupon compressive tests: axial stress ( $\sigma_{c,L}$ ) vs. strain ( $\varepsilon_{c,L}$ ) in the longitudinal direction of I200 flange specimens.

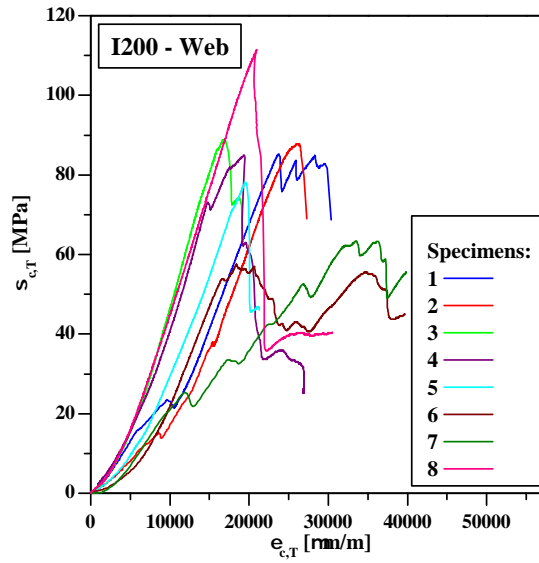


Figure 4.19.: Coupon compressive tests: axial stress ( $\sigma_{c,T}$ ) vs. strain ( $\varepsilon_{c,T}$ ) in the transverse direction of I200 web specimens.

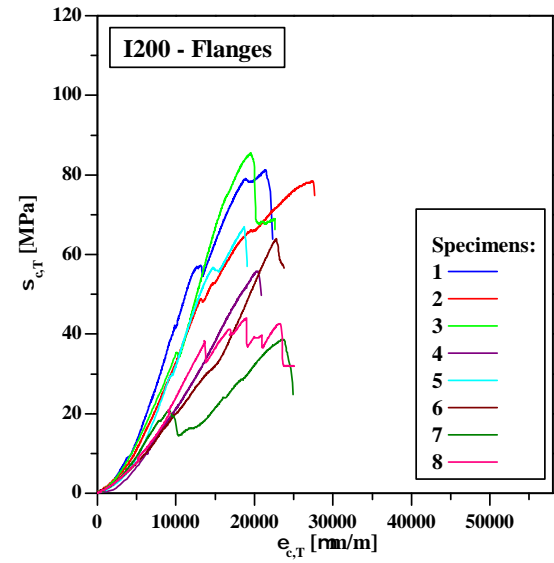


Figure 4.20.: Coupon compressive tests: axial stress ( $\sigma_{c,T}$ ) vs. strain ( $\varepsilon_{c,T}$ ) in the transverse direction of I200 flange specimens.

These results show that the specimens tested in the longitudinal direction (*cf.* Figures 4.17 and 4.18), after an initial adjustment period, presented linear behaviour up to the brink of collapse, where some specimens presented non-linear behaviour (in a very short period). Regarding the compressive tests in the transverse direction (*cf.* Figures 4.19 and 4.20), for both the flanges and the web, the behaviour varied from linear up to failure (after an initial adjustment) to remarkably non-linear during the entire test. The compressive behaviour in the transverse direction is governed by the polymeric matrix properties, while

in the longitudinal direction the fibres (higher content oriented in this direction) play a more significant role, hence the higher proneness for non-linear behaviour in the transverse direction. Tables 4.4 and 4.5 summarize the results obtained in the tests for the specimens extracted from the I200 profile, for both the web and the flanges, respectively (detailed results are presented in Tables A.3 and A.4, page 304). It should be mentioned that, due to the lack of an elastic range, as mentioned earlier, it was not possible to determine the transverse elasticity modulus ( $E_{c,T}$ ) of specimens no. 7 of the web and flanges.

Table 4.4.: Coupon compressive tests: summary of results for I200 web specimens.

Direction	Longitudinal				Transverse			
Property	$F_{cu,L}$ (kN)	$\sigma_{cu,L}$ (MPa)	$\varepsilon_{cu,L}$ ( $\mu\text{m}/\text{m}$ )	$E_{c,L}$ (GPa)	$F_{cu,T}$ (kN)	$\sigma_{cu,T}$ (MPa)	$\varepsilon_{cu,T}$ ( $\mu\text{m}/\text{m}$ )	$E_{c,T}$ (GPa)
Average	51.22	434.37	20705	27.06	10.31	88.92	22296	5.74
Std. Dev.	6.02	51.42	1532	1.99	2.22	16.08	5463	0.73
CoV	11.8%	11.8%	7.4%	7.4%	21.5%	18.1%	24.5%	12.7%

Table 4.5.: Coupon compressive tests: summary of results for I200 flange specimens.

Direction	Longitudinal				Transverse			
Property	$F_{cu,L}$ (kN)	$\sigma_{cu,L}$ (MPa)	$\varepsilon_{cu,L}$ ( $\mu\text{m}/\text{m}$ )	$E_{c,L}$ (GPa)	$F_{cu,T}$ (kN)	$\sigma_{cu,T}$ (MPa)	$\varepsilon_{cu,T}$ ( $\mu\text{m}/\text{m}$ )	$E_{c,T}$ (GPa)
Average	47.05	388.55	21748	33.93	8.26	64.31	21507	4.35
Std. Dev.	7.08	59.18	2212	3.35	1.96	17.25	2894	0.93
CoV	15.1%	15.2%	10.2%	9.9%	23.7%	26.8%	13.5%	21.3%

The scatter (CoV) of the experimental results obtained with the different specimens, up to 27%, is most likely due to small imperfections in the specimens' geometry, namely the not completely levelled extremity sections due to the lack of precision of the preparation/extraction (cutting) process of these small specimens. It can be observed, both for the web and the flanges, that the compressive strength ( $\sigma_{cu,X}$ ) is significantly higher in the longitudinal direction than in the transverse one (+388% and +504% for the webs and flanges, respectively). A similar result is observed when comparing the compressive elasticity modulus ( $E_{c,X}$ ) in the longitudinal and transverse directions (+371% and +680%, respectively). These results attest the importance of the glass fibers — which are mainly oriented in the longitudinal direction — in the compressive behaviour of the GFRP material. Notwithstanding, the fact that the longitudinal compressive strength is higher for the web than for the flanges, which have more fibres disposed longitudinally, shows the importance of the confinement effect that transversely and obliquely oriented fibres have in the compressive behaviour. Regarding the ultimate strains, similar values were observed for both directions, which indicates that the variation of the elasticity modulus and of the compressive strength is proportional (*cf.* Eq. (4.3)):

$$\varepsilon_{cu,X} = \frac{\sigma_{cu,X}}{E_{c,X}} \quad (4.3)$$

Regarding the tests performed in the I400 profile specimens, Figures 4.21 and 4.22 plot the axial compressive stress ( $\sigma_{c,L}$ ) *vs.* the estimated axial strain ( $\varepsilon_{c,L}$ ) curves obtained for the specimens extracted from the web and flanges, respectively. The equivalent curves



for specimens tested in the transverse direction ( $\sigma_{c,T}$  vs.  $\varepsilon_{c,T}$ ) are plotted in Figures 4.23 and 4.24.

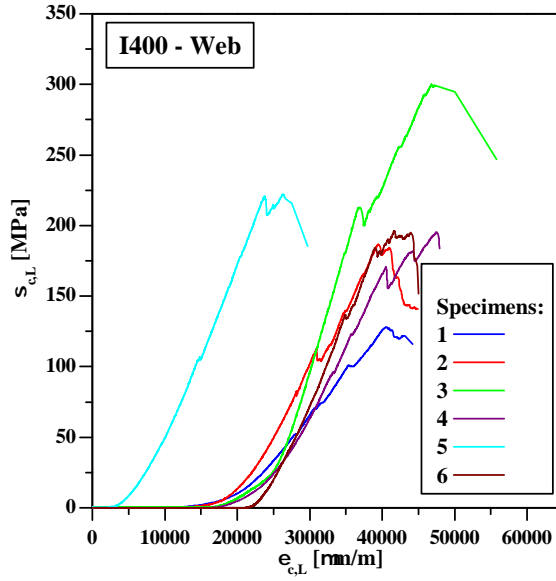


Figure 4.21.: Coupon compressive tests: axial stress ( $\sigma_{c,L}$ ) vs. strain ( $\varepsilon_{c,L}$ ) in the longitudinal direction of I400 web specimens.

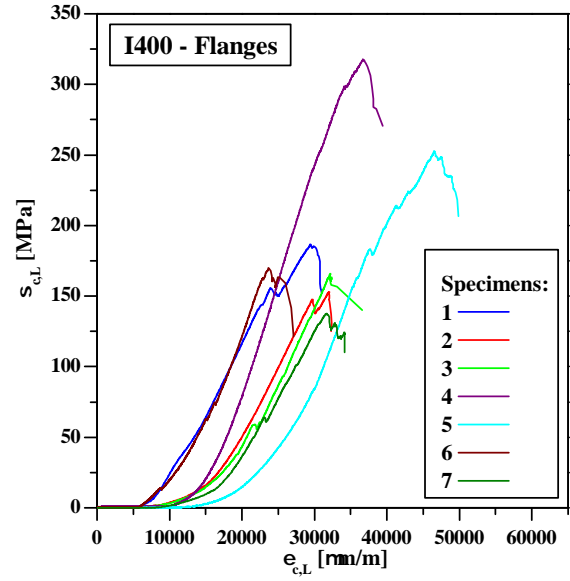


Figure 4.22.: Coupon compressive tests: axial stress ( $\sigma_{c,L}$ ) vs. strain ( $\varepsilon_{c,L}$ ) in the longitudinal direction of I400 flange specimens.

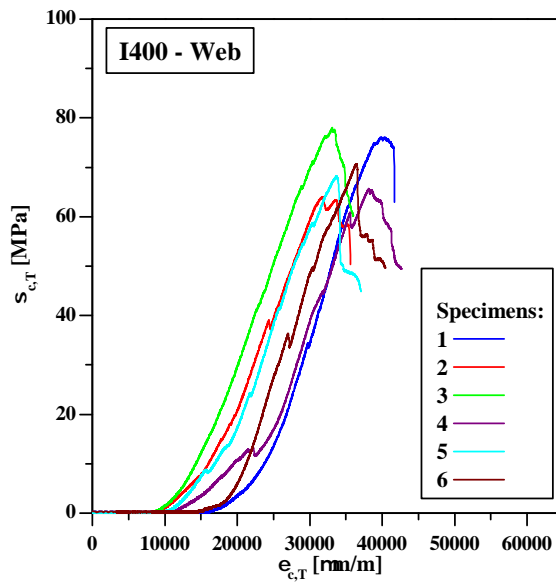


Figure 4.23.: Coupon compressive tests: axial stress ( $\sigma_{c,T}$ ) vs. strain ( $\varepsilon_{c,T}$ ) in the transverse direction of I400 web specimens.

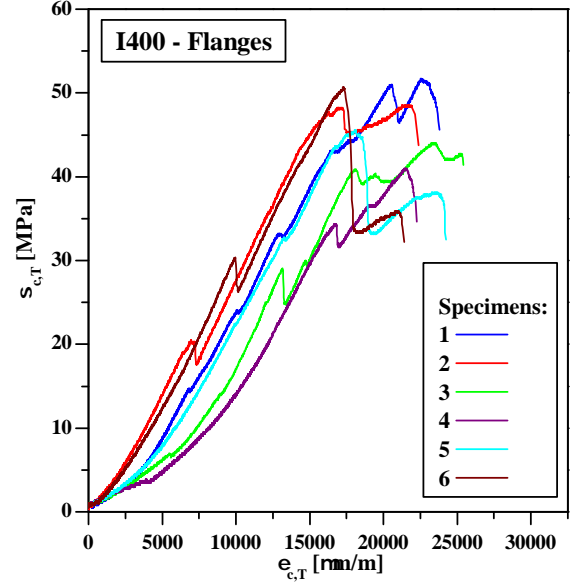


Figure 4.24.: Coupon compressive tests: axial stress ( $\sigma_{c,T}$ ) vs. strain ( $\varepsilon_{c,T}$ ) in the transverse direction of I400 flange specimens.

Similarly to what was observed in the I200 specimens, Figures 4.21 and 4.22 show that the specimens tested in the longitudinal direction presented linear behaviour after an initial non-linear (adjustment) stage and before the brink of collapse. Additionally, some specimens

presented minute reduction of the applied load within the linear regime, which may reflect the beginning of the (internal) delamination process, without apparent (visual) signs of damage. In what concerns the compressive tests in the transverse direction (*cf.* Figures 4.23 and 4.24), the behaviour observed was mostly linear (after the initial adjustment) with some perturbations (sometimes significant) during this regime, unlike what was observed for the I200 profile specimens. These differences may stem from a different fibre architecture, namely with the I400 profile presenting higher content of fibres oriented in the transverse and/or oblique directions. Tables 4.6 and 4.7 summarize the results obtained for the web and flange specimens, respectively. The complete records of all specimens are presented in Tables A.5 and A.6 (*cf.* page 305).

Table 4.6.: Coupon compressive tests: summary of results for I400 web specimens.

Direction	Longitudinal				Transverse			
Property	$F_{cu,L}$ (kN)	$\sigma_{cu,L}$ (MPa)	$\varepsilon_{cu,L}$ ( $\mu\text{m}/\text{m}$ )	$E_{c,L}$ (GPa)	$F_{cu,T}$ (kN)	$\sigma_{cu,T}$ (MPa)	$\varepsilon_{cu,T}$ ( $\mu\text{m}/\text{m}$ )	$E_{c,T}$ (GPa)
Average	36.91	204.72	26658	12.21	12.93	70.43	23636	4.55
Std. Dev.	8.98	56.15	4090	3.24	0.97	5.60	2076	0.52
CoV	24.3%	27.4%	15.3%	26.6%	7.5%	7.9%	8.8%	11.4%

Table 4.7.: Coupon compressive tests: summary of results for I400 flange specimens.

Direction	Longitudinal				Transverse			
Property	$F_{cu,L}$ (kN)	$\sigma_{cu,L}$ (MPa)	$\varepsilon_{cu,L}$ ( $\mu\text{m}/\text{m}$ )	$E_{c,L}$ (GPa)	$F_{cu,T}$ (kN)	$\sigma_{cu,T}$ (MPa)	$\varepsilon_{cu,T}$ ( $\mu\text{m}/\text{m}$ )	$E_{c,T}$ (GPa)
Average	38.20	197.65	25919	12.26	8.76	46.92	20624	3.57
Std. Dev.	11.88	64.43	4782	2.99	0.79	4.12	2445	0.36
CoV	31.1%	32.6%	18.5%	24.4%	9.0%	8.8%	11.9%	10.2%

The results presented in Tables 4.6 and 4.7 regarding the compressive tests on I400 specimens show general higher scatter (up to CoV +33%) than their I200 counterparts. Once again, this relatively high variability is most likely due to small imperfections in the specimens dimensions, particularly the flatness of their end sections (due to the aforementioned reasons). The relations between the parameters obtained in these tests are similar to those observed for the I200 specimens, namely, (i) the compressive strength ( $\sigma_{cu,X}$ ) is significantly higher in the longitudinal direction than in the transverse direction (+191% and +321% for the webs and flanges, respectively), and (ii) the compressive elasticity modulus ( $E_{c,X}$ ) in the longitudinal direction is higher than in the transverse direction (+168% and 243%, respectively). Although the specimens derived from both the I200 and the I400 profiles present a similar pattern regarding their compressive characteristics in the longitudinal and transverse directions, the differences are mitigated for the I400 specimens.

Regarding the failure mode, as depicted in Figures 4.15 and 4.16, all specimens failed due to the separation of the fibre plies in the thickness direction — delamination.

Table 4.8 compares the average compressive strength, the elasticity modulus and the ultimate strain in the longitudinal and transverse directions for the GFRP material of the I200 and the I400 pultruded profiles. These results show a significant strength decrease for the I400 specimens when compared to the I200 specimens (-49% and -63% in the longitudinal direction and -27% and -21% in the transverse direction for the flanges and

webs, respectively). It can also be observed that the reduction on the elasticity modulus is, approximately, proportional to the strength reduction between the I400 and the I200 specimens. It should also be referred that the decrease of the longitudinal properties, from the I400 to the I200 profiles, is much more pronounced for the compressive properties than for their tensile counterparts (*cf.* Section 4.2.2.1).

Table 4.8.: Coupon compressive tests: I200 *vs.* I400.

Profile	$\sigma_{cu,L}^{flanges}$ MPa	$\varepsilon_{cu,L}^{flanges}$ $10^{-4}$ m/m	$E_{c,L}^{flanges}$ GPa	$\sigma_{cu,T}^{flanges}$ MPa	$\varepsilon_{cu,T}^{flanges}$ $10^{-4}$ m/m	$E_{c,T}^{flanges}$ GPa
I200	388.55	21748	33.93	64.31	21507	4.35
I400	197.65	25919	12.26	46.92	20624	3.57
diff.	-49.1%	19.2%	-63.9%	-27.0%	-4.1%	-18.0%
Profile	$\sigma_{cu,L}^{web}$ MPa	$\varepsilon_{cu,L}^{web}$ $10^{-4}$ m/m	$E_{c,L}^{web}$ GPa	$\sigma_{cu,T}^{web}$ MPa	$\varepsilon_{cu,T}^{web}$ $10^{-4}$ m/m	$E_{c,T}^{web}$ GPa
I200	434.37	20705	27.06	88.92	22296	5.74
I400	204.72	26658	12.21	70.43	23636	4.55
diff.	-52.9%	28.7%	-54.9%	-20.8%	6.0%	-20.7%

#### 4.2.2.3. Off-axis tensile tests

The coupon off-axis tensile tests were performed in order to determine the in-plane shear strength ( $\tau_{u,XY}$ ) and the shear modulus ( $G_{XY}$ ) of the webs of both I200 and I400 profiles.

These tests were performed using the same multipurpose universal test machine (from *Instron*, model 1343, with a load capacity of 250 kN) used in the tensile tests (*cf.* Section 4.2.2.1). The tests were performed according to the recommendations of Hodgkinson [89], namely by tensioning the specimens at an angle of  $10^\circ$  with respect to the longitudinal direction. Tests were performed at a speed of 1 mm/min in specimens with the following dimensions (with a 1% error margin): (i) 250 mm of length; (ii) 150 mm of free length; and (iii) 25 mm of width. The strains of the specimens were measured at their mid-length by installing strain gauge rosettes comprising: (i) a longitudinal gauge ( $\varepsilon_{11}$ ); (ii) a transverse gauge ( $\varepsilon_{22}$ ); and (iii) a gauge installed at an angle of  $45^\circ$  with reference to the main axes of the specimens ( $\varepsilon_{12}$ ). During the tests, data was gathered with a datalogger (from *HBM*, model *Spider8*) at a rate of 5 Hz and stored in a PC.

For the I200 profile, 12 specimens were tested, 6 of which were instrumented with strain gauge rosettes. In what concerns the I400 profile, 5 specimens were tested, 4 of which with strain gauge rosettes. For the specimens of the former profile the rosettes were made with strain gauges from *HBM*, model *HBM-1-LY11-10/120*, while for the latter profile, strain gauges from *TML*, model *FLK-1-11-3L* were used.

Figures 4.25 and 4.26 show specimens of the I200 and I400 profiles, respectively, being tested in off-axis tension.

Regarding the relative positioning of strain gauge  $\varepsilon_{12}$ , some specimens were tested at  $+10^\circ$  off-axis and others at  $-10^\circ$  off-axis, as illustrated in Figure 4.27.

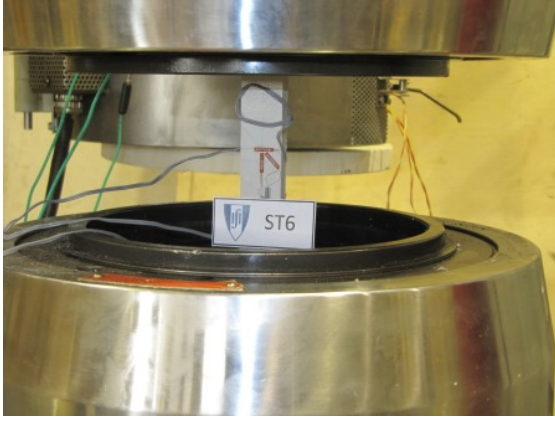


Figure 4.25.: Coupon off-axis tensile tests: I200 specimen.



Figure 4.26.: Coupon off-axis tensile tests: I400 specimen.

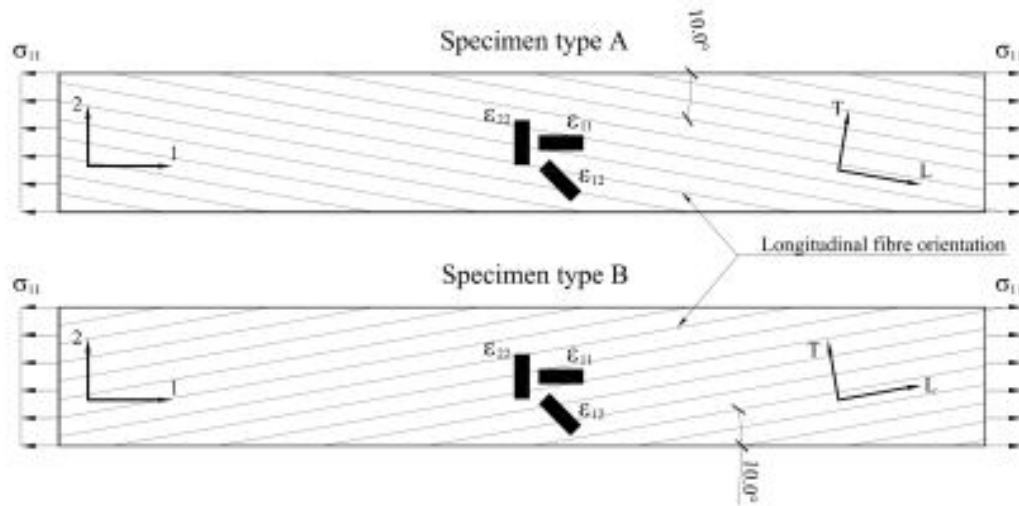


Figure 4.27.: Coupon off-axis tensile test: specimen types A and B, respectively, tested at a  $+10^\circ$  (top) or  $-10^\circ$  (bottom) off-axis direction.

From the experimental tests, the stress developed in the off-axis direction ( $\sigma_{11}$ ) can be readily determined by dividing the applied load by the area of the specimen, adapting, for this effect, Eq. (4.1). Thereafter, in order to derive the shear properties of the materials,  $\sigma_{11}$  may be related with the shear stress ( $\tau_{LT}$ ) considering the linear elasticity theory or based on the Mohr's circle, applying Eq. (4.4),

$$\tau_{LT} = \frac{1}{2} \sigma_{11} \sin(2\theta) \quad (4.4)$$

where  $\theta$  represents the angle between the longitudinal direction ( $L$ ) and the test direction (1) (cf. Figure 4.27).

Considering the main directions of the test (1 and 2), the distortion may be calculated as follows,

$$\begin{aligned}\gamma_{12} &= 2\varepsilon_{12} + \varepsilon_{11} + \varepsilon_{22}, & \text{for specimens type A} \\ \gamma_{12} &= 2\varepsilon_{12} - \varepsilon_{11} - \varepsilon_{22}, & \text{for specimens type B}\end{aligned}\quad (4.5)$$

where  $\varepsilon_{XY}$  represents the strains in direction  $XY$  (*cf.* Figure 4.27). Finally, the distortion between the main directions of the pultruded laminates ( $\gamma_{LT}$ ) may be calculated with Eq. (4.6):

$$\begin{aligned}\gamma_{LT} &= -(\varepsilon_{11} - \varepsilon_{22}) \sin(2\theta) + \gamma_{12} \sin(2\theta), & \text{for specimens type A} \\ \gamma_{LT} &= (\varepsilon_{11} - \varepsilon_{22}) \sin(2\theta) + \gamma_{12} \sin(2\theta), & \text{for specimens type B}\end{aligned}\quad (4.6)$$

The determination of the shear properties, namely of  $\tau_{LT}$  and  $\gamma_{LT}$ , allows defining the shear stress *vs.* distortion curves regarding the main directions of the pultruded laminates (longitudinal and transverse). Figures 4.28 and 4.29 plot such curves for the I200 and I400 specimens, respectively. Note that due to premature failure/debonding of the strain gauges these curves are not plotted up to failure.

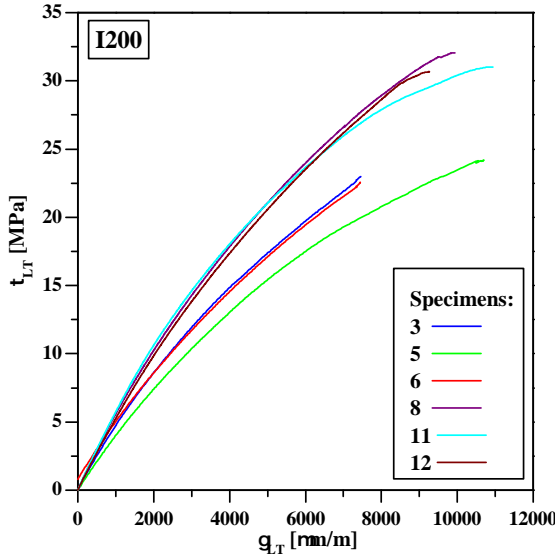


Figure 4.28.: Coupon off-axis tensile tests:  $\tau_{LT}$  *vs.*  $\gamma_{LT}$  — I200 specimens.

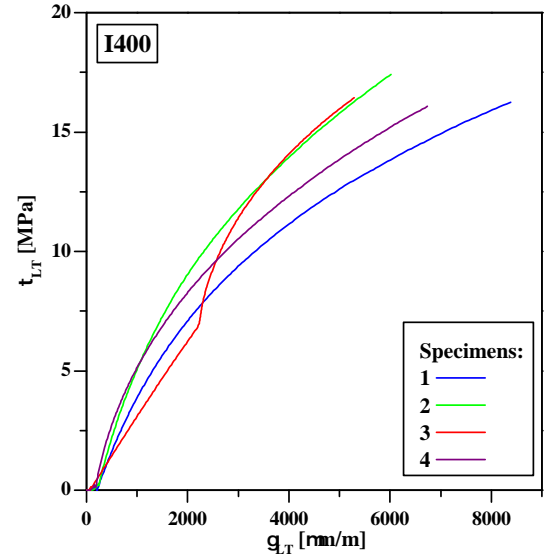


Figure 4.29.: Coupon off-axis tensile tests:  $\tau_{LT}$  *vs.*  $\gamma_{LT}$  — I400 specimens.

Figures 4.28 and 4.29 show that the shear behaviour is non-linear with continuous loss of stiffness up to failure for both I200 and I400 profiles, with the exception of specimen no. 3 of I400 profile, which presented an (apparently anomalous) initial linear behaviour (up to  $\approx 7.5$  MPa), which then changed to non-linear similarly to that presented by the remaining specimens. This exception, nonetheless, is most likely due to errors in the strain measurements of this specific specimen rather than to a different mechanical behaviour. The determination of the shear modulus ( $G_{LT}$ ) was performed based on the linear regression of the data presented in Figures 4.28 and 4.29 between distortion values ( $\gamma_{LT}$ ) ranging from  $500 \times \mu/m$  to  $2500 \times \mu/m$  [89]. Table 4.9 summarizes the results obtained in these tests for

both the I200 and the I400 specimens. The complete records are presented in Table A.7 (page 306).

Table 4.9.: Coupon off-axis tensile tests: summary of results.

Profile	I200			I400		
Property	$F_{u,11}$ (kN)	$\tau_{u,LT}$ (MPa)	$G_{LT}$ (GPa)	$F_{u,11}$ (kN)	$\tau_{u,LT}$ (MPa)	$G_{LT}$ (GPa)
Average	38.42	27.47	3.68	44.45	20.43	3.49
Std. Dev.	5.77	3.37	0.19	3.85	1.15	0.43
CoV	15.0%	12.3%	5.2%	8.7%	5.6%	12.4%

Regarding the failure modes, as illustrated in Figures 4.30 and 4.31, specimens presented an oblique fracture, indicative of shear failure [89].

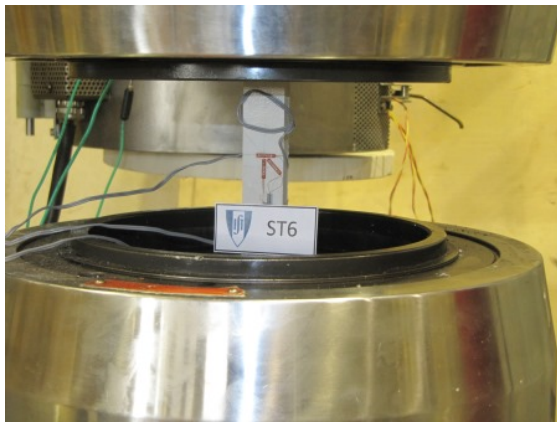


Figure 4.30.: Coupon off-axis tensile tests: failure mode of I200 specimen.

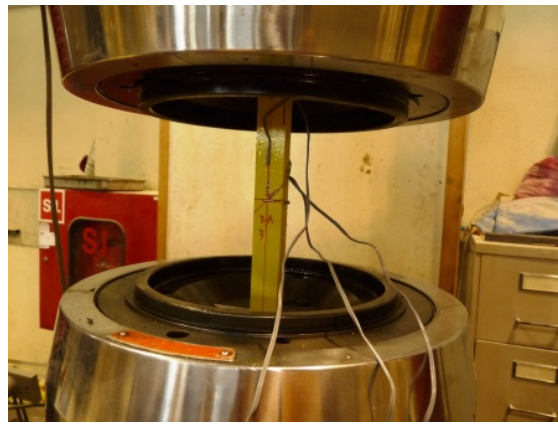


Figure 4.31.: Coupon off-axis tensile tests: failure mode of I400 specimen.

The results presented in Table 4.9 show that for both profiles the different specimens presented similar shear strength ( $\tau_{u,LT}$ ) and shear modulus ( $G_{LT}$ ), with CoV of 12% and 5%, respectively, for the I200 specimens, and 6% and 12%, respectively, for the I400 specimens. Regarding the comparison between the GFRP material of the different profiles, the I400 specimens presented lower shear strength than that of the I200 specimens (-26%), similarly to what happened with the properties measured in the previous tests. In what concerns the shear modulus, the results were similar for both profiles, with the I400 specimens presenting a slightly lower modulus (-5%) when compared to the I200 specimens.

#### 4.2.2.4. Flexural tests

The coupon flexural tests were performed in order to determine the flexural strength ( $\sigma_{fu,L}$ ), the ultimate strain in flexure ( $\varepsilon_{fu,L}$ ) and the elasticity modulus in flexure ( $E_{f,L}$ ) in the longitudinal direction.

These tests were performed using a press tester from *Form+Test Seidner* with a load capacity of 10 kN. The simply supported specimens were loaded at their midspan section, according to the specifications of EN ISO 14125 [90]. Load was applied in displacement control at a speed of 6.0 mm/min in specimens with the following dimensions (with a 1%

error margin): (i) 300 mm of length; (ii) 15 mm of width; and (iii) 192 mm of span, ensuring failure in flexure and minimizing the relative contribution of shear to the overall deformation. The midspan displacements were measured with an electric displacement transducer (from *APEK*, with a 50 mm stroke and 0.01 mm precision) mounted on the moving crosshead of the press and measuring the relative displacement to the support plate. Data was gathered with a datalogger (from *HBM*, model *Spider8*) at a rate of 5 Hz and stored in a PC. It should be referred that the test speed was set manually in each test and a 8.2 mm/min average velocity was in fact applied.

For this particular material characterization test, due to the limited material available for the I400 profile, only specimens from the I200 profile were tested, 8 extracted from the web and 6 from the flanges. Figures 4.32 and 4.33 show, as an example, one specimen being tested before and after failure, respectively. With this respect, it should be mentioned that, for all specimens, failure started due to the tensile rupture of the bottom fibres. Failure propagation continued with the successive failure of the fibre plies, towards the upper part of the midspan section of the specimens, until the final failure occurred.



Figure 4.32.: Coupon flexure test before specimen failure.



Figure 4.33.: Coupon flexure test after specimen failure.

Regarding the analysis of the experimental results, the flexural stress ( $\sigma_{f,L}$ ) was determined with Eq. (4.7),

$$\sigma_{f,L} = \frac{3F_f L_{f,0}}{2b_s t_s^2} \quad (4.7)$$

where  $F_f$  is the load applied by the press,  $L_{f,0}$  is the span,  $b_s$  is the specimens' width and  $t_s$  is the specimens' thickness (10 mm). The maximum strain ( $\varepsilon_{f,L}$ , in the extremity fibres of the specimens), on the other hand, may be determined using Eq. (4.8),

$$\varepsilon_{f,L} = \frac{6d_f t_s}{L_{f,0}^2} \quad (4.8)$$

where  $d_f$  is the midspan deflection of the specimen.

Figures 4.34 and 4.35 plot the flexural stress ( $\sigma_{f,L}$ ) *vs.* maximum strain ( $\varepsilon_{f,L}$ ) curves obtained in the tests of the specimens extracted, respectively, from the web and flanges of the I200 profile.

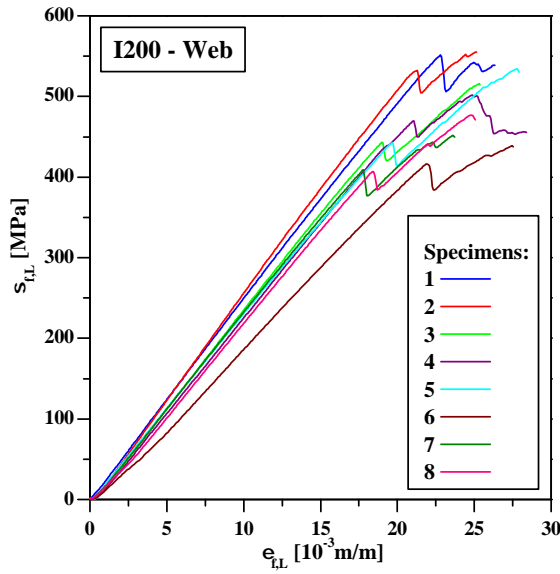


Figure 4.34.: Coupon flexure tests:  $\sigma_{f,L}$  vs.  $\varepsilon_{f,L}$  — web specimens.

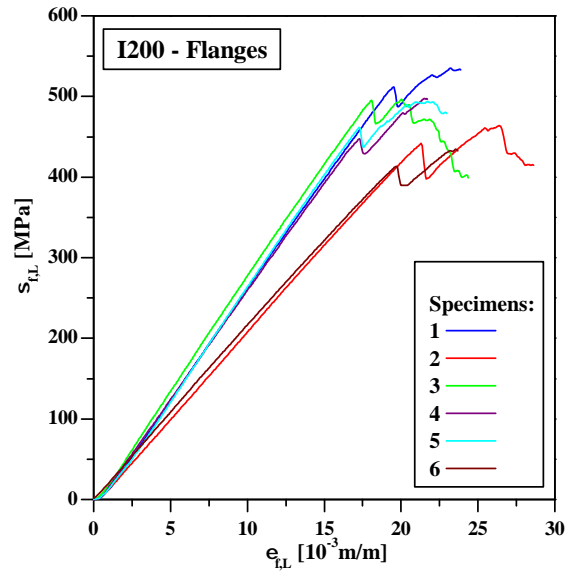


Figure 4.35.: Coupon flexure tests:  $\sigma_{f,L}$  vs.  $\varepsilon_{f,L}$  — flange specimens.

The curves plotted in Figures 4.34 and 4.35 show that the specimens' behaviour was linear up to the failure of the first fibres (at the bottom of the specimens). After this point, load decreased and increased again, one or several times, while the different layers of fibres progressively failed (in the upward direction), until the final failure of the specimens (*cf.* Figure 4.33).

Regarding the determination of the elasticity modulus ( $E_{f,L}$ ), it is often performed based on the linear regression between stresses  $\sigma_{f,L}$  and strains  $\varepsilon_{f,L}$  ranging from 500  $\mu\text{m/m}$  to 2500  $\mu\text{m/m}$  [90]. However, for this particular case, it was considered that the elastic behaviour was better represented for strains ranging from 500  $\mu\text{m/m}$  to 10000  $\mu\text{m/m}$ . Tables 4.10 and 4.11 summarize the results derived from the coupon flexure tests, for the web and flange specimens, respectively, including the initial fibre failure load ( $F_{fu-i,L}$ ) and the corresponding initial failure strain ( $\varepsilon_{fu-i,L}$ ), the ultimate load attained in each test ( $F_{fu,L}$ ), *i.e.* the maximum load, the corresponding ultimate stress ( $\sigma_{fu,L}$ ) and, additionally, as a measure of the reserve strength after the initial failure, the relation between the maximum load and the initial fibre failure load ( $F_{fu,L}/F_{fu-i,L}$ ). Tables A.8 and A.9 (page 307) present the complete records for all specimens.

Table 4.10.: Coupon flexural tests: summary of results of the web specimens (I200).

Property	$F_{fu-i,L}$ (kN)	$F_{fu,L}$ (kN)	$F_{fu,L}/F_{fu-i,L}$ -	$\sigma_{fu,L}$ (MPa)	$\varepsilon_{fu-i,L}$ ( $\mu\text{m/m}$ )	$E_{f,L}$ (GPa)
Average	2.37	2.62	1.11	543.62	21219	22.25
Std. Dev.	0.25	0.20	0.09	41.36	3166	3.00
CoV	10.7%	7.6%	7.9%	7.6%	14.9%	13.5%

The results obtained show a good agreement between the behaviour of the different specimens, presenting a maximum CoV of 15%. Regarding the absolute values of the mechanical properties measured in these tests, it should be mentioned that the results



Table 4.11.: Coupon flexure tests: summary of results of the flange specimens (I200).

Property	$F_{fu-i,L}$ (kN)	$F_{fu,L}$ (kN)	$F_{fu,L}/F_{fu-i,L}$ -	$\sigma_{fu,L}$ (MPa)	$\varepsilon_{fu-i,L}$ ( $\mu$ m/m)	$E_{f,L}$ (GPa)
Average	2.44	2.57	1.05	533.46	18848	23.67
Std. Dev.	0.19	0.18	0.03	37.54	1583	2.70
CoV	7.9%	7.0%	3.3%	7.0%	8.4%	11.4%

for the web and the flanges are very similar concerning the strength ( $\sigma_{fu,L}$ ) and elasticity modulus ( $E_{f,L}$ ), with differences of +6% and +3%, respectively. In what concerns the failure behaviour, the ratio  $F_{fu,L}/F_{fu-i,L}$  provides a measure of the reserve strength after initial failure, which varies from 0 to 17% in the web and from 0 to 11% in the flanges (considering all specimens from those laminates). Although this failure behaviour could be considered as pseudo-ductile, the consideration of such phenomenon in the design of FRP pultruded members may not be possible for most cases, since it is difficult to quantify this pseudo-ductility especially for the confidence levels assumed when designing civil engineering structures. Moreover, the failure mode of these elements is seldom governed by the flexural failure of the FRP laminates, normally being more susceptible to failure modes involving the entire section of the element, instability phenomena or localized crushing.

#### 4.2.2.5. Interlaminar shear tests

The coupon interlaminar shear tests were performed in order to determine the ultimate shear strength between fibre layers across the material thickness ( $\tau_{isu,L}$ ) in the longitudinal direction.

These tests were performed with a very similar test apparatus as that described for the flexural tests (*cf.* Section 4.2.2.4), namely using the same press tester (from *Form+Test Seidner* with a load capacity of 10 kN) and the same displacement measurement and data acquisition systems. The specimens were also loaded at the midspan section in a span of 40 mm, which ensured that failure was due to interlaminar shear. The tests were performed according to the specifications of ASTM D 2344 [91], at a speed of 1.0 mm/min in specimens with the following dimensions (with a 1% error margin): (i) 60 mm of length; and (ii) 20 mm of width. Regarding the actual test speed (which was set manually in each test) a 1.9 mm/min average velocity was in fact applied.

For this particular material characterization test, only specimens from the I200 profile were tested, in the longitudinal direction. Overall, 15 specimens were tested, 7 extracted from the web and 8 from the flanges. Figures 4.36 and 4.37 show, as an example, one specimen being tested before and after failure, respectively.

The maximum interlaminar shear stress developed in the specimens during the tests ( $\tau_{is,L}$ ) may be derived from the load applied by the press ( $F_{is,L}$ ) calculated with Eq. (4.9),

$$\tau_{is,L} = \frac{3 F_{is,L}}{4 b_{is} t_{is}} \quad (4.9)$$

where  $b_{is}$  is the width of the specimens and  $t_{is}$  is the thickness of the specimens. Given that for this particular test only I200 specimens were tested, the thickness is 10 mm for all specimens.

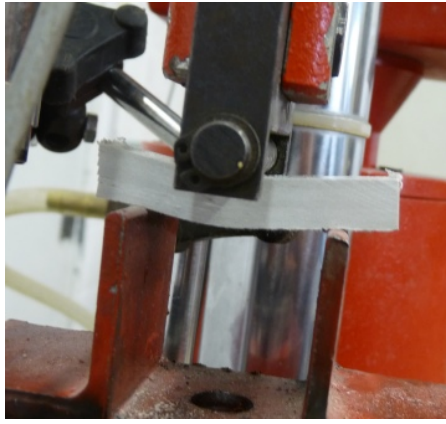


Figure 4.36.: Coupon interlaminar shear test before specimen failure.



Figure 4.37.: Coupon interlaminar shear test after specimen failure.

Figures 4.38 and 4.39 illustrate the behaviour of the specimens extracted both from the web and flanges, respectively, by plotting the stress ( $\tau_{is,L}$ ) vs. midspan deflections ( $d_{is,L}$ ) curves obtained in the tests.

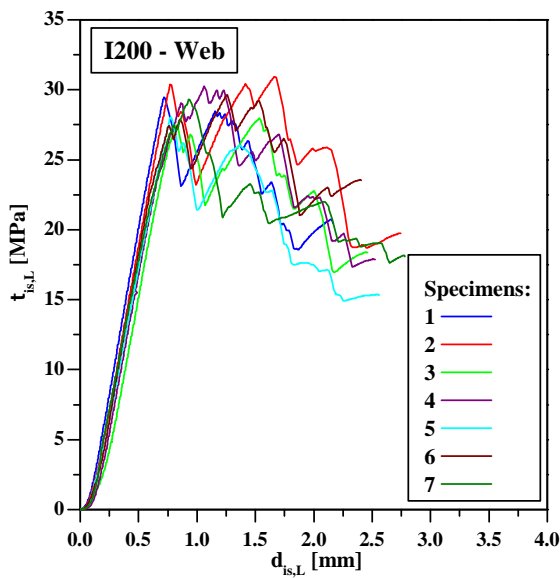


Figure 4.38.: Coupon interlaminar shear tests:  $\tau_{is,L}$  vs.  $d_{is,L}$  — web specimens.

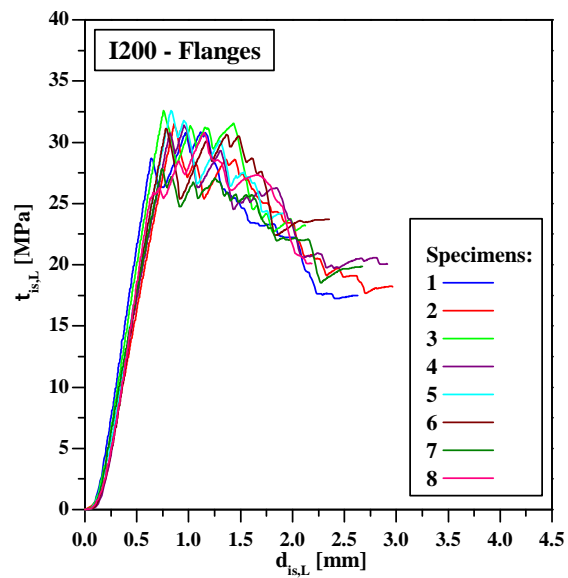


Figure 4.39.: Coupon interlaminar shear tests:  $\tau_{is,L}$  vs.  $d_{is,L}$  — flange specimens.

The curves plotted in Figures 4.38 and 4.39 show that the specimens behaved similarly regardless of the plate they were extracted from (web or flanges). The specimens presented a linear behaviour until failure, which was due to delamination of the central layers of the specimens (for which shear stresses are maximum). After the initial failure, the specimens were still able to sustain load, recovering a fraction of the maximum load until delamination occurred in another layer. This process repeated until the specimens were no longer able to sustain any load.

Table 4.12 summarizes the results obtained in these tests, namely the ultimate load ( $F_{isu,L}$ ) and the ultimate shear strength ( $\sigma_{isu,L}$ ). Table A.10 (page 308) presents the complete results for all specimens.

Table 4.12.: Coupon interlaminar shear tests: summary of results (I200).

Plate	Web		Flange	
Property	$F_{isu,L}$ (kN)	$\tau_{isu,L}$ (MPa)	$F_{isu,L}$ (kN)	$\tau_{isu,L}$ (MPa)
Average	7.42	29.35	7.85	30.21
Std. Dev.	0.21	1.11	0.38	1.14
CoV	2.9%	3.8%	4.8%	3.8%

As shown in Table 4.12, the results of all specimens were very consistent with maximum CoV of 5%. Moreover, the specimens extracted from the flanges presented very similar strength to those extracted from the web (+3%). This result was expected and should be due to the fact that this particular failure mode is less influenced by the fibre orientation or content being more susceptible to the number of layers of fibres and to the polymer matrix used in the composite material.

#### 4.2.2.6. Summary of results

Table 4.13 presents the material strengths, elasticity and shear moduli determined by experimental testing on coupons, described in the previous Sections, and the mechanical properties provided by the manufacturer (*ALTO Perfis Pultrudidos, Lda.*), which are given within an error of 10% [92].

Table 4.13.: Summary of the main mechanical properties of the GFRP material for both I200 and I400 profiles: experimental data and values declared by the manufacturer [92].

Property	Unit	I200		I400		Producer
		Web	Flange	Web	Flange	
$\sigma_{tu,L}$	MPa	376.69±7.44	410.67±18.60	279.90±23.78	336.94±37.51	450±45
$E_{t,L}$	GPa	32.85±1.09	35.94±2.35	23.98±1.60	35.71±1.83	-
$\sigma_{tu,T}$	MPa	-	-	29.09±2.84	-	-
$E_{t,T}$	GPa	-	-	7.73±0.90	-	-
$\nu_{LT}$	-	0.29	0.30	-	-	-
$\sigma_{cu,L}$	MPa	434.37±51.42	388.55±59.18	204.72±56.15	197.65±64.43	350±35
$E_{c,L}$	GPa	27.06±1.99	33.93±3.35	12.21±3.24	12.26±2.99	23±2.3
$\sigma_{cu,T}$	MPa	88.92±16.08	64.31±17.25	70.43±5.60	46.92±4.12	-
$E_{c,T}$	GPa	5.74±0.73	4.35±0.93	4.55±0.52	3.57±0.36	-
$\sigma_{f,L}$	MPa	493.05±52.78	506.21±39.81	-	-	450±45
$E_{f,L}$	GPa	22.25±3.00	23.67±2.70	-	-	-
$\tau_{is,L}$	MPa	29.35±1.11	30.21±1.44	-	-	-
$\tau_{LT}$	MPa	27.47±3.37	-	20.43±1.15	-	-
$G_{LT}$	GPa	3.68±0.19	-	3.49±0.43	-	-
$\gamma$	kN/m <sup>3</sup>	-	-	-	-	18±1.8

The results summarized in Table 4.13 show that the mechanical properties derived from the coupon tests presented herein are often outside the margin of error provided by the manufacturer [92], especially for the I400 profile, for which the properties obtained in the tests are always lower than those provided by the manufacturer (and outside the error margin indicated). On the other hand, it should be stated that the I400 profiles used in the experiments are from the very first batch made by the producer and are not yet commercially available. Nevertheless, this comparison highlights the relevance of experimental characterization tests in GFRP materials and the importance of safety factors in structural design.

### 4.2.3. Full-scale flexural tests

As mentioned earlier (*cf.* Section 4.2.1), the full-scale flexural tests of the profiles were performed in order to determine (i) the full-section elasticity and shear moduli ( $E_{full}$  and  $G_{full}$ , respectively), (ii) the local buckling stress ( $\sigma_{cr,local}$ ) and moment ( $M_{cr,local}$ ), and (iii) the ultimate bending moment ( $M_u$ ). In this regard, two sets of full-scale flexural tests were performed: (i) serviceability tests; and (ii) failure tests. These tests were performed for both the I200 and I400 profiles.

#### 4.2.3.1. Serviceability tests

For the full-scale serviceability flexural tests, which were performed in order to determine the full-section elasticity and shear moduli ( $E_{full}$  and  $G_{full}$ , respectively) of the I200 and I400 profiles, one specimen of each profile was tested. The tests were performed by loading the profiles in a 3-point bending configuration with the load being applied at the midspan section, while deflections were measured at the bottom of the profiles at that same section. The profiles were simply supported with a fixed support on one side and a sliding support on the other side. Additionally, for the I400 profile, lateral bracings were provided near the extremities of the profile in order to avoid global instability phenomena. This process was repeated for each beam, according to the specifications of EN 13706-2 [37] for different span lengths (4 and 6 span lengths were used for the I200 and I400 profiles, respectively) allowing the measurement of load *vs.* deflection curves with different ratios of flexure and shear deflections ( $\delta_{flex}$  and  $\delta_{shear}$ , respectively).

During the tests the load was applied with a hydraulic jack from *Enerpac* with a load capacity of 600 kN, which was installed in a loading steel frame anchored to the laboratory strong floor. For the I200 profile, an open loading frame was used, whereas for the I400 profile a closed frame was used. The deflections were measured with *TML* electric displacement transducers with strokes of 100 mm for the I200 profile and 50 mm for the I400 profile, both with a 0.01 mm precision. For both cases, the load was measured with a load cell from *Novatech* with measuring capacity of 10 kN placed between the hydraulic jack and a steel plate which rested on top of the profiles. During the tests data was acquired with a data logger from *HBM*, model *Spider8*. Figures 4.40 and 4.41 depict the test setup for profiles I200 and I400, respectively.

The specimens tested presented a total length of either 3.80 m or 4.85 m, for the I200 and the I400 profiles, respectively. As mentioned earlier, specimens were tested for different span lengths ( $L$ ), which are indicated in Table 4.14 along with the maximum load ( $F_{max}$ ) and midspan deflection ( $\delta_{max}$ ) for each span. In this respect, it should be mentioned that



Figure 4.40.: Full-scale flexural serviceability tests: test setup for the I200 profile.



Figure 4.41.: Full-scale flexural serviceability tests: test setup for the I400 profile.

although the test standard [37] recommends subjecting the profiles to a midspan deflection of  $L/200$  for each span, these tests were performed until maximum loads of  $\approx 5$  kN and  $\approx 30$  kN were attained for the I200 and the I400 profiles, respectively. These restrictions were set due to concerns regarding the premature failure of the specimens. In fact, preliminary analytical predictions indicated that the global instability critical load for the I200 specimen (regarding the largest span) was only  $\approx 14$  kN, while the ultimate failure load of the I400 specimen (governed by web shear failure) was around 115 kN.

Table 4.14.: Full-scale flexural serviceability tests: spans tested, maximum loads ( $F_{max}$ ) and midspan deflection ( $\delta_{max}$ ) attained.

Property	Unit	I200				I400					
		$L_1$	$L_2$	$L_3$	$L_4$	$L_1$	$L_2$	$L_3$	$L_4$	$L_5$	$L_6$
Span length	m	1.40	2.10	2.70	3.50	1.00	1.50	2.00	3.00	4.00	4.70
$F_{max}$	kN	5.25	5.08	5.24	5.05	30.85	31.01	30.37	30.99	30.19	30.29
$\delta_{max}$	mm	0.74	1.64	3.46	6.07	0.97	1.37	1.68	3.48	5.87	8.31
$L/\delta_{max}$	-	1897	1284	780	577	1031	1096	1190	862	682	565

Given the fact that the test method used [37] is very susceptible to small perturbations [93], such as support settlements, at least two load cycles were performed for each span presented in Table 4.14. Each load cycle was performed within the time range of 30 s to 90 s, suggested in EN 13706-2 [37].

Finally, the above mentioned test standard [37] suggests that the full-section elasticity and shear moduli ( $E_{full}$  and  $G_{full}$ , respectively) may be determined from the linear regression of the inverse of the stiffness presented at each cycle times the length of the span —  $\left(\frac{F_{max}}{\delta_{max}} \cdot L\right)^{-1}$  — by the inverse of the span squared ( $L^{-2}$ ). Figures 4.42 and 4.43 plot these curves for the I200 and I400 specimens, respectively, along with the linear regressions, their equations ( $y = a_{full}x + b_{full}$ ) and coefficients of determination  $R^2$ .

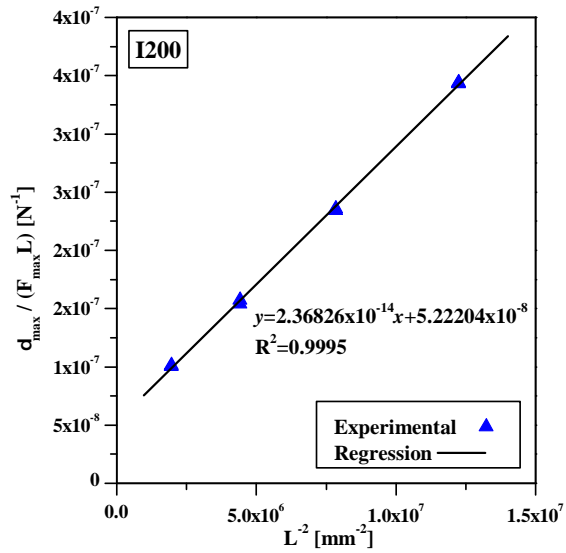


Figure 4.42.: Full-scale flexural serviceability tests: determination of the full-section moduli ( $E_{full}$  and  $G_{full}$ ) for the I200 profile.

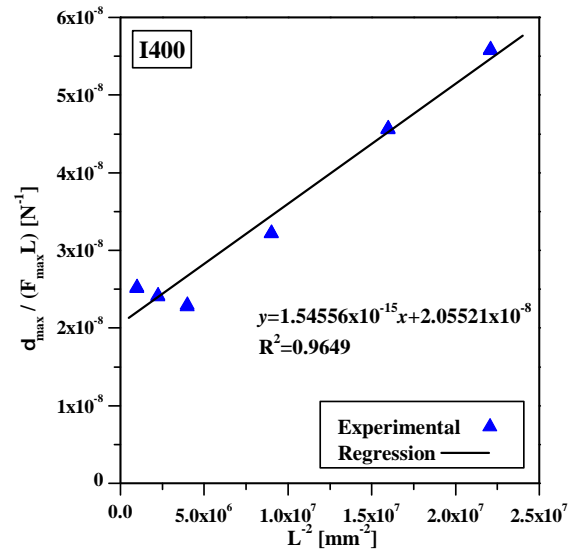


Figure 4.43.: Full-scale flexural serviceability tests: determination of the full-section moduli ( $E_{full}$  and  $G_{full}$ ) for the I400 profile.

The linear regressions presented in Figures 4.42 and 4.43 may be used to determine the full-section elasticity and shear moduli using Eqs. (4.10) and (4.11), respectively,

$$E_{full} = \frac{1}{48 \times a_{full} \times I} \quad (4.10)$$

$$G_{full} = \frac{1}{4 \times b_{full} \times kA} \quad (4.11)$$

where,  $I$  is the second moment of area of the profile around the bending axis and  $kA$  is the shear area in the direction of the applied load. Table 4.15 presents these geometrical parameters for both profiles. Regarding the determination of the shear area, it should be referred that it was considered to be the same as the area of the webs ( $A_w$ ), a common assumption for this type of profiles [60–62].

Table 4.15.: Geometrical properties of the profile sections.

Property	Unit	I200	I400
$I$	$\times 10^4 \text{ mm}^4$	2352.6	26877.9
$kA$	$\text{mm}^2$	1666.7	5775.0

Table 4.16 presents the full-section moduli derived from the full-scale flexural tests for each profile and compares these results with those derived from coupon testing.

The results for the I200 profile show a reasonable to good agreement between the elasticity and shear moduli derived from full-scale flexural test and those derived from coupon testing, namely when comparing with  $E_{t,L}^{Flanges}$  and  $G_{LT}^{Web}$ , which are the governing moduli for the flexural behaviour, presenting differences of +4% and -22%, respectively. Regarding the I400

Table 4.16.: Full-scale flexural serviceability tests: results and comparison with coupon testing.

Profile	$E_{full}$ GPa	$E_{full}/$ $E_{t,L}^{Web}$	$E_{full}/$ $E_{t,L}^{Flanges}$	$E_{full}/$ $E_{c,L}^{Web}$	$E_{full}/$ $E_{c,L}^{Flanges}$	$G_{full}$ GPa	$G_{full}/$ $G_{LT}^{Web}$
I200	37.39	1.14	1.04	1.38	1.10	2.87	0.78
diff.	-	13.8%	4.0%	38.2%	10.2%	187.2%	-21.9%
I400	50.15	2.09	1.40	4.11	4.09	2.11	0.60
diff.	-	109.1%	40.4%	310.7%	309.1%	110.6%	-39.6%

profile, the results of full-scale serviceability tests presented a poor agreement with those from coupon testing, with differences of +40% and -40%, respectively.

It should be mentioned that the EN 13706-2 [37] standard suggests the use of 5 different spans: (i) a span with 12% shear deformability ( $L_{12\%}$ , Eq. (4.12)); (ii) two shorter spans; and (iii) two longer spans.

$$L_{12\%} = \sqrt{\frac{100 \cdot EI}{GkA}} \quad (4.12)$$

In the present case, and using the moduli determined with coupon testing (*cf.* Table 4.13),  $L_{12\%}$  is 3.15 m and 5.02 m, for the I200 and I400 profiles, respectively. These results mean that, for both profiles, all spans tested presented an influence of the shear deformations higher than 12%, with the exception of the higher span for the I200 profile, which may hinder the validity of the method and the quality of the results, particularly for the I400 profile.

In this regard, it should be mentioned that the unexpected results obtained for the three lower spans of profile I400 (*cf.* Figure 4.43) could be due to the high influence of shear deformations, ultimately resulting in the determination of an unexpectedly high elasticity modulus ( $E_{full}$ , *cf.* Table 4.16), which is considered to be not accurate given the results obtained in the coupon testing (*cf.* Table 4.13).

In this respect, and given the known susceptibility of the method presented by EN 13706-2 [37] to small perturbations in the test procedure [93], the moduli derived from coupon testing will be used in the remainder of this work, namely in the analytical and numerical modelling.

#### 4.2.3.2. Failure tests

The full-scale flexural failure tests were performed by loading the profiles, monotonically, in a 4-point bending configuration. The boundary conditions were similar to those used in the serviceability tests with the profiles being simply supported with a fixed support on one side and a sliding support on the other side. Additionally, lateral bracing systems were provided for all profiles, namely, 6 supports along the length for the I200 profile and 4 for the I400 profiles. These lateral bracings were provided in order to avoid failure modes related with global instability phenomena, in particular, lateral-torsional buckling.

#### 4.2.3.2.1 Profile I200

Regarding the I200 profile, one specimen with a total length of 4.39 m was tested in a 4.00 m span ( $L$ ). As illustrated in Figure 4.44, the loads were applied symmetrically with respect to the longitudinal centre of the span, at a distance of the support sections of 1.30 m ( $a = 1.30$  m and  $b = 1.40$  m).

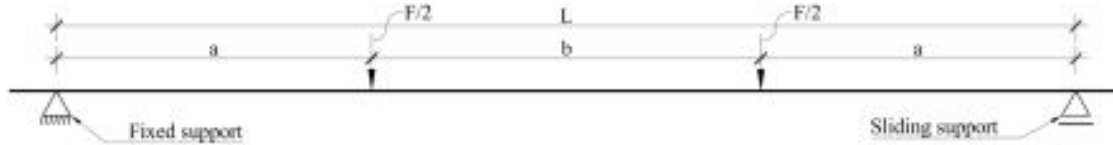


Figure 4.44.: Full-scale flexural failure tests: 4-point bending load configuration.

The load was applied with a hydraulic jack from *Enerpac* with a load capacity of 600 kN, which was installed in an open steel loading frame anchored to the laboratory strong floor. The hydraulic jack was connected to a steel beam, centred with the jack, which, by its turn, transferred the load along the span  $b$  (cf. Figure 4.44) to the loading points of the GFRP profile. The steel beam loaded the GFRP profile through steel cylinders that allowed rotations around the bending axis. Additionally, underneath the steel cylinders, steel spreading plates (160 mm long, 80 mm wide and 10 mm thick) were provided, in order to avoid premature failure modes, such as crushing or instability phenomena under concentrated loads. The supports were materialized by steel cylinders with 200 mm long and 80 mm wide steel spreading plates on top (thickness of 10 mm). The load was measured with a load cell from *Novatech*, with a capacity of 400 kN, which was placed in-between the steel loading frame and the hydraulic jack. This load cell was installed with a steel cylinder that allowed the loading system to rotate around the bending axis.

The vertical deflections were measured underneath the profile at the midspan section with an *APEK* electric displacement transducer and at two sections distanced of 1000 mm from the midspan with *TML* electric displacement transducers, all with a stroke of 100 mm and 0.01 mm precision. Additionally, at a section positioned at 450 mm from the midspan, the vertical deflections at the extremities of the top flange ( $\delta_{s1}$  and  $\delta_{s2}$ , as illustrated in Figure 4.45), were measured with string pot electric displacement transducers from *TML* with a range of 500 mm and precision of 0.1 mm.

Regarding the measurement of axial strains, the midspan section was instrumented with nine electric strain gauges (from *HBM*, model *HBM-1-LY11-10/120*), as schematized in Figure 4.46, five installed in the top flange and four installed in the bottom one.

Figure 4.47 illustrates the test setup, which, as mentioned earlier, included a lateral bracing system, provided to avoid the triggering of global instability phenomena. The bracing system was provided by six supports along the length, each support constituted by a pair of braces on each side of the profile. Two lateral supports were placed near the vertical support, at a distance of 400 mm from the midspan of the profile, and were materialized by triangular steel frames with a 300 mm width. Near the midspan of the profile, the four remaining lateral supports were displaced symmetrically with respect to the midspan at distances from the latter section of 260 mm and 840 mm. These supports were materialized by adjustable steel props, which were locked in-between the laboratory floor and a steel beam that was connected to the loading frame. In order to minimize the friction forces between the profile and the lateral supports, the contact areas were thoroughly greased.



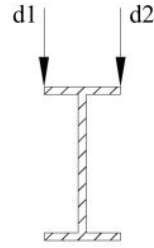


Figure 4.45.: Full-scale flexural failure tests: I200 profile — positioning of string pot displacement transducers.

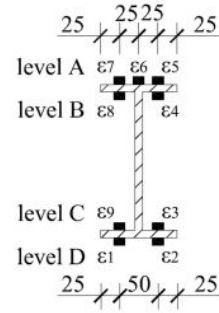


Figure 4.46.: Full-scale flexural failure tests: I200 profile — positioning of the strain gauges at mid-span section (dimensions in mm).



Figure 4.47.: Full-scale flexural failure tests: test setup of the I200 specimen.

Test data was acquired with two built-in data loggers, from *HBM*, model *Spider8*, at a rate of 10 Hz, and stored in a PC. In order to avoid the effects of the initial settlement of the test setup on the measurements, an initial load/unload cycle was performed, up to 5 kN, before the profile was finally loaded up to failure. Loading was performed at an average rate of 0.1 kN/s.

Figures 4.48 and 4.49 present the applied load as a function of (i) the deflections and (ii) the midspan axial strains, respectively. Regarding Figure 4.49, in order to enhance and simplify the analysis of the experimental results, the axial strains presented are the average of the strains measured at each level of the profile (outer and inner levels of the top and bottom flanges, *cf.* Figure 4.46). The results obtained in this test show that the behaviour of the profile was linear up to failure.

The I200 profile specimen failed at an ultimate load of 61.3 kN, for which the midspan deflection was 85.26 mm ( $\approx L/46.9$ ). The deflections measured at quarter-span (d1 and d3, *cf.* Figure 4.48) were very similar throughout the test indicating that the test setup and response were symmetric, as intended. Regarding the axial strains, they developed almost symmetrically with reference to the geometric centre of the cross-section, implying that the neutral axis position was coincident with the geometrical centre (there is a small deviation of 1.3 mm towards the compression flange). From this result, one may conclude

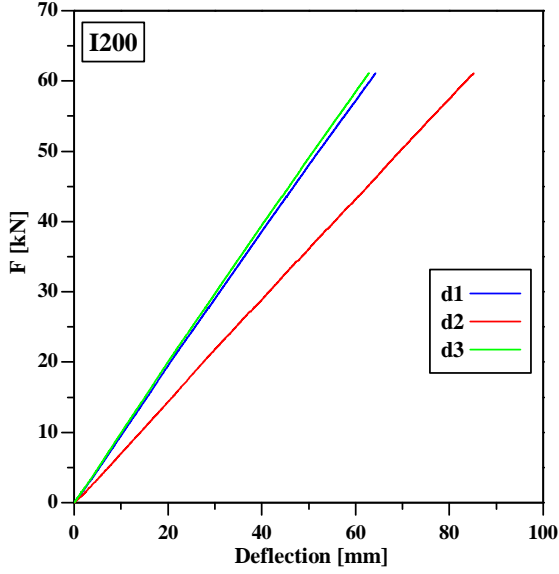


Figure 4.48.: Full-scale flexural failure tests: I200 profile — load *vs.* deflections.

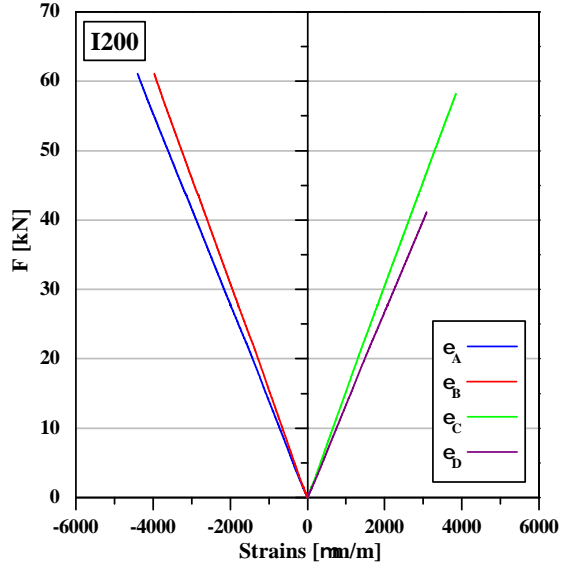


Figure 4.49.: Full-scale flexural failure tests: I200 profile — load *vs.* midspan axial strains.

that the longitudinal elasticity modulus in compression ( $E_{c,L}$ ) is very similar to that in tension ( $E_{c,L}$ ), a result confirmed by the coupon testing for the flanges but not for the web (*cf.* Section 4.2.2.6). Nevertheless, it should be mentioned that the influence of the web material in the flexure behaviour is much smaller than that of the flanges. In this regard, the full-section elasticity modulus ( $E_{full}$ ) observed in this test was estimated based on the axial strain measurements ( $\varepsilon$ ), considering, similarly to what was assumed in the serviceability test analysis, an homogeneous response of the profile, using Eq. (4.13),

$$E_{full} = \frac{M}{I\chi} \quad (4.13)$$

where  $M$  is the bending moment,  $I$  is the second moment of area with regard to the main direction, and  $\chi$  is the curvature of the section. The last parameter was obtained based on the linear regression between the strain gauges position along the cross-section's depth (*cf.* Figure 4.46) against the measured strains at each level. The theoretical bending moment ( $M$ ), by its turn, may be calculated with reference to the applied load ( $F$ ) and the 4-point bending load configuration (*cf.* Figure 4.44, for the present case  $a = 1300$  mm and  $b = 1400$  mm) using Eq. (4.14):

$$M = \frac{Fa}{2} \quad (4.14)$$

Table 4.17 presents the curvature and elasticity modulus calculated for bending moments ranging from 5 to 25 kNm.

These results show a good agreement between the different load levels (CoV of 0.6%), while the average elasticity modulus obtained compares well to that obtained in the serviceability tests, with a relative difference of -4%.

Table 4.17.: Full-scale flexural failure tests: determination of the elasticity modulus ( $E_{full}$ ) with axial strain measurements (I200).

$M$ (kNm)	$\chi$ ( $10^{-3}/m$ )	$E_{full}$ (GPa)
5	5.67	35.46
10	11.21	35.91
15	16.73	36.04
20	22.47	35.79
25	28.12	35.73
Average	-	35.79
Std. dev.	-	0.22
CoV	-	0.6%

Failure of the specimen occurred for a bending moment at the midspan ( $M$ ) section of 39.7 kNm. Failure occurred due to local buckling of the profile near one of the loading sections, as depicted in Figures 4.50 and 4.51. The buckling phenomenon was presumably triggered by the instability of the compressed flange, which was accompanied by the web. It was not clear, however, if the web-flange junction failed prior or after the buckling occur.



Figure 4.50.: Full-scale flexural failure tests: configuration of the local buckling wave in the I200 profile (near one of the loading sections).



Figure 4.51.: Full-scale flexural failure tests: damage detail on the top flange and web of the I200 profile (near one of the loading sections).

Regarding the local buckling of the top flange, it is possible to estimate the critical load ( $F_{cr}$ ) associated to the instability behaviour of the beam based on the experimental results, namely, based on the measurements of the vertical deflections at the extremities of the top flange ( $\delta_{s1}$  and  $\delta_{s2}$ ). These are plotted in Figure 4.52 as a function of the applied load ( $F$ ) along with the difference between those deflection measurements ( $\Delta\delta_s$ ), which provides an estimate of the rotation of the top flange. To this end, the modified Southwell method [94] may be applied by performing a linear regression of the load ( $F$ ) *vs.* differential vertical deflection of the flange ( $\Delta\delta_s$ ) curve, before and after the buckling phenomenon. Finally, the critical load ( $F_{cr}$ ) may be estimated by the interception of the resulting linearized curves. Figure 4.53 shows the curve  $F$  *vs.*  $\Delta\delta_s$  together with the application of the modified Southwell method. It should be mentioned that due to the relatively low precision of the

displacement transducers available for this test (0.1 mm), the  $F$  vs.  $\Delta\delta_s$  curve presents high variation, especially before instability occurred.

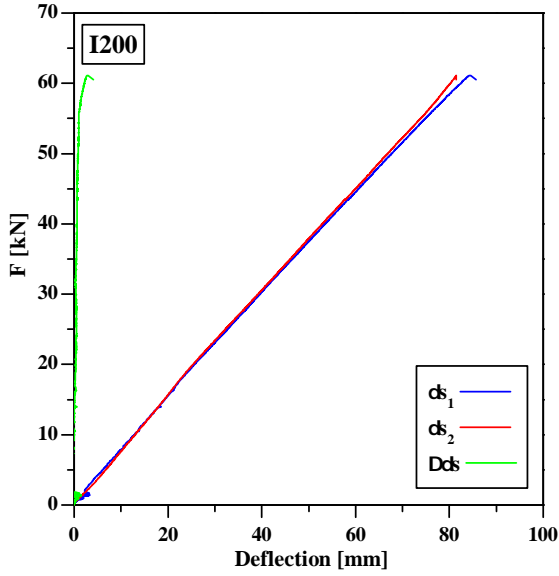


Figure 4.52.: Full-scale flexural failure tests: I200 profile — Load vs. upper flange deflections.

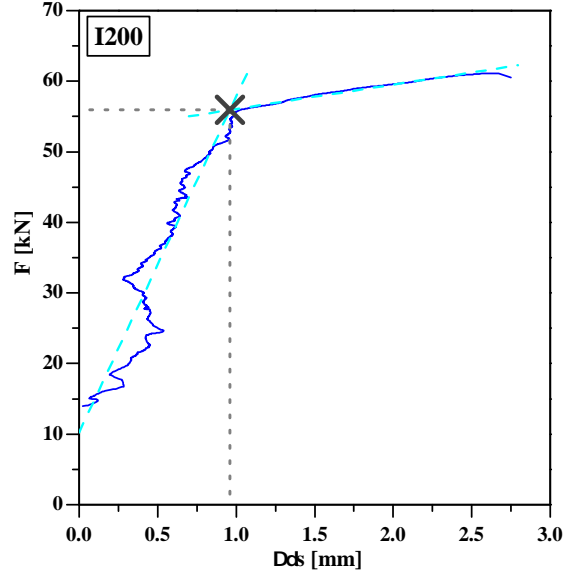


Figure 4.53.: Full-scale flexural failure tests: I200 profile — Upper flange differential vertical deflection and application of the modified Southwell method.

With this analysis, it was possible to estimate the critical load ( $F_{cr}$ ) as 55.9 kN, which corresponds to a critical bending moment (*cf.* Eq. (4.14)) of 36.4 kNm. Thereafter, the compressive critical axial stress ( $\sigma_{cr}$ ) estimated using Eq. (4.15) is 144.2 MPa,

$$\sigma = \frac{M}{W} \quad (4.15)$$

where  $W$  is the first moment of area with respect to the main direction of the profile's cross-section.

#### 4.2.3.2.2 Profile I400

In what concerns the I400 profile, three specimens were tested, two of which presented a total length of 4.85 m, while one had a total length of 3.85 m. The specimens were loaded in a 4-point bending configuration, the first two in a span of 4.00 m (specimens P400-1 and P400-2) and the other one in a span of 3.00 m (specimen P400-3). The load was applied symmetrically with reference to the profiles midspan with the following geometrical parameters: (i)  $a = 1.40$  m and  $b = 1.20$  m for the longer specimens; and (ii)  $a = b = 1.00$  m for the shorter specimen (*cf.* Figure 4.44).

The load was applied with a hydraulic jack from *Enerpac* with a load capacity of 600 kN, which was installed in a closed steel loading frame anchored to the laboratory strong floor. The test setup was centred with the the loading frame in order to enable an easier quantification of the effects of the loading frame deformations in the test measurements.

Similarly to what happened with the I200 specimen, the hydraulic jack was connected to a steel beam, centred with the jack, which, by its turn, transferred the load along the loading span  $b$  (cf. Figure 4.44) to the GFRP profile. The steel beam loaded the GFRP profile through steel cylinders that allowed rotations around the bending axis. Underneath these steel cylinders, steel spreading plates were provided in order to distribute the load evenly to the GFRP profile. These spreading plates were 100 mm long and 200 mm wide with a thickness of 20 mm for specimen P400-1, and were 200 mm long and 200 mm wide with similar thickness for the remaining specimens (P400-2 and P400-3). Similarly, at the support sections, steel cylinders were provided with steel spreading plates, 100 mm long and 200 mm wide with a thickness of 25 mm for the first specimen, and 200 mm long and 200 mm wide with a thickness of 25 mm for the remaining specimens. These differences in the boundary conditions of the different specimens were implemented in order to investigate experimentally the possibility of premature failure of the GFRP profiles due to web crushing or web buckling under concentrated loads (web-crippling).

As for the I200 specimen, the load was measured with a load cell from *Novatech* with a capacity of 600 kN, which was placed in-between the steel loading frame and the hydraulic jack. This load cell was installed with a steel cylinder that allowed the loading system to rotate around the bending axis. The vertical deflections were measured underneath the profile at the midspan section with two *TML* electric displacement transducers with a stroke of 100 mm and 0.01 mm precision. As shown in Figures 4.54 and 4.55, due to lack of free space between the loading frames and the GFRP profiles, the pistons of the displacement transducers were attached to a small steel plate, which was connected to the profiles with clamps and separated from them by means of two small plastic spacers in order to provide free space for the strain gauges installed at the midspan section (in specimen P400-2). Additionally, the displacements of the loading frame under one of the support sections was also measured, with an electric displacement transducer from *TML* with a stroke of 10 mm and precision of 0.01 mm, in order to measure any potential deformation of the closed loading frame.

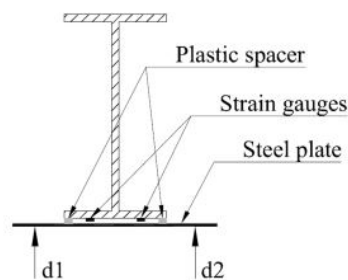


Figure 4.54.: Full-scale flexural failure tests: I400 profiles — scheme of the vertical displacement measurement apparatus.

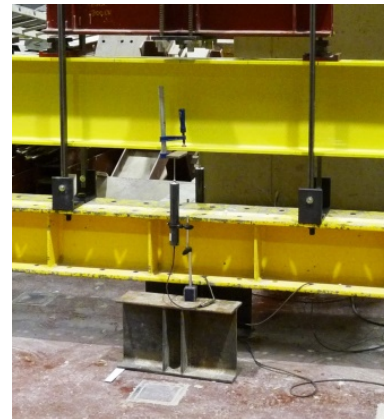


Figure 4.55.: Full-scale flexural failure tests: I400 profiles — vertical displacement measurement apparatus.

The axial strains were measured in the longer specimens, P400-1 and P400-2, at a section distanced of 200 mm from the midspan (P400-1) or at the midspan section (P400-2). The axial strains were measured in the flanges at the utmost exterior fibres of the cross-section

with two electric strain gauges per flange, from *TML*, model *FLK-6-11-3L*, as shown in Figure 4.56. Additionally, a strain gauge rosette, made with the same strain gauges, was installed in the P400-2 specimen at mid-height of the web and at a distance of 700 mm from one of the supports, as shown in Figure 4.57.

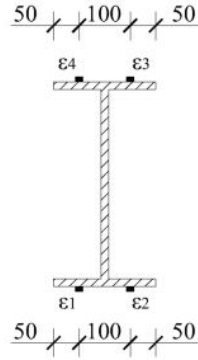


Figure 4.56.: Full-scale flexural failure tests: I400 profiles — positioning of the strain gauges in the cross-section (dimensions in mm).

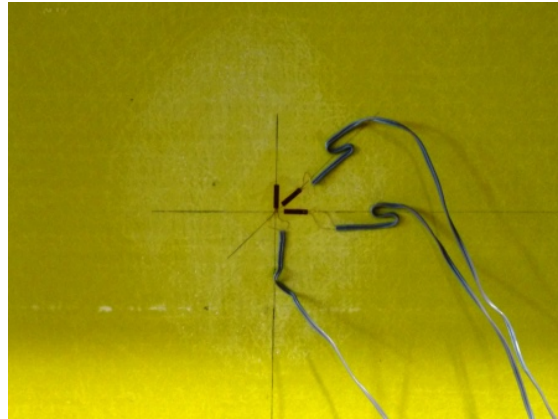


Figure 4.57.: Full-scale flexural failure tests: I400 profile — strain gauge rosette used in for specimen P400-2.

The lateral bracing system used in the I400 specimens tests, in order to avoid the triggering of global instability phenomena, comprised four pairs of vertical bars along the length. All lateral supports (bracings) were materialized by a tailor made support system comprising steel tubes ( $80 \times 20(\times 4) \text{ mm}^2$ ), which were connected to the loading frame with small length steel angle profiles. The connections between all the bracing elements were bolted. Since the bracing system was connected to the loading frame, the positioning of the lateral supports was defined based on the drills of the loading frame and could not be perfectly symmetrical with respect to the midspan of the profile. Thereafter, the positioning of the lateral supports, with respect to the distance to the left-hand support, was the following: (i) 335 mm, (ii) 1460 mm, (iii) 2575 mm, and (iv) 3685 mm, for the longer specimens (P400-1 and P400-2); and (i) 150 mm, (ii) 1070 mm, (iii) 1875 mm, and (iv) 2685 mm, for the shorter specimen (P400-3). All the contact areas between the lateral supports and the profiles were thoroughly greased in order to minimize friction forces. Figures 4.58 and 4.59 illustrate the test setup for the longer and shorter specimens, respectively.

During the tests, data was acquired with data loggers from *HBM*, model *Spider8*, at a rate of 10 Hz and stored in a PC. In order to avoid the effects of the initial settlement of the test setup on the measurements, an initial load/unload cycle was performed up to 30 kN, before the profile was loaded up to failure. Loading was performed at an average rate of 0.5 kN/s.

Figures 4.60 to 4.62 present the load deflection curves observed for each test including the average midspan deflection ( $d_{ms}$ ) and the individual deflections  $d1$  and  $d2$  (duly corrected based on the displacement of the loading frame). Although all specimens presented a linear load-average midspan displacement behaviour, specimens P400-2 and P400-3 also presented non-linear behaviour regarding the load-individual displacement curves  $d1$  and  $d2$ .

As depicted in Figures 4.60 to 4.62, at a certain point, all specimens presented a difference between the deflections measured at positions  $d1$  and  $d2$ , which indicates that the specimens



Figure 4.58.: Full-scale flexural failure tests: I400 profiles — test setup for the longer specimens.



Figure 4.59.: Full-scale flexural failure tests: I400 profiles — test setup for the shorter specimen.

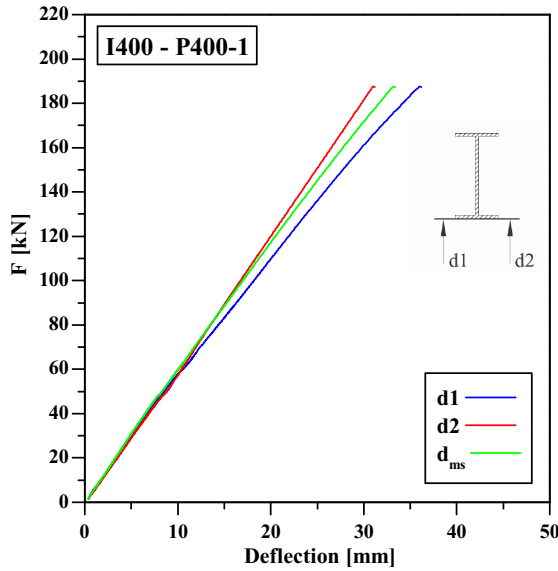


Figure 4.60.: Full-scale flexural failure tests: P400-1 specimen — load vs. midspan deflection.

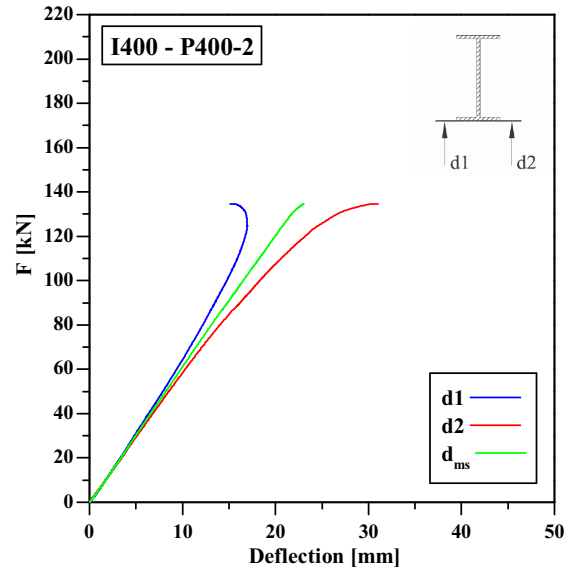


Figure 4.61.: Full-scale flexural failure tests: P400-2 specimen — load vs. midspan deflection.

exhibited torsional deformations. For specimen P400-1, this difference presented a roughly linear growth with the load until the failure of the specimen, indicating that torsion was induced most likely by the specimens own geometrical imperfections and by some transverse eccentricities of the load setup. In this regard it should be mentioned that due to the relative large geometrical imperfections observed in all specimens it was not possible to fully centre the load setup with the profile in the transverse direction.

Regarding specimens P400-2 and P400-3, they also presented a linear difference between the midspan deflections  $d1$  and  $d2$  in the earlier stages of the tests, but this difference started to increase non-linearly prior to failure. This indicates that, in both cases, a buckling phenomenon was triggered before the collapse of the specimens. Furthermore, given that the displacements were measured in the bottom flange, which is not susceptible to local buckling phenomena (since it is in tension), these results indicate that a global buckling phenomenon



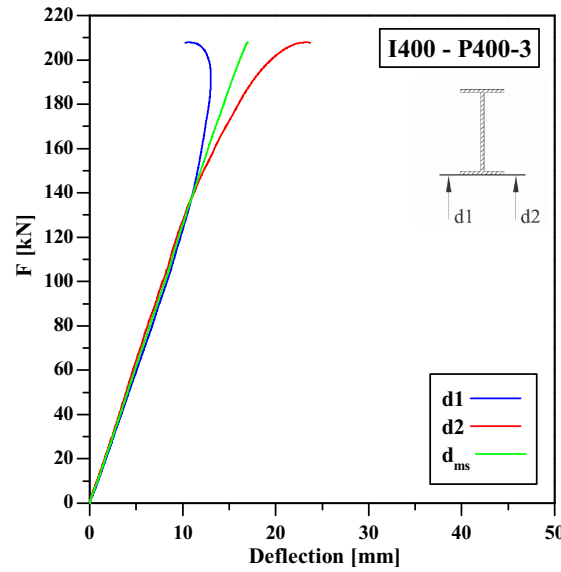


Figure 4.62.: Full-scale flexural failure tests: P400-3 specimen — load *vs.* midspan deflection.

occurred despite the lateral bracings installed. Additionally, the fact that the previously referred difference evolved faster (within its linear range) for the longer specimens confirms that the torsional deformations were magnified by geometrical imperfections of the profiles, to which the longer specimens are more susceptible to.

Figures 4.63 and 4.64 plot the load *vs.* axial strain curves for specimens P400-1 and P400-2, respectively, showing similar behaviour to that observed for the deflections. Specimen P400-1 presented linear load *vs.* axial strain curves up to failure, although the strains in the bottom flange exhibited significant differences. These differences may stem from the fact that the profile may have also exhibited some torsion, as mentioned earlier. Regarding specimen P400-2, load *vs.* axial strain curves were also linear in the earlier stages of the test and, similarly to the deflections, even if less prominently, then became non-linear and diverged before failure. This non-linear behaviour indicates the occurrence of an instability phenomenon. Furthermore, the evolution of the response of the axial strains from linear to non-linear indicates that the nature of the instability phenomenon was global.

From Figures 4.63 and 4.64 it may be depicted that the compressive and tensile strains developed almost symmetrically for both specimens, which indicates that the neutral axis of the profile is near the profiles' geometrical centre and, thereafter, the compressive and tensile elasticity moduli in the longitudinal direction are similar. In fact, based on the strain gauge measurements, the neutral axis presented an average deviation of 3.31 mm from the geometric centre towards the upper flange for specimen P400-1, whereas for specimen P400-2 this deviation was 2.33 mm towards the bottom flange. Based on these results, the full-section elasticity modulus ( $E_{full}$ ) was estimated using Eqs. (4.13) and (4.14). It should be noted that since the bending moment remains constant in-between load application points for the 4-point bending configuration, Eq. (4.14) is valid for all the sections in-between these points. Table 4.18 presents the curvature ( $\chi$ ), which was determined based on the (two-point) linear regression between the depth of the profile and the average strains measured in each flange, and the elasticity modulus ( $E_{full}$ ) calculated for bending moments ranging from 15 to 60 kNm.



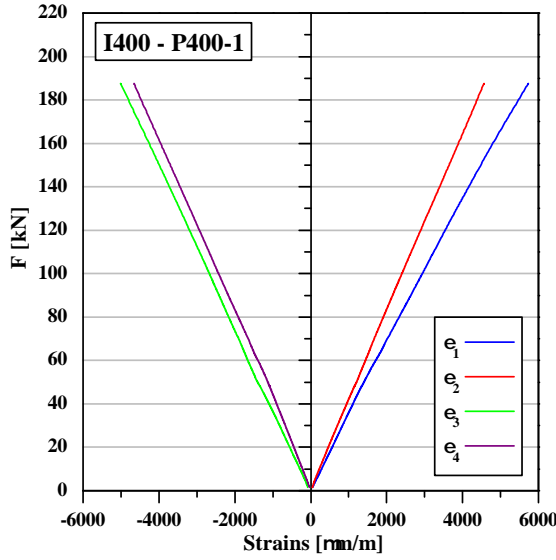


Figure 4.63.: Full-scale flexural failure tests: P400-1 specimen — load vs. axial strains.

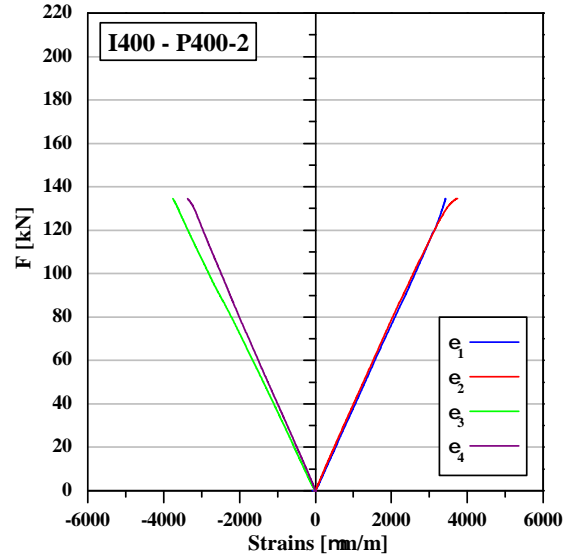


Figure 4.64.: Full-scale flexural failure tests: P400-2 specimen — load vs. axial strains.

The results obtained for the two specimens are very consistent, presenting maximum CoV of 1.4%, and similar. Nevertheless, and unlike the results observed for the I200 specimen, the elasticity modulus obtained with this method presents a high deviation from that obtained with the serviceability tests of approximately -62%. The fact that these results present such high differences is unexpected and may stem from the geometrical imperfections of the profiles mentioned earlier and the lack of accuracy in the procedure implemented for the serviceability tests. Moreover, due to the lack of confidence in both results, the elasticity moduli obtained in the coupon testing will be used henceforth in this document, namely in the analytical and numerical modelling.

Regarding the measurements of the strain gauge rosettes, Figure 4.65 presents the evolution of the strains with the load for specimen P400-2. It may be observed that the longitudinal strain gauge ( $r1$ ) presents very low deformations, which was expected due to the fact that it was installed in the vicinity of the neutral axis (which is deviated 2.33 mm from the

Table 4.18.: Full-scale flexural failure tests: determination of the elasticity modulus ( $E_{full}$ ) with axial strain measurements for I400 specimens.

$M$ (kNm)	Specimen P400-1		Specimen P400-2	
	$\chi$ ( $10^{-3}/m$ )	$E_{full}$ (GPa)	$\chi$ ( $10^{-3}/m$ )	$E_{full}$ (GPa)
15	2.71	19.38	2.78	18.90
30	5.44	19.28	5.57	18.88
45	8.33	18.90	8.36	18.83
60	11.16	18.82	11.21	18.74
Average	-	19.10	-	18.84
Std. dev.	-	0.28	-	0.07
CoV	-	1.4%	-	0.4%

geometrical centre of the section towards the bottom flange). In this respect, this strain gauge measured negative strains in the earlier stages of the test, coherently with the position where it was installed, and then retrieved positive strains, possibly due to the effects of the global instability phenomenon mentioned earlier. Notwithstanding, the absolute strains measured at this position were always the lowest within the rosette. In what concerns the transverse and oblique strain measurements ( $r2$  and  $r3$ , respectively) they both measured compressive strains, which is coherent with the load path between the load application and support sections. The oblique strain gauge ( $r3$ ) presented the highest absolute strains.

Using these results it is possible to determine the distortion between the longitudinal and transverse directions ( $\gamma_{LT}$ ) using Eq. (4.16):

$$\gamma_{LT} = 2 \cdot r3 - r1 - r2 \quad (4.16)$$

The shear stress ( $\tau_{LT}$ ), on the other hand, may be derived from Eq. (4.17),

$$\tau_{LT} = \frac{V \cdot W}{I \cdot t} \quad (4.17)$$

where  $t$  is the plate thickness. In order to calculate the shear stress ( $\tau_{LT}$ ) in the fibres corresponding to the rosette (the fibres at the geometrical centre of the section), the first moment of area ( $W$ ) to be considered in Eq. (4.17) should correspond to that of half of the section. Figure 4.66 plots the  $\tau_{LT}$  vs.  $\gamma_{LT}$  curve, which reflects a slightly non-linear behaviour (similar to that observed in the off-axis tensile coupon tests, *cf.* Section 4.2.2.3)

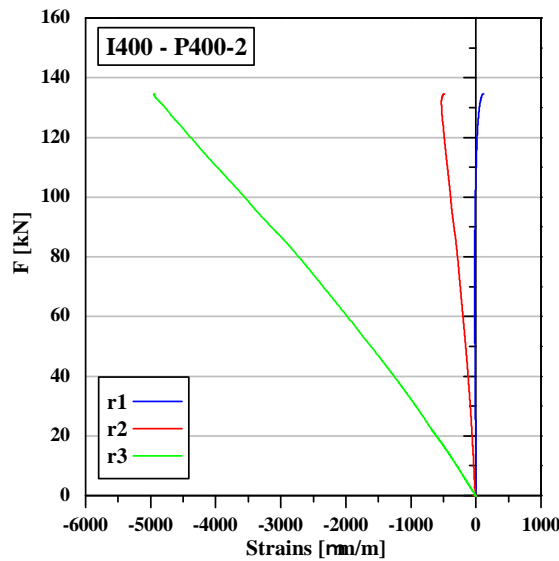


Figure 4.65.: Full-scale flexural failure tests: P400-2 specimen — load vs. rosette strains.

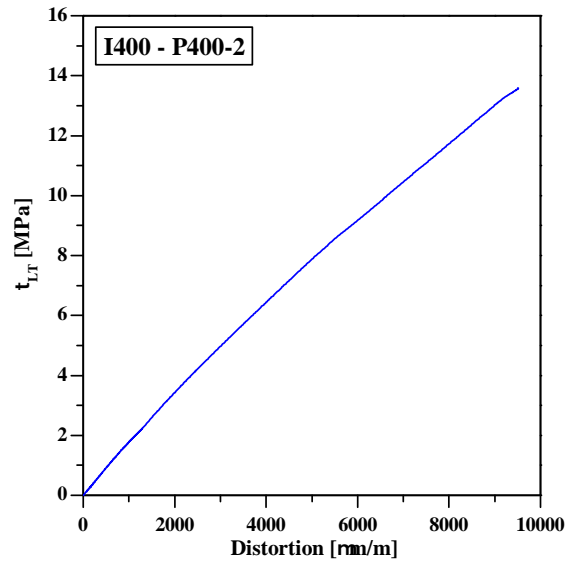


Figure 4.66.: Full-scale flexural failure tests: P400-2 specimen — shear stress vs. distortion.

From the linear regression of the curve plotted in Figure 4.66 it is possible to estimate the shear modulus ( $G_{LT}$ ) for this specimen. For the present case, this linear regression was performed between distortion values of  $500 \mu\text{m/m}$  to  $2500 \mu\text{m/m}$  (similarly to the regressions performed to the off-axis tensile coupon test results, *cf.* Section 4.2.2.3) indicating a 1.65 GPa modulus. The modulus obtained corresponds to approximately half of that

obtained with the coupon testing (-53%, *cf.* Section 4.2.2.6)), while it is 22% smaller than that determined in the full-scale flexural serviceability tests (*cf.* Section 4.2.3.1). These high relative differences are similar to those observed regarding the elasticity modulus, and should, likewise, be explained by the large geometrical imperfections of the specimen, which may have contributed to magnify the deformations, resulting in lower (apparent) elasticity and shear moduli.

In what concerns the failure behaviour, the first specimen, P400-1, failed for a load ( $F$ ) of 187.7 kN, corresponding to a maximum bending moment ( $M$ ) of 131.4 kNm and a shear force ( $V$ ) of 93.8 kN, with an average midspan deflection ( $d_{ms}$ ) of 33.2 mm. Failure occurred due to web-crippling, which may have been caused by both web-crushing and local web-buckling in the transverse direction [14], in the vicinity of the sliding support section, as shown in Figures 4.67 and 4.68, while the remaining areas of the profile were apparently undamaged.



Figure 4.67.: Full-scale flexural tests: failure mode of specimen P400-1, front side view.

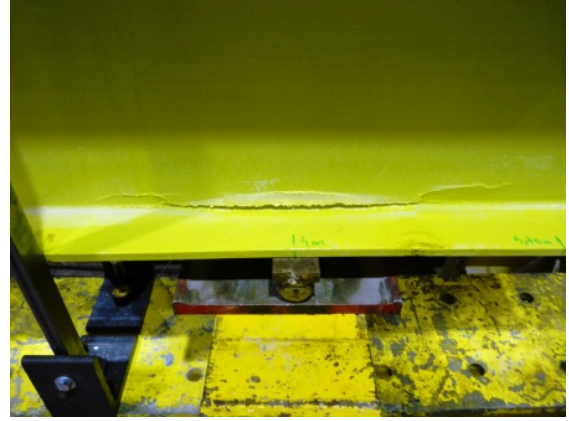


Figure 4.68.: Full-scale flexural tests: failure mode of specimen P400-1, back side view.

The crushing stress involved in this particular failure mode may be estimated with Eq. (4.18),

$$\sigma_T^{crush} = \frac{V}{A_{eff}} \quad (4.18)$$

where  $A_{eff}$  is the area supporting the stresses that are transmitted to the support. For the present case (a simply supported beam), following the recommendations of Bank [4], it may be considered as follows,

$$A_{eff} = t_w \left( L_{eff} + \frac{d_w}{2} \right) \quad (4.19)$$

where,  $t_w$  and  $d_w$  are the thickness and depth of the web plate, respectively, and  $L_{eff}$  is the length of the support. Thereafter, for this case, where  $L_{eff} = 150 \text{ mm}$ , the transverse crushing stress ( $\sigma_T^{crush}$ ) may be estimated as 37.3 MPa.

The failure of specimen P400-2 occurred for a load ( $F$ ) of 134.6 kN with an average midspan deflection ( $d_{ms}$ ) of 23.0 mm. This failure load, 28.3% lower than that of specimen P400-1, corresponds to a bending moment of 94.2 kNm and a maximum compressive stress ( $\sigma_{c,L}$ )

of 66.7 MPa. Failure occurred following an instability phenomenon. Although it is not possible to completely disregard the hypothesis of a mixed local–global buckling mode, the phenomenon observed was apparently global lateral–torsional buckling. Since the profile was clearly not properly laterally supported and this phenomenon was not observed in the P400–1 specimen (which failed for a higher load), the main reason for the inability of the bracing system to avoid the global buckling phenomenon may be the particularly large geometrical imperfections of this specimen. In fact, the lateral forces to which the bracing bars were subjected to were high enough to cause the yielding of the steel. After the instability phenomenon occurred, the profile failed in the web–flange junction due to the large rotation of the upper flanges under one of the load application points, possibly due to eccentric loading after the global buckling. Figures 4.69 and 4.70 illustrate the failure of this specimen.

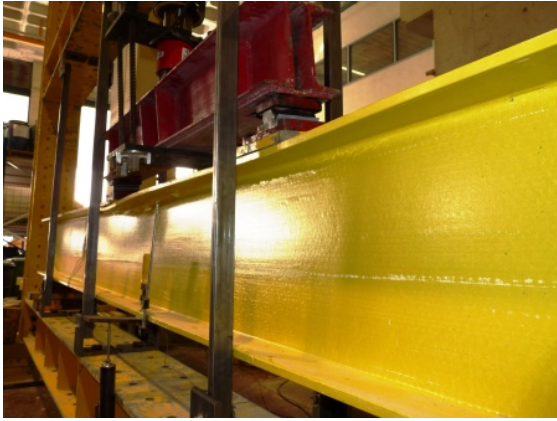


Figure 4.69.: Full-scale flexural tests: failure mode of specimen P400–2, global view.

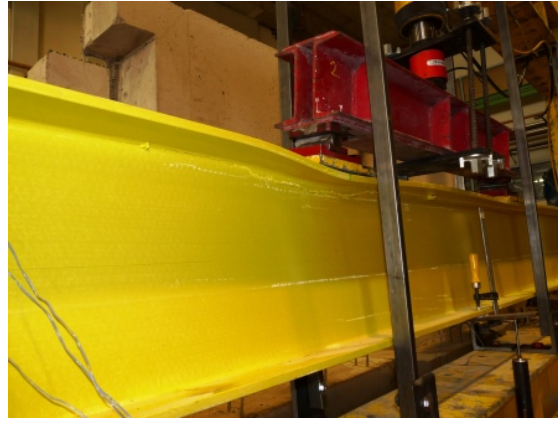


Figure 4.70.: Full-scale flexural tests: failure mode of specimen P400–2, damage on the web–flange junction.

Finally, specimen P400–3 failed in the web–flange junction near one of the loading sections. Failure occurred for a load of 207.9 kN, corresponding to a maximum bending moment ( $M$ ) of 103.9 kNm and a shear force ( $V$ ) of 103.9 kN, with an average midspan deflection ( $d_{ms}$ ) of 26.0 mm. The maximum compressive axial stress ( $\sigma_{c,L}$ ), considering the neutral axis coincident with the geometrical centre, was estimated as 101.8 MPa. The failure load was 11% higher than that of specimen P400–1. Failure is likely to have been caused by the combination of shear and axial longitudinal and transverse stresses, a point that was clarified with the development of numerical models (*cf.* Section 4.2.3.4). After the web–flange junction failed, local buckling of the top flange and of the web was observed, with extensive rotation of the upper flange in the areas where the junction had failed. The failure mode of specimen P400–3 is illustrated in Figures 4.71 and 4.72.

Table 4.19 summarizes the main results of the failure tests on the different I400 profile specimens.

The comparison between the transverse crushing stresses ( $\sigma_T^{crush}$ ) of specimens P400–1 and P400–2 (–4% for the latter) shows that the failure of specimen P400–2 may have been deeply influenced by the crushing of the web underneath the load section. It should be noted that given the lack of transverse force in-between loaded sections for the 4–point bending load configuration, the effective area ( $A_{eff}$ ) under the loading sections may also be given by Eq. 4.19. Furthermore, in the present case, given that the steel spreading plates used in the



Figure 4.71.: Full-scale flexural tests: failure mode of specimen P400-3, global view.



Figure 4.72.: Full-scale flexural tests: failure mode of specimen P400-3, damage on the web-flange junction.

support and load sections had similar lengths, the transverse crushing stress ( $\sigma_T^{crush}$ ) is the same for both sections.

#### 4.2.3.3. Analytical simulation

Analytical models were used to simulate the full-scale flexural tests on GFRP profiles in order to assess the accuracy of these design tools, namely regarding the serviceability behaviour, *i.e.* the ability to predict the deflections, the failure modes and loads observed in the tests.

Given the orthotropic behaviour of FRP materials (as attested by the results presented in Section 4.2.2.6), the flexural behaviour of these materials should not be predicted using standard Euler-Bernoulli beam theory, since it does not account for shear deflections [4]. In this context, in order to predict the **deflections in bending of FRP materials**, the Timoshenko beam theory, which accounts for shear deformations, should be used, according to Eqs. (4.20) and (4.21) [86],

$$\frac{d\phi}{dx} = \frac{M_y}{EI} \quad (4.20)$$

$$\frac{dz}{dx} - \phi = \frac{V_z}{kAG} \quad (4.21)$$

Table 4.19.: Full-scale flexural failure tests: summary of main results for the I400 specimens.

Specimen	$F_u$ (kN)	$M$ (kNm)	$V$ (kN)	$d_{ms}$ (mm)	$\sigma_{c,L}$ (MPa)	$\sigma_T^{crush}$ (MPa)	Failure mode
P400-1	187.7	131.4	93.8	33.2	90.3	37.3	Web-crippling at support section
P400-2	134.6	94.2	67.3	23.0	66.7	23.3	Global buckling
P400-3	207.9	103.9	103.9	26.0	72.7	35.8	In-plane shear (web)

where  $x$  is the longitudinal development of the beam,  $y$  is the direction perpendicular to the loading plane,  $z$  is the direction of loading,  $\phi$  is the slope of the deflection,  $M_y$  is the bending moment about  $y$ ,  $EI$  represents the flexural stiffness around  $y$ ,  $V_z$  is the shear force in the  $z$  direction and  $kAG$  represents the shear stiffness in the  $z$ — $x$  plane.

Applying the boundary conditions of a particular case to Eqs. (4.20) and (4.21) it is possible to determine the deflections along the beam span. Namely, considering a simply supported beam loaded in a 3-point or 4-point bending configuration, the deflections along the span may be determined with Eqs. (4.22) and (4.23), respectively,

$$\begin{aligned}\delta(x) &= \frac{F}{4 \times EI} \times \left[ \frac{L^2 x}{4} - \frac{x^3}{3} \right] + \frac{F}{2 \times kAG} \times x, & 0 \leq x < \frac{L}{2} \\ \delta(x) &= \frac{F}{4 \times EI} \times \left( \frac{x^3}{3} - Lx^2 + \frac{3L^2 x}{4} - \frac{L^3}{12} \right) + \frac{F \times (L - x)}{2 \times kAG}, & L/2 \leq x \leq L\end{aligned}\quad (4.22)$$

$$\begin{aligned}\delta(x) &= \frac{F}{4EI} \left[ a(L - a)x - \frac{x^3}{3} \right] + \frac{F}{kAG}x, & 0 \leq x < a \\ \delta(x) &= \frac{F}{4EI} \left( Lx - x^2 - \frac{a^3}{3} \right) + \frac{Fa}{2 \times kAG}, & a \leq x < b \\ \delta(x) &= \frac{F}{4EI} \left[ x \left( \frac{x^2}{3} + L(a - x) + (a + b)^2 \right) \right] + \\ &\quad \frac{F}{4EI} \left[ L \left( \frac{2L^2}{3} - La - (a + b)^2 \right) \right] + \frac{F(L - x)}{2 \times kAG}, & a + b \leq x \leq L\end{aligned}\quad (4.23)$$

where  $F$  is the total applied load,  $a$  and  $b$  are geometrical parameters (*cf.* Figure 4.44),  $EI$  represents the flexural stiffness and  $kAG$  is the shear stiffness. Note that Eq. (4.22) is a particular solution of Eq. (4.23) when  $a = L/2$  and  $b = 0$ .

In order to apply the above mentioned equations in the simulation of the experimental tests, the shear area ( $kA$ ) may be taken as the area of the web ( $A_w$ ), a common assumption for I-shaped profiles [4]. In this context, Table 4.20 presents the mechanical properties of the I200 and I400 cross-sections, including the neutral axis position with respect to the utmost upper fibre of the sections ( $NA$ ), when considering the elasticity and shear moduli obtained by (i) coupon testing and (ii) the full-scale flexural serviceability tests.

*Table 4.20.:* Cross-section properties of the profiles with the mechanical properties derived from coupon and full-scale testing.

Profile	Properties	$NA$ (mm)	$EI$ (kNm <sup>2</sup> )	$kAG$ (kN)
I200	Coupon	99.86	788.4	6992.0
	Full-scale	100.00	873.2	5457.6
I400	Coupon	229.97	5772.0	20154.8
	Full-scale	200.00	14532.1	12164.2

In order to compare the analytical predictions regarding the deformability of the profiles with the experimental results, the stiffness ( $K$ ) of the beams in terms of midspan deflections when subjected to a 3-point load configuration (Eq. (4.22)) was determined considering the

section properties presented in Table 4.20. Figures 4.73 and 4.74 plot these analytical curves and compare them to the experimental results for the I200 and I400 profiles, respectively, while Table 4.21 summarizes those same results.

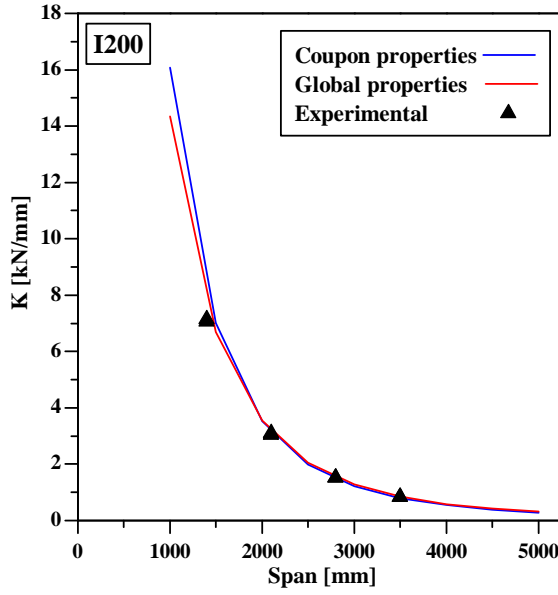


Figure 4.73.: Midspan deflection stiffness *vs.* span: analytical and numerical results for the I200 profile.

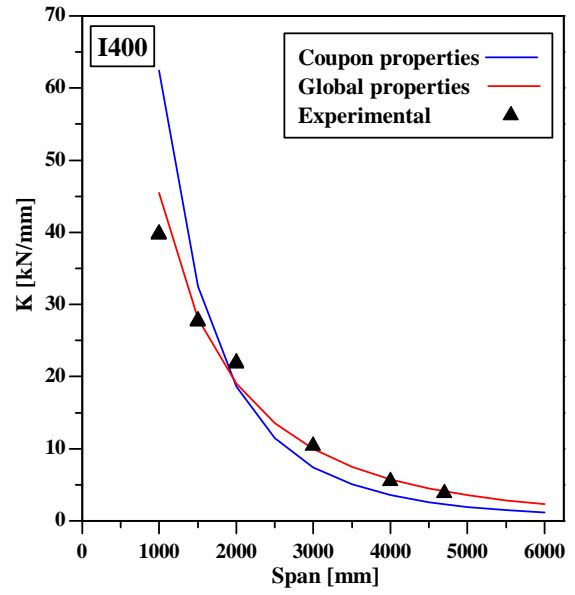


Figure 4.74.: Midspan deflection stiffness *vs.* span: analytical and numerical results for the I400 profile.

The experimental results compare very well with the analytical curves considering the full-section properties for both profiles, especially for the I200 profile (differences up to 1.1% and 14% for the I200 and the I400 profiles, respectively), which was expected since these properties were derived from the same experimental results based on the Timoshenko beam theory, namely Eq. (4.22). Regarding the analytical curves based on coupon properties, for the I200 profile the comparison with the experimental results is very good, with a maximum difference of 16%; in fact, this curve diverges from that obtained with the global properties only for short length spans (less than 1.50 m). For the I400 profiles the difference between the curves is much higher, up to 57%. Nevertheless, the comparison of the experimental results with coupon properties based predictions shows that the analytical model is still able to reproduce the overall behaviour of the stiffness decay *vs.* span curve. The fact that the analytical model is able to predict the experimental behaviour with coupon properties which are independent of the structural configuration and may be considered as intrinsic characteristics of the FRP material is of the utmost importance as it allows structural designers to predict the structural behaviour of FRP structures based on the material properties (*i.e.* independently of the structural system), and these can be more easily provided by manufacturers.

Regarding the **failure simulation** with the analytical models, as mentioned earlier, **specimen I200** failed in the web-flange junction, following the local buckling of the top flange. The critical local buckling stress of the top flange may be estimated, conservatively,

Table 4.21.: GFRP profiles serviceability behaviour: stiffness ( $K$ ) derived from experimental and analytical results.

Profile	$L$ (mm)	$Test$ kN/mm	Analytical model			
			Coupon properties		Global properties	
			kN/mm	diff.	kN/mm	diff.
I200	1400	7.06	8.16	15.5%	7.10	0.6%
	2100	3.03	3.13	3.4%	3.06	1.1%
	2800	1.51	1.47	-2.9%	1.52	0.3%
	3500	0.83	0.79	-4.6%	0.83	-0.1%
I400	1000	39.78	62.45	57.0%	45.48	14.3%
	1500	27.65	32.48	17.5%	28.04	1.4%
	2000	21.89	18.63	-14.9%	19.02	-13.1%
	3000	10.37	7.43	-28.4%	9.96	-3.9%
	4000	5.48	3.56	-35.0%	5.75	4.8%
	4700	3.81	2.31	-39.4%	4.07	6.8%

considering a wall simply supported on one edge and free in the other, under uniform compressive stress, as expressed in Eq. (4.24) [95],

$$\begin{aligned}
 \sigma_{free}^{ss} &= \frac{\pi^2}{t_f(b_f/2)^2} \left[ D_L \left( \frac{b_f/2}{a_{free}^{ss}} \right)^2 + \frac{12}{\pi^2} D_S \right] \\
 &= \frac{\pi^2 E_L}{12(1 - \nu_L \nu_T)} \left( \frac{t_f}{a_{free}^{ss}} \right)^2 + G_{LT} \left( \frac{2t_f}{b} \right)^2
 \end{aligned} \tag{4.24}$$

where,  $t_f$  and  $b_f$  are, respectively, the thickness and the (entire) width of the flange,  $D_L$  and  $D_S$  are the longitudinal flexural and torsional plate stiffnesses (*cf.* Eqs. (4.25) and (4.26)), respectively, and  $a_{free}^{ss}$  is the length of the buckle half-wave, which, according to Bank [4], may be taken as two to three times the free width of the wall (in this case,  $b_f/2$ ).

$$D_L = \frac{E_L t^3}{12(1 - \nu_L \nu_T)} \tag{4.25}$$

$$D_S = \frac{G_{LT} t^3}{12} \tag{4.26}$$

For long plates, where the ratio  $t/a_{free}^{ss}$  is small, the first term of Eq. (4.24) may be conservatively neglected, which means that the length of the buckle half-wave  $a_{free}^{ss}$  does not need to be estimated [4].

Since, in reality, the local buckling phenomenon involves all the plates of a section, in the experimental tests it is not possible to determine if the buckling was triggered by the instability of the top flange or by the instability of the web. Therefore, it is necessary to estimate the critical stress of the web in order to analytically predict the behaviour of the



profiles, which may be performed considering the web as a wall simply supported in both edges subjected to linearly varying compressive stress [95],

$$\begin{aligned}\sigma_{ss,var.lin.}^{ss} &= \frac{\pi^2}{t_w d_w^2} \left( 13.9 \sqrt{D_L D_T} + 11.1 D_{LT} + 22.2 D_S \right) \\ &= \left( 13.9 \sqrt{\frac{E_T}{E_L}} + 11.1 v_T \right) \frac{\pi^2 E_L}{12(1 - v_L v_T)} \left( \frac{t_w}{d_w} \right)^2 + \frac{22.2 G_{LT}}{12} \left( \frac{t_w}{d_w} \right)^2\end{aligned}\quad (4.27)$$

where,  $t_w$  and  $d_w$ , respectively, are the thickness and the depth of the web (with respect to the centreline of the walls), and  $D_T$  and  $D_{LT}$  are the transverse flexure and longitudinal to transverse flexure stiffnesses:

$$D_L = \frac{E_T t^3}{12(1 - v_L v_T)} \quad (4.28)$$

$$D_{LT} = \frac{v_L E_T t^3}{12(1 - v_L v_T)} = \frac{v_T E_L t^3}{12(1 - v_L v_T)} \quad (4.29)$$

For this buckling mode, the buckle half-wave length ( $a_{ss,var.lin.}^{ss}$ ) may be determined with Eq. (4.30):

$$a_{ss,var.lin.}^{ss} = \frac{\sqrt{2}}{2} d_w \sqrt[4]{\frac{E_L}{E_T}} \quad (4.30)$$

As mentioned earlier, the local buckling phenomenon involves all the walls of the section, whereas the above presented formulae respect to individual/isolated plates only. The fact that the plates are not isolated but are part of a more complex cross-section implies that they are not simply supported in the other walls, as assumed in Eqs. (4.24) and (4.27), but are in fact rotationally restrained by the remaining plates. The influence of this restraint may be determined with Eq. (4.31) [4],

$$\zeta_{rest.} = \frac{D_T}{k_\theta L_T} \quad (4.31)$$

where  $D_T$  and  $L_T$  are the flexural stiffness and the width of the plate being restrained in the transverse direction, and  $k_\theta$  is the rotational spring of the junction under consideration. Thereafter, for the present case, which regards the flexural behaviour of I-shaped profiles about their major axis, there are two hypotheses: (i) the flange buckles before the web, in which case the web restrains the flange ( $(\sigma_{free}^{ss})_{flange}/E_{c,L}^{Flanges} < (\sigma_{ss,var.lin.}^{ss})_{web}/E_{c,L}^{Web}$ ); or (ii) the web buckles before the flange and is restrained by the latter ( $(\sigma_{free}^{ss})_{flange}/E_{c,L}^{Flanges} > (\sigma_{ss,var.lin.}^{ss})_{web}/E_{c,L}^{Web}$ ). Table 4.22 presents such parameters for the present I200 profile considering the material mechanical properties derived from the coupon testing (*cf.* Section 4.2.2.6).

With respect to these results, it should be mentioned that the determination of the critical stress of the top flange considering the complete Eq. (4.24) was performed assuming a buckle half-wavelength ( $a_{free}^{ss}$ ) of three times the free width of the plate ( $b_f/2$ ). Considering the

Table 4.22.: Critical stresses of the several walls of the I200 cross-section.

Property	Unit	Flange		Web
		Eq. (4.24)	2 <sup>nd</sup> term of Eq. (4.24)	Eq. (4.27)
$\sigma_{cr}$	MPa	178.6	147.2	630.8
$E_{c,L}$	GPa		33.9	27.1
$\sigma_{cr}/E_{c,L}$	10 <sup>3</sup>	5.3	4.3	23.3

ratios  $\sigma_{cr}/E_{c,L}$  presented in Table 4.22 it is clear that the local buckling is triggered by the instability of the top flange and, therefore, the web acts as a restraining plate. In this context, the rotational spring of the junction may be determined from Eq. (4.32),

$$k_{\theta}^{flange} = \frac{2D_T^{web}}{d_w} \left[ 1 - \frac{\sigma_{free}^{ss,flange} E_{c,L}^{Web}}{\sigma_{ss,var.lin.}^{ss,web} E_{c,L}^{Flanges}} \right] \quad (4.32)$$

and the coefficient of restraint is:

$$\zeta_{rest.}^{flange} = \frac{D_T^{flange}}{k_{\theta}^{flange} b_f/2} \quad (4.33)$$

The buckle half-wavelength comes:

$$a^{flange} = 1.675 \frac{b_f}{2} \sqrt[4]{\frac{D_L^{flange}}{D_T^{flange}} (1 + 4.12 \zeta_{rest.}^{flange})} \quad (4.34)$$

Substituting Eq. (4.34) in Eq. (4.24), the critical stress may be expressed as follows:

$$\sigma_{flange}^{local} = \frac{\pi^2}{t_f(b_f/2)^2} \left[ 1.675^{-2} \sqrt{\frac{D_L D_T}{1 + 4.12 \zeta_{rest.}^{flange}}} + \frac{12}{\pi^2} D_S \right] \quad (4.35)$$

Table 4.23 compares the local buckling stresses, considering both the isolated plates and the web-flange interaction, with that derived from the experimental tests.

Table 4.23.: Critical stress of the I200 cross-section: experimental results *vs.* analytical predictions.

Critical stress	MPa	diff. (%)
Experimental	144.2	-
Isolated flange — Eq. (4.24)	178.6	+23.9%
Isolated flange — 2 <sup>nd</sup> term of Eq. (4.24)	147.2	+2.1%
Section (with web-flange interaction) — Eq. (4.35)	196.8	+36.5%

These results show that, unlike what was expected, the simplest and most conservative analytical estimate of the critical stress is the most accurate when comparing with the experimental results. Regarding the difference between using the complete expression given by Eq. (4.24) or only the second term of that expression, as suggested earlier, it should be noticed that this difference is highly dependent on the buckle half-wavelength ( $a_{free}^{ss}$ )

assumed — in this case, three times the free width of the plate ( $b_f/2$ ) — a parameter that, *a priori*, can only be estimated. On the other hand, the higher difference obtained when considering the web-flange interaction (Eq. (4.35)) was not expected since the latter method should be more accurate than the previous simplifications. Nevertheless, for the present case, the poorer agreement of the more sophisticated Eq. (4.35) may be due to the fabrication process of the profiles (pultrusion), which is known to create "weaker" areas at the web-flange junctions [4], mainly due to a lower fibre content than the flange and web plates. This "weaker" area can drastically reduce the stiffness of the rotational spring restraining the flange  $k_\theta^{flange}$ , which could mean that the consideration of such restraint is, in fact, unrealistic. These results suggest that designers should use the more conservative analytical formulae in order to determine the local critical stress of GFRP profiles in flexure and, consequently, their local critical bending moment.

In what concerns the **failure modes of specimens I400**, three different failure mechanisms were involved, although it was not always clear which exact failure mechanism governed the failure of each specimen: (i) web crushing / buckling under concentrated loads; (ii) in-plane shear failure of the web; and (iii) global lateral torsion-flexure buckling.

In order to determine the ultimate load due to web crushing/buckling (web-crippling) under concentrated loads, the governing ultimate stress was determined, *i.e.* the minimum value between the material compressive strength in the transverse direction ( $\sigma_{c,T}^{Web}$ , *cf.* Section 4.2.2.6) and the critical transverse stress ( $\sigma_{cr,T}^{Web}$ ). The latter was determined considering that the web is a plate, simply supported on its unloaded edges, under constant compressive stresses [4] as expressed by Eq. (4.36),

$$\sigma_{cr,T}^{Web} = \frac{2\pi^2}{t_w b_{eff}^2} \left( \sqrt{D_L D_T} + D_{LT} + 2D_S \right) \quad (4.36)$$

where  $b_{eff}$  is the effective width in which the stress is distributed and, according to Bank [4], it may be considered as (i)  $d_w$  for interior supports/load application points, or (ii)  $L_{eff} + d_w/2$  for extremity supports, such as those of simply supported beams. Thereafter, the ultimate concentrated transverse force  $V_{u,T}$  may be determined with Eq. (4.37),

$$V_{u,T} = A_{eff} \cdot \min \left( \sigma_{c,T}^{Web}; \sigma_{cr,T}^{Web} \right) \quad (4.37)$$

where  $A_{eff}$  is the effective area, which may be determined by Eq. (4.38):

$$A_{eff} = t_w b_{eff} \quad (4.38)$$

Similarly, the second failure mode, in-plane shear failure of the web, may be governed by the local buckling of the walls ( $\tau_{cr}^{local}$ ) or by the material strength ( $\tau_{LT}^{Web}$ , *cf.* Section 4.2.2.6), depending on which of those stresses is higher. The critical shear stress of the web ( $\tau_{cr}^{local}$ ) may be calculated with Eq. (4.39), considering that all borders are simply supported,

$$\tau_{cr}^{local} = \frac{4k_{LT} \sqrt[4]{D_L D_T^3}}{t_w d_w^2} = k_{LT} \frac{\sqrt[4]{E_L E_T^3}}{3(1 - \nu_L \nu_T)} \left( \frac{t}{b} \right)^2 \quad (4.39)$$

where  $k_{LT}$  is the shear buckling coefficient that may be taken as [95],

$$k_{LT} = 8.125 + 5.045K \quad (4.40)$$

which is valid for  $K \leq 1$  and  $K$  is given by:

$$K = \frac{2D_S + D_{LT}}{\sqrt{D_L D_T}} \quad (4.41)$$

Thereafter, the ultimate shear load due to in-plane shear may be calculated with Eq. (4.42):

$$V_u^{in-plane} = \frac{I \cdot t}{W} \min(\tau_{LT}^{Web}, \tau_{cr}^{local}) \quad (4.42)$$

With the expressions above, for each local failure mode, it is possible to compare the material strengths to the (buckling) critical stresses, determining the governing ultimate stresses, as summarized in Table 4.24.

Table 4.24.: Material strength and critical stress for each local failure mode.

Profile	Failure mode	Stress (MPa)		Governing mechanism
		Material	Buckling	
I200	Bending ( $\sigma_{c,L}$ )	388.6±59.2	147.2	Buckling
	In-plane shear ( $\tau_{LT}$ )	27.5±3.4	93.2	Material
	Concentrated loads ( $\sigma_{c,T}$ )	88.9±16.1	99.1	Material
I400	Bending ( $\sigma_{c,L}$ )	197.7±64.4	78.5	Buckling
	In-plane shear ( $\tau_{LT}$ )	20.4±1.2	41.4	Material
	Concentrated loads ( $\sigma_{c,T}$ )	70.4±5.6	40.0	Buckling

Regarding the local failure modes, Table 4.24 shows that buckling phenomena govern the bending failure over the material strength for both profiles and the local failure under concentrated loads for the I400 profile, which has a slender web (namely when compared to that of the I200 profile).

Finally, regarding the determination of the critical lateral-torsional bending moment of the profiles ( $M_{cr}^{global}$ ), it is generally accepted that the same equation used for isotropic materials may be used given that the orthotropic moduli are provided [4]. In this context, the well-known formulae presented in Eurocode 3 [96] may be adapted in order to be used with orthotropic materials, namely, the following expression for doubly symmetric cross-sections (as is the case of I-shaped profiles),

$$M_{cr}^{global} = C_1 \frac{\pi^2 E_L I_z}{(kL)^2} \left[ \sqrt{\left(\frac{k}{k_w}\right)^2 \frac{I_w}{I_z} + \frac{(kL)^2 G_{LT} I_t}{\pi^2 E_L I_z} + (C_2 z_g)^2} - C_2 z_g \right] \quad (4.43)$$

where  $L$  is the free length between lateral restraints,  $I_z$  is the second moment of area about the minor axis of the cross-section,  $k$  and  $k_w$  are factors accounting for boundary conditions, namely the end rotation on plan and the end warping fixity, respectively,  $C_1$  and  $C_2$  are

factors which account for the influence of the bending moment diagram over the length  $L$  and for  $k$  and  $k_w$ ,  $I_t$  is the torsional constant,  $I_w$  is the warping constant of the cross-section, and  $z_g$  is the distance between the shear centre and the load application point.

When applying Eq. (4.43) to the profiles under study, and in order to simplify the analysis, the following simplifications were assumed: (i) a constant elasticity modulus in the longitudinal direction  $E_L$  was considered (that of the flanges in compression  $E_{c,L}^{Flanges}$ , cf. Section 4.2.2.6), and (ii) the shear modulus of the flanges  $G_{LT}$  was considered to be the same as that of the webs ( $G_{LT}^{Web}$ , cf. Section 4.2.2.6).

Table 4.25 presents, for all specimens, the ultimate load ( $F_u$ ) considering each of the previous mentioned failure modes, comparing them to the experimental results, along with the corresponding maximum shear force and bending moment ( $V$  and  $M$ ). The results presented in Table 4.25 correspond to each of the individual failure modes, *i.e.* no interaction is considered (failure interaction will be discussed later in this Section). Furthermore, it should be noticed that in the preparation of this table the following assumptions were considered: (i) the failure due to local buckling in bending was calculated based on the most conservative critical stress, which compared better with the experimental results of specimen I200 (cf. Table 4.23); (ii) since in the test of specimen P400-2 it was observed that the lateral bracings were not able to support the beam laterally, the failure due to global lateral-torsional buckling of this specimen was calculated considering that the two central bracings did not exist.

Regarding specimen I200, the results show that the analytical models were able to determine the failure mode correctly (local buckling in bending, as observed experimentally) and with excellent accuracy in what concerns the ultimate load (-6.1% when compared to the experimental result).

For specimen P400-1, however, the analytical models were not able to successfully predict the failure mode observed experimentally. In fact, these models suggest that the failure mode of the specimen should comprise local buckling in bending, while failure due to concentrated loads at the supports was observed in the tests; furthermore, the predicted failure load was -23.0% lower than that achieved in the test. This is an unexpected result, since the analytical formulae predicted the failure behaviour of the I200 specimen with high accuracy. It is worth mentioning two factors regarding the calculation of the failure load for local buckling in bending: (i) as mentioned earlier, the critical stress is being conservatively calculated, considering the flange as being an isolated plate and disregarding the first term of Eq. (4.24); and (ii) the coupon testing elasticity modulus in compression ( $E_{c,L}$ ) is being used in these calculations and for the I400 profile, unlike what happened for the I200 profile, these moduli were much lower than their tensile counterparts (difference of -5.6% for the I200 profile and -65.7% for the I400 profile, concerning the flanges, cf. Table 4.13). In this context, it is reasonable to assume that (i) for the I400 profile, in opposition to the I200 profile, Eq. (4.35) is more accurate than Eq. (4.24) and (ii) the elasticity modulus in compression was underestimated and is closer to its tensile counterpart. Thereafter, using Eq. (4.35) with the tensile elasticity modulus ( $E_{t,L}$ ), a local buckling critical stress of 129.2 MPa is obtained, corresponding to a failure load ( $F_u$ ) of 263.7 kN, a critical local bending moment ( $M_{cr}^{local}$ ) of 184.6 kNm and a shear force ( $V$ ) of 131.8 kN. The latter failure load is 82.5% higher than that predicted with Eq. (4.24) and 40.5% higher than experimental failure load. Thereafter, the in-plane shear failure mode presents the best comparison with the experimental result, in terms of failure load — 20.9% higher than the test. Nevertheless, the experimental failure mode does not correspond to either of the previous modes. In fact, the failure mode due to concentrated loads at the supports, which corresponds to the experimental observation,

Table 4.25.: Failure load and forces for each specimen considering each failure mode.

Specimen	Failure mode		$F_u$		$V$	$M$
			kN	%	kN	kNm
I200	Experimental		55.9	-	28.0	36.4
	Bending	Local	52.5	-6.07%	26.3	34.1
		Global	168.7	+201.6%	84.3	109.6
	In-plane shear		98.9	+76.8%	49.4	64.3
	Conc. Loads	at supports	453.5	+711.0%	226.7	294.8
		at load points	337.9	+504.2%	168.9	219.6
P400-1	Experimental		187.7	-	93.8	131.4
	Bending	Local	144.5	-23.0%	72.2	101.1
		Global	549.2	+192.7%	274.6	384.4
	In-plane shear		226.8	+20.8%	113.4	113.4
	Conc. Loads	at supports	351.4	+87.3%	175.7	246.0
		at load points	462.5	+146.5%	231.3	231.3
P400-2	Experimental		134.6	-	67.3	94.2
	Bending	Local	144.5	+7.32%	72.2	101.1
		Global	50.7	-62.4%	25.3	35.5
	In-plane shear		226.8	+68.5%	113.4	158.7
	Conc. Loads	at supports	351.4	+161.0%	175.7	246.0
		at load points	462.5	+243.6%	231.3	323.8
P400-3	Experimental		207.9	-	103.9	103.9
	Bending	Local	202.3	-2.70%	101.1	101.1
		Global	995.3	+378.8%	497.6	497.6
	In-plane shear		226.8	+9.09%	113.4	113.4
	Conc. Loads	at supports	351.4	+69.0%	175.7	175.7
		at load points	462.5	+122.5%	231.3	231.3

was predicted for a failure load almost two times higher than the experimental failure load (+87.3%). This particular result suggests that the experimental failure mode may have been influenced by local buckling of the web in the transverse direction, an important phenomenon in GFRP profiles (*e.g.* [7, 14]).

Regarding specimen P400-2, the global lateral-torsional buckling failure load disregarding the interior bracings is predicted for a load level -62.4% lower than the experimental failure load. This result indicates that the interior bracings, although unable to fully support the profile laterally, were able to provide some lateral stiffness to the profile, momentarily avoiding the triggering of global buckling.

Finally, for specimen P400-3, similarly to what happened with specimen P400-1, the analytical formulae predicts bending failure due to local buckling for a load 2.7% lower than the experimental one. However, if the critical local buckling stress is recalculated following the same assumptions made for specimen P400-1, the failure load for this failure mode increases 155.5% to almost twice that of the experimental test (+96.7%). Thereafter, the governing failure mode becomes the in-plane shear failure of the web, with a failure load +9.1% higher than its experimental counterpart, which is consistent with the failure

mode observed experimentally. In this regard, the position of the failure initiation may be estimated considering the shear — bending interaction, using Eq. (4.44):

$$\left( \frac{\tau(x, z)}{\tau_{u,LT}(z)} \right)^2 + \left( \frac{\sigma(x, z)}{\sigma_{u,L}(z)} \right)^2 \leq 1 \quad (4.44)$$

Figure 4.75 shows the shear force and bending moment diagrams as a function of the applied load and of the geometrical parameters (*cf.* Figure 4.44), while Figure 4.76 shows the shear and axial stress distributions along the depth of the web as a function of the shear force and bending moment, respectively. The stress distributions were determined for the I400 profile following the assumptions made in the previous calculations, namely the consideration of the tensile elasticity moduli (*i.e.* disregarding the compressive elasticity moduli).

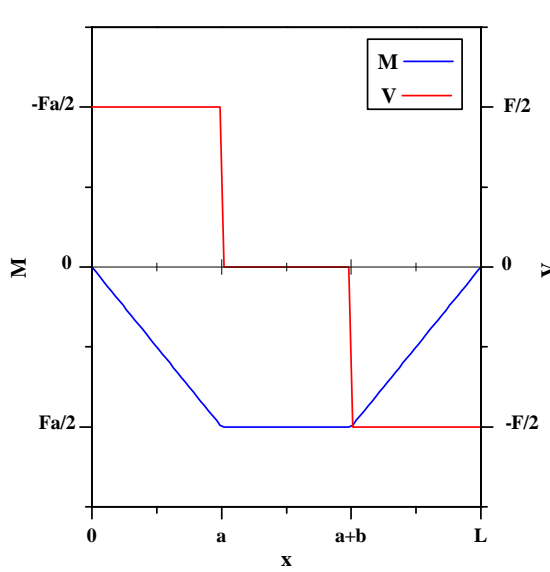


Figure 4.75.: Bending moment and shear force diagrams along the length of the beam.

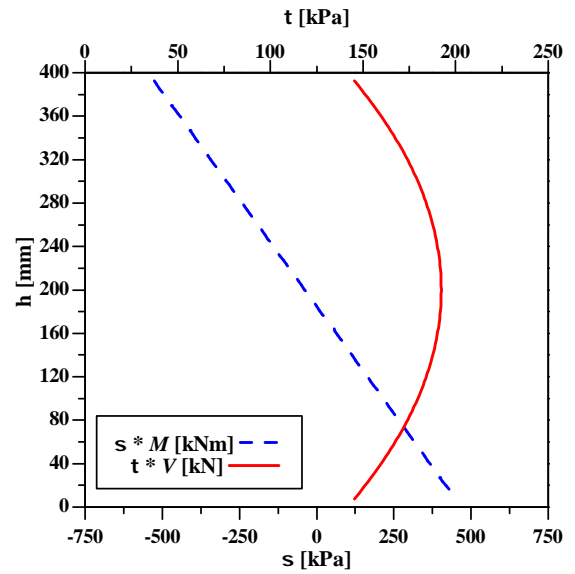


Figure 4.76.: Axial and shear stress distributions along the depth of the web of the I400 profile.

Considering the force and stress distributions presented in Figures 4.75 and 4.76, respectively, and introducing such stresses in Eq. (4.44) an ultimate load of 212.5 kN is predicted for the P400-3 specimen. This failure load prediction compares very well with the experimental failure load (+2.2%). Furthermore, failure is predicted in the sections under the applied loads, which is consistent with the experimental observations. Regarding the failure initiation point within the cross-section, Eq. (4.44) predicts that failure is initiated slightly over the geometrical centre of the profile (which, given the assumptions made, is also the stiffness and shear centres), where the shear stresses are maximum (*cf.* Figure 4.75), with a 99.9% contribution of the shear stress and only 0.1% contribution of the axial stress. This result is not consistent with the experimental observations given that failure was observed near the web-top flange junction. This difference may be due to the already mentioned material properties variation over the section, namely the lower strength in the web-flange junction regions due to a lower fibre content.

#### 4.2.3.4. Numerical simulation

All full-scale flexural tests in beams were simulated using tri-dimensional finite element (FE) models developed with the commercial package *ABAQUS*. The models comprised two different shell quadrilateral elements: (i) 4-node general purpose shell elements with reduced integration (*S4R*), simulating the geometry of the profiles; and (ii) 4-node tri-dimensional bilinear rigid shell elements, simulating the connection between the profiles and the support/load contact areas [97]. Both profile sections were simulated with the same number of nodes (27) and with the same element length (10 mm).

The profiles were simulated considering different material properties for the web and flanges, according to the coupon tests results (*cf.* Section 4.2.2.6). In this regard, and accounting for the poorer accuracy of the analytical models when using the compressive elasticity moduli<sup>1</sup> (*cf.* Section 4.2.3.3), the tension elasticity moduli were used.

In order to simulate the vertical supports and the load application points, the contact areas were modelled with rigid shell elements connecting to a reference point, whose alignment was centred with the respective centre of the support/load area and 25 mm apart of the utmost extreme fibres of the cross-sections in the vertical direction. These elements were constrained to a rigid body and the boundary conditions/load application was performed in the reference alignment only. Regarding the lateral bracings, in order to avoid the restriction of vertical displacements due to non-linear geometrical effects, they were simulated by restricting the web-flange junction points instead of the extreme points of the flanges.

Additionally, the torsional rotations of the upper flanges in the load application areas were also restrained since this effect was visible in the experimental tests owing to the use of cylinders between the loading beam and the profiles (*cf.* Section 4.2.3.2).

Figures 4.77 and 4.78 show the overall aspect of the FE models for the I200 and the P400-1 (as an example of the I400 specimens) profiles, respectively, including the boundary restrictions and applied loads.

Two sets of analyses were performed with these models: (i) buckling analyses, performed in order to estimate the buckling modes and critical loads for each configuration; and (ii) failure initiation analyses performed in order to determine the ultimate load of each specimen. Regarding the former type of analysis, a small geometrical imperfection was considered, with maximum amplitude of 0.02 mm and the shape of the first positive buckling mode (*i.e.*, the first buckling mode that occurs for a critical load applied in the same direction as that of the experimental load), which should avoid numerical problems near the bifurcation point and should not influence the postbuckled shape [98]. For the latter type of analysis, the failure criterion chosen was the Tsai-Hill failure criterion developed for FRP composite materials. This criterion, although being usually conservative (*e.g.* [99]), has proven to provide reasonable agreement with experimental data when using GFRP coupon strength data [100]. For plane stress states, the Tsai-Hill failure criterion may be expressed by Eq. (4.45),

$$\frac{\sigma_1^2}{X^2} - \frac{\sigma_1\sigma_2}{X^2} + \frac{\sigma_2^2}{Y^2} + \frac{\tau_{12}^2}{S^2} \leq 1 \quad (4.45)$$

---

<sup>1</sup>It should be noted that the coupon compressive tests may have provided unreliable data regarding the compressive strains, since the procedure does not account for the effects of (potential) local crushing of the extremities of the specimens, thereby providing less reliable elasticity moduli than the tensile tests.



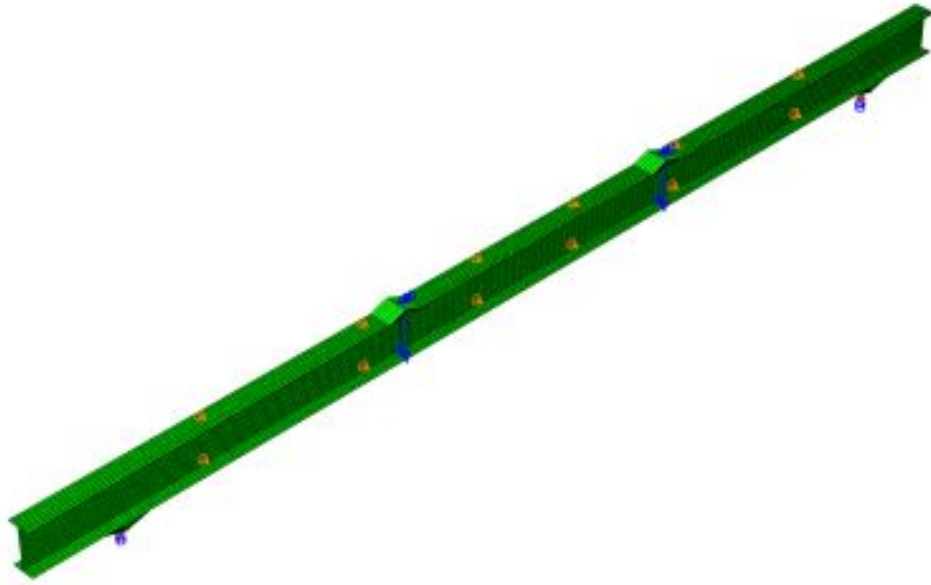


Figure 4.77.: Overall perspective of the I200 specimen FE model.

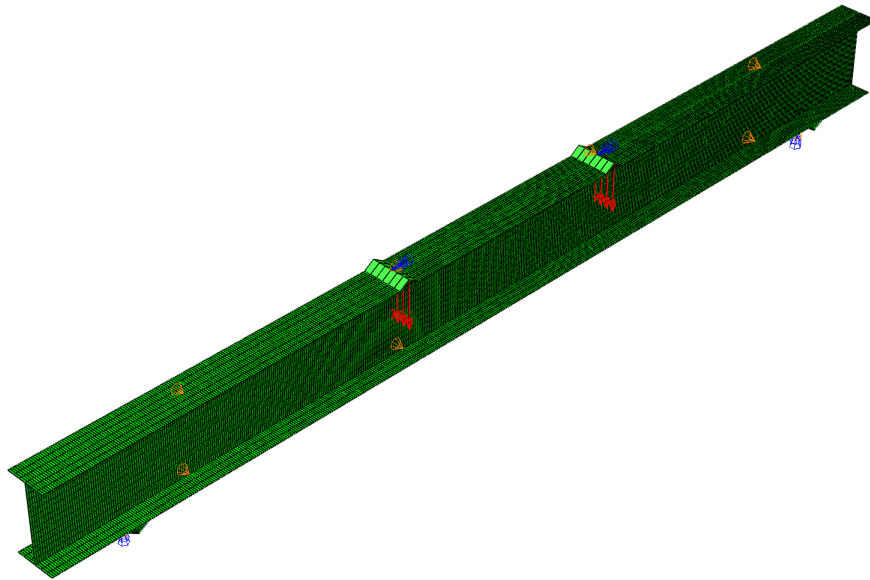


Figure 4.78.: Overall perspective of the I400 specimens FE models (P400-1 specimen).

where  $\sigma_1$  and  $\sigma_2$  are the axial stresses in the principal directions 1 and 2, respectively,  $\tau_{12}$  is the shear stress in the plane defined by those same directions,  $X$  and  $Y$  are the strengths in the principal directions, 1 and 2, respectively, while  $S$  is the shear strength in such plane (obtained from coupon testing). Applying Eq. (4.45) to the present case study, the principal directions 1 and 2 may be taken as the longitudinal and transverse directions, replacing  $\sigma_1$ ,  $\sigma_2$  and  $\tau_{12}$  by  $\sigma_L$ ,  $\sigma_T$  and  $\tau_{LT}$ , respectively, and  $X$ ,  $Y$  and  $S$  by  $f_{tu,L}$ ,  $f_{cu,T}$  and  $\tau_{u,LT}$ , respectively. It should be mentioned that for the longitudinal direction (the main direction) the material tensile properties were used given the higher accuracy of the coupon test methods, while for the transverse direction the compressive properties were used since, due to geometrical limitations, coupon tensile tests in the transverse direction were only performed on the web of the I400 profile.

Regarding the **I200 profile model**, the buckling analysis indicated that the first buckling mode corresponded to the local instability of the top flange between the load application points, as shown in Figure 4.79. The critical load ( $F_{cr}$ ) predicted by the FE model is 113.2 kN which corresponds to a critical bending moment ( $M_{cr}$ ) and compressive critical stress ( $\sigma_{cr}$ ) of respectively 73.6 kNm and 317.1 MPa. This critical load is considerably higher than that observed experimentally (+120.0%) and those predicted by the analytical formulae (+61.2% to +115.4%).

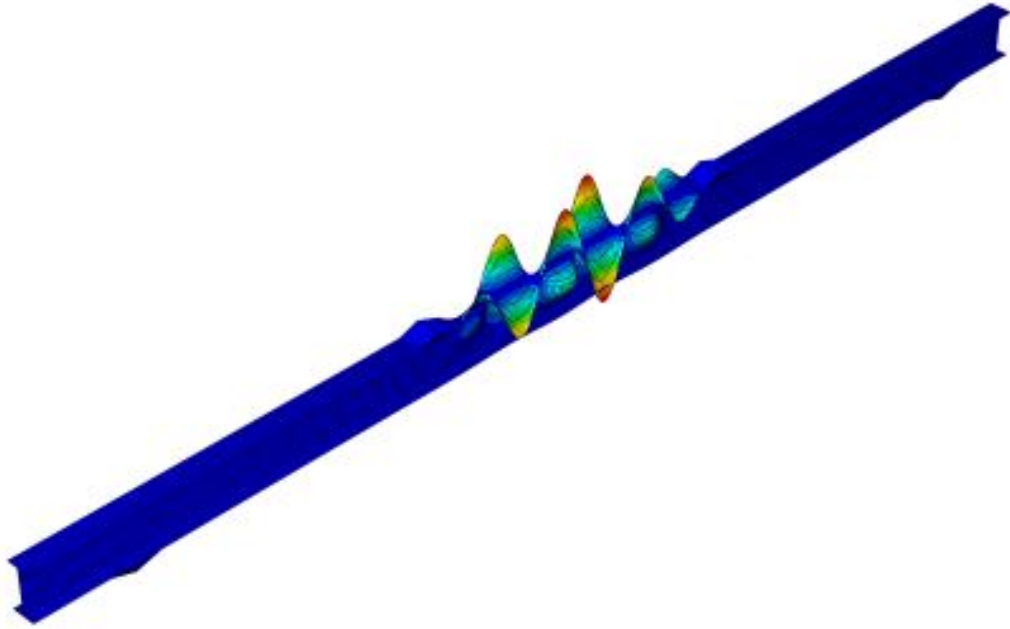


Figure 4.79.: FE analysis: first buckling mode configuration for the I200 specimen.

The failure initiation analysis, by its turn, indicates that the initial failure starts for a load ( $F_u$ ) of 34.0 kN under the load application points, at the web-flange junction. The distribution of the Tsai-Hill failure index at failure may be depicted from Figure 4.80.

According to the FE model, the failure initiation occurs in the web-flange junction of the compressed flange at the centre of each buckle half-wave, due to local concentration of transverse and shear stresses. This fact, together with the prediction of a lower failure initiation load, when compared to that observed experimentally (-44.6%) and a predicted critical load higher than that observed in the experimental tests, as stated earlier, indicates that the instability phenomenon observed in the experimental tests might have happened after an initial local failure of the web-flange junction (undetected in the tests) allowing the upper flange to buckle unrestrained (hence, the better approximation of the analytical formulae that do not account for support restriction in determining the critical stress, *cf.* Table 4.23).

The FE model developed for simulating the test of **specimen P400-1** predicts the first positive buckling mode (*i.e.*, with the critical load applied in the same direction as the experimental load) as a local instability phenomenon, with buckling of the flanges (triggering) and web between the load application points, presenting two buckle halfwaves as may be depicted from Figure 4.81. The critical load ( $F_{cr}$ ) for this buckling mode is predicted as 360.0 kN, corresponding to a critical bending moment ( $M_{cr}$ ) of 252.0 kNm and a compressive critical stress ( $\sigma_{cr}$ ) of 176.4 MPa. The critical load predicted by the FE model

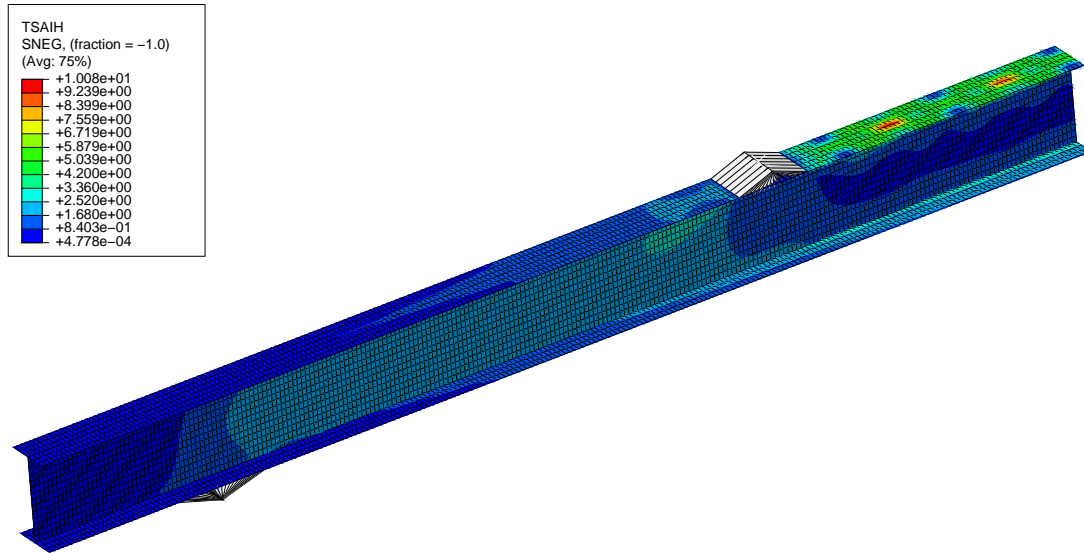


Figure 4.80.: FE analysis: Tsai-Hill failure index distribution of the I200 specimen for  $F = 34.9$  kN (half-model).

is, once again, higher than its analytical counterparts (*cf.* Section 4.2.3.3), namely +36.6% than the higher analytical estimate.

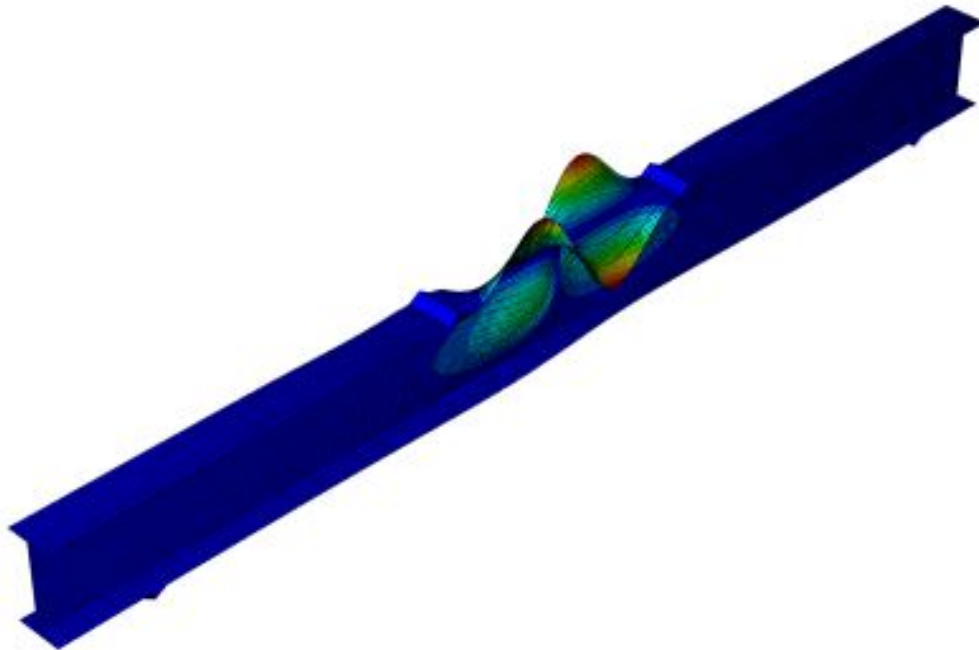


Figure 4.81.: FE analysis: first buckling mode configuration for the P400-1 specimen.

Regarding the failure initiation, the model predicts a failure initiation load ( $F_u$ ) of 97.8 kN (-47.9% than the experimental failure load) with failure occurring in the web-flange junction underneath the load application points, as shown in Figure 4.82, unlike the experimental tests where failure occurred in the web at a support section. It should be noted that the loading areas and the support areas present similar transverse compressive stresses, but the shear stresses are much higher in the loading areas, which could be due to local effects.

In this context, disregarding the failure under the support sections (*i.e.*, considering that failure initiation began in that region but did not propagate, having a reduced influence in the overall behaviour of the structure), the next failure load ( $F_u$ ) is 143.6 kN (-23.5% than the ultimate load observed experimentally), corresponding to failure in the web-flange junction at the support sections, being governed by transverse compressive and shear stresses, similarly to what was observed in the experimental tests.

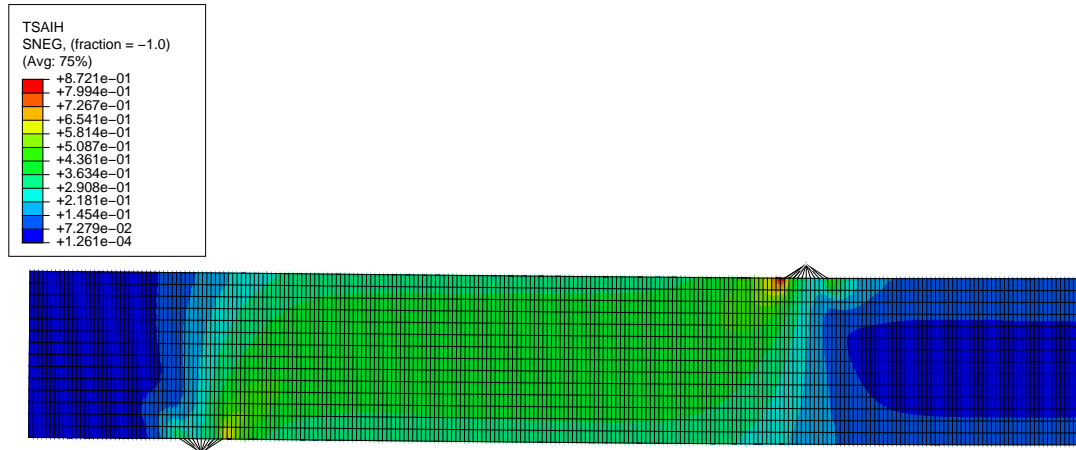


Figure 4.82.: FE analysis: Tsai-Hill failure index distribution of the P400-1 specimen for  $F = 91.1$  kN (half-model).

In what concerns **specimen P400-2**, the results obtained from the FE model are identical to those regarding specimen P400-1 when considering all the lateral bracings (the small differences stem from the fact that the support and load plates are larger for specimen P400-2). Nevertheless, in the experimental test it was clear that the central bracings were not able to support laterally this particular specimen. With this regard, an additional FE model was developed in which the central lateral bracings were removed. Figure 4.83 presents the shape of the first buckling mode obtained with the latter model, which corresponds to the global buckling of the profile and occurs for a critical load ( $F_{cr}$ ) of 187.9 kN.

Concerning the failure analyses, however, and even without the central lateral bracings, failure initiation occurs in the same fashion as for specimen P400-2 with a very similar failure initiation load ( $F_u$ ) of 102.5 kN (+4.8%, possibly owing to the larger load application area). Figure 4.84 presents the distribution of the Tsai-Hill failure index at failure for this specimen. The failure load predicted by the FE model is -23.9% lower than that observed experimentally, which occurred following global buckling phenomena. Once again, these results seem to indicate that an initial failure of the web-flange junction may have occurred, unnoticed in the experimental tests, triggering the instability phenomenon, which, for the present specimen and due to the lack of effective bracing, was global buckling.

Finally, for **specimen P400-3**, the FE model predicts the shape of the first positive buckling mode as a local instability phenomenon, with buckling of the flanges (triggering) and web between the load application points, presenting two buckle halfwaves, similarly to P400-1, as may be depicted from Figure 4.85. The critical load ( $F_{cr}$ ) for this buckling mode is predicted as 533.5 kN, corresponding to a critical bending moment ( $M_{cr}$ ) of 266.7 kNm

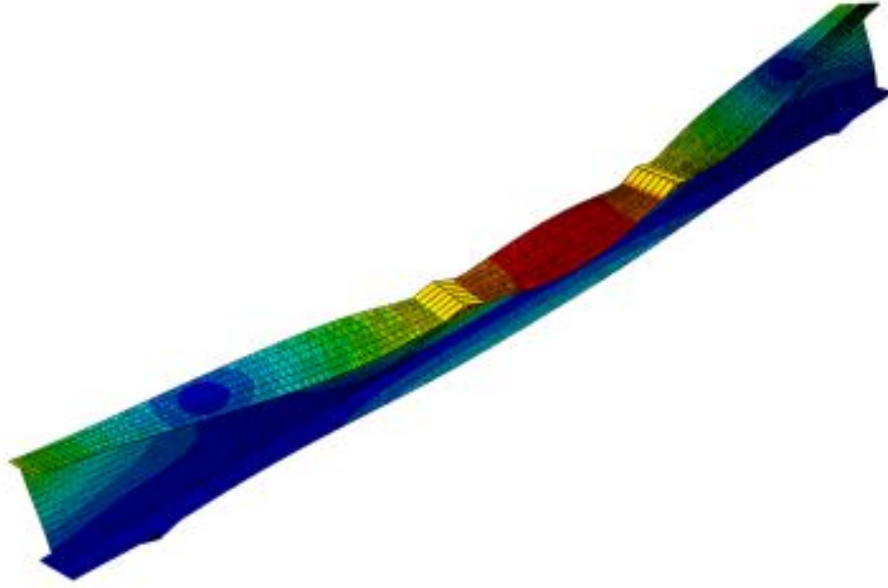


Figure 4.83.: FE analysis: first buckling mode configuration for the P400-2 specimen.

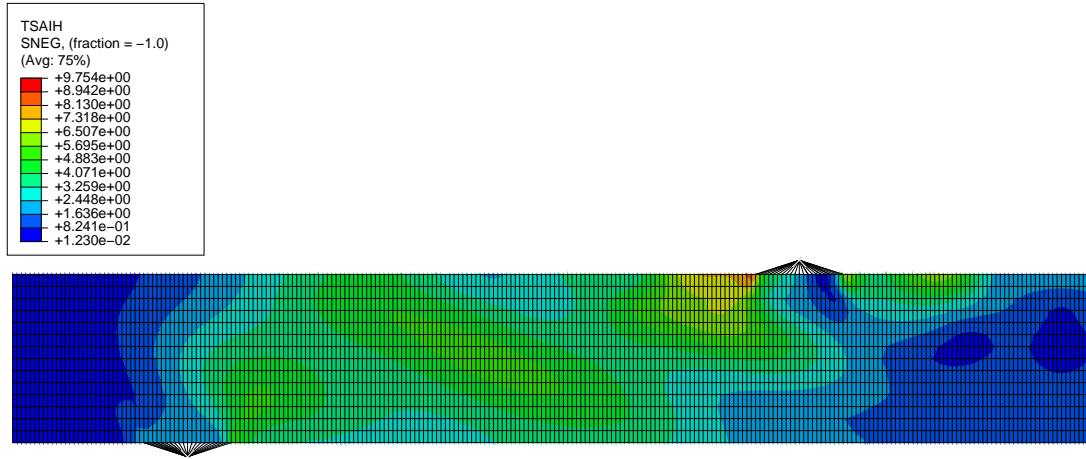


Figure 4.84.: FE analysis: Tsai-Hill failure index distribution of the P400-2 specimen for  $F = 91.1$  kN (half-model).

and a compressive critical stress ( $\sigma_{cr}$ ) of 186.7 MPa. Once more, the numerical critical load is higher than its analytical counterparts (*cf.* Section 4.2.3.3), namely +44.52% than the highest analytical estimate.

For this specimen the FE model predicts failure in the web-flange junction under the load sections, as can be depicted from Figure 4.86. The failure initiation load ( $F_u$ ) predicted by the numerical model is 113.1 kN, which is -45.6% lower than its experimental counterpart. Following the results obtained for the previous specimens, these results reinforce the hypothesis of early and unnoticed failure of the web-flange junction on the experimental tests, which enhanced the proneness of the profiles to instability phenomena and explain

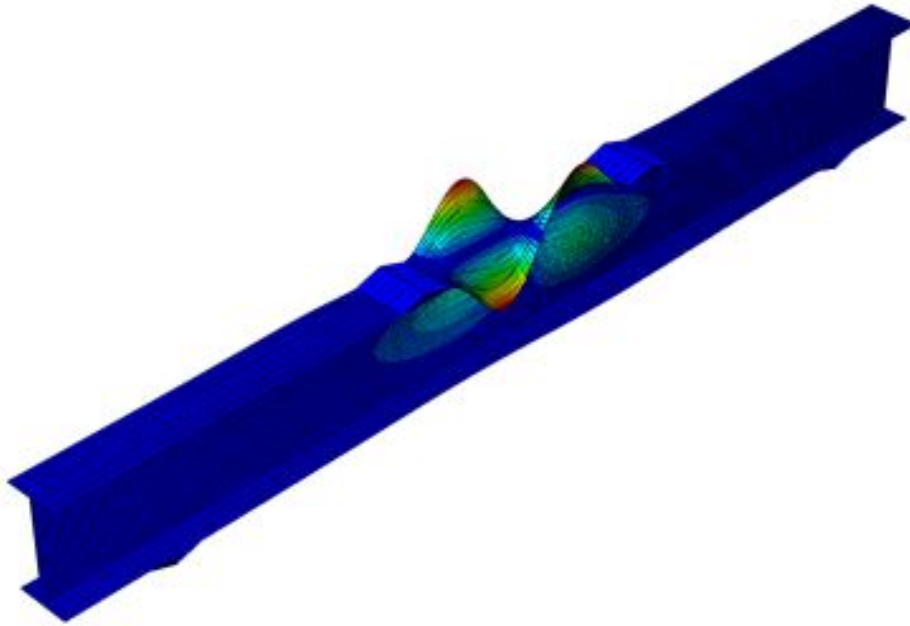


Figure 4.85.: FE analysis: first buckling mode configuration for the P400-3 specimen.

the better accuracy of the simpler analytical formulae regarding the local buckling of the upper flange (*cf.* Section 4.2.3.3). This hypothesis could be duly confirmed with FE models which consider material damage. The development of such models, however, falls out of the scope of the present thesis. Furthermore, the Tsai–Hill criterion, which, as mentioned earlier, provides a measure of the failure initiation (not of damage), has been known to underestimate the experimental failure loads of GFRP profiles, *e.g.* [7,98,99].

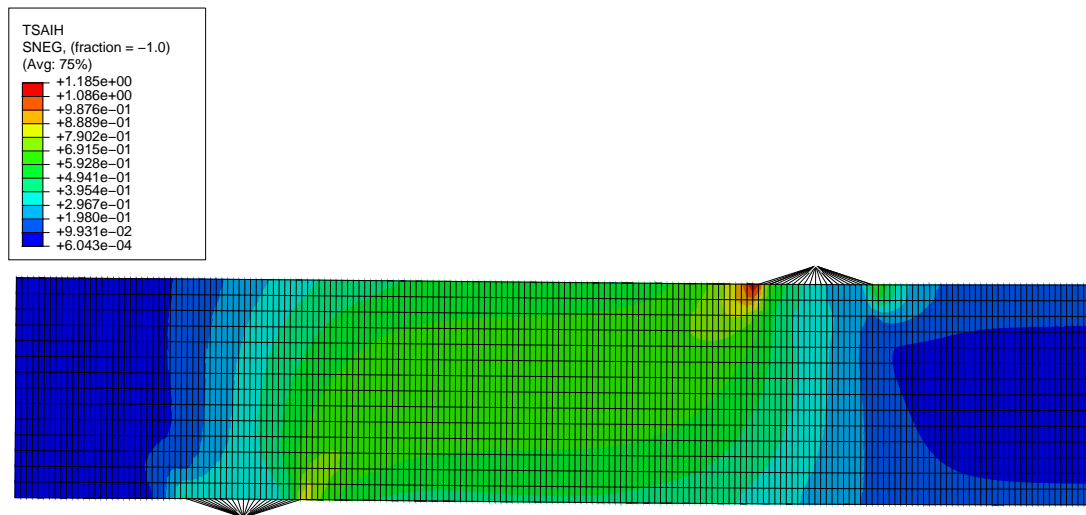


Figure 4.86.: FE analysis: Tsai–Hill failure index distribution of the P400-3 specimen for  $F = 141.7$  kN (half-model).

## 4.3. SFRSCC

### 4.3.1. Experimental programme

The steel fibre reinforced self-compacting concrete (SFRSCC) used in the deck of the footbridge prototypes was developed by *CiviTest, Pesquisa para Novos Materiais para a Engenharia Civil, Lda.*, which also provided the material for the small-scale prototype, while *Tecnipor* provided the SFRSCC for the full-scale prototype. The SFRSCC used in the small- and full-scale prototypes have slightly different compositions, which are given in Table 4.26.

Table 4.26.: Component mix proportions for the SFRSCC used in the small- and full-scale prototypes.

Component	Proportion (kg/m <sup>3</sup> )	
	Small-scale	Full-scale
Cement	380.5	413.0
Limestone filler	326.2	353.0
Water	126.8	140.0
Superplasticizer	6.09	7.83
Fine sand	362.6	237.0
River sand	574.6	710.0
Crushed stone	510.1	590.0
Steel fibres	45.0	60.0
W/C ratio	0.33	0.34

The steel fibres used were hooked-end fibres with 35 mm of length and 0.55 mm of diameter and presented a 1100 MPa characteristic tensile strength.

For the SFRSCC used in the small-scale prototype, two sets of material characterization tests were performed: (i) coupon tests, and (ii) full-scale transverse bending tests. The first set included tests on SFRSCC cubes and cylinders and were performed at 28 days of age and at 905 days of age, which was the same age as the small-scale prototype's SFRSCC deck when it was tested up to failure (*cf.* Chapter 6). The full-scale tests were performed by testing precast slab specimens with dimensions of  $2000 \times 1000 \times 40$  mm<sup>3</sup> in a 4-point bending configuration.

The characterization of the SFRSCC used in the full-scale prototype was performed by *CiviTest* and included coupon (i) compressive tests on cubes, and (ii) flexural tests on small-scale slabs.

### 4.3.2. Material characterization tests

#### 4.3.2.1. Tests on cubes

Compressive tests were performed on 150 mm cubes made of the SFRSCC used in the small-scale prototype in order to determine the compressive strength ( $f_c$ ) of the material. The tests were performed using a press tester from *Tonipact*, model 3000, with a control unit from *Form+Test Seidner*, model *CSRG5500*. The tests were performed according to

the specifications of EN 12390-3 [101]. Figure 4.87 shows the test apparatus with one of the specimens being tested.



Figure 4.87.: Compressive tests on SFRSCC cube specimens.

Based on the ultimate load achieved in these tests ( $F_{cu}$ ), it was possible to determine the compressive strength  $f_c$  of each specimen using Eq. (4.46),

$$f_c = \frac{F_{cu}}{A_{specimen}} \quad (4.46)$$

where  $A_{specimen}$  is the area of the specimen. Regarding the SFRSCC material used in the small-scale prototype, three specimens were tested at 28 days of age and four specimens were tested at 905 days of age. Table 4.27 summarizes the results obtained in these tests, while Table A.11 (page 308) presents the results for all specimens.

Table 4.27.: Summary of the compressive tests on small-scale prototype SFRSCC cube specimens

Property	$f_c$ (MPa)	
Age	28 days	905 days
Average	80.65	93.01
Std. Dev.	2.07	7.42
CoV	2.6%	8.0%

As expected, the compressive strength of the SFRSCC material increased over time as the concrete hardened.

For the SFRSCC material used in the full-scale prototype, similar tests were performed by *CiviTest* on four cube specimens, at 28 days of age, following the same test standard. These tests indicated an average compressive strength ( $f_c$ ) of 60.76 MPa, with a standard deviation of 6.95 MPa (CoV of 11.4%).



#### 4.3.2.2. Tests on cylinders

Two sets of tests were performed in cylinders of the SFRSCC material used in the small-scale prototype: (i) compressive tests in the slender direction in order to determine the elasticity modulus ( $E_c$ ) and the Poisson ratio ( $\nu_c$ ), following the recommendations of LNEC E 397 [102]; and (ii) compressive tests in the transverse direction in order to determine the splitting tensile strength  $f_{cr}$ , following the recommendations of EN 12390-6 [103]. For both tests, the cylinders had standard dimensions of 150 mm of diameter and 300 mm of height.

The first set of tests was performed using a multipurpose universal test machine from *Instron*, model 1343, with a load capacity of 250 kN. Longitudinal and transverse strains were monitored with a mechanical strain gauge comprised by steel bracings and three electric displacement transducers from *TML* with a stroke of 5 mm and precision of 0.01 mm. During the tests, data was gathered with a datalogger (from *HBM*, model *Spider8*) at a rate of 5 Hz and stored in a PC. Figure 4.88 shows the test apparatus with one of the specimens being tested. These tests were performed by first loading the specimens up to a compressive stress of 1 MPa ( $\sigma_1$ ) and registering the longitudinal strain ( $\varepsilon_1$ ). After this initial stage, the standard [102] recommends that the specimens are loaded at a rate of 9 kN/s, until a third of their ultimate compressive stress ( $\sigma_2$ ), registering the corresponding longitudinal strain ( $\varepsilon_2$ ). For the present case, however, due to the load limit of the test machine used, it was only possible to load the specimens up to  $\approx 22\%$  and  $\approx 19\%$  of their ultimate compressive strength ( $f_c$ , cf. Section 4.3.2.1), for 28 and 905 days, respectively. As mentioned earlier, these tests were performed in cylinders of the SFRSCC material used in the small-scale prototype, namely, three at 28 days of age and four at 905 days of age. The elasticity modulus in compression of the SFRSCC ( $E_c$ ) was then determined using Eq. (4.47):

$$E_c = \frac{\sigma_2 - \sigma_1}{\varepsilon_2 - \varepsilon_1} \quad (4.47)$$

The Poisson ratio ( $\nu_c$ ), on the other hand, was determined by dividing the transverse strains by the longitudinal strains as expressed in Eq. (4.48),

$$\nu_c = \frac{\varepsilon_{T,2} - \varepsilon_{T,1}}{\varepsilon_2 - \varepsilon_1} \quad (4.48)$$

where  $\varepsilon_{T,1}$  and  $\varepsilon_{T,2}$  are the transverse strains for the initial and final stress levels ( $\sigma_1$  and  $\sigma_2$ ), respectively.

The splitting tensile strength tests were performed with a press tester from *Tonipact*, model 3000, with a control unit from *Form+Test Seidner*, model *CSRG5500*. In order to ensure that the load was applied to the generatrix of the specimens, a steel positioning system was provided between the press plates and the specimens. Specimens made of the SFRSCC used in the small-scale prototype were tested, namely, three at 28 days of age and eight at 905 days of age, Figure 4.89 shows the test apparatus with one of the specimens being tested.



Figure 4.88.: Compressive tests on SFRSCC cylinder specimens.



Figure 4.89.: Splitting tensile strength tests on SFRSCC cylinder specimens.

Based on the ultimate load attained in these tests ( $F_{cr}$ ), it was possible to determine the splitting tensile strength,  $f_{cr}$ , using Eq. (4.49),

$$f_{cr} = \frac{2 \cdot F_{cr}}{\pi \cdot L_{cy} \cdot d_{cy}} \quad (4.49)$$

where  $L_{cy}$  and  $d_{cy}$  are the cylinders length and diameter, respectively.

Table 4.28 summarizes the experimental results, with the complete results for all specimens being presented in Table A.13 (page A.13).

Table 4.28.: Summary of the test results on small-scale prototype SFRSCC material cylinder specimens.

Age	28 days			905 days		
Property	$E_c$ (GPa)	$\nu_c$ -	$f_{cr}$ (MPa)	$E_c$ (GPa)	$\nu_c$ -	$f_{cr}$ (MPa)
Average	36.97	0.33	9.42	40.88	0.29	11.19
Std. Dev.	1.94	0.03	1.63	1.53	0.12	1.08
CoV	5.3%	10.5%	17.3%	3.7%	42.6%	9.6%

Again, these results show that, as expected, as the concrete hardens with time its mechanical properties increase.

#### 4.3.2.3. Tests on small-scale beams

As mentioned earlier, the flexural properties of the SFRSCC used in the full-scale prototype were determined experimentally by the manufacturer (*CiviTest*). By testing small-scale SFRSCC beams, in accordance with the recommendations of RILEM TC 162 TDF [104], it was possible to determine the cracking strength in flexure ( $f_{cr}$ ), the equivalent flexural tensile strengths ( $f_{eq,2}$  and  $f_{eq,3}$ ), and the residual flexural tensile strengths ( $f_{R,1}$  to  $f_{R,4}$ ), as summarized in Table 4.29.

These results show that the SFRSCC used in the full-scale prototype presents strain-hardening behaviour (*cf.* Section 2.5) after cracking, with a relatively low decrease on the

Table 4.29.: Summary of the flexural test results on full-scale prototype SFRSCC material coupons.

Property	$f_{cr}$ (MPa)	$f_{eq,2}$ (MPa)	$f_{eq,3}$ (MPa)	$f_{R,1}$ (MPa)	$f_{R,2}$ (MPa)	$f_{R,3}$ (MPa)	$f_{R,4}$ (MPa)
Average	6.21	10.42	10.56	10.17	10.27	9.71	9.01
Std. dev.	1.25	2.42	2.4	2.16	2.34	2.26	2.15
CoV	20.1%	23.2%	22.7%	21.2%	22.8%	23.3%	23.9%

residual flexural tensile strength (from  $f_{R,1}$  to  $f_{R,4}$ ) as the tensile strain increases, resulting in a ductile failure behaviour.

#### 4.3.2.4. Summary

Table 4.30 summarizes the main results of the SFRSCC material characterization tests, presenting the average properties and standard deviations.

Table 4.30.: Summary of the SFRSCC main mechanical properties derived from coupon testing.

Material	Age (days)	$E_c$ (GPa)	$\nu_c$ -	$f_c$ (MPa)	$f_{cr}$ (MPa)
Small-scale prototype	28	37.0±1.9	0.33±0.03	80.7±2.1	9.42±1.63
	905	40.9±1.5	0.29±0.12	93.0±7.4	11.19±1.08
Full-scale prototype	28	37.8±1.3 <sup>1</sup>	n.a.	60.8±7.0	6.21±1.25 <sup>2</sup>

<sup>1</sup> estimated.

<sup>2</sup> obtained from flexural tests.

Regarding the elasticity modulus in compression ( $E_c$ ) of the SFRSCC used in the full-scale prototype, since it was not determined experimentally, it was estimated using Eq (4.50), provided by Eurocode 2 [85]:

$$E_c = 22 \left[ \frac{0.8 \cdot f_c}{10} \right]^{0.3} \quad (4.50)$$

Using Eq (4.50), the elasticity modulus in compression of the SFRSCC used in the full-scale prototype was estimated as 37.75 GPa with a standard deviation of 1.31 GPa (CoV of 3.5%). It should be mentioned that the latter equation was able to estimate the elasticity modulus of the SFRSCC used in the small-scale prototype with relatively low error when compared to the experimental results, namely 10.8% and 5.1% for ages of 28 and 905 days, respectively.

Regarding the mechanical properties of the SFRSCC used in the small-scale prototype, as expected, all increased with time. Concerning the comparison between the small- and full-scale prototypes SFRSCC materials, the composition of the small-scale material, which has less steel fibre content (*cf.* Table 4.26 and 4.26), presents better mechanical properties. However, the benefits of adding more steel fibres in the concrete composition can only be evaluated in the post-cracking behaviour, which was not tested for the small-scale prototype material, preventing the comparison of both materials. Additionally, it should be added that both materials present similar specific weight ( $\gamma$ ) of 24 kN/m<sup>3</sup>.

### 4.3.3. Full-scale flexural tests

Precast slabs made of the SFRSCC used in the small-scale prototype, with dimensions of  $2000 \times 1000 \times 40 \text{ mm}^3$ , were tested in a 4-point bending load configuration with a 1100 mm span ( $a = 300 \text{ mm}$  and  $b = 500 \text{ mm}$ , *cf.* Figure 4.44), corresponding to the transverse span of the footbridge prototypes (*cf.* Chapters 6 and 7). The slabs were tested when the concrete's age was 905 days.

Figure 4.91 presents the test setup. These tests were performed in a closed steel loading frame anchored to the laboratory strong floor. Load was applied with a hydraulic jack from *Enerpac* with a load capacity of 50 kN, which was installed on the loading frame. The load was distributed to the loading sections with a steel beam. A steel sphere was installed between the hydraulic jack and the distribution beam in order to allow for rotations in both directions, together with a *Novatech* load cell, with 100 kN capacity, in order to measure the applied load. Steel circular tubes were positioned (i) in the load sections, in order to distribute the load in the transverse direction while allowing for rotation in the bending direction, and (ii) in the support sections, to act like pinned supports, one of which was restrained from sliding in the longitudinal direction. During the tests, the vertical deflections were measured at the midspan sections, in two different transverse positions, with electric displacement transducers from *TML* with a stroke of 50 mm and precision of 0.01 mm. The axial strains were also measured in the midspan section with electric strain gauges, from *HBM*, model *HBM-1-LY41-50/120*. Figure 4.90 shows the positioning of all gauges in the midspan section. During the tests, data was gathered with a datalogger from *HBM*, model *Spider8*, at a rate of 5 Hz and stored in a PC. The load was applied at an average rate of 0.25 kN/s.

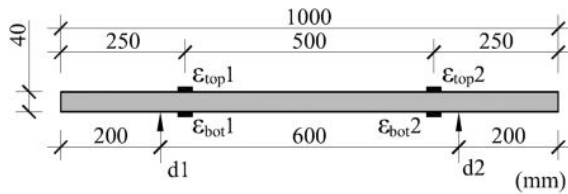


Figure 4.90.: Positioning of the strain gauges and displacement transducers in the midspan section.



Figure 4.91.: Flexural tests on SFRSCC slabs: test setup.

Figure 4.92 presents the load–deflection curves for both specimens tested (the average midspan deflection is considered), while Figure 4.93 shows the evolution of the average axial strains at the top and bottom fibres of the cross-section with the applied load. Both specimens presented a similar behaviour with linear load–deflection curves almost up to the maximum load. At the maximum load, specimens presented transverse cracking, starting in the bottom fibres, at the midspan section. After the maximum load was attained, a ductile plateau was observed where the deformations grew with little change of the applied load. This post-cracking behaviour was accompanied with the progressive opening of the midspan crack while the individual failure of the steel fibres could be heard. Finally, the specimens collapsed with the crack reaching the top fibres of the cross-section. Figure 4.94 shows the

initial cracking in one of the specimens, while Figure 4.95 depicts the crack opening in the vicinity of failure of that same specimen.

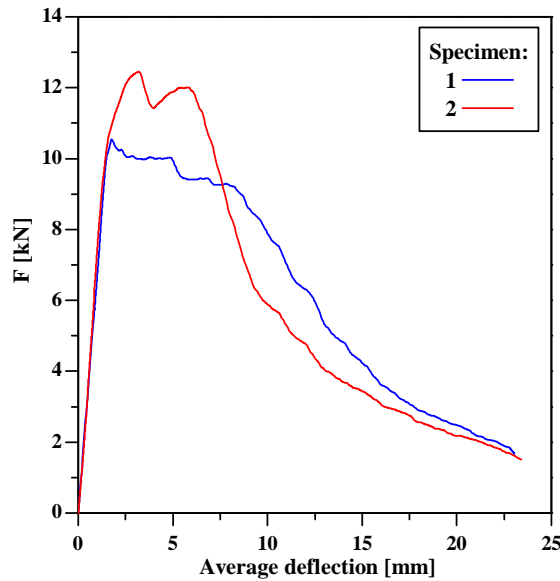


Figure 4.92.: Flexural tests on SFRSCC slabs: load vs. average deflection curves.

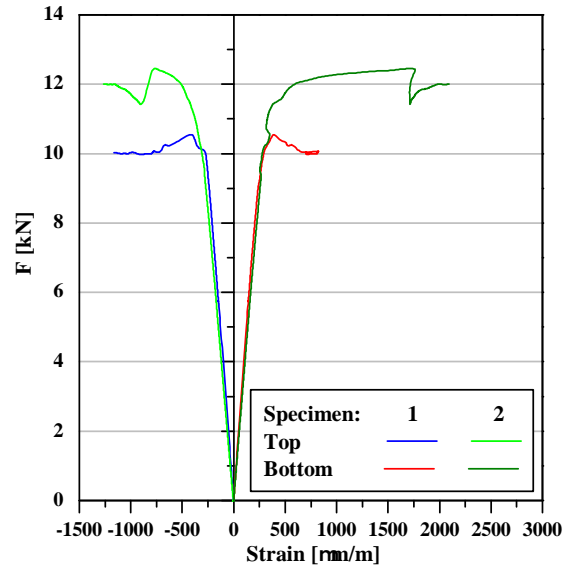


Figure 4.93.: Flexural tests on SFRSCC slabs: load vs. average strain curves.



Figure 4.94.: Flexural tests on SFRSCC slabs: initial crack opening.



Figure 4.95.: Flexural tests on SFRSCC slabs: crack opening in the brink of failure (overall and detail views).

The structural behaviour of the specimens described earlier may be depicted from Figures 4.92 and 4.93. Additionally, it can be seen that the deflection curves are very similar to those of the bottom axial strains where the cracking occurs. Another important conclusion to be drawn from Figure 4.93 is that, for both specimens, the bottom and top strains are symmetrical up until cracking occurs, showing that the neutral axis of the cross-section is roughly located at its geometrical centre.

Table 4.31 summarizes the results of the flexural tests on SFRSCC slabs, including the elastic stiffness ( $K$ ), the cracking load ( $F_{cr}$ ) and corresponding bending moment ( $M_{cr}$ ), the

cracking stress ( $f_{cr}$ ) and the average midspan deflection ( $d_{cr}$ ). Additionally, the maximum post-cracking load ( $F_{post-cr}$ ) is also presented with its corresponding bending moment ( $M_{post-cr}$ ), strength ( $f_{post-cr}$ ) and average midspan deflection ( $d_{post-cr}$ ). As a measure of the structural ductility of the slabs, the ratio between  $d_{post-cr}$  and  $d_{cr}$  is also provided.

Table 4.31.: Flexural tests on SFRSCC slabs: summary of results.

Specimen	$K$ kN/mm	$F_{cr}$ kN	$M_{cr}$ kNm	$f_{cr}$ MPa	$d_{cr}$ mm
1	6.62	10.55	1.58	5.93	1.76
2	7.85	12.45	1.87	7.00	1.71
Average	7.24	11.50	1.72	6.47	1.74
Specimen	$F_{post-cr}$ kN	$M_{post-cr}$ kNm	$f_{post-cr}$ MPa	$d_{post-cr}$ mm	$\frac{d_{post-cr}}{d_{cr}}$
1	10.02	1.50	5.64	4.95	2.81
2	12.01	1.80	6.76	5.34	3.12
Average	11.02	1.65	6.20	5.15	2.96

These results indicate an average cracking stress of 6.47 MPa, which is significantly lower (-42.2%) than that determined by the splitting tensile strength tests on SFRSCC cylinders with the same age (*cf.* Section 4.3.2.4). This difference is more likely due to the nature of the test (flexure *vs.* transverse compression) than to differences in the material itself. More importantly, the tests of both specimens presented significant maximum post-cracking strength ( $f_{post-cr}$ ) when compared to the cracking strength ( $f_{cr}$ , -5.0% and -3.5% for specimens 1 and 2, respectively). Moreover, the deflection at this point ( $d_{post-cr}$ ) was considerably higher than the deflection at cracking ( $d_{cr}$ ), +181% and 212% for specimens 1 and 2, respectively, presenting a clear ductile plateau. In summary, these tests confirmed that, unlike conventional concrete, the SFRSCC presents a ductile flexural failure, owing to the steel fibres embedded in the concrete.

## 4.4. Other materials

This section describes the additional materials used in the construction of the footbridge prototypes, indicating their mechanical properties of such materials, whenever available.

### 4.4.1. GFRP angle profiles

The footbridge prototypes developed in the context of the present thesis included secondary girders. For the small-scale prototype, the connection between main and secondary girders was materialized with the aid of small length angle section GFRP profiles (*cf.* Figures 6.2 and 6.3 (page 170), Chapter 6). These angle sections were extracted from square tubular sections produced by *Fiberline Composites A/S*. The square sections present 100 mm of length/width and an 8 mm thickness, being made of type-E glass fibres embedded in a polyester resin matrix. The mechanical characterization of the GFRP material constituting these profiles was performed at IST by Nunes *et al.* [105]. The summary of the results derived from coupon tests is presented in Table 4.32.

Table 4.32.: Summary of the mechanical properties of the square tubular GFRP profiles [105].

$\sigma_{tu,L}$	$E_{t,L}$	$\sigma_{cu,L}$	$E_{c,L}$	
MPa	GPa	MPa	GPa	
336.5±87.7	39.9±2.7	416.4±22.2	25.3±2.5	
$\sigma_{cu,T}$	$E_{c,T}$	$\sigma_{f,L}$	$E_{f,L}$	$\tau_{is,L}$
MPa	GPa	MPa	GPa	MPa
93.1±14.9	8.3±1.8	352.7±76.1	28.0±6.1	37.0±2.9

Regarding the connection between main and secondary girders of the full-scale prototype, similar small angle section GFRP profiles were used (*cf.* Section 7.2). In this case, however, they were produced by *ALTO Perfis Pultrudidos, Lda.*, the same producer of the main and secondary girders used in both prototypes, and are also constituted by E-glass fibres embedded in an isophthalic polyester resin matrix. The angle section presents equal sides with 60 mm of length and an 8 mm thickness. The general mechanical properties of the GFRP pultruded products produced by ALTO are listed in Table 4.33 [92]:

Table 4.33.: Mechanical properties of the L60×8 GFRP section provided by the manufacturer [92].

$\sigma_{tu,L}$	$\sigma_{cu,L}$	$E_{c,L}$	$\sigma_{f,L}$
MPa	MPa	GPa	MPa
450±45	350±35	23±2.3	450±45

#### 4.4.2. Stainless steel

The connection between main and secondary girders of the footbridge prototypes was materialized by stainless steel bolts, rods, washers and nuts, aided by small length angle GFRP profiles, as mentioned in the previous section (*cf.* Figures 6.2 and 6.3 (page 170), Chapter 6). Additionally, stainless steel bolts, washers and nuts were also provided as a means of connection between the SFRSCC slab and the GFRP main girders (*cf.* Figures 6.12 and 6.14 (page 173) Chapter 6). All stainless steel elements used were provided by *INTEC — Sociedade Técnica de Equipamentos Industriais, S.A.*, and are grade A2-70 [106], which presents a characteristic yielding stress ( $f_{yk}$ ) of 700 MPa.

Regarding the dimensions and type of elements used, the bolts and rods presented a 10 mm diameter. The length of the bolts was 55 mm (M10×55) and they fulfilled the ISO 4017 standard [107].

It should be referred that the materials described in this section, namely the bolts, nuts and washers, used in the construction of the footbridge prototypes, as stated earlier, were identical to those used in the GFRP-concrete shear connection tests (*cf.* Chapter 5).

#### 4.4.3. Epoxy adhesive

The connection between main and secondary girders of the footbridge prototypes comprised (i) a bolted connection provided by stainless steel bolts (as mentioned in the last section), and (ii) an adhesively bonded connection. The epoxy adhesive chosen was *S&P Resin 220*, produced by *S&P, Clever Reinforcement Iberica*, due to its known efficacy in bonding FRP

laminates to concrete surfaces [31, 108]. The manufacturer establishes minimum strengths for this product, namely (i) 90 MPa in compression, (ii) 30 MPa in bending, and (iii) 3 MPa in shear [31]. Regarding the tensile mechanical characteristics, this adhesive was subjected to coupon testing at IST by Firmo *et al.* [108], who determined the following mechanical properties in tension: (i) elasticity modulus ( $E_a = 8.76 \pm 0.54$  GPa); (ii) tensile strength ( $f_{au} = 17.33 \pm 1.30$  MPa); and (iii) ultimate tensile strain ( $\varepsilon_{au} = 2482 \pm 302$   $\mu\text{m/m}$ ).

Additionally, Firmo *et al.* [108, 109] evaluated experimentally the glass transition temperature ( $T_g$ ) of this adhesive with two different methods, estimating this parameter between 47°C and 55°C.

#### 4.4.4. Epoxy mortar

The small-scale prototype was built with precast SFRSCC slabs which had negatives in order to create sockets for the bolts (*cf.* Chapter 6). After the precast slabs were bonded to the girders, these sockets needed to be sealed. To this end, an epoxy mortar was selected due to two main reasons: (i) this product has a similar base as the adhesive (epoxy); and (ii) the high fluidity of this material does not require vibration inside the small sockets. The product chosen was *SIKA Icosit KC 220 N* [110] commercialized in Portugal by *SIKA Portugal — Produtos, Construção e Indústria, S.A.*. A very similar product is commercialized in other countries under the name *SIKA Icosit 220/60 TX* [111].

The epoxy mortar was mixed with mineral filler (*SIKA Carga 2*, from the same producer) in a proportion of 1:1 in weight. For this mixture, the manufacturer indicates elasticity moduli of (i)  $9.9 \pm 1.0$  GPa in compression ( $E_{m,c}$ ), and (ii)  $7.0 \pm 0.9$  GPa in bending ( $E_{m,f}$ ), and strengths of (i)  $100 \pm 5$  MPa in compression ( $f_{m,c}$ ), (ii)  $40 \pm 5$  MPa in bending ( $f_{m,f}$ ), and (iii)  $19 \pm 5$  MPa in shear ( $\tau_m$ ) [110].

#### 4.4.5. Conventional concrete

The concrete jackets were provided at the support sections of the small-scale prototype (*cf.* Figures 6.2 and 6.3 (page 170), Chapter 6), and were materialized by conventional concrete, unlike those of the full-scale prototype, which were made of SFRSCC. The composition of this conventional concrete is given in Table 4.34.

Table 4.34.: Conventional concrete, used in the concrete jackets of the small-scale prototype, component mix proportion.

Component	Cement	Coarse sand	Fine sand	Gravel	Water	Superplasticizer
Proportion (kg/m <sup>3</sup> )	450	614	269	642	158	9

Compressive tests were performed on three cubes of this concrete at the time of the failure flexural tests on the small-scale prototype, when the material had 842 days. An average compressive strength of  $63.63 \pm 10.23$  MPa (CoV of 16.1%) was obtained. The results obtained in each specimen are presented in Table A.12 (page 309).



#### 4.4.6. Regular steel

In order to test the feasibility of a simple external prestress system in hybrid GFRP–concrete structures (*cf.* Section 6.4.6.2), two additional steel elements were used: (i) A500 NR steel rebars with an 8 mm diameter, provided by *Chagas, S.A.*, and (ii) 8 mm diameter threaded rod, according to DIN 976 standard [112], made of steel grade 8.8 [113] provided by *INTEC — Sociedade Técnica de Equipamentos Industriais, S.A.*. According to their classes, the rebars present yielding strength ( $f_{yk}$ ) of 500 MPa and an elasticity modulus ( $E_s$ ) of 200 GPa, while the rod presents yielding strength ( $f_{yk}$ ) of 640 MPa and an elasticity modulus ( $E_s$ ) of 200 GPa.

### 4.5. Concluding remarks

This chapter presented all the materials used in the experimental tests and in the construction of the prototypes, including their most relevant properties, derived from experimental testing for the main materials (GFRP and SFRSCC) or taken from the literature for the secondary materials.

Regarding the full-scale flexural tests on the GFRP profiles, these proved to be difficult to perform and analyse due to the large geometrical imperfections of the profiles, especially for the I400 specimens. Moreover, the experimental results regarding failure were difficult to predict both by analytical and experimental models. The deviations between the experimental results and the models' predictions are likely to be due to premature failure of the web–top flange junction (a weaker region of the cross-section), which is unnoticeable in the stiffness of the specimens but may lead to the early triggering of instability phenomena. Thereafter, in the design of GFRP pultruded profiles the simpler analytical formulae regarding the local buckling of the compressed flange is recommended, *i.e.* without considering the restriction by the web, at least until further research is reported on this theme. On the other hand, GFRP–concrete hybrid structural systems such as that proposed in this thesis are not susceptible to local buckling of the top flange, making their design more reliable.

In what concerns the flexural tests on SFRSCC slabs, the material characterization tests performed confirm that, unlike conventional concrete, these materials are able to present ductile failure modes in flexure. Moreover, it was shown that the SFRSCC used in the full-scale prototypes presents tensile hardening behaviour.



## 5. GFRP–concrete shear connection

### 5.1. Preliminary remarks

The current chapter presents the experimental and numerical investigations concerning the shear connection between the GFRP and the SFRSCC materials. As mentioned earlier (*cf.* Chapter 3), the hybrid GFRP–concrete structural system proposed in this thesis comprises a connection system materialized by both (i) adhesive bonding and (ii) bolts.

*A priori*, the adhesive bonding should govern the stiffness behaviour of the interface GFRP–SFRSCC interface, while the bolts are expected to provide a redundant connection system in case of premature deterioration of the adhesive resin due to vandalism, environmental and/or rheological phenomena. Additionally, the bolted connection may be designed in order to promote a progressive collapse mechanism for the interface failure, *i.e.* where the ultimate strength of the bolted connection shall be higher than that of the adhesive connection.

Within the scope of the Pontalumis project (*cf.* Chapter 3), an experimental campaign on the GFRP–SFRSCC connection system was performed at Minho University [114], in order to investigate the short-term and fatigue behaviour of adhesively bonded GFRP–SFRSCC specimens subjected to push-out tests. Additionally, the effects of accelerated aging by means of thermal and humidity (with salt) cycles on the performance of the GFRP–SFRSCC interface was also investigated.

Also in the scope of the Pontalumis project and within the present thesis, complementary experimental investigations were developed at IST in order to determine the stiffness and strength of different GFRP–SFRSCC connection systems, namely (i) adhesive bonding, (ii) bolting, and (iii) hybrid, combining adhesive bonding and bolting. For the last two connection systems, the influence of the number of connectors on the short-term behaviour was investigated, while the effects of aging were studied for both systems comprising adhesive bonding. Additionally, finite element (FE) models were developed in order to simulate the mechanical behaviour observed in the experimental tests with adhesive bonded specimens.

Regarding the materials used in the experimental programme, as described in Chapter 4, the adhesive bonding was provided by an epoxy resin (*SE&P Resin 220* [31]) chosen due to its known ability to bond FRP laminates to concrete elements [31, 108] (*cf.* Section 4.4.3). The bolted connection, on the other hand, was materialized by stainless steel bolts, washers and nuts (*cf.* Section 4.4.2) embedded in negative sockets of the SFRSCC slabs, which were sealed with an epoxy mortar (*SIKA Icosit KC 220 N* [110], *cf.* Section 4.4.4). The I200 GFRP profile ( $200 \times 100(\times 10)$  mm<sup>2</sup>, *cf.* Chapter 4) was used in these tests.

It should be noted that a direct comparison between the results presented in [114] (tests performed at Minho University) and those presented in this thesis is not possible, due to the (slightly) different geometries of the specimens used.

This Chapter is divided in four sections. After these (i) preliminary remarks, the (ii) experimental tests are presented, followed by the (iii) numerical investigations and, finally, (iv) the concluding remarks.

## 5.2. Experimental tests

### 5.2.1. Experimental programme and test series

The experimental tests performed in order to investigate the mechanical behaviour of the GFRP-SFRSCC connection systems consisted of push-out tests. The test procedure was adapted from the recommendations provided by Eurocode 4 — Annex B [115], for steel-concrete mechanical connections. The tests consisted of loading a GFRP profile connected to two concrete SFRSCC slabs, while measuring the slip between the materials, as illustrated in Figure 5.1.

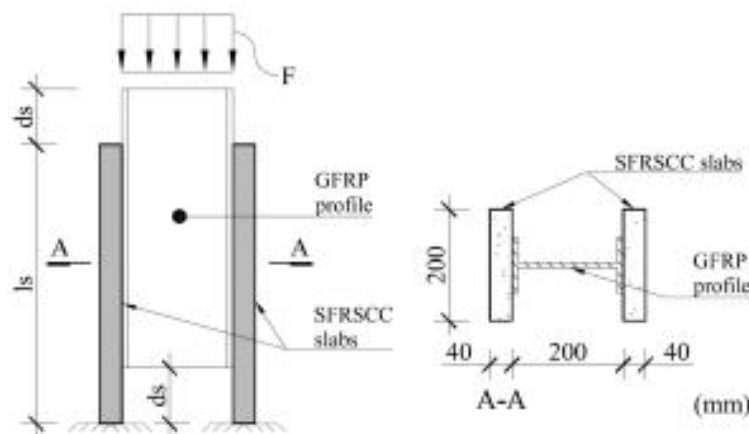


Figure 5.1.: Scheme of the push-out tests: frontal view (left) and setion view A-A (right).

The test series are divided in three main categories: (i) preliminary tests; (ii) un-aged specimens; and (iii) aged specimens. The following sections present each test series, detailing its objectives, as well as the geometry and the materials used in the specimens.

#### 5.2.1.1. Preliminary tests

In order to better understand the behaviour of the proposed GFRP-SFRSCC connection, three test series were studied in the preliminary tests (P), namely specimens connected with: (i) adhesive bonding (series P-A); (ii) bolts (series P-M), and (iii) a hybrid connection (series P-AM). The P-M series was further divided into four subseries, comprising a different numbers of bolts per flange, namely, (a) one pair (P-M1), (b) two pairs (P-M2), (c) three pairs (P-M3), and (iv) four pairs (P-M4). Figure 5.2 shows the dimensions of the specimens of series P-A, P-M1 and P-AM used in the preliminary tests. In the first and third series a 2 mm thick epoxy adhesive layer was applied over all the interface areas, while the specimens

of second and third series were provided with steel bolts (one pair for series P-AM), in each flange of the GFRP profile, at mid-height of the SFRSCC slabs.

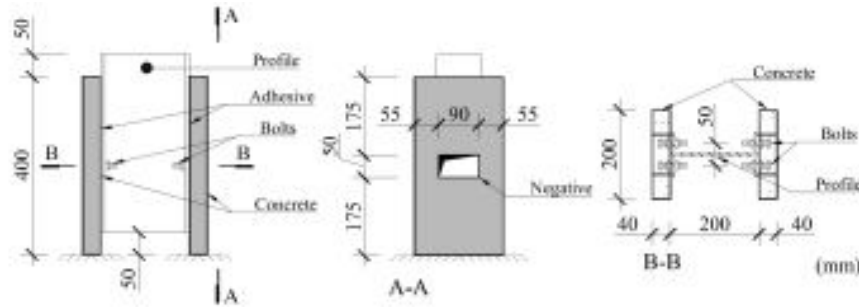


Figure 5.2.: Preliminary test specimens: adhesive provided for specimens P-A and P-AM only; and bolts and negatives provided for specimens P-M1 and P-AM only.

Figure 5.3 shows the dimensional details of the specimens provided with more than one pair of bolts per flange, series P-M2 to P-M4. It should be mentioned that these specimens are shorter than the specimens used in the remaining tests (*cf.* Sections 5.2.1.2 and 5.2.1.3), because the GFRP profile segments and the SFRSCC slabs of series P-A, P-M1 and P-AM provided by the manufacturers presented a length of 400 mm instead of the 500 mm that had been ordered. The different geometries of the specimens, however, do not hinder the quality/relevance of the results obtained in the preliminary tests, but prevent their direct comparison with those obtained for the remaining specimens, particularly those with an adhesive connection (which have different bonding areas).

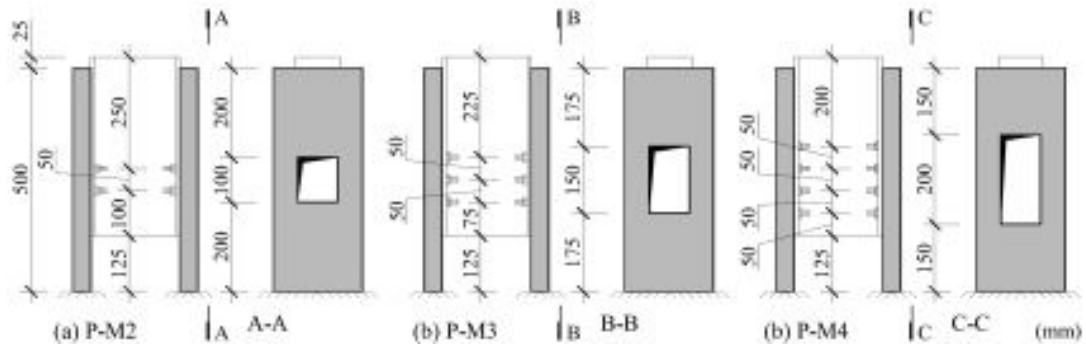


Figure 5.3.: Preliminary test specimens: (a) P-M2; (b) P-M3; (c) P-M4.

### 5.2.1.2. Un-aged specimens

After performing the preliminary tests, another campaign of shear connection tests was developed in order to determine the un-aged behaviour of the GFRP-SFRSCC interface. Three test series were built at this stage, (i) series A, with an adhesive connection at the interface, (ii) series AM, with both adhesive bonding and four pairs of bolts acting as mechanical connectors in each flange, and (iii) series M, with four pairs of bolts.

The main objective of the first series (A) was to set an un-aged reference for the mechanical behaviour of the adhesive bonding with the same geometrical properties of the aged specimens described in the following section (*cf.* Section 5.2.1.3), since the specimens used in the preliminary tests presented a slightly different geometry (*cf.* Section 5.2.1.1). Series AM was built in order to (i) test the mechanical behaviour of the hybrid interface, using four pairs of bolts per flange (which was the configuration adopted in the small-scale footbridge

prototype, *cf.* Section 6.2), and (ii) to set the un-aged reference for this connection system. Finally, since the testing of the preliminary series P–M showed that the epoxy mortar used to seal the negatives of the bolts might be acting as an adhesive itself (*cf.* Section 5.2.4), series M was developed in order to characterize the behaviour of the bolted connection, using four pairs of bolts per flange, without GFRP–epoxy mortar bonding. In order to achieve this effect, a thin cellophane film was installed between the GFRP profile and the epoxy mortar.

Figure 5.4 shows the dimensional properties of the specimens used in the un-aged tests. It should be noted that the epoxy adhesive was used in series A and AM, while the cellophane film was used in series M. The bolts were only used in series AM and M. Regarding series A, two specimens of this series were instrumented with eight electrical strain gauges, from *TML*, model *FLK-1-11-3L*, installed on one of the flanges of the GFRP profile, thus allowing to monitor the longitudinal strains at the GFRP–SFRSCC interface, as schematized in Figure 5.4.

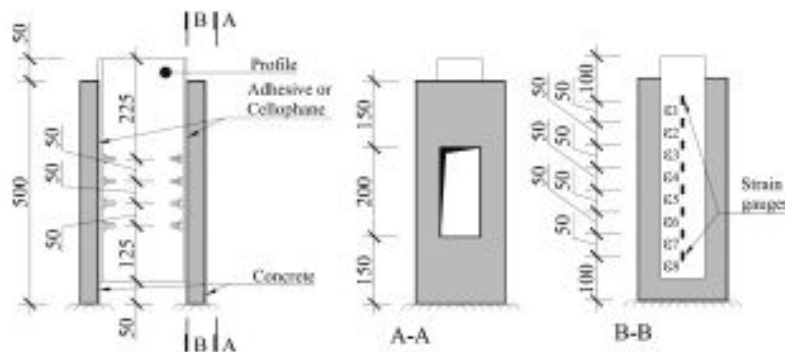


Figure 5.4.: Un-aged test specimens: adhesive provided for specimens A and AM while the cellophane film was provided for specimens M only; bolts and negatives provided for specimens AM and M; and strain gauges used in 2 specimens of series A.

### 5.2.1.3. Aged specimens

As mentioned earlier (*cf.* Section 5.1), one of the objectives of the present experimental campaign was to characterize the long-term behaviour of the GFRP–SFRSCC connection. In this context, shear connection specimens were subjected to two accelerated aging processes: (i) thermal cycles; and (ii) wet–dry cycles.

The thermal cycles performed were devised based on EN 13687–3 [116] standard, which refers to products for protecting and repairing concrete structures. For each 24 hour cycle, temperatures ranged from  $-15^{\circ}\text{C}$  to  $60^{\circ}\text{C}$ , as illustrated in Figure 5.5, while the relative humidity ( $RH$ ) was planned to vary between 0% to 95% as shown in Figure 5.6. This aging process was conducted in a climate chamber, from *Aralab*, model *Fitoclima 6400*, at Minho University. Although the temperature protocol was fairly well reproduced, the climate chamber was not able to follow the target  $RH$  curve, as shown in Figure 5.6. Figure 5.7 shows the test specimens inside the climate chamber.

Since there are no standardized protocols for thermal-cycle accelerated aging of GFRP–concrete connection systems, there were no requirements in the literature for the number of cycles to be performed. For other construction materials, on the other hand, there are readily available standards that define a number of thermal cycles ranging from 5 to 50, namely: (i) 5 thermal cycles for adhesives (ASTM D7149 [117]); (ii) 20 thermal cycles

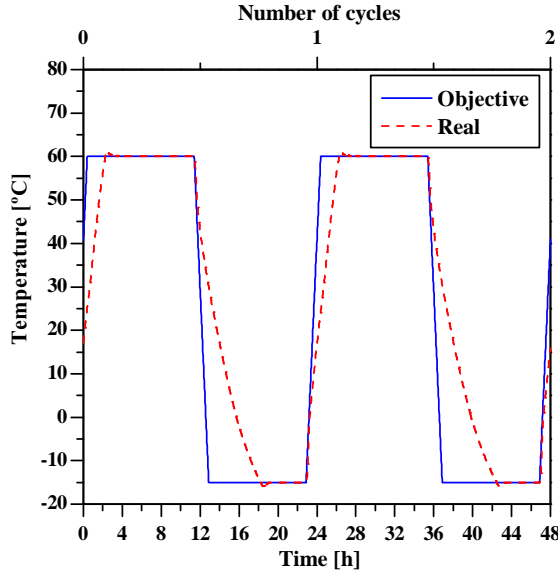


Figure 5.5.: Thermal cycle aging: objective and real (measured) temperature curves.

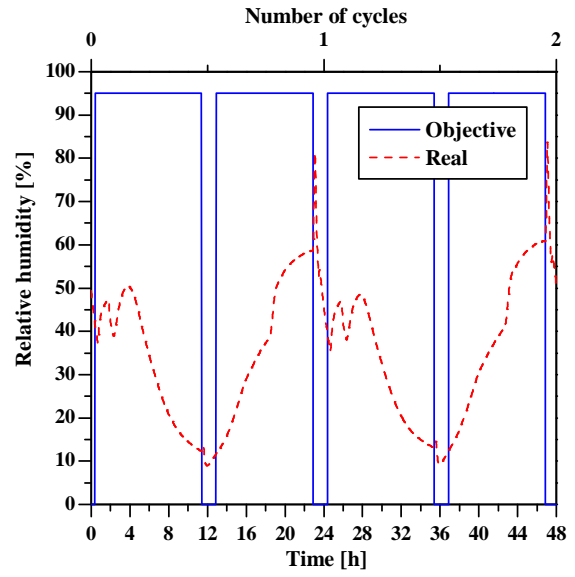


Figure 5.6.: Thermal cycle aging: objective and real (measured)  $RH$  curves.

for FRP strengthening systems for concrete and masonry structures (ICBO-AC125 [118]); (iii) 30 thermal cycles for cured coatings (ASTM D6944 [119]); and 50 thermal cycles for (iv) ceramic tiles (EN 539-2 [120]); (v) surface protection systems for concrete (EN 1504-2 [121]); (vi) products and systems for non-structural repair of concrete (EN 1504-3 [122]); and (vii) structural bonding materials for concrete structures (EN 1504-4 [123]). Given that the structural concept proposed herein is for new structures (not retrofitting of existing structures) and that GFRP based structures are generally designed for long service life periods (between 50 and 100 years), the maximum number of thermal cycles was set around 200.

Regarding the wet-dry cycles, these were performed using a large scale wet-dry chamber, which permanently maintained the  $RH$  over 95%. Each cycle lasted two weeks, with specimens remaining inside the wet-dry chamber (set at 20°C) during one week and outside the chamber (in the laboratory indoor environment) for the remaining week (the temperature in the laboratory environment was not controlled). Figure 5.8 shows the test specimens inside the wet-dry chamber.

The definition of the maximum number of wet-dry cycles presents the same uncertainty issues as that of the thermal cycles. Therefore, in order to better compare the effects of the wet-dry and thermal cycles accelerated aging, it was decided that the maximum number of wet-dry cycles should correspond to the same aging period as that of the maximum number of thermal cycles.

In total, 16 adhesively bonded specimens, with identical geometry to that of specimens of the un-aged A series (*cf.* Figure 5.4) were subjected to thermal cycles aging. For the wet-dry cycles, 15 specimens were used: 12 of which were adhesively bonded (similar to those of A series), while the remaining three presented hybrid connection, with the same geometry as the un-aged AM series specimens, *cf.* Figure 5.4. Table 5.1 summarizes the aging process of each subseries.



Figure 5.7.: Thermal cycle aging: specimens inside the climate chamber.



Figure 5.8.: Wet-dry cycle aging: specimens inside the wet-dry chamber.

### 5.2.2. Specimen preparation

The preparation of the specimens was very similar regardless of the test series, *i.e.* preliminary, un-aged or aged series. Regarding the preparation of the specimens comprising an adhesive connection, the first step was to prepare the SFRSCC slabs' surface in order to enhance the bond. This operation was performed by roughening the surface with an air needle scaler, until the aggregates were visible, as shown in Figures 5.9 and 5.10 for a slab without and with negative, respectively.

After the slab surface was prepared and all dust eliminated with compressed air, the epoxy resin used in the GFRP-SFRSCC connection (*SE&P Resin 220*), was prepared according to the recommendations of the manufacturer [31] and applied to the slabs, as shown in Figure 5.11. The GFRP profile segments were then positioned on top of the slabs, a weight was placed over the profile in order to guarantee the quality of the bonding, and the squeezed adhesive was cleaned. The thickness of the adhesive layer was guaranteed by means of 2 mm thick plastic spacers previously bonded to the profiles' flanges. After a period of 24 hours, given for the resin to set, this process was repeated in order to connect the second slab to the specimens, as depicted in Figure 5.12.

Table 5.1.: Accelerated aging: series, number of specimens and number of cycles.

Aging process	Series	Aging time (weeks)	Nr. of cycles (-)	Nr. of specimens (-)
Thermal cycles	A-Th-T1	16	112	4
	A-Th-T2	24	168	4
	A-Th-T3	32	224	8
Wet-dry cycles	A-H-T1	16	8	4
	A-H-T2	24	12	4
	A-H-T3	32	16	4
	AM-H-T3	32	16	3





Figure 5.9.: Surface preparation of a SFRSCC slab for the adhesive bonding.



Figure 5.10.: Surface preparation of a SFRSCC slab (with negative) for the adhesive bonding.



Figure 5.11.: Preparation of the adhesively bonded specimens: application of the resin.



Figure 5.12.: Preparation of the adhesively bonded specimens: application of the weight.

Additionally, in the specimens with only adhesive connection, strain gauges were used at one of the interfaces (specimens A-3 and A-4, *cf.* Section 5.2.1.2), as shown in Figures 5.13 and 5.14.

The preparation of the bolted specimens began with the drilling of the profiles, as shown in Figure 5.15. In order to fit the M10×55 stainless steel bolts used as connectors, the diameter of the holes was  $\phi 11$  mm. The stainless steel bolts, nuts and washers were then prepared to be embedded in the slab with a 25 mm length, as shown in Figure 5.16.

The bolts were installed on one side of slab and screwed tight, as shown in Figure 5.17. Regarding the un-aged specimens with bolted connection only (series M, *cf.* Section 5.2.1.2), they were provided with a cellophane film separating the GFRP flange from the SFRSCC slab and the epoxy mortar, in order to avoid any bonding between the profile and the mortar (*cf.* Figure 5.18).

The specimens with hybrid connection (series P-AM, AM and AM-H-T3) were first bonded, following the preparation steps described earlier for the adhesive connections, and were subsequently subjected to the procedures (described earlier) to provide them with a bolted



*Figure 5.13.: Preparation of the adhesively bonded specimens: installation of strain gauges.*



*Figure 5.14.: Preparation of the adhesively bonded specimens: specimens instrumented with strain gauges.*



*Figure 5.15.: Preparation of the bolted specimens: drilling of the profiles.*



*Figure 5.16.: Preparation of the bolted specimens: embedded length of the connectors.*

connection. These procedures included (i) the sealing of the SFRSCC-GFRP internal joints around the negative with common silicone adhesive in order to avoid filling material losses, as depicted in Figure 5.19, a procedure not performed for the latter specimens; and (ii) the filling of the negative with epoxy mortar, as shown in Figure 5.20. After a period of 24 hours, given for the initial setting of the mortar, the process was repeated for the other flange of the profile.

### 5.2.3. Test setup, instrumentation and procedure

The experimental series were tested at different periods and using different, but equivalent, test setups, illustrated in Figures 5.21 to 5.23. For the preliminary tests and un-aged specimens, the test setup comprised open loading steel frames, anchored to the laboratory strong floor. A hydraulic jack, from *Enerpac* with a capacity of 600 kN, was installed in the beam of the loading frames. The test specimens rested on the laboratory floor, or on top of a concrete block in the case of specimens P-M2, P-M3 and P-M4. In either case a thin

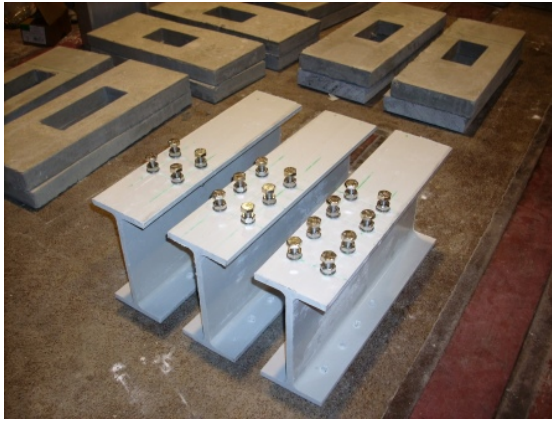


Figure 5.17.: Preparation of the bolted specimens: aspect after installation of the bolts.



Figure 5.18.: Preparation of the bolted specimens: series M specimens provided with cellophane film.



Figure 5.19.: Preparation of the bolted specimens: sealing of the GFRP-SFRSCC joints (M series only).



Figure 5.20.: Preparation of the bolted specimens: filling of the negatives with epoxy mortar.

plaster embedment was executed to guarantee the full contact with the floor and to avoid the effects of geometric irregularities. A 10 mm thick steel spreading plate ( $200 \times 200 \text{ mm}^2$ ) was positioned over the specimens' top surface, to ensure an uniform stress distribution throughout the top of the GFRP profile. A steel sphere was placed over the spreading plate in order to avoid applying transverse loads due to geometrical deviations. Finally, a load cell from *Novatech* with a capacity of 800 kN (400 kN for series P-A, P-M1 and P-AM) was placed in-between the hydraulic jack and the steel sphere, to measure the applied load. The relative displacements were measured with four displacement transducers, with a stroke of 25 mm and precision of 0.01 mm, positioned at the four corners of the spreading plate. Additionally, for some specimens, lateral steel plates connected by dywidag bars were installed in order to avoid potential damages on the transducers in case of explosive failure. It should be stressed that these plates were not screwed tight against the specimens and did not influence their behaviour.

The aged specimens were tested with a hydraulic press from *Enerpac*, with a capacity of 3000 kN, depicted in Figure 5.24. Specimens were placed in the bottom (moving) plate of the





Figure 5.21.: Test setup: specimens P-A, P-M1 and P-AM.



Figure 5.22.: Test setup: specimens P-M2, P-M3 and P-M4.

press, on top of a thin plaster embedment. The top plate was provided with a steel sphere and a load cell, from *Microtest*, with a load capacity of 3000 kN. The relative displacements were measured with four displacement gauges, with a stroke of 25 mm and precision of 0.01 mm, one of which positioned at the bottom plate of the press (the moving plate), while the remaining three were placed on the corners of the top plate of the press, which could rotate owing to the presence of the steel sphere.



Figure 5.23.: Test setup: specimens A, M and AM.



Figure 5.24.: Test setup: specimens A-Th, A-H and AM-H.

During the tests data was gathered with a datalogger from *HBM*, model *Spider8*, at a rate of 5 Hz and stored in a PC, with the exception of specimens A1 and A2, for which, in order to collect data from the strain gauge measurements at the interface (*cf.* Section 5.2.1.2), two similar built-in dataloggers were used.

The tests started with a loading/unloading cycle, up to about 10% of the expected failure load. After this first cycle, the specimens were tested monotonically under load control, at a rate of approximately 1 kN/s, set manually. Specimens were loaded until failure, which was typically characterized by a sudden load reduction without further recovery.

## 5.2.4. Results and discussion — preliminary tests

### 5.2.4.1. Series P-A

Figure 5.25 presents the load–relative displacement curves for all P-A specimens. It can be seen that, after an initial accommodation, the load presented fairly linear growth until a peak load was achieved, which corresponded to the failure initiation at the GFRP–SFRSCC interface, due to the debonding of the epoxy resin. After this peak load was attained, specimens were able to maintain most of the load, in some cases even sustaining higher loads, accommodating higher relative displacements, indicating a non-linear behaviour, until the specimens collapsed due to the failure of the GFRP web–flange junction at the opposite side of the specimen. This failure mechanism was observed for all specimens, with the exception of P-A-6, which failed simultaneously at the web–flange junction and at the GFRP–SFRSCC interface. After the collapse of the specimens, it was possible to observe that the failure of the interface occurred within the SFRSCC material.

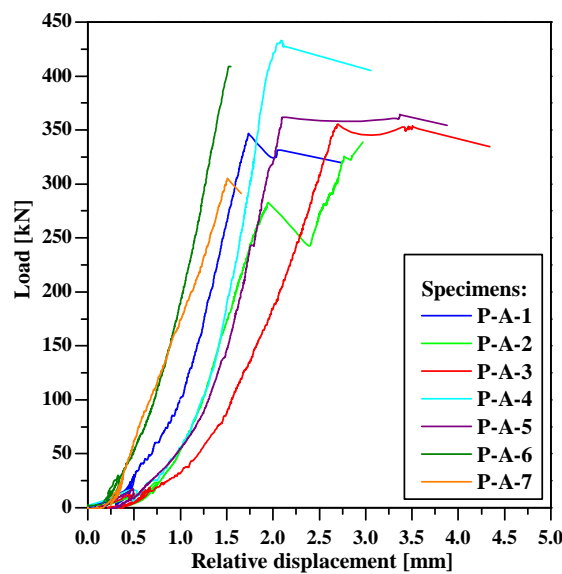


Figure 5.25.: Shear connection tests: load *vs.* relative displacement curves for P-A specimens.

Figure 5.26 shows, as an example, several stages of the test of specimen P-A-6. An average ultimate load ( $F_u$ ) of 362.8 kN (CoV of 12%) and stiffness ( $K$ , computed according to the definition given by Johnson and May [124]) of 277.1 kN/mm (CoV of 20%) were obtained in these tests. The complete results of all specimens are presented in Table B.1 (page 311).

### 5.2.4.2. Series P-M1

The load–relative displacement curves of all P-M1 specimens are presented in Figure 5.27. After the initial stage of the test, all specimens behaved very similarly, with load increasing linearly up to a first load peak, and then presenting a second load peak, after which the behaviour of all specimens followed a markedly non-linear behaviour.

The initial linear behaviour presented by all specimens was not expected *a priori*. In fact, this type of behaviour is typical of adhesively bonded specimens, whereas the second stage of the behaviour, the non-linear stage, is typical of bolted connection specimens. This mixed



Figure 5.26.: Specimen P-A-6: a) beginning of the test; b) failure of the specimen; c) detail of the web-flange junction failure — complete separation; and d) detail of the failure at the interface — complete separation.

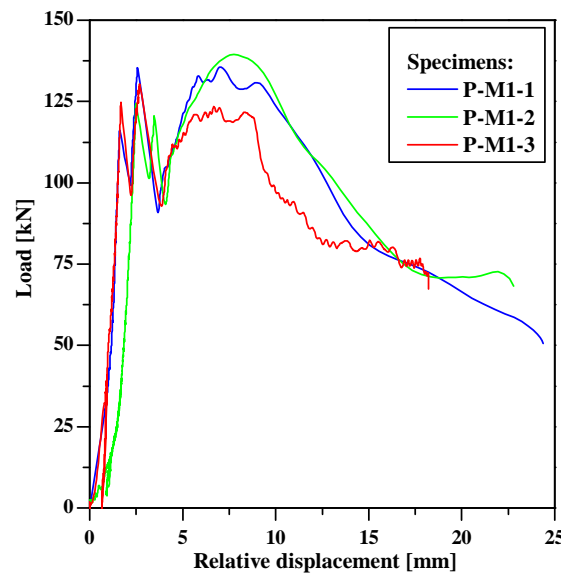


Figure 5.27.: Shear connection tests: load *vs.* relative displacement curves for P-M1 specimens.

behaviour suggests that the epoxy mortar used to seal the negative in the SFRSCC slabs acted as an adhesive, governing the early stages of the load–relative displacement behaviour of the specimens. An average ultimate load ( $F_u$ ) of 135.13 kN (CoV of 3.4%) and stiffness ( $K$ ) of 91.12 kN/mm (CoV of 4.8%) were obtained in these tests. The complete results of all specimens are presented in Table B.2, page 312.

Figure 5.28 presents, as an example, the several stages of the test of specimen P-M1-2. All specimens presented similar failure modes. Initially, when the load peaks were achieved after the linear stages (*cf.* Figure 5.27), loud cracks were heard followed by load losses. Although no external damage was visible at this stage, this behaviour was attributed to the debonding between the GFRP flanges and the epoxy mortar. After this stage, the specimens' behaviour was non-linear, with the GFRP flanges being crushed against the bolts, which also deformed visibly, until the specimens could not sustain any load.



Figure 5.28.: Specimen P-M1-2: a) beginning of the test; b) beginning of the crushing, and of bolts' deformation; c) failure due to crushing of the flange; and d) detail of the interaction between the bolts and the profile.

#### 5.2.4.3. Series P-M2

The load–relative displacement curves of specimens P-M2 are plotted in Figure 5.29. Similarly to what was observed for series P-M1, the behaviour was linear up to one or more peak loads, after which the behaviour was non-linear. The average ultimate load ( $F_u$ ) was of 222.9 kN (CoV of 6%) and the stiffness ( $K$ ) of 140.7 kN/mm (CoV of 14%). The complete results of all specimens are presented in Table B.3 (page 312).

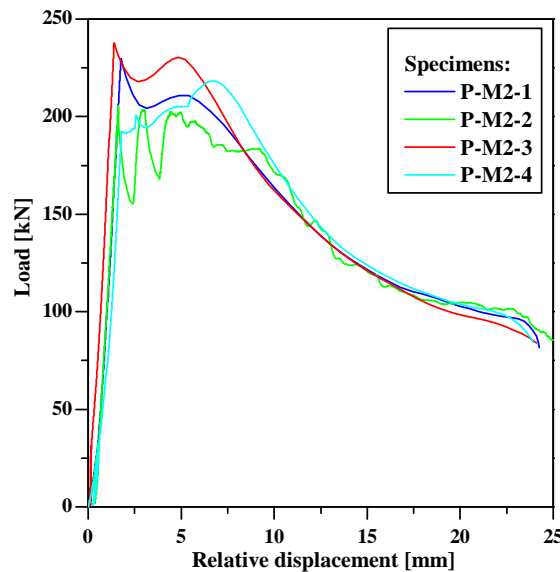


Figure 5.29.: Shear connection tests: load *vs.* relative displacement curves for P-M2 specimens.

Figure 5.30 presents, as an example, several stages of the test of specimen P-M2-1. As mentioned earlier, most specimens presented a linear regimen up to a peak load, which corresponded to the debonding of the epoxy mortar–GFRP interface. After this stage, the behaviour was markedly non-linear, with the GFRP flanges being crushed against the bolts, with visible bolt deformation, specially for the top pair. Specimen P-M2-2 behaved slightly differently, exhibiting two linear branches in the load *vs.* displacement curve, before starting to present a non-linear behaviour.



Figure 5.30.: Specimen P-M2-1: a) beginning of the test; b) deformation on the bolts/beginning of GFRP flange crushing on the GFRP flange; c) collapsed specimen; d) detail of the GFRP flange crushing.

#### 5.2.4.4. Series P-M3

Specimens P-M3 presented linear behaviour up to a load peak, after which they exhibited a non-linear behaviour, as depicted in Figure 5.31.

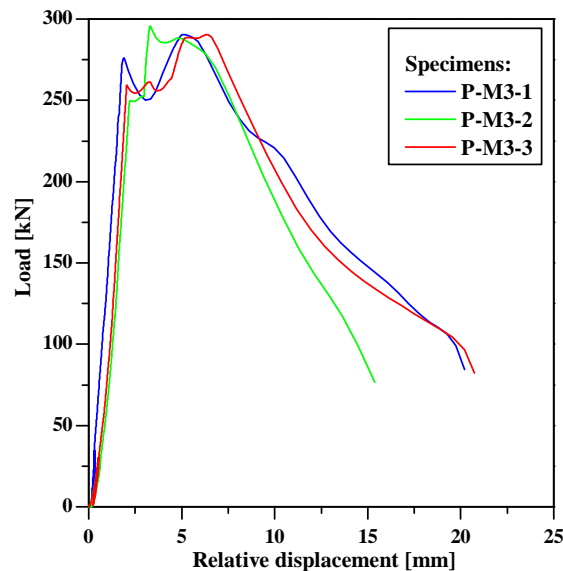


Figure 5.31.: Shear connection tests: load *vs.* relative displacement curves for P-M3 specimens.

Unlike what was observed for the previous series (P-M1 and P-M2), the maximum load was achieved at the non-linear stage of the behaviour, showing that the three pairs of bolts on each flange have higher strength than the adhesive connection provided by the epoxy mortar. An average ultimate load ( $F_u$ ) of 286.3 kN (CoV of 4%) and stiffness ( $K$ ) of 140.0 kN/mm (CoV of 7%) were obtained. The complete results of all specimens are presented in Table B.4 (page 313).

Figure 5.32 depicts several stages of the test of specimen P-M3-4, as an example. As in the previous M series, the first load peak is attributed to the debonding of the epoxy mortar-GFRP interface, after which the GFRP flanges started to be crushed by the bolts, with visible deformations on the latter, particularly in the top pairs.





Figure 5.32.: Specimen P-M3-4: a) linear stage; b) non-linear stage (deformation of the bolts on the left side only); c) crushing of the GFRP flange; d) crushing of the GFRP flange — detail.

#### 5.2.4.5. Series P-M4

Figure 5.33 plots the load–relative displacement curves for all P-M4 specimens. Again, specimens presented linear load–relative displacement behaviour up to a peak load, after which the behaviour was non-linear. The maximum load was observed in the non-linear stage for all specimens, with the exception of specimen P-M4-3. An average ultimate load ( $F_u$ ) of 363.7 kN (CoV of 3%) and stiffness ( $K$ ) of 221.8 kN/mm (CoV of 19%) were obtained in these tests. The complete results of all specimens are presented in Table B.5 (page 313).

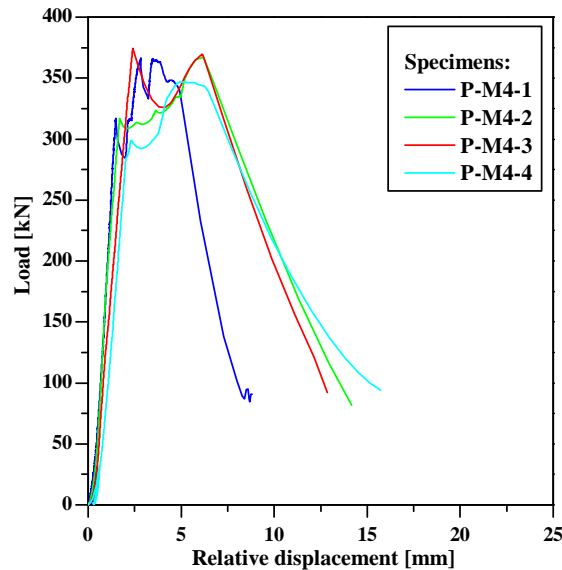


Figure 5.33.: Shear connection tests: load *vs.* relative displacement curves for P-M4 specimens.

The failure mode of these specimens was identical to the one described earlier for all P-M test series. Figure 5.34 shows, as an example, several stages of the test of specimen P-M4-4.



Figure 5.34.: Specimens P-M4-4: a) linear stage; b) non-linear stage — deformation of the bolts; c) collapsed specimen; and d) detail of the GFRP flange crushing.

#### 5.2.4.6. Series P-AM

Figure 5.35 plots the load–relative displacement curves obtained in the P-AM series. The specimens presented very similar behaviour to that observed for series P-A, showing that the behaviour was governed by the epoxy adhesive, both regarding the stiffness and the ultimate load. In these tests, an average ultimate load ( $F_u$ ) of 398.6 kN (CoV of 11%) and stiffness ( $K$ ) of 300.6 kN/mm (CoV of 24%) were obtained. The complete records for all specimens are presented in Table B.6 (page 314).

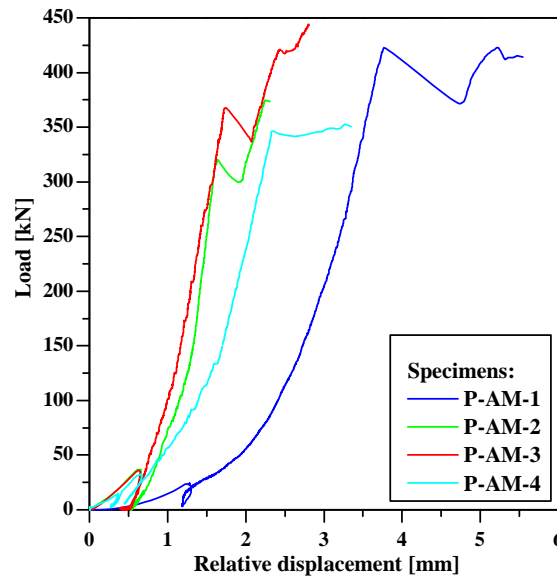


Figure 5.35.: Shear connection tests: load vs. relative displacement curves for P-AM specimens.

It should be noted that specimen P-AM-3 was not tested up to failure due to concerns of damaging the load cell (capacity of 400 kN, *cf.* Section 5.2.3). Figure 5.36 depicts several stages of the test of specimen P-AM-2, as an example. The failure mode of the remaining specimens was identical to that observed for the P-A series, with debonding of the GFRP-SFRSCC connection at one side of the specimen, followed by web-flange junction failure on the opposite side. The bolts failed immediately with the collapse of the specimens, not being able to sustain the applied load.



Figure 5.36.: Specimen P-AM-2: a) beginning of the test; b) failure of the web-flange junction; c) failure of the SFRSCC-adhesive interface; d) failure of both bolts of the same flange.

#### 5.2.4.7. Comparative analysis

The results obtained in the shear connection tests of all preliminary series, described above, are compared in Figure 5.37, which plots the load-relative displacement curves for a representative specimen of each series. Table 5.2 summarizes those same results.

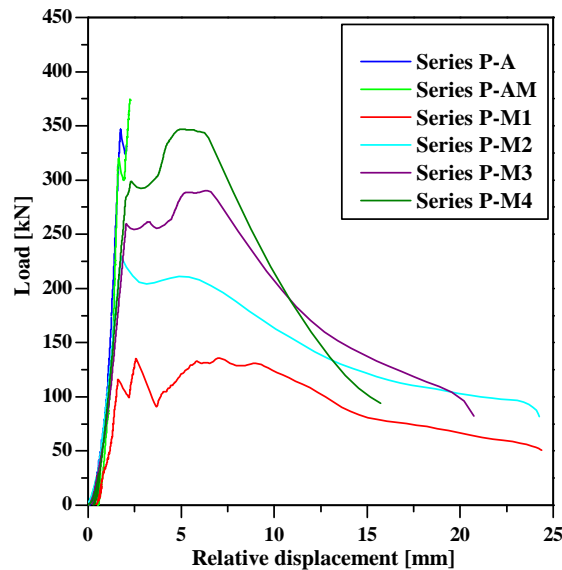


Figure 5.37.: Shear connection tests: load *vs.* relative displacement curves for all preliminary series.

These results show that the redundant connection with epoxy adhesive and one pair of bolts per flange (series P-AM) does not constitute any short-term improvement when compared to the adhesive connection alone (series P-A). However, as mentioned earlier (*cf.* Section 5.1), the redundant bolted connection was provided as a mean of ensuring the connection between both materials in case of premature deterioration of the adhesive. Nonetheless, the fact that the bolted connection with four pairs of bolts per flange (series P-M4) presents similar failure loads to those of the series using epoxy adhesive (P-A and P-AM) shows that the redundant bolted connection may create a ductile/progressive failure system, a hypothesis to be tested with series AM of the un-aged specimens (*cf.* Section 5.2.1.2).

Table 5.2.: Shear connection tests: summary of all preliminary series results.

Series	$F_u$ (kN)	$d_u$ (MPa)	$K$ (kN/mm)	Typical failure mode
P-A	$362.8 \pm 44.8$	$2.25 \pm 0.73$	$277.1 \pm 54.3$	1 <sup>st</sup> web-flange junction; 2 <sup>nd</sup> debonding
P-AM	$398.6 \pm 42.1$	$3.38 \pm 1.29$	$300.6 \pm 71.8$	1 <sup>st</sup> web-flange junction; 2 <sup>nd</sup> debonding & bolts' failure
P-M1	$135.1 \pm 4.6$	$5.81 \pm 2.73$	$91.1 \pm 4.4$	1 <sup>st</sup> debonding; 2 <sup>nd</sup> crushing of the flanges
P-M2	$222.9 \pm 14.1$	$2.87 \pm 2.55$	$140.8 \pm 19.3$	1 <sup>st</sup> debonding; 2 <sup>nd</sup> crushing of the flanges
P-M3	$286.3 \pm 12.1$	$4.94 \pm 1.57$	$140.0 \pm 9.6$	1 <sup>st</sup> debonding; 2 <sup>nd</sup> crushing of the flanges
P-M4	$363.7 \pm 11.9$	$4.12 \pm 1.79$	$221.8 \pm 42.7$	1 <sup>st</sup> debonding; 2 <sup>nd</sup> crushing of the flanges

Regarding all series comprising only bolted connection (series P-M), a two-staged behaviour was observed consistently for most specimens, the first stage corresponding to a linear behaviour up to a peak load, governed by the adhesive properties of the epoxy mortar sealing the slabs negatives, and the second stage reflecting a non-linear behaviour governed by the bolted connection. In this context, it is important to separate the failure load of the adhesive ( $F_{u,lin.}$ ) and the failure load of the bolted connection ( $F_{u,non-lin.}$ ). Table 5.3 presents this data along with the negative area ( $A_{neg}$ ) and number of bolts ( $Nr$ ), as well as ratios ( $F_{u,lin.}/A_{neg}$ ) and ( $F_{u,non-lin.}/Nr$ ) for each P-M series.

Table 5.3.: Shear connection tests: comparison of the results for all P-M series.

Series	$F_{u,lin}$ (kN)	$A_{neg.}$ (cm <sup>2</sup> )	$F_{u,lin}/A_{neg.}$ (kN/cm <sup>2</sup> )	$F_{u,non-lin}$ (kN)	$Nr$ (-)	$F_{u,non-lin}/Nr$ (kN/bolt)
P-M1	$121.5 \pm 4.7$	80	1.52	$132.8 \pm 8.4$	4	33.21
P-M2	$216.4 \pm 21.1$	160	1.35	$215.6 \pm 11.8$	8	26.95
P-M3	$261.9 \pm 13.3$	240	1.09	$274.6 \pm 14.4$	12	22.88
P-M4	$326.8 \pm 33.0$	320	1.02	$362.3 \pm 10.4$	16	22.64

Table 5.3 shows that both the first peak load ( $F_{u,lin.}$ ) and the non-linear maximum load ( $F_{u,non-lin.}$ ) seem to grow in an approximately direct proportion with the bonding area ( $A_{neg}$ ) and the number of bolts ( $Nr$ ), respectively. However, the average stress in the bonding area ( $F_{u,lin.}/A_{neg}$ ), as well as the strength per bolt ( $F_{u,non-lin.}/Nr$ ) seem to decrease with the bonding area ( $A_{neg}$ ) and the number of bolts ( $Nr$ ), respectively, towards an asymptote, as shown in Figures 5.38 and 5.39.

## 5.2.5. Results and discussion — un-aged specimens

### 5.2.5.1. Series A

All specimens of series A presented very similar behaviour between each other and to those of preliminary series P-A. Figure 5.40 shows that the load-relative displacement curves presented an initial linear behaviour up to a peak load, which corresponded to the failure initiation of the GFRP-SFRSCC interface. After this stage, specimens were able to maintain most of the load for a brief period until the GFRP profile web-flange junction failed at the other side of the specimen, leading to collapse. For all specimens, it was observed that the failure of the interface occurred in the SFRSCC material. Figure 5.41 shows, as an example, several stages of the test of specimen A-1. An average ultimate load ( $F_u$ ) of 393.1 kN (CoV

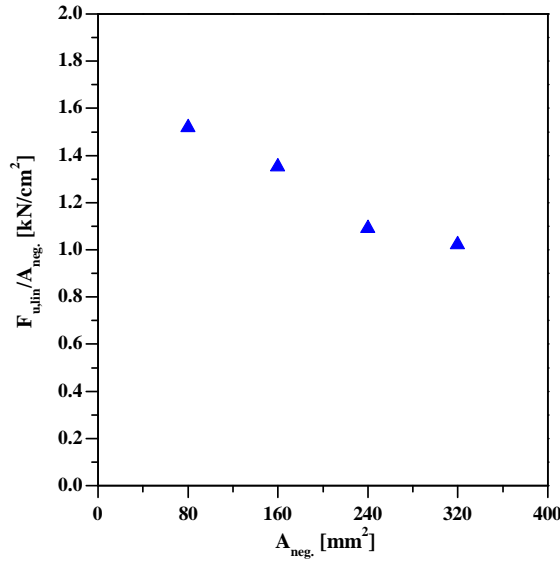


Figure 5.38.: Shear connection tests:  $F_{u,lin.}/A_{neg}$  vs.  $A_{neg}$  for all P-M specimens.

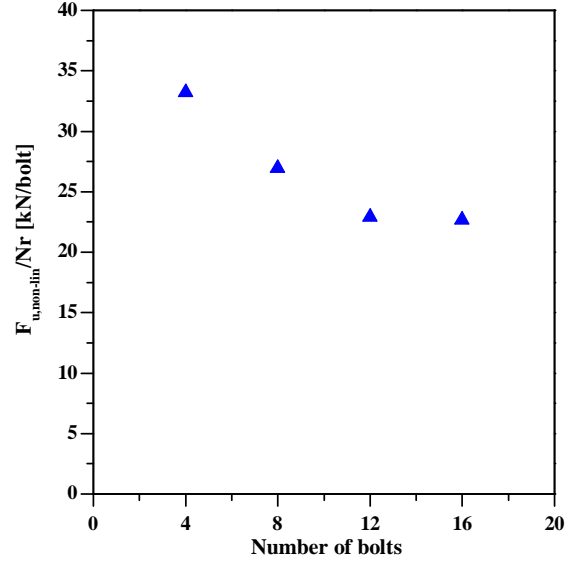


Figure 5.39.: Shear connection tests:  $F_{u,non-lin.}/Nr$  vs.  $Nr$  for all P-M specimens.

of 9%) and stiffness ( $K$ ) of 249.7 kN/mm (CoV of 12%) were obtained in these tests, whose complete results are presented in Table B.7 (page 314).

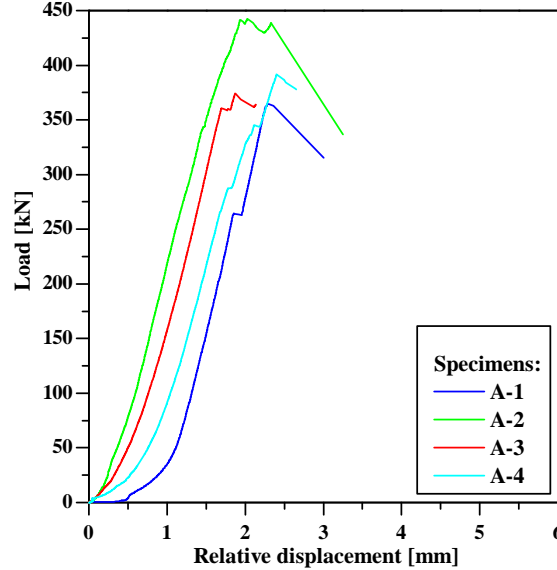


Figure 5.40.: Shear connection tests: load vs. relative displacement curves for series A.

Regarding the axial strains measured in the GFRP-SFSRCC interface, the measurements of all strain gauges used in specimen A-3, as well as the strain gauge  $\varepsilon_1$  of specimen A-4 (*cf.* Figure 5.4, page 122) were inconsistent, possibly due to a deficient installation. Thereafter, it was only possible to measure the strains for specimen A-4, at positions  $\varepsilon_2$  to  $\varepsilon_8$ , as shown in Figure 5.42, for several load levels.

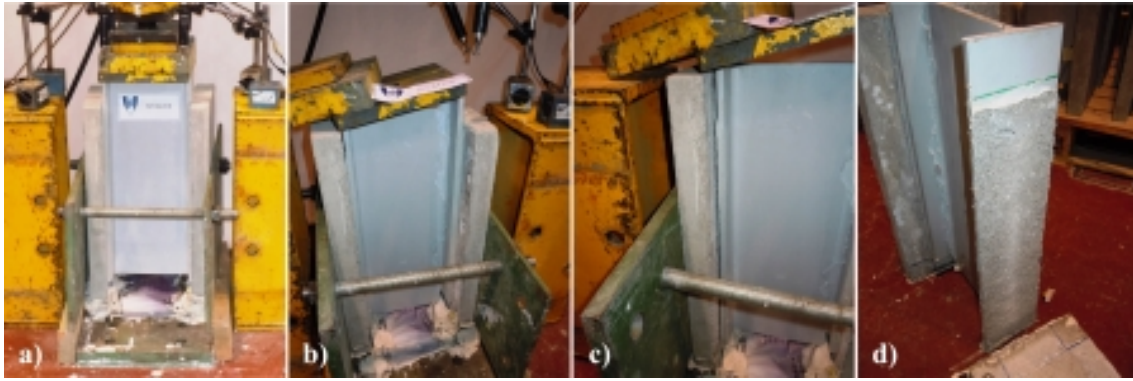


Figure 5.41.: Specimen A-1: a) beginning of the test; b) detail of the web-junction damage; c) detail of the GFRP-SFRSCC debonding; d) debonding in the SFRSCC.

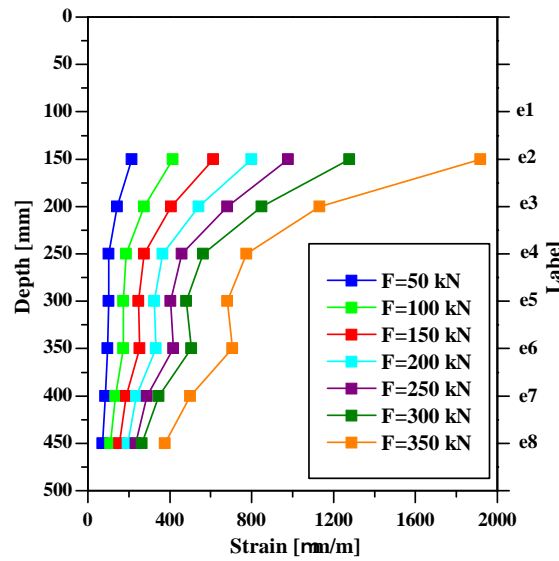


Figure 5.42.: Shear connection tests: strain measurements at the interface for specimen A-4.

These results show that the strains in the interface decrease with the depth, *i.e.* are higher near the load section, and increase with the applied load, as expected. These results will be further discussed in Section 5.3.3.1, together with the results of numerical models.

#### 5.2.5.2. Series M

In spite of the cellophane film installed between the GFRP and the SFRSCC in this series, which ensured that the epoxy mortar (sealing the negatives) did not bond the profiles and the SFRSCC, the load–relative displacement curves obtained in these tests showed an initial linear behaviour, as depicted in Figure 5.43. Near the maximum load levels, specimens started to present a non-linear behaviour, with limited ductility. For this series, an average ultimate load ( $F_u$ ) of 360.3 kN (CoV of 4%) and stiffness ( $K$ ) of 90.9 kN/mm (CoV of 7%) were obtained. The complete results for all specimens are presented in Table B.8 (page 315).

Several stages of the test of specimen M-2 (as an example) are presented in Figure 5.44. All specimens failed due to the progressive crushing of the flanges by the bolts, which occurred with considerable bolt deformation, most visible for the top pairs. Additionally,

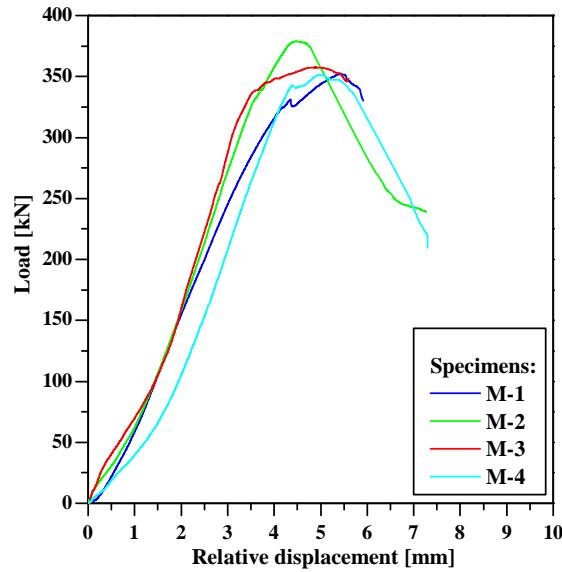


Figure 5.43.: Shear connection tests: load *vs.* relative displacement curves for series M.

specimens presented extensive damage on the SFRSCC slabs, which occurred, however, after failure.



Figure 5.44.: Specimen M-2: a) beginning of the test; b) deformation of the bolts; c) crushing of the GFRP flanges; d) damage on the SFRSCC (after failure).

Regarding the strength of the bolted connection for steel–concrete shear connection tests, Eurocode 4 [115] suggests that the characteristic strength provided by each bolt ( $R_{bk}$ ) is taken as 90% of the ultimate load divided by the number of bolts ( $F_u/Nr$ ). Applying such principle to the present case, a characteristic strength per bolt of 20.3 kN is determined.

### 5.2.5.3. Series AM

Figure 5.45 plots the load–relative displacement curves for specimens of series AM, showing that all specimens presented a linear behaviour up to approximately 250 kN, after which load continued to increase irregularly and with lower stiffness. This first transition point corresponded to the beginning of the interface debonding process. For all specimens, the maximum load was attained in this second stage, after which a load decrease was registered accompanied by large increases of relative displacement. These large displacements were



due to the necessary accommodation of the GFRP profile to the bolts in order to mobilize the bolted connection. Finally, load started to increase again, owing to the presence of the bolted connection, until the specimens' collapse. An average ultimate load ( $F_u$ ) of 508.7 kN (CoV of 16%) and stiffness ( $K$ ) of 297.0 kN/mm (CoV of 11%) were obtained in these tests. The complete results for all specimens are presented in Table B.9 (page 315).

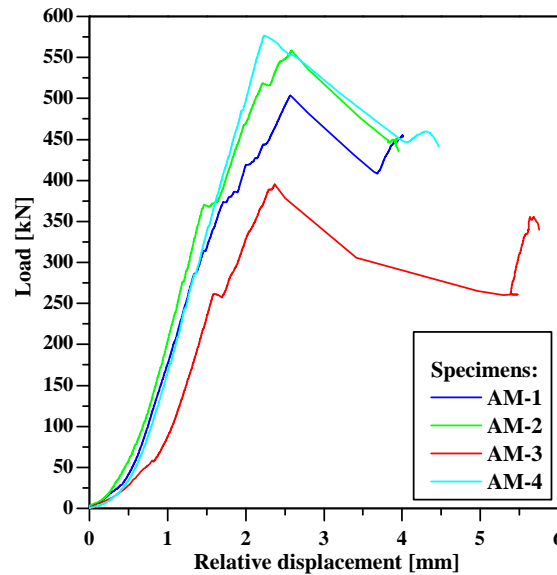


Figure 5.45.: Shear connection tests: load vs. relative displacement curves for series AM.

Figure 5.46 presents, as an example, several stages of the test of specimen AM-2. Regarding the failure modes, the adhesive interface failed initially within the SFRSCC, transferring the load to the bolted connection, which then started to crush the GFRP flanges. However, specimens collapse was due to the failure of the web-flange junction on the other side of the profile, except for specimen AM-3, which actually failed due to the crushing of the GFRP flange by the bolts. In this regard, it is worth mentioning that, with the exception of specimen AM-3, the strength of the bolted connection was not fully exploited.



Figure 5.46.: Specimen AM-2: a) beginning of the test; b) collapsed specimen; c) debonding and crushing of the flange; d) web-flange junction failure.



#### 5.2.5.4. Comparative analysis

The results obtained in the shear connection tests of the un-aged series are compared in Figure 5.47, which plots the load–relative displacement curves for a representative specimen of each series, and in Table 5.4, which summarizes the results of each series.

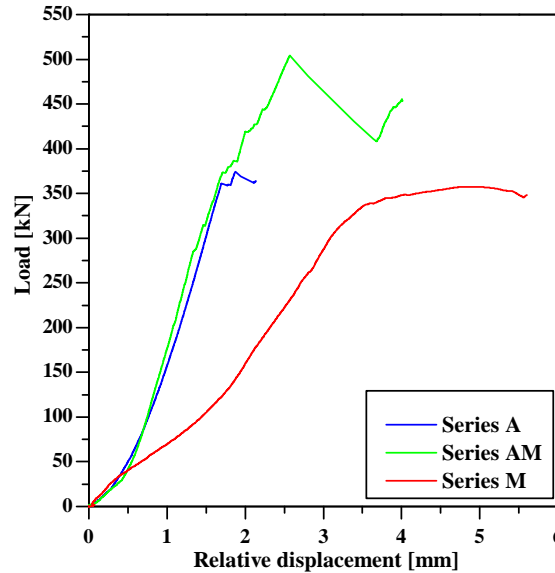


Figure 5.47.: Shear connection tests: load vs. relative displacement curves for all un-aged series.

Table 5.4.: Shear connection tests: summary of all un-aged series results.

Series	$F_u$ (kN)	$d_u$ (mm)	$K$ (kN/mm)	Typical failure mode
A	$393.1 \pm 34.7$	$2.14 \pm 0.24$	$249.7 \pm 30.0$	1 <sup>st</sup> web-flange junction; 2 <sup>nd</sup> debonding
M	$360.3 \pm 12.9$	$4.93 \pm 0.39$	$90.9 \pm 6.5$	Crushing of the flanges
AM	$508.7 \pm 81.6$	$2.24 \pm 0.16$	$297.0 \pm 32.5$	1 <sup>st</sup> debonding; 2 <sup>nd</sup> web-flange junction

The results obtained show that specimens of series A and AM behaved similarly prior to failure, with the behaviour being governed at this stage by the epoxy adhesive, which provided identical stiffness. For series A, after the first initial damage (debonding of the interface), the failure of the web-flange junction occurred almost simultaneously on the other side of the specimens, leading to collapse. For series AM, the initial damage was also due to the debonding of the GFRP-SFRSCC interface, which occurred gradually and started at lower load levels than for series A. In this respect, it is interesting to observe that the smaller area of epoxy resin provided in specimens of series AM does not seem to influence the stiffness but has major influence in the failure load of the adhesive connection. This result suggests that the epoxy mortar is able to provide similar stiffness to that provided by the epoxy resin, but lower strength. Furthermore, the presence of the bolts seems to delay the failure of the adhesive connection, significantly increasing its strength, possibly due to the fact that the bolts are able to sustain the peeling stresses developed at the interface.

More importantly, the comparison between the results of series A and AM show that adding a bolted connection may not only provide a redundant connection system in case of premature

deterioration of the adhesive bond, but it may also provide a pseudo-ductile/progressive failure.

Regarding the comparison between series A and series P-A, the former series, which has a higher bonding area (+29%), provided by the longer length of the bond (*cf.* Figures 5.4 and 5.2, pages 122 and 120, respectively), presented higher strength and stiffness (+8% and +6%, respectively) than the latter. These differences, however, are well within the coefficient of variation (CoV) observed in the tests, indicating that the strength and stiffness did not depend significantly on the bond length (for these geometries).

Concerning the bolted connection, the comparison between series M and series P-M4, plotted in Figure 5.48, shows that the stiffness of the former series was much smaller than that of the latter (-59.1%). This particular result confirms the doubts about the mechanical behaviour of specimens P-M, showing that, in fact, up to the first load peak, it was governed by the bond between the epoxy mortar and the GFRP. The strength of the bolted connection ( $F_{u,non-lin}$ , for the preliminary series, *cf.* Table 5.3) presented identical magnitudes for both series (-0.6% for series M) and failure occurred for similar relative displacement ranges, again confirming that the non-linear behaviour of the P-M series was governed by the bolted connection.

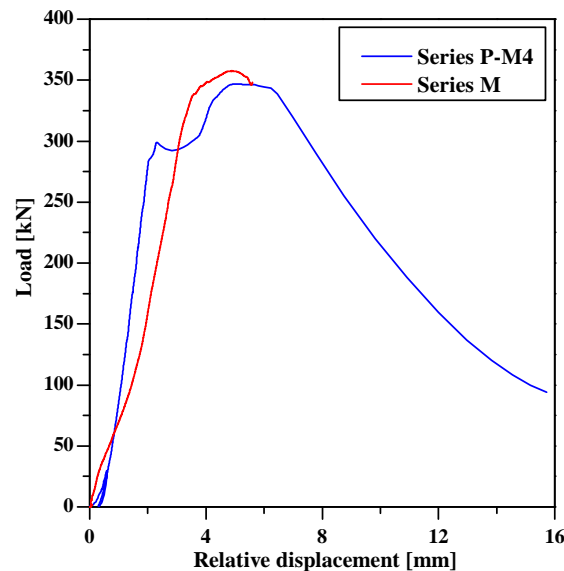


Figure 5.48.: Shear connection tests: load *vs.* relative displacement curves of series P-M4 and M.

The main difference between series M and P-M is the fact that the latter allowed for much higher post-failure relative displacement, while being able to sustain some load. This difference stems from the fact that the bond between the GFRP flanges and the epoxy mortar reinforced the flanges in the transverse direction, delaying the tearing of the flanges, which occurred after crushing.

## 5.2.6. Results and discussion — aged specimens

### 5.2.6.1. Thermal cycles

#### 5.2.6.1.1 Series A–Th–T1

Adhesively bonded specimens aged with thermal cycles during a period of 4 months, series A–Th–T1, presented little external (visible) signs of the accelerated aging process. All specimens presented linear behaviour almost up to failure, which occurred with a sudden loss of load, as depicted in the load–relative displacement curves plotted in Figure 5.49. It should be noted that the relative displacement for specimen A–Th–T1–2 could not be accurately measured for loads higher than approximately 270 kN due to the accidental movement of one of the displacement transducers.

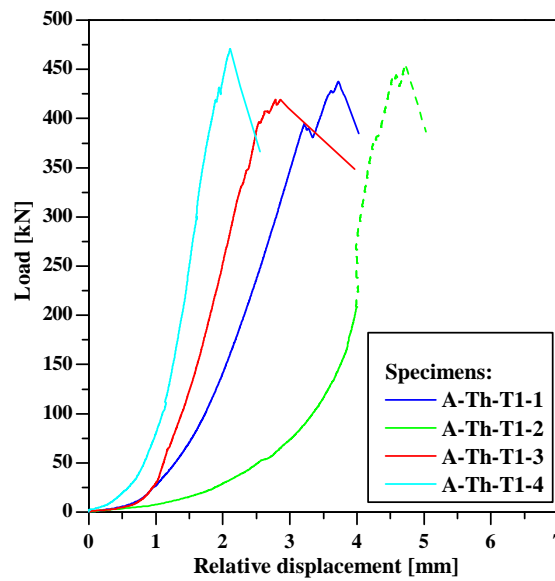


Figure 5.49.: Shear connection tests: load vs. relative displacement curves for series A–Th–T1.

For the present series, an average ultimate load ( $F_u$ ) of 445.9 kN (CoV of 5%) and stiffness ( $K$ ) of 241.4 kN/mm (CoV of 37%) were obtained. The complete results for all specimens are presented in Table B.10 (page 316). Unlike what was observed for their un-aged counterparts (*cf.* Section 5.2.5.1), the specimens of this series presented high scatter in terms of stiffness.

Figure 5.50 depicts several stages of the test of specimen A–Th–T1–2, as an example. All specimens failed due to debonding at the GFRP–SFRSCC interface, with no visible damage in the GFRP profile, namely at the web–flange junction, similarly to what was observed for the un-aged A series (*cf.* Section 5.2.5.1). The debonding damage occurred within the SFRSCC material, with a considerable thickness of the material being pulled out during the failure process.

#### 5.2.6.1.2 Series A–Th–T2

Specimens of series A–Th–T2, which also did not present external visible signs of aging, behaved similarly to those of the previous series. Figure 5.51 plots the load–displacement curves for all specimens. It should be noted that relative displacements of specimen



Figure 5.50.: Specimen A-Th-T1-2: a) beginning of the test; b) collapsed specimen; c) debonding failure in the SFRSCC; d) debonded surfaces.

A-Th-T2-1 could not be accurately determined for a load higher than approximately 320 kN, again due to the accidental movement of one of the displacement transducers. Additionally, specimen A-Th-T2-4 could not be tested up to failure due to an oil leakage in the hydraulic press system.

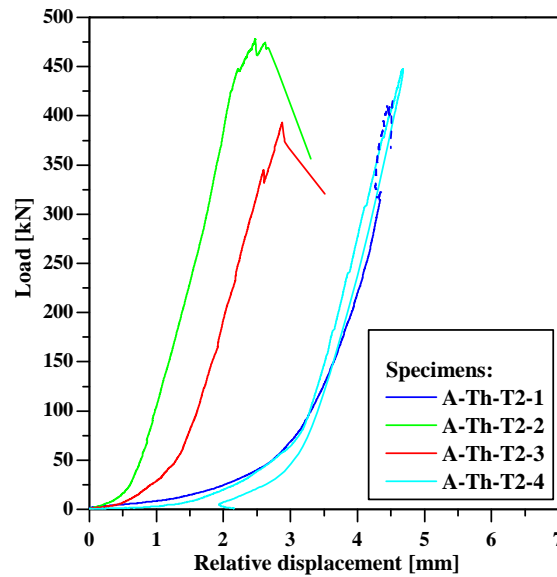


Figure 5.51.: Shear connection tests: load *vs.* relative displacement curves for series A-Th-T2.

An average ultimate load ( $F_u$ ) of 433.5 kN (CoV of 9%) and stiffness ( $K$ ) of 224.0 kN/mm (CoV of 16%) were obtained in these tests. The complete results for all specimens are presented in Table B.11 (page 316).

Specimens A-Th-T2-1 and A-Th-T2-3 failed due to the debonding of the interface, within the SFRSCC material. Specimen A-Th-T2-2, on the other hand, failed due to the debonding in one side of the specimen, presenting web-flange junction failure on the other side. During the test, it was possible to observe that the debonding process started before the web-flange junction failure. As an example of the typical failure mode, Figure 5.52 presents several stages of the test of specimen A-Th-T2-3.



Figure 5.52.: Specimen A-Th-T2-3: a) beginning of the test; b) collapsed specimen; c) SFRSCC failure surface; d) GFRP failure surface.

### 5.2.6.1.3 Series A-Th-T3

Specimens subjected to 8 months of thermal cycles accelerated aging showed external signs of the aging process, namely, corrosion of superficial steel fibres, as depicted in Figure 5.53.



Figure 5.53.: External signs of fibre corrosion in A-Th-T3 series, specimens: a) A-Th-T3-1; b) A-Th-T3-2; c) A-Th-T3-4; d) A-Th-T3-7.

The specimens of this series behaved similarly to the specimens of the remaining adhesively bonded series in terms of load–relative displacement curves, presenting linear behaviour almost up to failure, as shown in Figure 5.54.

For this series, an average ultimate load ( $F_u$ ) of 469.3 kN (CoV of 9%) and stiffness ( $K$ ) of 113.3 kN/mm (CoV of 23%) were obtained. The complete results for all specimens are presented in Table B.12 (page 317).

Figure 5.55 shows, as an example, several stages of the test of specimen A-Th-T3-2. All specimens failed due to the debonding of the GFRP–SFRSCC interface. Specimens presented visible debonding at both interfaces with failure occurring due to the complete debonding of one of the interfaces, with the exception of specimen A-Th-T3-5, which suffered complete debonding at both interfaces. The failure of the interfaces occurred mainly in the SFRSCC material, but with localized debonding patches in the epoxy adhesive itself, a phenomenon that had not been observed in the previous adhesively bonded series.

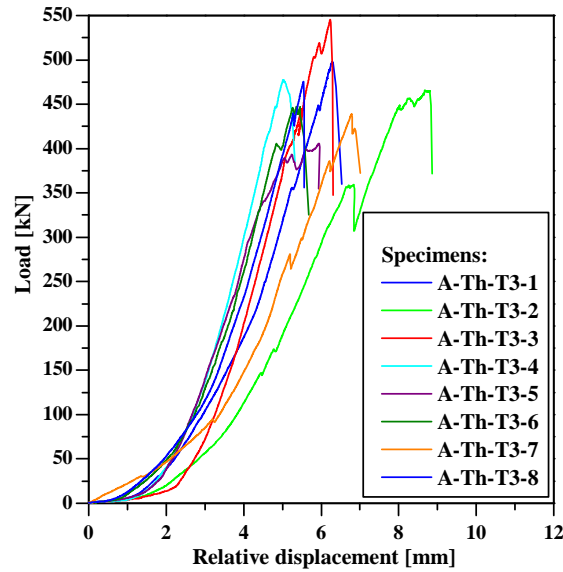


Figure 5.54.: Shear connection tests: load *vs.* relative displacement curves for series A-Th-T3.



Figure 5.55.: Specimen A-Th-T3-2: a) beginning of the test; b) collapsed specimen; c) incomplete debonding; d) failure surfaces.

#### 5.2.6.1.4 Comparative analysis

Figure 5.3.3.2 compares representative load-displacement curves of the adhesively bonded series (A) exposed to different periods of thermal cycles aging, while Table 5.5 summarizes the results for each test series. Figures 5.57 and 5.58 plot the evolution of the ultimate load ( $F_u$ ) and stiffness ( $K$ ), respectively, with the aging period.

These results indicate that the strength of the GFRP-SFRSCC adhesive connection increases with the number of thermal cycles, up to 19% after 32 weeks (or 224 cycles).

Although the scatter of the results obtained was relatively high (*cf.* Figure 5.57), preventing drawing definitive conclusions, the above mentioned increase may be due to the beneficial effect of the thermal cycles, namely of the elevated temperature on the strength of some of the constituent materials, as well as on the adhesive bonding itself.

Regarding the epoxy resin and the GFRP material, it is likely that further curing of the polymeric resins (of the adhesive itself and of the GFRP polymeric matrix) may have taken place during the thermal cycles [125–127]. Moussa *et al.* [126] have shown that heating epoxy adhesives (similar to that used in the present experiments) to temperatures

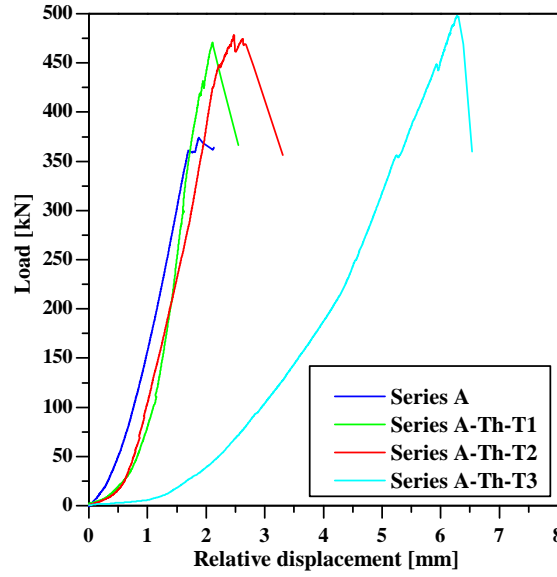


Figure 5.56.: Shear connection tests: comparison of load *vs.* relative displacement curves for different durations of thermal cycles aging (A series).

slightly exceeding their glass transition temperature ( $T_g$ ) and then cooling them to ambient temperature improves their strength and stiffness. Regarding the GFRP material, previous studies have shown that this type of thermal cycles has (very) limited deleterious effects or may even lead to improvements in material properties. As an example, Sousa *et al.* [125] have shown that GFRP profiles, made with a similar polyester matrix to those used in these test, subjected to dry thermal cycles between  $-5^\circ\text{C}$  and  $40^\circ\text{C}$ , up to 16 weeks, present relatively low mechanical properties variations, namely, ranging from  $-6.0\%$  to  $-13.1\%$  regarding the axial tensile strength ( $\sigma_{tu,L}$ ), and from  $-2.2\%$  to  $-14.7\%$  concerning the axial elasticity modulus in tension ( $E_{t,L}$ ).

The strength of the SFRSCC material, on the other hand, is not expected to suffer significant variations with this aging process, given the relatively low  $RH$  measured during the thermal cycles (*cf.* Figure 5.6) and the low porosity of the self-compacting concrete [127].

Regarding the effects of the thermal cycles in the stiffness of the connection, although the scatter was also relatively high, results show that this type of accelerated aging had remarkable effects, reducing the average stiffness down to half of that of the un-aged specimens ( $-54.6\%$ ) after 32 weeks (or 224 cycles). The unexpected drastic reduction of the stiffness of the connection from 24 to 32 weeks of aging (in particular, given the continuous strength increase), to magnitudes similar to those observed for the bolted connection

Table 5.5.: Shear connection test: summary of the results of series aged with thermal cycles.

Series	$F_u$		$K$		Typical failure mode
	(kN)	diff. (%)	(kN/mm)	diff. (%)	
A	$393.1 \pm 34.7$	-	$249.7 \pm 30.0$	-	1 <sup>st</sup> web-flange junction; 2 <sup>nd</sup> debonding
A-Th-T1	$445.9 \pm 22.4$	13.4%	$241.4 \pm 89.8$	-3.4%	Debonding
A-Th-T2	$433.5 \pm 37.2$	10.3%	$224.0 \pm 36.6$	-10.3%	Debonding
A-Th-T3	$469.3 \pm 41.6$	19.4%	$113.3 \pm 25.8$	-54.6%	Debonding

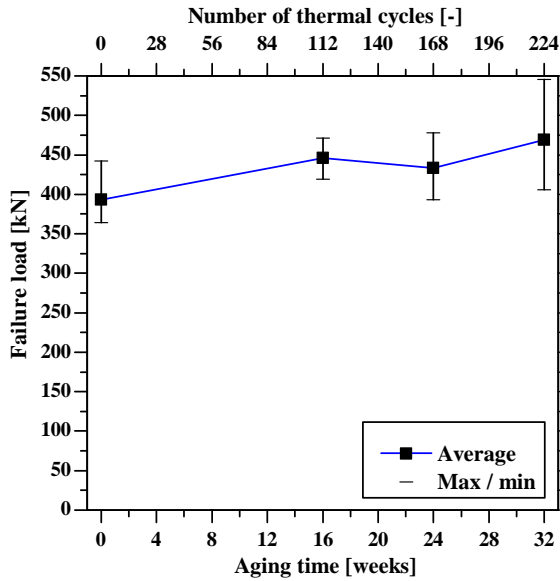


Figure 5.57.: Ultimate load vs. number of thermal cycles.

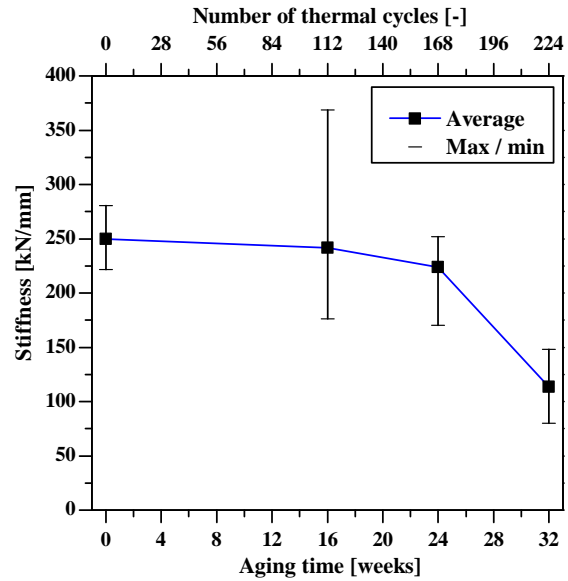


Figure 5.58.: Stiffness vs. number of thermal cycles.

(M series,  $K = 90.9 \pm 6.5$  kN/mm), indicates that the cumulative effect of the thermal cycles may have contributed to debond patches of the interface, possibly due to thermal fatigue effects in response to the internal stresses developed owing to different coefficients of thermal expansion of the materials. This hypothesis seems to agree with the slight change on the failure mode observed in series A-Th-T3, where failure did not occur exclusively on the SFRSCC, with failure patches being easily identified on the epoxy adhesive (*cf.* Figure 5.55d). It should be mentioned that the interface failure is generally governed by peak shear and peeling stresses, which usually develop in the extremities of the connection, with the bonding interface being able to present stress redistribution. This may explain why those failure patches in the adhesive did not cause a reduction in strength.

Overall, the results obtained attest the possibility of premature deterioration of the interface (even if the strength of the epoxy adhesive and of the interface increased) due to thermal effects, most likely caused by restrictions to free expansion and contraction of the constituent materials. This justifies the adoption of a redundant connection system.

### 5.2.6.2. Wet-dry cycles

#### 5.2.6.2.1 Series A-H-T1

Unlike the specimens aged with thermal cycles during the same period of time (series A-Th-T1), the specimens of the present series exhibited visible exterior signs of deterioration, namely, corrosion of the external steel fibres, as exemplified in Figure 5.59.

As shown in Figure 5.60, specimens of this series presented linear load-relative displacement behaviour almost up to failure, with the exception of specimen A-H-T1-2. In this specimen, the top of the GFRP profile, where the load was applied, presented an irregular surface, which caused the behaviour to be governed by the crushing of the GFRP top section instead





Figure 5.59.: External signs of fibre corrosion in A-H-T1 series, specimens: a) A-H-T1-2; b) A-H-T1-3; c) A-H-T1-4; d) A-H-T1-4.

of being governed by the GFRP-SFRSCC interface. Thereafter, the results obtained from this specimen were not considered in the determination of the average and standard deviation of the series; an average ultimate load ( $F_u$ ) of 375.5 kN (CoV of 16%) and stiffness ( $K$ ) of 119.3 kN/mm (CoV of 22%) were obtained. The complete results for all specimens are presented in Table B.13 (page 317).

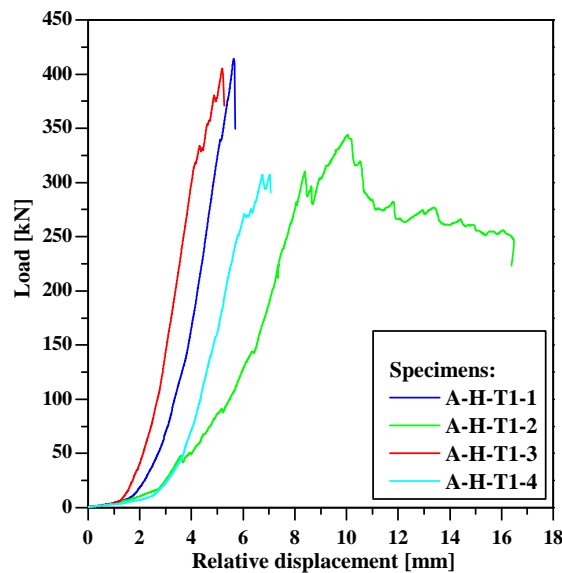


Figure 5.60.: Shear connection tests: load *vs.* relative displacement curves for series A-H-T1.

Figure 5.61 shows several stages of the test of specimen A-H-T1-3 (as an example). With the exception of specimen A-H-T1-2, which behaved irregularly as described earlier, all specimens failed due to the complete debonding at one of the GFRP-SFRSCC interfaces, with visible signs of debonding at the top of the interface on the opposite side of the specimen. The debonding surfaces show that failure was mixed with damage both on the SFRSCC and on the epoxy adhesive itself.

#### 5.2.6.2.2 Series A-H-T2

The specimens of this series also presented external signs of the effects of the aging process, namely corrosion of the steel fibres, as depicted in Figure 5.62.



Figure 5.61.: Specimen A-H-T1-3: a) beginning of the test; b) collapsed specimen; c) incomplete debonding; d) failure surfaces.



Figure 5.62.: External signs of fibre corrosion in A-H-T2 series, specimens: a) A-H-T2-1; b) A-H-T2-2; c) A-H-T2-3; d) A-H-T2-4.

All specimens presented similar load–relative displacement behaviour, with the exception of specimen A-H-T2-4. The remaining specimens presented linear behaviour almost up to failure, as shown in Figure 5.63. The behaviour of specimen A-H-T2-4 was governed by the crushing of the top of the GFRP profile, due to the irregularity of its loading surface. The results obtained with this specimen were not considered in the average and standard deviation results computed for the series. Regarding the apparent slip in the load–relative displacement curve of specimen A-H-T2-2, it was due to an adjustment made on the test setup during the test, and is not representative of the mechanical response of the specimen. Thus, the stiffness of this specimen was computed for loads over 105 kN only. Thereafter, an average ultimate load ( $F_u$ ) of 388.3 kN (CoV of 7%) and stiffness ( $K$ ) of 132.1 kN/mm (CoV of 25%) were obtained. The complete results for all specimens are presented in Table B.14 (page 318).

All specimens of this series presented different failure modes. Specimen A-H-T2-1 failed at both web–flange junctions, although it presented signs of debonding at the top of one of the interfaces. Specimen A-H-T2-2 presented web–flange junction failure at one of the sides of the specimen, which was followed by the complete debonding of the interface on the other side of the profile. Specimen A-H-T2-3 failed due to the complete debonding of one of the GFRP–SFRSCC interfaces. In both specimens, the debonding occurred mainly in the epoxy adhesive itself, unlike what was observed in the previous series. Finally, as mentioned earlier, specimen A-H-T2-4 failed due to the crushing of the GFRP profile top surface, not providing consistent information regarding the GFRP–SFRSCC connection. Figure 5.64 depicts several stages of the test of specimen A-H-T2-3.

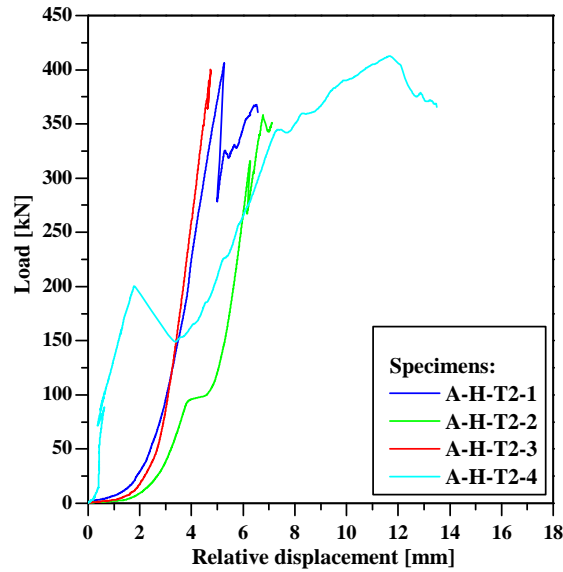


Figure 5.63.: Shear connection tests: load *vs.* relative displacement curves for series A-H-T2.



Figure 5.64.: Specimen A-H-T2-3: a) beginning of the test; b) collapsed specimen; c) failure surfaces; d) debonding in the epoxy resin.

#### 5.2.6.2.3 Series A-H-T3

Once again, specimens of series A-H-T3 presented external signs of fibre corrosion, due to the accelerated aging process to which they were subjected to, as shown in Figure 5.65.



Figure 5.65.: External signs of fibre corrosion in A-H-T3 series, specimens: a) A-H-T3-3; b) A-H-T3-3; c) A-H-T3-4; d) A-H-T3-4.

All specimens presented linear behaviour almost up to failure, with the exception of specimen A-H-T3-4, as depicted in Figure 5.66. The behaviour of specimen A-H-T3-4 was, for the most part, non-linear owing to the crushing of the top of the GFRP profile, due to the irregularity of the GFRP top surface. An average ultimate load ( $F_u$ ) of 387.6 kN (CoV of 12%) and stiffness ( $K$ ) of 99.3 kN/mm (CoV of 4%) were obtained for this series. The complete results for all specimens are presented in Table B.15 (page 318). In this case, the failure load of specimen A-H-T3-4 was accounted for in the calculations of the average and standard deviation values because, albeit the initial crushing of the GFRP, the final failure of the specimen was consistent with a typical shear connection failure (according to the previous results).

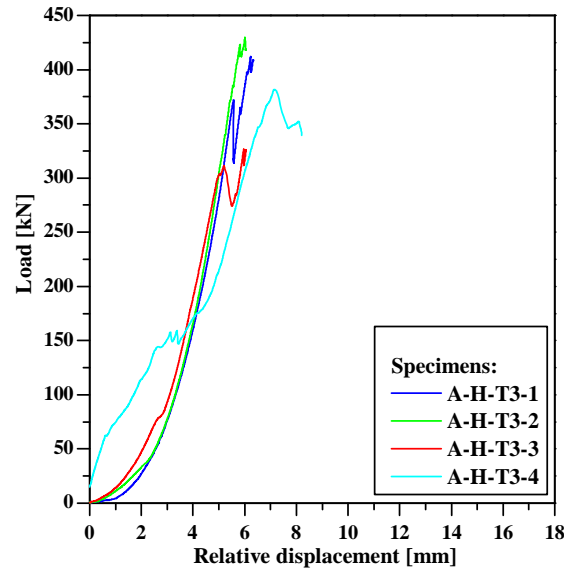


Figure 5.66.: Shear connection tests: load vs. relative displacement curves for series A-H-T3.

Figure 5.67 presents several stages of the test of specimen A-H-T3-1. Specimens A-H-T3-1 and A-H-T3-3 presented a similar failure mode, with the first damage appearing at the GFRP-SFRSCC interface, followed by the rupture of the web-flange junction on the other side of the specimens, which ultimately collapsed due to the complete debonding of the damaged interface. Specimen A-H-T3-2, on the other hand, failed due to the complete debonding of one of the interfaces without apparent signs of damage on the other side of the specimen. Finally, specimen A-H-T3-4 presented extensive crushing damage since the beginning of the test, but ultimately collapsed due the separation of one of the web-flange junctions.

#### 5.2.6.2.4 Series AM-H-T3

The specimens of series AM-H-T3 also presented significant external signs of fibre corrosion, as documented in Figure 5.68.

The three specimens tested in this series presented linear behaviour almost up to failure, as shown in Figure 5.69. The relative displacement of specimen AM-H-T3-3 could only be measured up to the first peak load, after which some of the displacement transducers moved. An average ultimate load ( $F_u$ ) of 498.4 kN (CoV of 4%) and stiffness ( $K$ ) of 127.0 kN/mm (CoV of 35%) were obtained in these tests.



Figure 5.67.: Specimen A-H-T3-1: a) beginning of the test; b) collapsed specimen; c) web-flange junction failure; d) failure surfaces.



Figure 5.68.: External signs of fibre corrosion in AM-H-T3 series, specimens: a) AM-H-T3-1; b) AM-H-T3-2; c) AM-H-T3-3; d) AM-H-T3-3.

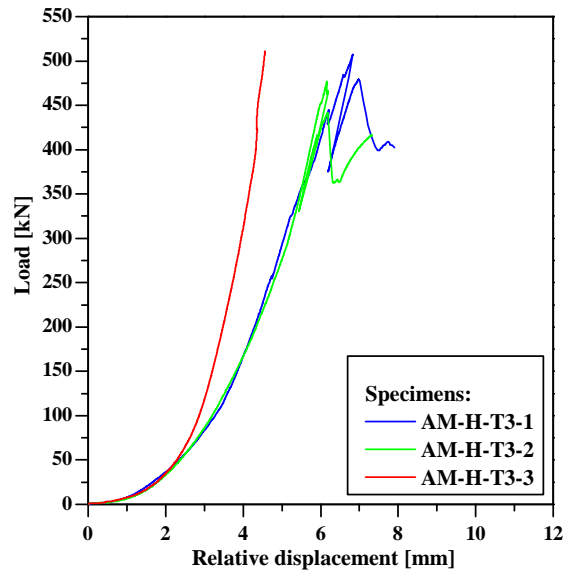


Figure 5.69.: Shear connection tests: load vs. relative displacement curves for series AM-H-T3.

The failure initiation of the first specimen (AM-H-T3-1) was due to the debonding of one of the GFRP-SFRSCC interfaces, after which the bolts began to crush the GFRP flange, with visible deformations on that same side of the specimens. Finally, the web-flange junction on the opposite side of the specimen failed, leading to its collapse. The failure of specimen



AM-H-T3-2 also began with the debonding of one of the GFRP-SFRSCC interfaces. In this case, however, instead of GFRP flanges' crushing by the bolts, the interface opening began to grow with the epoxy mortar sliding out of its slab negative. The collapse of the specimen occurred when the web-flange junction on the opposite side failed. Finally, the failure of specimen AM-H-T3-3 began with the debonding of the GFRP-SFRSCC interface at one side of the specimen, followed by the debonding on the opposite side. After the debonding of both adhesive connections, bolts began to deform visibly, while crushing both GFRP flanges until the specimen collapsed, due to the failure of one of the web-flange junctions. Figure 5.70 presents several stages of the test of the latter specimen as an example.



Figure 5.70.: Specimen AM-H-T3-3: a) beginning of the test; b) collapsed specimen; c) crushing of the flange; d) web-flange junction failure.

### 5.2.6.2.5 Comparative analysis

Figures 5.71 and 5.72 plot representative load-relative displacement curves for the series subjected to different periods of aging under wet-dry cycles, regarding series A and AM, respectively.

Table 5.6 summarizes the results of the test series aged with wet-dry cycles and compares the results obtained to those obtained with their un-aged counterparts (series A or AM). Figures 5.73 and 5.74 plot those same results with respect to the failure load ( $F_u$ ) and the stiffness ( $K$ ).

Table 5.6.: Shear connection tests: summary of the results of series aged with wet-dry cycles.

Series	$F_u$		$K$		Typical failure mode
	(kN)	diff. (%)	(kN/mm)	diff. (%)	
A	393.1±34.7	-	249.7±30.0	-	1 <sup>st</sup> web-flange junction; 2 <sup>nd</sup> debonding
A-H-T1	375.5±59.3	-4.5%	119.3±26.5	-52.2%	Debonding
A-H-T2	388.3±26.1	-1.2%	132.1±33.1	-47.1%	Various
A-H-T3	387.8±45.3	-1.4%	99.3±4.2	-60.3%	1 <sup>st</sup> web-flange junction; 2 <sup>nd</sup> debonding
AM	508.7±81.6	-	297.0±32.5	-	1 <sup>st</sup> debonding; 2 <sup>nd</sup> web-flange junction
AM-H-T3	498.4±18.5	-2.0%	127.0±44.5	-57.3%	1 <sup>st</sup> debonding; 2 <sup>nd</sup> crushing; 3 <sup>rd</sup> web-flange junction

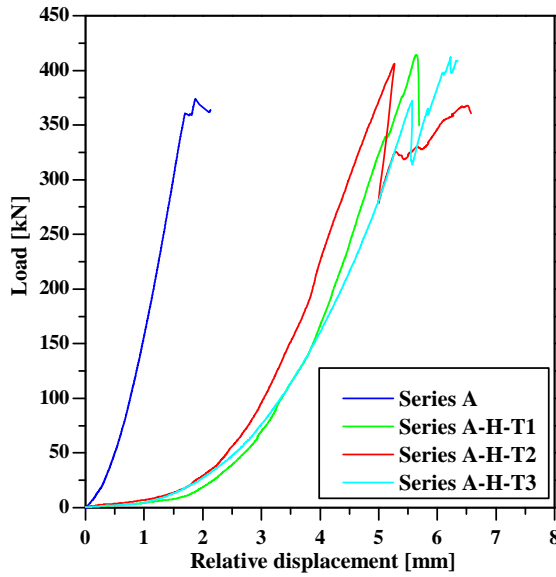


Figure 5.71.: Shear connection tests: comparison of load *vs.* relative displacement curves for different durations of wet-dry cycles aging (A series).

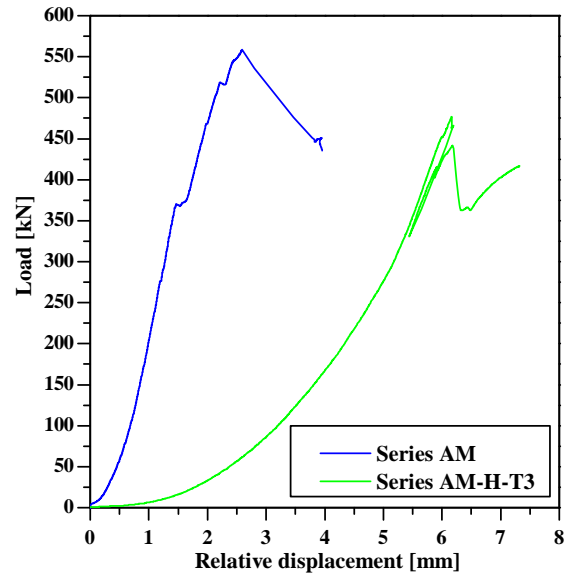


Figure 5.72.: Shear connection tests: comparison of load *vs.* relative displacement curves for different durations of wet-dry cycles aging (AM series).

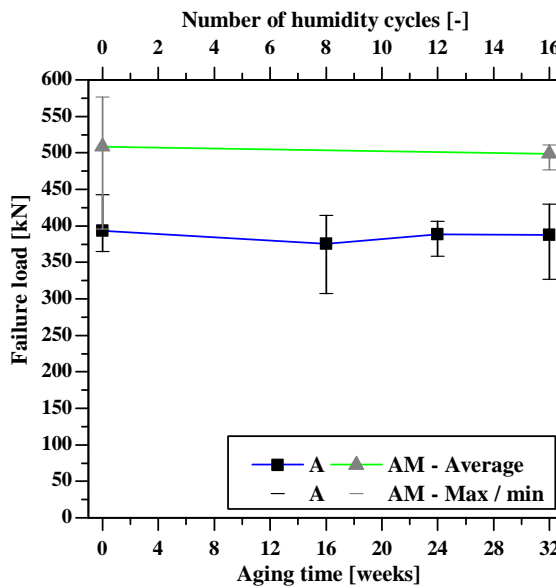


Figure 5.73.: Ultimate load *vs.* number of wet-dry cycles.

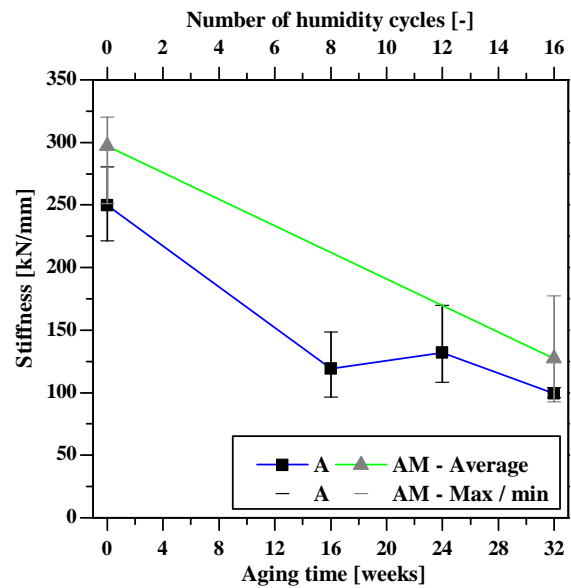


Figure 5.74.: Stiffness *vs.* number of wet-dry cycles.

The results indicate that the wet-dry cycles do not influence the strength of the GFRP-SFRSCC connection, with results presenting small variations (maximum of 5%) with the time of aging, well within the experimental scatter, for both A and AM series.

The stiffness of the connection, on the other hand, appears to be strongly influenced by the wet-dry cycles, with a reduction, when compared to series A, of -52% after 16 weeks of aging, and up to -60% after 32 weeks of aging. Although the specimens were not subjected

to high temperatures during the wet–dry cycles, the water saturation of the thermosetting resins (polyester of the GFRP profiles and epoxy adhesive), which seems to have occurred after 16 weeks of aging (given the low additional deterioration that followed) causes a phenomenon known as plasticization that involves considerable reduction of both stiffness and strength [128,129]. When subjected to wet–dry cycles aging, the mechanical behaviour of thermosetting resins is also known to degrade, owing to chemical reactions at the molecular level, which include chain scission [129]; this phenomenon, known as hydrolysis, must also have contributed to the stiffness reduction observed in these tests.

As an example, Borges [130] has shown that the tensile properties of a GFRP pultruded material (with a similar polyester matrix to that used here) present small variations when subjected to water immersion at 20°C up to 24 weeks, namely ranging from -7.3% to -7.5% regarding the tensile strength ( $\sigma_{tu,L}$ ), and from +1.1% to -4.5% concerning the elasticity modulus in tension ( $E_{t,L}$ ) in the longitudinal direction. Cabral–Fonseca *et al.* [128], adopting a similar aging process but testing the GFRP material in a saturated condition, reported considerably higher reductions on those material properties.

In summary, the faster degradation of the stiffness of specimens subjected to wet–dry cycles, when compared to those subjected to thermal cycles, is likely to be due to a combination of both degradation phenomena: plasticization and hydrolysis.

Regarding the fact that the AM series presented a similar reduction of stiffness (-57% after 32 weeks of aging) to that observed for the A series, confirms that the stiffness of the former specimens is governed by the adhesive bond.

### 5.2.6.3. Summary

The results presented in the previous sections show that the accelerated aging of GFRP–SFRSCC shear connection test specimens, both with thermal and wet–dry cycles, has a strong influence in the behaviour of the specimens, namely concerning the stiffness of the adhesive connection. On the other hand, the aging processes seem to have little influence on the strength of the connections. In fact, the thermal cycle aging even appears to have caused a post–curing effect on the interface, increasing its strength (up to +19%). Figures 5.75 and 5.76 illustrate the evolution of the ultimate load and stiffness of adhesively bonded specimens (A series), respectively, with the aging time, comparing the influence of the thermal cycles with that of the wet–dry cycles.

Figure 5.75 shows that the specimens aged with wet–dry cycles maintain the same magnitude of strength independently of the aging time, while specimens aged with thermal cycles show a slight increase of the ultimate load with the increase of the aging time. Regarding the stiffness of the adhesive connection, both aging processes led to similar decreases after 32 weeks of aging (-55% and -60% for the thermal and wet–dry cycles, respectively). Nevertheless, Figure 5.76 shows that the trends of the reduction were very different. The specimens subjected to wet–dry cycles presented a large reduction from 16 weeks of aging (-52%) and the results suggest that the performance reduction stabilized from that point on. Specimens aged with thermal cycles, on the other hand, presented a relatively low stiffness decrease at 24 weeks of aging (-10%), which was followed by a sharp drop at 32 weeks of aging, raising concerns about the stiffness variation for longer aging periods. This result, which must be confirmed by more (and longer) experimental campaigns, further attests the importance of providing a redundant shear connection system, such as the hybrid system proposed herein.



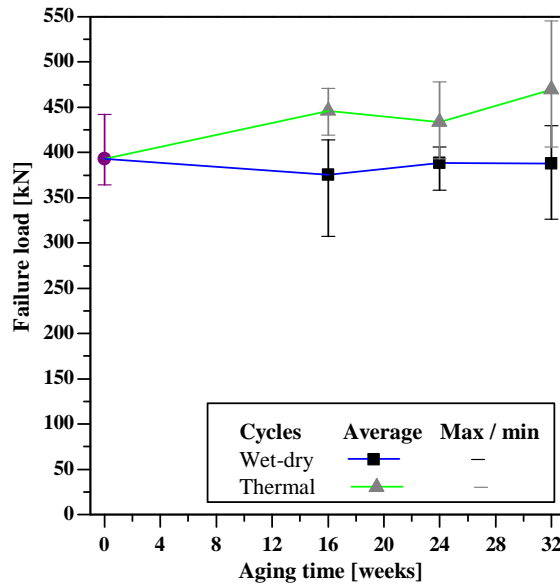


Figure 5.75.: Ultimate load vs. duration of aging.

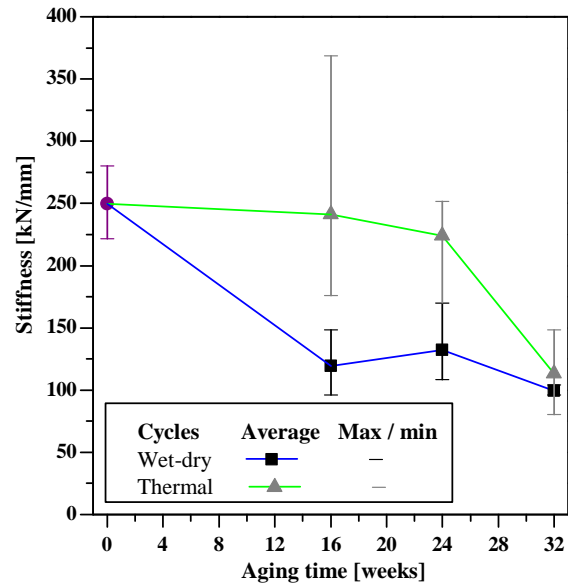


Figure 5.76.: Stiffness vs. duration of aging.

## 5.3. Numerical simulations

### 5.3.1. Objectives

In order to improve the understanding of the mechanical behaviour of the GFRP-SFRSCC adhesively bonded connections, numerical models were developed to simulate the shear connection tests described earlier. The development of these models aimed at assessing the feasibility of using simple bi-linear bond-slip laws to simulate the behaviour of GFRP-concrete adhesive connections, in order to integrate these laws in the modelling of full-scale hybrid GFRP-concrete structures.

The numerical models developed aimed at simulating the load-relative displacement behaviour observed both for the un-aged specimens (series A) and for the specimens aged with thermal (series A-Th) and wet-dry (series A-H) cycles. Furthermore, these models aimed at predicting the failure load and typical failure mode observed for each series, helping to further explain the evolution of these parameters with the aging time.

In order to achieve those objectives, the relevant parameters governing the GFRP-SFRSCC interface behaviour were calibrated to provide a good agreement between experimental and numerical results.

### 5.3.2. Description of the FE models

#### 5.3.2.1. Geometry, elements and boundary conditions

The tri-dimensional FE models used in these analyses were developed with the commercial package *ABAQUS* [97]. In order to reduce the computational costs, only a quarter of the shear connection specimens was modelled using symmetry boundary conditions.

The models comprise 8-node brick elements (*C3D8*), with three degrees of freedom (translation) per node, simulating the GFRP and SFRSCC materials. The epoxy adhesive was not explicitly modelled, with no gap being considered between the GFRP and SFRSCC materials. As an alternative, the properties of the interface were directly considered in the model, as will be further explained, including its 2 mm thickness.

In addition to the symmetry boundary conditions mentioned earlier, all degrees of freedom were fully restrained at the bottom nodes of the SFRSCC slab, simulating the contact of the specimen with the floor/bottom plate of the hydraulic press. Figure 5.77 shows an overview of the model.

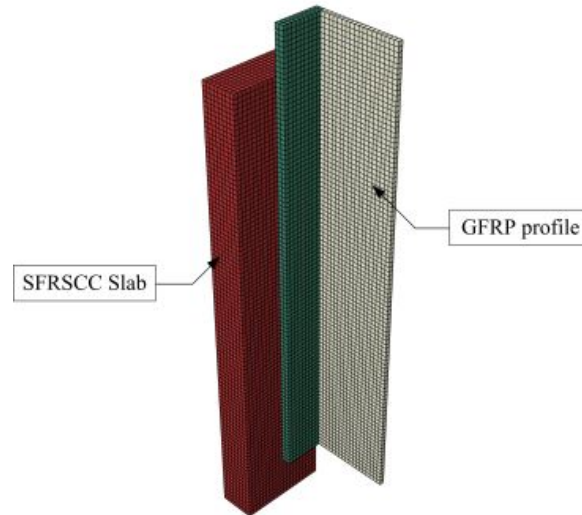


Figure 5.77.: Overview of the FE model.

### 5.3.2.2. Material properties

The GFRP pultruded profiles were modelled considering two different materials for the flange and the web. Both materials were modelled as orthotropic, considering the material properties obtained in the coupon tests (*cf.* Table 4.13, page 71). With this respect, it should be mentioned that the shear properties were considered to be the same in every direction, and that the properties in the direction normal to the plates were considered to be the same as those in the transverse direction. With respect to the latter assumption, it should be mentioned that, although the mechanical properties of the flange plates in the normal direction may have some influence in the interface behaviour (namely in the response to peeling stresses), since the interface failure modes observed in the experiments were due to the cohesive failure inside the concrete substrate or, for some cases, in the adhesive itself (and never in the GFRP profile), the relative importance of these properties is deemed to be low. The GFRP materials were considered to be linear-elastic.

The SFRSCC material was modelled as isotropic, considering the material properties derived from coupon testing at 28 days of age (*cf.* Table 4.30, page 111). The models allowed for concrete damage, namely in compression and in tension, using standard damage and plasticity models of the FE commercial package [97]. Nevertheless, all simulations performed were well within the elastic range considered for the SFRSCC and, therefore, concrete damage was not actually used.

The effects of the aging processes on the mechanical properties of the materials were not considered in the FE models because, since the primary failure mode of adhesively bonded specimens was on the interface, relatively small variations on these properties are deemed to have little influence on the behaviour of the specimens, which is governed by the GFRP–SFRSCC interface, modeled with constitutive laws.

### 5.3.2.3. GFRP–concrete interface constitutive laws

The GFRP–concrete interface constitutive laws adopted in the present study were defined based on bi-linear bond-slip curves, as depicted in Figure 5.78. This type of constitutive law was chosen owing to its simplicity and due to the fact that it was successfully used to describe the mechanical behaviour of FRP–concrete interfaces, namely carbon fibre reinforced polymer (CFRP)–concrete interfaces [21].

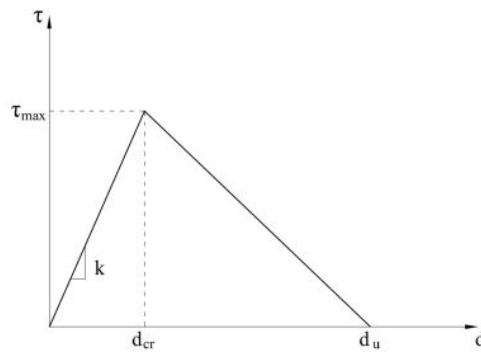


Figure 5.78.: Bi-linear shear bond-slip law adopted.

In the FE software package used [97], the calibration of the bi-linear bond-slip law is performed by adjusting three parameters: (i) the maximum stress ( $\sigma_{max}$  and  $\tau_{max}$ , for normal and shear stresses, respectively); (ii) the stiffness of the interface ( $k$ ); and (iii) the softening slip ( $d_{soft}$ ), which is defined by the difference between the ultimate slip ( $d_u$ ) and the critical slip ( $d_{cr} = \sigma_{max}$  (or  $\tau_{max})/k$ , cf. Figure 5.78). The first parameter governs the interface failure initiation, while the third parameter governs the behaviour of the softening stage. Together, these parameters can be used to define the strength and failure behaviour of the modelled specimens. The second parameter, on the other hand, governs the stiffness.

The constitutive law can be defined independently for normal stresses and shear stresses in both directions. In this particular case, since the specimens' response is governed by the shear behaviour in the longitudinal direction, the behaviour of the interface was modelled as isotropic. The calibration of the above mentioned parameters was performed considering a 2 mm thick interface, which corresponds to the thickness of the epoxy adhesive layer used in the experimental tests (cf. Section 5.2.2).

Since the strength predicted by the FE models can be calibrated with two different parameters,  $\tau_{max}$  and  $d_{soft}$ , the first parameter was adjusted in order for the FE models' first stiffness loss (which corresponds to the beginning of the interface slip) to occur for load levels of the same magnitude as those observed in the experimental tests' first discontinuity/stiffness loss. It should be mentioned that, for some cases, these stiffness reductions were minor and, therefore, not evident from the load *vs.* relative displacement curves. Thereafter, the second parameter ( $d_{soft}$ ) was calibrated in order for the ultimate load ( $F_u$ ) of the FE models to match such average value for each series. The stiffness parameter

( $k$ ) was calibrated in order for the stiffness ( $K$ ) of the FE models to match the average stiffness observed for each series.

#### 5.3.2.4. Type of analyses

In order to simulate the behaviour of the specimens, namely their load *vs.* relative displacement curves up to the post-failure softening regime, the numerical analyses were performed by applying an imposed displacement to the top of the GFRP profile, rather than applying a load. This method allows the control of the post-peak responses, which occur in the softening stage of the bond-slip law used [131]. Owing to the low load application rate used in the experimental test, it was possible to perform static non-linear analyses. The analyses were performed for the complete range of imposed displacement, except for the cases in which the final iteration diverged in the post-peak stage, indicating the collapse of the specimen.

### 5.3.3. Results and discussion

#### 5.3.3.1. Un-aged specimens

The bi-linear bond-slip law (*cf.* Figure 5.78) calibrated according to the experimental results comprised the following parameters: (i)  $\sigma_{max} = \tau_{max} = 6$  MPa; (ii)  $k = 6$  MPa/mm; and (iii)  $d_{soft} = 0.5$  mm. Figure 5.79 compares the load *vs.* relative displacement curves observed in the experimental tests (the initial accommodation was eliminated in order to enable the comparison) to those obtained with the FE model.

Figure 5.80 presents the evolution of the axial strains in the GFRP side of the interface, comparing the experimental results obtained for specimen A-4 to those obtained with the FE model. The results show that the FE model was able to simulate the overall evolution of the axial strains, presenting larger differences from the experimental results at depths between 200 mm and 300 mm. It should be referred that the inflection measured in the experimental tests in the latter depth range was not expected and could be due to a faulty installation of the strain gauges, as mentioned earlier. Furthermore, most likely owing to the smaller accuracy of the gauges in measuring relatively low strains, the comparison between experimental and numerical results improves with the load increase.

Overall, the results predicted with the FE model show an excellent agreement with those measured in the tests, namely regarding the ultimate load ( $F_u$ ) and the stiffness ( $K$ ), with relative differences of +5% and +3%, respectively. Additionally, the FE model was able to predict the overall strain distribution throughout the depth of the interface.

Regarding the failure mode, the FE model correctly predicted the initial failure in the GFRP-SFRSCC interface, as observed experimentally. Figure 5.81 plots the load *vs.* relative displacement curve obtained with the FE model together with the evolution of the Tsai-Hill index (*cf.* Eq. (4.45), Section 4.2.3.4) on the web-flange junction of the GFRP, which is the area with higher stresses. Regarding this issue, it should be mentioned that the SFRSCC material remained in the elastic regime throughout the simulation. These results show that the failure is triggered well before the failure initiation in the GFRP material.

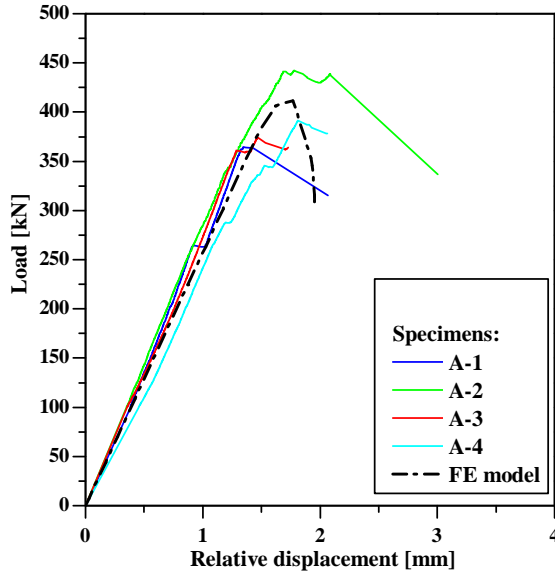


Figure 5.79.: Shear connection tests: load vs. relative displacement curves for series A — experiments and FE model.

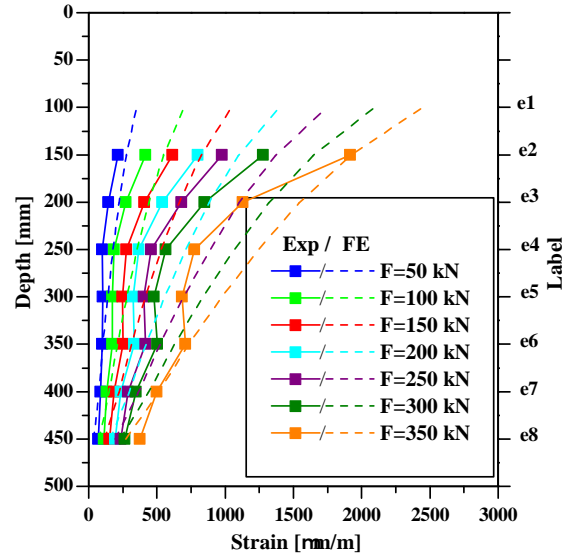


Figure 5.80.: Shear connection tests: strain measurements at the interface for specimen A-4 — experimental and numerical results.

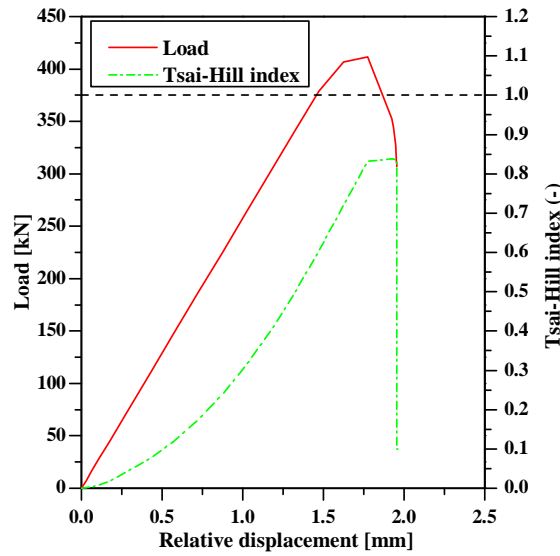


Figure 5.81.: Shear connection tests: load and Tsai-Hill index vs. relative displacement curves obtained with the FE model.

### 5.3.3.2. Specimens aged with thermal cycles

Regarding the specimens aged with thermal cycles, the bi-linear bond-slip law (*cf.* Figure 5.78) was calibrated for each aging period according to the corresponding experimental results. The calibrated parameters are listed in Table 5.7, which also summarizes the results obtained with the FE models showing the relative differences compared to the experimental results.

Table 5.7.: Shear connection FE model, thermal cycles: calibration parameters, numerical results and comparison with experimental results.

Series	Calibration parameters			Results				Failure on
	$\tau_{max}$	$k$	$d_{soft}$	$F_u$		$K$		
	MPa	MPa/mm	mm	kN	diff.	kN/mm	diff.	
A	6	6	0.5	411.4	+4.7%	257.6	+3.2%	Interface
A-Th-T1	6	6	0.75	429.1	-3.8%	257.6	+6.7%	Interface
A-Th-T2	6	5	0.75	438.7	+1.2%	234.6	+4.8%	Interface
A-Th-T3	6	1.5	1	490.6	+4.5%	105.4	-7.0%	Interface

The value of  $\tau_{max}$  was calibrated in order for the FE model to present similar failure initiation load to that obtained in the experimental tests (for some cases, it was hard to detect by analysing the load–relative displacement curves). In this regard, since the failure initiation occurred at sensibly the same load regardless of the aging period, the latter parameter was equal for all specimens. Accordingly, the  $d_{soft}$  parameter was then calibrated with regard to the ultimate load, resulting in larger softening branches for specimens subjected to larger aging periods. This evolution is in accordance with the effects of the thermal cycles aging process, previously discussed in Section 5.2.6.1.4. Additionally, it should be noticed that the  $k$  parameter has a minor influence on the ultimate load, as attested by the different ultimate loads obtained for specimens A–Th–T1 and A–Th–T2, which have the same  $\tau_{max}$  and  $d_{soft}$ .

Figure 5.82 compares the load *vs.* relative displacement curves predicted with the FE models with those obtained in the experimental tests, showing a good agreement. As for the previous series, the initial non-linear behaviour of the experimental curves (*cf.* Figure ), due to the accommodation of the experimental setup, was eliminated in order to facilitate the comparison with the numerical results.

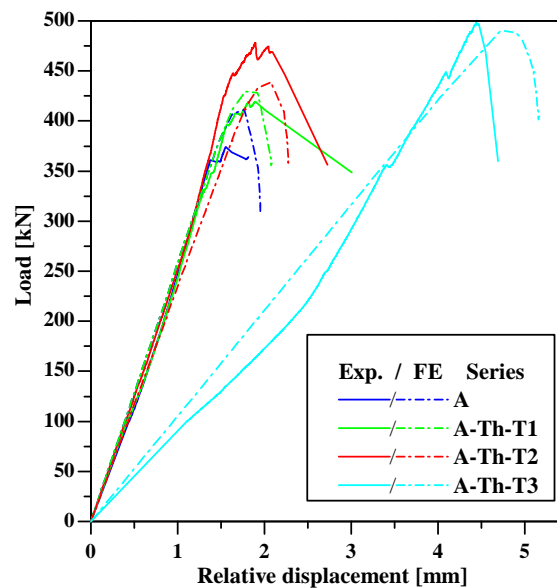


Figure 5.82.: Shear connection tests: load *vs.* relative displacement curves for series A specimens aged with thermal cycles — experiments and FE model.

Figures 5.83 and 5.84 compare the experimental and numerical results regarding the evolution of the ultimate load ( $F_u$ ) and the stiffness ( $K$ ), respectively, with the aging time. These results show that the FE models were able to determine the experimental results well within the maximum and minimum values obtained for each series.

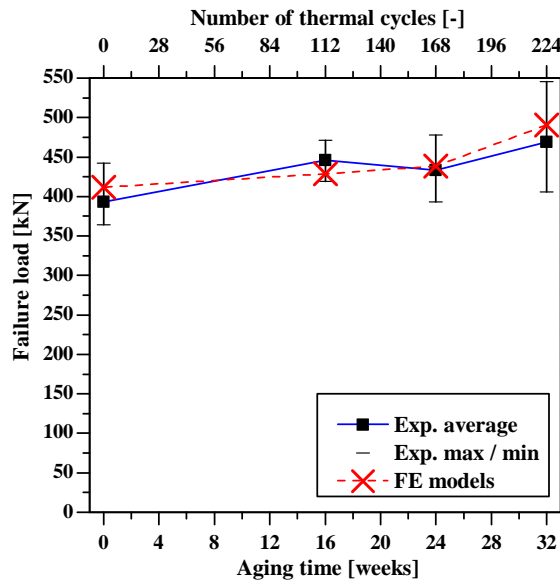


Figure 5.83.: Ultimate load *vs.* duration of thermal cycles aging: experimental and numerical results.

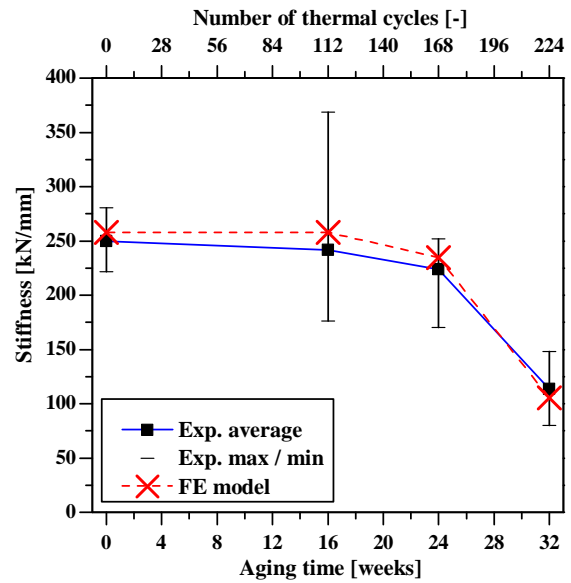


Figure 5.84.: Stiffness *vs.* duration of thermal cycles aging: experimental and numerical results.

All the modelled specimens failed due to the debonding of the interface, as shown in Figure 5.85, which plots both the load *vs.* relative displacement and the Tsai-Hill index (for the GFRP) *vs.* relative displacement curves obtained with the FE model, for all periods of aging. However, Figure 5.85 shows that, for series A-Th-T3, the Tsai-Hill index is higher than 1.0 before the ultimate load ( $F_u$ ) is achieved. This result indicates that at this point, which is after the beginning of the debonding process, failure initiation at the GFRP web-flange junction should occur, a phenomenon that was not observed experimentally. This apparent contradiction with the experimental results may be due to several reasons: (i) after failure initiation, the FE model, unlike the specimens used in the experimental tests, is not able to redistribute stresses between the two GFRP-SFRSCC interfaces; (ii) the GFRP material strength is known to increase when subjected to thermal cycles aging [125]; and (iii) the Tsai-Hill failure criterion estimates, conservatively, the failure initiation, which may occur in the GFRP material without visible signs of damage.

### 5.3.3.3. Specimens aged with wet-dry cycles

Similarly to what was performed for the specimens aged with thermal cycles, the bi-linear bond-slip law (*cf.* Figure 5.78) of the specimens aged with wet-dry cycles was calibrated, for each aging period, according to the experimental results. Table 5.8 presents the calibrated parameters and summarizes the results obtained with the FE models, showing the relative difference when compared to the corresponding experimental results.

For the wet-dry cycles aged specimens, unlike what occurred for the specimens aged with thermal cycles, the failure initiation occurred for a lower load than that of the un-aged

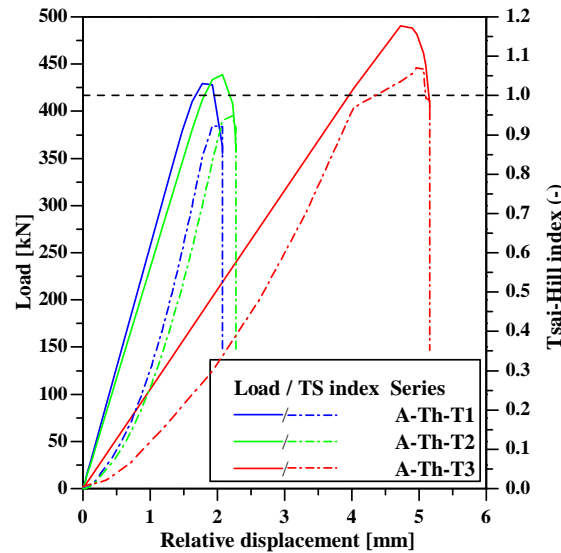


Figure 5.85.: Shear connection tests: load and Tsai–Hill index *vs.* relative displacement curves obtained with the FE model considering thermal cycles aging.

specimens, resulting in the adoption of a lower  $\tau_{max}$  parameter. On the other hand, the ultimate load variations with the aging period were almost null, allowing the adoption of the same  $d_{soft}$  parameter for all specimens. Regarding the stiffness variations, since series A–H–T1 and series A–H–T2 presented very similar experimental results, the same  $k$  parameter was adopted in both simulations, resulting in the adoption of the same exact GFRP–concrete interface constitutive law. Once again, comparing the failure loads obtained for specimens A–H–T1/T2 and A–H–T3, it is possible to attest the minor influence of the  $k$  parameter in the failure of the modelled specimens. It should also be mentioned that the evolution of the  $k$  parameter with the aging period is in accordance with the effects of the plasticization and hydrolysis phenomena discussed earlier in Section 5.2.6.2.5.

Figure 5.86 plots the load *vs.* relative displacement curves predicted with the FE models and compares them to those observed experimentally, showing once again a good agreement (the initial non–linear behaviour of the experimental curves was eliminated in this figure in order to facilitate the comparison with the numerical results).

The evolution of the ultimate load ( $F_u$ ) and the stiffness ( $K$ ) with the aging time is plotted in Figures 5.87 and 5.88, respectively. These results confirm the accuracy of the FE models, which were able to predict the experimental results within the scatter of each series, with

Table 5.8.: Shear connection FE model, wet–dry cycles: calibration parameters, numerical results and comparison with experimental data.

Series	Calibration parameters			Results				
	$\tau_{max}$	$k$	$d_{soft}$	$F_u$		$K$		Failure on
	MPa	MPa/mm	mm	kN	diff.	kN/mm	diff.	
A	6	6	0.5	411.4	+4.7%	257.6	+3.2%	Interface
A-H-T1	5	2	0.5	395.1	+5.2%	131.0	+9.9%	Interface
A-H-T2	5	2	0.5	395.1	+1.8%	131.0	-0.8%	Interface
A-H-T3	5	1.5	0.5	398.8	+2.9%	105.4	+6.2%	Interface



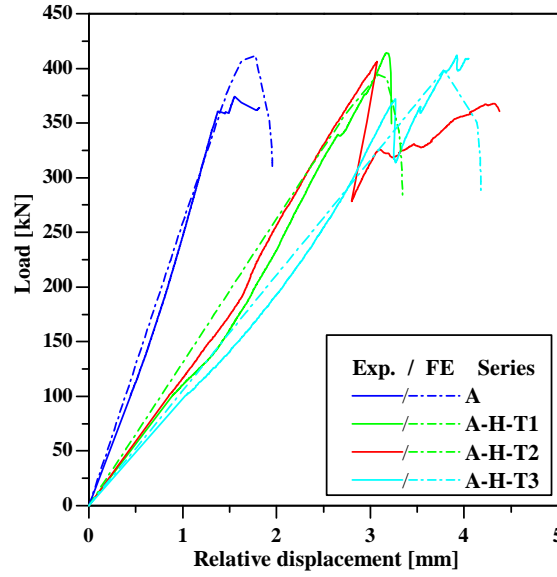


Figure 5.86.: Shear connection tests: load *vs.* relative displacement curves for A specimens aged with wet-dry cycles — experiments and FE model.

the exception of the stiffness for series A-H-T3, which presented the smallest scatter within the experimental campaign (CoV of 4.3%, *cf.* Table 5.6).

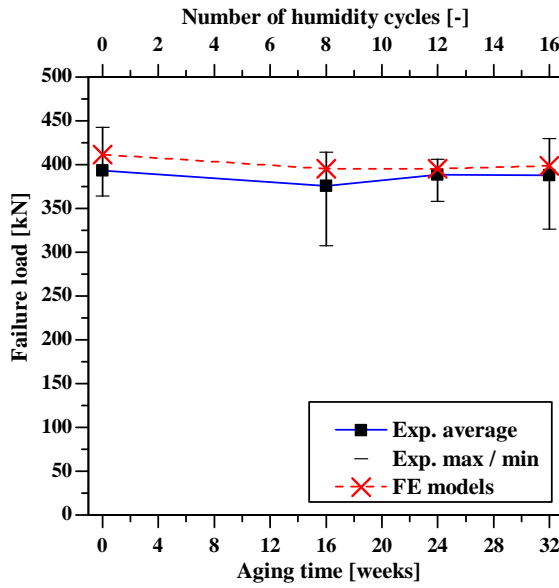


Figure 5.87.: Ultimate load *vs.* duration of wet-dry cycles aging: experimental and numerical results.

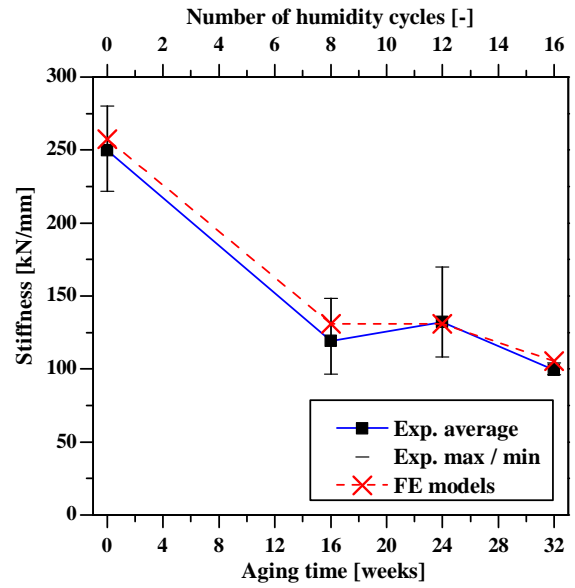


Figure 5.88.: Stiffness *vs.* duration of wet-dry cycles aging: experimental and numerical results.

The FE models indicate that failure is due to the debonding at the interface, which occurs, in all cases, for relatively low values of the Tsai-Hill index (approx. 0.7), as shown in Figure 5.89. These results are in agreement with the failure modes observed experimentally (*cf.* Table 5.6), except for series A-H-T2, for which it was not possible to determine a typical failure mode.

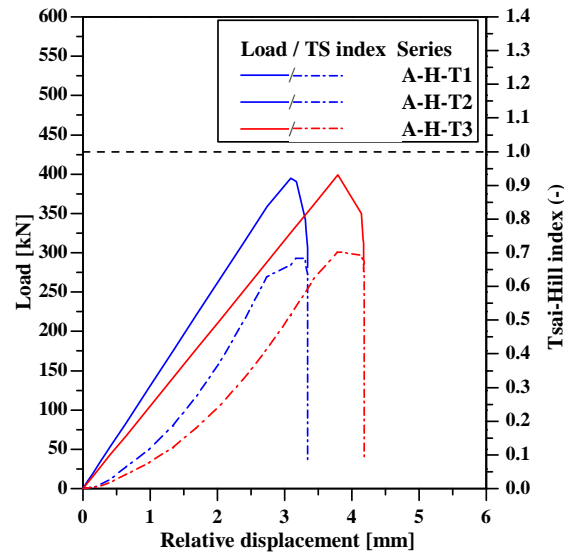


Figure 5.89.: Shear connection tests: load and Tsai–Hill index *vs.* relative displacement curves obtained with the FE model considering wet–dry cycles aging.

## 5.4. Final remarks

The experiments presented in this chapter have shown that the GRFP–SFRSCC connection can be effectively performed with both (i) an epoxy adhesive, and (ii) a bolted connection.

The bolted connection was tested with several arrangements of connectors, showing that it is possible to group connectors in relatively small sockets, increasing the overall strength with relatively low reductions of strength per bolt.

The adhesive connection proved to be much stiffer than the bolted connection (+175%), but presented similar strength when four pairs of bolts were used (+9%). The hybrid (redundant) connection system, with both adhesive and bolts, presented higher stiffness than that of the adhesive connection alone (+19%), although due to the high scatter of the test series (CoV of 11% and 12%) this difference may not be significant. Regarding strength, the redundant connection presented higher ultimate load than the adhesive connection alone (+29%). This result may be due to the fact that the bolts delay the opening of the interface by withstanding the peeling stresses developed during the test. Another important difference between the redundant and the simply bonded connection is the fact that the failure of the former is pseudo–ductile, while the failure of the latter is brittle.

The results obtained indicate that a hybrid connection system, provided by both adhesive bonding and bolts, may increase the strength of the interface and lead to a pseudo–ductile failure instead of the brittle failure achieved with a simply bonded connection.

Regarding the possible deterioration of the connection system with time, the results of the specimens aged with thermal cycles showed that the strength of the interface could in fact increase up to 19% after 32 weeks of aging. For the same aging process the stiffness presented significative reductions, up to -55% after 32 weeks. Specimens aged with wet–dry cycles, on the other hand, presented almost constant strength, with a maximum difference of -5%, while the stiffness presented a sharp drop, even for the early period of aging, reaching -60% after 32 weeks.

Although the strength of the connection does not seem to be affected with the aging processes (in fact, for the thermal cycles, it even increases), the high stiffness reduction clearly shows that the GFRP-SFRSCC interface undergoes deterioration processes. These processes are likely to be related with premature debonding of interface patches due to fatigue to thermal contraction/expansion internal stresses. For the wet-dry cycles it is likely that deterioration of the mechanical behaviour stems from plasticization and hydrolysis phenomena that affect the thermosetting resins used (polyester in the GFRP matrix and epoxy adhesive). In this context, and given that it is not possible to relate the accelerated aging periods with the natural aging, which occurs throughout the service life, the use of a hybrid (adhesive and bolts) connection is recommended.

In this respect, specimens with hybrid connection aged with wet-dry cycles presented similar results to those obtained with the adhesive connection, with a small (-2%) reduction of strength and a -57% decrease of stiffness after 32 weeks. Nevertheless, given that the stiffness was still higher than that obtained with the simply bolted specimens, which means that the behaviour was still governed by the adhesive bond.

The FE models developed, using a bi-linear bond-slip constitutive law for the GFRP-SFRSCC interface, were well able to reproduce the behaviour of the simply adhesively bonded specimens, including those subjected to accelerated aging processes. Furthermore, these models were able to predict the failure mode of the specimens, proving to be a valid tool for simulating GFRP-SFRSCC interface problems. In this regard, it should be mentioned that, when simulating GFRP-concrete full-scale structures, the parameters calibrated herein could be used if a similar adhesive connection is used (similar materials and thickness). As an alternative, the bi-linear bond-slip law parameters could be calibrated using new shear connection tests and their respective FE modeling.



## 6. Small–scale prototype

### 6.1. Preliminary remarks

The present Chapter presents the investigations performed on the small–scale hybrid GFRP–SFRSCC footbridge prototype. These investigations included (i) experimental tests and the development of (ii) analytical and (iii) numerical models.

The small–scale prototype built in the context of this thesis was not formally designed in order to comply with Ultimate or Serviceability Limit States. In fact, the objectives behind the construction and testing of the small–scale prototype were (i) to test the feasibility of the hybrid GFRP–concrete structural system proposed and (ii) to assess the ability of current design tools in predicting its behaviour, rather than using it as a footbridge in a real environment.

This Chapter is divided in seven main sections: (i) preliminary remarks, (ii) characteristics of the prototype, in which the structural details of the prototype are presented; (iii) construction of the prototype, where the step–to–step construction process is described; (iv) static behaviour; (v) dynamic behaviour; and (vi) creep behaviour, which present the investigations conducted in the small–scale prototype regarding its static, dynamic and creep behaviour, respectively. In each of the last three sections, experimental investigations are presented and the results obtained are compared to those obtained with analytical and/or numerical models. Finally, the last section presents the (vii) final remarks that conclude this chapter.

### 6.2. Characteristics of the prototype

The small-scale footbridge prototype was built with two 6000 mm long GFRP pultruded profiles as main girders connected to a thin SFRSCC slab, constituted by 6 precast slabs with plan dimensions of  $2000 \times 1000 \text{ mm}^2$ , positioned at the top of the girders and serving as the deck of the footbridge. The GFRP profiles have a I-shaped section  $200 \times 100 \times (10) \text{ mm}^2$  while the SFRSCC slab presents a 40 mm thickness. The connection between the main girders and the SFRSCC slab is materialized by a 2 mm thick epoxy adhesive layer and stainless steel bolts. Figure 6.1 illustrates the small-scale prototype cross-section.

The structure was tested in a simply supported configuration with a 5500 mm span. Vertical displacements were prevented in all supports, which also allowed rotations over the transverse axis of the structure, whereas longitudinal sliding was prevented only on one side of the structure. In order to avoid the premature collapse due to web–crippling failure over the support sections [4, 5, 7, 14, 15], concrete jackets were provided between the flanges on both sides of the web. Additionally, accounting for the possibility of using external

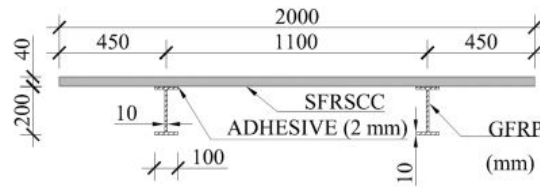


Figure 6.1.: Cross-section of the small-scale prototype.

prestress,  $\phi 9$  mm negatives were provided in the concrete jackets, positioned at a distance of 50 mm from the bottom fibre of the cross-section, in order to accommodate  $\phi 8$  mm straight rebars.

Secondary girders, connecting the two main girders, were provided at the support and midspan sections with two main purposes: (i) to avoid the distortion of the cross-section when loads are applied eccentrically; and (ii) to diminish the large initial imperfections of the GFRP pultruded profiles (*cf.* Section 6.3). The secondary girders were materialized by the same GFRP I-profiles that constitute the main girders and were connected to the latter with stainless steel bolts and small angle ( $80 \times 8$  mm<sup>2</sup>) GFRP profiles. Figure 6.2 shows the positioning of the supports, of the concrete jackets and of the secondary girders. Figure 6.3 shows the details of the connection between main and secondary girders and illustrates the details of the concrete jackets including the positioning of the aforementioned external prestress bars used in serviceability tests.

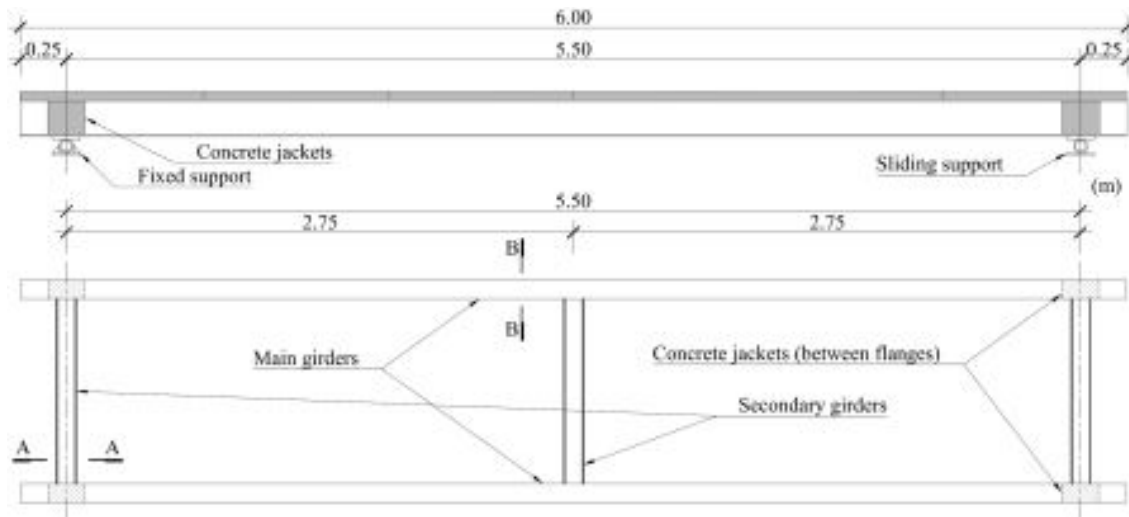


Figure 6.2.: Side- and bottom-view of the small-scale prototype.

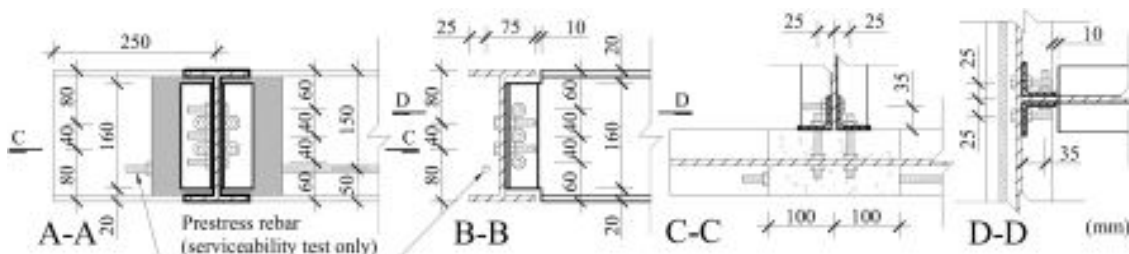


Figure 6.3.: Details of the concrete jackets and connections between main and secondary girders.

As mentioned earlier, the shear connection between the main girders and the SFRSCC deck was provided by a 2 mm thick epoxy adhesive layer and stainless steel bolts. The

adhesive layer thickness was defined based on standard recommendations for bonding CFRP laminates to concrete substrates [31]. The results of shear connection tests, reported in Section 5, show that the mechanical behaviour of the connection is governed by the epoxy adhesive layer, in terms of both strength and stiffness. Notwithstanding, the stainless steel bolts provide a redundant connection system, for the case of premature failure of the adhesive connection due to possible rheological deterioration of the epoxy adhesive properties, vandalism or accidental loads (*e.g.* fire). In this regard, the bolted connection was conservatively designed to fully withstand the shear loads between the GFRP profiles and the SFRSCC slab when the SFRSCC is crushed, considering a uniform distribution of shear load along the span, *i.e.*, the shear force ( $F_{cm}$ ) may be computed with Eq. (6.1) while the number of mechanical connectors needed ( $Nr$ ) may be derived from Eq. (6.2),

$$F_{cm} = 0.80 \times A_c \times f_c \quad (6.1)$$

where,  $A_c$  is the cross-section area of the concrete deck and  $f_c$  is the average compressive strength of the concrete.

$$Nr = 2 \times \frac{F_{cm}}{R_b} \quad (6.2)$$

Using the particular characteristics at 28 days of age of the SFRSCC used in the small-scale prototype (*cf.* Section 4.3.2.4) and the strength per bolt ( $R_b$ ) derived from experimental testing (results of preliminary series P–M4, *cf.* Section 5.2.4.7) in Eq. (6.2), a total of 228 mechanical connectors is obtained. Given that the SFRSCC deck is constituted by 6 precast slabs, as mentioned earlier, the connectors (materialized by stainless steel bolts, washers and nuts) were grouped in 6 sockets per precast slab each containing 8 connectors — summing a total of 288 connectors. Figure 6.4 shows the dimensional details of the precast slabs containing negatives for the connectors.

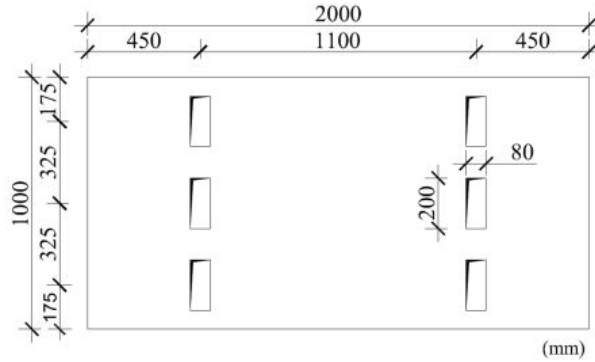


Figure 6.4.: Dimensions of the precast SFRSCC slabs.

### 6.3. Construction of the prototype

The construction of the small-scale prototype began with the preparation of the individual components. The surface of the SFRSCC precast slabs that would be in contact with the GFRP main girders (*cf.* Figure 6.1) was roughened with a needle scaler, thus enhancing the adhesive bond, as shown in Figures 6.5 and 6.6.



Figure 6.5.: Roughening of the slab.



Figure 6.6.: Roughening of the slab (detail).

The GFRP profiles were marked-up in order to be drilled (to accommodate the stainless steel bolts acting as mechanical connectors, *cf.* Section 6.2), in previously determined positions compatible with the negatives of the precast slabs (*cf.* Figure 6.4). Figures 6.7 and 6.8 show the mark-up of these positions for the bolted connections between the slab and the girder, and between the main and secondary girders (at the support sections), respectively.



Figure 6.7.: Mark-up for drilling of the bolts position.

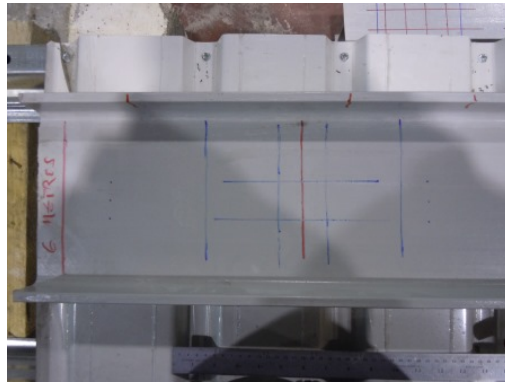


Figure 6.8.: Mark-up for drilling for the main/secondary girders connection.

The profiles were drilled with an  $\phi 11$  mm drill in order to accommodate  $\phi 10$  mm bolts and rods (for the webs in the support sections). Figures 6.9 to 6.11 show the drilling process undergoing for the flanges and the webs.

After the profiles were drilled, the stainless steel bolts, connecting the main girders and the SFRSCC slabs, and the threaded rods, connecting the main girders to the concrete jackets casted in the support sections (*cf.* Figure 6.3), were installed. The bolts were installed with an embedment length (inside the deck) of 25 mm, as illustrated in Figure 6.12, while the threaded rods were installed with a minimum embedded length (inside the concrete jackets) of 35 mm, as shown in Figure 6.13. Figures 6.14 and 6.15 show a group of bolts and a group of threaded rods, respectively, after being installed.

In order to cast the concrete jackets in the support sections, plywood formworks were tailored to the space in-between flanges of the profile section and installed with an adhesive (liquid nail), as shown in Figures 6.16 and 6.17.





Figure 6.9.: Drilling of the flanges.



Figure 6.10.: Drilling of the flanges (detail).

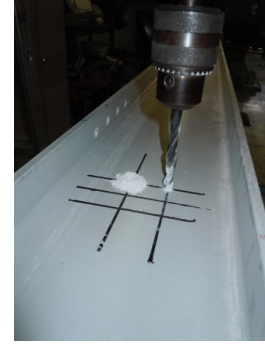


Figure 6.11.: Drilling of the webs.



Figure 6.12.: Embedded length of the bolts.

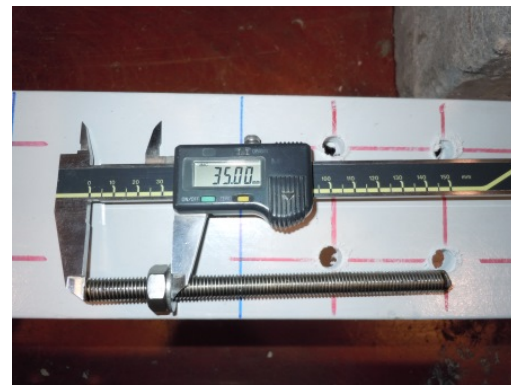


Figure 6.13.: Embedded length of the threaded rods.



Figure 6.14.: Group of bolts installed.

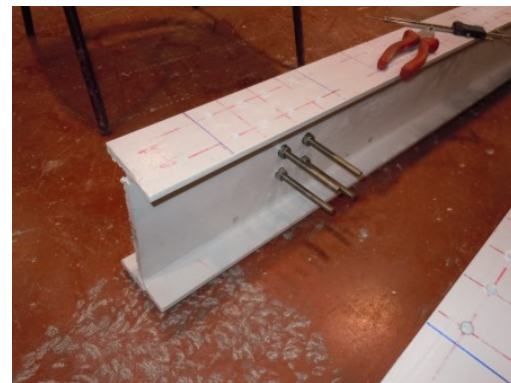


Figure 6.15.: Group of threaded rods installed.

Before casting the concrete jackets, PVC tubes with an inner diameter of  $\phi 9$  mm were provided inside the formwork in order to allow the installation of prestress straight rebars, as mentioned in the previous section (*cf.* Section 6.2). Figures 6.18 and 6.19 show the final aspect of the formwork after installation.



*Figure 6.16.: Tailoring of the formwork.*



*Figure 6.17.: Installation of the formwork.*



*Figure 6.18.: Final aspect of the formwork.*



*Figure 6.19.: Final aspect of the formwork (side view).*

After the adhesive used to install the formwork was hardened, the concrete of the jackets was prepared (*cf.* 4.4.5), casted and duly vibrated, as shown in Figures 6.20 and 6.21, respectively. After a waiting period of 48 hours, given for the concrete to dry, the profiles were turned on the other side and this process was repeated.



*Figure 6.20.: Casting of the concrete.*



*Figure 6.21.: Vibration of the concrete.*

When the concrete of the jackets was dry and the girders could be moved, the process of assembling the main and secondary girders was performed. This process started with the transformation of the GFRP squared-section profiles ( $100 \times 8 \text{ mm}^2$  manufactured by *Fiberline Composites A/S*, cf. Section 4.4.1) in angle-section profiles used to connect main and secondary girders (cf. Section 6.2 and Figure 6.3). This was performed by cutting two corners of small-length (160 mm) squared profiles, as shown in Figure 6.22, and later drilling  $\phi 11 \text{ mm}$  holes, on the resulting angle-section profiles, to fit the  $\phi 10 \text{ mm}$  stainless steel bolts used in the connections, as illustrated in Figure 6.23.



Figure 6.22.: Cutting of the square-section profiles.



Figure 6.23.: Drilling of the angle-section profiles.

After the angle sections were prepared, the secondary girders were cut to fit from a long profile with the same shape as the main girders. The secondary girders in the support section were cut to a length of 980 mm, in order to ensure a 10 mm gap to the main girder on each side, while the secondary girder of the midspan section, which connected to the web of the main girders (cf. Figure 6.3) presented a total length of 1070 mm, as illustrated in Figure 6.24, also ensuring a 10 mm gap to the main girder on each side. Figure 6.25 shows the final aspect of the midspan secondary girder, while Figures 6.26 and 6.27 show the assembly process of the main and secondary girders and the final aspect of the assembled girders, respectively.

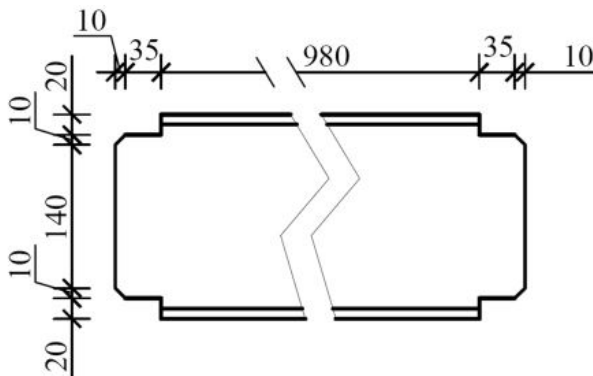


Figure 6.24.: Dimensions of the midspan secondary girder (mm).



Figure 6.25.: Final aspect of the midspan secondary girder.





Figure 6.26.: Assembly of the main and secondary girders.



Figure 6.27.: Final aspect of the assembled girders.

Before connecting the main and secondary girders, 2 mm thick plastic spacers were bonded onto the top of the main girders in order to guarantee a 2 mm thick layer of epoxy adhesive in the GFRP–SFRSCC interface, as shown in Figure 6.28a. Additionally, after performing a final inspection of each element in order to find any geometrical incompatibility, it was necessary (i) to trim the outer edge of some of the precast slabs (Figure 6.28b) due to the fact that some unembedded steel fibres prevented the full contact in the interface area, and (ii) to trim an inner edge of a precast slab (Figure 6.28c), whose negative had been cast with an incorrect geometry (Figure 6.28d).

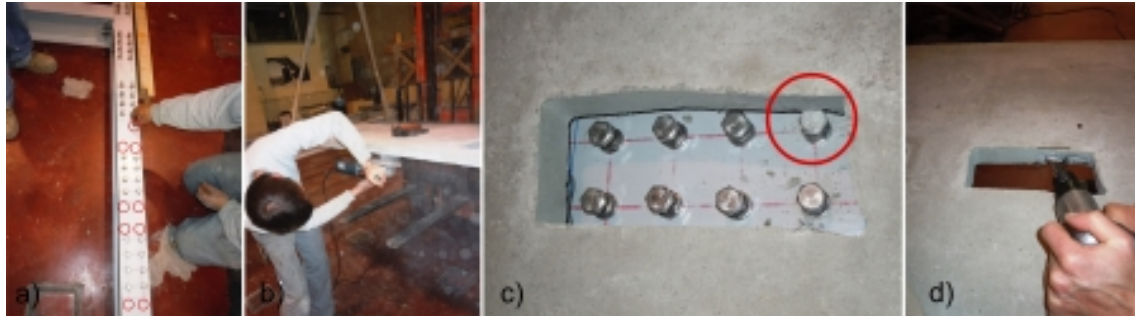


Figure 6.28.: Construction details: a) installation of plastic spacers; b) trimming of slabs' outer edges; c) trimming of a slab's inner edge; and d) geometrical incompatibility.

Prior to the installation of the SFRSCC slabs, and in order to assess the possibility of introducing a precamber in GFRP–concrete hybrid structures, two props were installed at the midspan section underneath each of the main girders, applying an upwards midspan deflection of 5 mm, as shown in Figure 6.29a. After these props were installed, the surface of the GFRP main girders' top flanges was dusted with compressed air in order to enhance the adhesive bonding between the GFRP material and the SFRSCC (Figure 6.29b). The epoxy adhesive was prepared according to the recommendations of the manufacturer (*cf.* Section 4.4.3, [31]) and applied on the main girders' top flanges (Figure 6.29c) and on the precast slabs' vertical surfaces (Figure 6.29d).



Figure 6.29.: Bonding of the elements: a) preamber props; b) dusting of the surface; application of the adhesive on the c) main girders; and d) on the SFRSCC slabs.

The precast slabs (6 in total) were bonded in pairs from the centre of the structure to the supports. After each pair of slabs was put in place, they were pressed against each other with a manual fastening system shown in Figure 6.30a and the bonded joints were cleaned from the excessive squeezed adhesive, both in the GFRP-SFRSCC interfaces and in the SFRSCC-SFRSCC interfaces.

An important note must be mentioned regarding the ease of erection of the structural system proposed herein: although the SFRSCC precast slabs were moved within the laboratory with the aid of a moving crane, as shown in Figure 6.30b, the final placing of the slabs was performed by manual labor of four men, as may be depicted from Figure 6.30c.

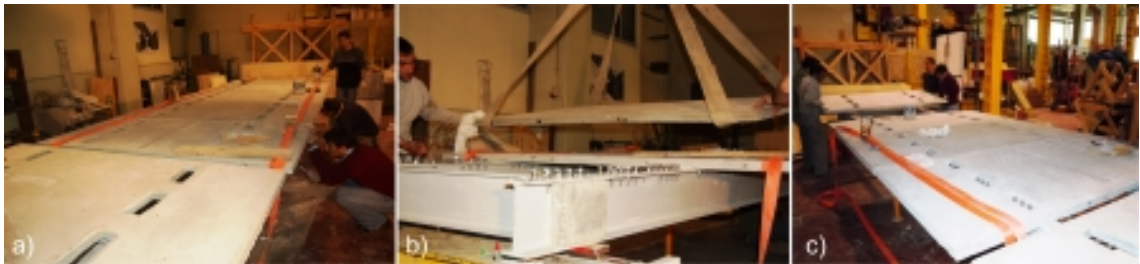


Figure 6.30.: Assembly of the prototype: a) fastening of the central pair of slabs; b) moving a slab with the aid of a moving crane; and c) final placing of the slabs by manual labor.

Figure 6.31 shows the overall aspect of the prototype after the SFRSCC precast slabs were bonded and during the initial drying period of the epoxy adhesive.



Figure 6.31.: Aspect of the small-scale prototype after the bonding of the slabs.

After a waiting period of 4 days, given for the epoxy adhesive to dry, the negatives for the bolts were ready to be sealed with an epoxy mortar (*cf.* Section 4.4.4, [110]). This process

was started by sealing the SFRSCC–GFRP junctions with silicone adhesive, as shown in Figures 6.32a and 6.32b, in order to minimize the leakage of the filling material. Afterwards, the epoxy mortar was prepared in a small container by mixing its two components with fine sand, as may be depicted from Figures 6.32c and 6.32d. The process was completed by pouring the epoxy mortar directly into the negatives, which was possible owing to its high fluidity as shown in Figure 6.33a. Figure 6.33b shows one of the negatives after being sealed, while Figure 6.33c shows the final aspect of the prototype.

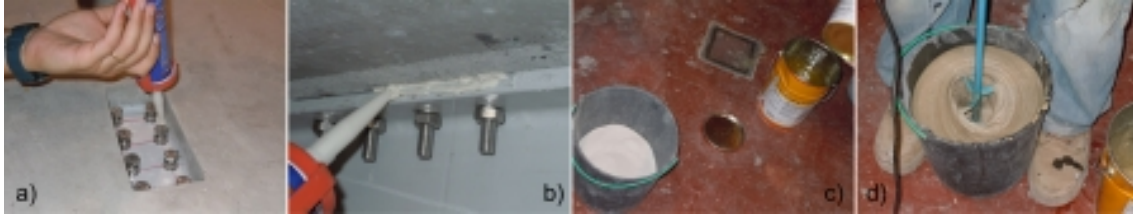


Figure 6.32.: Preparation for sealing the negatives: a) and b) sealing of the SFRSCC–GFRP junctions; c) components of the epoxy mortar; and d) mixing of the epoxy mortar.



Figure 6.33.: Sealing the negatives: a) pouring the epoxy mortar; b) sealed negative; and c) final aspect of the prototype.

After the epoxy mortar sealing the holes hardened, permanent instrumentation — namely electric strain gauges — were installed in the midspan section in order to monitor the structural behaviour during the experimental tests. In the SFRSCC material the strain gauges installed were *HBM-1-LY41-50/120* whereas in the GFRP material the strain gauges were *HBM-1-LY11-10/120*, both models from *HBM*. Figure 6.34 shows the positioning of the strain gauges in the midspan section (please note that the strain gauges in the bottom flanges of the GFRP profiles were only installed after the precamber props were removed).

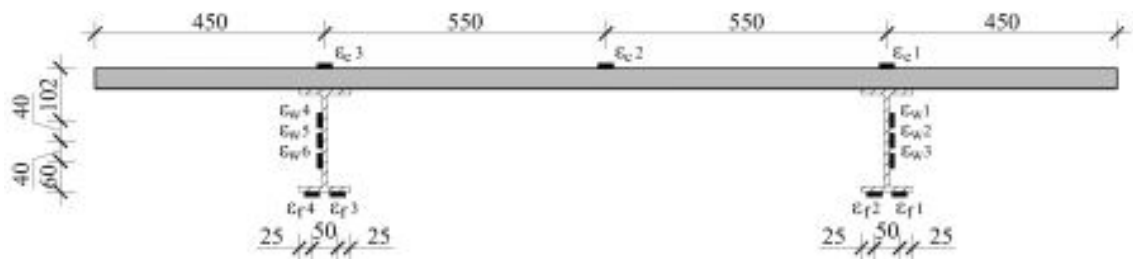


Figure 6.34.: Permanent instrumentation of the small-scale prototype: position of electric strain gauges at the midspan section.

## 6.4. Static behaviour of the prototype

### 6.4.1. Context

This section presents the experimental investigations regarding the static flexural behaviour of the hybrid GFRP–SFRSCC small-scale footbridge prototype, as well as the analytical and numerical modeling of those experiments. The need to fully understand the static behaviour of this type of GFRP–concrete hybrid structure is of the utmost importance because some of the main safety requirements, namely Serviceability and Ultimate Limit States requirements, are based on static behaviour criteria.

In this context, the experimental investigations presented herein comprised (i) the monitoring of the removal of the precamber polls, and static flexural tests, namely, (ii) serviceability tests; (iii) serviceability tests with prestress; and (iv) a failure test. The first set of static flexural tests allowed to assess the structural response to vertical loading and unloading; the second set allowed to verify the feasibility of a cost effective prestress solution; and the failure tests allowed the assessment of the structural response of the prototype up to failure, as well as the failure modes involved in the collapse of the structure.

The analytical and numerical modeling of these tests and the comparison between the predictions and the actual structural behaviour observed experimentally, aimed at assessing the quality/accuracy of the design tools for GFRP–concrete structures available to structural designers.

### 6.4.2. Monitoring of precamber effects

Eight days after the filling of the slab negatives, given for the epoxy mortar to dry and cure, the props applying the precamber were removed. During this process, strains were measured in the midspan section in positions  $\varepsilon_c1$  to  $\varepsilon_c3$  and  $\varepsilon_w1$  to  $\varepsilon_w6$  (*cf.* Figure 6.34), while deflections were measured also at the midspan section with two electric displacement gauges, from *TML* with a stroke of 10 mm and precision of 0.01 mm, placed beneath the SFRSCC transverse cantilevers, one in each extremity of the cross-section. Data was gathered with two built-in dataloggers, from *HBM*, model *Spider 8*, at a rate of 5 Hz and registered in a PC.

After the precamber props were removed, an instantaneous average midspan deflection ( $\delta_{ms}$ ) of 6.63 mm was measured, while the average axial strains measured along the cross-section height were those depicted in Figure 6.35.

These results show that the precamber system used was effective since upon removal of the props, the structure deformed and the slab was compressed achieving both goals of the precamber system: (i) obtaining smaller deflections; and (ii) introducing compressive stresses in the slab.

### 6.4.3. Serviceability tests (without prestress)

As mentioned earlier, serviceability tests were performed in the small-scale prototype in order to assess the static flexural response of this structure. These tests were performed with two different load configurations: (i) a 3–point bending configuration materialized by two concrete blocks,  $1000 \times 500 \times 500$  mm<sup>3</sup>, weighing 522 kgf and 524 kgf, which were placed

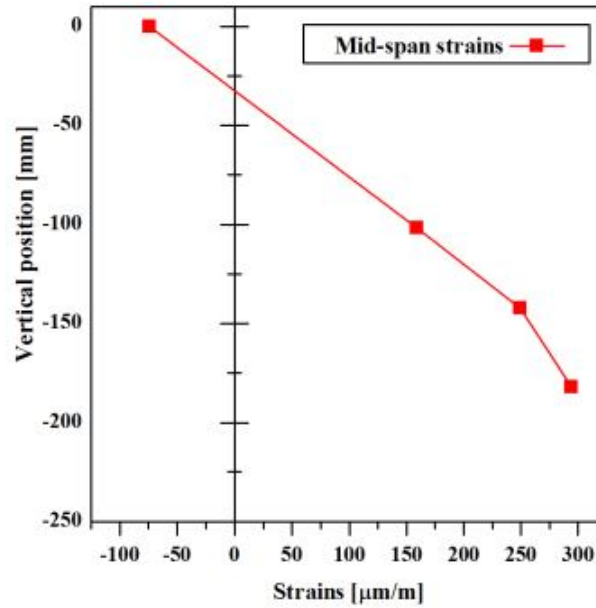


Figure 6.35.: Axial strains measured upon the removal of the precamber props (position 0 mm corresponds to  $\varepsilon_c1$  to  $\varepsilon_c3$ , *i.e.* the top of the deck).

(using a moving crane) on top of the prototype’s deck at the midspan section, in a symmetric position, each block being aligned with one of the main girders (*cf.* Figure 6.36); and (ii) a 4-point bending load configuration comprising two concrete blocks,  $1200 \times 400 \times 200 \text{ mm}^3$ , weighing 640 kgf each, which were placed at a distance of  $a = 1.90 \text{ m}$  from each support and spaced between each other by  $b = 1.70 \text{ m}$  (*cf.* Figure 6.37).

The total load used in the first configuration corresponds approximately to 1/6 of the characteristic load for footbridges ( $5 \text{ kN/m}^2$ , according to Eurocode 1 [65]), causing a bending moment at midspan of approximately 1/3 of that caused by such characteristic load applied uniformly over the span. This load configuration allowed testing the flexural and torsional static behaviour of the footbridge structure by applying the concrete blocks in the following three sequential stages: (a) first block loaded over the left girder (stage 1); (b) both blocks loaded over both girders (stage 2); and (c) right block loaded over the right girder (stage 3). During this test, vertical deflections were measured at five different positions across midspan section with displacement transducers from *Mitutoyo* (with a stroke of 50 mm and precision of 0.01 mm). Two displacement transducers were positioned underneath the GFRP girders and three were positioned below the SFRSCC slab, one at the transverse midspan and two at a distance of 10 mm from the edges of the cantilevers. Figure 6.36 shows the deflections measured at midspan for each stage. These results show that the GFRP–concrete hybrid structure presented a symmetrical behaviour, as expected, for load stages 1 and 3, showing the same response to torsional moments regardless of the direction of those same moments. For load configuration 2, the slight slope of the deflections over the cross-section, which may be disregarded, is most likely due to the effects of small deviations on the positioning of concrete blocks. The average midspan deflection ( $\delta_{ms}$ ) attained, 6.41 mm, corresponds to  $L/858$ .

Regarding the second load configuration, the total load used,  $F = 12.56 \text{ kN}$  (*cf.* Figure 6.37), corresponds to approximately 1/5 of the characteristic load defined in Eurocode 1 [65] for footbridge structures —  $5 \text{ kN/m}^2$  — when applied to the entire deck. The concrete blocks were lifted with the laboratory crane and smoothly positioned (and removed) over the deck



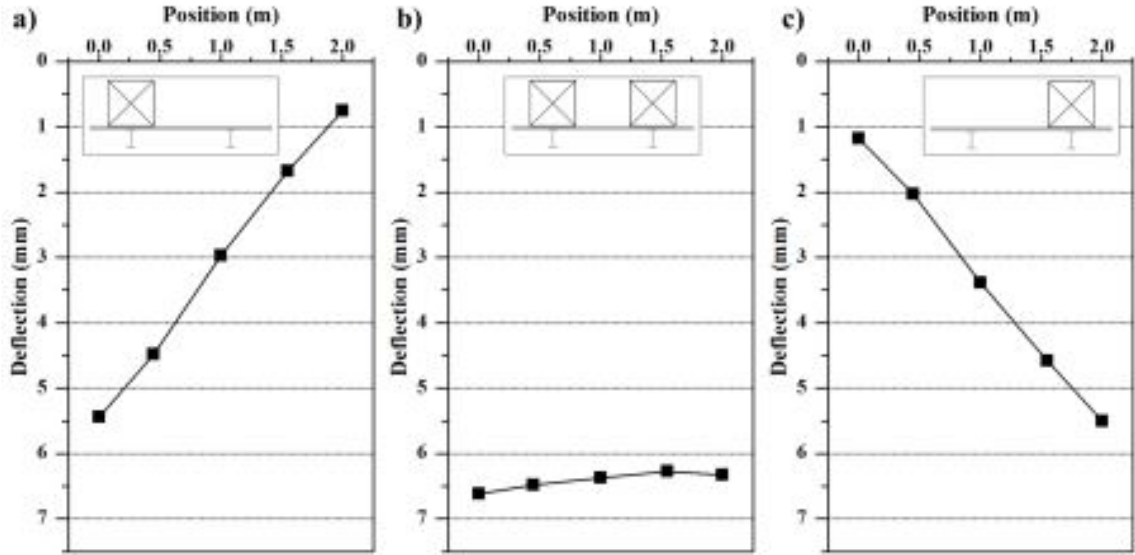


Figure 6.36.: Small-scale prototype serviceability tests: midspan deflections for load configuration (i): a) load stage 1; b) load stage 2; and c) load stage 3.

in the predefined positions so as to avoid any dynamic effects. Deflections were measured at midspan section underneath both main girders with *TML* electric displacement transducers with a stroke of 25 mm and precision of 0.01 mm. Strains were also measured at different positions of midspan cross-section with strain gauges  $\varepsilon_{c1}$ ,  $\varepsilon_{f1}$  and  $\varepsilon_{f2}$  (cf. Figure 6.34). Data was gathered with a data logger (model *QuantumX* from *HBM*) at a rate of 10 Hz and registered in a PC. Figure 6.38 shows the structure loaded for this test.



Figure 6.37.: Small-scale prototype serviceability tests: load configuration 2.

In this test, the structure exhibited linear-elastic load-deflection behaviour, as expected, which was possible to observe due to the (time) continuous measurement of the displacements and strains with the datalogger. These tests allowed determining the average midspan deflections ( $\delta_{ms} = 6.79$  mm) —  $L/810$  — and stiffness ( $K = 1.85$  kN/mm) of the structure for the load configuration used. Based on the strain gauge measurements, the curvature ( $\chi = 19.29 \times 10^{-4} \text{ m}^{-1}$ ) and the neutral axis position ( $NA = 24.55$  mm, with reference to the top of the cross-section) at the midspan cross-section were estimated.

#### 6.4.4. Serviceability tests with prestress

As mentioned earlier (cf. Section 6.2), the feasibility of a cost-effective external prestress system for GFRP-concrete structures was one of the objectives of the present investigation. With this aim, flexural serviceability tests were conducted for the small-scale prototype with the application of a prestress system materialized by two steel straight rebars with small length threaded steel rods welded in both extremities. The prestress force was applied by tensioning the rebars, which were positioned in the negatives of the concrete jackets (cf.



Figure 6.38.: Small-scale prototype serviceability tests: structure loaded in load configuration 2.

Section 6.2) and tightened with the help of 10 mm thick steel plates (in order to distribute the stresses evenly to the concrete jackets), washers and nuts (*cf.* Figure 6.39a). Figure 6.39b shows the prestress being applied by tightening the rebar, while Figures 6.39c and 6.39d show a prestress rebar before and after being tightened.

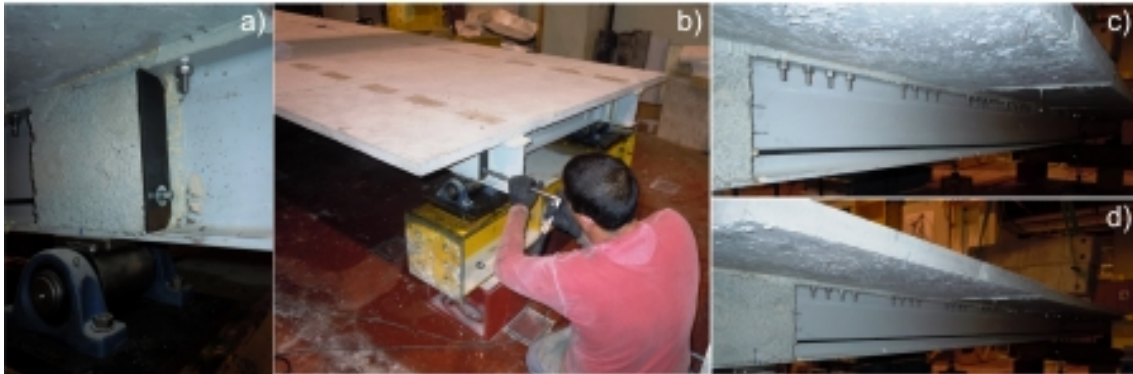


Figure 6.39.: Small-scale prototype serviceability tests with prestress: a) positioning of the prestress rebars; b) applying prestress; prestress rebar c) without and d) with applied force.

In this test, the load configuration 2 of the serviceability tests was used with the same load level (*cf.* Section 6.4.3). The test procedure was the following: (i) a force of 10 kN was applied in each rebar; (ii) the static load was applied; and (iii) the rebars were further tighten until a force of 20 kN was attained in each one. The maximum prestress force installed in each rebar (20 kN/rebar), which corresponds to approximately 80% of its characteristic yield strength ( $\approx 25$  kN, *cf.* Section 4.4.5), was evaluated with electric strain gauges (model *FLK-6-11-3L* from *TML*) installed on the rebars.

Figure 6.40 shows the evolution of the midspan average deflection ( $\delta_{ms}$ ) with the prestress force per cable ( $P$ ). As expected, the structure deflected upwards when the rebars were first tightened, showing that this simple external prestress system is capable of uplifting this type of hybrid structure. When the structure was loaded with the concrete blocks, it presented a downwards deflection, which was finally reduced when the prestress rebars

were further tightened. These results attest the possibility of using simple external prestress systems in GFRP–concrete hybrid structures, which may provide a cost effective and durable (if using FRP non–corrodible rebars) solution for limiting deformation restrictions. In this particular case of a hybrid footbridge, the prestress system can be used to mitigate part of the permanent load deflections, namely those caused by pavements, parapets, guardrails and other secondary elements. In this respect, the concrete blocks used in the tests can be regarded as those other permanent loads. Table 6.1 summarises the main results of this test, presenting separately the effects of the load application and the effects of the (total) prestress. The average midspan deflection ( $\delta_{ms}$ ) caused by the static loads was lower than that measured in the serviceability tests without prestress for load configuration 2 (*cf.* Section 6.4.3). This comparison shows that although the prestress rebars are external to the structure, they provide a slight stiffness increase (+3.9%) as the rotation of the supports may cause the elongation of the rebars.

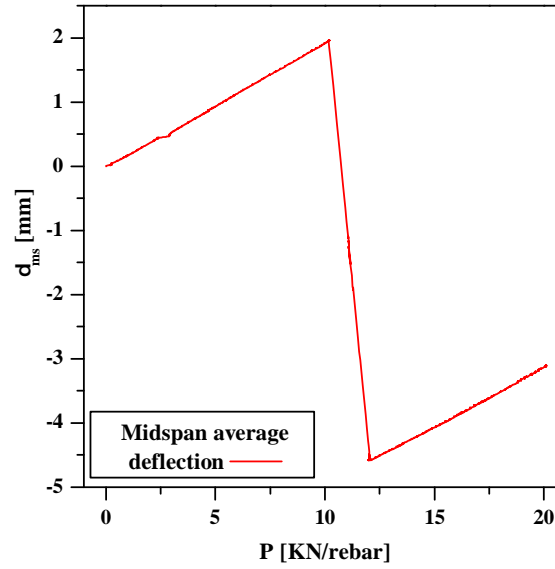


Figure 6.40.: Small-scale prototype serviceability tests with prestress: midspan average deflection *vs.* prestress force per rebar.

Table 6.1.: Small-scale prototype serviceability tests with prestress: midspan average deflection ( $\delta_{ms}$ ) and stiffness ( $K$ ) for applied loads and prestress.

Loads		Prestress	
$\delta_{ms}$ (mm)	$K$ (kN/mm)	$\delta_{ms}$ (mm)	$K$ (kN/mm)
6.53	1.92	3.41	5.30

### 6.4.5. Failure test

The static flexural test up to failure of the small-scale prototype was performed with a 4–point bending load configuration — similar to load configuration 2 of the serviceability tests (*cf.* Section 6.4.3) — with geometrical parameters  $a = 1.85$  m and  $b = 1.80$  m (*cf.* Figure 6.37). No prestress system was used in this test.

Load was applied with a hydraulic jack (from *Enerpac*) with a load capacity of 600 kN, installed on a loading frame, comprising two steel columns and a beam, which was anchored to the laboratory strong floor. Load was measured with a *Novatech* load cell, with a capacity

Table 6.2.: Small-scale prototype failure test: failure load ( $F_u$ ), average midspan deflection at failure ( $\delta_{ms-u}$ ), stiffness ( $K$ ) and neutral axis position ( $NA$ ) with reference to the top of the cross-section.

$F_u$ (kN)	$\delta_{ms-u}$ (mm)	$K$ (kN/mm)	$NA$ (mm)
232.4	126.29	1.95	27.39

of 800 kN, installed between the hydraulic jack and the footbridge prototype. Load was distributed to the structure with three steel beams, one oriented longitudinally, transferring the load from the jack within the central load span ( $b$ , cf. Figure 6.37), and two oriented transversely in order to apply the load along the entire width of the deck. A metal sphere was positioned between the load cell and the longitudinal distribution steel beam, while steel cylinders were installed between the longitudinal and transversal steel beams allowing for rotation in the longitudinal direction. The deflections of the structure were measured at the midspan section, over the deck and centered with both main girders —  $\delta_{ms1}$  and  $\delta_{ms2}$ , with *TML* electric displacement transducers with a stroke of 100 mm and precision of 0.01 mm. Strains were measured in all positions shown in Figure 6.34. The load was applied monotonically under load control at an approximate rate of 0.6 kN/s. Data was gathered with two built-in data loggers (from *HBM*, model *QuantumX*) at a rate of 5 Hz and registered in a PC. Figure 6.41 shows the test configuration.



Figure 6.41.: Small-scale prototype failure test: test configuration.

The structural behaviour of the hybrid structure was linear-elastic up to failure, as may be depicted from Figures 6.42 and 6.43, which show, respectively, the applied load as a function of the midspan deflections and the average strains as a function of the applied load. Moreover, strain gauge measurements (Figure 6.43) confirm that no slip occurred in the GFRP-adhesive-concrete interfaces, in accordance with the results of the shear connection tests presented in Chapter 5. Table 6.2 summarises the most relevant results obtained in this test, including the failure load ( $F_u$ ), the average midspan deflection at failure ( $\delta_{ms-u}$ ), the stiffness ( $K$ ) for this load configuration and the neutral axis position ( $NA$ ) derived from the measured strains.

The collapse of the structure was brittle and triggered by the shear failure of the web-flange junction of one of the GFRP main girders. This shear failure was apparently followed by flexural buckling of the web, whose upper edge was no longer supported, at a distance

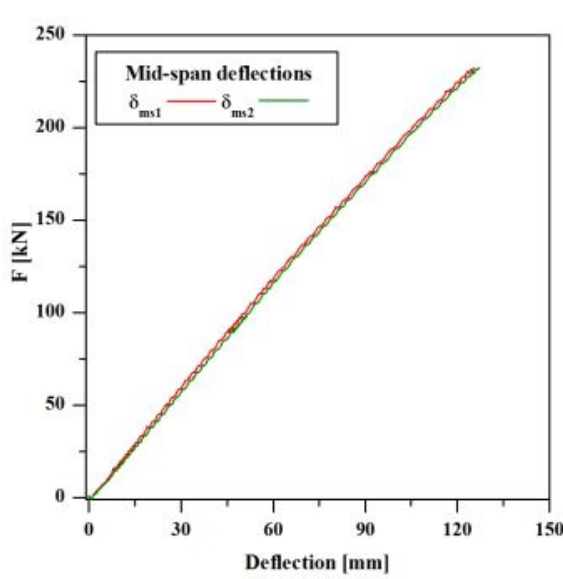


Figure 6.42.: Small-scale prototype failure test: load vs. midspan average deflections up to failure.

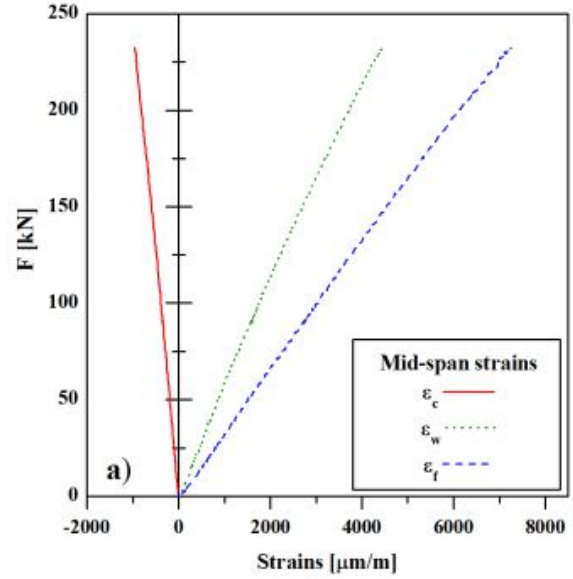


Figure 6.43.: Small-scale prototype failure test: load vs. midspan average strains up to failure.

of about 0.50 m from the midspan section. The other main girder remained apparently undamaged. The SFRSCC deck, which had not exhibited any signs of damage (cracking, crushing) prior to failure, suffered extensive damage after the GFRP girder failed. However, although the footbridge structure did collapse, the deck was able to support its own weight after failure. Figure 6.44 shows several details of the structure after collapse. Failure occurred for a total load ( $F$ , cf. Figure 6.37) of 232.4 kN, which corresponds to approximately 4.2 times the characteristic load for footbridge structures [65] when applied to the entire deck. This failure load corresponds to a maximum bending moment ( $M_{max}$ ) of  $\approx 215.0$  kNm and an ultimate shear force ( $V_u$ ) of  $\approx 116.2$  kN.

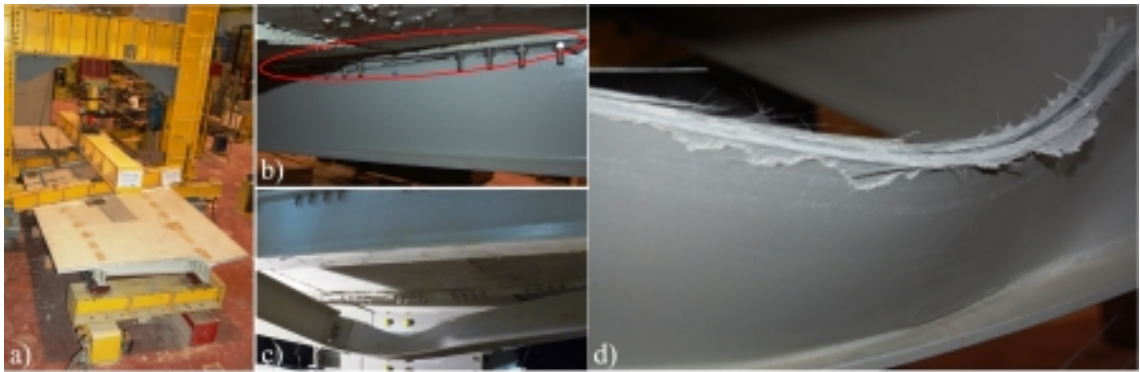


Figure 6.44.: Small-scale prototype failure test: (a) prototype after failure; (b) GFRP main girder web-flange junction failure; (c) complete separation of web and flange followed by web buckling; and (d) detail of web-flange separation.

The failure of the structure occurred when the mid-span average deflection was 126.3 mm (cf. Table 6.2), which corresponds to approximately  $L/43.5$  ( $L$  being the longitudinal span) — about 6–12 times higher than the deflection limits defined for building floors in Eurocode 2 [85] and in the Italian guidelines for FRP structures [68] (both for the quasi-

permanent load combination), and more than 2.25 times higher than the deflection limit for pedestrian footbridges defined in the Italian guidelines [68] (for the rare load combination). In this regard, and although the structure did not present any obvious loss of stiffness prior to failure (*cf.* Figures 6.41 and 6.42), such high deformations constitute a clear warning for a possible structural malfunction as may be depicted from Figure 6.45, which shows the deformed configuration of the structure prior to failure. Therefore, even without pseudo-ductility and featuring a brittle type of failure, this hybrid structure did not collapse without visible signs of malfunction, providing clear warning of imminent failure for both users and infrastructure management authorities.



Figure 6.45.: Small-scale prototype failure test: deformed configuration immediately prior to failure.

## 6.4.6. Analytical simulation

### 6.4.6.1. Serviceability behaviour without prestress

As mentioned earlier, the shear deflections should not be neglected in the design of FRP based structural solutions. In this context, in order to predict the instantaneous deflections of the hybrid GFRP-concrete structure under study, Eqs. (4.22) and (4.23) (*cf.* page 90) were developed, based on the Timoshenko beam theory [86], to determine the vertical deflections along the span for (i) 3-point and (ii) 4-point bending load configurations, respectively.

Regarding the determination of the shear stiffness for this type of hybrid structure, comprising GFRP I-shaped profiles, an assumption is generally made that it is provided only by the webs of the profiles [60–62], therefore the general shear area ( $kA$ ) may be substituted by the area of the webs of the profiles ( $A_w$ ), while the general shear modulus ( $G$ ) should be substituted by the in-plane shear modulus ( $G_{LT}$ ) of the web plates. Additionally, considering that the slip at the GFRP-SFRSCC interface is negligible, in accordance with the experimental data of shear connection tests (*cf.* Chapter 5), the position of the cross-section neutral axis ( $NA$ ) may be determined with Eq. (6.3),

$$NA = \frac{\sum_i^n E_i A_i z_i}{\sum_i^n E_i A_i} \quad (6.3)$$

where  $E_i$  is the elasticity modulus of element  $i$ ,  $A_i$  is the area of element  $i$  and  $z_{gi}$  is the distance between the stiffness centroid of element  $i$  and a chosen fixed point (in the present case the neutral axis position is always determined with reference to the top of the

cross-section). Furthermore, accounting for the orthotropic nature of the GFRP material, the elasticity moduli in the longitudinal direction ( $E_{L,i}$ ) of the GFRP plates should be used. For the cross-section under study, 4 types of elemental areas were considered: (i) the SFRSCC slab; (ii) the 2 mm epoxy adhesive layer; (iii) the GFRP flanges; and (iv) the GFRP webs. The flexural stiffness ( $EI$ ) may then be calculated with the Lagrange–Steiner theorem as shown in Eq. (6.4),

$$EI = \sum_i^n E_i I_i + E_i I_i \times (NA - z_{gi})^2 \quad (6.4)$$

where  $I_i$  is the second moment of area of each element  $i$  around its own stiffness centroid ( $z_{gi}$ ). In Eq. (6.4) the elasticity moduli in the longitudinal direction ( $E_{L,i}$ ) of the GFRP plates should also be used, in order to account for their orthotropic behaviour.

Additionally, for the present case, the full width of the SFRSCC slab was considered in the determination of the flexural stiffness, according to the method presented in Eurocode 4 [115] to define the effective width of concrete slabs in steel–concrete composite structures. These formulae allowed the determination of the shear and flexural stiffness of the cross-section,  $G \times kA = 12636$  kN and  $EI = 5793$  kNm<sup>2</sup>, respectively.

Table 6.3 shows that the midspan deflections and stiffness predicted by the analytical formulae presented compare well with the results observed experimentally — for load configuration 2 — with relative errors around 10%. The predicted curvature ( $\chi$ ) was also correctly estimated ( $\approx 7\%$  relative error), while the predicted neutral axis presented a deviation of 4.51 mm (in a 242 mm section) from the measured neutral axis. These results show that the analytical formula presented herein are well able to predict the flexural behaviour of hybrid GFRP–concrete structures for service conditions.

*Table 6.3.: Small-scale prototype serviceability behaviour — load configuration 2: experimental and analytical estimates of average midspan deflection ( $\delta_{ms}$ ), stiffness ( $K$ ), curvature ( $\chi$ ) and neutral axis position ( $NA$ ) with reference to the top of the cross-section.*

Source	$\delta_{ms}$		$K$		$\chi$		$NA$
	(mm)	diff. (%)	(kN/mm)	diff. (%)	$10^{-4}/m$	diff. (%)	(mm)
Experimental	6.79	-	1.85	-	19.29	-	24.55
Analytical	7.50	10.44	1.67	-9.45	20.61	6.82	29.06

#### 6.4.6.2. Serviceability behaviour with prestress

Regarding the prediction of the effects of the application of external prestress to the structure, two additional effects must be considered in the analytical formulae: (i) the deflections caused by the bending moment introduced by the prestress rebars; and (ii) the additional stiffness that these rebars may provide to the structure. The external prestress rebars are straight and are anchored in the concrete jackets at the support sections (*cf.* Section 6.2), therefore, the prestress forces ( $P$ ) induce a constant bending moment along the entire span of the structure (negative bending moments as the rebars are tensioned).



The upwards deflection caused by the prestress rebars ( $\delta_P$ ) may then be computed with Eq. (6.5),

$$\delta_P(x) = \frac{P \cdot e}{2EI}(x^2 - Lx) \quad (6.5)$$

where  $e$  is the eccentricity of the prestress rebars, measured with respect to the neutral axis of the cross section.

Additionally, the elongation of the rebars, caused by the rotation of the supports when the structure is loaded, must be taken into consideration when calculating the deflections of the prestressed structure. In order to do so, the rotation of the supports must be calculated with reference to the theoretical supports of the Timoshenko's beam theory (located in the neutral axis) depicted in Figure 6.46.

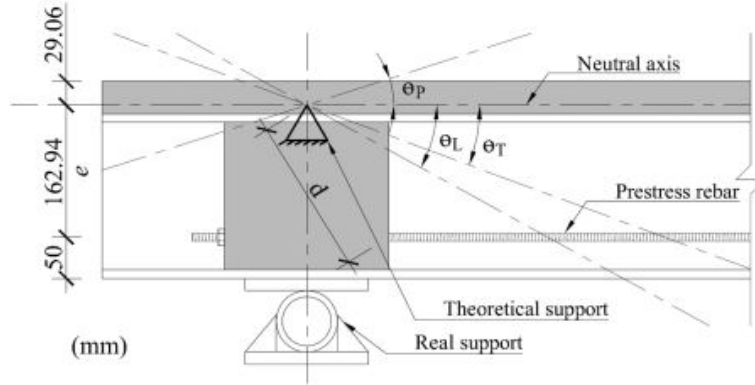


Figure 6.46.: Prestress: rotation around the theoretical support.

The total rotation of the support ( $\theta_T$ ) may then be computed by adding the rotation caused by the loads ( $\theta_L$ ) to the rotation due to the prestress ( $\theta_P$ ) previously installed in the structure, as defined by Eq. (6.6):

$$\theta_T = \theta_L + \theta_P = \left( \frac{Fa}{4EI}(L - a) + \frac{F}{2GkA} \right) - \frac{P \cdot e}{2EI}L \quad (6.6)$$

For this particular case, the flexural deformations account for 88.1% of the rotation caused by the loads ( $\theta_L$  — first two terms of Eq. (6.6)), whereas the remaining 11.9% are due to the shear deformations. The elongation of the rebars ( $\Delta_s$ ) may then be expressed as follows,

$$\Delta_s = 2d \cdot \sin(\theta_T) \quad (6.7)$$

where  $d$  is the distance between the theoretical support and the rotation point of the rebars ( $\approx 191$  mm), just outside the concrete jackets (*cf.* Figure 6.46). Finally, the additional force on the rebars caused by the vertical loads ( $\Delta P$ ) may be written as,

$$\Delta P = \frac{\Delta_s}{l} E_s A_s \quad (6.8)$$

where  $l$  is the free length of the rebars (5250 mm),  $E_s$  is the elasticity modulus of the rebars and  $A_s$  is the area of the rebars (*cf.* Section 4.4.6). The deflections caused by the vertical



loads after prestress installation may then be calculated by re-writing Eq. (4.23) (page 90) into the following form:

$$\begin{aligned}
 \delta(x) &= \frac{F}{4EI} \left[ a(L-a)x - \frac{x^3}{3} \right] + \frac{F}{2A_w G} x - \frac{\Delta P \cdot e}{2EI} (x^2 - Lx), & 0 \leq x < a \\
 \delta(x) &= \frac{F}{4EI} \left( Lx - x^2 - \frac{a^3}{3} \right) + \frac{Fa}{2A_w G} - \frac{\Delta P \cdot e}{2EI} (x^2 - Lx), & a \leq x < b \\
 \delta(x) &= \frac{F}{4EI} \left[ x \left( \frac{x^2}{3} + L(a-x) + (a+b)^2 \right) \right] + & \\
 &\quad \frac{F}{4EI} \left[ L \left( \frac{2L^2}{3} - La - (a+b)^2 \right) \right] + \frac{F(L-x)}{2A_w G} - & (6.9) \\
 &\quad \frac{\Delta P \cdot e}{2EI} (x^2 - Lx), & a+b \leq x \leq L
 \end{aligned}$$

The comparison between the results obtained with these analytical formulae and those observed experimentally, shown in Figure 6.47 and Table 6.4, prove that these straightforward analytical expressions are able to predict with good accuracy the experimental results obtained in the flexural test with prestress application. Predicted midspan deflections are similar to those observed in the tests, with relative errors of  $\approx 12.9\%$  for the prestress deflections and  $\approx 8.6\%$  for the vertical load deflections after prestress installation. These results show that simple analytical beam models are well able to predict the behaviour of this type of prestressed hybrid structures, constituting reliable design tools especially for the early stages of the design process.

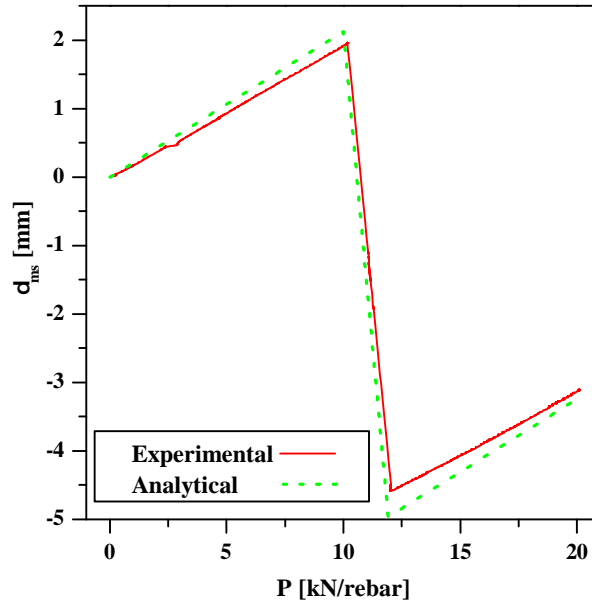


Figure 6.47.: Small-scale prototype serviceability behaviour with prestress: experimental test *vs.* analytical simulation

Table 6.4.: Small-scale prototype serviceability behaviour with prestress: midspan average deflection ( $\delta_{ms}$ ) and stiffness ( $K$ ) for loads and prestress. Experimental test *vs.* analytical simulation.

Source	Load				Prestress			
	$\delta_{ms}$		$K$		$\delta_{ms}$		$K$	
	(mm)	diff. (%)	(kN/mm)	diff. (%)	(mm)	diff. (%)	(kN/mm)	diff. (%)
Test	6.53	-	1.92	-	3.41	-	5.30	-
Analytical	7.09	8.58	1.77	-7.90	3.85	12.92	4.70	-11.40

#### 6.4.6.3. Failure behaviour

Concerning the analytical simulation of the flexural failure behaviour of the structure, it is necessary to determine the ultimate bending moment and shear force that the structure is able to sustain. In this particular case, due to the hybrid nature of the structure and the use of secondary bracing girders, no instability phenomena play part in the failure mode of the structure; therefore, the resistance is only limited by the cross-section strength, allowing a full exploitation of the materials' capacity.

Regarding the ultimate shear force ( $V_u$ ), a common (conservative) assumption is made for this type of hybrid structures that the strength is provided only by the webs of the profiles [60–62] (*i.e.* neglecting the contribution of the concrete member), which, thus, can be calculated with Eq. (6.10),

$$V_u \approx \tau_{u,LT} \cdot A_w \quad (6.10)$$

where  $\tau_{u,LT}$  is the in-plane shear strength of the GFRP webs.

The ultimate bending moment ( $M_u$ ), on the other hand, is computed considering the contribution of the different materials that constitute the hybrid structure and assuming full interaction at the interface. In this particular case, due to the geometry and mechanical properties of the materials involved, the ultimate bending moment is achieved within the linear-elastic range of the materials, due to tensile failure of the GFRP, and thus can be computed with Eq. (6.11),

$$M_u = EI \cdot \min \left( \frac{f_{tu,L}^{Flanges}}{E_{L,t}^{Flanges} \cdot (h_t - NA)}; \frac{f_{tu,L}^{Webs}}{E_{L,t}^{Webs} \cdot (h_t - NA - t_f)} \right) \quad (6.11)$$

where  $f_{tu,L}^{Flanges}$  and  $f_{tu,L}^{Webs}$  are the tensile strengths of the GFRP material for the longitudinal direction of the flanges and webs, respectively,  $E_{L,t}^{Flanges}$  and  $E_{L,t}^{Webs}$  represent the elasticity modulus in tension of the GFRP material for the longitudinal direction of the flanges and webs, respectively,  $h_t$  is the total height of the cross-section, and  $t_f$  is the thickness of the GFRP profiles' flanges. Applying Eqs. (6.10) and (6.11) to the present structure, the ultimate shear force and bending moment are 104.4 kN and 309.1 kNm, respectively.

In order to simulate the experimental flexural failure test (*cf.* Section 6.4.5), the two loads that acted on the structure must be considered: (i) the self-weight (2.14 kN/m); and (ii) the force applied by the hydraulic jack (*cf.* Figure 6.37). Using the ultimate forces in order to determine the failure load, one can use either (i) a simple failure criterion (Eqs. (6.10) and (6.11)), or (ii) the following second-order shear-flexure failure interaction

equation (suggested by Bank [4] and by the Italian design guidelines for FRP pultruded members [68]),

$$\left(\frac{V_{SW}(x) + V_F(x)}{V_u}\right)^2 + \left(\frac{M_{SW}(x) + M_F(x)}{M_u}\right)^2 \leq 1 \quad (6.12)$$

where  $V_{SW}$  and  $M_{SW}$  are, respectively, the shear force and bending moment due to the self-weight, whereas  $V_F$  and  $M_F$  are the shear force and bending moment due to the applied load.

Eq. (6.12) was used to predict the failure load ( $F_u$ ) and the correspondent failure cross-section, while Eq. (4.23) (page 90) was used to predict the deflections up to failure. Table 6.5 and Figure 6.48 summarise the results obtained and compare them with the experimental data.

Table 6.5.: Small-scale prototype failure behaviour: failure load ( $F_u$ ), midspan average deflection at failure ( $\delta_{ms-u}$ ), stiffness ( $K$ ) and neutral axis position ( $NA$ ). Experimental test and analytical simulations.

Source	$F_u$		$\delta_{ms-u}$		$K$		$NA$
	(kN)	diff.	(mm)	diff.	(kN/mm)	diff.	(mm)
Experimental	232.4	—	126.29	—	1.95	—	27.39
Analytical — Eq. (6.12)	172.4	-25.82%	101.08	-19.97%	1.71	-12.71%	29.06
Analytical — Eq. (6.13)	207.0	-10.93%	121.37	-3.90%			

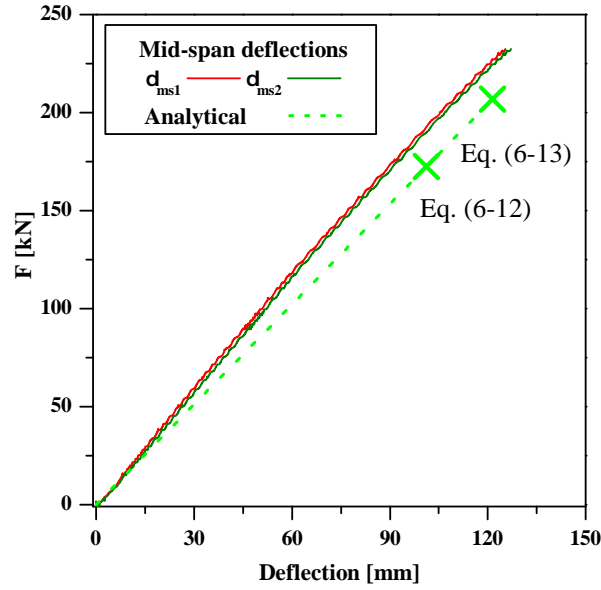


Figure 6.48.: Small-scale prototype failure behaviour: midspan deflections. Experimental tests and analytical predictions.

The analytical formulae presented predicted a similar behaviour to that observed experimentally with similar stiffness (-12.7%) and neutral axis position (difference of 1.67 mm). However, Eq. (6.12) underestimated the ultimate load ( $F_u$ ) and, consequently, the corresponding ultimate midspan deflection ( $\delta_{ms-u}$ ) was also underestimated (relative differences of -25.8% and -20.0%, respectively). The contribution of the shear force to the predicted failure load was 71.3%, whereas that of the bending moment was 28.7%. According to this failure criterion, failure should occur in the sections underneath the loading points.

Regarding the high relative difference in predicting the failure load with Eq. (6.12), one should note that the maximum shear stresses do not occur in the same fibres where maximum axial stresses develop. As an example, at the web-flange junction, where failure was triggered, the axial stresses are almost null. Conversely, at the bottom flange, where axial stresses are maximum, the shear stresses are minimum. Thereafter, for FRP structures in general (that do not yield), and for FRP-concrete hybrid structures in particular (where maximum shear stresses develop in fibres with low axial stresses, *cf.* Figure 6.49), failure load predictions using Eq. (6.12) may be overly conservative. Another quadratic failure criterion, also suggested by Bank [4], compares the maximum shear and axial stresses as follows,

$$\left( \frac{\tau_{SW}(x, z) + \tau_F(x, z)}{\tau_{u,LT}(z)} \right)^2 + \left( \frac{\sigma_{SW}(x, z) + \sigma_F(x, z)}{f_{tu,L}(z)} \right)^2 \leq 1 \quad (6.13)$$

where  $\tau_{SW}$  and  $\sigma_{SW}$  are, respectively, the shear and axial stresses due to the self-weight,  $\tau_F$  and  $\sigma_F$  are the shear and axial stresses due to the applied load and  $z$  represents the vertical development of the cross-section. In order to use this criterion, a shear stress distribution was calculated for a simplified thin-walled cross-section where the GFRP profiles' upper flanges were disregarded and the web was extended until the SFRSCC slabs' mid-line. This simplified cross-section presents a very similar flexural stiffness to that of the original cross-section (relative difference of -0.2%). It is also worth mentioning that, unlike the simple failure criterion expressed by Eq. (6.10) (which only considers the contribution of the GFRP webs), the shear stress distribution used to compute Eq. (6.13) takes into account the contribution of the concrete slab to the shear strength.

Figure 6.49 shows the analytical distribution of shear and axial stresses in the GFRP profiles' webs, as a function of the applied load ( $F$ ) for longitudinal position  $x = 1.025$  m (in which both bending moments and shear forces develop), calculated with Eqs. (6.14) and (6.15), respectively,

$$\tau(x, z) = b_p z_{NA} \frac{E_{L,t}^{Flanges}}{EI} V(x) + (z_{NA} - z)(z_{NA} + z) \frac{E_{L,t}^{Webs}}{2EI} V(x) \quad (6.14)$$

$$\sigma(x, z) = \frac{M(x) \cdot z}{EI} E_{L,t}^{Webs} \quad (6.15)$$

where  $z_{NA}$  represents the neutral axis height with reference to the mid-line of the bottom flanges of the GFRP profiles and  $z$  is the vertical distance to  $z_{NA}$ .

Using Eq. (6.13) with stresses computed by Eqs. (6.14) and (6.15) a failure load ( $F_u$ ) of 207.0 kN is determined, which is much closer to the experimental failure load when compared with the previous prediction (-10.9% *vs.* -25.8%, respectively). Accordingly, the prediction of the midspan deflection at failure ( $\delta_{ms-u}$ ) is also significantly improved (-3.9% *vs.* -20.0%, respectively), as summarized in Table 6.5 and illustrated in Figure 6.48. According to Eq. (6.13), failure is predicted to occur at the support sections, where the shear force ( $V(x=0)$ ) is maximum and the bending moment ( $M(x=0)$ ) is null and at the web-flange junction where the vertical shear stresses are maximum (*cf.* Figure 6.49 and Eq. (6.14)) — this was precisely the part of the cross-section where failure was observed in the tests (*cf.* Section 6.4.5). These results indicate that, according to the failure criterion expressed by Eq. (6.13) and for the present case, failure would be caused only by the shear stresses.

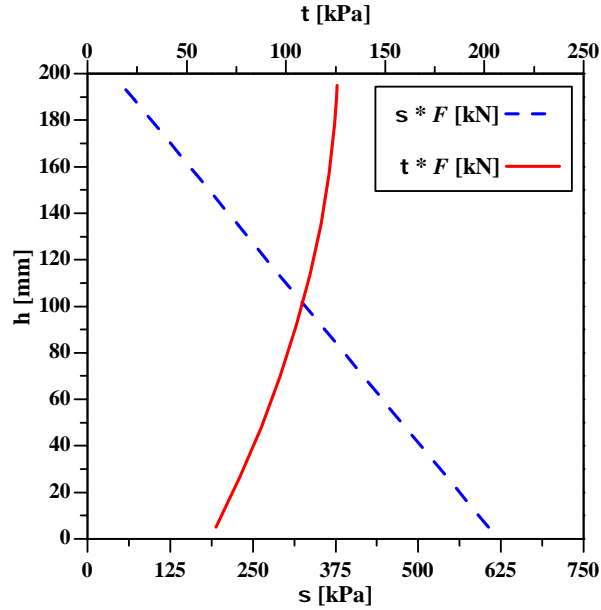


Figure 6.49.: Analytical prediction of the axial ( $\sigma$ ) and shear ( $\tau$ ) stress distributions along the depth of the web for  $x = 1.025$  m.

#### 6.4.7. Numerical simulation

The numerical simulations of the flexural tests described in Sections 6.4.3 to 6.4.5 were performed with a three-dimensional finite element (FE) model, illustrated in Figure 6.50, developed with the commercial package SAP2000.

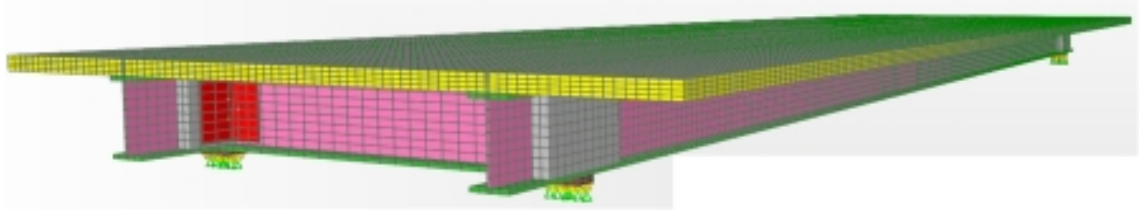


Figure 6.50.: Tri-dimensional illustration of the FE model.

Three types of finite elements were used: (i) 8-node solid brick elements; (ii) two-joint rigid links; and (iii) frame elements. The first elements were used to simulate the geometry of the prototype, namely the GFRP profiles' (i) webs and (ii) flanges, (iii) the SFRSCC slab, (iv) the epoxy adhesive layer, (v) the concrete jackets, (vi) the GFRP angle sections (*cf.* Figure 6.3), and (vii) the steel support plates. The two-joint rigid link elements were used to simulate the bolts connecting the main and secondary girders (*cf.* Figure 6.3) and to connect the steel support plates to the rotation centre of the supports. The frame elements were used only to simulate the prestress rebars.

The material properties used were those described in Section 4, derived from coupon testing. The GFRP material was modelled as orthotropic while all other materials were considered isotropic. Only linear-elastic numerical analyses were performed (similarly to the analytical simulations performed, *cf.* Section 6.4.6), according to the structural behaviour observed in the experiments (*cf.* Sections 6.4.3 to 6.4.5). The connection between the main girders and the slab (modelled explicitly by considering the 2 mm thick epoxy adhesive layer as solid brick elements), was also taken as fully linear-elastic in accordance with the results of the

shear connection tests performed (*cf.* Section 5) and with the experimental results of the static flexural tests reported earlier.

The vertical forces, simulating the loads used in the serviceability and failure tests, were applied as surface pressures at the top of the SFRSCC slab, considering the actual geometry of the loads used and the setup of each test (*cf.* Figures 6.36, 6.37, 6.38 and 6.41). The prestress applied in the serviceability tests was considered by applying horizontal point loads on the rebar frame elements, which were anchored to the concrete jackets (*cf.* Figures 6.39 and 6.46).

#### 6.4.7.1. Serviceability behaviour without prestress

The FE model developed was able to simulate the behaviour of the hybrid GFRP–concrete structure exhibited in the serviceability test with very high accuracy for both load configurations. Regarding load configuration 1, the FE model predicted the midspan deflections with a very good agreement when compared to the experimental results, with a maximum relative error (at the centre of the cross-section) of 6.7%. More importantly, the FE model was not only able to predict the flexural response but also the torsional response, which is depicted in Figure 6.51 that compares the experimental and numerical midspan vertical deflections for each load stage.

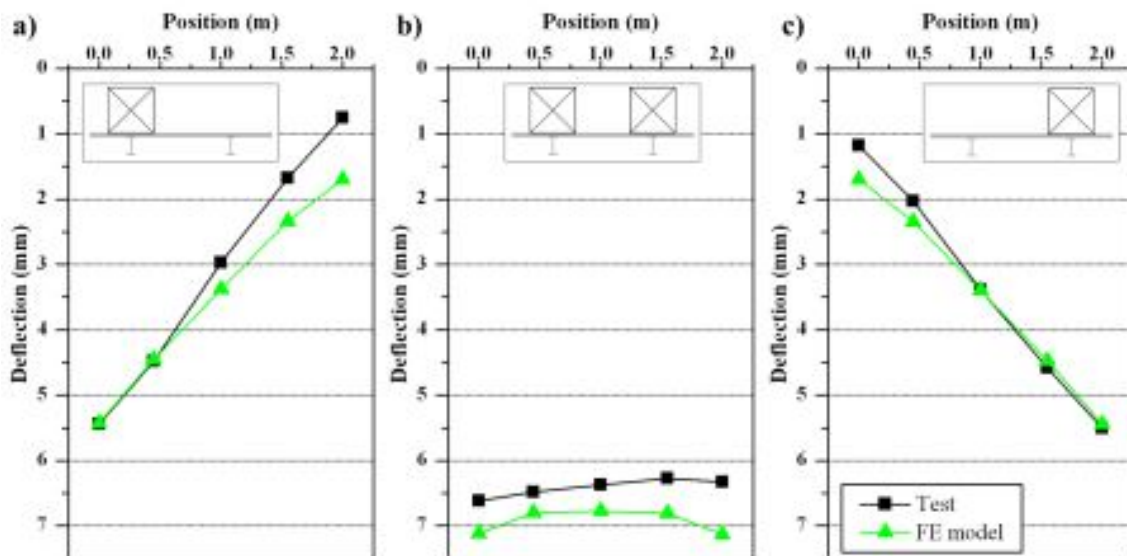


Figure 6.51.: Small-scale prototype serviceability behaviour without prestress for load configuration 1: a) load stage 1; b) load stage 2; and c) load stage 3. Experimental test *vs.* FE model prediction.

Regarding load configuration 2, the FE model predicted very similar midspan deflections and stiffness (relative differences of +3.6% and -3.5%, respectively). The predicted curvature and neutral axis position were also similar to those observed experimentally. Table 6.6 summarizes the results obtained with the numerical model and compares them with their experimental and analytical counterparts.

Moreover, Table 6.6 shows that the serviceability behaviour predicted by the FE model was much closer to the behaviour observed in the tests, compared with that simulated with the analytical model (*cf.* Section 6.4.3).

Table 6.6.: Small-scale prototype serviceability behaviour without prestress for load configuration 2: average midspan deflection ( $\delta_{ms}$ ), stiffness ( $K$ ), curvature ( $\chi$ ) and neutral axis position ( $NA$ ) with reference to the top of the cross-section. Experimental results, analytical and numerical predictions.

Source	$\delta_{ms}$		$K$		$\chi$		$NA$
	(mm)	diff. (%)	(kN/mm)	diff. (%)	$10^{-4}/m$	diff. (%)	(mm)
Experimental	6.79	-	1.85	-	19.29	-	24.55
Analytical	7.50	10.44	1.67	-9.45	20.61	6.82	29.06
Numerical	7.03	3.58	1.79	-3.46	20.43	5.89	29.51

#### 6.4.7.2. Serviceability behaviour with prestress

Regarding the simulation of the effects of external prestress, Figure 6.52 and Table 6.7 show that the FE model was also very accurate in predicting the experimental behaviour, namely regarding the deflections due to the vertical loads and the prestress action (relative differences of -4.4% and 0.3%, respectively). Once more, the numerical predictions were more accurate than those provided by the simpler analytical models.

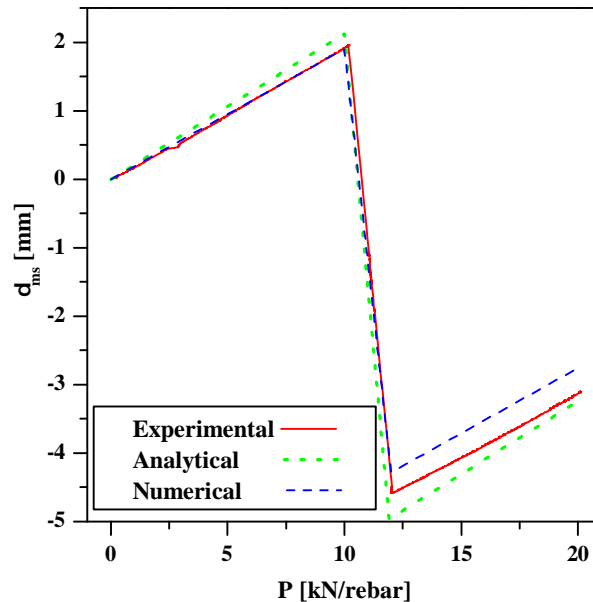


Figure 6.52.: Small-scale prototype serviceability behaviour with prestress: experimental results *vs.* analytical and numerical predictions.

#### 6.4.7.3. Failure behaviour

In what concerns the simulation of the flexural test up to failure, Figures 6.53 and 6.54 compare the experimental, analytical and numerical midspan deflections and axial strains, respectively, both as a function of the applied load. Once more, the FE model was able to simulate the flexural response in terms of stiffness, midspan deflections and neutral axis with very good accuracy, as summarized in Table 6.9.

The failure load was predicted (i) using the shear and axial stresses computed with the FE model and (ii) applying a failure criterion developed for FRP composite materials, the

Table 6.7.: Small-scale prototype serviceability behaviour with prestress: midspan average deflection ( $\delta_{ms}$ ) and stiffness ( $K$ ) for loads and prestress. Experimental test *vs.* analytical simulation.

Source	Load				Prestress			
	$\delta_{ms}$		$K$		$\delta_{ms}$		$K$	
	(mm)	diff. (%)	(kN/mm)	diff. (%)	(mm)	diff. (%)	(kN/mm)	diff. (%)
Experimental	6.53	-	1.92	-	3.41	-	5.30	-
Analytical	7.09	8.58	1.77	-7.90	3.85	12.92	4.70	-11.40
Numerical	6.24	-4.41	2.01	4.61	3.42	0.30	5.26	-0.78

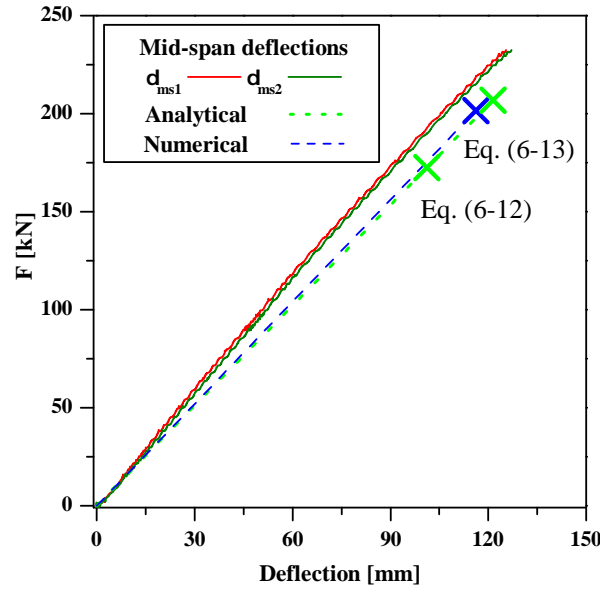


Figure 6.53.: Small-scale prototype flexural behaviour up to failure: midspan deflections. Experimental tests, analytical and numerical predictions.

Tsai–Hill failure criterion (*cf.* Section 4.2.3.4). This criterion is expressed by Eq. (4.45) (page 100).

The Tsai–Hill failure criterion provided a failure (initiation) load ( $F_u$ ) of 201.6 kN and predicted failure to start at the web–flange junction, at a distance of 1.025 m from the support sections. Table 6.9 shows, for the failure load, the Tsai–Hill index for the webs and flanges (this index was calculated for the flanges considering the same value of the in–plane shear strength  $\tau_{u,LT}$  as that of the webs) of the GFRP main girders and the maximum and minimum stresses in the SFRSCC slab. It can be seen that the failure criterion indicates that failure occurs in the webs, being largely governed by the shear strength (contribution of 99.4% for the Tsai–Hill failure index), which is corroborated by experimental observations. Regarding the SFRSCC deck, the results presented in Table 6.9 show that it is subjected to relatively low stresses, when compared to its ultimate strengths (*cf.* Table 4.30, page 111), confirming that in the brink of collapse the material was still in its linear–elastic range, thereby validating the linear analysis performed. Figure 6.55 plots the numerical variation of axial and shear stresses across the depth of the GFRP webs as a function of the applied load  $F$  (*cf.* Figure 6.37) in the failure section ( $x = 1.025$  m) and compares them with their analytical counterparts. It can be seen that the FE model predicts very similar distributions to those determined from the analytical formulae presented earlier, with the maximum shear stresses occurring in the top of the web where the axial stresses are minimum. However, unlike the quadratic criterion based on stresses (*cf.* Eq. (6.13)), the Tsai–Hill criterion does



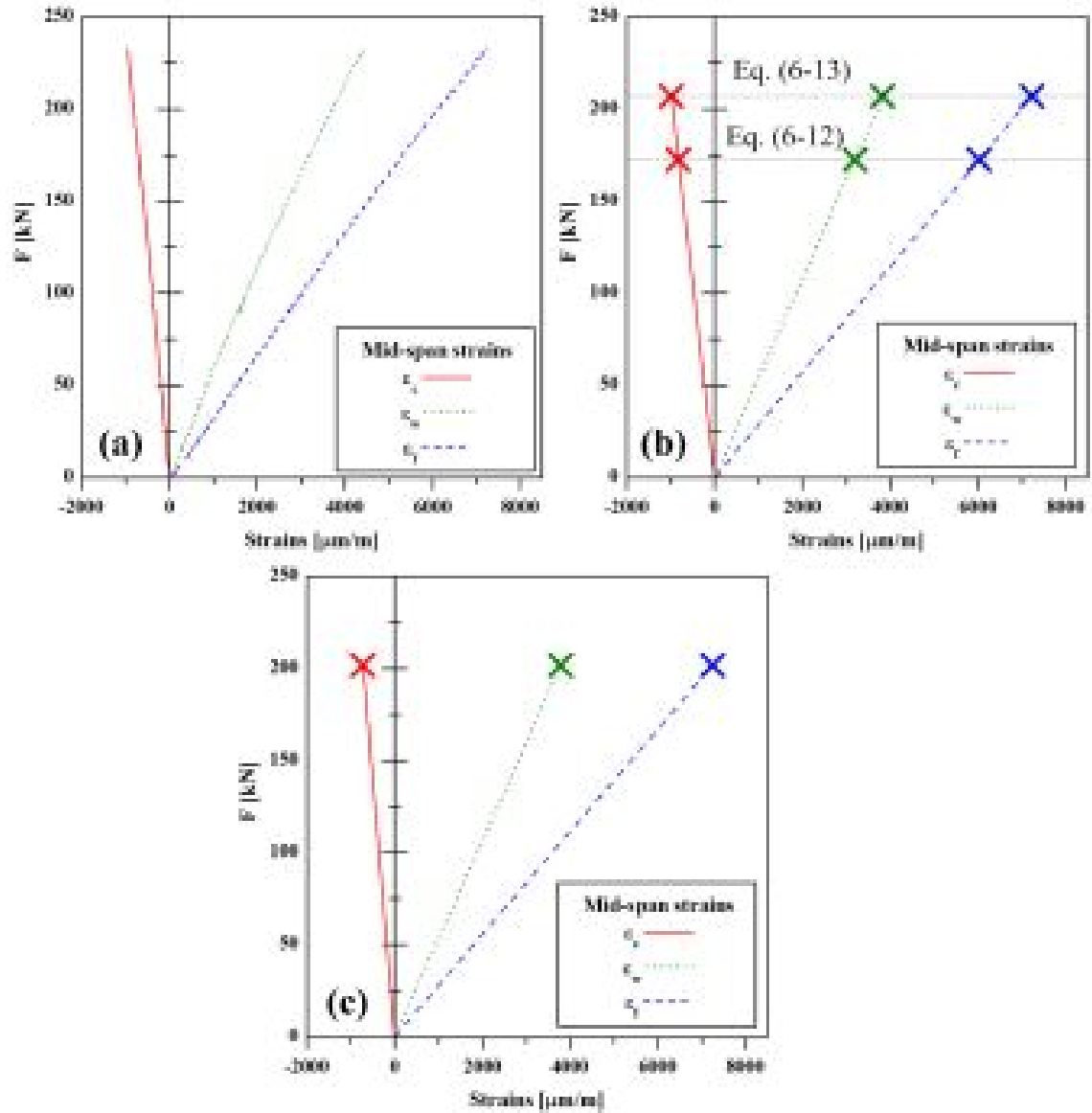


Figure 6.54.: Small-scale prototype flexural behaviour up to failure: midspan average strains results for a) experimental tests, b) analytical and c) numerical predictions.

not predict failure to occur in the support sections, indicating that axial and transverse stresses had a small contribution to failure ( $\leq 0.6\%$ ).

#### 6.4.8. Conclusions

This Section presented the study about the static flexural behaviour of the small-scale prototype, namely in what concerns the (i) serviceability and failure responses of this particular GFRP-concrete hybrid structure, and (ii) the ability of current analytical and numerical tools in predicting such behaviour.

The experimental tests showed that the flexural behaviour of the footbridge prototype is linear-elastic up to failure. Collapse was brittle and triggered by shear failure at the web-flange junction of one of the GFRP profiles. Although no loss of stiffness was observed prior to failure, the high deflections in the brink of collapse ( $\approx L/43.5$ ) should provide a

Table 6.8.: Small-scale prototype failure behaviour: failure load ( $F_u$ ), midspan average deflection at failure ( $\delta_{ms-u}$ ), stiffness ( $K$ ) and neutral axis position ( $NA$ ). Experimental test, analytical and numerical simulations.

Source	$F_u$		$\delta_{ms}$		$K$		$NA$
	(kN)	diff.	(mm)	diff.	(kN/mm)	diff.	(mm)
Experimental	232.4	—	126.29	—	1.95	—	27.39
Analytical — Eq. (6.12)	172.4	-25.82%	101.08	-19.97%	1.71	-12.71%	29.06
Analytical — Eq. (6.13)	207.0	-10.93%	121.37	-3.90%			
Numerical	201.6	-13.24%	116.24	-7.96%	1.74	-11.22%	24.88

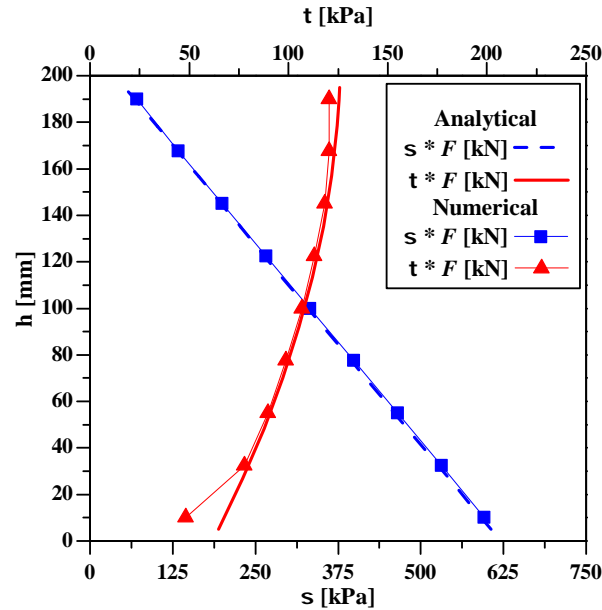


Figure 6.55.: Small-scale prototype failure behaviour: analytical and numerical axial ( $\sigma$ ) and shear ( $\tau$ ) stress distributions along the depth of the web for  $x = 1.025$  m.

clear warning of structural malfunction. It was also shown that the introduction of external prestress is an effective way to mitigate the instantaneous deflections of GFRP–concrete hybrid structures. Further studies are required to investigate (i) the use of FRP rebars instead of steel to increase durability; (ii) the use of deviators in order to achieve a pseudo-ductile failure (in which the FRP prestress rebars fail prior to the remaining structural components); and (iii) the long-term behaviour of the prestress solution, including the effects of creep and relaxation.

The analytical and numerical models developed in this study were able to predict the serviceability and failure structural static responses of the footbridge prototype with good accuracy, proving to be reliable tools for the design of GFRP–concrete hybrid structures. In fact, both types of models were able to predict (i) the linear elastic behaviour of the structure up to failure, (ii) the effects of the external prestress, (iii) the failure mode and location (shear failure in the web–flange junction), and (iv) the strength. In what concerns the analytical models, because maximum shear and axial stresses do not concomitantly develop in the same fibres (particularly for this type of hybrid cross-section), in order to avoid overly conservative strength predictions, the failure criterion should be based on stresses and not on applied forces.

Table 6.9.: Numerical failure analysis for the small-scale prototype — maximum Tsai–Hill index for GFRP laminates and maximum stresses in the SFRSCC.

$F_u$ (kN)	Tsai–Hill index (-)			SFRSCC stress (MPa)	
	Webs	Top flanges	Bottom flanges	Tension	Compression
201.61	1.00	0.29	0.53	3.2	41.1

## 6.5. Dynamic behaviour of the prototype

The present Section presents the study of the dynamic behaviour of the small-scale GFRP–SFRSCC footbridge prototype. This study includes experimental investigations regarding the modal identification of the footbridge structure and its response under pedestrian loads. Additionally, the results of the experimental investigations are compared with analytical and numerical predictions.

### 6.5.1. Modal identification

#### 6.5.1.1. Context

The design of structures made of traditional materials (reinforced concrete, prestressed concrete, steel), unlike that of FRP structures, is generally governed by the material strength, leading to structures with higher stiffness and weight than comparable FRP structures. Although stiffness and weight have contrary effects in the vibration frequencies, structures made of traditional materials, especially concrete structures, tend to exhibit higher structural vibration frequencies than their FRP counterparts. On the other hand, the lower self-weight of FRP structures, in principle an inherent advantage, raises concerns about their dynamic behaviour under human-induced loads, namely in footbridges. The relatively low material damping of FRP [132] also contributes to those concerns. When compared to all-FRP structures, GFRP–concrete hybrid structural solutions present higher stiffness and damping (due to the addition of concrete), thus mitigating the previous concerns and increasing their potential in footbridge structural solutions.

Modal identification tests have been an important tool in determining the dynamic characteristics of civil engineering structures, namely of the following modal parameters: (i) vibration frequencies, (ii) mode shapes, and (iii) damping ratios. The determination of these parameters is particularly important to validate the design models of structures that are particularly complex and/or involve non-traditional materials and structural systems, which is the case of GFRP–concrete hybrid solutions.

There are several examples in the literature of modal identification tests performed on civil engineering structures in general and bridge structures in particular (*e.g.* [133–137]). In order to determine the modal parameters by means of experimental tests, there are several methods of analysis available, namely input–output methods and output-only methods [138].

There are only a few studies reported in the literature regarding modal identification tests on FRP bridges. Bai and Keller [132] tested a two span all-GFRP truss footbridge, one of the spans presenting bolted connections and the other bonded connections. In this study, two different output only methods were used, namely (i) the peak peaking (PP) method, and (ii) stochastic subspace identification based on the state space model (SSI), to

estimate mode shapes, frequencies and damping ratios (only SSI). The two methods provided similar results. The experimental results were compared with analytical predictions based on the Euler–Bernoulli beam theory; a good agreement was obtained regarding mode shapes and frequencies. The authors showed that the connection between the pultruded elements considerably influences the dynamic behaviour, namely in what concerns the mode frequency and damping. Burgueño *et al.* [139] tested a bridge structural system constituted by carbon fibre reinforced polymer (CFRP) concrete filled tubular girders and a GFRP deck. This study confirmed the possibility of detecting and measuring damage in this type of structural system by means of modal identification tests. Experimental results were predicted with a good accuracy using finite element models.

The study presented in this Section concerns the modal parameter identification of the GFRP–concrete hybrid footbridge small-scale prototype. The experimental data is analysed in order to retrieve the modal parameters of the first four vibration modes with (i) an input–output identification algorithm based on the Rational Fraction Polynomial method [140] and with (ii) a simpler output–only method directly based on the Fast Fourier Transform (FFT) of the structural response. The former method allowed the determination of the mode shapes, frequencies and damping ratios, while the latter method was used to provide only the mode frequencies and shapes. The experimental results were then compared with predictions from analytical and numerical models, in order to assess the quality of these simulation tools for GFRP–concrete hybrid structures.

### 6.5.1.2. Experimental tests

The preliminary numerical analysis of the footbridge pointed to a frequency range of interest of 10 — 40 Hz. This aspect, combined with the reduced mass, suggested the interest of performing input–output testing based on the excitation by an adequate impact hammer and the measurement of both the applied excitation and the structural response, in order to apply conventional input–output modal identification techniques. To that end an impact load was applied on the top surface of the deck at two predefined positions and the structural response was measured in terms of vertical accelerations at 18 pre-determined positions. Figure 6.56 shows the positions over the deck of the impact load points (S#) and of the acceleration measurement points (A#).

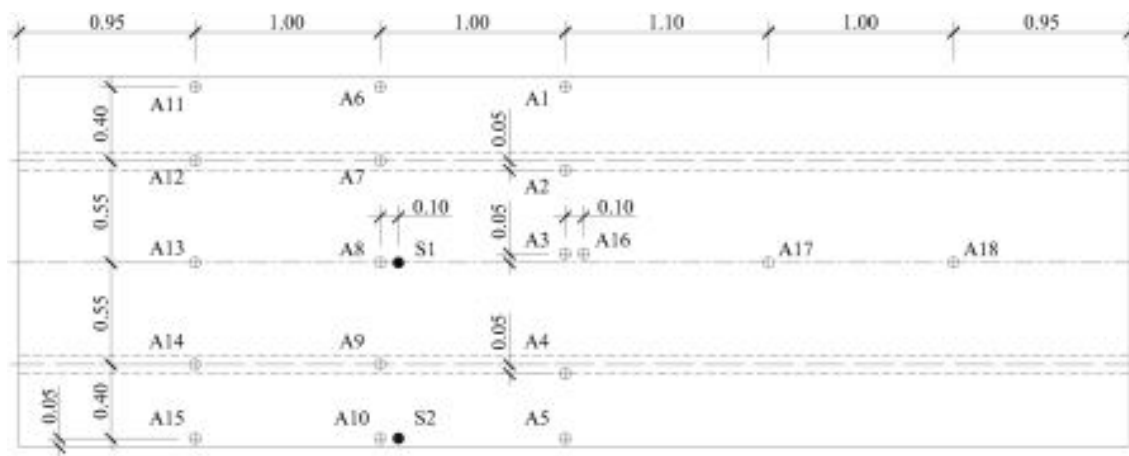


Figure 6.56.: Small-scale prototype modal identification tests: top plan view and instrumentation (S# load points and A# acceleration measurement points).

The loads were applied by means of an impact hammer with a rubber tip containing a built-in load cell (from *PCB*, model *086D50*). Accelerations were measured with two equivalent accelerometers (one from *Endevco* and the other from *Brüel&Kjær*) both connected to signal amplifiers (from *Brüel&Kjær*). Data was sampled at a rate of 400 Hz with a datalogger (from *HBM*, model *Spider8*) and stored in a PC. Figure 6.57 shows one of the modal identification tests being performed.



Figure 6.57.: Small-scale prototype modal identification tests: example of impact load being applied.

Considering the two excitation locations and the 18 response measurement positions depicted in Figure 6.56, as well as the available instrumentation, 15 s records were stored, each containing the time series of one impact hammer excitation applied at one location and the acceleration recorded simultaneously at two of the measurement points. Figure 6.58 shows, as an example, one of the time records collected simultaneously when exciting the structure at S1 and recording the acceleration at positions A1 and A5 (*cf.* Figure 6.56). In order to reduce the measurement noise, five impacts were applied for each configuration of the instrumentation; therefore, the total number of stored records was 90.

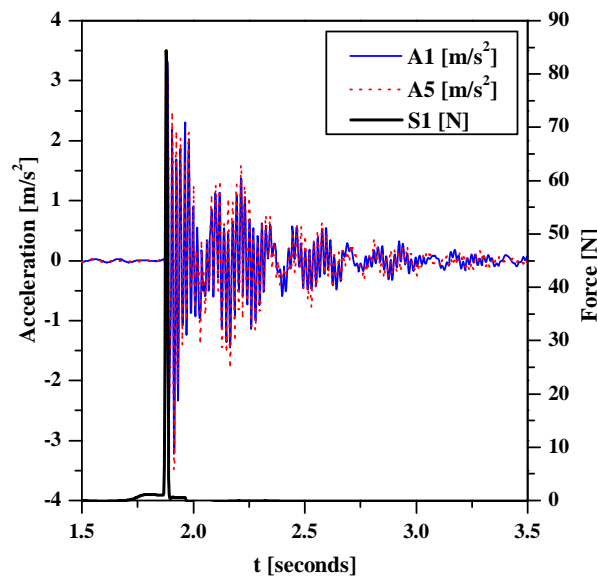


Figure 6.58.: Small-scale prototype modal identification tests: impact at point S1 and corresponding deck acceleration recorded at points A1 and A5.

In order to confirm the preliminary numerical results which, as mentioned earlier, set the frequency range of interest between 10 Hz and 40 Hz, a preliminary analysis of the experimental results was performed with a simple output-only method. This method consisted of applying the Fast Fourier Transform (FFT) algorithm to the acceleration measurements, identifying the frequencies for which the FFT presents its peak values. In order to identify these frequencies for both flexural and torsional modes, this method was performed to the half-sum and half-difference of the accelerations measured at points A6 and A10 when the impact load was applied in position S2. Figure 6.59 shows an example of the FFT obtained with one of these tests. This process allowed to determine the vibration frequencies presented in Table 6.10. These results are in accordance with the frequency range of interest predetermined earlier. The first and third vibration frequencies correspond to flexural modes (FFT of the half-sum of accelerations), while the second and fourth frequencies are concerned with torsional modes (FFT of the half-difference of accelerations). One should also note that the third and fourth mode frequencies are quite similar. Furthermore, from the analysis of Figure 6.59, it is clear that the first two vibration frequencies are very well defined, whereas the FFT shows a higher dispersion around the third and fourth vibration frequencies.

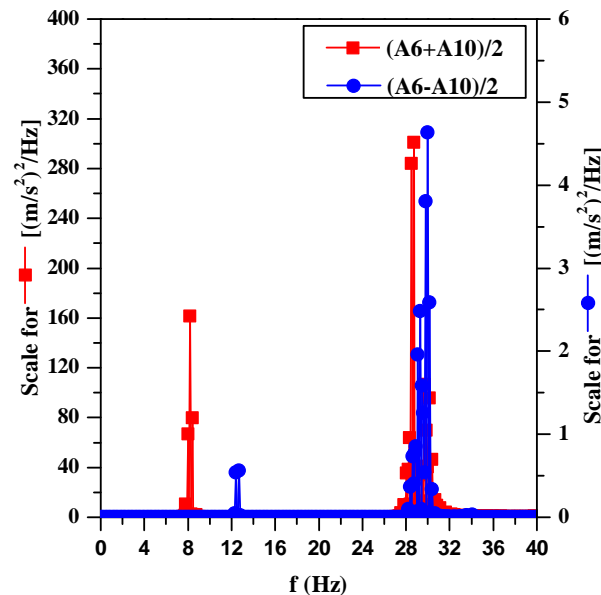


Figure 6.59.: Small-scale prototype modal identification tests, output-only method: example of the FFT of the half-sum and half-difference of accelerations at A6 and A10 for an impact load at S2.

Table 6.10.: Small-scale prototype modal identification tests: vibration frequencies and nature of identified modes (output-only method).

Mode no.	Vibration frequency (Hz)		Nature of mode
	(Avg.)	(Std. dev.)	
1	8.320	0.0837	1 <sup>st</sup> bending
2	12.520	0.1304	1 <sup>st</sup> torsion
3	28.576	0.1290	2 <sup>nd</sup> bending
4	29.962	0.1601	2 <sup>nd</sup> torsion

Regarding the full identification of the vibration modes, power spectra density estimates of force and accelerations were obtained, on the basis of the collected time records, as well

as cross-power estimates of the simultaneously collected force and accelerations records. These estimates were averaged considering the 5 sets of records collected for each setup. Finally, Frequency Response Functions (FRFs) were determined, relating the excitation at one location with the response measured at each of the 18 points by means of the ratio between the average power spectral densities of the response and excitation. Coherence function estimates were also obtained. Figure 6.60 shows an example of one FRF amplitude curve and the corresponding coherence function relating the excitation applied at point S2 with the acceleration measured at point A6 (*cf.* Figure 6.56).

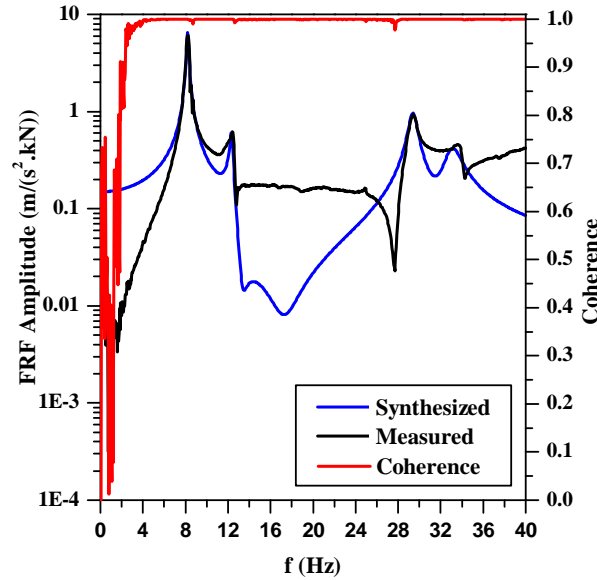


Figure 6.60.: Small-scale prototype modal identification tests: example of FRF amplitude relating excitation at point S2 with acceleration measured at point A6. Measured and synthesized in range 0–40 Hz, and coherence.

The identification of modal parameters was then made by individual fitting of sets of FRF estimates. This was achieved on the basis of an algorithm based on the rational fraction polynomial method [140]. Table 6.11 summarizes the identified natural frequencies and damping ratios, and characterises the modal configurations represented in Figure 6.61. The vibration frequencies obtained with the input–output method compare relatively well with the frequencies determined by the simpler output–only method used earlier for the first two vibration modes. For the third and fourth vibration modes, the frequencies obtained differ from those determined by the output–only method. This comparison indicates that the simpler output–only method is able to determine the frequency range of interest, but may not be able to determine the higher frequencies with accuracy, especially when two modes have similar frequencies, as is the case.

These results have shown that the first two vibration modes respect to symmetric flexure and torsion, respectively, while the third and fourth vibration modes respect to anti-symmetric flexure and torsion deformations, respectively. The deformations measured on position A1 were not in accordance with the global shape defined by the deformations on the other positions for all modes and were, therefore, disregarded in the construction of Figure 6.61. Additionally, for the third vibration mode (anti-symmetric bending) the deformation at position A8 was unexpectedly low. These (very rare) errors may be due to a poor calibration of the accelerometer in these positions, not detected during the test procedure. The vibration frequencies were successfully measured with low standard deviations (less than 1.08%, *cf.*

Table 6.11.: Small-scale prototype modal identification tests: vibration frequencies, damping ratios and nature of identified modes (input-output method).

Mode no.	Vibration frequency (Hz)		Damping ration (%)		Nature of mode
	(Avg.)	(Std. dev.)	(Avg.)	(Std. dev.)	
1	8.18	0.04	1.32	0.16	Symmetric bending
2	12.44	0.03	0.77	0.97	Symmetric torsion
3	28.21	0.24	1.54	0.46	Anti-symmetric bending
4	29.81	0.37	1.43	1.24	Anti-symmetric

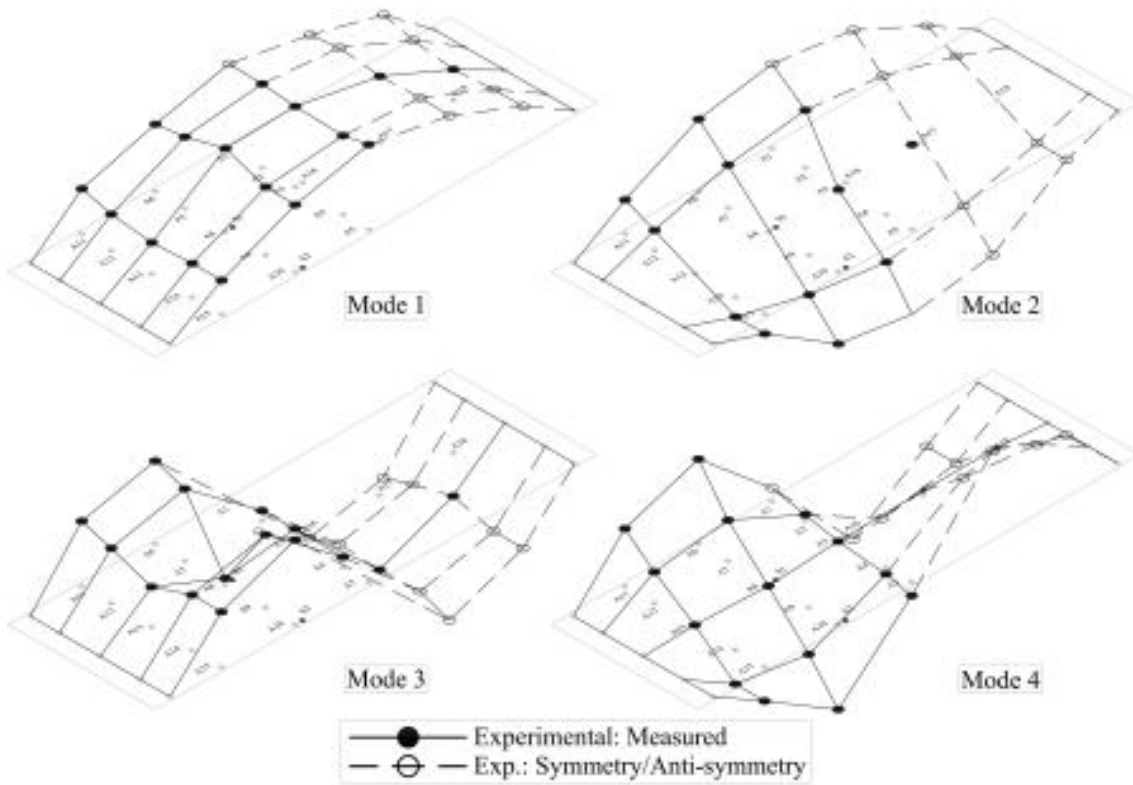


Figure 6.61.: Small-scale prototype modal identification tests: mode shapes attained (normalized to maximum deformation).

Table 6.11) providing further validation to the experimental results. Regarding the damping ratios, the experimental results indicate that the damping is slightly higher for the flexural vibration modes (1.32% and 1.54% respectively for the first and third modes) than for the torsional vibration modes (0.77% and 1.43%, respectively for the second and fourth modes), albeit the standard deviations obtained were relatively high (especially for the torsion modes) preventing definitive conclusions to be drawn on this subject. Nevertheless, these parameters, which are difficult to predict, requiring very complex analytical or numerical models [141], are very important for the prediction of forced vibration structural response, which is particularly relevant for footbridge structures. It is interesting to compare the damping ratios obtained here with those from other studies, namely the ones presented by Bai and Keller [132] and Burgueño *et al.* [139]. For the comparable mode shapes, Bai and Keller [132] obtained damping ratios higher than 5% for an all-GFRP footbridge. Albeit the addition of concrete elements is expected to lead to higher damping ratios, the footbridge tested by these authors is comprised of a truss structural system (with several



joints), whereas the structure studied herein is a simply supported beam element. Thus, the higher damping ratios of the all–GFRP structure should stem from the truss structural system and not from the materials used. Regarding the results presented by Burgueño *et al.* [139] for a hybrid CFRP–GFRP–concrete structural system, the comparable damping ratios were also higher (over 1.95%) than those presented herein, which can be explained from (i) the higher relative volume of concrete in the solution studied by those authors, and (ii) the fact that, unlike the structure presented herein, the connection between the deck and the girders may not be very stiff.

### 6.5.1.3. Analytical simulation

#### 6.5.1.3.1 Flexure: Euler–Bernoulli beam theory

Based on the equilibrium of an infinitesimal element of a vibrating beam, it is possible to obtain analytical predictions of its mode frequencies and shapes. The dynamic equilibrium of a uniform and straight beam may be expressed by Eqs. (6.16) and (6.17) in terms of transverse forces and bending moments, respectively [86], where  $M$  is the bending moment,  $V$  is the shear force,  $A$  is the cross–section area,  $I$  is its second moment of area,  $dx$  is the infinitesimal length,  $z$  is the transverse displacement,  $\theta$  is the rotation angle of the infinitesimal,  $t$  is the time and  $\rho$  is the volumetric weight.

$$\sum V = 0 \Rightarrow V - V - \frac{\partial V}{\partial x}dx - \rho A \frac{\partial^2 z}{\partial t^2}dx = 0 \Rightarrow \rho A \frac{\partial^2 z}{\partial t^2}dx + \frac{\partial V}{\partial x}dx = 0 \quad (6.16)$$

$$\begin{aligned} \sum M = 0 &\Rightarrow -M - \rho I \frac{\partial^2 \theta}{\partial t^2}dx + M + \frac{\partial M}{\partial x}dx - Vdx + \frac{\rho A}{2} \frac{\partial^2 z}{\partial t^2}(dx)^2 = 0 \\ &\Rightarrow \frac{\partial M}{\partial x} - V - \rho I \frac{\partial^2 \theta}{\partial t^2} + \frac{\rho A}{2} \frac{\partial^2 z}{\partial t^2}dx = 0 \end{aligned} \quad (6.17)$$

Furthermore, the slope of the transverse deformation ( $z$ ) may be expressed by Eq. (6.18),

$$\frac{\partial z}{\partial x} = \theta + \beta \quad (6.18)$$

where  $\beta$  represents the distortional angle of the infinitesimal. Consequently, the shear force ( $V$ ) and bending moment ( $M$ ) may be expressed by Eqs. (6.19) and (6.20), respectively:

$$V = -k\beta AG = -kAG \left( \frac{\partial z}{\partial x} - \theta \right) \quad (6.19)$$

$$M = -EI \frac{\partial \theta}{\partial x} \quad (6.20)$$

The Euler–Bernoulli beam theory does not consider the contribution of the shear deformations to the global deflections and, therefore, the distortional angle ( $\beta$ ) may be disregarded in Eq. (6.18) and the shear force ( $V$ ) is simply given by the first derivative of the bending moment ( $M$ ) with respect to the longitudinal development of the beam ( $x$ ). Thereafter, and

neglecting the contribution of the mass force (a simplification commonly made [86]) — the second order infinitesimal in Eq. (6.17) — it can be shown that for each vibration mode  $n$  the equilibrium of the infinitesimal is given by Eq. (6.21),

$$\frac{d^4 \bar{z}_n(x)}{dx^4} - \bar{z}_n(x) \cdot p_n^2 \frac{\rho A}{EI} = 0 \quad (6.21)$$

where  $\bar{z}_n(x)$  represents the  $n^{th}$ -mode shape and  $p_n$  is the  $n^{th}$ -mode vibrating frequency. The general solution of this equation is given by Eq. (6.22),

$$\begin{aligned} \bar{z}_n(x) = & A_n \cosh \left( \sqrt[4]{p_n^2 \frac{m}{EI}} x \right) + B_n \sinh \left( \sqrt[4]{p_n^2 \frac{m}{EI}} x \right) + \\ & C_n \cos \left( \sqrt[4]{p_n^2 \frac{m}{EI}} x \right) + D_n \sinh \left( \sqrt[4]{p_n^2 \frac{m}{EI}} x \right) \end{aligned} \quad (6.22)$$

where  $A_n$ ,  $B_n$ ,  $C_n$  and  $D_n$  give the relative magnitude of each arch (cosh, sinh, cos or sin, respectively) and are dependent of the boundary conditions. Applying the boundary restraints of a simply supported beam (expressed in Eq. (6.23)) to Eq. (6.22), the particular solution is found in the well-known forms of Eqs. (6.24) and (6.25) for the  $n^{th}$  mode shape and frequency ( $p_n$  in rad/s and  $f_n$  in Hz), respectively,

$$\bar{z}_n(0) = 0; \quad \bar{z}_n(L) = 0; \quad M(0) = 0 \approx \frac{d^2 \bar{z}_n}{dx^2}(0) = 0; \quad M(L) = 0 \approx \frac{d^2 \bar{z}_n}{dx^2}(L) = 0 \quad (6.23)$$

$$\bar{z}_n(x) = \sin \left( \frac{n\pi}{L} x \right) \quad (6.24)$$

$$p_n = \left( \frac{n\pi}{L} \right)^2 \sqrt{\frac{EI}{\rho A}} \quad \text{or} \quad f_n = \frac{\pi}{2} \left( \frac{n}{L} \right)^2 \sqrt{\frac{EI}{\rho A}} \quad (6.25)$$

### 6.5.1.3.2 Flexure: Timoshenko beam theory

In the Timoshenko beam theory, unlike the Euler–Bernoulli beam theory, shear deflections are not neglected, being considered in the computation of vibration frequencies and mode shapes. Thereafter, Eqs. (6.16) to (6.20) regarding the infinitesimal equilibrium are still valid, but the distortion angle ( $\beta$ ) is not disregarded. Once again, neglecting the contribution of the mass force, the infinitesimal equilibrium may be expressed by Eq. (6.26),

$$\frac{d^4 \bar{z}_n(x)}{dx^4} + r_g^2 \left( 1 + \frac{E}{kG} \right) K^4 \frac{d^2 \bar{z}_n(x)}{dx^2} + \left( r_g^2 \frac{\rho A}{kAG} p_n^2 - 1 \right) K^4 \cdot \bar{z}_n(x) = 0 \quad (6.26)$$

where

$$r_g^2 = \frac{I}{A}; \quad K^4 = \frac{p_n^2}{e^2} \quad e^2 = \frac{EI}{\rho A} \quad (6.27)$$

The general solution of the equilibrium expressed by Eq. (6.26) may be written as Eq. (6.28),

$$\bar{z}_n(x) = A_n \cos(\zeta x) + B_n \sin(\zeta x) + C_n \cosh(\xi x) + D_n \sinh(\xi x) \quad (6.28)$$

where

$$\zeta = \frac{\sqrt{2}}{2} \sqrt{(k^2 - 4w)^{0.5} + b}; \quad \xi = \frac{\sqrt{2}}{2} \sqrt{(k^2 - 4w)^{0.5} - b} \quad (6.29)$$

and

$$k = r_g^2 \left( 1 + \frac{E}{kG} \right) K^4; \quad w = \left( r_g^2 \frac{\rho A}{kAG} p_n^2 - 1 \right) K^4 \quad (6.30)$$

As an approximation, the same boundary conditions of the simply supported beam presented in Eq. (6.23) may be applied to Eq. (6.28) [86] providing an approximate solution for the vibration frequency (the mode shape achieved is the same than that for Euler-Bernoulli beam theory, *cf.* Eq. (6.24)) in which the shear deformation is taken into account. These frequencies are expressed by Eq. (6.31),

$$p_n = \pm \left( \sqrt{\frac{(v^2 - 4rj)^{0.5} - v}{2r}} \right) \quad \vee \quad \pm \left( \sqrt{\frac{(v^2 - 4rj)^{0.5} + v}{2r}} \right) \quad (6.31)$$

*or*  
 $f_n = \frac{p_n}{2\pi}$

where

$$r = r_g^2 \frac{\rho A}{kAG}; \quad v = - \left( \frac{n\pi}{L} \right)^2 r_g^2 \left( 1 + \frac{E}{kG} - 1 \right); \quad j = e^2 \left( \frac{n\pi}{L} \right)^4 \quad (6.32)$$

#### 6.5.1.3.3 Torsion

Regarding the torsion vibrations, the equilibrium on an infinitesimal may be expressed by Eq. (6.33) [86], similarly to the flexure equilibrium (*cf.* Eqs. (6.16) and (6.17)),

$$T + \frac{\partial T}{\partial x} dx - T - \rho I_p \frac{\partial^2 \phi}{\partial t^2} dx = 0 \Rightarrow \frac{\partial T}{\partial x} - \rho I_p \frac{\partial^2 \phi}{\partial t^2} = 0 \quad (6.33)$$

where  $T$  is the torque,  $I_p$  is the polar moment of inertia and  $\phi$  is the torsion rotation angle.

Considering the open wall geometry of the cross-section (*cf.* Figure 6.1), both uniform and warping torsion should be duly considered. Therefore, the torque ( $T$ ) may be expressed by Eq. (6.34),

$$T = GJ \frac{\partial \phi}{\partial x} - EI_w \frac{\partial^3 \phi}{\partial x^3} \quad (6.34)$$

where  $J$  is the torsion constant and  $I_w$  is the warping constant. Substituting Eq. (6.34) in Eq. (6.33), the equilibrium may be rewritten as in Eq. (6.35),

$$-EI_w \frac{\partial^4 \bar{\phi}_n(x)}{\partial x^4} + GJ \frac{\partial^2 \bar{\phi}_n(x)}{\partial x^2} + p_n^2 I_p \bar{\phi}_n(x) = 0 \quad (6.35)$$

where  $\bar{\phi}_n(x)$  represents the  $n^{th}$ -torsion mode shape. The general solution of Eq. (6.35) is identical to the one expressed in Eq. (6.28) with:

$$k = -\frac{GJ}{EI_w}; \quad w = -p_n^2 \frac{\rho I_p}{EI_w} \quad (6.36)$$

Applying the boundary conditions of the present case — a simply supported beam with fixed torque and free warping at both ends — one obtains:

$$\bar{\phi}_n(0) = \bar{\phi}_n(L) = \frac{\partial^2 \bar{\phi}_n(0)}{dx^2} = \frac{\partial^2 \bar{\phi}_n(L)}{dx^2} = 0 \quad (6.37)$$

The particular solution of Eq. (6.28), with  $k$  and  $w$  as expressed in Eq. (6.36), is found and may be expressed by Eqs. (6.38) and (6.39) with respect to the mode shape and vibration frequency ( $p_n$  in rad/s and  $f_n$  in Hz),

$$\bar{\phi}_n(x) = \sin\left(\frac{n\pi}{L}x\right) - \frac{\sin\left(\frac{n\pi}{L}L\right)}{\sinh(\xi L)} \sinh(\xi x) \quad (6.38)$$

$$p_n = \sqrt{\left(\frac{n\pi}{L}\right)^4 \frac{EI_w}{\rho I_p} + \left(\frac{n\pi}{L}\right)^2 \frac{GJ}{\rho I_p}} \quad \text{or} \quad f_n = \frac{p_n}{2\pi} \quad (6.39)$$

#### 6.5.1.3.4 Application to the present case study

In the present calculations the same principles and assumptions regarding the flexural and shear stiffness of the hybrid GFRP-concrete structure reported in Section 6.4 were taken into account. Regarding the torsional characteristics of the structure, the warping stiffness of the section was calculated considering an homogenized section with respect to the elasticity modulus of the GFRP flanges ( $E_{L,t}$ ) using the CUFSM [142] open-source software. The main torsion properties of the cross-section are the following: (i)  $GJ = 594 \text{ kNm}^2$ ; (ii)  $EI_w = 1684 \text{ kNm}^4$ ; and (iii)  $\rho I_p = 68.6 \text{ kgm}$ .

Figure 6.62 compares the experimental mode shapes to those obtained with the analytical models (*cf.* Eqs. (6.24) and (6.38)). Table 6.12 compares the analytically predicted mode frequencies for flexure, with both Euler-Bernoulli and Timoshenko beam theories, and torsion using the models discussed earlier.

The vibration frequencies predicted by the analytical models were able to correctly sort the vibration modes order. Regarding the flexural vibration modes, both Euler-Bernoulli and Timoshenko beam models provided very accurate predictions of the symmetric flexural mode vibration frequency, with relative errors of only 4.64% and -2.22%, respectively. For the anti-symmetric flexural mode, the frequency predicted by the Timoshenko beam model

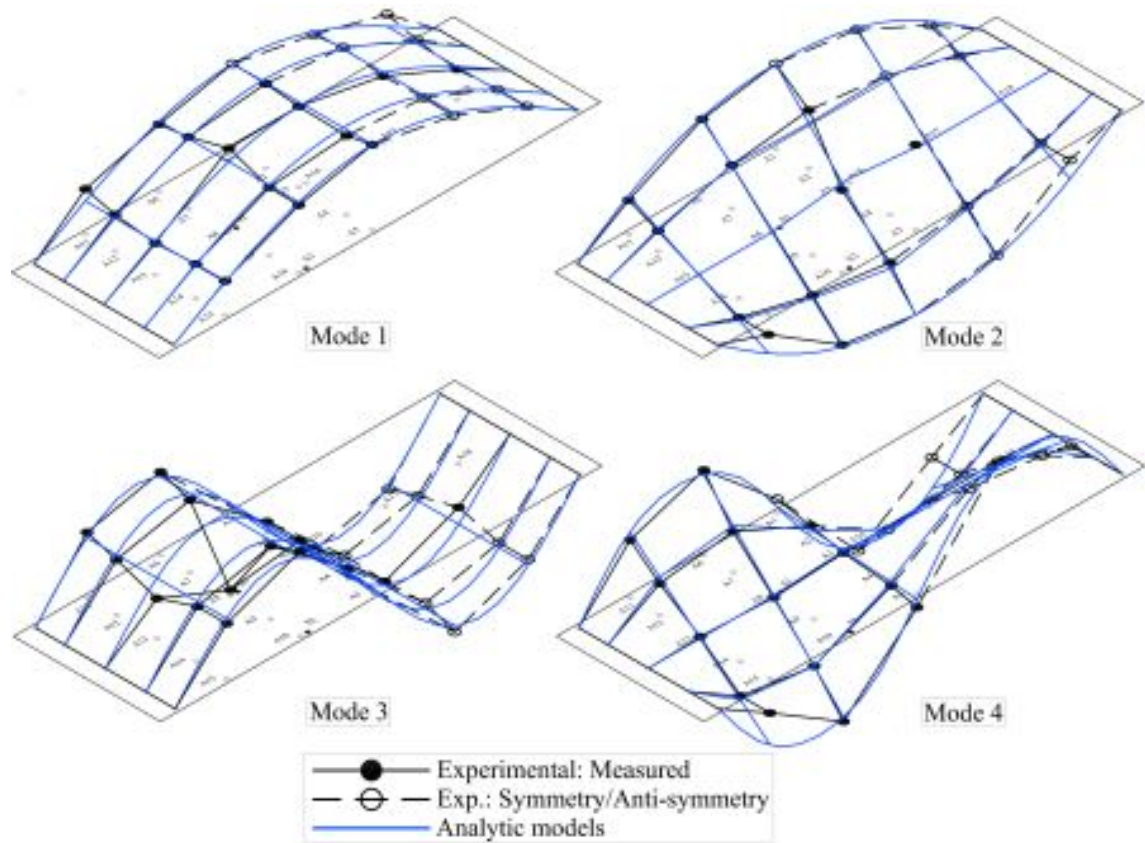


Figure 6.62.: Small-scale prototype modal identification: mode shapes (normalized to maximum deformation). Experimental results *vs.* analytical predictions.

was much closer to the one measured experimentally than the prediction obtained from Euler-Bernoulli's model (relative errors of -6.75% and 17.21%, respectively). These results, for both the symmetric and anti-symmetric flexural vibration mode frequencies, confirm the importance of the shear deformability in the dynamic flexural behaviour of this type of structures, pointing out the need of using the model presented in Section 6.5.1.3.2 for all-GFRP and GFRP-concrete hybrid structures. Regarding the torsional vibration modes, the model proposed was able to predict the vibration frequencies measured experimentally with excellent accuracy — relative errors of -5.66% and 8.48% for the symmetric and antisymmetric torsional vibration modes. These results point out the importance of both uniform and warping torsion in the behaviour of these structures and show that the concrete jackets and secondary girders provided at the support sections provide very limited, if any, warping fixity. The mode shapes predicted by the analytical models also compared very well with the experimental results, as shown in Figure 6.62, indicating that these analytical models may be used to predict the dynamic response of the hybrid structure for both free and forced vibrations.

#### 6.5.1.4. Numerical simulation

The FE model used to simulate the dynamic behaviour of the small-scale prototype was identical to that used to simulate its static behaviour (*cf.* Section 6.4.7). The only difference between these models consisted of substituting the fixed supports by very stiff springs ( $3.5 \times 10^6$  kN/m) in order to perform the dynamic analyses. On one side of the structure,

these support springs were provided in all directions, while on the opposite side no restraints were adopted in the longitudinal direction, simulating the sliding supports used in the experiments (*cf.* Figure 6.2).

The vibration mode frequencies obtained with the FE model are presented in Table 6.12, while Figure 6.63 plots the mode shapes obtained from the modal analyses.

Table 6.12.: Small-scale prototype mode frequencies: experimental results *vs.* analytical and numerical (FE) predictions.

Mode no.	Experimental	Analytical models						FE model	
		Euler–Bernoulli		Timoshenko		Torsion			
		Hz	diff.	Hz	diff.	Hz	diff.	Hz	diff.
1 <sup>a</sup>	8.18±0.04	8.56	+4.64%	8.00	-2.22%	-	-	7.89	-3.50%
2 <sup>b</sup>	12.44±0.03	-	-	-	-	11.74	5.66%	13.98	12.37%
3 <sup>a</sup>	29.21±0.24	34.24	+17.21%	27.27	-6.75%	-	-	27.01	-7.52%
4 <sup>b</sup>	33.81±0.37	-	-	-	-	33.19	8.48%	33.19	-1.84%

<sup>a</sup> Flexure

<sup>b</sup> Torsion

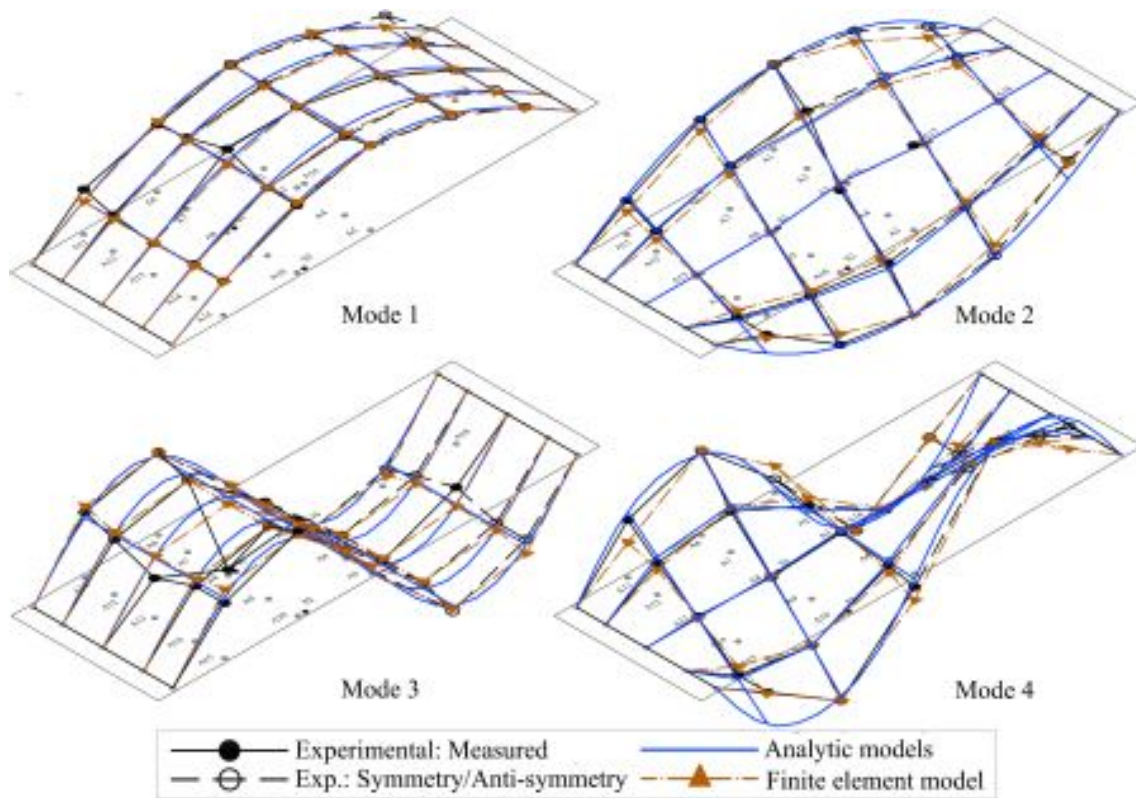


Figure 6.63.: Small-scale prototype modal identification: mode shapes (normalized to maximum deformation). Experimental results *vs.* analytical and numerical predictions.

It can be seen that the FE model was able to correctly predict the order of the vibration modes. In addition, the mode shapes compare very well with the experimental results (*cf.* Figure 6.63). Regarding the predictions of the vibration frequencies, the FE model was also able to predict the experimental results with good accuracy. The highest deviation from the experimental results was obtained for the symmetric torsional mode (+12.37%) and it may stem from the higher complexity of the torsional behaviour of this structure (the analytical model for torsion also presented poorer results than the models for flexure) and

its dependency on connection details and boundary conditions. In this regard, it is worth mentioning that the use of rigid links to simulate the bolted connections between main and secondary girders (*cf.* Section 6.4.7) might have increased the warping fixity at the support sections. Nevertheless, it seems fair to claim that in general the FE model was able to predict with good accuracy the dynamic modal behaviour of the GFRP–SFRSCC footbridge observed experimentally, proving to be an adequate tool in the simulation and design of hybrid GFRP–concrete structures.

#### 6.5.1.5. Conclusions

The results and analyses presented in this Section have shown that the experimental modal identification of the structure was successfully performed with resource to an input–output method, relating the excitation and the structural response with Frequency Response Functions (FRFs). The modal parameters were then identified by individually fitting the FRFs estimates with an algorithm based on the rational fraction polynomial method [140]. This process allowed the identification of the vibration mode frequencies, shapes and damping ratios for the first 4 modes. It was also shown that a simpler output–only method, based directly on the Fast Fourier Transform (FFT) of the structural response, could be used to determine the frequency range of interest. However, the latter method showed lower accuracy, especially for the higher vibration frequencies.

The analytical models presented were able to predict the vibration mode frequencies and shapes observed experimentally with an excellent accuracy for both flexural and torsional modes. Regarding the flexural modes, as expected, the Timoshenko beam model was more precise in predicting the vibration frequencies than the Euler–Bernoulli beam model. In fact, the former model takes into account the effects of shear deformability, which are generally non–negligible in this type of GFRP–concrete hybrid structures. Analytical results also showed the importance of both uniform and warping torsion in the overall behaviour of the footbridge prototype.

The FE model of the footbridge prototype developed was also able to predict the vibration mode frequencies and shapes with good accuracy. With the exception of the first torsional mode frequency, relative errors between experimental data and numerical predictions were very low.

The results presented show that it is possible to predict the modal behaviour of GFRP–concrete hybrid structures with common design tools, often used with conventional solutions made with traditional materials, provided that simple adaptations are performed, namely (i) the consideration of shear deformation for the flexural analytical models, (ii) the consideration of both uniform and warping torsion in analytical simulations (at least for open thin–walled sections), and (iii) the consideration of the material orthotropic properties in the numerical models. Moreover, the good comparison of the analytical predictions with both experimental results and numerical predictions proves that these models are an excellent tool for the earlier stages of design, providing excellent results with simple expressions, namely Eqs. (6.31) and (6.39).

## 6.5.2. Behaviour under pedestrian loads

### 6.5.2.1. Context

In the previous Section (*cf.* Section 6.5.1) experimental investigations regarding the intrinsic dynamic characteristics of the small-scale GFRP–concrete hybrid footbridge prototype were presented and the ability of current design tools in predicting those same characteristics was attested. The full understanding of these dynamic characteristics is of the utmost importance in footbridge structures given that the design of these structures is often governed by their serviceability behaviour, namely in what concerns the fulfilment of pedestrian comfort criteria [69, 74] (*cf.* Section 2.7). Potential problems regarding the serviceability behaviour of footbridges rise with the slenderness of the structural solutions [69] and, therefore, with the use of more deformable materials, such as GFRP. Thereafter, it is particularly important to correctly assess and predict the structural behaviour of GFRP–concrete hybrid structures under pedestrian loading with readily available design tools, namely commercial finite element (FE) packages.

In this context, experimental investigations regarding the dynamic response of the small-scale prototype under pedestrian loads were performed, namely (i) tests with one pedestrian, and (ii) crowd tests comprising several pedestrians travelling the footbridge. In order to assess the ability of current numerical design tools in predicting the structural response under pedestrian loads, the tests with one pedestrian are replicated with a FE model. To this end, the pedestrian induced load was measured experimentally and used as an input in the aforementioned FE model.

### 6.5.2.2. Experimental tests

#### 6.5.2.2.1 Definition of the pedestrian loads

Pedestrian loads depend considerably on a large number of variables that include the type of footwear, the type of pavement and the type of human induced load, which naturally varies from individual to individual [70]. Therefore, in order to ensure a proper comparison between the results of experimental dynamic tests under pedestrian actions and corresponding numerical simulations, the pedestrian loads induced by the specific individuals who performed the experimental tests should be properly characterised, namely with respect to the following parameters: (i) frequency between steps; (ii) velocity; (iii) step size; and (iv) load-time function. In the present study, the following three types of human motion were analysed: (i) walk slow; (ii) walk normal; and (iii) walk fast.

The first three parameters referred above were measured for each type of human motion using a chronograph and a ruler. In order to measure the fourth parameter, the load–time function, the pedestrian who performed the one–pedestrian test stepped over an SFRSCC slab ( $2.00 \times 1.00 \times 0.04 \text{ m}^3$ ) that was simply supported by four load cells from *Novatech*, with a load capacity of 10 kN, as shown in Figure 6.64. The load on each cell was measured at a rate of 50 Hz using a data logger from *HBM* (model *Spider8*) and registered in a PC. The load induced by the pedestrian (weighing 98 kgf) was calculated from the sum of the values measured by each load cell.

Figure 6.65 shows the load–time functions obtained for each type of motion and compares them with the functions proposed by Bachmann and Ammann [70] for the same motion





Figure 6.64.: Pedestrian induced actions: experimental evaluation of load-time functions.

types. Table 6.13 compares the remaining parameters, which defined the pedestrian loads, obtained in these tests with the values proposed by those authors [70].

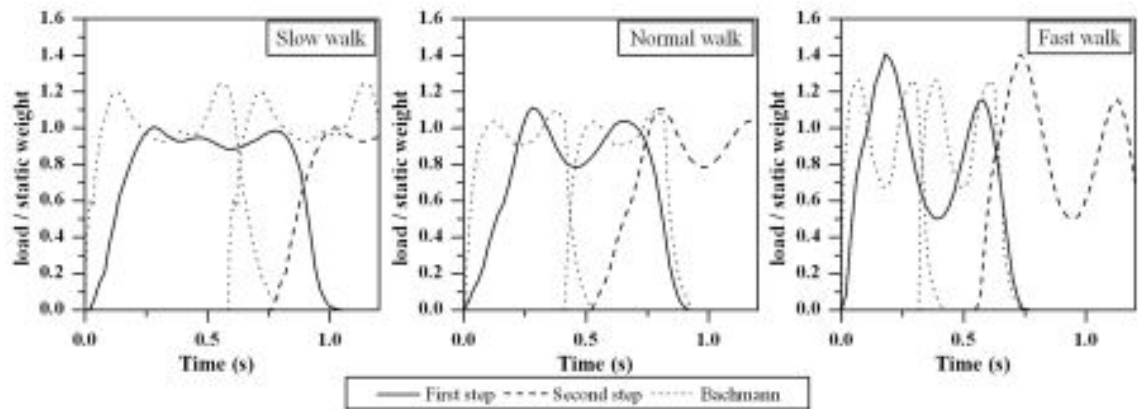


Figure 6.65.: Load-time functions for pedestrian action (slow, normal and fast walk): tests *vs.* Bachmann and Ammann [70].

The comparison between the results measured in the present study and those reported by Bachmann and Ammann [70] clearly shows that human induced actions can be highly variable for different individuals. In this particular case, Figure 6.65 shows that although the load-time curves have similar peak values and general shapes, the period of contact of the foot is much longer for the pedestrian who conducted the experiments than that considered by Bachmann and Ammann [70]. Table 6.13 also shows that the present pedestrian walks much more slowly (for every motion type) than what is proposed by those authors. In this regard, one should note that general load-time functions may be suitable for serviceability limit states design, but are not recommended for direct comparison with experimental results, as intended in the present Section.

### 6.5.2.3. One pedestrian tests

As already mentioned, the test regarding the dynamic response under pedestrian loads were performed above all to assess the quality of the numerical simulation. In addition, experimental tests were expected to provide a measure of the dynamic performance of

Table 6.13.: Main characteristics of pedestrian motion: experimental tests *vs.* Bachmann and Ammann [70].

Motion	Frequency (Hz)		Velocity (m/s)		Step size (m)	
	Test	Literature	Test	Literature	Test	Literature
Walk slow	$1.36 \pm 0.10$	$\sim 1.70$	$0.78 \pm 0.06$	1.10	$\sim 0.55$	0.60
Walk normal	$1.76 \pm 0.16$	$\sim 2.00$	$1.20 \pm 0.07$	1.50	$\sim 0.67$	0.75
Walk fast	$1.81 \pm 0.13$	$\sim 2.30$	$1.81 \pm 0.18$	2.20	$\sim 0.86$	1.00

the hybrid system proposed; although being a small-scale model, one did not expect the footbridge prototype to necessarily comply with standard limits.

The dynamic tests on the small-scale footbridge prototype were carried out for the same kinematic conditions adopted in the static flexural and modal identification tests (*cf.* Sections 6.4 and 6.5.1), *i.e.* it was tested in a simply supported span of 5.50 m.

The tests with one pedestrian consisted of subjecting the structure to the effect of a pedestrian (weighing 98 kgf) travelling along the deck, with vertical accelerations (on the top of the deck) being measured at the predefined positions (A#) shown in Figure 6.66. As mentioned earlier, three types of human motion were considered in this study: slow walk, normal walk and fast walk. Due to the reduced length of the prototype, jogging and running were not considered to be suitable for this study. Additionally, two transversal motion paths were considered, as depicted in Figure 6.66, one along the longitudinal axis of the prototype (centred path) and the other along the centre of one of the cantilevers (eccentric path).

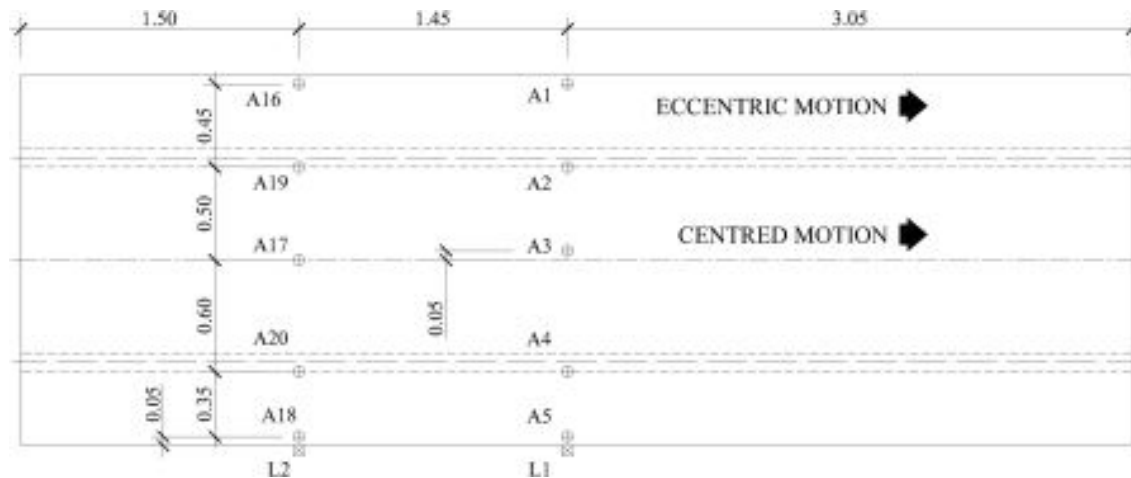


Figure 6.66.: Small-scale prototype behaviour under pedestrian loads tests: instrumentation and motion positioning (dimensions in meters).

Figure 6.67 shows a one pedestrian test undergoing for slow walk travelling in the eccentric path.

Accelerations were measured with two equivalent accelerometers (one from *Endevco* and the other from *Brüel&Kjær*), connected to two amplifiers (from *Brüel&Kjær*) with precision of  $0.01 \text{ m/s}^2$ , in paired positions. The data acquisition was performed using data loggers from *HBM* (models *Spider8* and *QuantumX*) at rates of 400 Hz and 200 Hz, respectively, and stored in a PC.

As an illustrative example, Figure 6.68 shows the vertical accelerations at location A3 for slow walk eccentric travelling. The full collection of the experimental records of vertical



Figure 6.67.: Small-scale prototype one pedestrian test.

acceleration for both paths and all motion types may be consulted in Appendix C. Table 6.14 presents a summary of the maximum accelerations (average  $\pm$  standard deviation) obtained in the dynamic tests with one pedestrian.

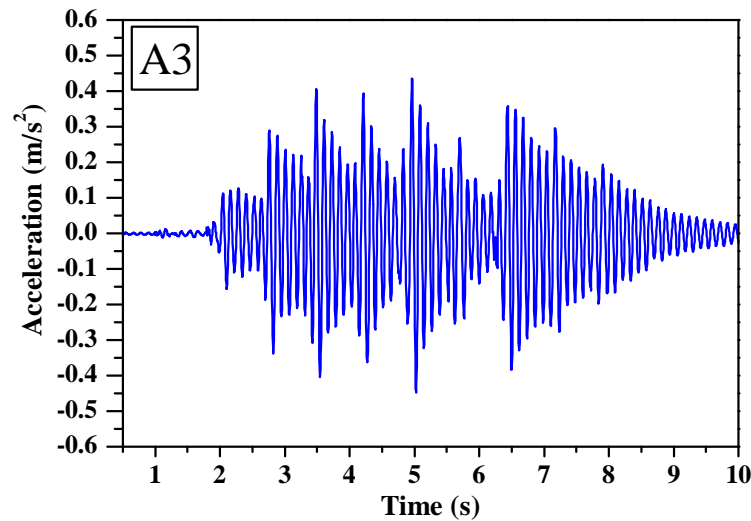


Figure 6.68.: Small-scale prototype one pedestrian tests: accelerations attained at A3 for slow walk at the cantilever.

These results show that the structural accelerations vary with the location within the structure, the motion type and the travelling position (centred or eccentric). While the structural accelerations rise with the walking pace, the results show that eccentric motion increases the accelerations in eccentric positions (even if those positions are in the opposite side of the pedestrian, *e.g.* A5 and A18). This effect clearly indicates that the eccentric motion excites the torsional vibration modes more than the centred motion, as expected. Regarding the magnitudes of the accelerations attained in these dynamic tests featuring one pedestrian, the results obtained show that in some cases the limit proposed in Eurocode 0 [64] for maximum vertical accelerations ( $0.70 \text{ m/s}^2$ ) is not fulfilled by this particular structure, although its first flexural frequency ( $8.18 \text{ Hz}$ , *cf.* Section 6.5.1.2) is higher than the minimum limit ( $5.0 \text{ Hz}$ ) established by Eurocode 0 [64], for which the direct assessment of the structural accelerations is not required to be performed in order to automatically fulfil with pedestrian comfort criteria (*cf.* Section 2.7).

These limits to the maximum accelerations, however, do not consider important parameters regarding pedestrian comfort such as human sensitivity and time of exposure to the vibrations or the frequency of those same vibrations. Furthermore, one should note that these

Table 6.14.: Small-scale prototype one pedestrian tests: maximum accelerations (mean  $\pm$  standard deviation).

Location	Path	Walk slow (m/s <sup>2</sup> )	Walk normal (m/s <sup>2</sup> )	Walk fast (m/s <sup>2</sup> )
A1	Centred	0.43 $\pm$ 0.04	0.70 $\pm$ 0.10	1.07 $\pm$ 0.25
	Eccentric	0.55 $\pm$ 0.08	1.23 $\pm$ 0.14	1.43 $\pm$ 0.14
A2	Centred	0.40 $\pm$ 0.08	0.70 $\pm$ 0.12	0.69 $\pm$ 0.12
	Eccentric	0.42 $\pm$ 0.07	0.77 $\pm$ 0.16	1.02 $\pm$ 0.11
A3	Centred	0.33 $\pm$ 0.09	0.75 $\pm$ 0.10	0.70 $\pm$ 0.22
	Eccentric	0.30 $\pm$ 0.09	0.57 $\pm$ 0.14	0.71 $\pm$ 0.05
A4	Centred	0.39 $\pm$ 0.07	0.63 $\pm$ 0.15	0.72 $\pm$ 0.10
	Eccentric	0.37 $\pm$ 0.06	0.76 $\pm$ 0.13	1.21 $\pm$ 0.13
A5	Centred	0.44 $\pm$ 0.08	0.61 $\pm$ 0.10	1.08 $\pm$ 0.30
	Eccentric	0.51 $\pm$ 0.04	1.03 $\pm$ 0.17	1.48 $\pm$ 0.15
A16	Centred	0.22 $\pm$ 0.04	0.52 $\pm$ 0.05	0.59 $\pm$ 0.14
	Eccentric	0.45 $\pm$ 0.06	0.84 $\pm$ 0.23	0.92 $\pm$ 0.23
A17	Centred	0.24 $\pm$ 0.07	0.48 $\pm$ 0.08	0.49 $\pm$ 0.15
	Eccentric	0.19 $\pm$ 0.06	0.37 $\pm$ 0.07	0.50 $\pm$ 0.04
A18	Centred	0.19 $\pm$ 0.03	0.48 $\pm$ 0.04	0.63 $\pm$ 0.11
	Eccentric	0.39 $\pm$ 0.07	0.76 $\pm$ 0.14	0.95 $\pm$ 0.26
A19	Centred	0.28 $\pm$ 0.03	0.45 $\pm$ 0.10	0.58 $\pm$ 0.17
	Eccentric	0.28 $\pm$ 0.04	0.55 $\pm$ 0.13	0.84 $\pm$ 0.10
A20	Centred	0.26 $\pm$ 0.02	0.46 $\pm$ 0.07	0.56 $\pm$ 0.13
	Eccentric	0.26 $\pm$ 0.03	0.56 $\pm$ 0.09	0.93 $\pm$ 0.19

accelerations should be reduced (assuming a linear-elastic behaviour) by approximately 30% before comparison with regulation limits, since it is recommended that these limits are verified for a pedestrian weighing 70 kgf [70] and the tests were performed by a pedestrian weighing 98 kgf.

#### 6.5.2.4. Crowd tests

In addition to the one pedestrian tests described in the former Section, the small-scale prototype was also subjected to dynamic tests under pedestrian crowd actions. These crowd tests were performed by requesting eight pedestrians (0.67 persons/m<sup>2</sup>, corresponding to a density classification between sparse and dense crowd, according to [74]) with weights ranging from 52.6 to 102.7 kgf to cross the small-scale footbridge prototype deck randomly for a period of over 5 minutes. During that period vertical accelerations were measured at positions A1 and A5 and transverse (lateral, horizontal) accelerations of the deck were measured at positions L1 and L2 (*cf.* Figure 6.66) with the same test apparatus used in the one pedestrian tests described earlier, but gathering the data at a rate of 50 Hz. Figure 6.69 shows a crowd test undergoing with multiple pedestrians circulating along the footbridge deck.

Figures 6.70 and 6.71 illustrate, respectively, the vertical and horizontal accelerations measured in these tests and compare them with the requirements set by Eurocode 0 [64]



Figure 6.69.: Small-scale prototype crowd test.

showing that the limits set by this document were surpassed several times, for both vertical and horizontal accelerations.

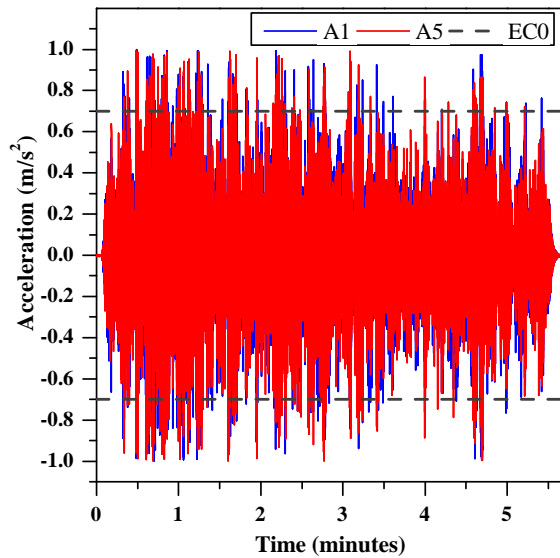


Figure 6.70.: Small-scale prototype crowd tests: vertical accelerations.

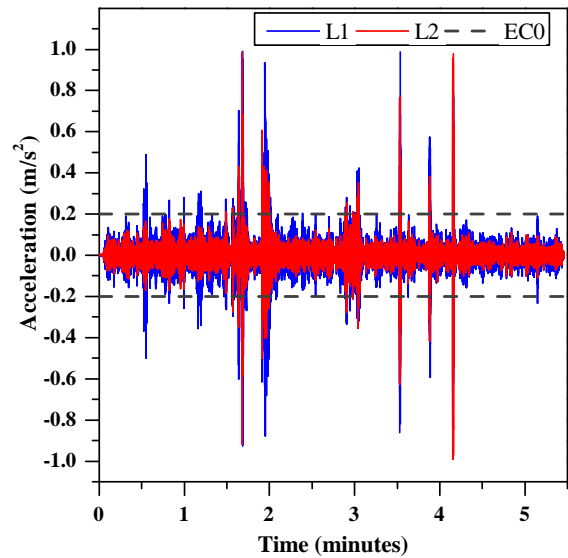


Figure 6.71.: Small-scale prototype crowd tests: horizontal accelerations.

Nevertheless, and given the above mentioned limitations of the Eurocode 0 [64] pedestrian comfort criteria, the accelerations observed in the crowd tests may be compared with more comprehensive pedestrian comfort criteria, namely those of ISO 10137 [75]. In order to do so, the acceleration-time records registered during the tests (*cf.* Figures 6.70 and 6.71) were transformed to root mean squared (RMS) accelerations in the frequency domain. Figures 6.72 and 6.73 compare the RMS vertical and horizontal accelerations, respectively, attained during the tests to the requirements of ISO 10137 [75]. For the verification of vertical accelerations, two comfort levels are compared, one for people traveling the footbridge and

other for people standing still on top of the footbridge while others travel along it (more severe situation); therefore, according to ISO 10137 [75], for the latter scenario, the base curve multiplying factor was reduced to half (from 60 to 30).

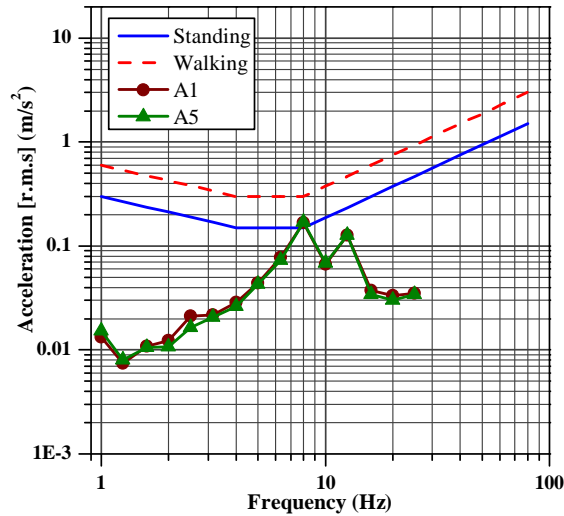


Figure 6.72.: Small-scale prototype crowd tests: expected vertical accelerations (RMS). Experimental tests *vs.* ISO 10137 [75].

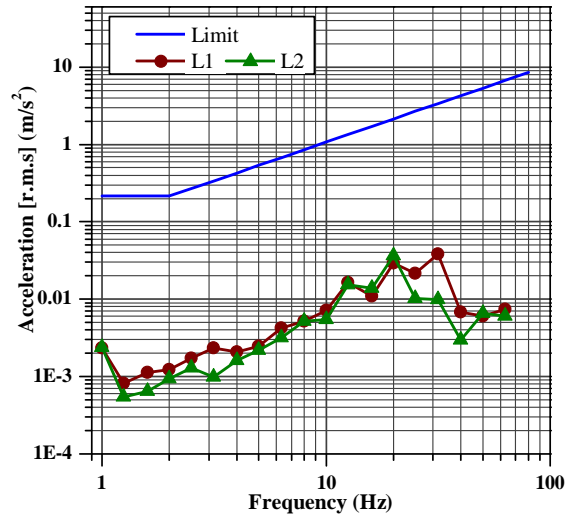


Figure 6.73.: Small-scale prototype crowd tests: expected horizontal accelerations (RMS). Experimental tests *vs.* ISO 10137 [75].

The results obtained show that, according to [75], there are low probabilities of complaints due to discomfort of pedestrians travelling the footbridge. Regarding pedestrians standing on the footbridge, the limit acceleration is slightly surpassed near the fundamental frequency of the structure which should not, therefore, cause discomfort.

#### 6.5.2.5. Numerical simulation

One of the main objectives of the experimental tests under pedestrian loads, namely the tests with one pedestrian, was to assess the ability of current design tools in predicting the structural response for this type of loads in GFRP–concrete structures. To that end, the one pedestrian tests described in Section 6.5.2.3 were modelled with the FE model, developed with the commercial package SAP2000, described earlier (*cf.* Sections 6.4.7 and 6.5.1.4). With this regard, two pairs of frame elements, with no mass, weight or stiffness, were added to the model and placed at the top of the deck, aligned with the longitudinal axis of the footbridge. One pair of frames was positioned centred with the longitudinal axis of the footbridge, while the other pair was positioned along the centre of one of the cantilevers, simulating the centred and eccentric motion paths (*cf.* Figure 6.66), respectively. For each pair, the frames were placed 30 cm apart from each other in the transverse direction, each frame simulating the pathway of one foot. For each type of motion (walk slow, walk normal and walk fast) and for each motion position (centred or eccentric), a point load of 98 kgf was assigned to the respective frame according to the motion characteristics presented in Table 6.13 simulating each footstep. The load cases were then combined in time history analysis with the respective load–time function (*cf.* Figure 6.65).

As an example, Figures 6.74 to 6.76 show the comparison between vertical accelerations measured in the dynamic tests and those determined from FE simulation at position A3,

for a pedestrian walking slowly along the eccentric path and at positions A1 and A3 for the pedestrian walking fast in the centred path, respectively. The complete records of accelerations (including experimental and numerical results) are presented in Appendix C.

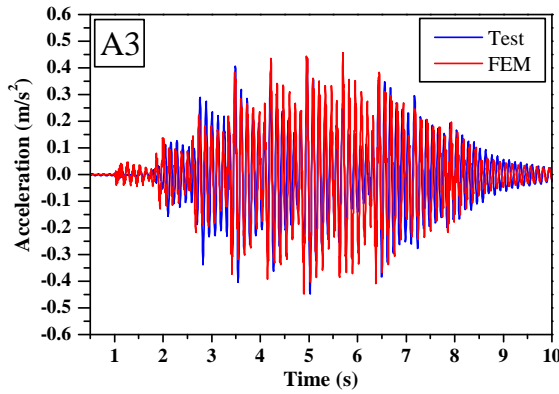


Figure 6.74.: Small-scale prototype one pedestrian tests: accelerations attained at A3 for slow walk at the cantilever. Experimental and numerical results.

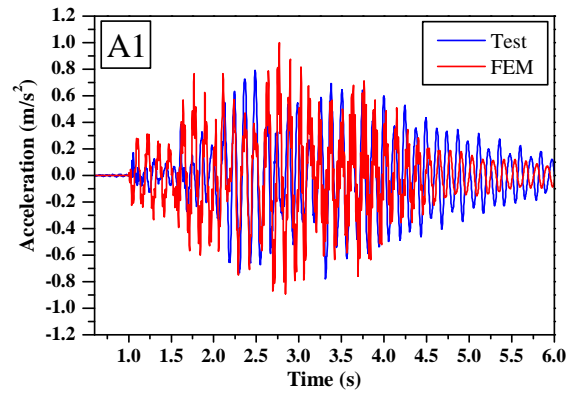


Figure 6.75.: Small-scale prototype one pedestrian tests: accelerations attained at A1 for fast walk at the centre. Experimental and numerical results.

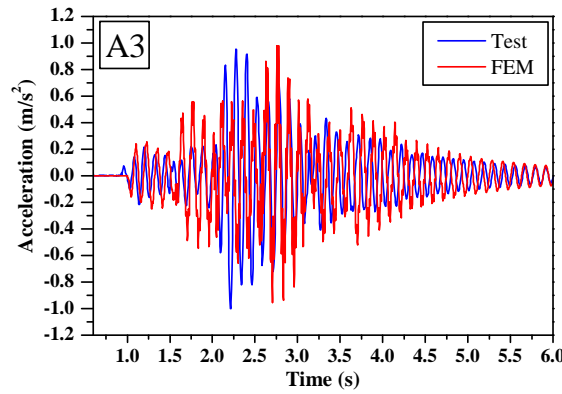


Figure 6.76.: Small-scale prototype one pedestrian tests: accelerations attained at A3 for fast walk at the centre. Experimental and numerical results.

Table 6.15 presents a detailed summary of the results obtained in the simulation of the dynamic response under pedestrian actions, comparing experimental and numerical values of maximum accelerations for all tests carried out.

The same comparison is illustrated in Figures 6.77 to 6.79 for each type of motion (walk slow, walk normal and walk fast), with the pedestrian traveling along the centred path and in Figures 6.80 to 6.82 with the pedestrian traveling along the eccentric path.

The comparison shown in Figures 6.74 to 6.76 reveals a very good agreement between the numerical predictions and the corresponding experimental data. Although the peak values may present some differences, the curves observed in the tests are generally well simulated by the model, proving the ability of the latter to predict the real dynamic behaviour of the structure. Such ability is attested by the comparison of peak accelerations for the three different types of motions presented in Figures 6.77 to 6.82. In addition, these figures show that the maximum accelerations obtained from FE simulation are generally very similar to

Table 6.15.: Small-scale prototype one pedestrian tests: experimental maximum accelerations (average  $\pm$  standard deviation) *vs.* numerical predictions.

Location	Path	Walk slow (m/s <sup>2</sup> )			Walk normal (m/s <sup>2</sup> )			Walk fast (m/s <sup>2</sup> )		
		Test	FE	diff.(%)	Test	FE	diff.(%)	Test	FE	diff.(%)
A1	Centred	0.43 $\pm$ 0.04	0.49	14.0	0.70 $\pm$ 0.10	0.66	-5.7	1.07 $\pm$ 0.25	1.00	-6.5
	Eccentric	0.55 $\pm$ 0.08	0.66	20.0	1.23 $\pm$ 0.14	0.88	-28.5	1.43 $\pm$ 0.14	1.90	-32.9
A2	Centred	0.40 $\pm$ 0.08	0.47	17.5	0.70 $\pm$ 0.12	0.57	-18.6	0.69 $\pm$ 0.12	0.80	15.9
	Eccentric	0.42 $\pm$ 0.07	0.52	23.8	0.77 $\pm$ 0.16	0.67	-13.0	1.02 $\pm$ 0.11	1.15	12.7
A3	Centred	0.33 $\pm$ 0.09	0.47	42.4	0.75 $\pm$ 0.10	0.55	-26.7	0.70 $\pm$ 0.22	0.98	40.0
	Eccentric	0.30 $\pm$ 0.09	0.46	53.3	0.57 $\pm$ 0.14	0.57	0.0	0.71 $\pm$ 0.05	0.90	26.8
A4	Centred	0.39 $\pm$ 0.07	0.44	12.8	0.63 $\pm$ 0.15	0.56	-11.1	0.72 $\pm$ 0.10	0.77	6.9
	Eccentric	0.37 $\pm$ 0.06	0.48	29.7	0.76 $\pm$ 0.13	0.56	-26.3	1.21 $\pm$ 0.13	1.27	5.0
A5	Centred	0.44 $\pm$ 0.08	0.50	13.6	0.61 $\pm$ 0.10	0.62	1.6	1.08 $\pm$ 0.30	1.02	-5.6
	Eccentric	0.51 $\pm$ 0.04	0.59	15.7	1.03 $\pm$ 0.17	0.71	-31.1	1.48 $\pm$ 0.15	1.81	22.3
A16	Centred	0.22 $\pm$ 0.04	0.36	63.6	0.52 $\pm$ 0.05	0.41	-21.2	0.59 $\pm$ 0.14	0.77	30.5
	Eccentric	0.45 $\pm$ 0.06	0.41	-8.9	0.84 $\pm$ 0.23	0.52	-38.1	0.92 $\pm$ 0.23	1.12	21.7
A17	Centred	0.24 $\pm$ 0.07	0.30	25.0	0.48 $\pm$ 0.08	0.35	-27.1	0.49 $\pm$ 0.15	0.61	24.5
	Eccentric	0.19 $\pm$ 0.06	0.35	84.2	0.37 $\pm$ 0.07	0.37	0.0	0.50 $\pm$ 0.04	0.66	32.0
A18	Centred	0.19 $\pm$ 0.03	0.36	89.5	0.48 $\pm$ 0.04	0.40	-16.7	0.63 $\pm$ 0.11	0.77	22.2
	Eccentric	0.39 $\pm$ 0.07	0.43	10.3	0.76 $\pm$ 0.14	0.46	-39.5	0.95 $\pm$ 0.26	0.93	-2.1
A19	Centred	0.28 $\pm$ 0.03	0.29	3.6	0.45 $\pm$ 0.10	0.35	-22.2	0.58 $\pm$ 0.17	0.51	-12.1
	Eccentric	0.28 $\pm$ 0.04	0.31	10.7	0.55 $\pm$ 0.13	0.40	-27.3	0.84 $\pm$ 0.10	0.79	-6.0
A20	Centred	0.26 $\pm$ 0.02	0.30	15.4	0.46 $\pm$ 0.07	0.35	-23.9	0.56 $\pm$ 0.13	0.54	-3.6
	Eccentric	0.26 $\pm$ 0.03	0.35	34.6	0.56 $\pm$ 0.09	0.35	-37.5	0.93 $\pm$ 0.19	0.66	-29.0

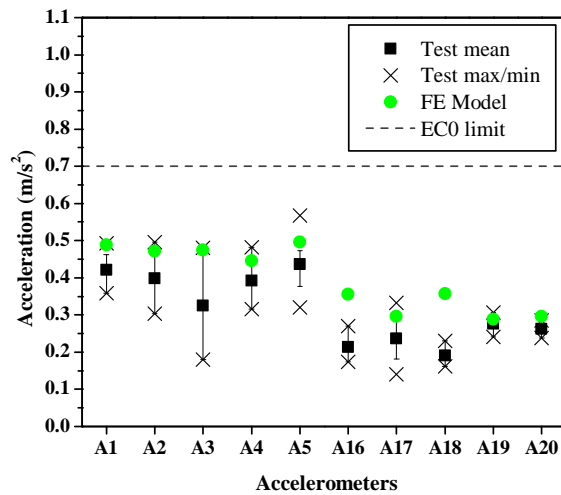


Figure 6.77.: Small-scale prototype one pedestrian tests: maximum accelerations attained for slow walk at the centred path.

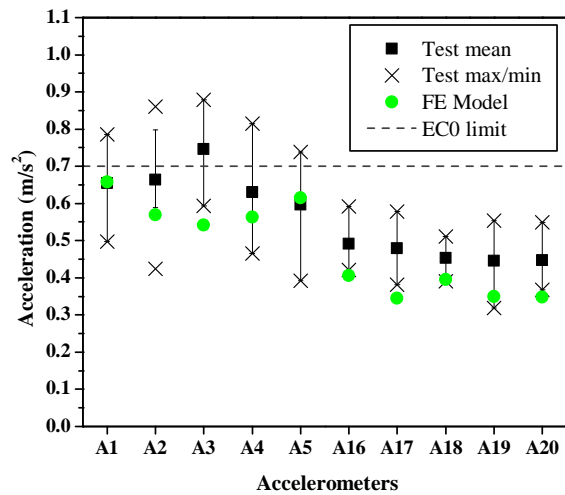


Figure 6.78.: Small-scale prototype one pedestrian tests: maximum accelerations attained for normal walk at the centred path.

the corresponding average experimental results, seldom being outside the range of maximum values measured in the dynamic tests.



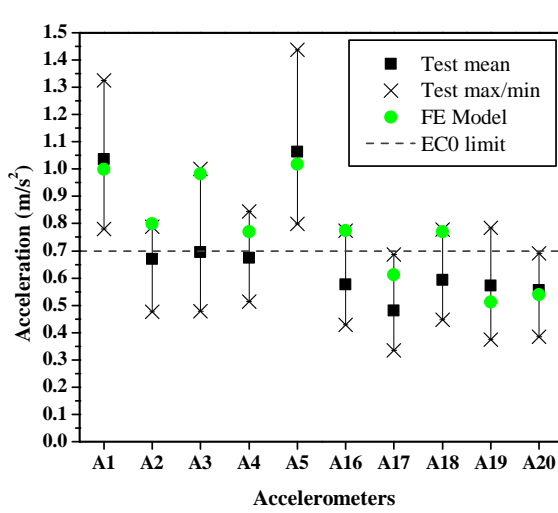


Figure 6.79.: Small-scale prototype one pedestrian tests: maximum accelerations attained for fast walk at the centred path.

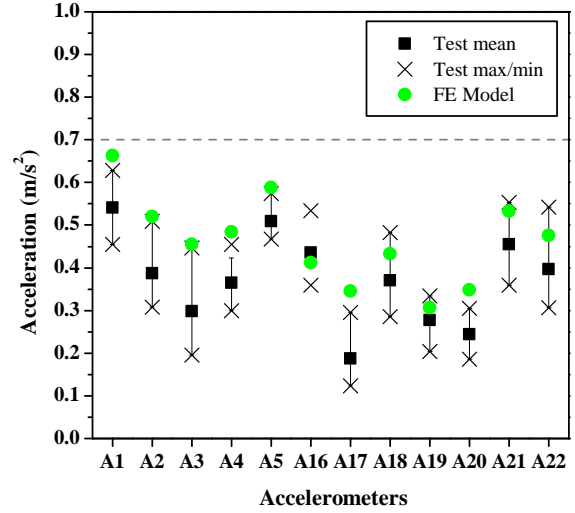


Figure 6.80.: Small-scale prototype one pedestrian tests: maximum accelerations attained for slow walk at the eccentric path.

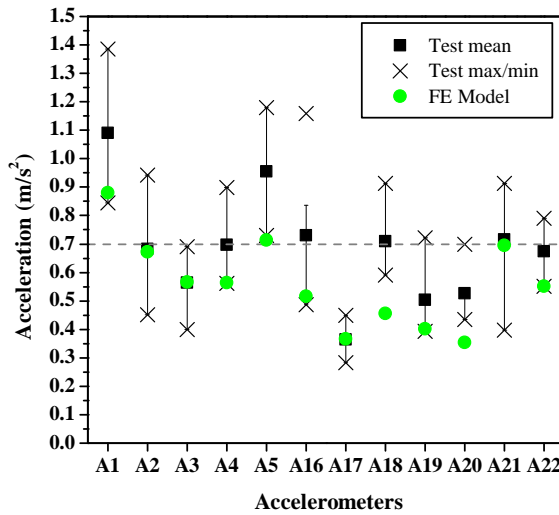


Figure 6.81.: Small-scale prototype one pedestrian tests: maximum accelerations attained for normal walk at the eccentric path.

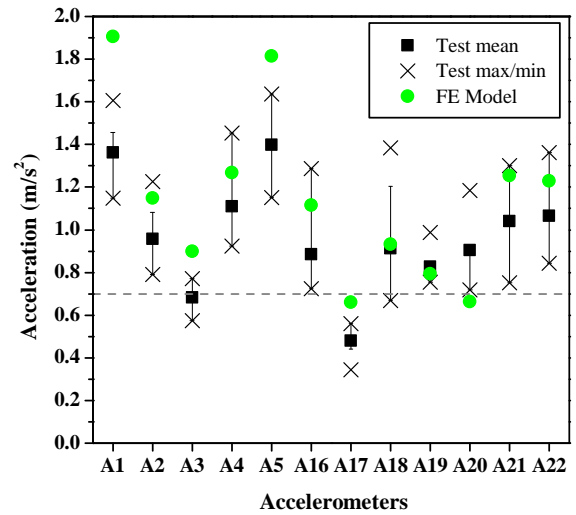


Figure 6.82.: Small-scale prototype one pedestrian tests: maximum accelerations attained for fast walk at the eccentric path.

#### 6.5.2.6. Conclusions

The results presented in this section regarding the definition of the pedestrian loads show that literature load models are not suitable for a direct comparison with experimental data obtained from dynamic tests, as pedestrian loads may vary considerably from individual to individual.

The FE model used proved to be able to predict with fairly good accuracy the dynamic response of the structure under pedestrian loads. The FE model was not only able to predict the maximum values of vertical accelerations attained in the dynamic tests, but it also proved

capable of reproducing the response of the structure over time with fairly good accuracy. Therefore, these numerical tools allow checking simple comfort requirements, such as those of Eurocode 0 [64], but they can also be used in more comprehensive comfort analysis of structures using, for instance, the criteria proposed in ISO 10137 [75].

Regarding the pedestrian comfort of the small-scale footbridge prototype, both experimental and numerical results showed that the peak values of vertical accelerations caused by a 98 kgf pedestrian are higher than the Eurocode 0 [64] limit. However, since literature [70, 74] indicates that comfort verifications should be performed considering a 70 kgf pedestrian, according to linear-elastic theory, a 29% reduction on the accelerations should be expected compared to those measured for the present pedestrian, which would allow fulfilling the above mentioned limit for the vast majority of situations analysed. Furthermore, acceleration peak values are not usually critical for the comfort of pedestrians subjected to vibration. In fact, the comparison of the experimental results with ISO 10137 [75] limits suggests that pedestrians should not feel discomfort due to the structural vibrations while crossing or standing on the footbridge (small-scale prototype).

## 6.6. Creep behaviour of the prototype

### 6.6.1. Context

FRP materials in general and GFRP pultruded profiles in particular, are known to present visco-elastic behaviour when subjected to sustained loads over time [143], commonly referred to as creep behaviour. Furthermore, the creep phenomenon in GFRP materials varies significantly with the type of solicitations the materials are subjected to, *i.e.*, compression, tension, flexure and shear. With this respect and although there are few studies regarding the creep of GFRP pultruded materials in tension (*e.g.* [38, 144]), it has been shown that creep is much less significant when these materials are tensioned than when they are compressed. Such difference stems from the higher susceptibility to creep of the polymeric matrices of GFRP profiles, which have a higher preponderance in the composite behaviour in compression, when compared to the glass fibres, which govern the composite behaviour in tension [143]. Consequently, these materials present an intermediate susceptibility to creep in flexure [38], because part of the material is compressed and part is tensioned. In this context, the combination of concrete elements (in compression) with GFRP pultruded profiles (in tension) may be advantageous in reducing not only the instantaneous deformability, but also the magnitude of GFRP creep deformation, thereby diminishing the long-term deformability.

This Section presents experimental and analytical investigations regarding the creep behaviour of the small-scale hybrid GFRP-concrete footbridge prototype. The creep tests were performed with different load levels and for different environmental conditions (temperature and relative humidity). The analytical study comprised the development of design formulae in order to predict the creep behaviour of GFRP-concrete hybrid flexural members. The model proposed, from now on referred to simply as analytical model, is based on the Timoshenko beam model using as input the material moduli provided by empirical creep models of the constituent materials, taking into account their actual stress state and overall environmental conditions. The proposed model is then validated through the comparison with test data.

### 6.6.1.1. Creep response of the GFRP material

As mentioned earlier, GFRP pultruded profiles, as well as other FRP composites, are known to be susceptible to creep phenomena [145]. Sá *et al.* [143] recently presented a literature review on the creep behaviour of GFRP pultruded elements in compression and in flexure. As mentioned earlier, these materials are more susceptible to creep in compression than in tension because the viscoelastic behaviour is more relevant in the polymeric matrixes than in the glass fibres [143]. The viscoelastic behaviour of GFRP materials is often predicted by empirical models based on experimental tests, namely with Findley's power law [4, 144, 146],

$$\Delta(t) = \Delta_0 + m \cdot t^n \quad (6.40)$$

where  $\Delta(t)$  is the time-dependent general deformation (strain or deflection),  $\Delta_0$  is the instantaneous general deformation,  $t$  represents time while  $m$  is a stress-dependent coefficient and  $n$  is a stress independent coefficient. Moreover, for low stress levels, the coefficient  $m$  may also be considered stress independent [144].

In order to determine the elasticity (or shear) modulus over time, Eq. (6.40) can be rewritten as follows [4, 146],

$$E(t) = \frac{E_0}{1 + \left(\frac{E_0}{E_t}\right) t^{n_E}} \quad \text{or} \quad G(t) = \frac{G_0}{1 + \left(\frac{G_0}{G_t}\right) t^{n_G}} \quad (6.41)$$

where  $E(t)$  and  $G(t)$  are the time-dependent elasticity and shear moduli, respectively,  $E_0$  and  $G_0$  are the instantaneous elasticity and shear moduli,  $E_t$  and  $G_t$  are known as the creep elasticity and shear moduli, while  $n_E$  and  $n_G$  are the Findley's power law stress independent coefficients with respect to the elasticity and shear moduli, respectively. The creep moduli may be determined with Eq. (6.42),

$$E_t = \frac{\sigma_m}{m'_\sigma} \quad \text{or} \quad G_t = \frac{\tau_m}{m'_\tau} \quad (6.42)$$

where  $\sigma_m$  (or  $\tau_m$  for shear) and  $m'_\sigma$  and  $m'_\tau$  are also determined empirically from creep tests [146] and

$$m_\sigma = m'_\sigma \sinh\left(\frac{\sigma}{\sigma_m}\right) \quad \text{or} \quad m_\tau = m'_\tau \sinh\left(\frac{\tau}{\tau_m}\right) \quad (6.43)$$

where  $\sigma$  is the applied axial stress (or  $\tau$  for shear stress).

Bank [4] proposed general creep models for GFRP pultruded profiles in service conditions subjected to compression and flexure, based on the empirical laws mentioned above. Table 6.16 shows the parameters proposed by Bank [4] for flexure, shear in flexure (relevant for the case study presented herein) and compression to be used in Eq. (6.41) with time ( $t$ ) in hours.

The EuroComp [38], on the other hand, presents graphical data on the evolution of the time-dependent moduli of unidirectional FRP composites in tension and in shear. Unlike the shear creep model presented by Bank [4], the model presented in EuroComp [38] does

Table 6.16.: Parameters of the GFRP creep model proposed by Bank [4].

Sustained loading type	$E_t$ (GPa)	$n_E$ (-)	$G_t$ (GPa)	$n_G$ (-)
Flexure	1241.06	0.3	186.16	0.3
Compression	1489.28	0.3	-	-

not specifically refer to shear in flexure; one assumes that this model refers to pure shear. The creep laws suggested in this document may be described by the following general equation:

$$E_t = E_0(\lambda - \varrho \cdot \ln t) \quad \text{or} \quad G_t = G_0(\lambda - \varrho \cdot \ln t) \quad (6.44)$$

The general creep laws defined by Eq. (6.44) are valid for  $t \geq 0.1$  h. Table 6.17 lists the parameters  $\lambda$  and  $\varrho$  (along with the corresponding coefficient of determination,  $R^2$ ) obtained by adjusting the graphical data for both tension and shear [38] to the logarithmic curve expressed by Eq. (6.44).

Table 6.17.: Parameters of the GFRP creep models derived from EuroComp [38].

Creep model for	$E_t$ (tension)	$G_t$
$\lambda$	0.99156	0.89676
$\varrho$	$5.96459 \times 10^{-5}$	$4.71867 \times 10^{-2}$
$R^2$	0.999	1.000

The Italian Guidelines [68] for the design of pultruded FRP members present discrete coefficients of viscosity for the elasticity and shear moduli as a function of time (1, 5, 10, 30 and 50 years). Table 6.18 shows the non-dimensional time-dependent moduli suggested by this document for the different periods.

Figure 6.83 compares the evolution of the several time-dependent elasticity and shear moduli with time, proposed in the above mentioned documents. For the models suggested in the EuroComp [38] and the Italian Guidelines [68], the reduction curves are general (*i.e.* independent of the instantaneous moduli), whereas for the model proposed by Bank [4] the curves refer to the instantaneous moduli of the GFRP used in the small-scale prototype (*cf.* Section 4.2.2.6). As expected, the model proposed by Bank [4] for the elasticity modulus in flexure reflects higher susceptibility to creep than the model proposed in the EuroComp [38] for the elasticity modulus in tension. Regarding the shear modulus evolution, the model proposed in EuroComp [38], presumably for pure shear, is more susceptible to creep than the model proposed by Bank [4] for shear in flexure. For both moduli, the models proposed by the Italian Guidelines [68] seem to fall in-between those of the other documents. It is also worth mentioning that the latter document [68], unlike Bank [4], suggests that the creep effects are more severe for the shear modulus than for the elasticity modulus. The Italian Guidelines [68], however, do not specify the loading type to which the time-dependent moduli refer, therefore a direct comparison may not be valid.

An external factor that may significantly influence the creep rates of FRP materials is temperature [144]. Although none of the previous documents specifies the temperatures for which the models are valid, a 25°C room temperature may be considered for these general

Table 6.18.: Time-dependent moduli proposed by the Italian guidelines [68].

t (years)	$E_t[\times E_0]$	$G_t[\times G_0]$
1	0.794	0.637
2	0.704	0.505
10	0.667	0.448
30	0.625	0.362
50	0.602	0.324

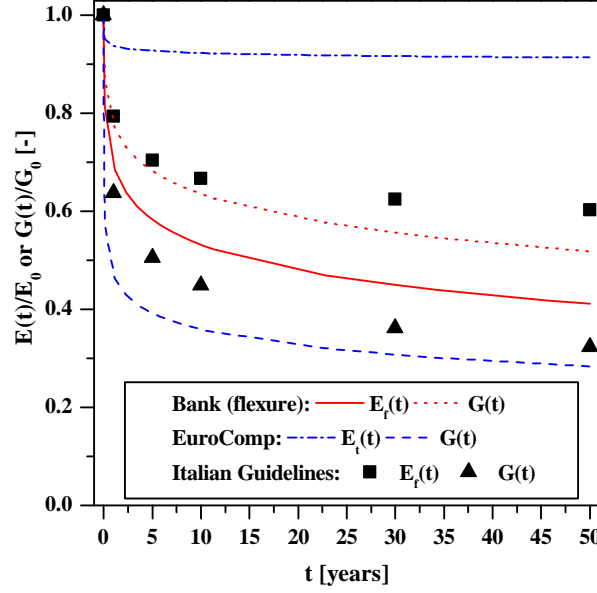


Figure 6.83.: Evolution of the elasticity and shear moduli of the GFRP material with time according to different creep models.

models [144]. Dutta and Hui [144] proposed the following modification to Findley's power law (Eq. (6.40)) in order to consider the effects of temperature in the empirical models,

$$\Delta(t) = \Delta_0 + m \cdot t^{n(T/T_0)} \quad (6.45)$$

where  $T_0$  is the reference temperature for which the regression parameters were determined and  $T$  is the temperature for which the creep behaviour is being predicted (in °C). Following this modification of Eq. (6.40), Eq. (6.41) may also be re-written as:

$$E(t) = \frac{E_0}{1 + \left(\frac{E_0}{E_t}\right) t^{n_E T/T_0}} \quad \text{or} \quad G(t) = \frac{G_0}{1 + \left(\frac{G_0}{G_t}\right) t^{n_G T/T_0}} \quad (6.46)$$

Similarly, the following adaptation can be performed in EuroComp's [38] general model (Eq. (6.44)) in order to consider the influence of temperature on the creep response, simply by modifying the slope of the logarithmic curve:

$$E_t = E_0 \left[ \lambda - \left( \frac{T}{T_0} \right) \varrho \cdot \ln t \right] \quad \text{or} \quad G_t = G_0 \left[ \lambda - \left( \frac{T}{T_0} \right) \varrho \cdot \ln t \right] \quad (6.47)$$

### 6.6.1.2. Creep response of the SFRSCC material

Since the small-scale prototype is a hybrid GFRP-concrete structure and concrete is also susceptible to creep phenomena [85] it is also necessary to quantify this material's creep response. For the SFRSCC, in particular, the influence of the steel fibres in the creep behaviour may be neglected if the volume of fibres is lower than 1.0% [147]. In the present case study, the SFRSCC used in the footbridge deck has a volumetric fibre content of  $\approx 2\%$ . However, due to the relatively low stress levels induced in the tests and due to the fact that the slab is mainly in compression (in the longitudinal direction), the slab does not present any cracking and, therefore, the fibre reinforcement is not effective [148] for these load levels. Thereafter, one assumes that the creep model presented by Eurocode 2 — Annex B [85] for regular concrete may be used. According to this model, the creep behaviour is influenced by the following parameters: relative humidity of the air ( $RH$ ), equivalent thickness of the element ( $h_0$ ), compressive strength of the concrete at 28 days of age ( $f_{cm}$ ), age of the concrete when loaded ( $t_0$ ) and, finally, temperature ( $T$ ).

The creep coefficient evolution with time,  $\varphi(t, t_0)$ , is given by Eq. (6.48),

$$\varphi(t, t_0) = \varphi_0 \cdot \beta_c(t, t_0) \quad (6.48)$$

where  $\varphi_0$  is a constant creep coefficient and  $\beta_c(t, t_0)$  accounts for the creep evolution with time. The constant creep coefficient ( $\varphi_0$ ) may be computed with Eq. (6.49),

$$\varphi_0 = \varphi_{RH} \cdot \beta(f_{cm}) \cdot \beta(t_0) \quad (6.49)$$

where

$$\varphi_{RH} = \left[ 1 + \frac{1 - RH/100}{0.1 \cdot \sqrt[3]{h_0}} \cdot \alpha_1 \right] \cdot \alpha_2 \quad \text{for } f_{cm} > 35 \text{ MPa} \quad (6.50)$$

$$\beta_{f_{cm}} = \frac{16.8}{\sqrt{f_{cm}}} \quad (6.51)$$

$$\beta_{t_0} = \frac{1}{0.1 + t_0^{0.20}} \quad (6.52)$$

$$h_0 = \frac{2A_c}{u} \quad (6.53)$$

$$\alpha_1 = \left[ \frac{35}{f_{cm}} \right]^{0.7} ; \quad \alpha_2 = \left[ \frac{35}{f_{cm}} \right]^{0.2} \quad (6.54)$$

in which  $A_c$  is the area of the concrete section and  $u$  is the perimeter of the section edge exposed to the environmental conditions. In the formulae above, the following units shall be used: (i) percentage (%) for  $RH$ ; (ii) mm for  $h_0$ ; (iii) MPa for  $f_{cm}$ ; and (iv) days for  $t_0$ . Regarding the creep evolution with time, coefficient  $\beta_c(t, t_0)$  is given by Eq. (6.55),

$$\beta_c(t, t_0) = \left[ \frac{t - t_0}{\beta_H + t - t_0} \right]^{0.3} \quad (6.55)$$

where  $t$  is the concrete age (in days) and therefore  $t - t_0$  is the load period.  $\beta_H$  accounts for the environmental conditions and, given that  $f_{cm} \geq 35$  MPa (*cf.* Section 4.3.2.4), it may be calculated with Eq. (6.56),

$$\beta_H = 1.5[1 + (0.012 \cdot RH)^{18}] \cdot h_0 + 250 \cdot \alpha_3 \leq 1500 \cdot \alpha_3 \quad (6.56)$$

and

$$\alpha_3 = \left[ \frac{35}{f_{cm}} \right]^{0.5} \quad (6.57)$$

The latter formulae show that the creep coefficient,  $\varphi(t, t_0)$ , is influenced by the relative humidity, in an inverse proportion, concerning both the constant coefficient ( $\phi_0$ ) and the creep evolution with time ( $\beta_c(t, t_0)$ ). Regarding the influence of temperature, the present model allows the consideration of temperatures between 0°C and 80°C [85]. The influence of temperature is indirectly considered in the model by correcting the concrete age ( $t$ ) in Eq. (6.55). The concrete age considering the effects of temperature ( $t_T$ ) is given by Eq. (6.58),

$$t_T = \sum_{i=1}^n e^{-(4000/[273+T(\Delta t_i)]-13.65)} \cdot \Delta t_i \quad (6.58)$$

where  $T(\Delta t_i)$  is the temperature (in °C) observed in a given number of days ( $\Delta t_i$ ). Introducing Eq. (6.58) in Eq. (6.55) will increase the creep rate for temperatures higher than 20°C and decrease it for temperatures lower than 20°C. It is also important to note that temperature does not affect the magnitude of creep in concrete but rather its time evolution, similarly to the creep model proposed by Dutta and Hui [144] for GFRP materials.

Finally, the adjusted elasticity modulus of concrete can be calculated considering concrete's age and creep,

$$E_c(t, t_0) = \frac{E_{c,28}}{1 + \chi(t, t_0) \cdot \varphi(t, t_0)} \quad (6.59)$$

where  $E_{c,28}$  is the concrete elasticity modulus at 28 days and  $\chi(t, t_0)$  is Trevino's aging coefficient given by Eq. (6.60) [149]:

$$\chi(t, t_0) \cong \chi(t_0) = \frac{\sqrt[3]{t_0}}{1 + \sqrt[3]{t_0}} \quad (6.60)$$

## 6.6.2. Experimental tests

### 6.6.2.1. Experimental series

The experimental campaign presented herein was performed to assess the flexural creep behaviour of the small-scale footbridge prototype. The programme comprised three different experimental tests, with varying load levels and environmental conditions: (i) test 1 was performed with a higher load level (defined below) in hot and dry climate conditions for

a total duration of 2590 h; (ii) test 2 was performed with a lower load level, with similar climate conditions to test 1, for a period of 2114 h; and (iii) test 3 was performed with a similar load level to that used in test 1, but in a colder and wetter climate (compared to that used in test 1 and 2), for a period of 2642 h.

All tests were performed by placing dead loads over the footbridge deck and measuring the corresponding evolution of deflections and axial deformations at midspan. During the test period the temperature and relative humidity, which were not constant (owing to the large-scale geometry of the prototype, it was not possible to test it in a chamber with environmental control), were also registered. Figure 6.84 shows the instrumentation position at the midspan section, where (i)  $\delta$  stands for displacement transducers, (ii)  $\varepsilon_f$  stands for strain gauges in the GFRP flanges, and (iii)  $\varepsilon_c$  stands for strain gauges in the SFRSCC. Figure 6.85 illustrates the loading configuration used in the creep tests.

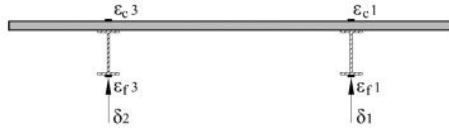


Figure 6.84.: Small-scale prototype creep tests: instrumentation at midspan.

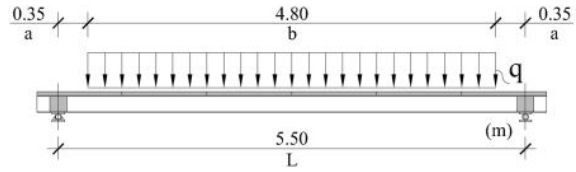


Figure 6.85.: Small-scale prototype creep tests: load configuration.

In the early stages of the tests (typically, in the first 72 h), vertical deflections were measured with *TML* electrical displacement transducers with a stroke of 50 mm and precision of 0.01 mm, whereas axial strains were measured with electrical strain gauges (models *HBM-1-LY41-50/120* for concrete and *HBM-1-LY11-10/120* for GFRP). Regarding the axial strains in the GFRP flanges during these early stages of the tests, the measurements  $\varepsilon_{f1}$  and  $\varepsilon_{f3}$  presented in this Section correspond to the average strain measured in the strain gauges installed in each GFRP flange (*cf.* Figure 6.34, page 178). Data was acquired with a *HBM Spider8* datalogger and registered in a PC. In a further stage of the tests, the electric equipment was disconnected and measurements were performed with analogical deflection gauges from *Mitutoyo* with (i) a 30 mm stroke and 0.01 mm precision for the measurement of vertical deflections, and (ii) a 5 mm stroke and a 0.001 mm precision for the monitoring of axial strains. For test 2, in which electrical strain gauges were used during the entire period of the test, reliable measurements could be obtained only for a short period of the test; therefore, only vertical deflections could be monitored during the entire duration of the test.

The loads  $q$  (*cf.* Figure 6.85) applied to the prototype were materialised by concrete tiles, concrete blocks and cement sacks. The higher load level, applied in tests 1 and 3, was approximately 5480 kgf, corresponding to a load of 11.19 kN/m or 5.59 kN/m<sup>2</sup> (higher than Eurocode 1 [65] characteristic load for footbridges — 5.00 kN/m<sup>2</sup>). This load caused a maximum bending moment of 20.81 kNm/m at the midspan section, corresponding to 13.2% of the ultimate bending moment, and a shear force of 13.43 kN/m, which corresponds to 32.7% of the ultimate shear strength (disregarding the strength of the concrete jackets at the supports, *cf.* Section 6.4). The lower load level, applied in test 2, was approximately 3210 kgf, *i.e.* 58.6% of the higher load. Consequently, the forces imposed upon the structure were also reduced to 58.6% of the previous forces — 7.7% and 19.2% of the ultimate bending moment and shear force, respectively. For all tests, the above mentioned load levels are higher than those concerning the quasi-permanent condition of footbridges. However, for this study,



which is not a design exercise, but rather a fundamental study about the creep response of GFRP–concrete hybrid flexural members, it was important to guarantee a reasonable stress level in the GFRP material. It is also worth mentioning that for building applications, for which this structural system is also envisaged [5], higher quasi–permanent load levels may be expected when compared to footbridges.

Figure 6.86 shows the prototype loaded for each test series, while Table 6.19 summarizes the most relevant information regarding each test.



Figure 6.86.: Small-scale prototype loaded for creep test: a) test 1; b) test 2; and c) test 3.

Table 6.19.: Small-scale prototype creep tests: relevant data.

Creep test	Period	Duration (h)	Load (kN/m <sup>2</sup> )	Avg. $T$ (°C)	Avg. $RH$ (%)	$t_0$ (days)
1	June 1 <sup>st</sup> — Sep. 20 <sup>th</sup> 2012	2590	5.59	23.0±1.4	60±9	562
2	July 29 <sup>th</sup> — Oct. 25 <sup>th</sup> 2011	2114	3.28	23.3±0.8	60 <sup>a</sup>	254
3	Nov. 8 <sup>th</sup> 2012 — Feb. 26 <sup>th</sup> 2013	2642	5.59	11.3±1.3	73±15	722

<sup>a</sup>Estimated value (based on creep test 1)

## 6.6.2.2. Experimental results

### 6.6.2.2.1 Test 1

Figure 6.87 shows the evolution of the environmental parameters during the period of test 1, namely the temperature and the relative humidity. Figure 6.88 plots the evolution of the midspan deflections underneath each main girder ( $\delta_1$  and  $\delta_2$ , *cf.* Figure 6.84), together with Findley's power law regressions (Eq. (6.40)) for each case. The difference between deflections registered in positions  $\delta_1$  and  $\delta_2$  may be due to some slight eccentricity in the applied load, causing one beam to bear more load than the other. This explanation is corroborated by the regressions performed, which present different  $m$  parameter values (stress dependent), but very similar  $n$  parameter values (*cf.* Eq. (6.40) and Figure 6.88). The regression parameters presented in Figure 6.88 were computed with high coefficients of determination ( $R^2$ ) of 0.990 and 0.982 for  $\delta_1$  and  $\delta_2$ , respectively. Nevertheless, these regressions seem to show a tendency to "outgrow" the experimental results expected projections for increasing duration, especially for  $\delta_2$ .

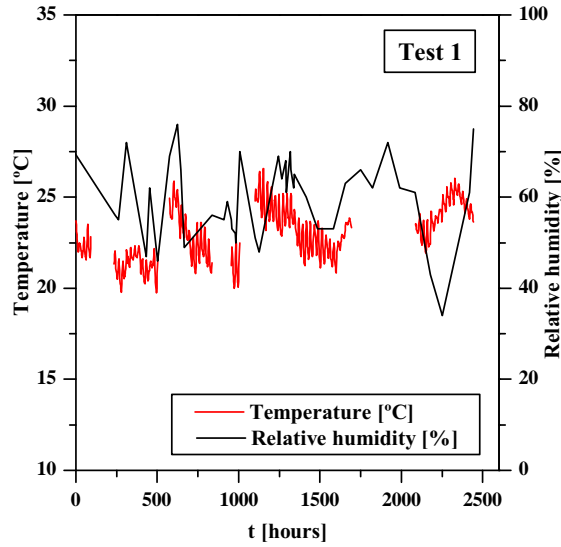


Figure 6.87.: Small-scale prototype creep tests: environmental — temperature and relative humidity.

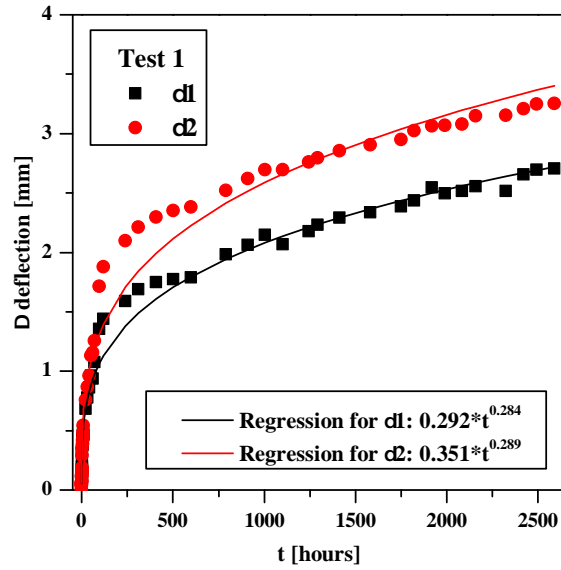


Figure 6.88.: Small-scale prototype creep test 1: evolution of the midspan deflections and Findley's power law regressions.

Figure 6.89 shows the evolution of midspan axial strains in the GFRP profiles ( $\varepsilon_{f1}$  and  $\varepsilon_{f3}$ , *cf.* Figure 6.84) and in the SFRSCC slab ( $\varepsilon_{c3}$ , *cf.* Figure 6.84) together with the corresponding Findley's power law regressions. The results obtained with strain gauge  $\varepsilon_{c1}$  (*cf.* Figure 6.84) were inconsistent and therefore discarded. These results show a higher dispersion than the results obtained for the deflections. Nevertheless, a similar difference may be observed between the strain results in the GFRP profiles and between the corresponding deflections. Once again, the regression parameters are coherent with the explanation presented earlier. It may also be observed that the  $\varepsilon_{c3}$  regression is steeper (higher  $n$  parameter) than the regressions for  $\varepsilon_{f1}$  and  $\varepsilon_{f3}$ . These regressions were obtained with coefficients of determination ( $R^2$ ) of 0.972, 0.790 and 0.952 for  $\varepsilon_{f1}$ ,  $\varepsilon_{f3}$  and  $\varepsilon_{c3}$ , respectively.

Additionally, Figure 6.90 shows the distribution of axial strains throughout the cross-section depth as well as the neutral axis position at the beginning and end of test 1. It can be seen that during the test the neutral axis moved towards the interface between the two materials, indicating a higher axial stiffness loss of the SFRSCC slab when compared to the GFRP profile.

#### 6.6.2.2.2 Test 2 (effect of load level)

During the period of test 2, the relative humidity was not measured, but it is likely to have been similar to that of test 1 as the test has been performed in a similar period, during which outdoor climatic conditions were fairly close (*cf.* Table 6.19). Figure 6.91 shows the evolution of temperature within the test period, while Figure 6.92 shows the evolution of mid-span deflections and the corresponding regressions, for each case, using Findley's power law.

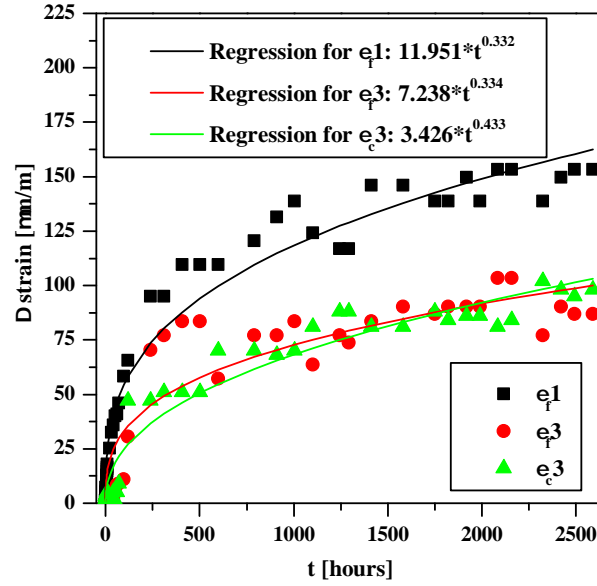


Figure 6.89.: Small-scale prototype creep test 1: evolution of strains at midspan and Findley's power law regressions.

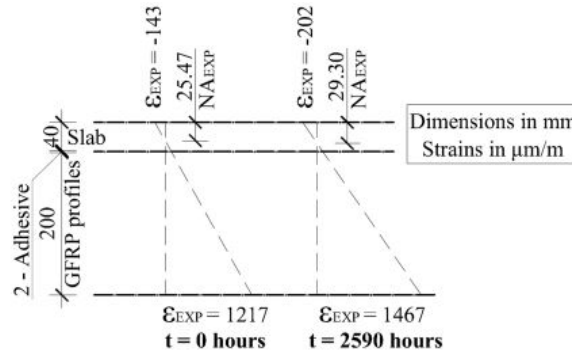


Figure 6.90.: Small-scale prototype creep test 1: axial strain distributions across the depth of the cross-section and neutral axis depth, measured from the top of the SFRSCC slab at the beginning and end of the test.

The regressions plotted in Figure 6.92 exhibit coefficients of determination ( $R^2$ ) of 0.959 and 0.972 for  $\delta_1$  and  $\delta_2$ , respectively. Similarly to the regressions obtained for the deflections in test 1, albeit the high coefficients of determination, these regressions show a tendency to deviate from the experimental results at the end of the test period.

As expected, the stress dependent parameters ( $m$ ) are lower for test 2 than for test 1, which is in accordance with Findley's power law creep theory (*cf.* Section 6.6.1.1). However, the average  $m$  parameter for test 2 is 17.3% lower than for test 1, which means that this variation is not directly proportional to the load. On the other hand, the stress independent parameters ( $n$ ) should be similar for both tests (which were performed in similar environmental conditions) but are lower (19.5% in average) for test 2. This seems to indicate that Findley's power law may not be fully suited for adjusting creep deformations in GFRP-concrete structures.

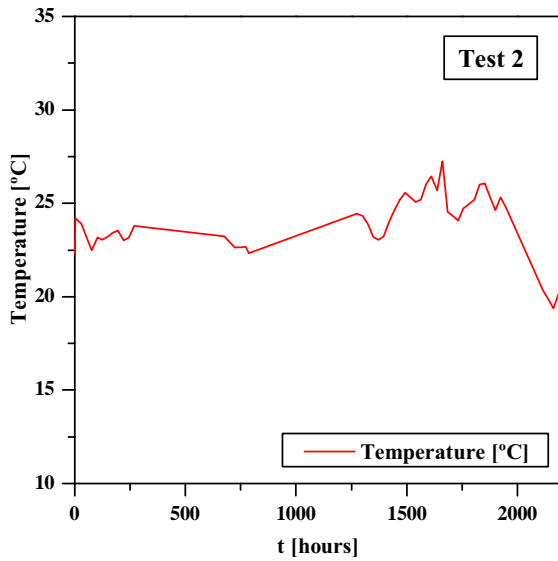


Figure 6.91.: Small-scale prototype creep test 2: evolution of the temperature.

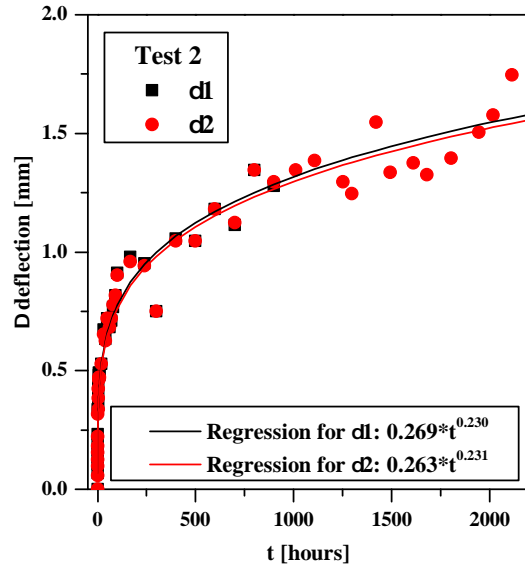


Figure 6.92.: Small-scale prototype creep test 2: evolution of midspan deflections and Findley's power law regressions.

#### 6.6.2.2.3 Test 3 (effect of temperature)

The environmental parameters evolution during the period of test 3, namely temperature and relative humidity, is plotted in Figure 6.93. The evolution of the deflections at midspan is shown in Figure 6.94 together with Findley's power law regressions for each case. These regressions present coefficients of determination ( $R^2$ ) of 0.969 and 0.968 for  $\delta_1$  and  $\delta_2$ , respectively. A very good agreement was obtained in both cases (similar  $m$  and  $n$  parameters). Similarly to what was observed in the other tests, these regressions show a tendency to deviate from the experimental results in the final period of the test. In this test, unlike test 1, the response is fully symmetric, because the effects of load eccentricity were completely prevented.

The stress dependent parameters ( $m$ ) obtained for this test are similar to those obtained in test 1 (-6.4% in average) and to those obtained in test 2 (+13.2% in average). According to Findley's power law creep theory (*cf.* Section 6.6.1.1) the  $m$  parameter should be closer to the parameters obtained in test 1 and higher than the parameters obtained in test 2. Furthermore, the stress independent parameter ( $n$ ) is lower in test 3 than in tests 1 (-28.8% in average) and 2 (-11.5% in average), which is in accordance with the model proposed by Dutta and Hui [144], since test 3 was performed with lower temperatures than tests 1 and 2 (*cf.* Table 6.19). However, as mentioned earlier, this parameter should be similar for tests 1 and 2.

#### 6.6.2.2.4 Comparative summary

The results obtained in the three creep tests, in terms of midspan deflections, are compared in Figure 6.95. As expected, the creep deformation is higher for test 1 than for tests 2 and 3. The fact that tests 2 and 3 present very similar creep deflections, especially in the early

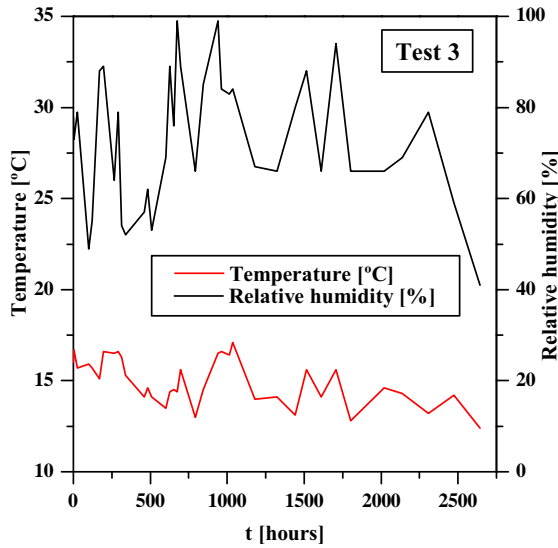


Figure 6.93.: Small-scale prototype creep test 3: environmental conditions — temperature and relative humidity.

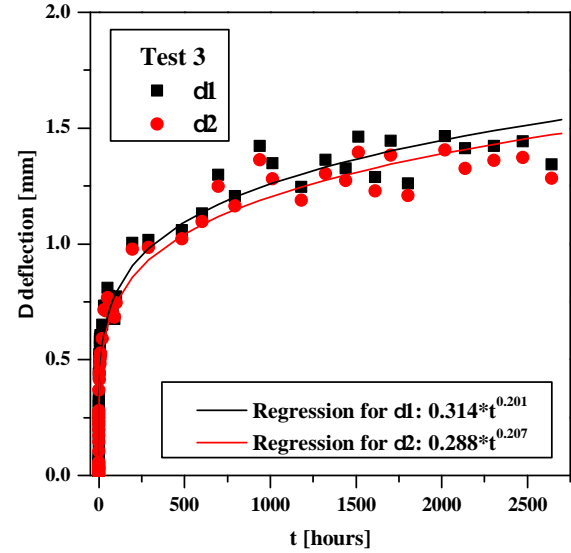


Figure 6.94.: Small-scale prototype creep test 3: evolution of midspan deflections and Findley's power law regressions.

stages of the tests, attests the importance of temperature in the creep phenomenon. In fact, the effects of a load reduction of 41.4% appear to be matched by a reduction in the average temperature of 12°C. Table 6.20 summarises the parameters obtained from the fittings of Findley's power law to the different experimental results.

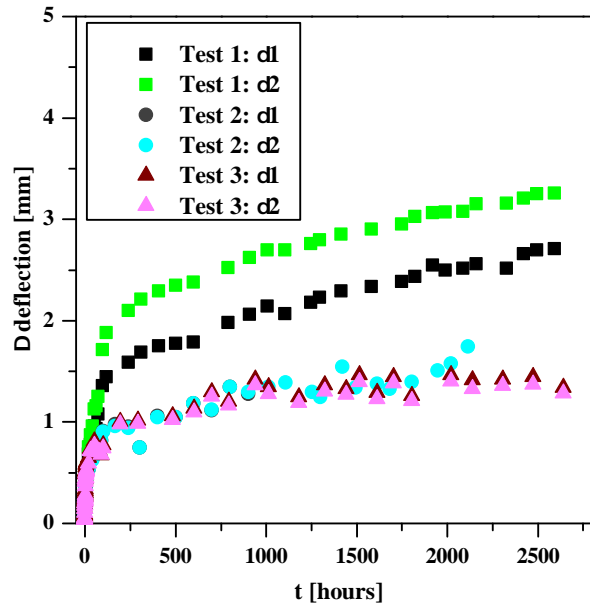


Figure 6.95.: Small-scale prototype creep tests: comparison between the creep deflections of all tests.

Regarding the regressions for the axial strains in the GFRP profiles ( $\varepsilon_f1$  and  $\varepsilon_f3$ ), it is more difficult to draw any definitive conclusions than for midspan deflections ( $\delta1$  and  $\delta2$ ). Parameter  $m$  seems to be lower for test 2 than for tests 1 and 3 (the regression for  $\varepsilon_f3$  — test 1 presents a low coefficient of determination and should be disregarded) but parameters

Table 6.20.: Small-scale prototype creep tests Findley power law regression parameters.

Test	1			2			3		
Parameter	$m$	$n$	$R^2$	$m$	$n$	$R^2$	$m$	$n$	$R^2$
$\delta 1$	0.292	0.284	0.99	0.269	0.23	0.959	0.314	0.201	0.966
$\delta 2$	0.351	0.289	0.982	0.263	0.231	0.972	0.288	0.207	0.968
$\varepsilon_f 1$	11.951	0.332	0.972	7.981	0.362	0.917	18.001	0.31	0.985
$\varepsilon_f 3$	7.238	0.334	0.79	4.866	0.439	0.951	12.648	0.371	0.981
$\varepsilon_c 1$	-	-	-	-	-	-	-	-	-
$\varepsilon_c 3$	3.426	0.433	0.952	-	-	-	-	-	-

$n$  are higher (in average) in test 3 than in test 1. For the strains in the SFRSCC slab, on the other hand, it was not possible to perform regressions, except for  $\varepsilon_c 3$  — test 1, due to the high dispersion of the results. The high dispersion of the strain measurement results, for both the GFRP and SFRSCC materials, may be explained by two main reasons: (i) on one hand, the electrical strain gauges presented long-term instability, while the analogical gauges presented a low sensitivity (approximately  $16 \mu\text{m/m}$ ); (ii) on the other hand, during the tests, the neutral axis of a hybrid structure in flexure may shift due to the different evolution of the elastic creep moduli of the constituent materials, affecting the strains along the sections without a direct relation with the creep deformation of the materials (*cf.* Figure 6.90).

These results and conclusions show that, although it is possible to adjust Findley's power law to the creep behaviour of a GFRP–concrete hybrid structure, this method may not be very accurate, especially for long-term predictions based on short-term tests.

### 6.6.3. Analytical simulation

#### 6.6.3.1. Model proposal

As mentioned earlier (*cf.* Section 6.4.6), shear deformations are not generally neglectable in GFRP structures. Therefore, the deflections of the hybrid structure studied herein should be calculated with Timoshenko's beam model [86]. For the load model presented in Figure 6.85, midspan deflections may be calculated with Eq. (6.61),

$$\delta_{ms} = \frac{C_1}{EI} + \frac{C_2}{G \cdot kA} \quad (6.61)$$

where the first term represents the flexural deflection and the second term the shear deflection. The terms  $C_1$  and  $C_2$  are given by Eqs. (6.62) and (6.63), respectively,

$$C_1 = q \cdot \left[ \frac{a^3 b}{6} + \frac{a^2 b^2}{4} + \frac{5ab^3}{48} + \frac{5b^4}{384} \right] \quad (6.62)$$

$$C_2 = q \cdot \left[ \frac{ab}{2} + \frac{b^2}{8} \right] \quad (6.63)$$

where  $q$  is the applied uniformly distributed load and  $a$  and  $b$  are the geometrical parameters of the load (*cf.* Figure 6.85).

The deflections obtained with the formulae presented above — using the  $EI$  and  $G \cdot kA$  calculated earlier, *cf.* Section 6.4.6 — show a good agreement with the instantaneous deflections measured experimentally for both higher and lower load levels (*cf.* Section 6.6.2): 25.80 mm (+9.9%) and 15.13 mm (+10.6%).

In order to use the formulae presented above to predict long-term deflections it is necessary to consider the time-dependent elasticity and shear moduli of the materials that constitute the hybrid structure, namely the GFRP profile and the SFRSCC slab. Therefore, for each time step, it is necessary to determine the position of the neutral axis, which may shift due to the different evolution of the constituent materials' elasticity modulus (*cf.* Figure 6.90), and the corresponding flexural and shear stiffness ( $EI$  and  $GkA$ , respectively).

Regarding the choice of the GFRP material creep models, the initial stress distribution within the section should be taken into account. The hybrid footbridge structure under study presents its neutral axis in the SFRSCC slab near the GFRP–concrete interface, which means that the slab is mainly in compression, while the profile is in tension. Thereafter, *a priori* a tension creep model should be more suited to describe the GFRP elasticity modulus evolution, instead of a flexure creep model. In addition, for the shear modulus variation, a shear in flexure creep model (as the one proposed by Bank [4]) is deemed to be more adequate than a pure shear creep model (as the one proposed in EuroComp [38]). The influence of such GFRP material creep models is assessed in the next section.

#### 6.6.3.2. Assessment of GFRP material creep models

Experimental results can be compared with predictions computed by the analytical model (Eq. (6.61)) with different material creep models. In order to assess which material creep models should be used, the experimental deflections are compared with analytical deflections using the following combinations of GFRP creep models: (i) Bank's [4] flexure model for both elasticity and shear moduli; (ii) tension and shear models proposed by EuroComp [38] for the elasticity and shear moduli, respectively; and (iii) tension model proposed by EuroComp [38] and shear in flexure model proposed by Bank [4] for the elasticity and shear moduli, respectively, thereby taking into account the actual stress distribution on the structure. One should note that these creep models were developed for different GFRP materials, namely with different fibre contents and architectures, and produced with different manufacturing methods. Nevertheless, given that they aim to be general creep models used in design, they should be able to reproduce fairly well the creep behaviour of most GFRP materials.

The above mentioned material creep models were adapted according to the recommendations by Dutta and Hui [144] in order to account for different temperatures (*cf.* Section 6.6.1.1, Eqs. (6.46) and (6.47), in which a reference temperature of  $T_0 = 25^\circ\text{C}$  was considered). For the SFRSCC the creep model proposed in Eurocode 2 [85] for regular concrete was used (*cf.* Section 6.6.1.2). Regarding the environmental conditions of each experimental series, they were taken into account introducing in the creep models the average temperature and relative humidity (SFRSCC), and the concrete's age (*cf.* Table 6.19). The latter parameter is of high importance for young concrete but has minor influence in the tests presented in this study. In the absence of relative humidity data for test 2, this parameter was considered to be equal to test 1 since both tests were performed in similar climate periods. Figures 6.96 to 6.98 show, for tests 1 to 3, respectively, the comparison between the deflections predicted with the analytical model using the three different material creep model combinations referred above and their experimental counterparts.

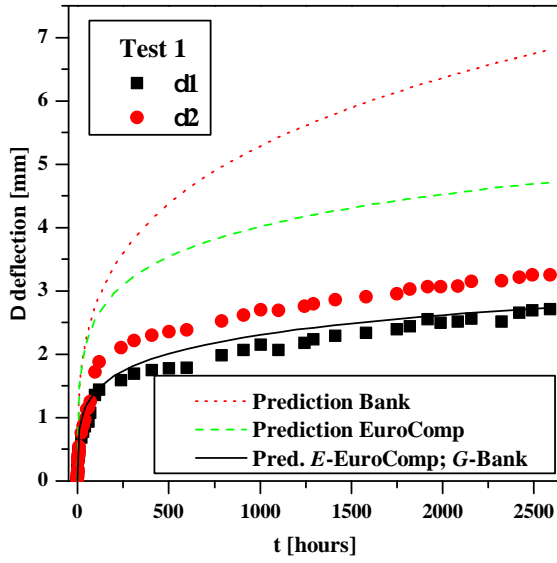


Figure 6.96.: Small-scale prototype creep test 1: analytical predictions *vs.* experimental results.

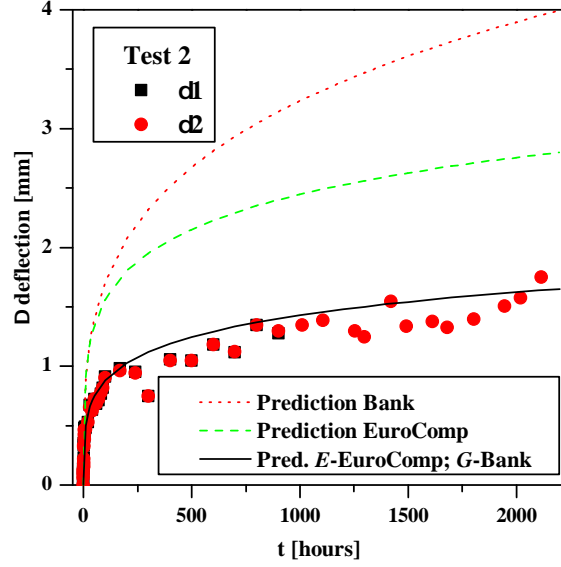


Figure 6.97.: Small-scale prototype creep test 2: analytical predictions *vs.* experimental results.

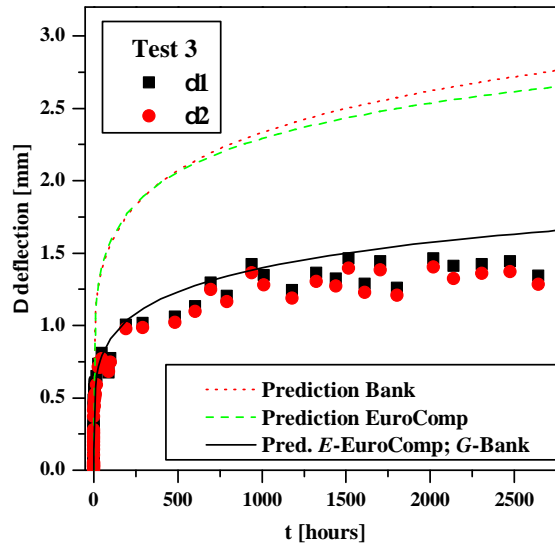


Figure 6.98.: Small-scale prototype creep test 3: analytical predictions *vs.* experimental results.

The results obtained show that in all cases predictions using the flexure creep models proposed by Bank [4] or the tension and pure shear creep models proposed by EuroComp [38] overestimate the creep deflections measured experimentally. On the other hand, the mixed model proposed herein, combining EuroComp's [38] tension creep model for the elasticity modulus and Bank's [4] shear in flexure model for the shear modulus, is able to predict the experimentally observed creep deflections with good accuracy. The ability of this mixed model in predicting the experimental results observed in test 3 is also remarkable (*cf.* Figure 6.98), showing that it is possible to predict the creep behaviour of hybrid GFRP–concrete structures in different environmental conditions by taking into account the recommendations of Dutta and Hui [144] in the GFRP material creep models.



### 6.6.3.3. Prediction of long-term response

Having defined the combination of GFRP material creep models to be used in the design of this type of hybrid structures (*cf.* Section 6.6.3.2) it is now possible to predict their long-term creep deformations. Figures 6.99 to 6.101 compare the long-term predictions according to the model proposed in this study for the small-scale prototype ( $E(t)$  — EuroComp [38];  $G(t)$  — Bank [4]) with the long-term predictions performed with Findley's power law regressions of the experimental results (*cf.* Table 6.20) for tests 1 to 3, respectively.

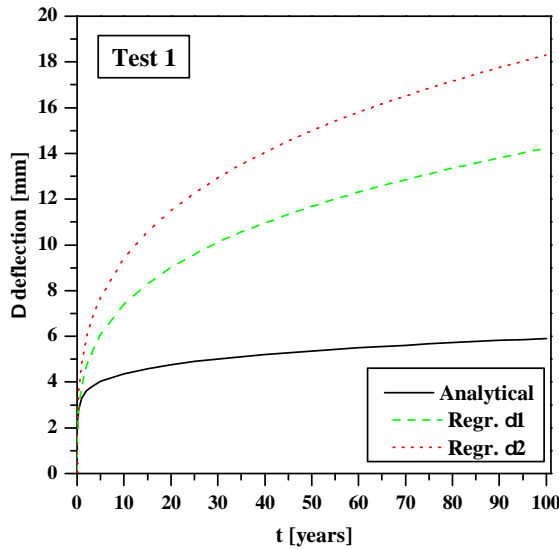


Figure 6.99.: Small-scale prototype creep test 1 long-term predictions: analytical *vs.* regressions.

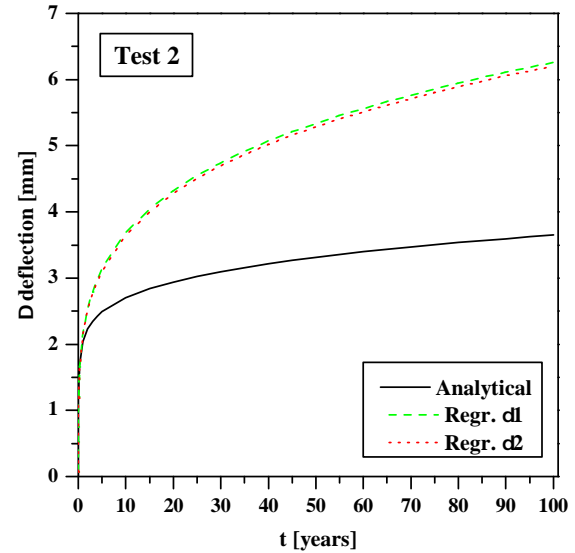


Figure 6.100.: Small-scale prototype creep test 2 long-term predictions: analytical *vs.* regressions.

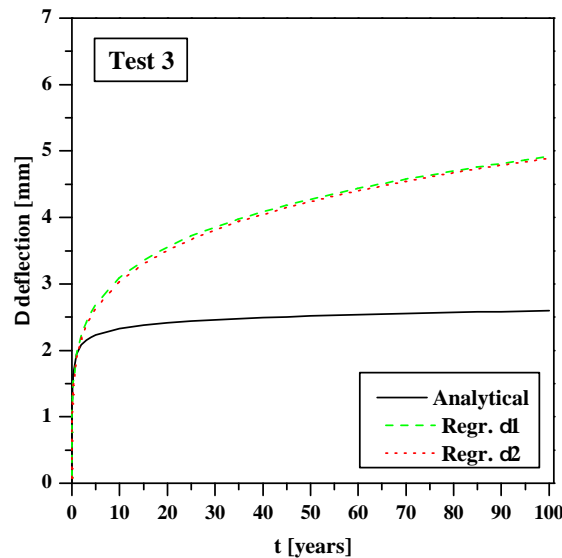


Figure 6.101.: Small-scale prototype creep test 3 long-term predictions: analytical *vs.* regressions.

Table 6.21 summarises the graphical comparison depicted in Figures 6.99 to 6.101 after 20, 50 and 100 years including the results for the analytical model using the material creep models proposed by Bank [4] for both elasticity and shear moduli and using the material

creep models proposed by EuroComp [38] for both elasticity and shear moduli, where  $\delta_0$  are the instantaneous deflections.

Table 6.21.: Small-scale prototype predictions of long-term creep deflections: analytical model and regressions.

Test		1			2			3		
Time elapsed (years)		20	50	100	20	50	100	20	50	100
Reg. $\delta_1$	$\Delta\delta$ [mm]	9.01	11.68	14.23	4.32	5.34	6.26	3.56	4.27	4.91
	$\Delta\delta/\delta_0$ [%]	38.4	49.8	60.6	31.6	39.0	45.7	15.1	18.2	20.9
Reg. $\delta_2$	$\Delta\delta$ [mm]	11.50	14.99	18.31	4.28	5.29	6.20	3.51	4.24	4.89
	$\Delta\delta/\delta_0$ [%]	49.0	63.8	78.0	31.3	38.6	45.3	14.9	18.1	20.8
Analytical model	$\Delta\delta$ [mm]	4.76	5.36	5.91	2.94	3.31	3.65	2.41	2.52	2.60
G-Bank [4]; E-EC [38]	$\Delta\delta/\delta_0$ [%]	18.4	20.8	22.9	19.4	21.9	24.1	9.3	9.8	10.1
Analytical model	$\Delta\delta$ [mm]	19.51	24.52	29.17	12.04	15.17	18.08	4.60	5.06	5.44
G & E-Bank [4]	$\Delta\delta/\delta_0$ [%]	75.6	95.1	113.1	79.6	100.3	119.5	17.8	19.6	21.1
Analytical model	$\Delta\delta$ [mm]	8.37	9.50	10.52	5.1	5.80	6.44	3.87	4.09	4.26
G & E-EC [38]	$\Delta\delta/\delta_0$ [%]	32.4	36.8	40.8	33.7	38.3	42.6	15.0	15.9	16.5

Additionally, Figure 6.102 shows, as an example and with reference to test 1, the strain distributions across the depth of the cross-section predicted based on the above mentioned mixed model, for both short- and long-term predictions. Predictions for strains and neutral axis position compare reasonably well with experimental results (the main differences stem from the relatively reduced strain values in the SFRSCC slab). Analytical results confirm the increase of the neutral axis depth in the short-term, showing also that in the long-term it tends to stabilise.

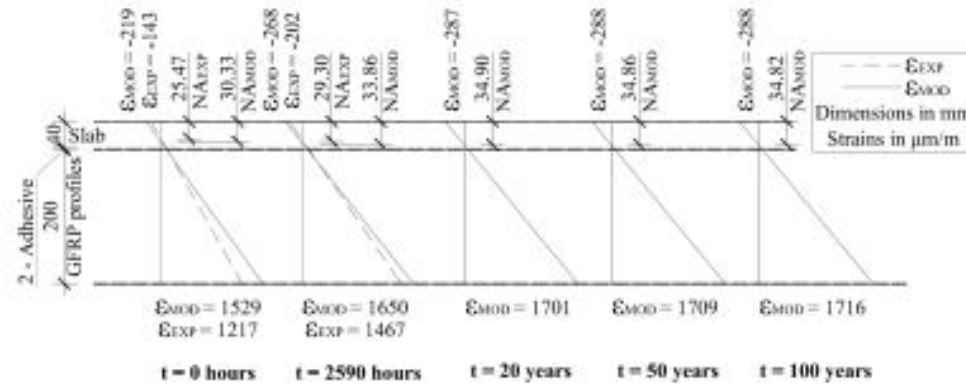


Figure 6.102.: Small-scale prototype creep test 1: experimental and predicted axial strain distributions ( $\varepsilon_{EXP}$  and  $\varepsilon_{MOD}$ , respectively) across the depth of the cross-section and neutral axis depth, measured from the top of the SFRSCC slab ( $NA_{EXP}$  and  $NA_{MOD}$ , respectively).

The analysis of these results shows that for the long-term predictions, Findley's power law regressions of short-term experimental tests deviate considerably from the analytical predictions, albeit the analytical model has proved to be very effective in simulating the experimental results. This fact, together with the previous concerns regarding the quality of Findley's power law regressions for the structure tested (*cf.* Section 6.6.2.2.4) seem to point out that this type of regression is not adequate for predicting the long-term creep deflections in GFRP-concrete hybrid structures. The poor results of these regressions may be explained by two reasons: (i) the creep behaviour of concrete does not follow Findley's power law; and (ii) the changes in the neutral axis of the section may change the logarithmic

slope of the curve representing the structural response ( $n$  parameter), which is constant in Findley's power law.

Regarding the comparison between the different analytical models, the use of a tension creep model for GFRP's elasticity modulus and a shear in flexure model for GFRP's shear modulus is consistent with the stress distribution along the cross-section and proved to provide an excellent fit to experimental results (*cf.* Section 6.6.3.2). Therefrom, these material creep models should be used in the analytical prediction of this structure or other hybrid structures with similar characteristics and stress distributions. The comparison with the results obtained with other GFRP material creep models, not coherent with the actual stress distribution, shows the importance of selecting the proper material creep models.

Although the small-scale footbridge prototype was not designed to fulfil serviceability requirements (only the full-scale one was) and the fact that the higher load applied in the creep tests corresponds to the characteristic live load for footbridges (for which, creep does not need to be considered in design), the following deflection limits included in the Italian Guidelines [68] are mentioned as indicative references:  $L/250$  (quasi-permanent load combination) and  $L/100$  (characteristic load combination), respectively 22 mm and 55 mm for the small-scale prototype. Using the prediction model proposed in the present study, for the characteristic load ( $5 \text{ kN/m}^2$  [65]), after 50 years this structure is expected to present a midspan deflection of 29.23 mm (124.4% of the instantaneous deflection, with 54.0% of the creep deflection being due to flexure and 46.0% due to shear). It is worth mentioning that an all-GFRP structure, with equivalent flexure and shear instantaneous stiffness, is expected to present a midspan deflection of 55.62 mm (236.6% of the instantaneous deflection, now with 91.8% of the creep deflection being due to flexure and 8.2% due to shear) after the same period. Although the full-GFRP structure mentioned above was not object of testing, these predictions indicate that GFRP–concrete hybrid structures are most likely much more efficient regarding the creep phenomenon.

#### 6.6.4. Conclusions

The experimental results obtained based on flexural creep tests on a GFRP–SFRSCC footbridge small-scale prototype showed that the creep behaviour of these structures is affected by the load level and by the environmental conditions, namely, temperature and relative humidity. Moreover, in the present study, a 41.4% reduction of load had very similar effects to a  $12^\circ\text{C}$  reduction in the average temperature (together with a 13% increase in relative humidity) in terms of creep deflections. Regarding Findley's power law regressions, it was shown that this power law may not be adequate to predict the creep deflections of GFRP–concrete hybrid structures.

The analytical study showed that it is possible to predict experimental results with comprehensive material creep models. It is necessary, however, to choose the material creep models coherently with the actual stress distribution, *i.e.*, taking into account the type of stress each material is subjected to. Furthermore, the analytical models proposed herein are able to predict the important effects of environmental changes (temperature and relative humidity) observed experimentally provided that proper adaptations are made in the material creep models. These analytical models proved to be the best tool in predicting the long-term behaviour and creep effects of GFRP–concrete structures.

Based on the analytical model proposed here, after 50 years the GFRP–SFRSCC small-scale footbridge prototype is expected to present a midspan creep deflection of 24.4% of the

instantaneous deflection, while in an equivalent all-GFRP structure such creep deflection would be 136.6% of the instantaneous deflection. This remarkable difference highlights the advantage of hybrid structures in reducing the magnitude of creep phenomenon and this is a very relevant finding of the present study.

Notwithstanding, further investigations are needed to develop more comprehensive material creep models for the GFRP material, namely, allowing the consideration of the effects, if any, of the following parameters: (i) age at loading; (ii) curing degree of the polymeric matrix of the GFRP profiles; (iii) fibre reinforcement ratio and architecture; (iv) relative humidity; and (v) thermal variations during the loading period. Also, the assessment of the behaviour of GFRP–concrete structures throughout their life-cycle in real service conditions is necessary in order to further validate the results and models presented herein.

## 6.7. Final remarks

This chapter presented the investigations performed regarding the small-scale hybrid GFRP–SFRSCC footbridge prototype. The ease of assembly and construction of this type of GFRP–concrete hybrid structure was shown in Section 6.3, which presented the construction process of this prototype with little use of heavy lifting machinery.

Owing to the results presented in this chapter, one may conclude that the analytical and numerical tools readily available to designers are well capable of predicting the structural behaviour of GFRP–concrete hybrid structures, namely regarding their (i) static behaviour up to failure (Section 6.4), (ii) dynamic behaviour (Section 6.5), and (iii) creep behaviour (Section 6.6). The ability of these common design tools in predicting the structural behaviour of these structures is of the utmost importance for structural designers and a keystone in the widespread of this structural solution.

The positive experimental results regarding pedestrian comfort criteria (*cf.* Section 6.5) — although hard to extrapolate to the full-scale prototype — attest the feasibility of this structural system for use in footbridge structures since these criteria are often governing for this type of structures.

One of the main findings presented in this chapter is that hybrid GFRP–concrete structures may be much less susceptible to creep phenomena than all-GFRP structures (*cf.* Section 6.6), proving the high potential of the structural system proposed given that the high deformability, namely the long-term deformability, is often pointed out as one of the main problems of all-GFRP structures.

The models developed in the context of this chapter will be used to design the full-scale footbridge prototype (*cf.* Chapter 7).

## 7. Full-scale prototype

### 7.1. Preliminary remarks

The present Chapter describes the design, construction and assessment of the behaviour of the full-scale hybrid GFRP–SFRSCC footbridge prototype. The investigations included (i) experimental tests and the simulation of those experiments with (ii) analytical and (iii) numerical models.

The full-scale prototype, unlike its small-scale counterpart (*cf.* Chapter 6), was designed in order to formally comply with ultimate and serviceability limit states (ULS and SLS, respectively) requirements, since it will ultimately be installed and used as a footbridge opened to the general public. The knowledge gathered with the investigations on the small-scale prototype, regarding the behaviour of GFRP–hybrid structural systems, was of the utmost importance in the design of the full-scale prototype for a real serviceability environment. Additionally, the results of the experimental tests performed in the full-scale prototype were used to further validate and calibrate the models used to predict the behaviour of the small-scale prototype.

This Chapter is divided in seven main sections: (i) preliminary remarks, (ii) characteristics and design of the prototype, which presents the structural details and design procedure; (iii) construction, where the step-to-step construction process is described; (iv) static behaviour; (v) dynamic behaviour; and (vi) creep behaviour of the prototype, which present the investigations conducted for the full-scale prototype regarding its static, dynamic and creep behaviour, respectively. In each of the last three sections experimental investigations are presented and the results obtained are compared with those from analytical and/or numerical models. Subsequently, some (vii) final remarks are presented.

### 7.2. Characteristics and design of the prototype

The full-scale hybrid GFRP–SFRSCC footbridge prototype has a total length of 11000 mm and a width ( $b$ ) of 2000 mm, and was installed in a simply supported span ( $L$ ) of 10500 mm. Figure 7.1 illustrates the cross-section of the the full-scale prototype. The structure comprises two main girders, materialized by I-shaped section ( $400 \times 200(\times 15)$  mm<sup>2</sup>) GFRP pultruded profiles, and a SFRSCC deck positioned on top of those girders. The SFRSCC deck was intended to have a 40 mm thickness, however, after construction, a nominal 37.5 mm thickness was measured. All calculations presented here refer to this nominal thickness.

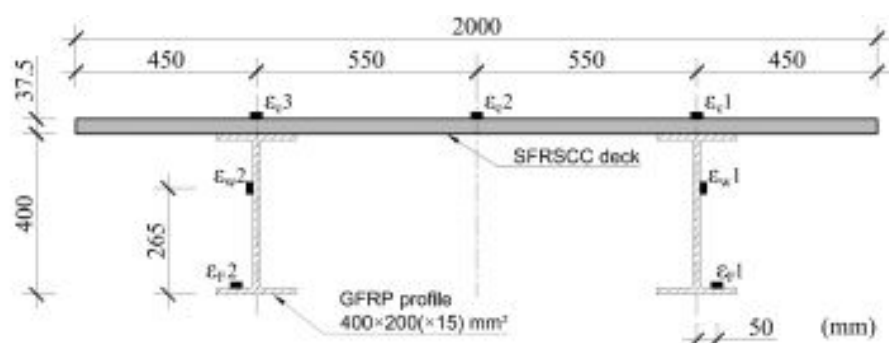


Figure 7.1.: Full-scale prototype cross-section.

In addition to the main elements, *i.e.* the main girders and the deck, and similarly to what was done for the small-scale prototype, the footbridge prototype was provided with secondary girders and concrete jackets at the support sections, as shown in Figure 7.2. The secondary girders were materialized by I-shaped section ( $200 \times 100(\times 10)$  mm<sup>2</sup>) GFRP pultruded profiles (the same used for the main and secondary girders of the small-scale prototype), while the concrete jackets were cast with SFRSCC with the same composition used in the deck (*cf.* Section 4.3).

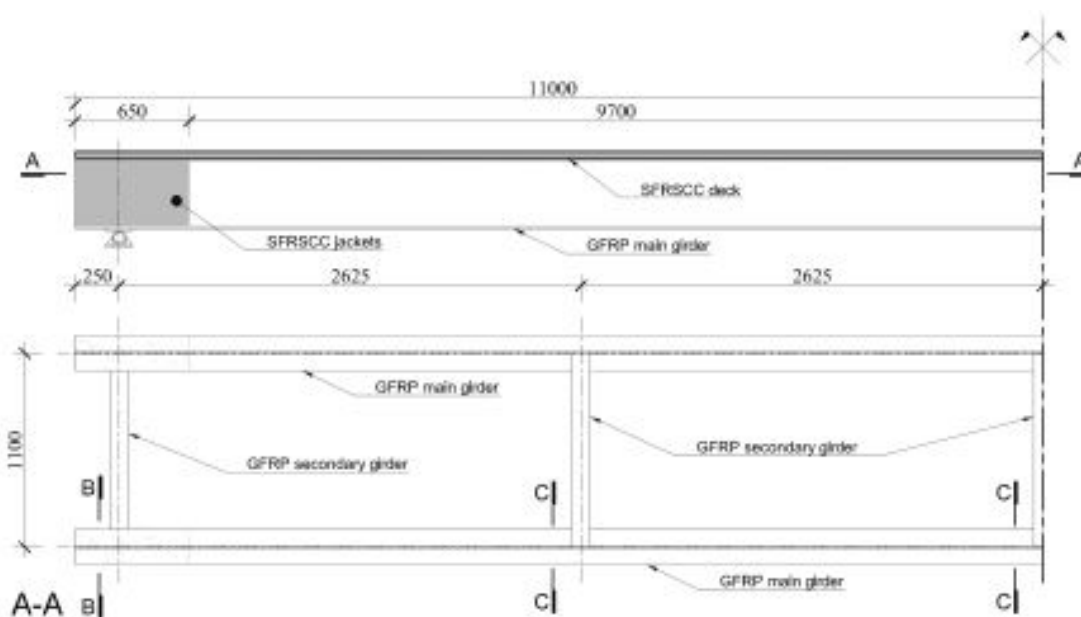


Figure 7.2.: Side- and A-A section-view of the full-scale prototype.

Figure 7.3 plots the details of the connections between the main and secondary girders, by depicting section-views B-B, C-C, D-D and E-E (*cf.* Figures 7.2 and 7.3). These connections were materialized by stainless steel bolts and threaded rods, which connected the different elements with the aid of small-length GFRP angle-section profiles.

The connection between the main girders and the deck was provided by both an adhesive connection and a bolted connection, following the recommendations made in Chapter 5. The bonded connection was materialized by a 2 mm layer of epoxy adhesive (*cf.* Section 4.4.3), the same used in the small-scale prototype. The bolted connection was materialized by two M10 stainless steel connectors per girder, installed with a 300 mm longitudinal spacing.

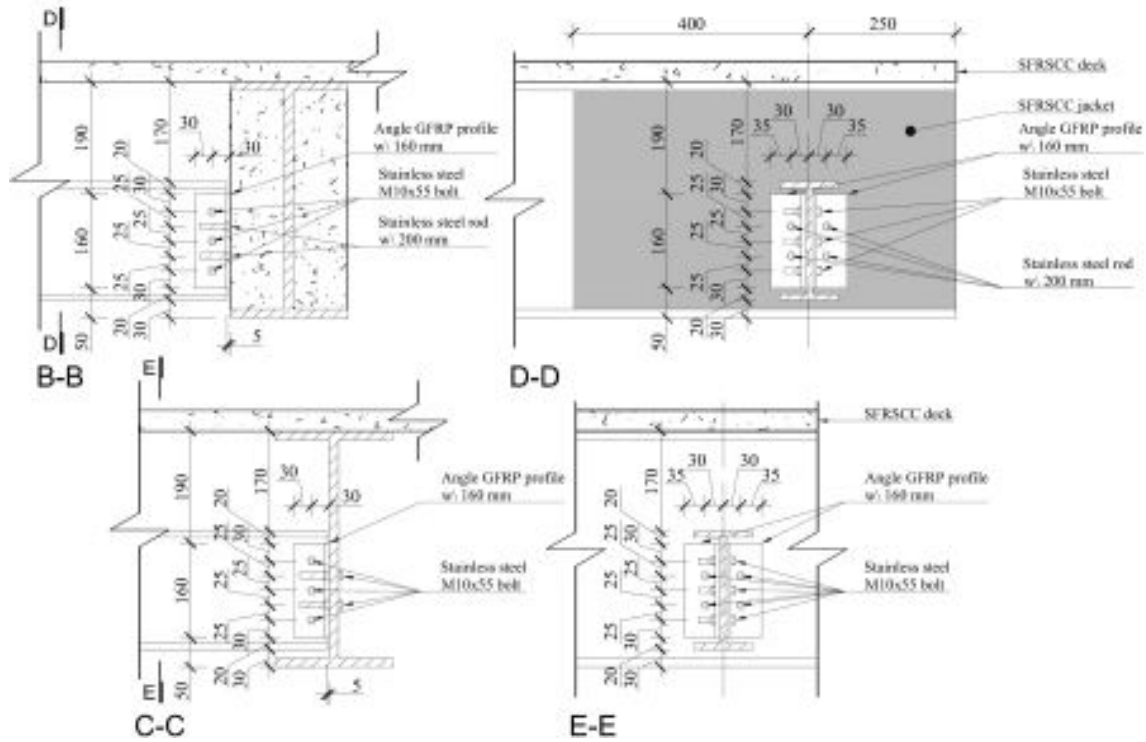


Figure 7.3.: Details of the connections between main and secondary girders of the full-scale prototype.

### 7.2.1. Ultimate limit states

Regarding the design of the full-scale footbridge prototype, it complied with the ULS requirements of Eurocodes 0 [64] and 1 [65], namely by considering the design loads and partial safety factors presented in Table 7.1.

Table 7.1.: Design loads and partial safety factors considered in the design of the full-scale footbridge prototype.

Loads				Materials	
Self-weight		Live load		$\gamma_M$ (-)	
$g_k$ (kN/m <sup>2</sup> )	$\gamma_G$ (-)	$q_{fk}$ (kN/m <sup>2</sup> )	$\gamma_Q$ (-)	GFRP	SFRSCC
1.11	1.35	5.00	1.50	2.00	1.50

It should be mentioned that the Eurocodes do not establish partial safety factors for the GFRP material ( $\gamma_M$ ) and, therefore, the value presented in Table 7.1 was defined within the *Pontalumis* project. The fact that the proposed coefficient is lower than those proposed by some existing standards/guidelines for composite materials, namely the EuroComp [38], stems from the extensive testing to which this particular GFRP material was subjected to, both at coupon and full-scale levels. Nevertheless, the chosen partial safety factor (2.0) is higher than that proposed in the more recent Italian Guidelines [68] (<1.5).

The basic ULS design requirement set in the Eurocodes is that the design strength ( $R_d$ ) is equal or higher than the design loads ( $S_d$ ) [64]:

$$S_d \leq R_d \quad (7.1)$$

The ultimate limit states design load combination may be written as follows:

$$S_d = \gamma_G \times g_k + \gamma_Q \times q_{fk} \quad (7.2)$$

Thereafter, using Eq. (7.2) with the data provided in Table 7.1, a design load  $q_{sd} = 9.0 \text{ kN/m}^2$  is determined. The design values of the internal forces, namely (i) the shear force ( $V_{sd} = 94.5 \text{ kN}$ ), (ii) the bending moment ( $M_{sd} = 248.1 \text{ kNm}$ ); and (iii) the support reaction ( $R_{sd} = 47.3 \text{ kN}$ ), are determined with Eqs. (7.3) to (7.5) using simple beam theory.

$$V_{sd} = (q_{sd} \cdot b) \frac{L}{2} \quad (7.3)$$

$$M_{sd} = (q_{sd} \cdot b) \frac{L^2}{8} \quad (7.4)$$

$$R_{sd} = \frac{V_{sd}}{2} \quad (7.5)$$

The ultimate design strengths, on the other hand, are obtained by dividing the characteristic strengths of the materials by the corresponding material partial safety factor:

$$R_d = R_k / \gamma_M \quad (7.6)$$

The characteristic strengths ( $R_k$ ) may be determined as the 5% percentile of the material strength determined experimentally, according to Eurocode 2 [85]. For the concrete material, the characteristic compressive strength ( $f_{ck}$ ) should be determined considering the tests on cylinder coupons [85]. Table 7.2 summarizes the material characteristic strengths relevant for the design of the full-scale prototype.

Table 7.2.: Material characteristic strengths relevant for the design (MPa).

Property	GFRP		SFRSCC
	Flange	Web	
$\sigma_{tu,Lk}$	284.5	246.3	–
$\sigma_{cu,Lk}$	41.8	64.4	–
$\tau_{LTk}$	–	19.2	–
$f_{ck}$	–	–	52.5
$f_{cr,k}$	–	–	4.15
$f_{R,4k}$ <sup>1</sup>	–	–	5.47

### 7.2.1.1. Longitudinal direction

Regarding the longitudinal direction, four failure modes were considered: (i) flexure failure, governed by the material strength or by the local buckling of the compressed plates; (ii) shear failure, governed by the material strength or by the local buckling of the distorted plates;

<sup>1</sup> $f_{R,4}$  corresponds to the ultimate tensile residual strength of the SFRSCC in flexure according to the RILEM TC 162 TDF [104], cf. Section 4.3.2.3.



(iii) shear–failure interaction; and (iv) crushing at the support sections. The redundant connection systems in the GFRP–SFRSCC interface were then designed, individually, so that failure does not occur in this interface.

#### 7.2.1.1.1 Flexural failure

The neutral axis ( $NA$ ) of the cross–section can be determined with Eq. (6.3) (*cf.* page 186), while the corresponding stiffness can be determined with Eq. (6.4) (*cf.* page 187). The above mentioned formulae predicts that the neutral axis of the full–scale prototype is positioned at a distance of 62.20 mm from the top fibre, while the flexural stiffness is predicted as 23211 kNm<sup>2</sup>.

Assuming that the flexural failure of the section is due to the tensile failure of the GFRP main girders' bottom flanges, an ultimate characteristic strain of  $\varepsilon_{tu,Lk} = 7967 \mu\text{m/m}$  is determined for the bottom fibre. In order to achieve such strain, a curvature of  $\chi_{rk} = 21.11 \cdot 10^{-3}/\text{m}$  must be imposed to the section. Thereafter, the ultimate characteristic bending moment is determined with Eq. (7.7):

$$M_{rk} = EI \cdot \chi_{rk} \quad (7.7)$$

Dividing the ultimate characteristic bending moment by the GFRP material partial safety factor (*cf.* Eq. (7.6)), the ultimate design bending moment ( $M_{rd}$ ) is determined as 490.3 kNm. This bending moment, governed by the material failure of the bottom flange, corresponds to maximum: (i) compressive stress of 8.56 MPa on the GFRP top flanges; (ii) compressive stress of 1.95 MPa; and (iii) tensile stress of 91.7 MPa on the GFRP webs; and (iv) compressive stress in the SFRSCC of 24.8 MPa, showing that the assumed hypothesis (*i.e.* tensile failure in the GFRP bottom flange) is valid. Moreover, the fact that the ultimate design bending moment corresponds to such low stress levels on the SFRSCC (less than 50% of  $f_{ck}$ ) shows that this material is in its linear branch, meaning that Eq. (6.4) is valid for determining the flexural stiffness of the cross–section ( $EI$ ).

On the other hand, if the flexural failure of the cross–section is due to the local buckling of the web<sup>2</sup>, then the critical compressive stress ( $\sigma_{cr}^{web}$ ) can be computed using Eq. (4.27) (*cf.* Section 4.2.3.3, page 93). This equation provides a conservative estimate of the critical compressive stress for the present situation, since it is formulated considering a symmetric and linearly varying compressive stress, while for the present case most of the web is in tension. The critical compressive stress of the web ( $\sigma_{cr}^{web}$ ) is then estimated as 213.5 MPa, more than 100 times the maximum compressive stress of the web considering material failure, as shown earlier. This result shows that the flexural failure of the cross–section is not governed by local buckling.

#### 7.2.1.1.2 Shear failure

For the design of the present structure, it was assumed that the shear stresses were supported only by the GFRP profiles' webs. As mentioned earlier, this is a common design assumption for hybrid GFRP–concrete structures with I–section profiles, which leads to conservative results [60–62]. Moreover, the concrete jackets at the support section are not accounted for

<sup>2</sup>Note that the compressed flange is restrained by the (much thicker) slab and, therefore, it does not buckle.

the shear strength of the structure. Thereafter, the shear strength may be governed (i) by the material strength, or (ii) by the critical buckling stress of the webs in shear ( $\tau_{cr}^{web}$ ). The critical shear stress was determined, using Eq. (4.39) (*cf.* page 95), as 42.9 MPa, more than twice the ultimate characteristic shear strength of the web plates ( $\tau_{LTk}$ , *cf.* Table 7.2), showing that this failure mode is also governed by the material strength.

The ultimate design shear strength ( $V_{sd}$ ) is then determined, using Eq. (4.37) (*cf.* page 95), as 111.0 kN.

### 7.2.1.1.3 Shear–flexure failure interaction

As discussed previously, regarding the failure of the small-scale prototype (*cf.* Section 6.4.6.3), the failure mechanism of the proposed structural system may result from shear–flexure failure interaction. Henceforth, Eq. (6.13) (*cf.* page 192) is used with the design strength and load values to determine a 0.79 safety coefficient (lower than 1, *i.e.* on the safe side). It should be mentioned that, similarly to what was done for the small-scale prototype, the stress distribution was estimated with a simplified thin-walled cross-section where the GFRP profiles' upper flanges were disregarded and the web was extended until the SFRSCC slab mid-line. This simplified cross-section presents a very similar flexural stiffness to that of the original cross-section (relative difference of -1.5%). Unlike what was observed for the small-scale prototype, for this case failure is predicted at the shear centre of the support sections. The web shear stress distribution at failure for the latter section is shown in Figure 7.4. It should be noted that the longitudinal axial stresses are null at the support sections.

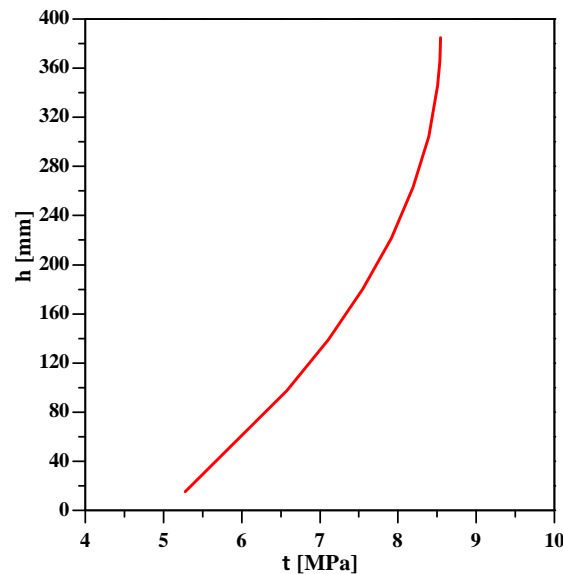


Figure 7.4.: Design web shear stress ( $\tau_{sd}$ ) distribution at the support section.

### 7.2.1.1.4 Crushing at the support sections

The design of the support sections, which have concrete jackets, may be conservatively estimated disregarding the contribution of the GFRP webs to the overall strength. However, Correia [5] has shown that the compressive strength of unreinforced concrete jackets loaded

in the transverse direction of the web at failure may be significantly lower (down to 60%) than its average compressive strength ( $f_c$ , measured on cylinder coupons). Thereafter, Eq. (7.8) is proposed in order to estimate the strength of the concrete jackets to concentrated loads:

$$R_{cj,k} = L_{eff} \cdot b_{cj} \times 0.5f_{ck} \quad (7.8)$$

where,  $L_{eff}$  is the support length and  $b_{cj}$  is the concrete jacket's width (width of the profile minus web thickness). With this formula, which conservatively considers only 50% of the concrete's compressive strength, the minimum design support length is estimated as 14.60 mm (in the experimental tests a 100 mm support length was used).

#### 7.2.1.1.5 Shear connection

As mentioned earlier, the shear connection is provided by both (i) an adhesive bond and (ii) a bolted connection, the latter provided as a redundant connection system in case of premature degradation of the mechanical properties of the epoxy adhesive.

Concerning the strength of the adhesive connection, the failure test of the small-scale prototype (*cf.* Section 6.4.5), in which failure occurred in the GFRP material, provides a lower bound for the strength of the interface. In this regard, the maximum shear stresses at the adhesive may be estimated with Eq. (6.14) in 30.8 MPa, which, being a lower bound, may be taken as the characteristic strength of the interface ( $\tau_{ak}$ ) for design purposes. On the other hand, for the full-scale the design shear stress at the interface due to the design load ( $q_{sd}$ ) is  $\tau_{sd} = 8.5$  MPa, as shown in Figure 7.4. Thereafter, considering a material partial safety factor of  $\gamma_M = 2.0$  for the bonded interface, the design shear strength obtained is  $\tau_{rd} = 15.4$  MPa, approximately 1.8 times higher than  $\tau_{sd}$ , showing that failure is not governed by the failure of the epoxy adhesive.

Regarding the design of the bolts, which, as mentioned earlier, does not consider the contribution of the adhesive, since the failure of the structure occurs when the SFRSCC is within its linear behaviour branch, the design method used for the small-scale profile (*cf.* Section 6.2) was deemed as overly conservative. Thereafter, the bolted connection was designed to present higher strength than the shear stresses applied when the governing failure mode occurs.

The calculations presented earlier show that the governing failure mode is the shear failure of the main girders webs, which occurs for a design strength load ( $q_{rd}$ ) of 10.6 kN/m<sup>2</sup>, corresponding to a 291.2 kNm bending moment at the midspan section. For this load level, the maximum compressive load on the SFSRCC deck ( $F_{rd}$ , considering a linear behaviour) is 771.4 kN.

The strength of the bolted connection, on the other hand, was determined experimentally; a characteristic strength per bolt ( $R_{bk}$ ) of 20.3 kN was obtained (*cf.* Section 5.2.5.2). Assuming a 1.5 material partial safety factor ( $\gamma_M$ ), the design strength per bolt ( $R_{bd}$ ) is 13.5 kN. Thereafter, the number of mechanical connectors ( $Nr$ ) needed may be estimated by conservatively considering the maximum compressive load of the deck (which is verified only at midspan), thereby adapting Eq. (6.2) (page 171) as follows:

$$Nr = 2 \times \frac{F_{rd}}{R_{bd}} \quad (7.9)$$

Using Eq. (7.9), the number of connectors needed is estimated as over 114 connectors. Using 4 connectors per section, *i.e.* a pair of connectors in each main girder, the maximum longitudinal spacing to ensure safety is 367.7 mm. In order to guarantee that failure does not occur in the bolted connection before it occurs in the GFRP webs, a longitudinal spacing of 300 mm between connectors was used.

#### 7.2.1.1.6 Summary

The ultimate limit states analysis concerning the longitudinal direction presented earlier shows that the full-scale footbridge prototype structure fulfils the ULS requirements (*cf.* Eq. (7.1)). The results are summarized in Table 7.3, including the strength factor ( $S.F. = S_d/R_d$ ), which evaluates the percentage of the strength required by the applied loads, showing that the shear failure is the governing mode. It should be noted that the strength factor is lower for the shear failure mode than for flexure–shear failure interaction. This difference is due to the fact that the latter failure was evaluated considering the contribution of the concrete to the shear stress distribution, while the former considered the contribution of the webs only. Additionally, it should be mentioned that the strength presented for the failure due to crushing at the support sections was determined considering a 100 mm support length.

Table 7.3.: Summary of ULS design in the longitudinal direction.

Failure mode	Flexure (kNm)	Shear (kN)	Interaction (–)	Crushing (kN)
$S_d$	248.1	94.5	–	47.3
$R_d$	490.3	111.0	–	323.6
$S.F.$	0.51	0.85	0.78	0.15

#### 7.2.1.2. Transverse direction

##### 7.2.1.2.1 Flexural failure

In the transverse direction the thin SFRSCC deck must be able to sustain the loads by itself without any rebar reinforcement. The deck has three transverse spans, two cantilevers and one interior span. Therefore, the design bending moments must be determined considering that the live load may not be distributed in the entire width of the deck. The governing bending moments, for the cantilever and interior span, can be determined as follows,

$$M_{trans, sd}^- = -\frac{q_{sd} \cdot L_{cant}^2}{2} \quad (7.10)$$

and

$$M_{trans, sd}^+ = \frac{q_{sd} \cdot L_{int}^2}{8} - \frac{g_{sd} \cdot L_{cant}^2}{2} \quad (7.11)$$

where,  $L_{cant}$  and  $L_{int}$  are the transverse cantilever and interior spans, respectively (450 mm and 1100 mm, *cf.* Figure 7.1).

The design strength bending moment ( $M_{trans,rd}$ ) was determined considering the SFRSCC stress-strain relationship depicted in Figure 7.5, idealized based on the recommendations proposed by Salehian [84], in which the design strengths were used, *i.e.* the cracking strength ( $f_{cr}$ ) was replaced by the design cracking strength ( $f_{cr,d}$ ), and the post-cracking strength ( $f_{post-cr}$ ) was replaced by the design residual cracking strength ( $f_{R,4d}$ ).

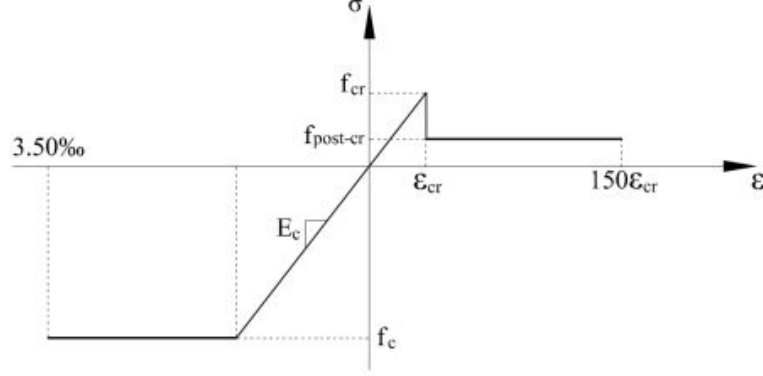


Figure 7.5.: Idealized stress-strain relationship of the SFRSCC.

Given the non-linear response of the SFRSCC material, as assumed in Figure 7.5, the stiffness of the slab was determined with Eq. (7.12), using an iteration routine,

$$K_{sec} = \int \frac{\sigma(\varepsilon)}{\varepsilon} \begin{bmatrix} 1 & z \\ z & z^2 \end{bmatrix} d\Omega \quad (7.12)$$

where  $\varepsilon$  is the axial strain,  $\sigma(\varepsilon)$  is the axial stress (which in the non-linear regime is a function of the axial strain) and  $\Omega$  is the cross-section area. Thereafter, it is possible to determine the ultimate bending moment of the cross-section with Eq. (7.13),

$$\begin{bmatrix} N \\ M \end{bmatrix} = K_{sec} \begin{bmatrix} \varepsilon \\ \chi \end{bmatrix} \quad (7.13)$$

by setting a null axial load ( $N$ ) and a maximum strain corresponding to the ultimate compressive or tensile strains ( $3.50\text{‰}$  or  $150\varepsilon_{cr}$ ), whichever case is governing. The design strength bending moment was, thereby, evaluated as 2.33 kNm/m, while the axial stress distribution over the SFRSCC slab cross-section depth ( $h_c$ ) is presented in Figure 7.6.

#### 7.2.1.2.2 Shear failure

In the transverse direction the design shear load can be determined for the cantilever and the interior span using Eqs. (7.14) and (7.15),

$$V_{sd}^- = -q_{sd} \cdot L_{cant} \quad (7.14)$$

and

$$V_{sd}^+ = \frac{q_{sd} \cdot L_{int}}{2} \quad (7.15)$$

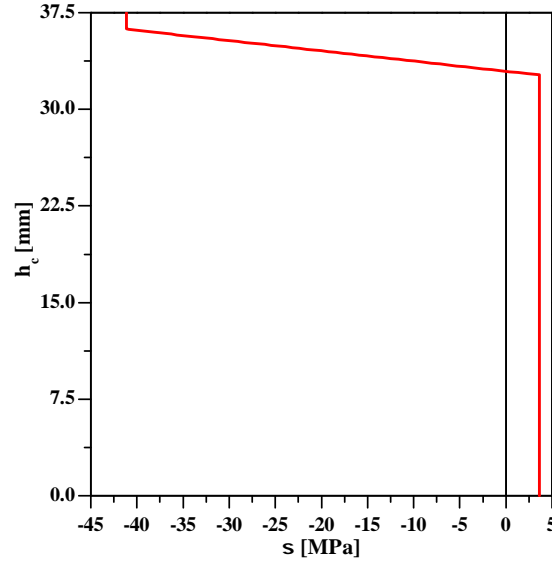


Figure 7.6.: Axial stress distribution over the SFRSCC slab at transverse failure.

The shear strength, on the other hand, can be conservatively estimated neglecting the contribution of the steel fibre reinforcement. Thereafter, the minimum design shear strength ( $v_{min}$ ) of the SFRSCC is determined using the recommendations of Eurocode 2 [85],

$$v_{min} = 0.035k^{3/2}f_{ck}^{1/2} \quad (7.16)$$

and

$$k = 1 + \sqrt{\frac{200}{d}} \leq 2.0 \quad (7.17)$$

where  $d$  (in mm) is the distance between the top fibre of the section and the centre of the longitudinal reinforcement. For the present case, since no longitudinal reinforcement is provided,  $d$  is considered to be the thickness of the deck. The design resistant shear load ( $V_{rd}$ ) is then estimated with Eq. (7.18):

$$V_{rd} = v_{min} \times b \cdot d \quad (7.18)$$

where  $b$  is the width of the cross-section, resulting in  $V_{rd} = 26.9$  kN/m.

#### 7.2.1.2.3 Summary

The results obtained in the preceding sections are summarized in Table 7.4, showing that the ULS requirements are fulfilled for the transverse direction without the need of adding any internal rebar reinforcement.

Table 7.4.: Summary of ULS design in the transverse direction.

Failure mode	Flexure (kNm/m)	Shear (kN/m)
$S_d$	1.21	4.95
$R_d$	2.33	26.89
$S.F.$	0.52	0.18

### 7.2.2. Serviceability limit states

The SLS requirements for footbridges defined in Eurocode 0 [64] do not include any deformation limits but only vibration limits in order to guarantee pedestrian comfort. In this regard, two alternative sets of requirements are proposed: (i) direct criteria, namely vertical accelerations under  $0.7 \text{ m/s}^2$  and horizontal accelerations under  $0.2 \text{ m/s}^2$  and  $0.4 \text{ m/s}^2$  for normal use and crowd conditions, respectively; and (ii) indirect criteria, namely fundamental frequencies of the deck higher than 5 Hz for vertical vibrations modes and 2.5 Hz for lateral and torsional vibrations modes. Furthermore, a maximum stress criterion for serviceability permanent stresses is included.

Using Eqs. (6.31) and (6.39) (cf. pages 207 and 208) in order to estimate the fundamental bending and torsional frequencies of the full-scale prototype, one obtains  $f_{bending} = 5.96 \text{ Hz}$  and  $f_{torsion} = 7.17 \text{ Hz}$ , both values fulfilling the requirements set by the indirect criteria mentioned earlier. Further information about these calculations is provided in Section 7.5.1.2.

Concerning the deformability limit states requirements, as Eurocode 0 [64] does not set any deformability requirements for footbridges, the partners of the Pontalumis project (cf. Chapter 3) decided to limit the long-term midspan deflection of the full-scale prototype when subjected to the quasi-permanent load combination to 26 mm, which corresponds to  $L/400$ . As a benchmark for this limit, Eurocode 2 [85] sets the maximum deflections for concrete floors in buildings at  $L/250$  or, for cases in which the deformations may damage non-structural elements, such as masonry walls, at  $L/500$ .

Using the creep models developed for the small-scale prototype (cf. Section 6.6.3), a long-term midspan deflection of 20.37 mm ( $\approx L/565$ ) is estimated for the quasi-permanent load combination (which, for footbridges, corresponds to the permanent loads according to Eurocode 1 [65]), after a period of 100 years, and considering an average temperature and relative humidity of  $25^\circ\text{C}$  and 60%, respectively. More details on creep behaviour predictions for the full-scale prototype are provided in Section 7.6.3.

On the other hand, the Italian guidelines for FRP structures [68] recommend the deflections to be limited to  $1/100$  of the span ( $L$ ) for the rare (characteristic) load combination. In order to check this criterion, the instantaneous deflections induced in the structure by the characteristic live load ( $q_{fk}$ ), which do not cause creep due to their short-term nature, should be added to the long-term deflections caused by the permanent loads, assuming the superposition principle. Thereby, the long-term midspan deflection for the rare load combination after 100 years is  $\delta_{long-term}^{rare} = 20.37 + 37.73 = 58.16 \text{ mm}$ , corresponding to  $L/180$ , thus below the proposed limit.

Additionally, owing to concerns regarding the rupture of the GFRP material under permanent stresses, it is recommended to limit the maximum stress under serviceability loads [4].

The Italian guidelines [68] suggest that the permanent stresses on the GFRP members should be limited to 30% of the design strength. For the present structure, the maximum stress on the GFRP main girders for the quasi-permanent load combination is 9.26 MPa, corresponding to 6.5% of  $\sigma_{tu,Ld}$ , thereby verifying the stress limit criterion.

Table 7.5 summarises the results of the SLS analyses.

Table 7.5.: Summary of SLS design.

Limit state	Vibration		Deformability		Stress
	Vertical	Horizontal/Torsion	Quasi-permanent	Rare	
Requirement	$\geq 5.0$ Hz	$\geq 2.5$ Hz	$\leq L/500$	$\leq L/100$	$\leq 30$
Result	5.96 Hz	7.17 Hz	$L/565$	$L/180$	6.5

### 7.3. Construction of the prototype

The construction of the full-scale prototype began with the manufacturing of the GFRP I400 section pultruded profiles at *ALTO Perfis Pultrudidos, Lda.* Figures 7.7 and 7.8 show the pultrusion process of the profiles, which were produced for the first time in the context of this project. Such production required a considerable extension of ALTO's pultrusion facilities due to the very large quantities of glass fibre reinforcement needed for the I400 profile production.



Figure 7.7.: Beginning of the pultrusion of the I400 profiles.



Figure 7.8.: Pultrusion of the I400 profiles in progress.

Afterwards, the GFRP profiles were assembled (I400, I200 and angle sections) according to the dispositions presented in Figures 7.2 and 7.3, using stainless steel bolts and rods to materialize the connections. Figure 7.9 shows the aspect of the assembled girders, while Figure 7.10 shows the GFRP girders loaded on a small truck and ready to be transported for the construction site, attesting the lightness and ease of transportation characteristic of FRP structural systems. Additionally, Figure 7.9 shows the holes made in the top flanges, near the extremities of the I400 profiles, in order to cast the SFRSCC of the concrete jackets.

In the meantime, at the facilities of *Tecnipor* (a precast concrete company), where the full-scale prototype was to be constructed, the slab formwork was being prepared. Figure 7.11





*Figure 7.9.: Assembled girders.*



*Figure 7.10.: Girders on the transport truck.*

shows the construction of the formwork, while Figure 7.12 shows the formwork ready for the SFRSCC cast with the release agent already applied.



*Figure 7.11.: Construction of the formwork.*



*Figure 7.12.: Formwork ready for the cast.*

Figure 7.13 shows the casting of the SFRSCC slab, while Figure 7.14 shows the regularization of the top surface of the slab.

Figure 7.15 shows the final aspect of the slab after the casting process was completed. Additionally, the casting of the SFRSCC jackets at the support sections was performed and the stainless steel connectors used at that interface areas were installed, as shown in Figure 7.16.



Figure 7.13.: Casting of the SFRSCC slab.



Figure 7.14.: Regularization of the slab surface.

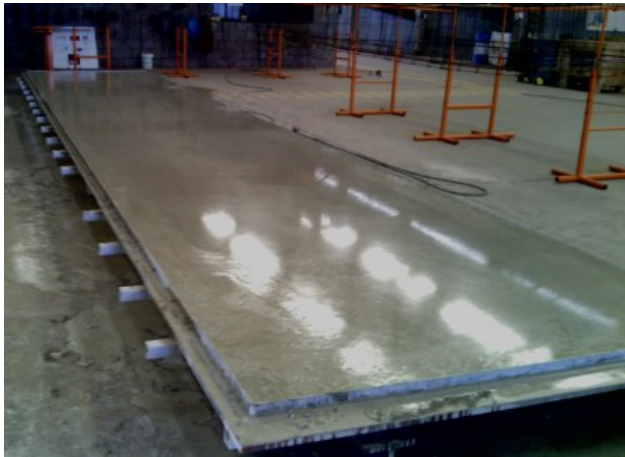


Figure 7.15.: Final aspect of the slab after being cast.



Figure 7.16.: Concrete jackets and stainless steel connectors.

After the SFRSCC of the slab was hardened, 30 mm deep holes were drilled in the deck, at predetermined positions, in order to accommodate the stainless steel connectors, as depicted in Figure 7.17. These stainless steel connectors were then installed in the previously drilled holes, as shown in Figure 7.18, using an epoxy resin (*S&P Resin 220*, cf. Section 4.4.3) to guarantee a monolithic connection with the slab.

After a 5 day period, set for the hardening of the epoxy adhesive that embedded the connectors, the interface areas (which would be in contact with the GFRP main girders) were roughened with sand paper and duly dusted, in order to enhance the bond, and an epoxy adhesive layer was applied, as shown in Figure 7.19. The 2 mm thickness preconized was guaranteed by gluing small 2 mm plastic spacers on the slab, scattered throughout the interface areas. After this process was completed, the GFRP girders were positioned, using a moving crane, into the top of the slab, as depicted in Figure 7.20.



*Figure 7.17.: Drilling of the SFRSCC slab.*



*Figure 7.18.: Installation of the stainless steel connectors.*



*Figure 7.19.: Application of the epoxy adhesive layer.*



*Figure 7.20.: Installation of the girders on the deck.*

Once all the structural elements were positioned, the washers and nuts were installed in the connectors, as shown in Figure 7.21, and were screwed tightened with an electric screwdriver. After all the nuts were tighten, the excessive squeezed adhesive was cleaned from the edges of the interface areas. Figure 7.22 shows the aspect of the assembled structure.

The footbridge prototype was rotated ( $180^\circ$ ) and put into position 9 days after the assembly of all elements, a period given for the epoxy adhesive of the GFRP-SFRSCC interface to fully harden. In order to avoid damaging the SFRSCC slab during this process, namely of its edges, an auxiliary system, especially designed for this purpose, comprising steel profiles, wood blocks and GFRP profiles, was installed. Figure 7.23 shows several stages of the rotation process that was performed with a moving crane. Figure 7.24 presents the final aspect of the full-scale prototype.





*Figure 7.21.: Installation of the washers and nuts.*



*Figure 7.22.: Aspect of the assembled structure.*



*Figure 7.23.: Rotation of the full-scale prototype.*



*Figure 7.24.: Final aspect of the full-scale prototype.*

## 7.4. Static behaviour of the prototype

### 7.4.1. Overview

Following the investigations regarding the static behaviour of the small-scale prototype (*cf.* Section 6.4), this section presents the experimental investigations regarding the static behaviour of the full-scale prototype. In this case, the experiments respect only the serviceability behaviour of the structure, since the footbridge prototype is meant to be installed in real service conditions and, therefore, could not be tested up to failure.

Similar design tools as those used in the previous chapter (*cf.* Section 6.4), namely analytical and numerical models, were used to predict the structural behaviour, with the results obtained with these simulation tools being compared to the experimental data.

### 7.4.2. Serviceability tests

As for the remaining tests, the footbridge prototype was installed with a 10.5 m simply supported span, with all supports allowing rotations in the bending axis, while longitudinal displacements were only allowed on one side of the prototype. These support systems laid on top of two concrete blocks, on each side, as shown in Figure 7.24.

The serviceability tests were performed by loading the prototype with closed water reservoirs, which had an average weight of 10.6 kN and plan dimensions of  $1.0 \times 1.2 \text{ m}^2$ , corresponding to a distributed load of  $8.8 \text{ kN/m}^2$  (76% higher than the characteristic load specified in Eurocode 1 [65] for footbridges,  $5 \text{ kN/m}^2$ ). The reservoirs were successively positioned with a stacker on top of the deck in three different uniformly distributed load configurations, as shown in Figure 7.25: (a) along the entire span, centred with the deck in a width of 1.20 m (total load of 106.0 kN); (b) in the central part of the span, in a length of around 2.70 m (with a small gap of 0.30 m in the vicinity of midspan), across the entire width of the deck (2.00 m, total load of 42.2 kN); and (c) in the central part of the span, in a length of 5.10 m (with a gap of 0.30 m in the vicinity of midspan), also across the entire width of the deck (total load of 84.4 kN). The loading and unloading operations were performed as fast as possible in order to minimize creep effects — the duration of these operations varied between 10 and 50 minutes.

During the tests vertical deflections were measured at the midspan section underneath both GFRP profiles, while axial strains were measured at different positions of that cross-section, as depicted in Figure 7.26. The deflections were measured with electrical transducers (precision of about 0.01 mm), whereas the axial strains were measured with electric strain gauges. Data was gathered at a rate of 1 Hz with data loggers and was registered in a PC.

The footbridge prototype exhibited linear-elastic load-deflection and load-axial strain behaviour in all the tests during both the loading and unloading processes. Table 7.6 presents the average midspan deflections ( $\delta_{ms,Avg}$ ) and axial strains ( $\varepsilon_{c,Avg}$ ,  $\varepsilon_{w,Avg}$  and  $\varepsilon_{f,Avg}$ , for the concrete, GFRP webs and flanges, respectively) measured at the end of the loading process (for each load configuration).

The results obtained are in agreement with a linear-elastic structural response, namely: (i) deflections/axial strains for load configuration (b) were around half of those for configuration (c) (similar configurations were used and the load in (c) was twice of that used



Figure 7.25.: Serviceability tests on the full-scale prototype: load configurations.

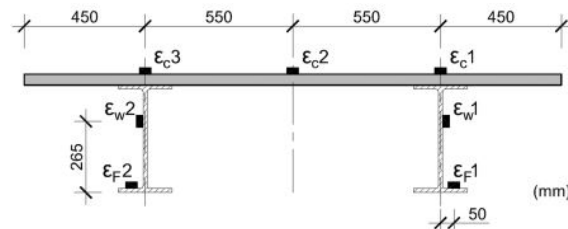


Figure 7.26.: Axial strain gauges positioning at the midspan section of the full-scale prototype.

in (b)); (ii) deflections/axial strains for load configuration (a) were lower than those for configuration (c) (a higher total load was used in (a), but in (b) loads were concentrated in the vicinity of midspan). Regarding the unloading process, the small residual deflections of 4.52%, 0.98% and 4.10% for load configurations (a), (b) and (c), respectively, may have been caused by (i) some initial accommodation of the support system and/or (ii) the initial creep developed during the loading process.

Table 7.6.: Summary of the results of the serviceability tests on the full-scale prototype.

Load configuration	$\delta_{ms,Avg}$ (mm)	$\varepsilon_{c,Avg}$ ( $\mu\text{m}/\text{m}$ )	$\varepsilon_{w,Avg}$ ( $\mu\text{m}/\text{m}$ )	$\varepsilon_{f,Avg}$ ( $\mu\text{m}/\text{m}$ )	$\chi$ ( $10^{-4}/\text{m}$ )
a	38.07	-190	320	1102	30.6
b	23.27	-145	220	712	20.3
c	43.28	-252	392	1208	34.6

### 7.4.3. Analytical simulation

Disregarding the midspan gap for load configurations (b) and (c), all load configurations may be schematized as shown in Figure 7.27, *i.e.* as uniformly distributed loads applied in a portion of the deck, centred with the structure's longitudinal and transverse midspan symmetry axes.

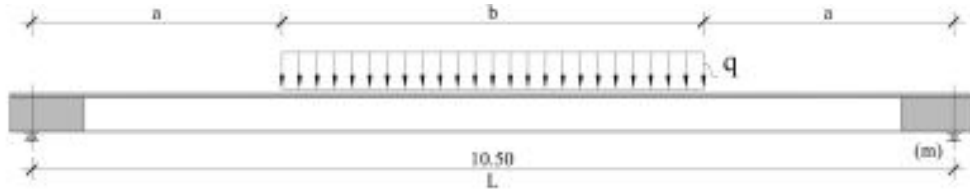


Figure 7.27.: Full-scale prototype serviceability tests: scheme of load configurations.

Table 7.7 presents the geometrical parameters ( $a$  and  $b$ ) for each load configuration as well as the respective load level ( $q$ ).

The bending moment at the midspan section can then be determined with Eq. (7.19):

$$M_{ms} = q \cdot \left( \frac{ab}{2} + \frac{b^2}{8} \right) \quad (7.19)$$

The midspan average deflections ( $\delta_{ms}$ ) can be estimated with Eq. (6.61) (*cf.* page (6.61)). The flexural and shear stiffness of the cross-section ( $EI$  and  $GkA$ , respectively) are determined based on the same assumptions made for the small-scale prototype (*cf.* Section 6.4.6.1) as 46443 kNm<sup>2</sup> and 40310 kN. Additionally, the curvature of the midspan section is determined with Eq. (7.20), while the strains at each position are determined with Eq. (7.21),

$$\chi_{ms} = \frac{M_{ms}}{EI} \quad (7.20)$$

and

$$\varepsilon_{ms} = \chi_{ms} \cdot z \quad (7.21)$$

where,  $z$  is the vertical distance between the neutral axis ( $NA$ ) and the fibre in which the strains are to be determined. Table 7.8 summarizes the analytical predictions and compares them to data obtained experimentally.

Concerning the midspan deflections, the analytical predictions show a good agreement with the experimental results for all loading cases with absolute relative differences ranging from

Table 7.7.: Full-scale prototype serviceability tests: load parameters.

Load configuration	$a$ (m)	$b$ (m)	$q$ (kN/m)
(a)	0.0	10.5	8.8
(b)	3.9	2.7	17.6
(c)	2.7	5.1	17.6

6.8% to 14.4%. A similar agreement was found for the small-scale prototype regarding the serviceability tests (*cf.* Table 6.3, page 187) and the instantaneous deflections measured in the creep tests (*cf.* Section 6.6.3.1). Regarding the predictions of the axial strains and curvature, a fair to good agreement was also observed, with absolute relative errors ranging from 0.4% to 19.5%.

#### 7.4.4. Numerical simulation

In order to simulate the structural behaviour of the footbridge prototype observed in the experimental tests, a finite element (FE) model was developed using the commercial package SAP2000, similarly to the model developed to simulate the behaviour of the small-scale prototype (*cf.* Section 6.4.7). This model included 8-node solid brick elements in order to simulate most structural components, namely: (i) the SFRSCC deck; (ii) the 2 mm thick epoxy adhesive layer; (iii) the GFRP main girders; (iv) the GFRP secondary girders, (v) the steel support plates, and (vi) the GFRP angle sections (*cf.* Figures 7.1 to 7.3). Two-joint link elements were also used to simulate the bolted connections between main and secondary girders and to connect the support sections to the rotation centre of the supports. Figure 7.28 presents a tri-dimensional view of the FE model, including a detail of the connection between the main girders and the interior secondary girders.

All materials were considered linear-elastic, using the material properties obtained from experimental coupon testing (*cf.* Chapter 4). The GFRP profiles were modelled as orthotropic materials (for the I400 profile, the longitudinal to transverse Poissons' coefficients ( $\nu_{LT}$ ), which were not obtained experimentally, were assumed to be the same as those of the I200 profile, *cf.* Table 4.13, page 71) and the remaining materials were modelled as isotropic. A perfect bond was assumed at the GFRP-epoxy and SFRSCC-epoxy interfaces, *i.e.* only the adhesive distortion was considered. This modelling approach is supported by the results of the shear connection tests (*cf.* Chapter 5) and validated by the present test results, namely

Table 7.8.: Full-scale prototype serviceability tests: analytical *vs.* experimental results.

Load configuration	$\delta_{ms}$ (mm)			$\chi$ ( $10^{-4}/m$ )		
	Exp.	Analytical	diff.	Exp.	Analytical	diff.
a	38.07	33.00	-13.3%	30.6	26.1	-14.7%
b	23.27	26.61	14.4%	20.3	23.4	15.3%
c	43.28	46.21	6.8%	34.6	38.4	11.0%

Load configuration	$\varepsilon_{c,Avg}$ ( $\mu m/m$ )			$\varepsilon_{w,Avg}$ ( $\mu m/m$ )			$\varepsilon_{f,Avg}$ ( $\mu m/m$ )		
	Exp.	Analytical	diff.	Exp.	Analytical	diff.	Exp.	Analytical	diff.
a	-190	-162	-14.5%	320	293	-8.4%	1102	946	-14.1%
b	-145	-146	0.4%	220	263	19.5%	712	848	19.1%
c	-252	-239	-5.2%	392	431	10.0%	1208	1392	15.2%



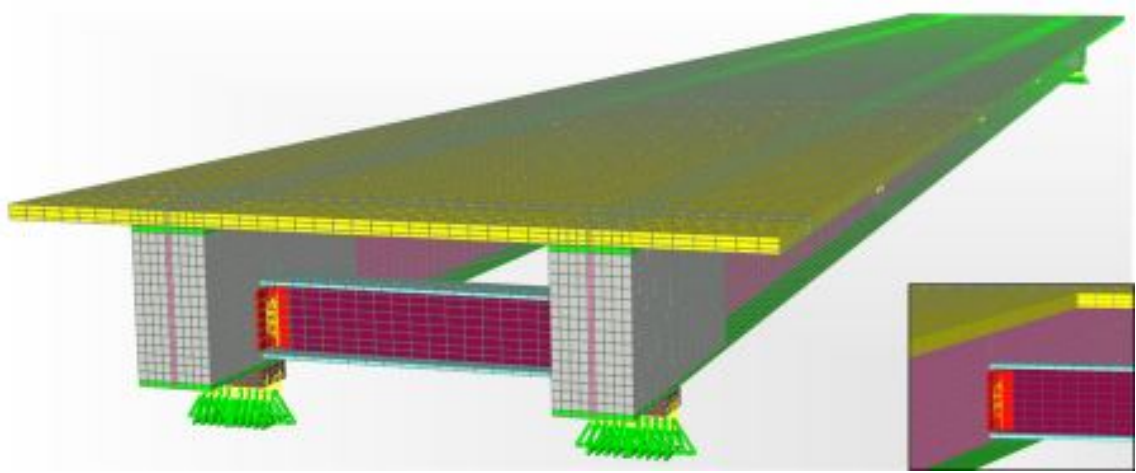


Figure 7.28.: Tri-dimensional view of the FE model of the full-scale prototype.

the axial strains measured throughout the depth of the hybrid section in the serviceability tests.

The static tests were simulated by applying surface pressure loads in the top elements of the deck with the geometry of each load configuration, described in Section 7.4.2, and performing a linear-elastic analysis, as all materials behaved within their linear-elastic range.

The numerical predictions are presented in Table 7.9, which also compares the experimental, analytical and numerical results for each load configuration.

The results obtained show an excellent agreement between the average midspan deflections predicted by the FE model and those measured in the tests, with a maximum absolute relative difference of 3.3% among the three load configurations. Regarding the average axial strains, the agreement between numerical results and experimental data varied from very good to reasonable, with a maximum relative difference of 33%; however, in general, the relative differences were lower than 12%. It should be noted that these results refer to relatively low axial strains and that the measurement of axial strains is typically less precise than that of deflections (especially in concrete, due to its heterogeneous nature and susceptibility to cracking). Furthermore, it is worth mentioning that very reduced relative differences (maximum of 7%) were registered regarding the midspan cross-section curvature. Overall, these results show that the FE model is able to simulate the static flexural behaviour of the hybrid structure with excellent accuracy, improving the predictions made with the analytical models.

Additionally, the FE model was used to predict the failure behaviour of the full-scale prototype, in order to validate the ULS design performed earlier with analytical models (*cf.* Section 7.2.1). To this end, two load configurations were considered: (i) load applied on the entire deck surface; and (ii) load applied over half of the deck width (to assess the torsional effects). Using the Tsai-Hill failure initiation criterion for the GFRP plates (*cf.* Eq. (4.45), page 100), the ultimate load was estimated as 22.8 kN/m<sup>2</sup> and 20.7 kN/m<sup>2</sup> (plus self-weight), for these load configurations (*i.e.* load applied in the entire deck or in half of its width), respectively. For both load configurations, failure was predicted in the webs of the main girders, at a distance of 650 mm from the support sections, near the web-flange junction. Moreover, for both cases, failure is almost solely due to shear stresses, which contributed with over 99.7% for the Tsai-Hill index, similarly to what was predicted with the simpler flexure-shear failure interaction analytical model (*cf.* Section 7.2.1.1.3).

Table 7.9.: Full-scale prototype serviceability tests: numerical, analytical and experimental results.

Load configuration			(a)	(b)	(c)
$\delta_{ms}$	Experimental	(mm)	38.07	23.27	43.28
	Analytical	(mm)	33.00	26.61	46.21
		diff.	-13.3%	14.4%	6.8%
	FE	(mm)	36.82	23.1	42.34
		diff.	-3.3%	-0.7%	-2.2%
$\chi$	Experimental	( $10^{-4}/m$ )	30.6	20.3	34.6
	Analytical	( $10^{-4}/m$ )	26.1	23.4	38.4
		diff.	-14.7%	15.3%	11.0%
	FE	( $10^{-4}/m$ )	30.6	21.3	37
		diff.	0.0%	4.9%	6.9%
$\varepsilon_{c,Avg}$	Experimental	( $\mu m/m$ )	-190	-145	-252
	Analytical	( $\mu m/m$ )	-162	-146	-239
		diff.	-14.5%	0.4%	-5.2%
	FE	( $\mu m/m$ )	-188	-117	-207
		diff.	-1.1%	-19.3%	-17.9%
$\varepsilon_{w,Avg}$	Experimental	( $\mu m/m$ )	320	220	392
	Analytical	( $\mu m/m$ )	293	263	431
		diff.	-8.4%	19.5%	10.0%
	FE	( $\mu m/m$ )	425	242	369
		diff.	32.8%	10.0%	-5.9%
$\varepsilon_{f,Avg}$	Experimental	( $\mu m/m$ )	1102	712	1208
	Analytical	( $\mu m/m$ )	946	848	1392
		diff.	-14.1%	19.1%	15.2%
	FE	( $\mu m/m$ )	1102	782	1354
		diff.	0.0%	9.8%	12.1%

Additionally, it should be noted that, for both cases, the maximum tensile stress in the SFRSCC is lower than 6 MPa ( $< f_{cr}$ ), with the exception of small areas over the support sections that present higher tensile stresses, owing to the small dimension of the FE elements ( $\leq 50$  mm), together with the vicinity of the point restrictions simulating the supports. The maximum compressive stress on the SFRSCC, on the other hand, is lower than 35 MPa ( $< 0.7 \times f_{ck}$ ), well within the elastic branch of the material behaviour, thereby validating the linear analysis performed with the FE model. It is also worth noting that the governing load configuration corresponded to the load applied in half of the deck width, attesting the importance of torsional effects on this type of structural system.

Using the FE model results to formally design the full-scale prototype with regard to the ULS requirements, *i.e.* considering the design load combinations and partial material safety coefficient presented in Section 7.2.1, a maximum Tsai–Hill index of 0.85 is obtained (as mentioned, governed by the load case in which the load is applied in half of the deck width), showing that the structure fulfils ULS requirements.

### 7.4.5. Conclusions

The current Section presented experimental investigations regarding the serviceability static flexural behaviour of the full-scale prototype. Analytical and numerical models were used to predict the experimental results showing good accuracy, proving once again to be reliable tools for the design of GFRP–concrete hybrid structures.

Additionally, the FE model was used to validate the structural design with regard to the ULS analysis, validating the design presented earlier and developed with analytical models, showing that the hybrid GFRP–SFRSCC footbridge prototype complies with ULS requirements.

## 7.5. Dynamic behaviour of the prototype

The present Section presents the study of the dynamic behaviour of the full-scale GFRP–SFRSCC footbridge prototype, including experimental investigations regarding the modal identification of the footbridge structure and its response under pedestrian loads.

The results observed in the experimental investigations are compared with analytical and numerical predictions.

### 7.5.1. Modal identification

#### 7.5.1.1. Experimental tests

The modal identification tests were performed using a simple output-only method, already described (*cf.* Section 6.5.1.2), by applying a stroke with a rubber hammer in the vicinity of the quarter-span section (near the cantilever edge), while vertical accelerations were measured at quarter and midspan sections, in positions A1 to A4 shown in Figure 7.29.

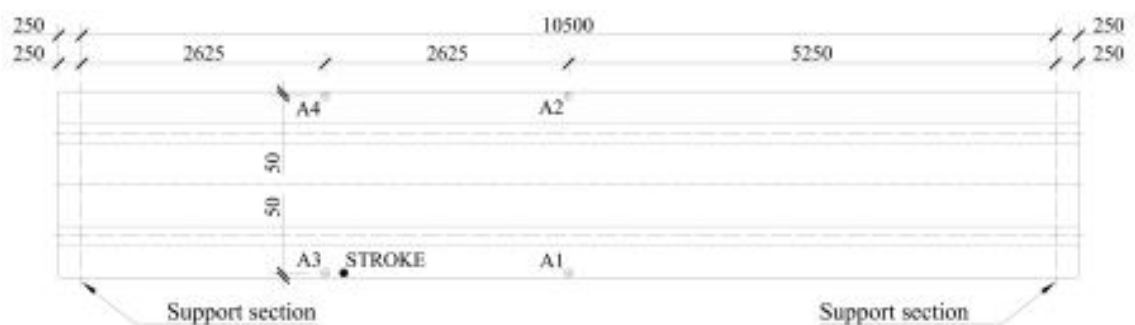


Figure 7.29.: Full-scale prototype modal identification tests: instrumentation (dimensions in mm).

During the tests, the accelerations were measured in pairs with two equivalent accelerometers (one from *Endevco* and the other from *Brüel&Kjær*) both connected to signal amplifiers (from *Brüel&Kjær*). Data was sampled at a rate of 600 Hz with a data logger (from *HBM*, model *QuantumX*) and stored in a PC. Six repetitions of each setup (accelerometer pair) were performed in order to have representative results. Figure 7.30 shows the modal identification test ongoing.

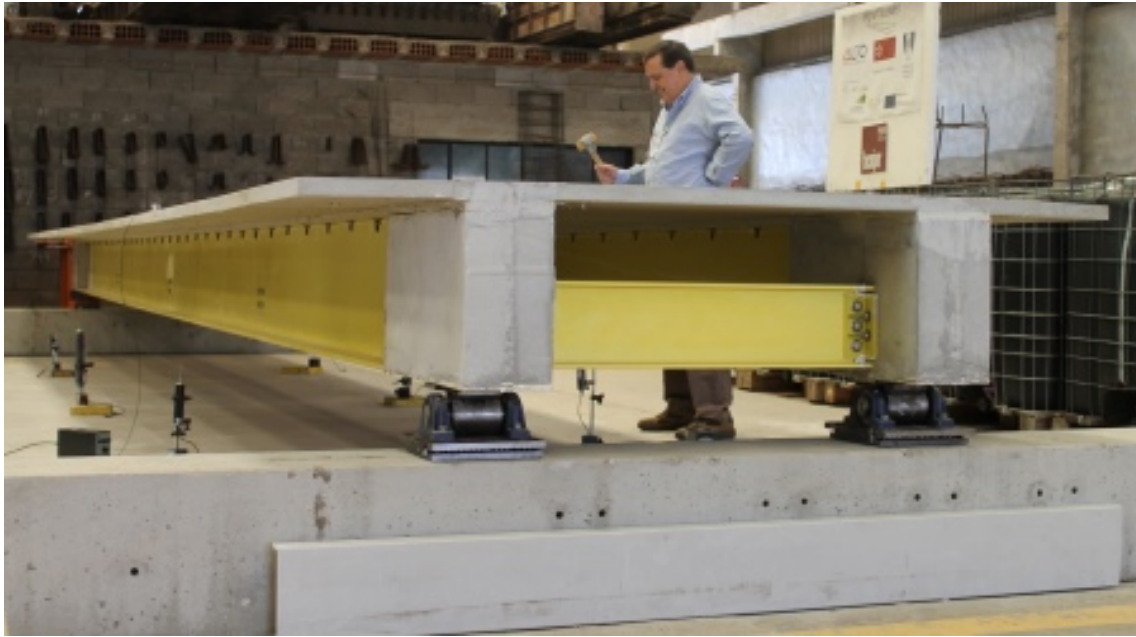


Figure 7.30.: Full-scale prototype modal identification test ongoing.

As an illustrative example, Figures 7.31 and 7.32 show the records of the accelerations measured at midspan and quarter-span sections with accelerometers A1+A2 and A3+A4, respectively.

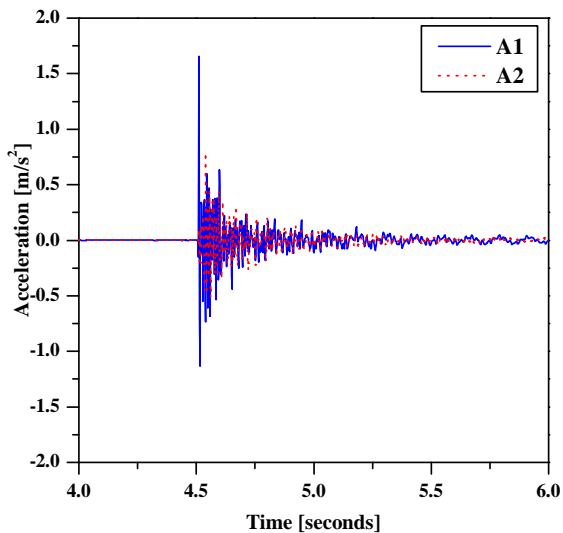


Figure 7.31.: Modal identification tests: accelerations at positions A1 and A2.

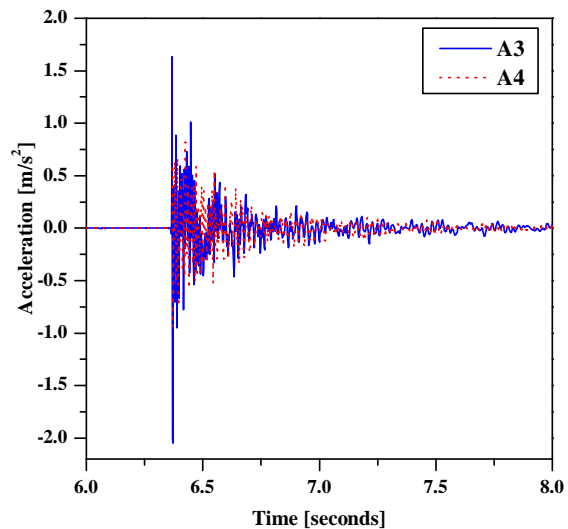


Figure 7.32.: Modal identification tests: accelerations at positions A3 and A4.

The experimental records were analysed by applying a Fast Fourier Transform (FFT) algorithm to the acceleration measurements, identifying the frequencies for which the FFT presents its peak values. In order to identify these frequencies for both flexure and torsion modes, this method was applied to the half-sum and half-difference of the accelerations measured at points A1+A2 and A3+A4, examples of which are presented in Figures 7.33 and 7.34, respectively.

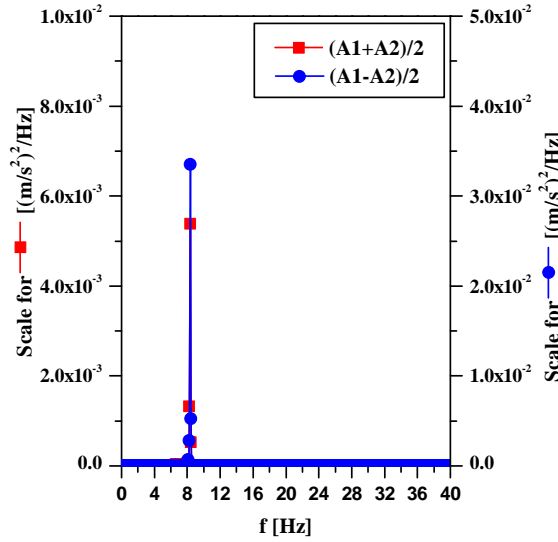


Figure 7.33.: Full-scale prototype modal identification tests: FFT of the half-sum and half-difference of accelerations at A1 and A2.

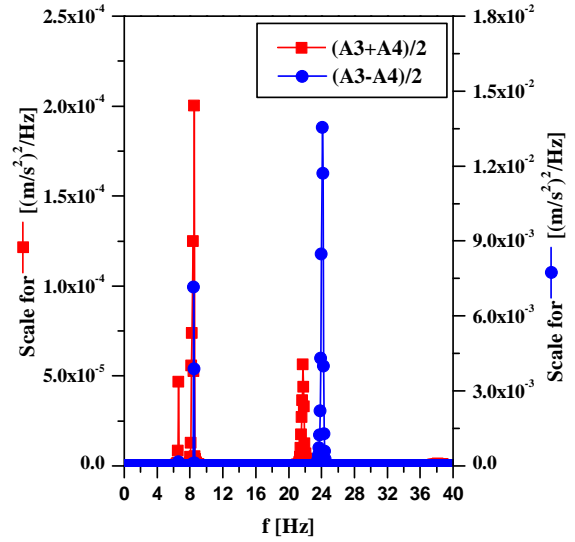


Figure 7.34.: Full-scale prototype modal identification tests: FFT of the half-sum and half-difference of accelerations at A3 and A4.

This analysis allowed the determination of the first four vibration modes, whose characteristics are summarized in Table 7.10. Furthermore, owing to the position of the stroke applied (eccentric, *cf.* Figure 7.29), the richer frequencies on the FFTs correspond to torsional modes, whereas the less rich vibration frequencies identified correspond to flexural modes. As expected, the anti-symmetric vibration frequencies (two half-waves) could only be identified for acceleration records at positions A3 and A4, since their expected deformation at midspan is null. Moreover, the anti-symmetric flexural mode was only identified for the half-sum of these accelerations, while the anti-symmetric torsional mode was only identified for the half-difference of the same records.

Table 7.10.: Full-scale prototype modal identification tests: summary of results.

Mode number	Vibration frequency (Hz)		Mode nature
	Average	Std. Dev.	
1	6.60	0.04	Flexure symmetric
2	8.35	0.07	Torsion symmetric
3	21.70	0.10	Flexure anti-symmetric
4	24.10	0.07	Torsion anti-symmetric

It should be mentioned that more sophisticated modal identification tests, using the Enhanced Frequency Domain Decomposition (EFDD) method, were carried out in the structure outside the scope of this thesis [13], presenting an excellent agreement to the results obtained with the simpler method, with maximum relative differences of 8.7% (for the torsion anti-symmetric mode, which was determined with a 6.1% CoV with the EFDD method [13]).

### 7.5.1.2. Analytical simulation

The vibration modes frequencies and shapes were estimated with the analytical models presented earlier with regard to the small-scale prototype (*cf.* Section 6.5.1.3), namely Eq. (6.31) for the flexure modes (Timoshenko beam theory, page 207), and Eq. (6.39) for the torsion modes (page 208).

Regarding the torsional characteristics of the structure, the warping stiffness of the section ( $EI_w$ ) was calculated considering an homogenized section with respect to the elasticity modulus of the SFRSCC ( $E_c$ ) using the CUFISM [142] open-source software. The main torsion properties of the cross-section are the following: (i)  $GJ = 505 \text{ kNm}^2$ ; (ii)  $EI_w = 13524 \text{ kNm}^4$ ; and (iii)  $\rho I_p = 75.7 \text{ kgm}$ .

Table 7.11 summarizes the analytical predictions and compares them with the experimental results.

Table 7.11.: Full-scale prototype modal identification tests: experimental results *vs.* analytical predictions.

Mode number	Vibration frequency			Mode nature
	Experimental	Analytical		
	(Hz)	(Hz)	diff.	
1	6.60±0.04	5.96	-9.6%	Flexure symmetric
2	8.35±0.07	7.17	-14.1%	Torsion symmetric
3	21.70±0.10	21.14	-2.6%	Flexure anti-symmetric
4	24.10±0.07	25.32	5.1%	Torsion anti-symmetric

These results show that the analytical models proposed were well able to predict the mode shape order, estimating the vibration frequencies with very good accuracy, with absolute relative differences under 10%, except for the second mode (symmetric torsion), for which an absolute relative difference of 14% was found.

### 7.5.1.3. Numerical simulation

The FE model described in Section 7.4.4 was used to predict the dynamic characteristics of the footbridge, namely regarding its vibration frequencies and mode shapes for the first four vibration modes. Table 7.12 summarizes these predictions and compares them with their analytical and experimental counterparts, and Figure 7.35 presents the mode shapes of the FE model.

Table 7.12.: Full-scale prototype modal identification tests: experimental results, analytical and numerical predictions.

Mode number	Vibration frequency					Mode nature
	Experimental (Hz)	Analytical		FE model		
		(Hz)	diff.	(Hz)	diff.	
1	6.56±0.04	5.96	-9.6%	6.02	-8.7%	Flexure symmetric
2	8.35±0.07	7.17	-14.1%	9.69	16.1%	Torsion symmetric
3	21.70±0.10	21.14	-2.6%	20.84	-4.0%	Flexure anti-symmetric
4	24.10±0.07	25.32	5.1%	24.52	1.7%	Torsion anti-symmetric

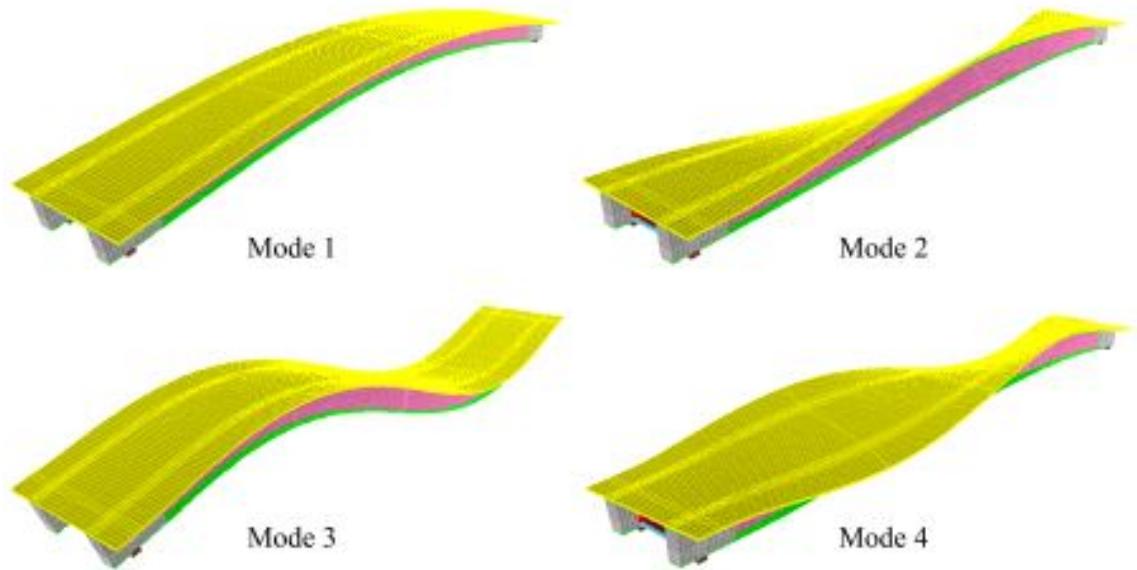


Figure 7.35.: Full-scale prototype FE model: modal shapes.

The FE model predicted with very good accuracy the mode shapes and frequencies of the first four modes, with absolute relative differences under 10%, except for the second mode (torsion symmetric), for which an absolute relative difference of 16% was found, similarly to the analytical predictions. Moreover, the relative differences obtained with the numerical and analytical predictions are very similar for all modes.

It should be mentioned that the modal identification tests using the EFDD method, performed outside the scope of this thesis, detected a lateral bending asymmetric vibration mode, with a vibration frequency of 12.13 Hz [13], which was not predicted by the FE model, as would be expected. However, this vibration mode may have been detected owing to irregularities due to (i) geometry deviations introduced during the construction, (ii) the very small (shrinkage) cracking observed in the footbridge deck at the time of those tests [13], or (iii) the inability of the support system to fully restrain very small lateral displacements, the effects of which cannot be predicted by a linear-elastic FE model.

## 7.5.2. Behaviour under pedestrian loads

### 7.5.2.1. Overview

As mentioned earlier (*cf.* Section 6.5.2.1), the design of footbridge structures is often governed by serviceability requirements concerned with pedestrian comfort criteria [69, 74], which are more difficult to be fulfilled in slender structures, such as the present full-scale footbridge prototype that exhibits geometric slenderness and incorporates relatively flexible materials (namely the GFRP). Thereafter, the assessment of the structural behaviour of this type of structures under pedestrian loads is of great importance. In this context, two sets of dynamic tests under pedestrian loads were performed: (i) tests with one pedestrian; and (ii) tests with several pedestrians simulating a crowd.

For both tests, accelerations were measured at quarter and midspan sections, positions A1 to A4 shown in Figure 7.36. The acceleration records were gathered with the same

instrumentation described earlier (*cf.* Section 7.5.1.1), at a rate of (i) 600 Hz for one pedestrian tests, and (ii) 200 Hz for the crowd tests.

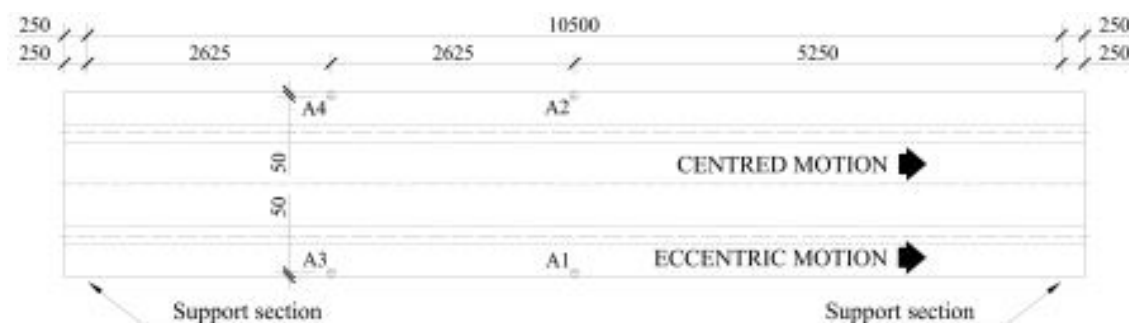


Figure 7.36.: Full-scale prototype response under pedestrian behaviour tests: instrumentation (dimensions in mm).

These tests allowed the direct assessment of pedestrian comfort criteria for the full-scale prototype, namely those proposed by Eurocode 0 [64] and ISO 10137 [75]. Moreover, the results gathered in the one pedestrian tests were compared with the predictions obtained with the FE model in order to assess the accuracy of the numerical design tool.

## 7.5.2.2. Experimental tests

### 7.5.2.2.1 One pedestrian tests

One pedestrian tests were performed by measuring the vertical accelerations at the previously referred positions, while one pedestrian (weighing 85 kgf) crossed the footbridge deck in a centred or eccentric path (*cf.* Figure 7.36) at different walking paces: (i) slow; (ii) normal; (iii) fast; and (iv) run. Figure 7.37 shows a one pedestrian test ongoing with the pedestrian running in the eccentric path.



Figure 7.37.: Full-scale prototype one pedestrian tests: pedestrian running in the eccentric path.

As an example, Figure 7.38 presents the accelerations measured at position A1 when the pedestrian walked normally in the centred and eccentric paths. The full acceleration records are available in Appendix D.

Table 7.13 summarizes the maximum vertical accelerations registered in this set of tests, showing that the maximum value for vertical acceleration specified in Eurocode 0 [64] ( $0.70 \text{ m/s}^2$ ) is generally not reached. The only exception was the maximum acceleration at position A1 when the pedestrian ran over the cantilever.

Regarding the fact that, even if seldom, vertical accelerations higher than  $0.70 \text{ m/s}^2$  (the limit imposed by Eurocode 0 [64]) were measured during the tests, it should be noted that



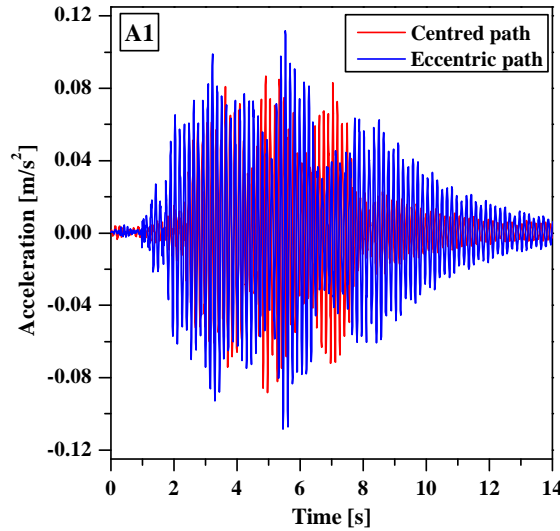


Figure 7.38.: Full-scale prototype one pedestrian tests: accelerations at position A1 when the pedestrian walked normally in the centred and eccentric paths.

the peak accelerations do not fully represent the overall response of the structure and are deemed to have little influence on the comfort of pedestrians travelling along the footbridge. Furthermore, Bachmann and Ammann [70] suggest that the regulation limits are verified for a pedestrian weighing 70 kgf, which means that the experimental accelerations should be reduced (assuming a linear-elastic behaviour) to approximately 82% of the measured values before comparison with Eurocode 0 [64] limits, owing to the fact that the tests were performed by a pedestrian weighing 85 kgf. This correction leads to maximum accelerations of  $0.77 \text{ m/s}^2$ , which are still (slightly) higher than the Eurocode 0 [64] limit.

Accounting for the previous statements, the experimental results of the one-pedestrian tests seem to be in accordance with the SLS design using the indirect criteria presented in Section 7.2.2, *i.e.* without the necessity of explicitly verifying the maximum accelerations, owing to the relatively low values of maximum accelerations measured (which exceeded the  $0.70 \text{ m/s}^2$  limit in a very particular single case).

Table 7.13.: Full-scale prototype one pedestrian tests: summary of the experimental results.

Position	Path	Walk slow	Walk normal	Walk fast	Run
A1 ( $\text{m/s}^2$ )	Centred	$0.10 \pm 0.03$	$0.10 \pm 0.01$	$0.14 \pm 0.02$	$0.46 \pm 0.05$
	Eccentric	$0.17 \pm 0.06$	$0.10 \pm 0.01$	$0.37 \pm 0.02$	$0.94 \pm 0.15$
A2 ( $\text{m/s}^2$ )	Centred	$0.05 \pm 0.02$	$0.05 \pm 0.00$	$0.07 \pm 0.01$	$0.49 \pm 0.09$
	Eccentric	$0.08 \pm 0.03$	$0.05 \pm 0.00$	$0.14 \pm 0.00$	$0.44 \pm 0.07$
A3 ( $\text{m/s}^2$ )	Centred	$0.09 \pm 0.04$	$0.07 \pm 0.01$	$0.09 \pm 0.01$	$0.40 \pm 0.09$
	Eccentric	$0.15 \pm 0.06$	$0.14 \pm 0.02$	$0.19 \pm 0.06$	$0.15 \pm 0.06$
A4 ( $\text{m/s}^2$ )	Centred	$0.05 \pm 0.02$	$0.04 \pm 0.00$	$0.07 \pm 0.01$	$0.36 \pm 0.12$
	Eccentric	$0.07 \pm 0.02$	$0.07 \pm 0.01$	$0.10 \pm 0.02$	$0.07 \pm 0.02$

### 7.5.2.2.2 Crowd tests

One pedestrian tests were performed by having a small crowd travelling the bridge at random pace and path for a period of around 5 minutes. The crowd comprised 6 or 7 pedestrians (corresponding to  $\approx 0.3$  pedestrians/m<sup>2</sup>, a lower density than that defined as a sparse crowd by [74], 0.5 pedestrians/m<sup>2</sup>) while vertical accelerations were measured at midspan (A1 and A2, cf. Figure 7.36) and at quarter-span (A3 and A4), respectively. The average weight of the pedestrians used in the tests was 81.3 kgf and 85.1 kgf for the accelerations measured at mid and quarter-span, respectively. Figure 7.39 shows these tests in progress.



Figure 7.39.: Full-scale prototype crowd tests in progress.

Figures 7.40 and 7.41 present the mid and quarter-span vertical accelerations, respectively, measured in the tests, and compare them with the Eurocode 0 [64] limit. These results show that the structural accelerations are relatively low, generally under 0.4 m/s<sup>2</sup> and 0.2 m/s<sup>2</sup> in the midspan and quarter-span sections, respectively. The Eurocode 0 [64] limit (0.70 m/s<sup>2</sup>) was (barely) exceeded at a single peak in position A1, reaching 0.703 m/s<sup>2</sup>, thus validating the analysis of the one pedestrian tests presented in the previous section.

These acceleration records were transformed from the time domain to root mean squared (RMS) acceleration records in the frequency domain, allowing the comparison with the limits proposed by ISO 10137 [75]. As mentioned earlier, unlike the pedestrian comfort direct criteria specified in Eurocode 0 [64], these limits account for the frequency of the structural response on the pedestrian comfort level, considering the overall response, thereby setting different limits for different structural uses.

Figure 7.42 compares the limits of ISO 10137 [75] with the structural response measured in the crowd tests. The limits shown refer to (i) a person standing still in the footbridge while other pedestrians travel along the deck (the most severe situation for footbridges) and (ii) to pedestrians travelling the footbridge. The results obtained show that there is a very low probability of pedestrian discomfort for both design situations.

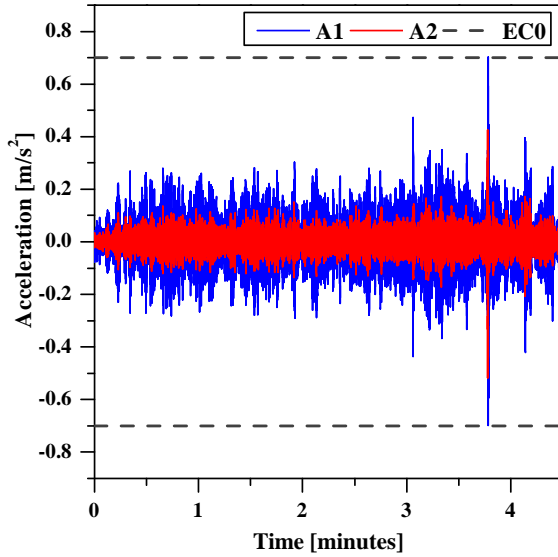


Figure 7.40.: Full-scale prototype crowd tests: accelerations at A1 and A2.

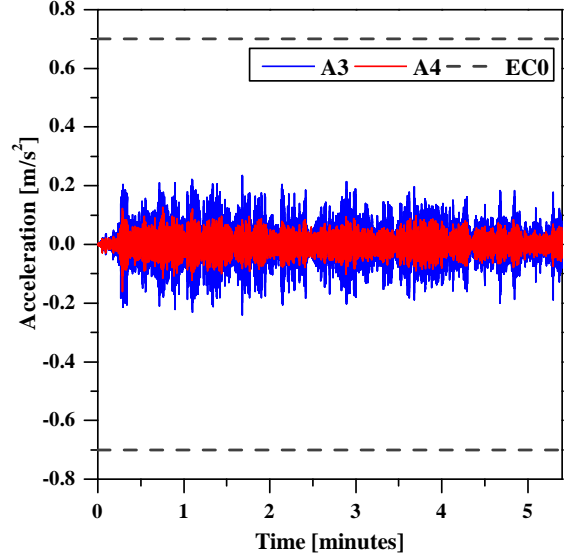


Figure 7.41.: Full-scale prototype crowd tests: accelerations at A3 and A4.

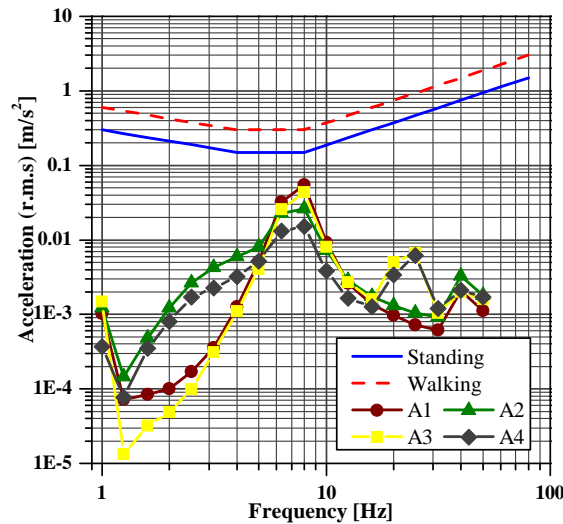


Figure 7.42.: Full-scale prototype crowd tests: comparison between the experimental expected vertical accelerations (RMS) and the ISO 10137 [75] limits.

### 7.5.2.3. Numerical simulation

The one pedestrian tests were modelled with the FE model described earlier (*cf.* Sections 7.4.4). To this end, two pairs of frame elements, with no mass, weight or stiffness, were added to the FE model and placed at the top of the deck, aligned with the longitudinal axis of the footbridge. One pair of frames was positioned centred with the longitudinal axis of the footbridge, while the other pair was positioned along the centre of one of the cantilevers, simulating the centred and eccentric motion paths (*cf.* Figure 7.36), respectively. For each pair, the frames were placed 30 cm apart from each other in the transverse direction, each frame simulating the pathway of one foot. For each type of motion (walk slow, walk normal, walk fast and run) and for each motion position (centred or eccentric), point

loads (85 kgf) were assigned to the respective frame, according to the motion characteristics presented in Table 6.13 (page 214) simulating each footstep. The load cases were then combined in time history analysis with the respective load–time function (*cf.* Figure 6.65, page 213). In this analysis, the first four vibration modes were considered and the modal damping ratios used for each mode were those determined with a modal analysis using the EFDD method, presented elsewhere [13].

Figures 7.43 and 7.44 show, as an example, the comparison between the vertical accelerations at position A1 obtained experimentally and with the FE model, when the pedestrian walked normally in the centred and eccentric paths, respectively. The full collection of the experimental records of vertical acceleration for both paths and all motion types are included in Appendix D.

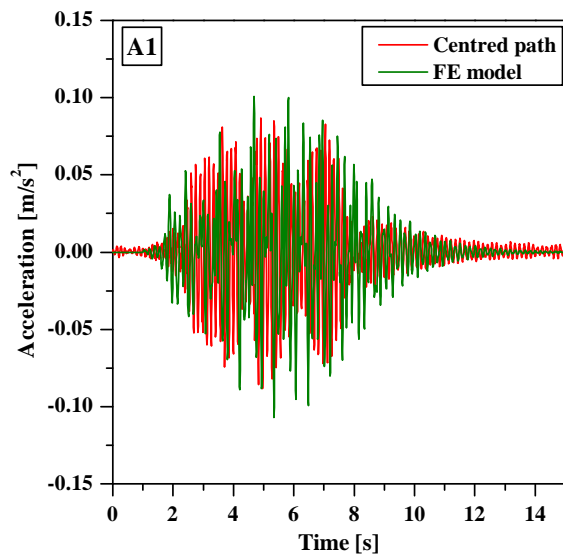


Figure 7.43.: Full-scale prototype one pedestrian tests: accelerations at A1 for normal walk in the centred path, experimental and numerical results.

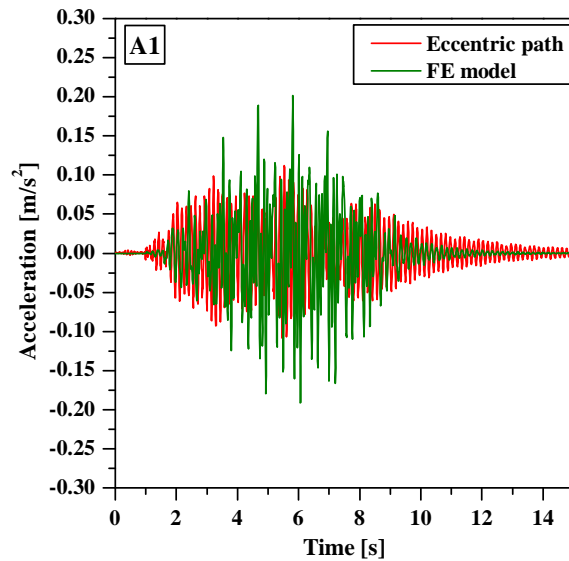


Figure 7.44.: Full-scale prototype one pedestrian tests: accelerations at A1 for normal walk in the eccentric path, experimental and numerical results.

Table 7.14 presents the summary of the maximum accelerations (average  $\pm$  standard deviation) obtained in the dynamic tests with one pedestrian and the comparison with the numerical predictions.

The same results are illustrated in Figures 7.45 to 7.48 for each type of motion (walk slow, walk normal, walk fast and run), with the pedestrian traveling along the centred path and in Figures 7.49 to 7.52 with the pedestrian traveling along the eccentric path.

The comparison between the experimental results and the numerical predictions showed worse agreement, compared to that obtained for the small-scale prototype (*cf.* Section 6.5.2.5). Overall, the fast walk was the motion with poorer results. This unexpected poor agreement may stem from two reasons: (i) the accelerations measured are relatively low when compared to the small-scale prototype, which may contribute to an "artificial" increase of the relative errors; and/or (ii) albeit the same pedestrian was used in these tests and their counterparts for the small-scale prototype, he presented a weight difference around 13 kgf from one set of tests to the other. The latter fact is especially relevant considering that the load functions used in both simulations were determined when the pedestrian was

Table 7.14.: Full-scale prototype one pedestrian tests: experimental results *vs.* numerical predictions.

Motion	Source	A1 (m/s <sup>2</sup> )		A2 (m/s <sup>2</sup> )	
		Centred	Eccentric	Centred	Eccentric
Walk slow	Test	0.10±0.03	0.17±0.06	0.05±0.02	0.08±0.03
	FE	0.20	0.32	0.21	0.32
	diff.	100%	91%	311%	304%
Walk normal	Test	0.10±0.01	0.10±0.01	0.05±0.00	0.05±0.00
	FE	0.11	0.20	0.11	0.20
	diff.	7%	101%	112%	304%
Walk fast	Test	0.14±0.02	0.37±0.02	0.07±0.01	0.14±0.00
	FE	0.41	0.76	0.39	0.77
	diff.	194%	105%	464%	450%
Run	Test	0.46±0.05	0.94±0.15	0.49±0.09	0.44±0.07
	FE	0.91	1.34	0.92	1.36
	diff.	97%	43%	88%	210%
Motion	Source	A3 (m/s <sup>2</sup> )		A4 (m/s <sup>2</sup> )	
		Centred	Eccentric	Centred	Eccentric
Walk slow	Test	0.09±0.04	0.15±0.06	0.05±0.02	0.07±0.02
	FE	0.14	0.19	0.14	0.22
	diff.	54%	26%	177%	215%
Walk normal	Test	0.07±0.01	0.14±0.02	0.04±0.00	0.07±0.01
	FE	0.07	0.12	0.07	0.11
	diff.	4%	-11%	82%	61%
Walk fast	Test	0.09±0.01	0.19±0.06	0.07±0.01	0.10±0.02
	FE	0.27	0.45	0.26	0.44
	diff.	199%	136%	276%	339%
Run	Test	0.40±0.09	0.15±0.06	0.36±0.12	0.07±0.02
	FE	0.62	0.84	0.61	0.84
	diff.	56%	457%	70%	1104%

heavier (*cf.* Section 6.5.2.2.1), and could, therefore, present significant differences with the pedestrian physiology changes [70].

Nevertheless, the FE model was able to estimate, for most cases, the magnitude of the maximum accelerations.

### 7.5.3. Conclusions

The results presented in this section showed that the full-scale footbridge prototype complies with the pedestrian comfort limit states, as predicted in the design of the structure (*cf.* Section 7.2.2).

The analytical and numerical models used proved to be able to predict the modal parameters of the structure accurately, namely its vibration mode frequencies and shapes. Regarding the response of the full-scale to pedestrian actions, the results predicted with the FE model showed a poorer agreement with experimental measurements, when compared to that obtained for the small-scale prototype. It should be noted, however, that the maximum

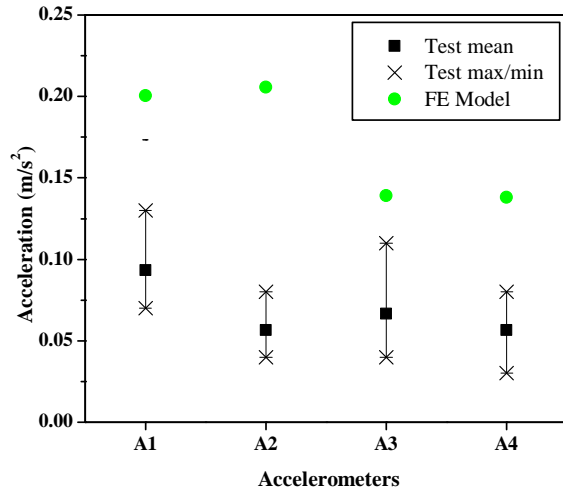


Figure 7.45.: Full-scale prototype one pedestrian tests: maximum accelerations for slow walk in the centred path, experimental and numerical results.

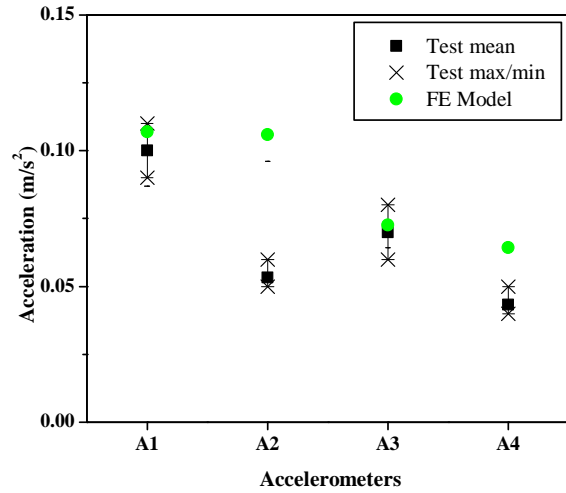


Figure 7.46.: Full-scale prototype one pedestrian tests: maximum accelerations for normal walk in the centred path, experimental and numerical results.

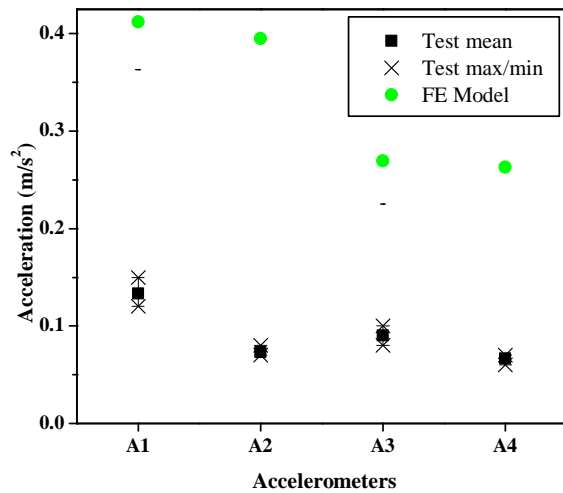


Figure 7.47.: Full-scale prototype one pedestrian tests: maximum accelerations for fast walk in the centred path, experimental and numerical results.

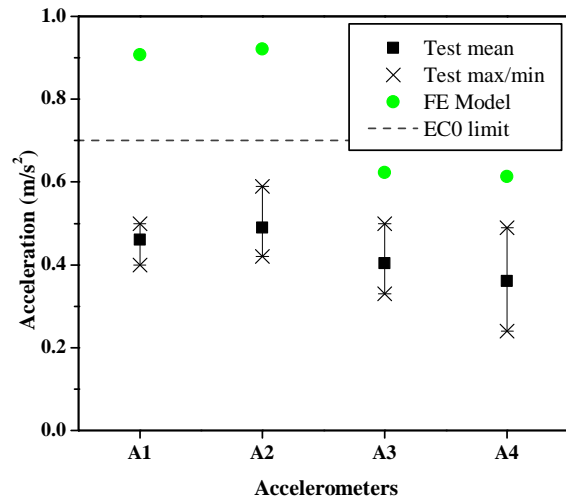


Figure 7.48.: Full-scale prototype one pedestrian tests: maximum accelerations for run in the centred path, experimental and numerical results.

accelerations predicted with the FE model were higher (on the safe side) than those measured in the tests but, for most cases, within the same magnitude and can, thus, be regarded as conservative estimates. Nonetheless, this topic should be further investigated in the future in order to develop numerical tools able to predict with better accuracy the structural dynamic behaviour under pedestrian actions.

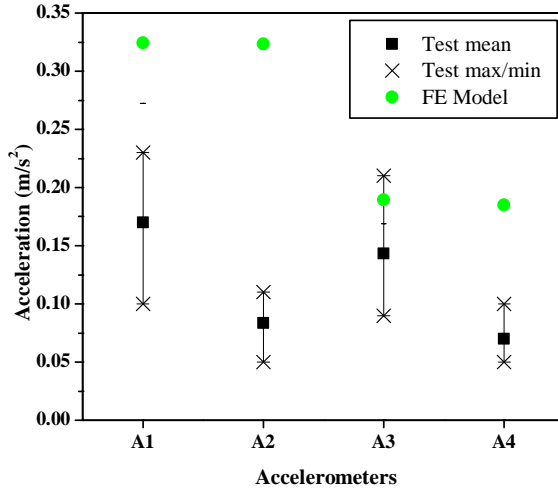


Figure 7.49.: Full-scale prototype one pedestrian tests: maximum accelerations for slow walk in the eccentric path, experimental and numerical results.

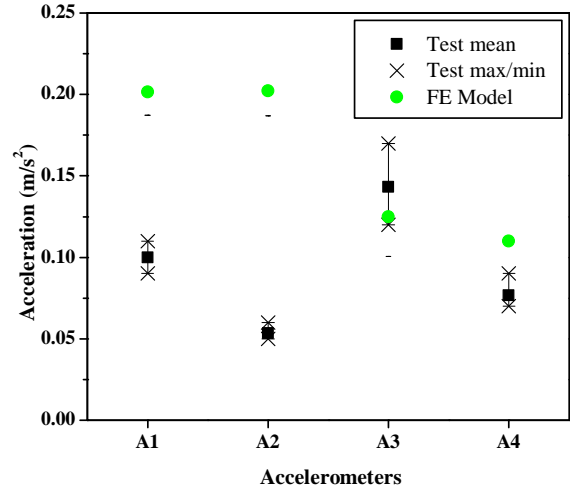


Figure 7.50.: Full-scale prototype one pedestrian tests: maximum accelerations for normal walk in the eccentric path, experimental and numerical results.

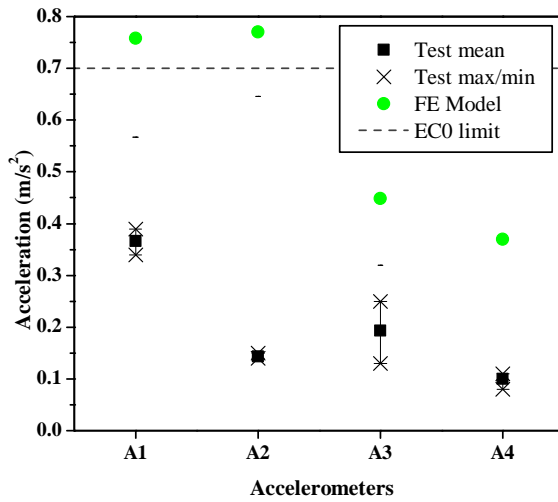


Figure 7.51.: Full-scale prototype one pedestrian tests: maximum accelerations for fast walk in the eccentric path, experimental and numerical results.

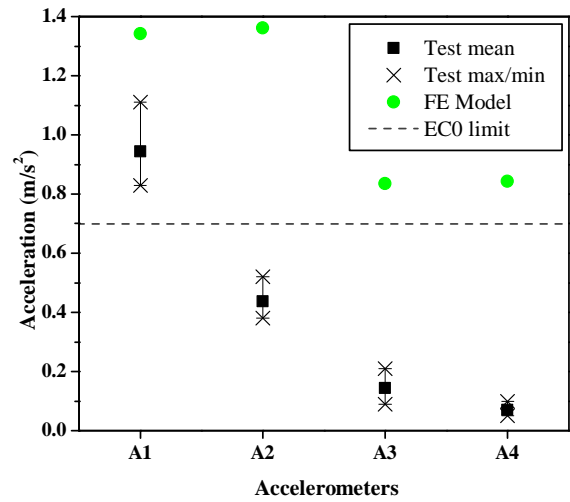


Figure 7.52.: Full-scale prototype one pedestrian tests: maximum accelerations for run in the eccentric path, experimental and numerical results.

## 7.6. Creep behaviour of the prototype

### 7.6.1. Overview

As already mentioned, the design of GFRP based structures is known to be governed by SLS, namely deformability limit states, owing to the materials' low elasticity moduli together with typical thin-walled geometry. Furthermore, the fact that these materials are known to present visco-elastic behaviour when subjected to sustained loads over time [143], justifies studying the creep behaviour of full-scale prototype.

In this context, the present Section presents experimental and analytical investigations regarding the creep behaviour of the full-scale hybrid GFRP–concrete footbridge prototype. The analytical study was based on the models presented with regard to the small-scale prototype creep investigations (*cf.* Section 6.6), proposing an additional change in the formulae developed then in order to account for the relatively high temperature variations measured during the tests.

### 7.6.2. Experimental test

The flexure creep test on the full-scale footbridge prototype was performed by applying a uniformly distributed load on the top of SFRSCC deck, materialized by 80 cement bags (each one weighing 40 kgf), as shown in Figure 7.53. Therefore, a total load of 31.4 kN was applied, corresponding to  $1.49 \text{ kN/m}^2$ , which is approximately 30% of the characteristic live load for footbridges defined in Eurocode 1 [65] ( $5.0 \text{ kN/m}^2$ ).



Figure 7.53.: Full-scale prototype loaded in the creep test.

During the test, the midspan deflections were measured underneath both main girders with analogical deflection gauges (precision of  $0.001 \text{ mm}$ ), during the loading process (which lasted approximately 30 minutes), and up to 3670 hours ( $\approx 153$  days) after the loading process was completed. Figure 7.54 presents the air temperature ( $T$ ) and the relative humidity ( $RH$ ) in the surroundings of the footbridge, which were also measured during the test period, gathered at a rate of  $\approx 0.083 \text{ Hz}$ .

Figure 7.55 shows the average creep deflections (results were very consistent for both girders) measured after the loading process had been concluded, together with the Findley's power law (*cf.* Eq. (6.40), page 223) regression of the experimental results, showing a good fitting to the experimental results ( $R^2 = 0.963$ ), with  $m = 0.945$  and  $n = 0.197$ .

The experimental observations show that the average creep deflection at the end of the test was  $4.71 \text{ mm}$ , which corresponds to a 39.9% increase of the instantaneous deflection. The Findley's power law regression predicts a  $4.75 \text{ mm}$  midspan deflection at the end of the test, agreeing well with the experimental result (+0.8%).

### 7.6.3. Analytical simulation

The analytical simulation of the creep tests was performed using the models proposed with regard to the creep tests on the small-scale prototype (*cf.* Section 6.6), namely by determining the deflections with Eq. (6.61) (page 234), obtaining an instantaneous midspan



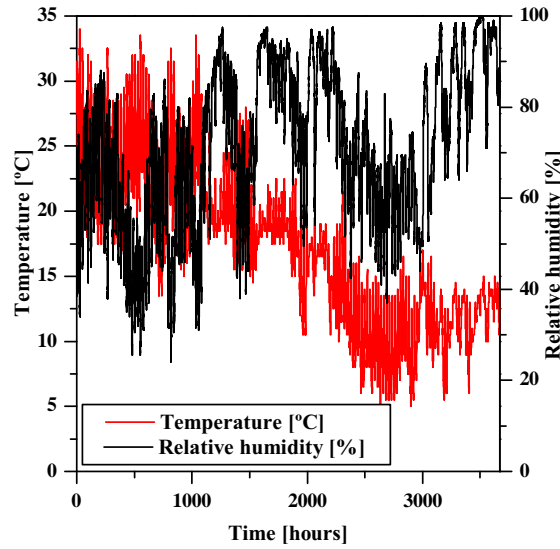


Figure 7.54.: Full-scale prototype creep test: air temperature ( $T$ ) and relative humidity ( $RH$ ) during the test period.

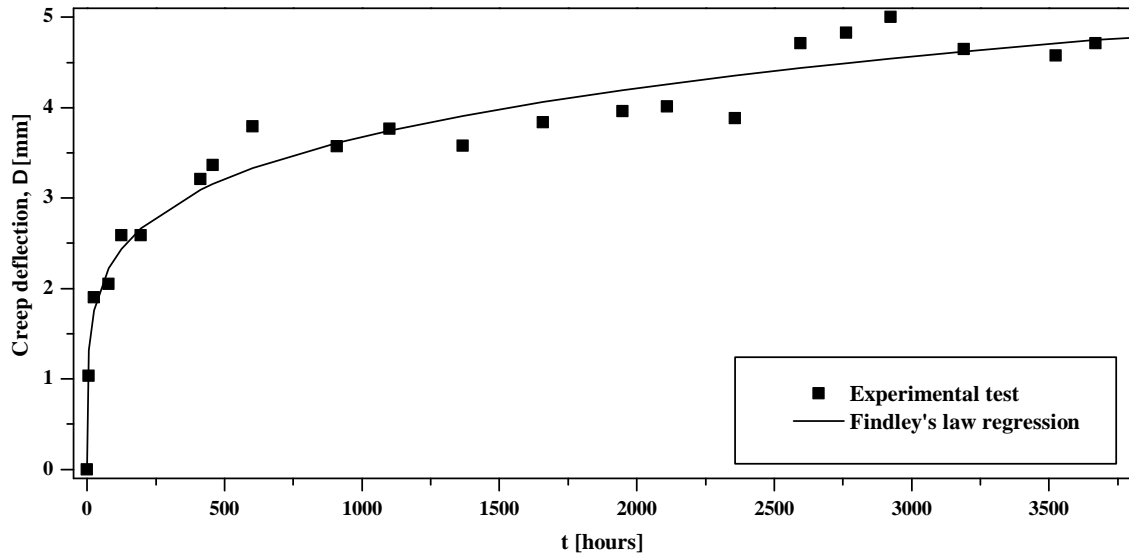


Figure 7.55.: Full-scale prototype creep test: experimental results and Findley's power law fitting.

deflection for the creep load ( $q = 1.49 \text{ kN/m}^2$ ) of 11.24 mm, in good agreement with its experimental counterpart (-4.9%).

Regarding the material creep models used to predict the time-dependent moduli ( $E(t)$  and  $G(t)$ ), accounting for the stress distribution over the cross-section (the instantaneous neutral axis is positioned in the GFRP webs, *cf.* Section 7.2.1.1), the flexure and shear in flexure creep models proposed by Bank [4] (*cf.* Section 6.6.1.1) were chosen for the GFRP material, while the standard creep model proposed by Eurocode 2 [85] for regular concrete (*cf.* Section 6.6.1.2) was chosen for the SFRSCC material.

As proposed earlier (*cf.* Section 6.6.1.1), these GFRP creep models may be modified in order to account for the temperature, as proposed by Dutta and Hui [144], using Eq. (6.46) (page 225). Moreover, for situations in which the temperature presents relatively high variations during the test period, a new change the GFRP material creep models is

proposed, in order to correct the slope of the time-dependent moduli taking into account the temperature variation according to the following equation:

$$\begin{aligned} E(t) &= E(t_{i-1}) + [E(t, T_i) - E(t_{i-1}, T_i)] \quad , \quad t_{i-1} < t \leq t_i \quad \text{or} \\ G(t) &= G(t_{i-1}) + [G(t, T_i) - G(t_{i-1}, T_i)] \quad , \quad t_{i-1} < t \leq t_i \end{aligned} \quad (7.22)$$

Eq. (7.22) considers a time-step ranging from  $t_{i-1}$  to  $t_i$ , for which an average temperature  $T_i$  is registered. Within a given time step, the elasticity (or shear) modulus is obtained by adding the elasticity (shear) modulus at the beginning of the time-step ( $E(t_{i-1})$ , known *a priori*) to the elasticity (shear) modulus variation at that given age and average temperature (*e.g.*,  $E(t, T_i) - E(t_{i-1}, T_i)$ , obtained from Eq. (6.46)). Therefore, a continuous curve is obtained for the time-dependent moduli, albeit its slope may present local discontinuities due to temperature variations.

Moreover, the creep parameters introduced in the creep models (*cf.* Section 6.6.1.1) are highly dependent on the FRP material used, namely on the (i) fibre architecture; (ii) type of resin, and (iii) curing process. In fact, a review by Sá *et al.* [143] of several studies regarding the creep response of GFRP flexural members has shown that the  $n_E$  parameter may range from 0.30 to 0.36. In this context, and given the relatively short curing period of the I400 profile GFRP material (performed at ambient temperature), the authors decided to perform a sensitivity analysis on the parameters governing the time-dependent elasticity modulus, namely on (i) the  $n_E$  parameter, varying between 0.30 (proposed by Bank [4]) and 0.36 (+20%) [143, 146], and (ii) the  $E_t$  parameter, ranging from 1241.06 GPa (proposed by Bank [4]) and 992.85 GPa (-20% — a similar variation to that of the previous parameter). The shear creep parameters considered were those suggested by Bank ( $G_t = 186.16$  GPa,  $n_G = 0.30$ ) [4].

Figure 7.56 compares the analytical predictions with the experimental results in terms of creep midspan deflection. The analytical predictions were performed considering the temperature variations observed experimentally within 5 minute periods (*cf.* Eq. (7.22)). The average  $RH$  of 72.5% observed in the tests was considered for the calculation of the time-dependent elasticity modulus of the SFRSCC. Figure 7.56 shows that the experimental results are well within the sensitivity analysis performed. It can also be seen that the initial experimental measurements (up to 1000 hours) are very well described by the GFRP creep model with  $n_E = 0.36$  and  $E_t = 992.85$  GPa, which are respectively higher and lower than the corresponding values proposed by Bank [4]. Subsequently, and up to the end of the test, the experimental data lie between the above mentioned modelling curve and that with  $n_E = 0.36$  and  $E_t = 1241.06$  GPa. In spite of the variation exhibited by the experimental data between 2300 and 2600 hours, which may be due to the environmental conditions, namely the relative humidity (whose average increased at this stage and is not accounted for in the GFRP creep model), results obtained in this study show that, for the GFRP material tested, a general better agreement is achieved with  $n_E = 0.36$  and  $E_t = 992.85$  GPa.

Additionally, long-term predictions of the creep behaviour were performed, with Figure 7.57 presenting the predictions of midspan deflections up to 100 years based on (i) Findley's power law (fitted with the experimental data), and (ii) the analytical model proposed by the authors (considering the average temperature (16.9°C) and  $RH$  (72.5%) measured in the creep test). These results show that the creep deformations predicted with Findley's power law deviate considerably from those obtained with the analytical model (for the various combinations of creep parameters). While Findley's power law prediction indicates an overall deflection of 25.8 mm ( $L/407$ ) after 100 years (more than twice the instantaneous

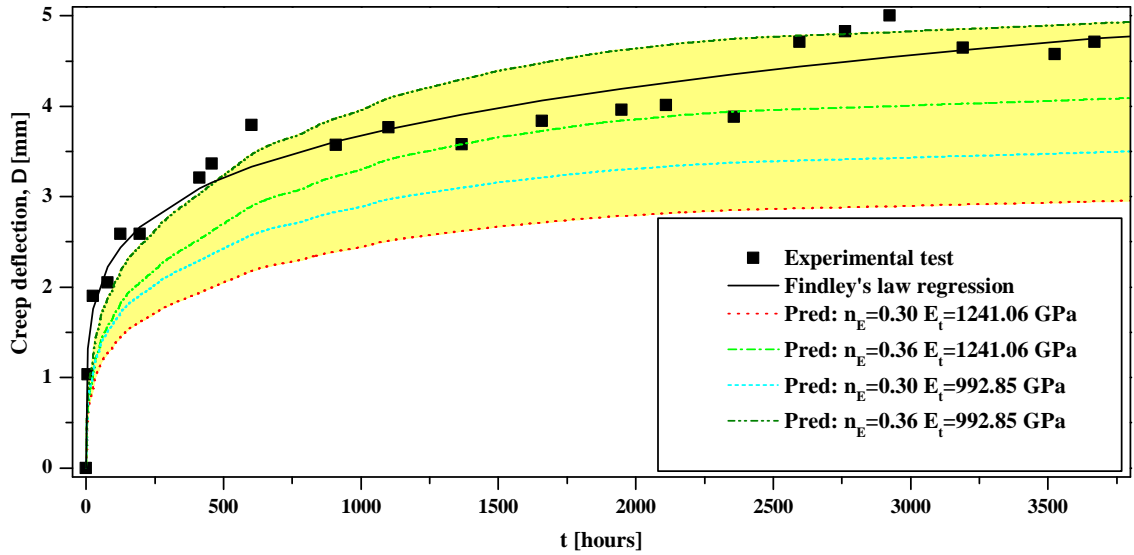


Figure 7.56.: Full-scale prototype creep test: experimental results *vs.* analytical predictions.

deflection), the other analytical predictions range from 16.2 mm to 20.5 mm (+44% to +82% higher than the instantaneous deflection), which correspond to  $L/648$  and  $L/512$ , respectively.

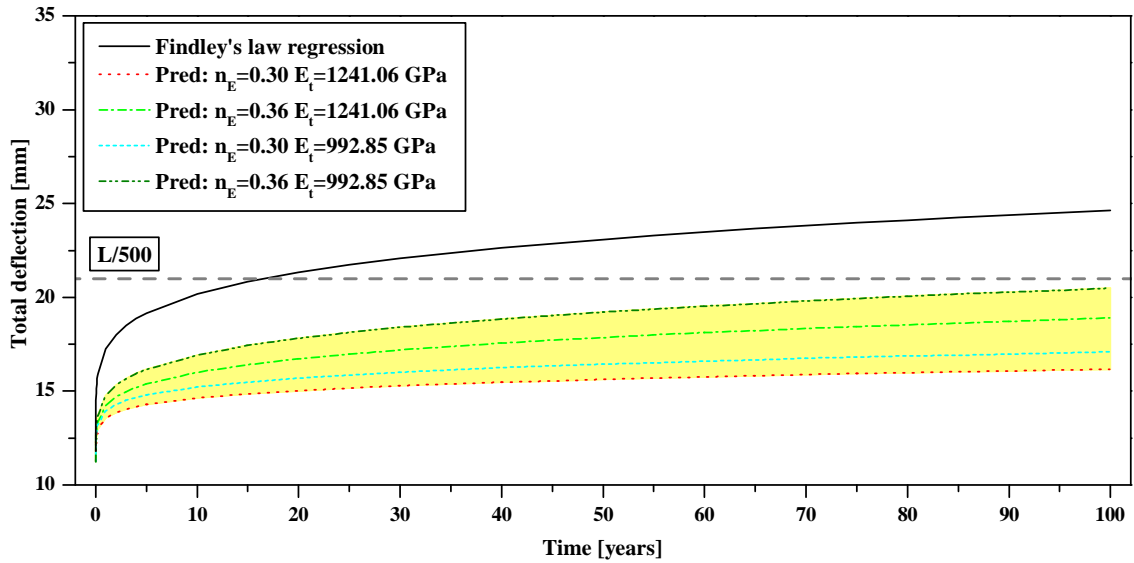


Figure 7.57.: Full-scale prototype creep test: long-term midspan deflection predictions.

Regarding the use of Findley's power law to predict long-term deformations of GFRP-concrete structures, although the results presented here have shown a good fitting of such law to the experimental data, the results of the creep tests on the small-scale prototype (*cf.* Section 6.6) indicate that using Findley's power law, based on short-term test results, may lead to unrealistic predictions of long-term deformations for GFRP-concrete hybrid structures. This has been attributed to (i) the nature of the creep response of the SFRSCC material (not complying with Findley's power law), and (ii) the changes in the neutral axis that may change the logarithmic slope of the curve representing the structural response ( $n$  parameter), which is constant in Findley's power law.

Additionally, for design purposes, the predictions of the long-term deflection for the quasi-permanent load combination were computed. These predictions were estimated using the creep parameters proposed by Bank [4] for flexure, considering a relative humidity of 60% and two different average temperatures: (i) 20°C and (ii) 25°C. Thereafter, the midspan long-term deflections after 100 years were predicted to be 14.14 mm and 20.37 mm, considering average temperatures of 20°C and 25°C, respectively. Figure 7.58 compares these predictions for different periods. These results show that a 5°C increase on the average temperature corresponds to a 44% increase of the midspan deflection prediction after 100 years.

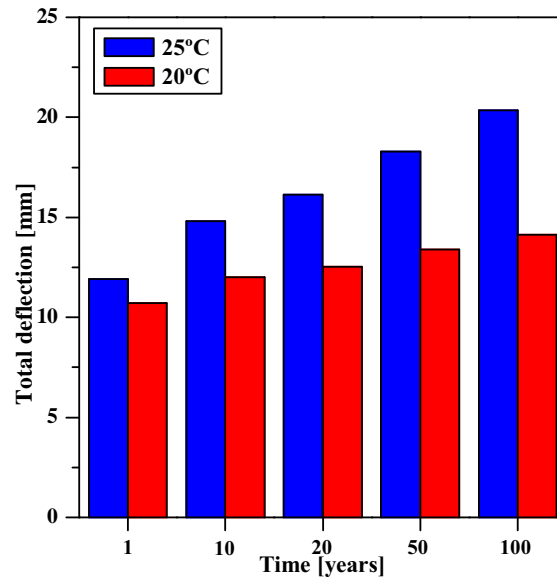


Figure 7.58.: Full-scale prototype midspan deflection creep predictions with 20°C and 25°C average temperature.

#### 7.6.4. Conclusions

The results obtained in the creep tests and analytical simulations have highlighted the high sensitivity of long-term deflections to  $n_E$  and  $E_t$  parameters, stressing the importance of defining reliable creep parameters for the GFRP material. In this regard, manufacturers should provide these very important material properties since the design of most FRP structures is governed by deformability requirements. Moreover, the effects of the relative humidity in the GFRP material creep models need to be further investigated in order to improve the reliability of the design tools available.

The long-term predictions performed estimate the long-term midspan deflection as (i)  $L/407$ , for the Findley's power law regression, and (ii) between  $L/648$  and  $L/512$ , for the analytical analysis. Both prediction methods estimate long-term deflections under  $L/400$ , which was the deformability limit state requirement set for this project (*cf.* Section 7.2.2).

## 7.7. Final remarks

This Chapter presented the design, construction and assessment of the structural behaviour of the full-scale GFRP-SFSRCC hybrid footbridge prototype.

The static tests performed for several loading configurations attested the adequate structural response of the hybrid footbridge. The experimental responses were accurately predicted using analytical and numerical models considering elastic behaviour for the constituent materials.

The modal identification tests allowed determining the modal parameters of the first four modes, namely the vibration frequency and mode shape. The analytical and numerical models developed were well able to predict the experimental results. The dynamics tests under pedestrian loads showed that the structure fulfils pedestrian comfort requirements, namely showing that there is very low probability of pedestrian discomfort due to the structural vibrations. Compared to what was observed for the small-scale prototype, the numerical model developed provided less accurate simulations of the dynamic response under one pedestrian tests. Although some hypotheses were put forward to explain this worse agreement, further investigation is needed to improve the modeling for this type of action.

In the flexural creep test the instantaneous deflection increased by approximately 40% after 5 months. The analytical model proposed to predict the long-term deflections of this type of hybrid structures was able to predict the experimental response of the structure within the period of the test and was, therefore, used to predict the long-term deflections of the structure.

Overall, the results presented showed that the structural behaviour of the GFRP-SFSRCC hybrid footbridge prototype is, for the most part, well predicted by readily available analytical and numerical tools, which were used to formally design the structure according to ULS and SLS requirements.



## 8. Conclusions and future developments

### 8.1. Conclusions

In spite of the considerable growth of GFRP pultruded profiles in structural civil engineering applications over the last few decades, the widespread use of these materials is being delayed due to a number of factors. In fact, albeit their several advantages over traditional materials, namely, high strength, lightness, strength-to-weight ratio, ease of erection, electromagnetic transparency, improved durability and thermal insulation properties, they are still not regarded as an effective alternative to structural materials by most structural engineers.

This stems mostly from some of the materials' disadvantages, including their low elasticity and shear moduli, which often lead to designs governed by deformability criteria or instability phenomena, their brittle failure and the lack of widely accepted guidelines and design codes (such as Eurocodes).

In order to overcome such disadvantages, while maintaining the main advantages of GFRP based structures, several hybrid structural solutions have been proposed, combining GFRP and concrete. These systems allow increasing the stiffness compared to all-GFRP structures and preventing some of the instability phenomena.

This PhD thesis was developed in this context and its main objective was to study hybrid GFRP–concrete structural systems and their applicability to footbridge structures. Thereafter, the research was developed along three main axes:

- GFRP–concrete connection systems;
- Static, creep and dynamic behaviour of GFRP–concrete structures;
- Development of a full-scale GFRP–SFRSCC footbridge prototype.

The objectives set *a priori* were accomplished. The research developed, allowed concluding that GFRP–concrete structures are a feasible solution for footbridge applications. In this regard, it must be highlighted that the judicious combination of GFRP and concrete, such that the GFRP members are mostly subjected to tension, while the concrete elements are mostly subjected to compression, leads to the development of lightweight structures with appropriate mechanical behaviour, especially compared to all-GFRP or concrete structures. Furthermore, it was shown that readily available analytical and numerical design tools are well able to predict the structural behaviour of the proposed hybrid GFRP–SFRSCC structure. Additionally, the ease of construction and assembly of the proposed hybrid system

was also demonstrated by the construction of two prototypes using different methods: (i) small-length precast slabs; and (ii) a cast in-situ slab. In the following sections, the specific conclusions and contributions to the state-of-the-art are drawn, organized according to the aforementioned research axes.

### **8.1.1. GFRP–concrete connection systems**

The research on GFRP–concrete connection systems included a vast experimental campaign comprising a total of 68 push-out tests.

The experimental investigations included three types of connection systems: (i) adhesively bonded, (ii) bolted; and (iii) hybrid connection, combining the adhesive bond with a bolted connection. For the bolted system, the influence of the number of connectors used was also investigated, namely by testing specimens with one to four pairs of connectors per flange.

The results of the experimental tests show that the bolted specimens using a larger number of connectors present higher strength, as expected. However, the strength per bolt decreases with the increase of the number of bolts, suggesting that the benefit of adding more connectors may be limited. At failure these specimens presented significant GFRP crushing around the bolts, leading to a failure behaviour with some ductility.

The adhesively bonded specimens presented an excellent mechanical behaviour, with a stiffness approximately 2.5 times higher than that of their bolted (with four pairs of bolts per flange) counterparts, while presenting similar strength. The failure of these specimens was brittle.

The specimens provided with hybrid connection presented the best mechanical behaviour with higher strength and stiffness compared to the remaining specimens. Additionally, the failure of the bolted connection occurred after the failure of the adhesive bond, leading to a pseudo-ductile failure mode.

Specimens connected with adhesive bond only and with hybrid connection were subjected to thermal (bonded specimens only) and humidity cycles up to 32 weeks in order to study the influence of accelerated aging conditions on their mechanical behaviour. The influence of the accelerated aging processes on the strength of the specimens was minimal. In fact, the thermal cycles aging process appeared to have a positive effect on the strength of the specimens, although this effect was within the scatter measured in the tests. The stiffness, however, was significantly affected by the accelerated aging processes, presenting reductions around 50% after 32 weeks, for both thermal and humidity cycles.

Finite element (FE) models were developed in order to simulate the experimental tests performed on adhesively bonded specimens. The parameters governing the GFRP–concrete interface were calibrated in accordance with the experimental results. The FE models developed were able to simulate the experimentally observed behaviour for unaged specimens, as well as for specimens aged with both thermal and humidity cycles. These results suggest that the methodology used to develop the FE models may be replicated for large-scale models (such as beam models) in order to account for the behaviour of the connection interface in design, whenever relevant.

Overall, the research on GFRP–concrete connection systems showed that both adhesively bonded and bolted connection systems are suitable for use in GFRP–concrete structures but



the adhesive bond provides better mechanical behaviour. Nevertheless, owing to durability concerns, corroborated by the results of the experimental campaign conducted in this thesis, the connection of GFRP–concrete structures should be provided by a hybrid connection system (bonded and bolted).

### **8.1.2. Static, creep and dynamic behaviour of GFRP–concrete structures**

The structural behaviour of hybrid GFRP–concrete structures was investigated, namely by performing experiments on the small–scale footbridge prototype with regard to its static, creep and dynamic behaviour.

The small–scale prototype was subjected to static flexural tests in order to investigate (i) the serviceability and failure flexural responses of GFRP–concrete structures, and (ii) to assess the ability of readily available analytical and numerical models to predict the aforementioned responses.

The small–scale prototype showed an appropriate serviceability behaviour, presenting linear–elastic flexural behaviour. The hypothesis of using a low–cost prestress system was tested, showing that the deflections of GFRP–concrete structures may be mitigated by using such prestress systems.

The failure tests showed that the prototype presented a linear behaviour up to failure, which was brittle and was triggered by the shear failure at the web–(top) flange junction of one of the GFRP main girders. This experiment showed that, although no loss of stiffness was observed prior to failure, the high deflection in the brink of failure constitutes a warning of structural malfunction.

Analytical and numerical models were able to predict the experimental results with good accuracy, for both service and failure conditions, proving to be reliable tools for the design of GFRP–concrete structures. The models were able to predict the experimental results regarding: (i) the effects of external prestress; (ii) the failure mode and failure location; and (iii) the strength at failure. With regard to the analytical models' ability to predict the failure behaviour, the investigations performed showed that the bending moment–shear interaction should be considered using failure criteria based on stresses and not on applied forces. For the FE model, the Tsai–Hill failure initiation criterion proved to be adequate for predicting the failure behaviour of the structure.

Dynamic tests were performed in the small–scale prototype, namely (i) modal identification tests, and (ii) tests under pedestrian loading. The modal identification tests consisted of applying a vertical impact load (on predetermined positions) on the deck while measuring the structural vertical accelerations. The pedestrian tests were performed by having one or multiple pedestrians traveling the footbridge deck at different paces (randomly in the case of multiple pedestrians) while measuring the structural response in terms of vertical and horizontal (multiple pedestrians only) structural accelerations.

The modal identification tests allowed the determination of the modal parameters, namely, (i) the mode shapes, (ii) the vibration frequencies, and (iii) the damping ratios. These parameters were determined using two different methods: (i) an output–only method based on the direct results of Fast Fourier Transforms (FFTs); and (ii) an input–output method, which consisted of the individual fitting of the Frequency Response Functions (FRFs) with

an algorithm based on the rational fraction polynomial method. Both methods delivered similar results.

The analytical models derived from the Euler–Bernoulli and Timoshenko beam theories were well able to predict the vibration modes and frequencies of the flexural vibration modes of the footbridge prototype, with the formulae based on the latter theory presenting a better accuracy, owing to the consideration of the shear deformability in the overall behaviour. Regarding the torsional vibration modes, the analytical models were also able to predict the experimental results with fair accuracy, showing the importance of considering both uniform and warping torsion in the overall behaviour of this type of GFRP–concrete structures.

The FE model developed was also able to predict the experimentally observed behaviour of the small-scale prototype with good accuracy, with the exception of the first torsional vibration mode, for which the comparison between experimental and numerical vibration frequencies presented a higher relative difference.

Overall, the modal identification tests and their correspondent analytical and numerical simulations showed that it is possible to predict the modal parameters of hybrid GFRP–concrete structures, namely the mode shapes and vibration frequencies. In order to enhance the quality of the simulations, the following adaptations to traditional models should be made: (i) consideration of the shear deformability on the flexure analytical models; (ii) consideration of both uniform and warping torsion in analytical simulations (at least when using open thin-walled pultruded profiles); and (iii) consideration of the orthotropic material properties of the GFRP in the numerical simulations.

The investigations about the response of hybrid GFRP–concrete structures included experimental tests on the small-scale prototype. The results of these tests showed that the probability of pedestrian discomfort when using the footbridge is low for both vertical and horizontal vibrations. This is a particularly important result regarding the feasibility of GFRP–concrete structures for footbridge applications, since pedestrian comfort often governs the design of pedestrian bridges.

The tests with one pedestrian were simulated with FE models, which were able to predict the dynamic response of the structure with fairly good accuracy, regarding both the maximum vertical accelerations obtained in the experimental tests, as well as the overall structural response over time. This result indicates that readily available numerical tools are suitable for checking pedestrian comfort criteria in design stages.

Finally, the investigations on the creep behaviour of GFRP–concrete hybrid structures included experimental tests, which were performed by loading the small-scale prototype in flexure with two different load levels for two different environmental conditions. The creep tests had a duration ranging from 2114 h to 2642 h.

The experimental results showed that the creep behaviour of GFRP–concrete structures is sensitive to the environmental conditions, in particular to temperature. It should be noticed that this parameter is not taken into account on conventional GFRP creep models. Furthermore, the experimental results also suggest that Findley’s power law regressions, commonly used to predict the creep behaviour of FRP materials, may not be adequate to describe the creep behaviour of hybrid GFRP–concrete structures.

An analytical model to predict the GFRP–concrete behaviour was proposed. This model is based on the judicious choice of GFRP creep material models, according to the stress state of the material in the hybrid structural system, along with the adaptation of those creep material models in order to consider the effects of environmental changes, namely

the temperature. The proposed models showed a good accuracy in predicting the creep deflections, being able to correctly consider the load and environmental differences of each test, proving to be an accurate tool to estimate the long-term creep behavior of GFRP–concrete structures.

Based on the analytical model proposed, it was shown that the hybrid GFRP–concrete structural system proposed is much less susceptible to the creep phenomenon than an all-GFRP equivalent structure.

### **8.1.3. Development of a full-scale GFRP–SFRSCC footbridge prototype**

A full-scale hybrid GFRP–SFRSCC footbridge prototype was developed for general public use. In order to do so, the knowledge gathered with respect to the small-scale prototype and to the investigations on GFRP–concrete connection systems was of the utmost importance.

The full-scale prototype was designed to formally fulfil ultimate (ULS) and serviceability (SLS) limit states requirements.

The static flexural behaviour of the full-scale prototype was experimentally tested and, once again, the analytical and numerical tools used in the formal design proved to have good accuracy. Moreover, regarding the ULS, the analytical and FE models used in the design showed a good agreement with each other, validating one another.

The full-scale prototype was subjected to modal identification tests which showed a good agreement with the analytical and numerical tools proposed earlier, with reference to the small-scale prototype. This result is of particular importance since the SLS pedestrian comfort criteria used in the formal design of the footbridge was the indirect criteria, which is based on the fundamental vibration frequencies.

Moreover, dynamic tests under pedestrian loads were also performed on the full-scale prototype. These tests corroborated the formal design by showing that the direct pedestrian comfort criterion was fulfilled. The FE model showed a poorer agreement, when compared to the small-scale prototype results, in simulating the response under one pedestrian actions, albeit being able to predict the magnitude of the maximum accelerations for most cases. Moreover, it should be mentioned that these prediction were higher than the corresponding experimental results, being, thereafter, conservative estimates.

The creep response of the full-scale prototype was also addressed by an experimental investigation which highlighted the need for GFRP manufacturers to provide characteristic creep moduli for their products, since they may be susceptible to the curing degree of the matrix. The results of this test allowed enhancing the previously proposed creep model, with respect to the small-scale prototype, by including an additional adaptation that allows the consideration of the temperature history (instead of the average temperature only).

## **8.2. Future developments**

The research presented in this thesis addressed several aspects of the behaviour of GFRP–concrete hybrid structural systems. Some aspects of the investigations presented, or their conclusions, led to the suggestion of other subjects that are relevant for the overall knowledge

on GFRP–concrete structures. These should be further addressed in future investigations, namely the following:

- Comprehensive experimental, analytical and numerical investigation on the behaviour of SFRSCC slender slabs in order to enhance the confidence on this new construction material;
- Shear connection testing of GFRP–concrete specimens subjected to a larger number of aging cycles and comparison to specimens subjected to *in situ* natural aging during the same period, allowing to relate accelerated and natural aging processes;
- Experimental testing of full-scale GFRP–concrete beams designed to fail on the GFRP–concrete interface, in order to exploit the pseudo-ductility failure of the hybrid (bonded and bolted) connection system and, additionally, to assess the accuracy of the GFRP–epoxy–SFRSCC interface FE models developed herein, namely with regard to their bi-linear bond-slip laws;
- Development of an analogous solution for application in continuous structures with intermediate supports, *i.e.* adapting the proposed solution to negative bending moments;
- Development of GFRP–concrete structural solutions for vertical members, namely columns and piers;
- Further investigation of the behaviour under one pedestrian loading of the full-scale prototype in order to determine the reasons why the FE model showed worse accuracy in predicting such behaviour (when compared to the predictions made for the small-scale prototype). This investigation may include additional experimental tests, performed when the full-scale prototype is installed in its final location, testing different support conditions to verify their influence on the behaviour;
- Monitoring the behaviour of the prototype in real service conditions with periodic testing in order to assess if the mechanical response of the structure deteriorates over time;
- Experimental investigations (at coupon level) on the influence of the relative humidity on the creep behaviour of the GFRP material and development of new/adapted material creep models which account for that parameter;
- Additional experimental creep investigations on large scale GFRP–concrete hybrid structures to obtain further validation of the models developed in this thesis and those stemming from the previous item;
- Investigation on the fatigue behaviour of GFRP–concrete structures, at (i) connection, (ii) isolated members and (iii) full-scale structural levels, in order to allow the application of the proposed structural system for road and railway bridge structures;
- Investigations on the long-term behaviour (and effectiveness) of prestress GFRP–concrete structures, namely using cost effective prestress systems such as that presented in this thesis;
- Development of prestress systems for GFRP–concrete structures that envisage progressive failure mechanisms, with the prestress rebars/tendons failing before the collapse of the structure;

- Life-cycle cost analysis of GFRP-SFRSCC structures, including data gathered by the continuous monitoring of the full-scale prototype developed in this thesis, and comparison with alternative solutions built with traditional materials;
- Investigation on the failure behaviour of the web-flange junctions of GFRP profiles and proposal of new fibre architectures and/or local reinforcements in order to surpass the strength limitations of this particular zone;
- Numerical simulations of isolated GFRP beams at failure using failure criteria able to simulate the progressive failure of the material (*e.g.* Hashin failure criteria or even micro-mechanics failure theory), in order to obtain better estimates of the failure load.



## Bibliography

- [1] T. Keller. Advanced materials: an introduction. *Structural Engineering International*, 9(4):250, 1999.
- [2] T. Keller. Use of fibre reinforced polymers in bridge construction. In *Structural Engineering Documents, Volume 7*. IABSE, Zurich, 2003.
- [3] ASCE’s 2013 Report Card for American’s Infrastructure. Website: <http://www.infrastructurereportcard.org/>, visited in 10/10/2014.
- [4] L.C. Bank. *Composites for Construction: Structural Design with FRP Materials*. John Wiley & Sons, Inc., Hoboken, NJ, 2006.
- [5] J.R. Correia. *GFRP pultruded profiles in civil engineering: hybrid solutions, bonded connections and fire behaviour*. PhD thesis, Instituto Superior Técnico, Universidade Técnica de Lisboa, 2008.
- [6] J.A. Barros. Technology, design and applications of steel fibre reinforced self-compacting concrete. In *6<sup>th</sup> International Conference Fibre Concrete*. Prague, 2011.
- [7] L.A. Fernandes. Structural behaviour of GFRP beams subjected to concentrated loading: experimental characterization, numerical modeling, and analytical study. Master’s thesis, Instituto Superior Técnico, 2014 (in portuguese).
- [8] J.R. Correia, F.A. Branco, J.A. Gonilha, N. Silva, and D. Camotim. GFRP pultruded flexure membes: assessing of existing design methods. *Structural Engineering International*, 4:362–369, 2010.
- [9] J.A. Gonilha, J.R. Correia, and F.A. Branco. Dynamic response under pedestrian load of a GFRP–SFRSCC hybrid footbridge prototype: Experimental tests and numerical simulation. *Composite Structures*, 95:453–463, 2013.
- [10] J.A. Gonilha, J.R. Correia, and F.A. Branco. Creep response of GFRP–concrete hybrid structures: Application to a footbridge prototype. *Composites Part B*, 53:193–206, 2013.
- [11] J.A. Gonilha, J.R. Correia, F.A. Branco, E. Caetano, and A. Cunha. Modal identification of a GFRP–concrete hybrid footbridge prototype: Experimental tests and analytical and numerical simulations. *Composite Structures*, 106:724–733, 2013.
- [12] J.A. Gonilha, J.R. Correia, and F.A. Branco. Structural behaviour of a GFRP–concrete hybrid footbridge prototype: Experimental tests and numerical and analytical simulations. *Engineering Structures*, 60:11–22, 2014.
- [13] J.A. Gonilha, J. Barros, J.R. Correia, J. Sena-Cruz, F.A. Branco, L.F. Ramos, D. Gonçalves, M.R. Alvim, and T. Santos. Static, dynamic and creep behaviour of a full-scale GFRP–SFRSCC hybrid footbridge. *Composite Structures*, 118:496–509, 2014.

- [14] L.A. Fernandes, J.A. Gonilha, J.R. Correia, N. Silvestre, and F. Nunes. Web-crippling of GFRP pultruded profiles. Part 1: experimental study. *Composite Structures*, in press, 2014 (DOI: 10.1016/j.compstruct.2014.09.027).
- [15] L.A. Fernandes, F. Nunes, J.R. Correia, N. Silvestre, and J.A. Gonilha. Web-crippling of GFRP pultruded profiles. Part 2: numerical analysis and design. *Composite Structures*, in press, 2014 (DOI: 10.1016/j.compstruct.2014.09.026).
- [16] M. Maalej, S.T. Quek, S.F.U. Ahmed, J. Zhang, V.W.J. Lin, and K.S. Leong. Review of potential structural applications of hybrid fiber engineered cementitious composites. *Construction and Building Materials*, 36:216–227, 2012.
- [17] C.D. Tracy. *Fire endurance of multicellular panels in an FRP building system*. PhD thesis, École Polytechnique Fédérale de Lausanne, 2005.
- [18] Retronaut the fotografic time machine. 1957: Monsanto “House of the Future”: [www.retronaut.com/2010/04/monsanto-house-of-the-future](http://www.retronaut.com/2010/04/monsanto-house-of-the-future), visited in 14/8/2014.
- [19] Retronaut the fotografic time machine. 1960s: Futuro House: [www.retronaut.com/2012/01/futuro-house-1960s](http://www.retronaut.com/2012/01/futuro-house-1960s), visited in 14/8/2014.
- [20] T. Keller. Fibre reinforced polymer materials in bridge construction. In *IABSE Symposium, Towards a Better Built Environment — Innovation, Sustainability, Information Technology*. Melbourne, 2002.
- [21] J.P. Firmo, M.R.T. Arruda, and J.R. Correia. Contribution to the understanding of the mechanical behaviour of CFRP-strengthened RC beams subjected to fire: Experimental and numerical assessment. *Composites Part B*, 66:15–24, 2014.
- [22] S&P Clever Reinforcement Company AG. S&P Clever Reinforcement Company web site: [www.reinforcement.ch/](http://www.reinforcement.ch/), visited in 14/8/2014.
- [23] ASDEA S.r.l. ASDEA web site: [www.asdea.net/](http://www.asdea.net/), visited in 14/8/2014.
- [24] Composite Construction Laboratory. CCLAB web site: [cclab.epfl.ch/](http://cclab.epfl.ch/), visited in 14/8/2014.
- [25] J.G. Ferreira and F.A. Branco. The use of glass fiber-reinforced concrete as a structural material. *Experimental Techniques*, 31(3):64–73, 2007.
- [26] B. Matos, J.R. Correia, L.M.S. Castro, and P. França. Structural response of hyperstatic concrete beams reinforced with GFRP bars: Effect of increasing concrete confinement. *Composite Structures*, 94(3):1200–1210, 2012.
- [27] University of Sheffield. Website: <http://mguadagnini.staff.shef.ac.uk/frp/frp.php>, visited in 16/8/2014.
- [28] Université de Sherbrooke. Website: <http://www.civil.usherbrooke.ca>, visited in 14/8/2014.
- [29] Fiberline Composite A/S. Website: <http://www.fiberline.com/>, visited in 16/8/2014.
- [30] Fiberline Composite A/S. Fiberline Design Manual, 2003.
- [31] S&P Clever Reinforcement Company AG. S&P resin 220 epoxy adhesive — two component epoxy resin-based adhesive for S&P FRP Systems, 2013.
- [32] Strongwell Corporation. Website: <http://www.strongwell.com/>, visited in 20/8/2014.



- [33] Creative Pultrusions Inc. The New and Improved Pultex Pultrusion Design Manual of Standard and Custom Fibre Reinforcement Polymer structural Profiles, Volume 4 — Revision 9, 2004.
- [34] T. Keller. Towards structural forms for composite fibre materials. *Structural Engineering International*, 9(4):297–300, 1999.
- [35] Jizhou Huarui FRP Co. Lda. Website: <http://www.hrljxc.com/>, visited in 20/8/2014.
- [36] Creative Pultrusions Inc. Website: <http://www.creativepultrusions.com/>, visited in 20/8/2014.
- [37] EN 13706:2002. *Reinforced Plastic Composites: Specifications for Pultruded Profiles*. European Committee for Standardization, Brussels, 2002.
- [38] J.L. Clarke (editor). *Structural Design of Polymer Composites — EuroComp Design Code and Handbook*. E&FN Spon, London, 1996.
- [39] Reinforced Plastics. Website: <http://www.reinforcedplastics.com/>, visited in 21/8/2014.
- [40] M. Vasile. Mogapan website: <http://www.mogapan.ro/>, visited in 21/8/2014.
- [41] Wikipedia Foundation. Website: <http://en.wikipedia.org/>, visited in 21/8/2014.
- [42] FIB. *Model Code 2010*. International Federation for Structural Concrete (FIB), Lausanne, 2012.
- [43] S. Balouch, J. Forth, and J. Granju. Surface corrosion of steel fibre reinforced concrete. *Cement and Concrete Research*, 40(3):410–414, 2010.
- [44] J.A.O. Barros, E.B. Pereira, and S.P.F. Santos. Lightweight panels of steel fiber reinforced self-compacting concrete. *ASCE Journal of Materials in Civil Engineering*, 19(4):295–304, 2007.
- [45] RILEM Technical Committees. Design of steel fibre reinforced concrete using the  $\sigma$ -w method: principles and applications. *Materials and Structures*, 35(5):262–278, 2002.
- [46] V.M.C.F. Cunha. *Steel fibre reinforced self-compacting concrete: from micro-mechanics to composite behaviour*. PhD thesis, University of Minho, 2010.
- [47] N. Deskovic, T. Triantafillou, and U. Meier. Innovative design of FRP combined with concrete: Short-term behaviour. *Journal of Structural Engineering*, 121(7):1069–1078, 1995.
- [48] J.E. Hall and J.T. Mottram. Combined FRP reinforcement and permanent formwork for concrete members. *Journal of Composites for Construction*, 2(2):78–86, 1998.
- [49] F.H. Garcia. Uso económico de composites de polímeros avanzados con hormigón en estructuras (proyecto i+d brite: Compcon). In *Asociación Científico-Técnica del Hormigón Estructural (ACHE)*, editor, *II Congreso de ACHE de Puentes y Estructuras*, pages 261–276. Madrid, 2001.
- [50] L. Canning, L. Hollaway, and A.M. Thorne. An investigation of the composite action of an FRP-concrete prismatic beam. *Construction and Building Materials*, 13:417–426, 1999.

- [51] J. Hulatt, L. Hollaway, and A.M. Thorne. The use of advanced polymer composites to form an economic structural unit. *Construction and Building Materials*, 17:55–68, 2003.
- [52] M.C.S. Ribeiro, A.J.M. Ferreira, and Marques A.T. Flexural behaviour of GFRP–polymer concrete hybrid structural systems. In *Fibre-Reinforced Polymer Reinforcement for Concrete Structures, Proceedings of the 6th International Symposium on FRP Reinforcement for Concrete Structures (FRPPCS-6)*, pages 695–703. Singapore, 2003.
- [53] J.M. Mieres, I. Calvo, L.F. Pineda, F. Botello, M.A. Gómez, C. López, A. Miravete, and E. Gutiérrez. First bridge constructed of carbon fibre–reinforced polymers in Spain. In *Third International Conference Composites in Construction*, pages 1037–1044. Lyon, 2005.
- [54] A. Hurtado, A. de Banzal, C. Paulotto, and S. Primi. FRP bridges: lessons learned in Spain in the last decade. In *6th International Conference on FRP Composites in Civil Engineering (CICE)*. Rome, 2012.
- [55] A. Arteaga, A. de Diego, C. López-Hombrados, A. Recuero, J.P. Gutiérrez, L.A. Pineda, and Botello F. Tests on models for a hybrid FRP and concrete bridge. In *Third International Conference Composites in Construction*, pages 963–970. Lyon, 2005.
- [56] F. Seible, V.M. Karbhari, and R. Burgueño. Kings Stormwater Channel and I–5/Gilman bridges, USA. *Structural Engineering International*, 9(4):250–253, 1999.
- [57] S. Black. Are hybrid designs the future for construction bridge decks? *Composites Technology*, 10(1):20–25, 2004.
- [58] X. Gai, A. Darby, T. Ibell, and M. Evernden. Experimental investigation into a ductile FRP stay-in-place formwork system for concrete slabs. *Construction and Building Materials*, 49:1013–1023, 2013.
- [59] T. Keller, E. Schaumann, and Vallée T. Flexural behavior of a hybrid FRP and lightweight concrete sandwich bridge deck. *Composites Part A*, 38(3):879–889, 2007.
- [60] J.R. Correia, F.A. Branco, and J.G. Ferreira. Flexural behaviour of GFRP–concrete hybrid beams with interconnection slip. *Engineering Structures*, 77(1):66–78, 2007.
- [61] J.R. Correia, F.A. Branco, and J.G. Ferreira. GFRP–concrete hybrid cross–sections for floors of buildings. *Engineering Structures*, 31(6):1331–1343, 2009.
- [62] J.R. Correia, F.A. Branco, and J.G. Ferreira. Flexural behaviour of multi–span GFRP concrete hybrid beams. *Engineering Structures*, 31(7):1369–1381, 2009.
- [63] Y. Zheng, J. Yang, and Y. Li. Novel concrete deck system without internal reinforcement: Experimental behavior and FE simulation. In *7th International Conference on FRP Composites in Civil Engineering (CICE)*. Vancouver, 2014.
- [64] CEN. EN 1990. *Eurocode 0: Basis of Structural Design*. European Committee for Standardization, Brussels, 2005.
- [65] CEN. EN 1991–2. *Eurocode 1: Actions on Structures – Part 2: Traffic Loads on Bridges*. European Committee for Standardization, Brussels, 2003.

- [66] AASHTO. *LFRD Guide Specifications for the Design of Pedestrian Bridges*. American Association of State Highway and Transportation Officials, Washington, DC, 2009.
- [67] J.R. Demitz, D.R. Mertz, and J.W. Gillespie. Deflection requirements for bridges constructed with advanced composite materials. *Journal of Bridge Engineering*, 8(2):73–83, 2003.
- [68] Advisory Committee on Technical Recommendations for Construction. *Guide for the Design and Construction of Structures Made of FRP Pultruded Elements*. CNR, Rome, 2008.
- [69] D.P. Thambiratnam, N.J. Perera, C.M. Abeysinghe, M. Huang, and S.S. de Silva. Experimental dynamic characterization of an FRP composite bridge superstructure assembly. *Structural Engineering International*, 22(2):238–245, 2012.
- [70] H. Bachmann and W. Ammann. Vibrations in structures: induced by Man and Machines. In *Structural Engineering Documents, Volume 3e*. IABSE, Zurich, 1987.
- [71] S. Zivanovic, A. Pavic, and P. Reynolds. Vibration serviceability of footbridges under human-induced excitation: a literature review. *Journal of Sound and Vibration*, 279(1–2):1–74, 2005.
- [72] T.P. Andriacchi, J.A. Ogle, and J.O. Galante. Walking speed as a basis for normal and abnormal gait measurements. *Journal of Biomechanics*, 10:261–268, 1977.
- [73] Y. Matsumoto, T. Nishioka, H. Shiojiri, and K. Matsuzaki. Dynamic design of footbridges. In *IABSE Proceedings No. 2*. Zurich, 1978.
- [74] Service d’études techniques des routes et autoroutes. *Assessment of Vibrational Behaviour of Footbridges Under Pedestrian Loading, Technical Guide*. SÉTRA, 2006.
- [75] ISO 10137. *Bases for Design of Structures — Serviceability of Buildings and Walkways Against Vibrations*. International Organization for Standardization, Genève, 2012.
- [76] BSI. *UK National Annex to Eurocode 1: Actions on Structures — Part 2: Traffic Loads on Bridges*. British Standards Institution, London, 2008.
- [77] Directorate-General for Research and Innovation. *Advanced Load Models for Synchronous Pedestrian Excitation and Optimised Design Guidelines for Steel Footbridges*. European Communities, Luxembourg, 2008.
- [78] BS 5400. *Standard for Steel, Concrete and Composite bridges*. British Standards Institution, London, 2006.
- [79] Ontario Ministry of Transportation. *Ontario Highway Bridge Design Code*. Toronto, 1983.
- [80] F. Mazzolani (Ed.). *STESSA 2003 — Behaviour of Steel Structures in Seismic Areas*. CRC Press, Boca Raton, 2003.
- [81] BS 6841. *Measurement and Evaluation of Human Exposure to Whole-Body Mechanical Vibration and Repeated Shock*. British Standards Institution, London, 1987.
- [82] BS 6471-1. *Guide to Evaluation of Human Exposure to Vibration in Buildings — Part 1: Vibration Sources Other than Blasting*. British Standards Institution, London, 2012.

- [83] A. Aquino, J.G. Gonilha, J.R. Correia, and F. Branco. Characterization of the geometrical properties of the existent footbridges over the Portuguese railway network. Technical report — Pontalumis project — 2009/003456 A1.T1.IST.1, Instituto Superior Técnico, Lisboa, 2009 (in Portuguese).
- [84] H.R. Salehian, J.A. Barros, and M. Taheri. A design-based approach to estimate the moment-curvature relationship of fiber reinforced elements failing in bending. Technical report A0.T0.UM.1 — PONTALUMIS project, Minho University, Guimarães, 2009.
- [85] CEN. EN 1992-1-1. *Eurocode 2: Design of Concrete Structures – Part 1-1: General Rules and Rules for Buildings*. European Committee for Standardization, Brussels, 2004.
- [86] S. Timoshenko, D.H. Young, and W. Weaver Jr. *Vibration Problems in Engineering*. John Wiley & Sons, Inc., New York, 4th edition, 1974.
- [87] ISO 527:1997. *Plastics — Determination of Tensile Properties*. International Organization for Standardization, Genève, 1997.
- [88] ASTM D 695. *Standard Test Method for Compressive Properties of Rigid Plastics*. American Society for Testing and Materials, West Conshohocken, Pennsylvania, 2002.
- [89] J.M. Hodgkinson. *Mechanical Testing of Advanced Fiber Composites*. CRC Press, Boca Raton, California, 2000.
- [90] ISO 14125:1998. *Fiber-Reinforced Plastic Composites: Determination of Flexure Properties*. International Organization for Standardization, Genève, 1998.
- [91] ASTM D 2344. *Standard Test Method for Short-Beam Strength of Polymer Matrix Composite Materials and Their Laminates*. American Society for Testing and Materials, West Conshohocken, Pennsylvania, 2000.
- [92] ALTO Perfis Pultrudidos Lda. ALTO website: [www.alto.pt](http://www.alto.pt), visited in 6/3/2014.
- [93] T.M. Roberts. Influence of shear deformation on buckling of pultruded fiber reinforced plastic I profiles. *Journal of Composites for Construction*, 6(4):241–248, 2002.
- [94] E.J. Barbero and J. Trovillion. Prediction and measurement of the post-critical behavior of fiber-reinforced composite columns. *Composites Science and Technology*, 58(8):1335–1341, 1998.
- [95] L.P. Kollár. Local buckling of fiber reinforced plastic composite structural members with open and closed cross sections. *Journal of Structural Engineering*, 129(11):1503–1513, 2003.
- [96] CEN. EN 1993. *Eurocode 3: Design of Steel Structures*. European Committee for Standardization, Brussels, 2005.
- [97] SIMULIA. ABAQUS 6.11 — *Analysis User’s Manual*. Dassault Systèmes, Maastricht.
- [98] M.M. Correia, F. Nunes, J.R. Correia, and N. Silvestre. Buckling behavior and failure of hybrid fiber-reinforced polymer pultruded short columns. *Journal of Composites for Construction*, 17(4):463–475, 2013.

- [99] F. Nunes, M. Correia, J.R. Correia, N. Silvestre, and A. Moreira. Experimental and numerical study on the structural behavior of eccentrically loaded GFRP columns. *Thin-Walled Structures*, 72:175–187, 2013.
- [100] R.M. Jones. *Mechanics of Composite Materials*. Taylor and Francis Ltd., London, 2nd edition, 1999.
- [101] EN 12390-3. *Testing Hardened Concrete — Part 3: Compressive Strength of Test Specimens*. European Committee for Standardization, Brussels, 2001.
- [102] LNEC Test Specification E 397. *Determination of Elasticity Modulus in Compression (in portuguese)*. National Laboratory of Civil Engineering (LNEC), Lisboa, 1993.
- [103] EN 12390-6. *Testing Hardened Concrete — Part 6: Tensile Splitting Strength of Test Specimens*. European Committee for Standardization, Brussels, 2009.
- [104] RILEM TC 162-TDF. Test and design methods for steel fibre reinforced concrete. *Materials and Structures*, 35:579–582, 2002.
- [105] F. Nunes, T. Morgado, J.R. Correia, and F. Branco. Task 5 — Structural behaviour of GFRP pultruded profiles under compression. FCT project PTDC/ECM/100779/2008, Technical report IST-5-1, Instituto Superior Técnico, Lisboa, 2012.
- [106] ISO 3506:2009. *Mechanical Properties of Corrosion-Resistant Stainless Steel Fasteners*. International Organization for Standardization, Genève, 2009.
- [107] ISO 4017:2011. *Hexagon Head Screws — Product Grades A and B*. International Organization for Standardization, Genève, 2011.
- [108] J.P. Firmo, J.R. Correia, and P. França. Fire behaviour of reinforced concrete beams strengthened with CFRP laminates: protection systems with insulation of the anchorage zones. *Composites Part B*, 43(3):1545–1556, 2012.
- [109] J.P. Firmo, D. Pitta, J.R. Correia, Tiago C., and Arruda M.R.T. Bond behavior at high temperatures between near surface mounted (NSM) CFRP strips and concrete. *Journal of Composites for Construction*, in press, 2014 (DOI: 10.1061/(ASCE)CC.1943-5614.0000535).
- [110] SIKA Portugal S.A. Icosit KC 220 N — High bearing fluid epoxy mortar (in Portuguese), 2009.
- [111] SIKA Deutschland GmbH. Icosit KC 220/60 TX — 2-pack epoxy binder, 2009.
- [112] DIN 976. *Stud bolts*. Deutsches Institut für Normung e. V., Berlin, 2002.
- [113] ISO 898:2013. *Mechanical Properties of Fasteners made of Carbon Steel and Alloy Steel*. International Organization for Standardization, Genève, 2013.
- [114] P.J.D Mendes, J.A.O Barros, J. Sena-Cruz, and M. Teheri. Influence of fatigue and aggressive exposure on GFRP girder to SFRSCC deck all-adhesive connection. *Composite Structures*, 110:152–162, 2014.
- [115] CEN. EN 1994-1-1. *Eurocode 4: Design of Composite Steel and Concrete Structures — Part 1-1: General Rules and Rules for Buildings*. European Committee for Standardization, Brussels, 2004.

- [116] EN 13687-3. *Products and Systems for the Protection and Repair of Concrete Structures - Test Methods; Determination of Thermal Compatibility - Part 3: Thermal Cycling without De-Icing Salt Impact*. European Committee for Standardization, Genève, 2002.
- [117] ASTM D 7149. *Standard Practice for Determining the Freeze Thaw Stability of Adhesives*. American Society for Testing and Materials, West Conshohocken, Pennsylvania, 2011.
- [118] ICBO-AC125. *Acceptance Criteria for Concrete and Reinforced and Unreinforced Masonry Strengthening using Fiber-Reinforced Polymer (FRP) Composite Systems*. ICBO Evaluation Service, Inc., Whittier, California, 2001.
- [119] ASTM D 6944. *Standard Practice for Resistance of Cured Coatings to Thermal Cycling*. American Society for Testing and Materials, West Conshohocken, Pennsylvania, 2009.
- [120] EN 539-2. *Clay Roofing Tiles for Discontinuous Laying — Determination of Physical Characteristics — Part 2: Test for Frost Resistance*. European Committee for Standardization, Brussels, 2013.
- [121] EN 1504-2. *Products and Systems for the Protection and Repair of Concrete Structures — Definitions, Requirements, Quality Control and Evaluation of Conformity — Part 2: Surface Protection Systems for Concrete*. European Committee for Standardization, Brussels, 2004.
- [122] EN 1504-3. *Products and Systems for the Protection and Repair of Concrete Structures — Definitions, Requirements, Quality Control and Evaluation of Conformity — Part 3: Structural and Non-Structural Repair*. European Committee for Standardization, Brussels, 2005.
- [123] EN 1504-4. *Products and Systems for the Protection and Repair of Concrete Structures — Definitions, Requirements, Quality Control and Evaluation of Conformity — Part 4: Structural Bonding*. European Committee for Standardization, Brussels, 2004.
- [124] R.P. Johnson and I.M. May. Partial-interaction design of composite beams. *Structural Engineer*, 8(53):305–311, 1975.
- [125] J.M. Sousa, J.R. Correia, S Cabral-Fonseca, and A.C. Diogo. Effects of thermal cycles on the mechanical response of pultruded GFRP profiles used in civil engineering applications. *Composite Structures*, 116:720–731, 2014.
- [126] O. Moussa, A.P. Vassilopoulos, J. Castro, and T. Keller. Time-temperature dependence of thermomechanical recovery of cold-curing structural adhesives. *International Journal of Adhesion and Adhesives*, 35:94–101, 2012.
- [127] P. Silva, P. Fernandes, J. Sena-Cruz, M. Azenha, and J. Barros. Effects of thermal cycles and ice/de-ice cycles in the structural behaviour of concrete members reinforced with CFRP laminates using the nsm technique (in portuguese). In *5as Jornadas Portuguesas de Engenharia de Estruturas (JPÉE)*. Lisboa, 2014.
- [128] S. Cabral-Fonseca, J.R. Correia, M.P. Rodrigues, and F.A. Branco. Artificial accelerated ageing of GFRP pultruded profiles made of polyester and vinylester resins: Characterisation of physical-chemical and mechanical damage. *Strain*, 48:162–173, 2012.

- [129] J.E. Yagoubi, G. Lubineau, S. Saghir, J. Verdu, and A. Askari. Thermomechanical and hygroelastic properties of an epoxy system under humid and cold-warm cycling conditions. *Polymer Degradation and Stability*, 99:146–155, 2014.
- [130] R.C. Borges. Durability of GFRP pultruded profiles made of unsaturated polyester and vinylester resins. Master’s thesis, Instituto Superior Técnico, 2014 (in portuguese).
- [131] M.A. Crisfield. *Non-Linear Finite Element Analysis of Solids and Structures*. John Wiley & Sons, Inc., New York, 1991.
- [132] Y. Bai and T. Keller. Modal parameter identification for a GFRP pedestrian bridge. *Composite Structures*, 82(1):90–100, 2008.
- [133] E. Caetano and A. Cunha. Experimental and numerical assessment of the dynamic behaviour of a stress-ribbon bridge. *Structural Concrete*, 5(1):29–38, 2004.
- [134] A. Cunha, E. Caetano, and R. Delgado. Dynamic tests on a large cable-stayed bridge. An efficient approach. *Journal of Bridge Engineering*, 6(1):54–62, 2001.
- [135] F. Benedettini and C. Gentile. Operational modal testing and FE model tuning of a cable-stayed bridge. *Engineering Structures*, 33(6):2063–2073, 2011.
- [136] P. Clemente, F. Marulo, L. Lecce, and A. Bifulco. Experimental modal analysis of the Garigliano cable-stayed bridge. *Soil Dynamics and Earthquake Engineering*, 17(7–8):485–493, 1998.
- [137] F. Magalhães, E. Caetano, A. Cunha, O. Flamand, and G. Grillaud. Ambient and free vibration tests on the Milau Viaduct: evaluation of alternative processing strategies. *Engineering Structures*, 45:372–384, 2012.
- [138] A. Cunha and E. Caetano. Experimental modal analysis of civil engineering structures. *Sound and Vibration*, 40(6):12–20, 2006.
- [139] R. Burgueño, V.M. Karbhari, F. Seible, and R.T. Kolozs. Experimental dynamic characterization of an FRP composite bridge superstructure assembly. *Composite Structures*, 54(4):427–444, 2001.
- [140] M.-C. Han and A.L. Wicks. On the application of the forsythe orthogonal polynomials for global modal parameter estimation. In *Proceeding of the 7th International Modal Analysis Conference*, pages 625–630. 1989.
- [141] A. De Fenza. *Experimental and numerical estimation of damping in composite plates with embedded viscoelastic treatments*. PhD thesis, University of Naples Federico II, 2011.
- [142] Z. Li and B.W. Schafer. Buckling analysis of cold-formed steel members with general boundary conditions using CUFSM: conventional and constrained finite strip methods. In *Proceedings of the 20th International Specialty Conference on Cold-Formed Steel Structures*. St. Louis, MO, 2010.
- [143] M.F. Sá, A.M. Gomes, J.R. Correia, and N. Silvestre. Creep behaviour of pultruded GFRP elements — Part 1: literature review and experimental study. *Composite Structures*, 93:2450–2459, 2011.
- [144] P.K. Dutta and D. Hui. Creep rupture of a GFRP composite at elevated temperatures. *Composite Structures*, 76(1–3):153–161, 2000.

- [145] D.W. Scott, J.S. Lai, and A.-H. Zureick. Creep behaviour of FRP composites: a review of technical literature. *Journal of Reinforced Plastics and Composites*, 14:588–617, 1995.
- [146] M.F. Sá, A.M. Gomes, J.R. Correia, and N. Silvestre. Creep behaviour of pultruded GFRP elements — Part 2: analytical study. *Composite Structures*, 93:2409–2418, 2011.
- [147] J.A. Barros. State-of-the-art of steel fibre reinforced concrete (in portuguese). Technical report 3, Minho University, Guimarães, 2006.
- [148] P. Dávila and J.A. Barros. An integral approach to simulate the creep behaviour of steel fibre reinforced self-compacting concrete (SFRSCC) laminar structures. In *Semana de Engenharia*. Guimarães, 2010.
- [149] J. Trevino. *Méthode directe de calcul de l'état de déformation et de contrainte à long terme d'une structure composée*. PhD thesis, École Polytechnique Fédérale de Lausanne, Thèse EPFL no. 728, 1988.



# Appendix



## A. Appendix A — Material characterization tests

### A.1. Introduction

The complete experimental data obtained in the material characterization tests described in Chapter 4 are provided in this appendix.

### A.2. GFRP tensile coupon tests

Table A.1.: Coupon tensile tests: results for I200.

Specimen	Web				Flanges			
	$F_{tu,L}$	$\sigma_{tu,L}$	$E_{t,L}$	$\nu_{LT}$	$F_{tu,L}$	$\sigma_{tu,L}$	$E_{t,L}$	$\nu_{LT}$
	kN	MPa	GPa	-	kN	MPa	GPa	-
1	96.7	386.80	-	-	98.38	393.52	-	-
2	93.81	375.24	-	-	107.66	430.64	39.28	-
3	92.55	370.20	-	-	107.99	431.96	34.94	-
4	92.75	371.00	32.23	-	106.53	426.12	-	-
5	94.3	377.20	34.42	0.29	97.7	390.8	35.68	0.30
6	92.26	369.04	32.74	-	98.42	393.68	-	-
7	97.21	388.84	32.02	-	101.99	407.96	33.87	-
8	93.81	375.24	-	-	-	-	-	-
Average	94.17	376.69	32.85	0.29	102.67	410.67	35.94	0.30
Std. Dev.	1.86	7.44	1.09	-	4.65	18.60	2.35	-
CoV	2.0%	2.0%	3.3%	-	4.5%	4.5%	6.5%	-

Table A.2.: Coupon tensile tests: results for I400.

Specimen	Web						Flanges		
	Longitudinal			Transverse			Longitudinal		
	$F_{tu,L}$ kN	$\sigma_{tu,L}$ MPa	$E_{t,L}$ GPa	$F_{tu,T}$ kN	$\sigma_{tu,T}$ MPa	$E_{t,T}$ GPa	$F_{tu,L}$ kN	$\sigma_{tu,L}$ MPa	$E_{t,L}$ GPa
1	103.33	275.55	23.09	12.01	32.03	7.79	101.90	271.72	37.41
2	114.66	305.76	25.84	10.42	27.79	6.81	137.32	366.20	33.78
3	104.36	278.30	23.02	8.95	23.87	8.59	138.21	368.57	35.93
4	88.69	236.51	-	10.86	28.96	-	121.04	322.77	-
5	105.51	281.36	-	9.83	26.21	-	123.59	329.57	-
6	110.98	295.95	-	11.14	29.71	-	136.06	362.82	-
Average	104.59	278.90	23.98	10.54	28.09	7.73	126.35	336.94	35.71
Std. Dev.	8.92	23.78	1.60	1.06	2.84	0.90	14.07	37.51	1.83
CoV	8.5%	8.5%	6.7%	10.1%	10.1%	11.6%	11.1%	11.1%	5.1%

### A.3. GFRP compressive coupon tests

Table A.3.: Coupon compressive tests: results for I200 web specimens.

Specimen	Longitudinal				Transverse			
	$F_{cu,L}$ (kN)	$\sigma_{cu,L}$ (MPa)	$\varepsilon_{cu,L}$ ( $\mu\text{m}/\text{m}$ )	$E_{c,L}$ (GPa)	$F_{cu,T}$ (kN)	$\sigma_{cu,T}$ (MPa)	$\varepsilon_{cu,T}$ ( $\mu\text{m}/\text{m}$ )	$E_{c,T}$ (GPa)
1	50.67	492.82	19515	31.50	9.42	85.28	23710	5.05
2	51.98	426.04	24049	24.78	10.08	87.85	26222	5.60
3	47.93	403.76	20609	26.04	10.96	88.80	16660	6.72
4	54.90	480.00	20815	26.92	11.36	84.91	19376	6.68
5	55.03	454.19	19893	25.96	10.47	78.17	19479	5.20
6	38.07	327.80	20287	27.44	7.22	111.44	18416	5.02
7	54.34	442.18	19108	26.48	8.34	63.45	33541	-
8	56.85	448.16	21367	27.40	14.64	111.44	20962	5.91
Average	51.22	434.37	20705	27.06	10.31	88.92	22296	5.74
Std. Dev.	6.02	51.42	1532	1.99	2.22	16.08	5463	0.73
CoV	11.8%	11.8%	7.4%	7.4%	21.5%	18.1%	24.5%	12.7%

Table A.4.: Coupon compressive tests: results for I200 flange specimens.

Specimen	Longitudinal				Transverse			
	$F_{cu,L}$ (kN)	$\sigma_{cu,L}$ (MPa)	$\varepsilon_{cu,L}$ ( $\mu\text{m}/\text{m}$ )	$E_{c,L}$ (GPa)	$F_{cu,T}$ (kN)	$\sigma_{cu,T}$ (MPa)	$\varepsilon_{cu,T}$ ( $\mu\text{m}/\text{m}$ )	$E_{c,T}$ (GPa)
1	43.16	366.35	24751	27.94	9.50	81.22	21317	5.98
2	48.35	410.42	24073	32.63	9.60	78.43	27235	4.61
3	50.50	413.33	23225	34.36	10.67	85.49	19500	4.76
4	33.26	270.77	19326	32.19	7.39	55.69	20141	3.14
5	47.58	380.80	20004	37.72	9.01	66.95	18702	3.67
6	54.82	453.09	20852	35.79	8.95	64.01	22780	4.51
7	51.67	425.06	20004	36.87	4.90	38.64	23446	-
8	-	-	-	-	6.08	44.09	18935	3.80
Average	47.05	388.55	21748	33.93	8.26	64.31	21507	4.35
Std. Dev.	7.08	59.18	2212	3.35	1.96	17.25	2894	0.93
CoV	15.1%	15.2%	10.2%	9.9%	23.7%	26.8%	13.5%	21.3%

Table A.5.: Coupon compressive tests: results for I400 web specimens.

Specimen	Longitudinal				Transverse			
	$F_{cu,L}$ (kN)	$\sigma_{cu,L}$ (MPa)	$\varepsilon_{cu,L}$ ( $\mu\text{m}/\text{m}$ )	$E_{c,L}$ (GPa)	$F_{cu,T}$ (kN)	$\sigma_{cu,T}$ (MPa)	$\varepsilon_{cu,T}$ ( $\mu\text{m}/\text{m}$ )	$E_{c,T}$ (GPa)
1	24.21	128.03	29407	7.75	14.05	75.99	23488	5.29
2	34.94	186.68	26465	10.49	11.67	64.00	22555	4.11
3	50.74	300.13	29934	17.42	14.03	77.98	24684	3.83
4	36.51	195.51	30267	11.32	12.17	65.68	27077	4.57
5	42.30	221.90	23901	13.17	12.62	68.24	23032	4.82
6	32.75	196.08	19973	13.14	13.06	70.66	20980	4.70
Average	36.91	204.72	26658	12.21	12.93	70.43	23636	4.55
Std. Dev.	8.98	56.15	4090	3.24	0.97	5.60	2076	0.52
CoV	24.3%	27.4%	15.3%	26.6%	7.5%	7.9%	8.8%	11.4%

Table A.6.: Coupon compressive tests: results for I400 flange specimens.

Specimen	Longitudinal				Transverse			
	$F_{cu,L}$ (kN)	$\sigma_{cu,L}$ (MPa)	$\varepsilon_{cu,L}$ ( $\mu\text{m}/\text{m}$ )	$E_{c,L}$ (GPa)	$F_{cu,T}$ (kN)	$\sigma_{cu,T}$ (MPa)	$\varepsilon_{cu,T}$ ( $\mu\text{m}/\text{m}$ )	$E_{c,T}$ (GPa)
1	36.08	186.84	24677	10.24	9.97	51.73	22559	3.26
2	29.48	153.10	26553	9.74	8.99	48.52	21251	3.71
3	33.44	165.84	27367	11.33	8.128	44.06	23267	3.97
4	60.12	317.69	27388	17.11	7.84	40.99	21392	3.37
5	48.25	252.54	33801	14.01	8.40	45.57	18035	3.13
6	33.86	169.82	17910	14.43	9.22	50.65	17237	3.95
7	26.20	137.70	23740	8.93	-	-	-	-
Average	38.20	197.65	25919	12.26	8.76	46.92	20624	3.57
Std. Dev.	11.88	64.43	4782	2.99	0.79	4.12	2445	0.36
CoV	31.1%	32.6%	18.5%	24.4%	9.0%	8.8%	11.9%	10.2%

## A.4. GFRP off-axis tensile coupon tests

Table A.7.: Coupon off-axis tensile tests results.

Specimen	I200			I400		
	$F_{u,11}$ (kN)	$\tau_{u,LT}$ (MPa)	$G_{LT}$ (GPa)	$F_{u,11}$ (kN)	$\tau_{u,LT}$ (MPa)	$G_{LT}$ (GPa)
1	37.29	25.12	-	42.70	20.13	3.32
2	35.20	25.05	3.88	51.00	22.02	4.13
3	33.04	25.04	-	42.03	19.82	3.19
4	29.69	23.54	-	44.80	21.10	3.31
5	32.64	24.17	3.41	41.74	19.06	-
6	31.70	23.17	3.58	-	-	-
7	42.26	29.52	-	-	-	-
8	43.99	32.06	3.84	-	-	-
9	41.50	29.64	-	-	-	-
10	44.47	30.62	-	-	-	-
11	43.38	31.01	3.55	-	-	-
12	45.82	30.69	3.80	-	-	-
Average	38.42	27.47	3.68	44.45	20.43	3.49
Std. Dev.	5.77	3.37	0.19	3.85	1.15	0.43
CoV	15.0%	12.3%	5.2%	8.7%	5.6%	12.4%

## A.5. GFRP flexural coupon tests

Table A.8.: Coupon flexural tests: results of the web specimens (I200).

Specimen	$F_{fu-i,L}$ (kN)	$F_{fu,L}$ (kN)	$F_{fu,L}/F_{fu,L}$ -	$\sigma_{fu,L}$ (MPa)	$\varepsilon_{fu-i,L}$ ( $\mu$ m/m)	$E_{f,L}$ (GPa)
1	2.65	2.65	1.00	551.61	22803	24.57
2	2.72	2.88	1.06	597.92	25317	26.26
3	2.25	2.72	1.21	565.41	19708	23.59
4	2.62	2.64	1.01	549.62	25307	21.85
5	2.33	2.82	1.21	585.53	19643	23.67
6	2.19	2.31	1.05	481.11	21926	17.18
7	2.07	2.38	1.15	495.25	16643	22.07
8	2.14	2.51	1.17	522.51	18404	18.77
Average	2.37	2.62	1.11	543.62	21219	22.25
Std. Dev.	0.25	0.20	0.09	41.36	3166	3.00
CoV	10.7%	7.6%	7.9%	7.6%	14.9%	13.5%

Table A.9.: Coupon flexure tests: results of the flange specimens (I200).

Specimen	$F_{fu-i,L}$ (kN)	$F_{fu,L}$ (kN)	$F_{fu,L}/F_{fu,L}$ -	$\sigma_{fu,L}$ (MPa)	$\varepsilon_{fu-i,L}$ ( $\mu$ m/m)	$E_{f,L}$ (GPa)
1	2.70	2.82	1.05	586.45	19491	24.46
2	2.33	2.44	1.05	508.05	21284	20.63
3	2.61	2.62	1.00	544.38	18067	27.35
4	2.36	2.62	1.11	544.88	17295	25.75
5	2.43	2.60	1.07	540.89	17273	23.10
6	2.18	2.29	1.05	476.12	19676	20.75
Average	2.44	2.57	1.05	533.46	18848	23.67
Std. Dev.	0.19	0.18	0.03	37.54	1583	2.70
CoV	7.9%	7.0%	3.3%	7.0%	8.4%	11.4%

## A.6. GFRP interlaminar shear coupon tests

Table A.10.: Coupon interlaminar shear tests results (I200).

Specimen	Web		Flange	
	$F_{isu,L}$ (kN)	$\tau_{isu,L}$ (MPa)	$F_{isu,L}$ (kN)	$\tau_{isu,L}$ (MPa)
1	7.54	29.47	7.79	30.28
2	7.74	30.95	7.95	30.22
3	7.35	30.26	8.23	30.82
4	7.30	27.97	7.93	30.99
5	7.53	29.74	8.23	31.89
6	7.40	29.10	7.85	29.70
7	7.06	27.97	7.02	28.02
8	-	-	7.77	29.72
Average	7.42	29.35	7.85	30.21
Std. Dev.	0.21	1.11	0.38	1.14
CoV	2.9%	3.8%	4.8%	3.8%

## A.7. SFRSCC compressive cube tests

Table A.11.: Results of the compressive tests on small-scale prototype SFRSCC cube specimens

Specimen	$f_c$ (MPa)	
	28 days	905 days
1	80.67	94.93
2	78.58	89.16
3	82.71	85.47
4	-	102.49
Average	80.65	93.01
Std. Dev.	2.07	7.42
CoV	2.6%	8.0%



*Table A.12.:* Results of the compressive tests on small-scale prototype conventional concrete (jackets) cube specimens.

Specimen	$f_c$ (MPa)
1	61.38
2	54.71
3	74.80
Average	63.63
Std. Dev.	10.23
CoV	16.1%

## A.8. SFRSCC compressive cylinder tests

*Table A.13.:* Test results on small-scale prototype SFRSCC material cylinder specimens.

Specimen	28 days			905 days		
	$E_c$ (GPa)	$\nu_c$ -	$f_{cr}$ (MPa)	$E_c$ (GPa)	$\nu_c$ -	$f_{cr}$ (MPa)
1	38.55	0.35	8.55	39.69	0.33	11.35
2	34.80	0.29	8.41	40.54	0.15	11.72
3	37.57	0.35	11.31	43.10	0.24	11.42
4	-	-	-	40.18	0.44	9.15
5	-	-	-	-	-	12.41
6	-	-	-	-	-	11.99
7	-	-	-	-	-	11.47
8	-	-	-	-	-	9.99
Average	36.97	0.33	9.42	40.88	0.29	11.19
Std. Dev.	1.94	0.03	1.63	1.53	0.12	1.08
CoV	5.3%	10.5%	17.3%	3.7%	42.6%	9.6%



## B. Appendix B — GFRP–SFRSCC shear connection tests

### B.1. Introduction

The complete experimental data obtained in the GFRP–SFRSCC shear connection tests described in Chapter 5 are provided in this appendix.

### B.2. Preliminary tests

#### B.2.1. Series P–A

*Table B.1.:* GFRP–SFRSCC shear connection tests: results for series P–A.

Specimen	$F_u$ (kN)	$d_u$ (MPa)	$K$ (kN/mm)	Failure mode
1	346.69	1.74	280.72	1 <sup>st</sup> debonding; 2 <sup>nd</sup> web–flange junction
2	325.89	2.85	285.85	1 <sup>st</sup> debonding; 2 <sup>nd</sup> web–flange junction
3	355.60	2.70	186.82	1 <sup>st</sup> debonding; 2 <sup>nd</sup> web–flange junction
4	432.79	2.09	336.17	1 <sup>st</sup> debonding; 2 <sup>nd</sup> web–flange junction
5	364.35	3.37	274.33	1 <sup>st</sup> debonding; 2 <sup>nd</sup> web–flange junction
6	409.10	1.52	341.52	Web–flange junction and debonding
7	305.24	1.51	234.54	1 <sup>st</sup> debonding; 2 <sup>nd</sup> web–flange junction
Average	362.81	2.25	277.14	-
Std. Dev.	44.78	0.73	54.31	-
CoV	12.3%	32.3%	19.6%	-

## B.2.2. Series P–M1

Table B.2.: GFRP–SFRSCC shear connection tests: results for series P–M1.

Specimen	$F_u$ (kN)	$d_u$ (MPa)	$K$ (kN/mm)	Failure mode
1	135.56	6.98	94.21	1 <sup>st</sup> debonding; 2 <sup>nd</sup> crushing of the flanges
2	139.49	7.76	93.02	1 <sup>st</sup> debonding; 2 <sup>nd</sup> crushing of the flanges
3	130.32	2.69	86.12	1 <sup>st</sup> debonding; 2 <sup>nd</sup> crushing of the flanges
Average	135.13	5.81	91.12	-
Std. Dev.	4.60	2.73	4.37	-
CoV	3.4%	47.0%	4.8%	-

## B.2.3. Series P–M2

Table B.3.: GFRP–SFRSCC shear connection tests: results for series P–M2.

Specimen	$F_u$ (kN)	$d_u$ (MPa)	$K$ (kN/mm)	Failure mode
1	229.80	1.77	148.29	1 <sup>st</sup> debonding; 2 <sup>nd</sup> crushing of the flanges
2	205.54	1.63	151.20	1 <sup>st</sup> debonding; 2 <sup>nd</sup> crushing of the flanges
3	237.83	1.40	151.59	1 <sup>st</sup> debonding; 2 <sup>nd</sup> crushing of the flanges
4	218.30	6.69	111.81	1 <sup>st</sup> debonding; 2 <sup>nd</sup> crushing of the flanges
Average	222.86	2.87	140.72	-
Std. Dev.	14.06	2.55	19.33	-
CoV	6.3%	88.8%	13.7%	-

**B.2.4. Series P-M3***Table B.4.: GFRP-SFRSCC shear connection tests: results for series P-M3.*

Specimen	$F_u$ (kN)	$d_u$ (MPa)	$K$ (kN/mm)	Failure mode
1	290.51	5.10	148.93	1 <sup>st</sup> debonding; 2 <sup>nd</sup> crushing of the flanges
2	272.63	3.29	129.80	1 <sup>st</sup> debonding; 2 <sup>nd</sup> crushing of the flanges
3	295.64	6.42	141.34	1 <sup>st</sup> debonding; 2 <sup>nd</sup> crushing of the flanges
Average	286.26	4.94	140.02	-
Std. Dev.	12.08	1.57	9.63	-
CoV	4.2%	31.8%	6.9%	-

**B.2.5. Series P-M4***Table B.5.: GFRP-SFRSCC shear connection tests: results for series P-M4.*

Specimen	$F_u$ (kN)	$d_u$ (MPa)	$K$ (kN/mm)	Failure mode
1	366.11	2.84	246.83	1 <sup>st</sup> debonding; 2 <sup>nd</sup> crushing of the flanges
2	367.18	6.15	268.68	1 <sup>st</sup> debonding; 2 <sup>nd</sup> crushing of the flanges
3	374.53	2.40	191.71	1 <sup>st</sup> debonding; 2 <sup>nd</sup> crushing of the flanges
4	346.78	5.10	179.94	1 <sup>st</sup> debonding; 2 <sup>nd</sup> crushing of the flanges
Average	363.65	4.12	221.79	-
Std. Dev.	11.85	1.79	42.74	-
CoV	3.3%	43.5%	19.3%	-

### B.2.6. Series P–AM

Table B.6.: GFRP–SFRSCC shear connection tests: results for series P–AM.

Specimen	$F_u$ (kN)	$d_u$ (MPa)	$K$ (kN/mm)	Failure mode
1	422.67	5.22	197.98	1 <sup>st</sup> debonding; 2 <sup>nd</sup> web–flange junction & bolts' failure
2	374.72	2.24	357.93	1 <sup>st</sup> debonding; 2 <sup>nd</sup> web–flange junction & bolts' failure
3	444.16 <sup>1</sup>	2.80 <sup>1</sup>	340.81	-
4	352.93	3.27	305.55	1 <sup>st</sup> debonding; 2 <sup>nd</sup> web–flange junction & bolts' failure
Average	398.62	3.38	300.57	-
Std. Dev.	42.08	1.29	71.79	-
CoV	10.6%	38.2%	23.9%	-

<sup>1</sup> not tested up to failure.

## B.3. Un-aged specimens

### B.3.1. Series A

Table B.7.: GFRP–SFRSCC shear connection tests: results for series A.

Specimen	$F_u$ (kN)	$d_u$ (mm)	$K$ (kN/mm)	Failure mode
1	364.46	2.28	280.28	1 <sup>st</sup> debonding; 2 <sup>nd</sup> web–flange junction
2	442.34	2.03	270.58	1 <sup>st</sup> debonding; 2 <sup>nd</sup> web–flange junction
3	374.13	1.87	226.54	1 <sup>st</sup> debonding; 2 <sup>nd</sup> web–flange junction
4	391.59	2.40	221.58	1 <sup>st</sup> debonding; 2 <sup>nd</sup> web–flange junction
Average	393.13	2.15	249.74	-
Std. Dev.	34.67	0.24	29.99	-
CoV	8.8%	11.2%	12.0%	-

### B.3.2. Series M

Table B.8.: GFRP-SFRSCC shear connection tests: results for series M.

Specimen	$F_u$ (kN)	$d_u$ (mm)	$K$ (kN/mm)	Failure mode
1	352.60	5.42	96.60	Crushing of the flanges
2	379.16	4.47	96.36	Crushing of the flanges
3	357.53	4.87	84.87	Crushing of the flanges
4	351.75	4.97	85.72	Crushing of the flanges
Average	360.26	4.93	90.89	-
Std. Dev.	12.86	0.39	6.46	-
CoV	3.6%	8.0%	7.1%	-

### B.3.3. Series AM

Table B.9.: GFRP-SFRSCC shear connection tests: results for series AM.

Specimen	$F_u$ (kN)	$d_u$ (mm)	$K$ (kN/mm)	Failure mode
1	504.09	2.26	297.54	1 <sup>st</sup> debonding; 2 <sup>nd</sup> web-flange junction
2	558.74	2.59	319.21	1 <sup>st</sup> debonding; 2 <sup>nd</sup> web-flange junction
3	395.38	2.37	250.97	1 <sup>st</sup> debonding; 2 <sup>nd</sup> crushing of the flanges
4	576.57	2.24	320.43	1 <sup>st</sup> debonding; 2 <sup>nd</sup> web-flange junction
Average	508.70	2.36	297.04	-
Std. Dev.	81.59	0.16	32.46	-
CoV	16.0%	6.8%	10.9%	-

## B.4. Aged specimens

### B.4.1. Thermal cycles

#### B.4.1.1. Series A–Th–T1

Table B.10.: GFRP–SFRSCC shear connection tests: results for series A–Th–T1.

Specimen	$F_u$ (kN)	$d_u$ (mm)	$K$ (kN/mm)	Failure mode
1	437.60	3.72	175.96	Debonding
2	455.70	— <sup>1</sup>	180.37	Debonding
3	419.26	2.86	240.58	Debonding
4	471.07	2.11	368.59	Debonding
Average	445.91	2.90	241.38	-
Std. Dev.	22.42	0.81	89.79	-
CoV	5.0%	27.9%	37.2%	-

<sup>1</sup> The measurement of the relative displacement is not accurate for loads over 268 kN because one of the transducers moved.

#### B.4.1.2. Series A–Th–T2

Table B.11.: GFRP–SFRSCC shear connection tests: results for series A–Th–T2.

Specimen	$F_u$ (kN)	$d_u$ (mm)	$K$ (kN/mm)	Failure mode
1	415.29	— <sup>1</sup>	170.47	Debonding
2	477.77	2.47	251.66	1 <sup>st</sup> debonding; 2 <sup>nd</sup> web–flange junction
3	392.98	2.88	231.38	Debonding
4	448.02 <sup>2</sup>	4.68 <sup>2</sup>	242.40	- <sup>2</sup>
Average	433.51	3.34	223.98	-
Std. Dev.	37.17	1.18	36.63	-
CoV	8.6%	35.2%	16.4%	-

<sup>1</sup> The measurement of the relative displacement is not accurate for loads over 318 kN because one of the transducers moved.

<sup>2</sup> Specimen did not collapse.



**B.4.1.3. Series A–Th–T3***Table B.12.: GFRP–SFRSCC shear connection tests: results for series A–Th–T3.*

Specimen	$F_u$ (kN)	$d_u$ (mm)	$K$ (kN/mm)	Failure mode
1	497.60	6.28	90.23	Debonding
2	465.87	8.68	80.26	Debonding
3	545.45	6.23	148.18	Debonding
4	477.52	5.01	143.62	Debonding
5	405.87	5.94	124.91	Debonding
6	447.77	5.37	119.22	Debonding
7	438.84	6.79	85.88	Debonding
8	475.79	5.54	113.98	Debonding
Average	469.34	6.23	113.29	-
Std. Dev.	41.64	1.14	25.86	-
CoV	8.9%	18.3%	22.8%	-

**B.4.2. Wet–dry cycles****B.4.2.1. Series A–H–T1***Table B.13.: GFRP–SFRSCC shear connection tests: results for series A–H–T1.*

Specimen	$F_u$ (kN)	$d_u$ (mm)	$K$ (kN/mm)	Failure mode
1	414.05	5.63	113.25	Debonding
2	344.13 <sup>1</sup>	10.04 <sup>1</sup>	51.43 <sup>1</sup>	Crushing of the GFRP
3	405.12	5.19	148.28	Debonding
4	307.19	6.74	96.30	Debonding
Average	375.45	5.85	119.27	-
Std. Dev.	59.29	0.80	26.51	-
CoV	15.8%	13.7%	22.2%	-

<sup>1</sup> These results were not considered for the average and standard deviation.

**B.4.2.2. Series A–H–T2***Table B.14.: GFRP-SFRSCC shear connection tests: results for series A–H–T2.*

Specimen	$F_u$ (kN)	$d_u$ (mm)	$K$ (kN/mm)	Failure mode
1	406.12	5.27	118.07	Web-flange junction
2	358.26	6.77	108.29	1 <sup>st</sup> web-flange junction; 2 <sup>nd</sup> debonding
3	400.41	4.74	169.90	Debonding
4	412.81 <sup>1</sup>	11.66 <sup>1</sup>	90.12 <sup>1</sup>	Crushing of the GFRP
Average	388.26	5.59	132.09	-
Std. Dev.	26.14	1.05	33.11	-
CoV	6.7%	18.9%	25.1%	-

<sup>1</sup> These results were not considered for the average and standard deviation.

**B.4.2.3. Series A–H–T3***Table B.15.: GFRP-SFRSCC shear connection tests: results for series A–H–T3.*

Specimen	$F_u$ (kN)	$d_u$ (mm)	$K$ (kN/mm)	Failure mode
1	412.31	6.23	97.72	1 <sup>st</sup> web-flange junction; 2 <sup>nd</sup> debonding
2	429.67	6.01	104.04	Debonding
3	326.53	5.97	96.01	1 <sup>st</sup> web-flange junction; 2 <sup>nd</sup> debonding
4	381.82	7.13 <sup>1</sup>	26.96 <sup>1</sup>	1 <sup>st</sup> crushing; 2 <sup>nd</sup> web-flange junction
Average	387.58	6.07	99.26	-
Std. Dev.	45.25	0.14	4.23	-
CoV	11.7%	2.3%	4.3%	-

<sup>1</sup> These results were not considered for the average and standard deviation.

**B.4.2.4. Series AM-H-T3***Table B.16.:* GFRP-SFRSCC shear connection tests: results for series AM-H-T3.

Specimen	$F_u$ (kN)	$d_u$ (mm)	$K$ (kN/mm)	Failure mode
1	507.52	6.83	110.88	1 <sup>st</sup> debonding; 2 <sup>nd</sup> crushing; 3 <sup>rd</sup> web-flange junction
2	477.02	6.16	92.82	1 <sup>st</sup> debonding; 2 <sup>rd</sup> web-flange junction
3	510.50	4.56	177.28	1 <sup>st</sup> debonding; 2 <sup>nd</sup> crushing; 3 <sup>rd</sup> web-flange junction
Average	498.35	5.85	126.99	-
Std. Dev.	18.53	1.17	44.48	-
CoV	3.7%	19.9%	35.0%	-



## C. Appendix C — One pedestrian dynamic test on the small-scale prototype

### C.1. Introduction

This appendix presents the comprehensive comparison between the experimental data of the small-scale prototype one pedestrian tests, described in Chapter 6, and the numerical results. In this regard, for each pedestrian motion, each path, and each measuring position, a representative curve of the accelerations measured in the experimental tests is compared with those obtained with the FE model.

### C.2. Walk slow

#### C.2.1. Centred path

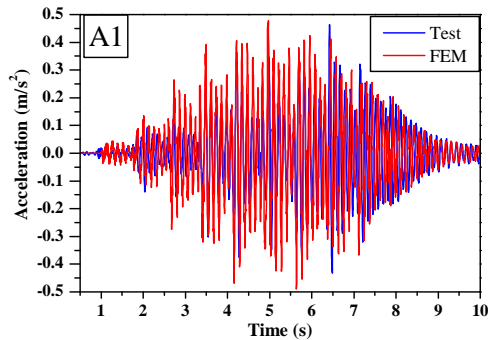


*Figure C.1.:* Small-scale prototype one pedestrian tests: accelerations attained at A1 for slow walk at the centred path. Experimental and numerical results.

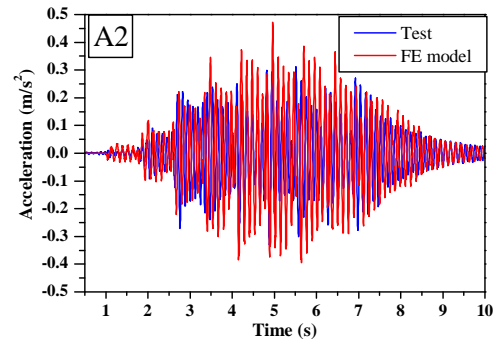


*Figure C.2.:* Small-scale prototype one pedestrian tests: accelerations attained at A2 for slow walk at the centred path. Experimental and numerical results.

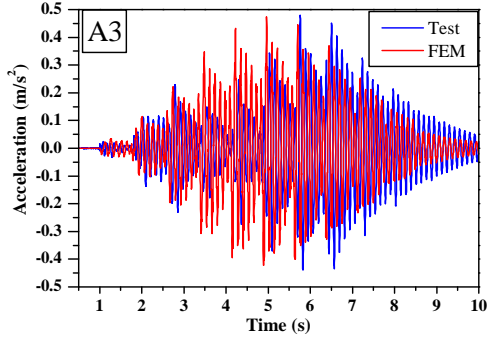


Figure C.3.: Small-scale prototype one pedestrian tests: accelerations attained at A3 for slow walk at the centred path. Experimental and numerical results.

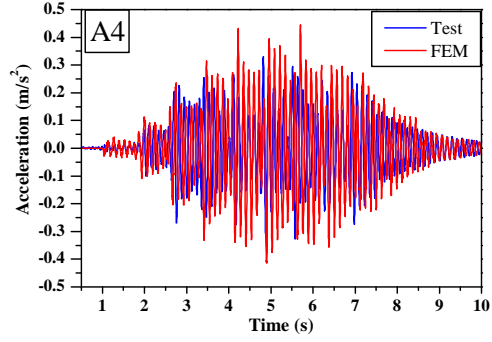


Figure C.4.: Small-scale prototype one pedestrian tests: accelerations attained at A4 for slow walk at the centred path. Experimental and numerical results.

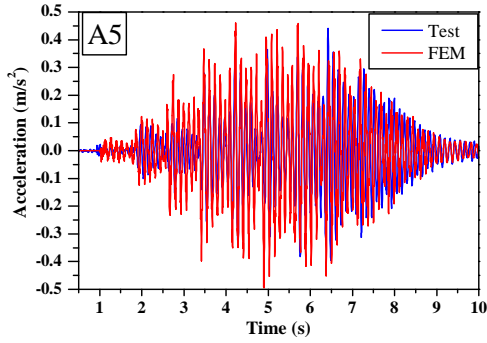


Figure C.5.: Small-scale prototype one pedestrian tests: accelerations attained at A5 for slow walk at the centred path. Experimental and numerical results.

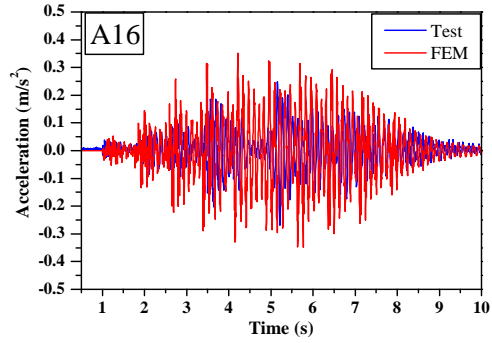


Figure C.6.: Small-scale prototype one pedestrian tests: accelerations attained at A16 for slow walk at the centred path. Experimental and numerical results.

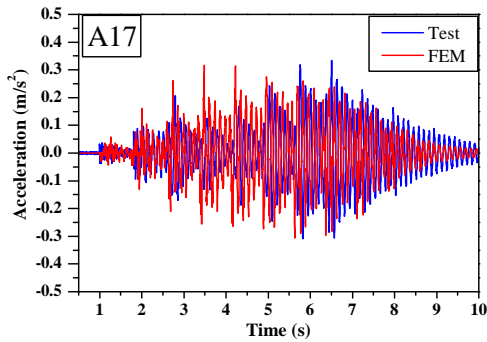


Figure C.7.: Small-scale prototype one pedestrian tests: accelerations attained at A17 for slow walk at the centred path. Experimental and numerical results.

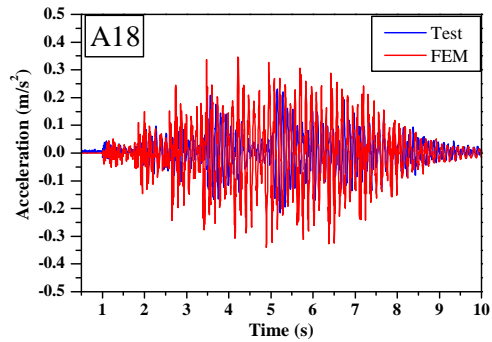


Figure C.8.: Small-scale prototype one pedestrian tests: accelerations attained at A18 for slow walk at the centred path. Experimental and numerical results.

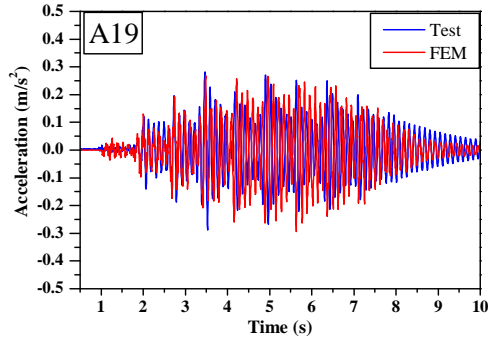


Figure C.9.: Small-scale prototype one pedestrian tests: accelerations attained at A19 for slow walk at the centred path. Experimental and numerical results.

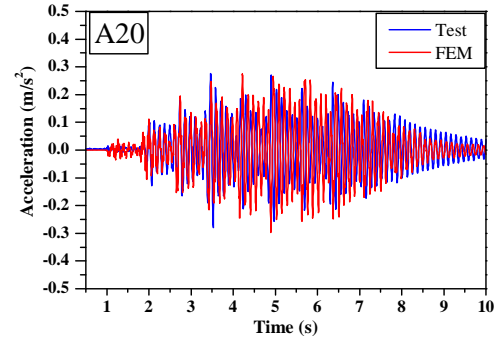


Figure C.10.: Small-scale prototype one pedestrian tests: accelerations attained at A20 for slow walk at the centred path. Experimental and numerical results.

### C.2.2. Eccentric path

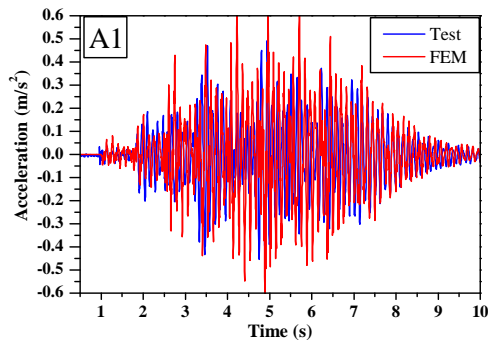


Figure C.11.: Small-scale prototype one pedestrian tests: accelerations attained at A1 for slow walk at the eccentric path. Experimental and numerical results.

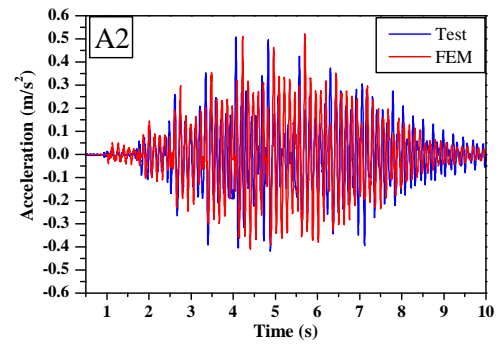


Figure C.12.: Small-scale prototype one pedestrian tests: accelerations attained at A2 for slow walk at the eccentric path. Experimental and numerical results.

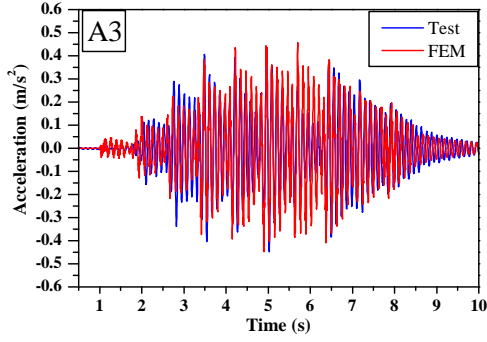


Figure C.13.: Small-scale prototype one pedestrian tests: accelerations attained at A3 for slow walk at the eccentric path. Experimental and numerical results.

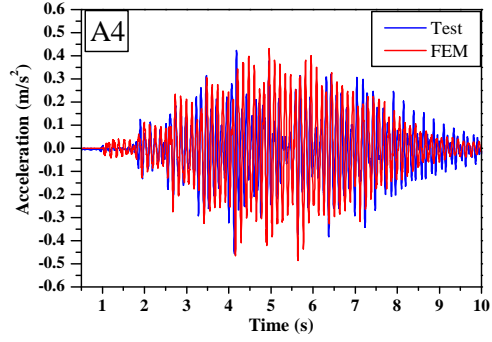


Figure C.14.: Small-scale prototype one pedestrian tests: accelerations attained at A4 for slow walk at the eccentric path. Experimental and numerical results.

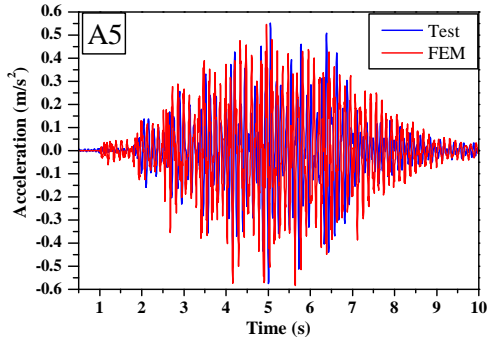


Figure C.15.: Small-scale prototype one pedestrian tests: accelerations attained at A5 for slow walk at the eccentric path. Experimental and numerical results.

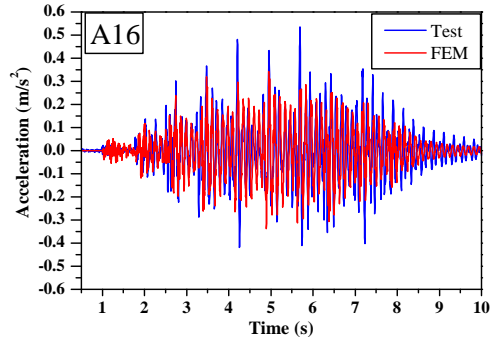


Figure C.16.: Small-scale prototype one pedestrian tests: accelerations attained at A16 for slow walk at the eccentric path. Experimental and numerical results.

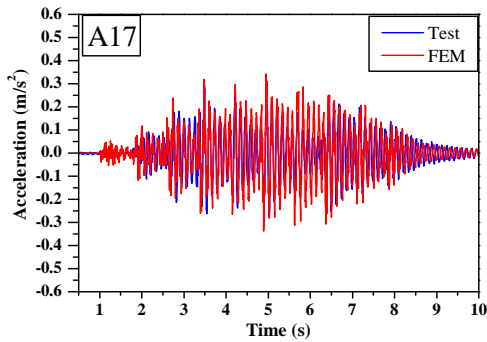


Figure C.17.: Small-scale prototype one pedestrian tests: accelerations attained at A17 for slow walk at the eccentric path. Experimental and numerical results.

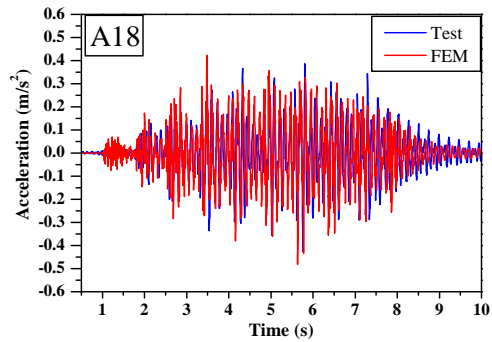


Figure C.18.: Small-scale prototype one pedestrian tests: accelerations attained at A18 for slow walk at the eccentric path. Experimental and numerical results.



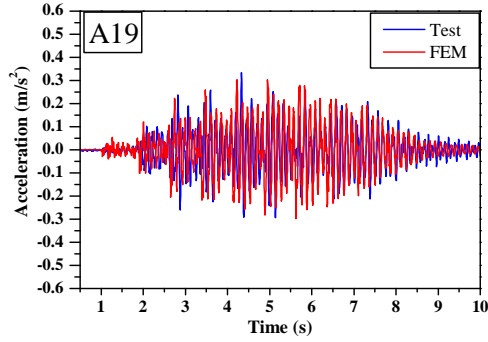


Figure C.19.: Small-scale prototype one pedestrian tests: accelerations attained at A19 for slow walk at the eccentric path. Experimental and numerical results.

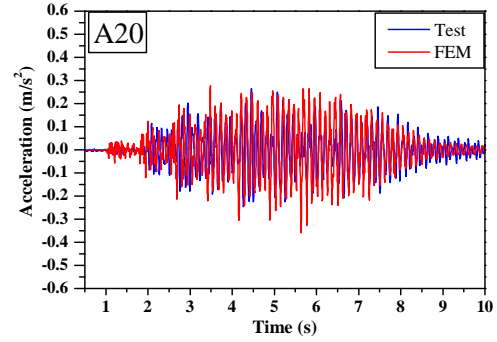


Figure C.20.: Small-scale prototype one pedestrian tests: accelerations attained at A20 for slow walk at the eccentric path. Experimental and numerical results.

### C.3. Walk

#### C.3.1. Centred path

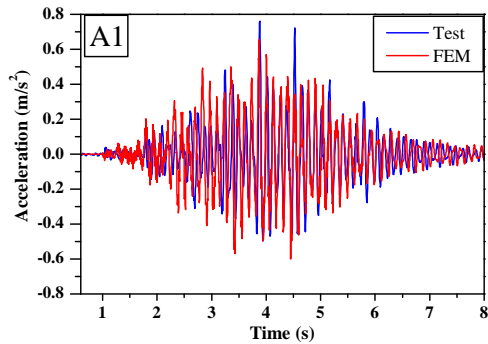


Figure C.21.: Small-scale prototype one pedestrian tests: accelerations attained at A1 for normal walk at the centred path. Experimental and numerical results.

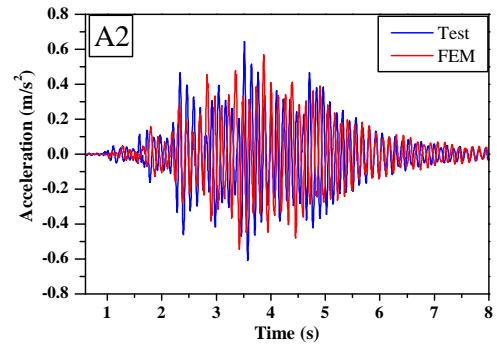


Figure C.22.: Small-scale prototype one pedestrian tests: accelerations attained at A2 for normal walk at the centred path. Experimental and numerical results.

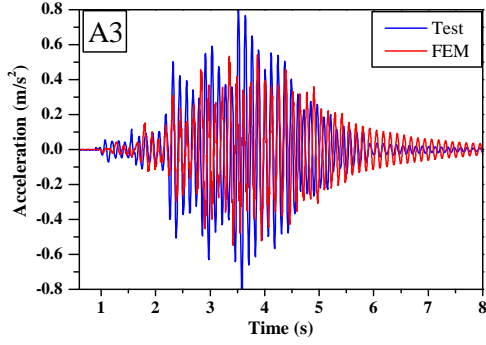


Figure C.23.: Small-scale prototype one pedestrian tests: accelerations attained at A3 for normal walk at the centred path. Experimental and numerical results.

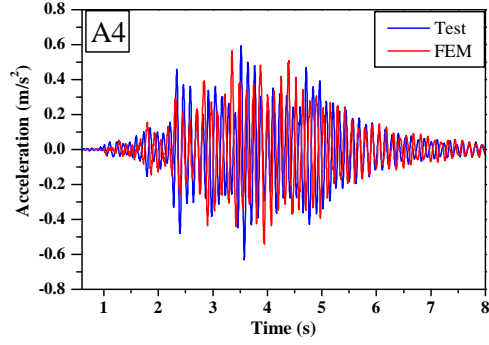


Figure C.24.: Small-scale prototype one pedestrian tests: accelerations attained at A4 for normal walk at the centred path. Experimental and numerical results.

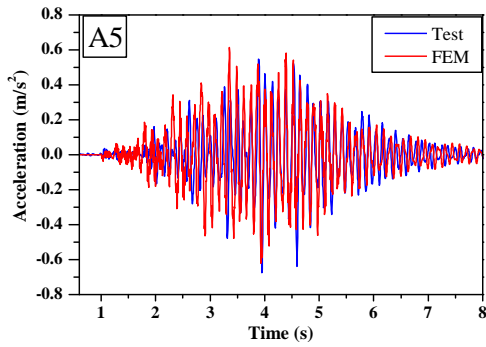


Figure C.25.: Small-scale prototype one pedestrian tests: accelerations attained at A5 for normal walk at the centred path. Experimental and numerical results.

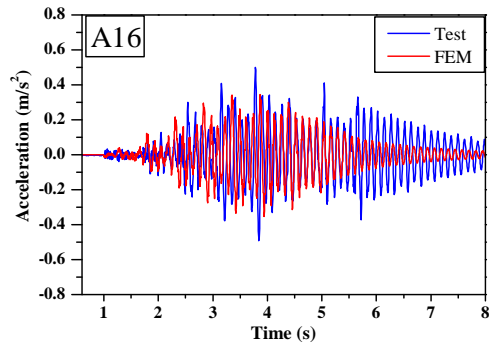


Figure C.26.: Small-scale prototype one pedestrian tests: accelerations attained at A16 for normal walk at the centred path. Experimental and numerical results.

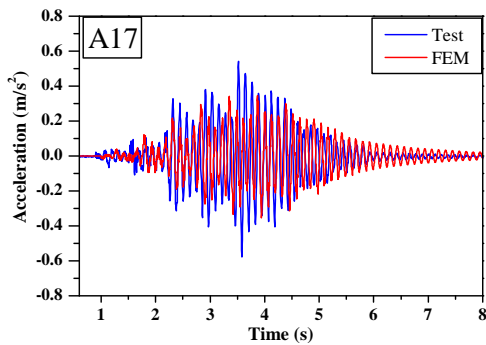


Figure C.27.: Small-scale prototype one pedestrian tests: accelerations attained at A17 for normal walk at the centred path. Experimental and numerical results.

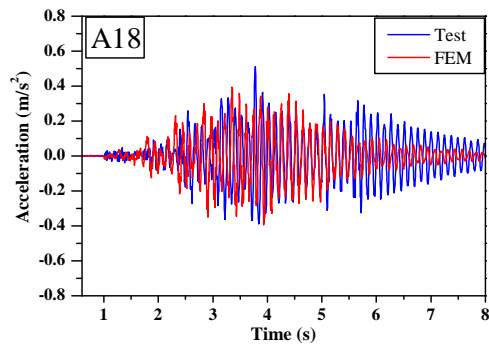


Figure C.28.: Small-scale prototype one pedestrian tests: accelerations attained at A18 for normal walk at the centred path. Experimental and numerical results.

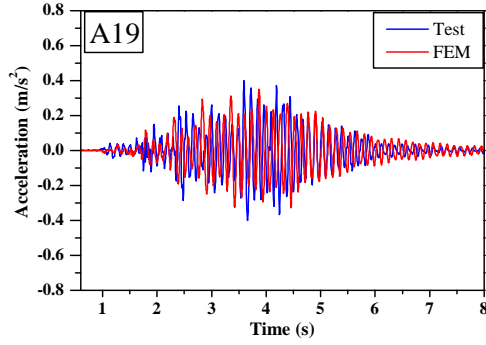


Figure C.29.: Small-scale prototype one pedestrian tests: accelerations attained at A19 for normal walk at the centred path. Experimental and numerical results.

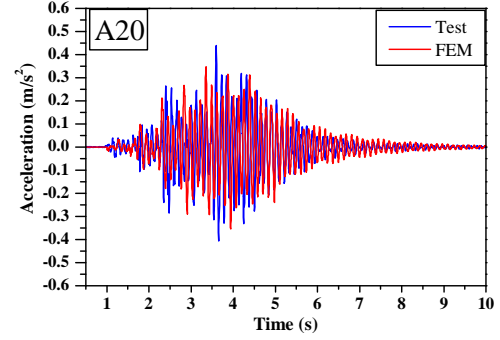


Figure C.30.: Small-scale prototype one pedestrian tests: accelerations attained at A20 for normal walk at the centred path. Experimental and numerical results.

### C.3.2. Eccentric path

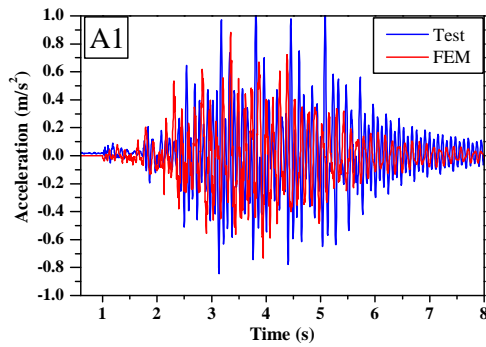


Figure C.31.: Small-scale prototype one pedestrian tests: accelerations attained at A1 for normal walk at the eccentric path. Experimental and numerical results.

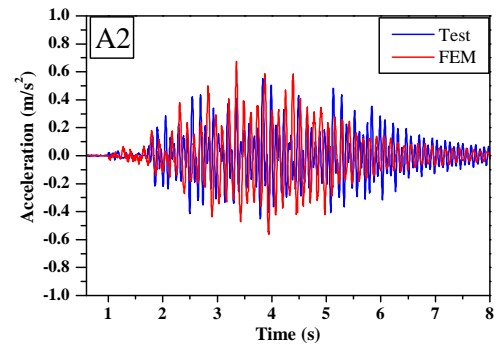


Figure C.32.: Small-scale prototype one pedestrian tests: accelerations attained at A2 for normal walk at the eccentric path. Experimental and numerical results.

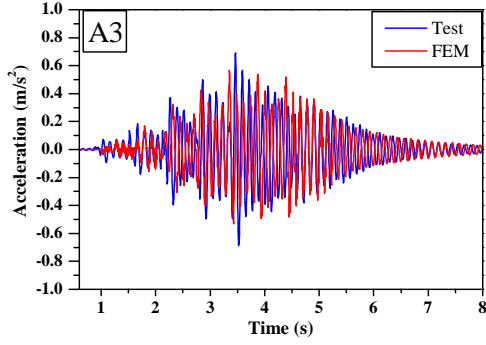


Figure C.33.: Small-scale prototype one pedestrian tests: accelerations attained at A3 for normal walk at the eccentric path. Experimental and numerical results.

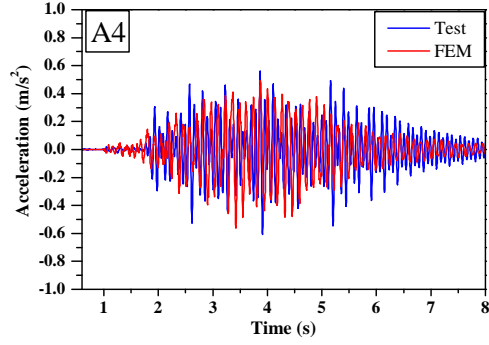


Figure C.34.: Small-scale prototype one pedestrian tests: accelerations attained at A4 for normal walk at the eccentric path. Experimental and numerical results.

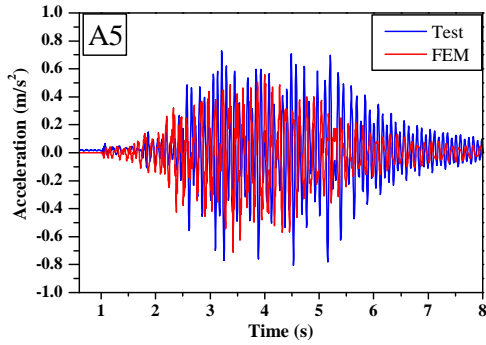


Figure C.35.: Small-scale prototype one pedestrian tests: accelerations attained at A5 for normal walk at the eccentric path. Experimental and numerical results.

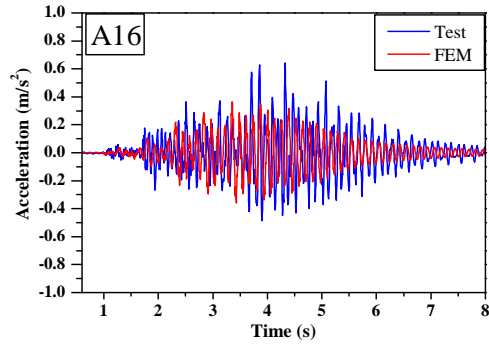


Figure C.36.: Small-scale prototype one pedestrian tests: accelerations attained at A16 for normal walk at the eccentric path. Experimental and numerical results.

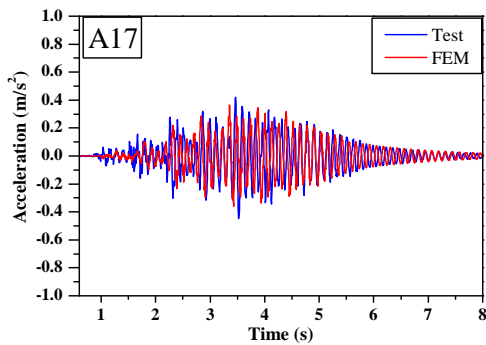


Figure C.37.: Small-scale prototype one pedestrian tests: accelerations attained at A17 for normal walk at the eccentric path. Experimental and numerical results.

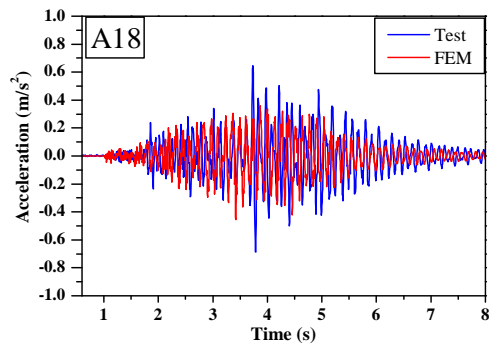


Figure C.38.: Small-scale prototype one pedestrian tests: accelerations attained at A18 for normal walk at the eccentric path. Experimental and numerical results.

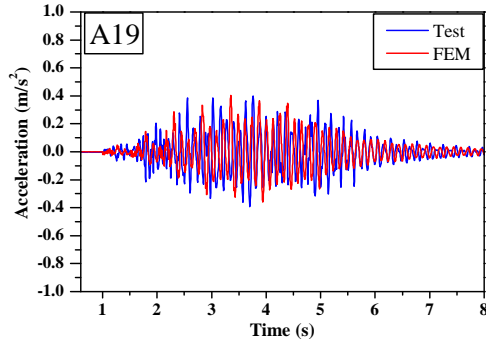


Figure C.39.: Small-scale prototype one pedestrian tests: accelerations attained at A19 for normal walk at the eccentric path. Experimental and numerical results.

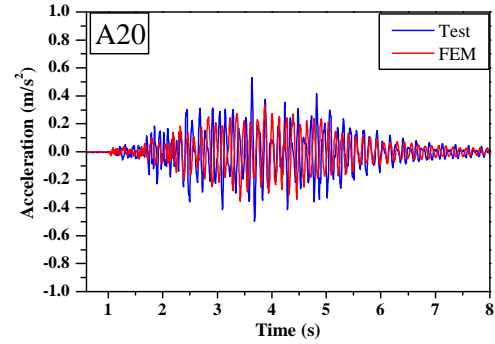


Figure C.40.: Small-scale prototype one pedestrian tests: accelerations attained at A20 for normal walk at the eccentric path. Experimental and numerical results.

## C.4. Walk fast

### C.4.1. Centred path

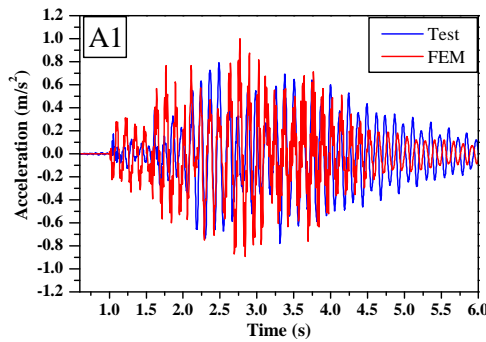


Figure C.41.: Small-scale prototype one pedestrian tests: accelerations attained at A1 for fast walk at the centred path. Experimental and numerical results.

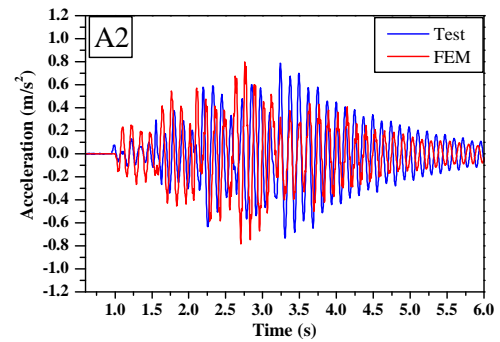


Figure C.42.: Small-scale prototype one pedestrian tests: accelerations attained at A2 for fast walk at the centred path. Experimental and numerical results.

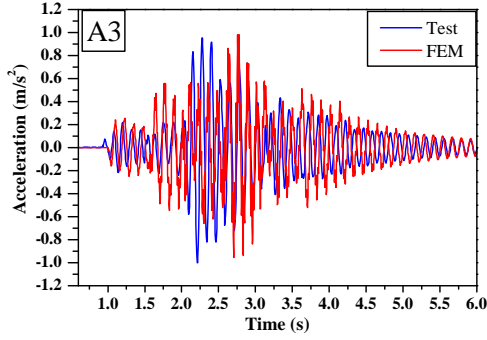


Figure C.43.: Small-scale prototype one pedestrian tests: accelerations attained at A3 for fast walk at the centred path. Experimental and numerical results.

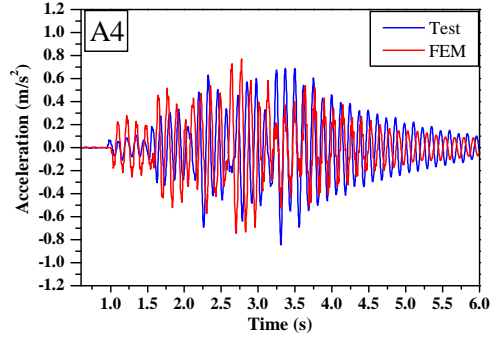


Figure C.44.: Small-scale prototype one pedestrian tests: accelerations attained at A4 for fast walk at the centred path. Experimental and numerical results.

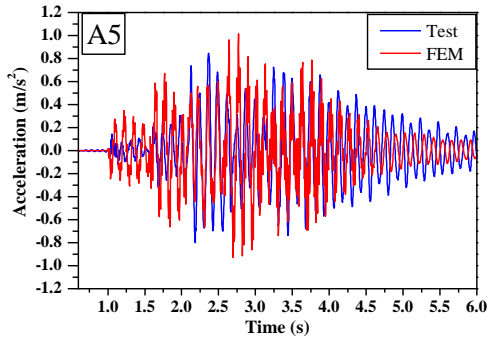


Figure C.45.: Small-scale prototype one pedestrian tests: accelerations attained at A5 for fast walk at the centred path. Experimental and numerical results.

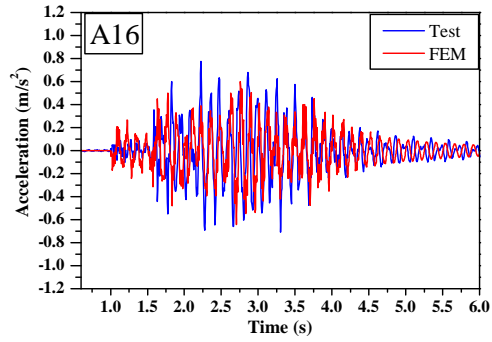


Figure C.46.: Small-scale prototype one pedestrian tests: accelerations attained at A16 for fast walk at the centred path. Experimental and numerical results.

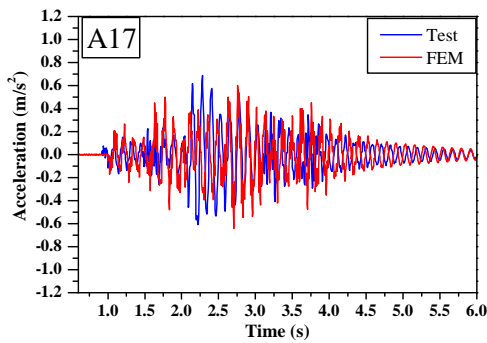


Figure C.47.: Small-scale prototype one pedestrian tests: accelerations attained at A17 for fast walk at the centred path. Experimental and numerical results.

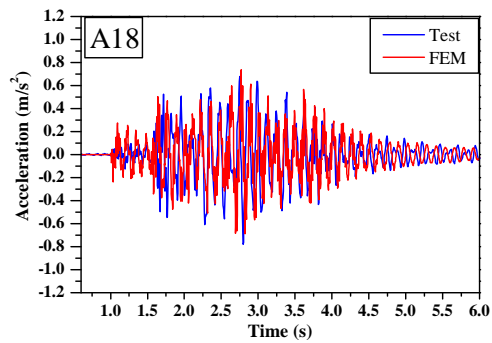


Figure C.48.: Small-scale prototype one pedestrian tests: accelerations attained at A18 for fast walk at the centred path. Experimental and numerical results.

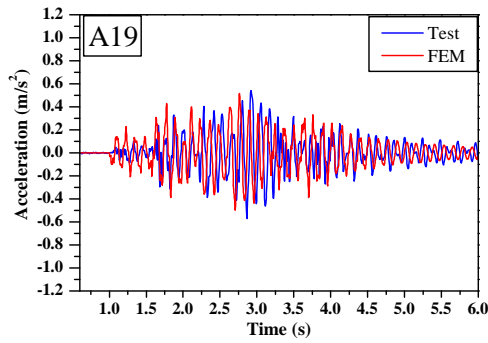


Figure C.49.: Small-scale prototype one pedestrian tests: accelerations attained at A19 for fast walk at the centred path. Experimental and numerical results.

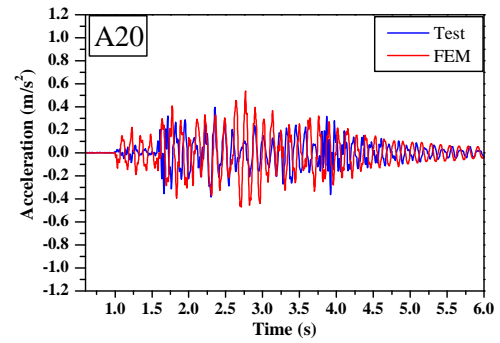


Figure C.50.: Small-scale prototype one pedestrian tests: accelerations attained at A20 for fast walk at the centred path. Experimental and numerical results.

#### C.4.2. Eccentric path

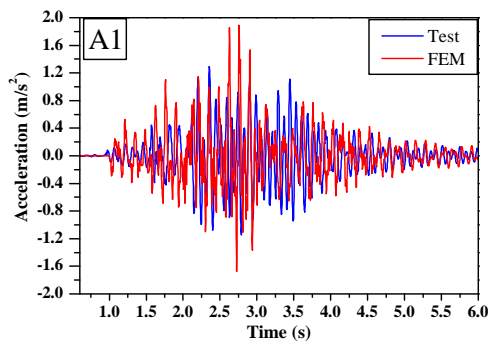


Figure C.51.: Small-scale prototype one pedestrian tests: accelerations attained at A1 for fast walk at the eccentric path. Experimental and numerical results.

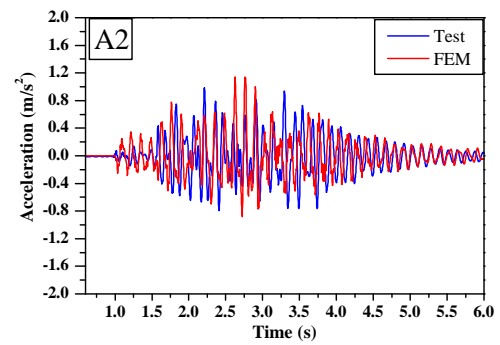


Figure C.52.: Small-scale prototype one pedestrian tests: accelerations attained at A2 for fast walk at the eccentric path. Experimental and numerical results.

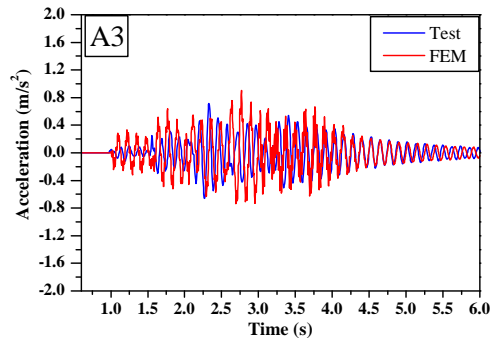


Figure C.53.: Small-scale prototype one pedestrian tests: accelerations attained at A3 for fast walk at the eccentric path. Experimental and numerical results.

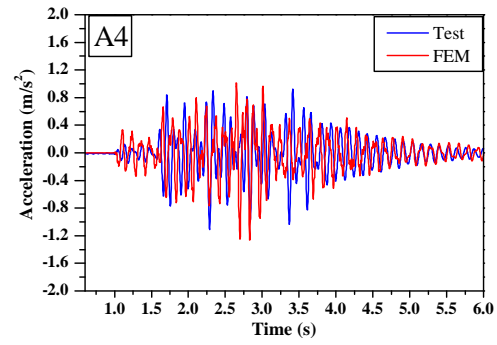


Figure C.54.: Small-scale prototype one pedestrian tests: accelerations attained at A4 for fast walk at the eccentric path. Experimental and numerical results.

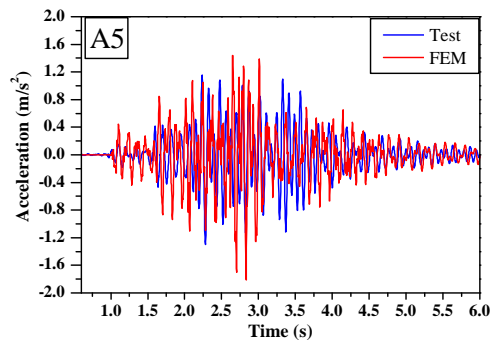


Figure C.55.: Small-scale prototype one pedestrian tests: accelerations attained at A5 for fast walk at the eccentric path. Experimental and numerical results.

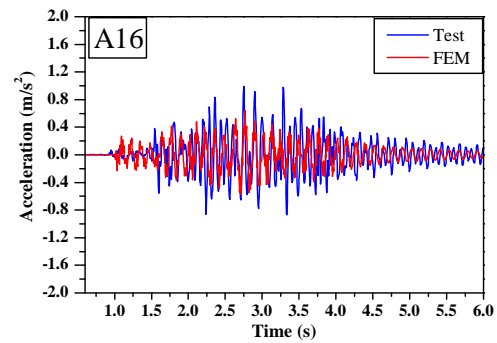


Figure C.56.: Small-scale prototype one pedestrian tests: accelerations attained at A16 for fast walk at the eccentric path. Experimental and numerical results.



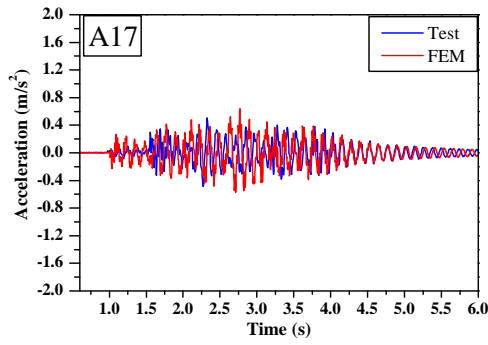


Figure C.57.: Small-scale prototype one pedestrian tests: accelerations attained at A17 for fast walk at the eccentric path. Experimental and numerical results.

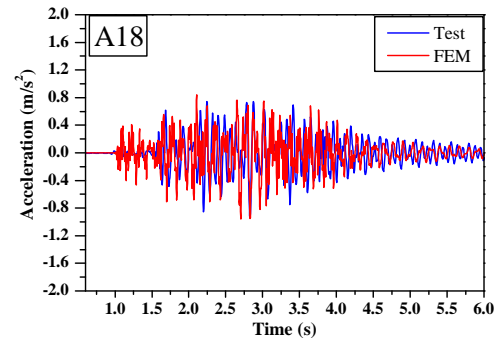


Figure C.58.: Small-scale prototype one pedestrian tests: accelerations attained at A18 for fast walk at the eccentric path. Experimental and numerical results.

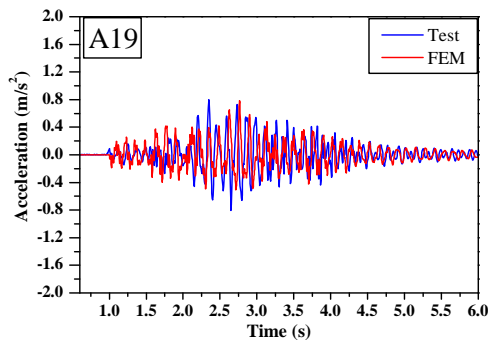


Figure C.59.: Small-scale prototype one pedestrian tests: accelerations attained at A19 for fast walk at the eccentric path. Experimental and numerical results.

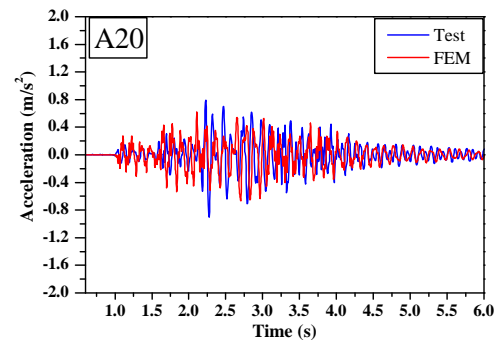


Figure C.60.: Small-scale prototype one pedestrian tests: accelerations attained at A20 for fast walk at the eccentric path. Experimental and numerical results.



## D. Appendix D — One pedestrian dynamic test on the full-scale prototype

### D.1. Introduction

This appendix presents the comprehensive comparison between the experimental data of the full-scale prototype one pedestrian tests, described in Chapter 7, and the numerical results. In this regard, for each pedestrian motion, each path, and each measuring position, a representative curve of the accelerations measured in the experimental tests is compared with those obtained with the FE model.

### D.2. Walk slow

#### D.2.1. Centred path

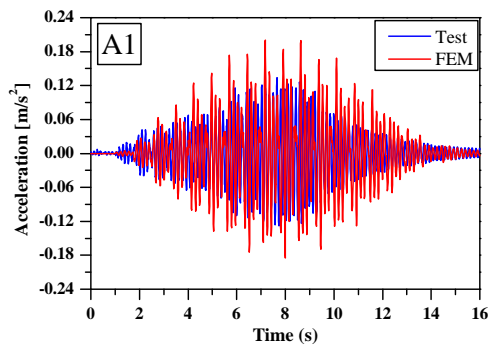


*Figure D.1.:* Full-scale prototype one pedestrian tests: accelerations attained at A1 for slow walk at the centred path. Experimental and numerical results.

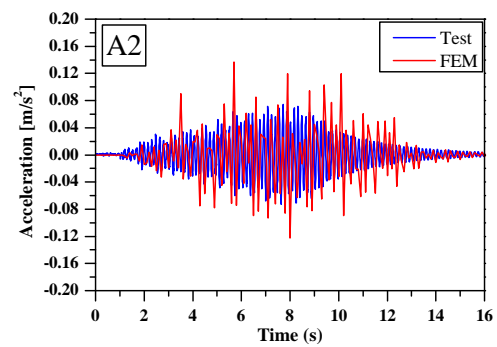


*Figure D.2.:* Full-scale prototype one pedestrian tests: accelerations attained at A2 for slow walk at the centred path. Experimental and numerical results.

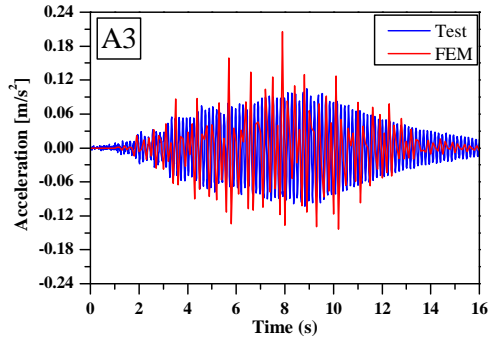


Figure D.3.: Full-scale prototype one pedestrian tests: accelerations attained at A3 for slow walk at the centred path. Experimental and numerical results.

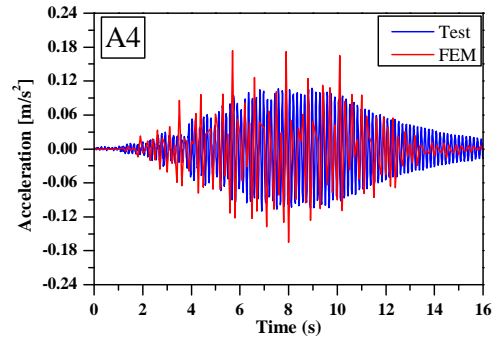


Figure D.4.: Full-scale prototype one pedestrian tests: accelerations attained at A4 for slow walk at the centred path. Experimental and numerical results.

## D.2.2. Eccentric path

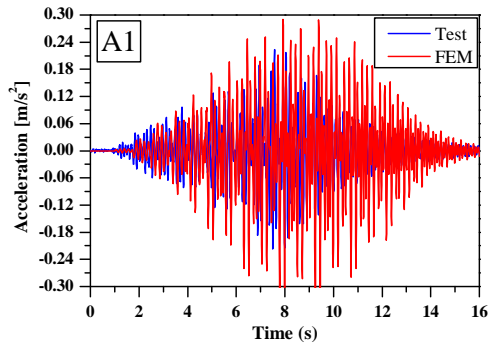


Figure D.5.: Full-scale prototype one pedestrian tests: accelerations attained at A1 for slow walk at the eccentric path. Experimental and numerical results.

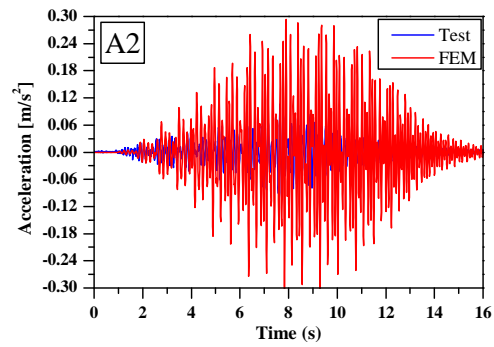


Figure D.6.: Full-scale prototype one pedestrian tests: accelerations attained at A2 for slow walk at the eccentric path. Experimental and numerical results.

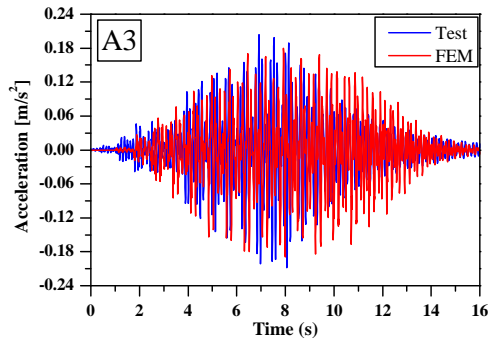


Figure D.7.: Full-scale prototype one pedestrian tests: accelerations attained at A3 for slow walk at the eccentric path. Experimental and numerical results.

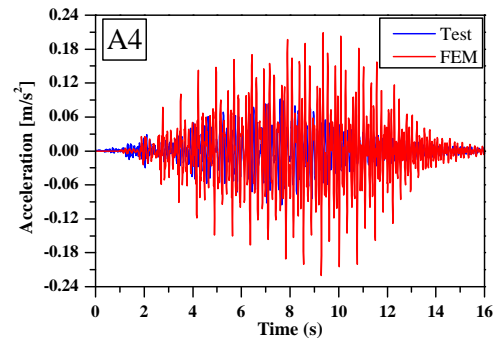


Figure D.8.: Full-scale prototype one pedestrian tests: accelerations attained at A4 for slow walk at the eccentric path. Experimental and numerical results.

## D.3. Walk

### D.3.1. Centred path

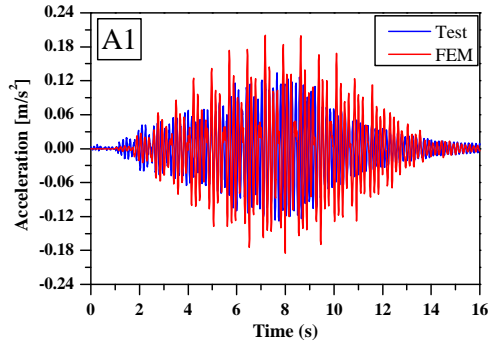


Figure D.9.: Full-scale prototype one pedestrian tests: accelerations attained at A1 for normal walk at the centred path. Experimental and numerical results.

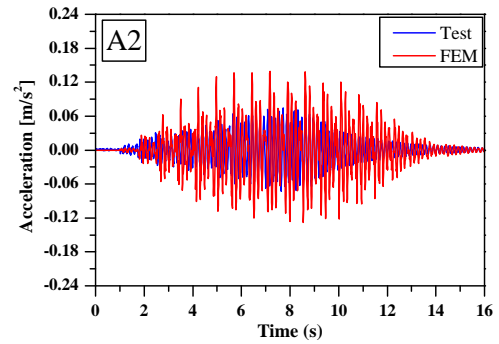


Figure D.10.: Full-scale prototype one pedestrian tests: accelerations attained at A2 for normal walk at the centred path. Experimental and numerical results.

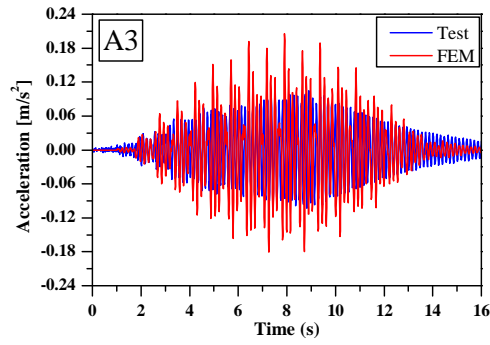


Figure D.11.: Full-scale prototype one pedestrian tests: accelerations attained at A3 for normal walk at the centred path. Experimental and numerical results.

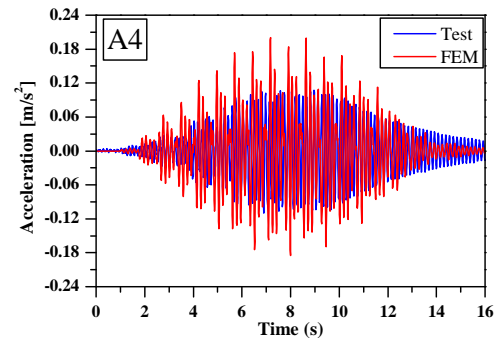


Figure D.12.: Full-scale prototype one pedestrian tests: accelerations attained at A4 for normal walk at the centred path. Experimental and numerical results.

### D.3.2. Eccentric path

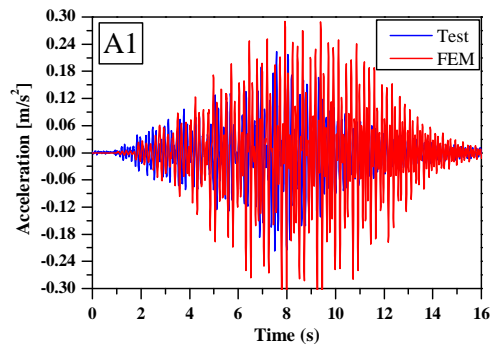


Figure D.13.: Full-scale prototype one pedestrian tests: accelerations attained at A1 for normal walk at the eccentric path. Experimental and numerical results.

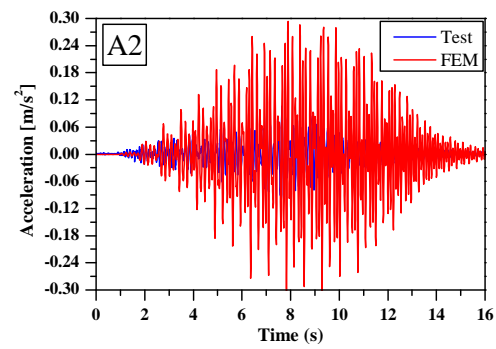


Figure D.14.: Full-scale prototype one pedestrian tests: accelerations attained at A2 for normal walk at the eccentric path. Experimental and numerical results.

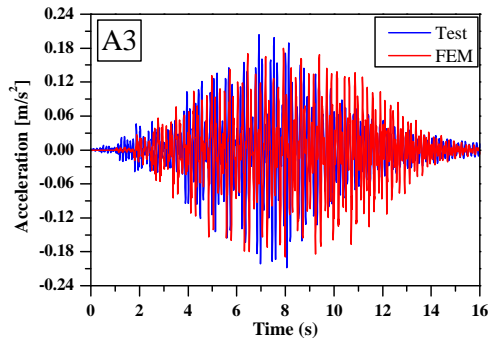


Figure D.15.: Full-scale prototype one pedestrian tests: accelerations attained at A3 for normal walk at the eccentric path. Experimental and numerical results.

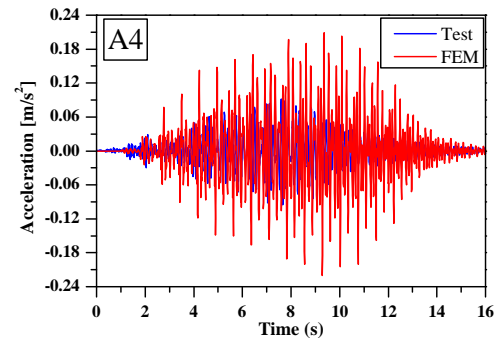


Figure D.16.: Full-scale prototype one pedestrian tests: accelerations attained at A4 for normal walk at the eccentric path. Experimental and numerical results.

## D.4. Walk fast

### D.4.1. Centred path

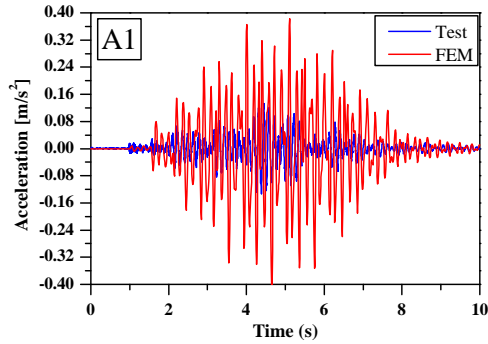


Figure D.17.: Full-scale prototype one pedestrian tests: accelerations attained at A1 for fast walk at the centred path. Experimental and numerical results.

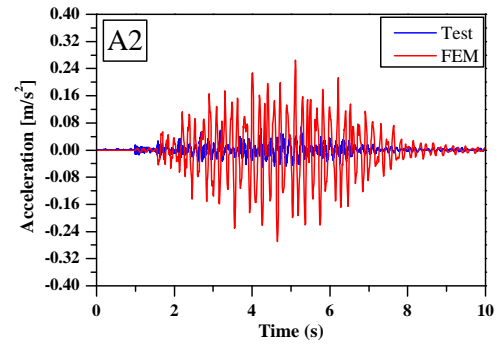


Figure D.18.: Full-scale prototype one pedestrian tests: accelerations attained at A2 for fast walk at the centred path. Experimental and numerical results.

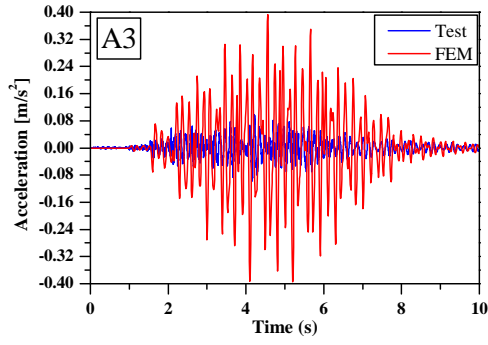


Figure D.19.: Full-scale prototype one pedestrian tests: accelerations attained at A3 for fast walk at the centred path. Experimental and numerical results.

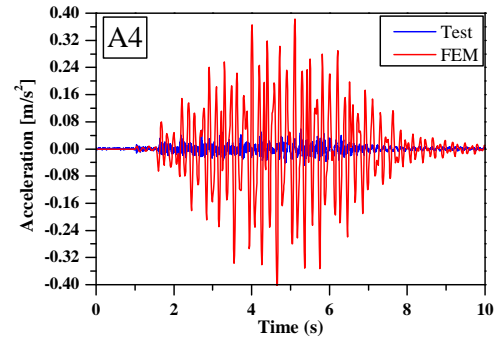


Figure D.20.: Full-scale prototype one pedestrian tests: accelerations attained at A4 for fast walk at the centred path. Experimental and numerical results.

#### D.4.2. Eccentric path

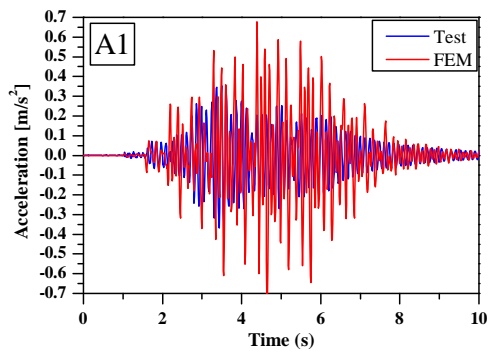


Figure D.21.: Full-scale prototype one pedestrian tests: accelerations attained at A1 for fast walk at the eccentric path. Experimental and numerical results.

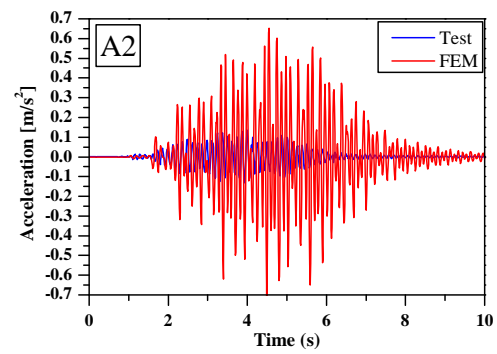


Figure D.22.: Full-scale prototype one pedestrian tests: accelerations attained at A2 for fast walk at the eccentric path. Experimental and numerical results.



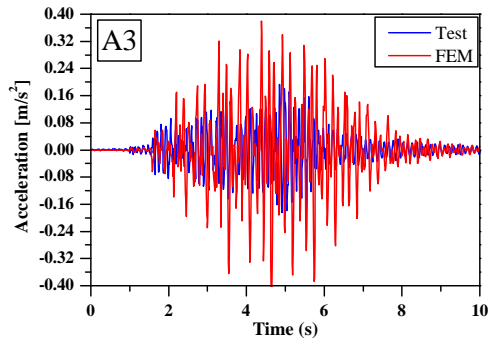


Figure D.23.: Full-scale prototype one pedestrian tests: accelerations attained at A3 for fast walk at the eccentric path. Experimental and numerical results.

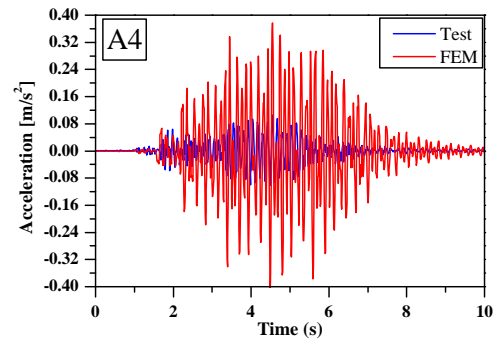


Figure D.24.: Full-scale prototype one pedestrian tests: accelerations attained at A4 for fast walk at the eccentric path. Experimental and numerical results.

## D.5. Walk fast

### D.5.1. Centred path

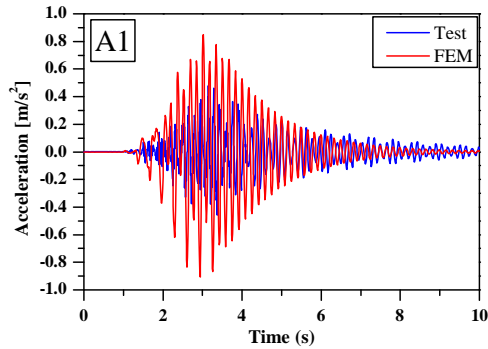


Figure D.25.: Full-scale prototype one pedestrian tests: accelerations attained at A1 for run at the centred path. Experimental and numerical results.

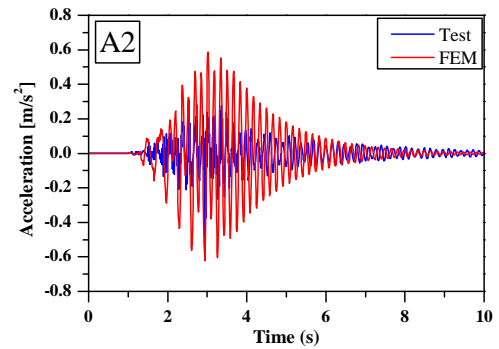


Figure D.26.: Full-scale prototype one pedestrian tests: accelerations attained at A2 for run at the centred path. Experimental and numerical results.

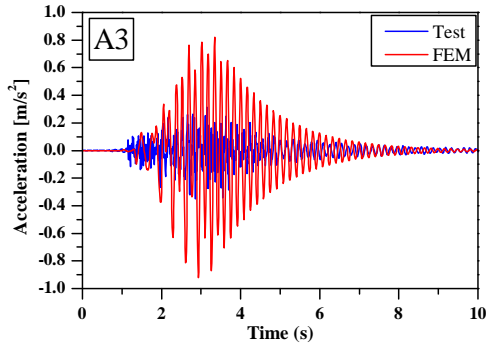


Figure D.27.: Full-scale prototype one pedestrian tests: accelerations attained at A3 for run at the centred path. Experimental and numerical results.

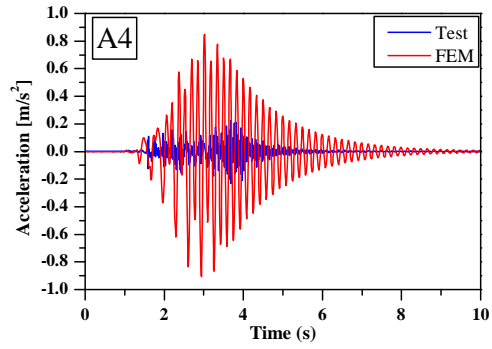


Figure D.28.: Full-scale prototype one pedestrian tests: accelerations attained at A4 for run at the centred path. Experimental and numerical results.

### D.5.2. Eccentric path

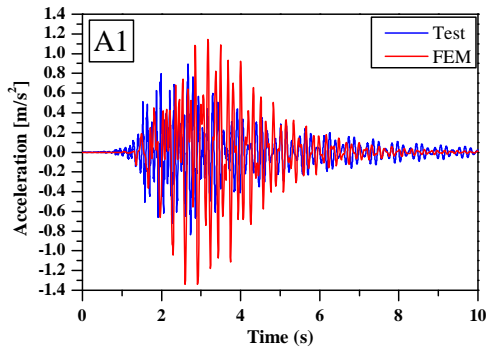


Figure D.29.: Full-scale prototype one pedestrian tests: accelerations attained at A1 for run at the eccentric path. Experimental and numerical results.

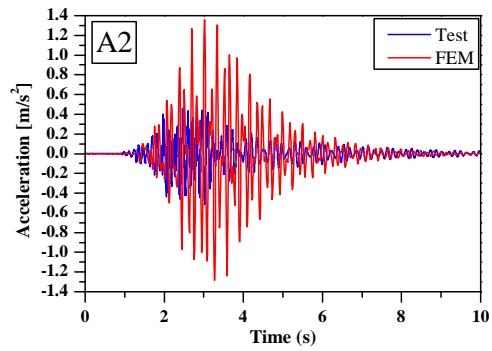


Figure D.30.: Full-scale prototype one pedestrian tests: accelerations attained at A2 for run at the eccentric path. Experimental and numerical results.

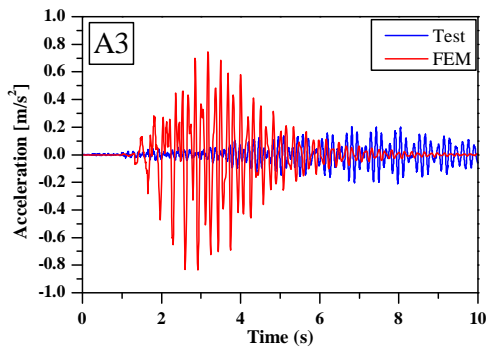


Figure D.31.: Full-scale prototype one pedestrian tests: accelerations attained at A3 for run at the eccentric path. Experimental and numerical results.

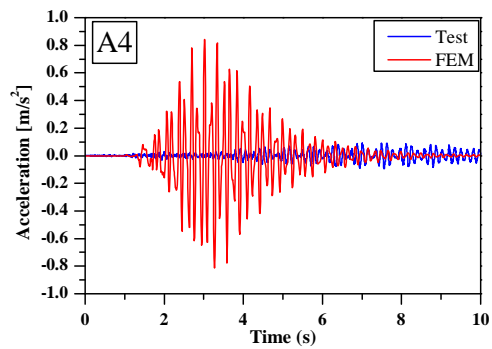


Figure D.32.: Full-scale prototype one pedestrian tests: accelerations attained at A4 for run at the eccentric path. Experimental and numerical results.